# Bio-Compatible Nanoparticles Based Electroactive Polymer Thin Films: Characterizations and Applications to Energy Harvesting from Environmental Mechanical Sources via Piezoelectric and Triboelectric Effect

Thesis submitted to

**Jadavpur University**

By

**Debmalya Sarkar**

In partial fulfilment of the requirements for the degree of

**Doctor of Philosophy (PhD) in Science**

**Department of Physics**

**Jadavpur University**

**Kolkata-700032**

**April 2024**

যাদবপুর বিশ্ববিদ্যালয়
কলকাতা-৭০০০৩২, ভারত

JADAVPUR UNIVERSITY
KOLKATA-700032, INDIA

FACULTY OF SCIENCE : DEPARTMENT OF PHYSICS

# CERTIFICATE FROM THE SUPERVISOR (S)

This is to certify that the thesis entitled ***"Bio-Compatible Nanoparticles Based Electroactive Polymer Thin Films: Characterizations and Applications to Energy Harvesting from Environmental Mechanical Sources via Piezoelectric and Triboelectric Effect"*** Submitted by Mr. Debmalya Sarkar who got his name registered on 11/11/2019 (Index no.: **125/19/Phys./26**) for the award of Ph.D. (Science) Degree of Jadavpur University, is absolutely based upon his own work under the supervision of Prof. Sukhen Das and Dr. Ruma Basu and that neither this thesis nor any part of it has been submitted for either any degree/diploma or any other academic award anywhere before.

Sukhen Das 18/09/2024
Prof. Sukhen Das
Professor
Department of Physics
Jadavpur University
Kolkata-700032

Prof. Sukhen Das
Department of Physics,
Jadavpur University
Kolkata - 700 032

Ruma Basu 18/9/24
Dr. Ruma Basu
Associate Professor
Department of Physics
Jogamaya Devi College
Kolkata-700026

Dr. Ruma Basu
Associate Professor
Physics Department
Jogamaya Devi College
92, S. P. Mukherjee Road
Kolkata-700 026

যাদবপুর বিশ্ববিদ্যালয়
কলকাতা-৭০০০৩২, ভারত

JADAVPUR UNIVERSITY
KOLKATA-700032, INDIA

FACULTY OF SCIENCE : DEPARTMENT OF PHYSICS

# CERTIFICATE OF SIMILARITY CHECK

This is to certify that the plagiarism checking for this thesis entitled ***"Bio-Compatible Nanoparticles Based Electroactive Polymer Thin Films: Characterizations and Applications to Energy Harvesting from Environmental Mechanical Sources via Piezoelectric and Triboelectric Effect"*** authored by Mr. Debmalya Sarkar has been performed using professional plagiarism prevention software iThenticate. According to the report generated after plagiarism checking there is an 9% similarity in this thesis, which is in the category "Level 0" (minor similarities) as per the "Promotion of Academic Integrity and Prevention of Plagiarism in Higher Education Institutions Regulations, 2018" of the University Grand Commission (UGC) of India. The common knowledge or coincidental terms up to 10 (ten) consecutive words (as prescribed in the above said UGC Regulation up to 14 (fourteen) terms for such common knowledge or coincidental terms can be excluded) and own works of the candidate published in various peer-reviewed journals (those are attached in the thesis) are excluded from the similarity checking. It is certified that the present thesis submitted by Mr. Debmalya Sarkar is plagiarism-free and has followed standard norms of academic integrity and scientific ethics.

Sukhen Das

Prof. Sukhen Das 18/04/2024
Professor
Department of Physics
Jadavpur University
Kolkata-700032

Prof. Sukhen Das
Department of Physics,
Jadavpur University
Kolkata-700 032

Ruma Basu

Dr. Ruma Basu 18/4/24
Associate Professor
Department of Physics
Jogamaya Devi College
Kolkata-700026

Dr. Ruma Basu
Associate Professor
Physics Department
Jogamaya Devi College
92, S. P. Mukherjee Road
Kolkata-700 026

*Dedicated to*

# *My Parents*

# *Abstract*

**THESIS TITLE: Bio-Compatible Nanoparticles Based Electroactive Polymer Thin Films: Characterizations and Applications to Energy Harvesting from Environmental Mechanical Sources via Piezoelectric and Triboelectric Effect**

**Submitted by: Debmalya Sarkar**

**Index no.: 125/19/Phys./26**

With the rapid growth of human civilizations, fossil fuels are limiting day by day. For this, human society will face some serious energy crises in the upcoming days. Along with this, the regular requirement of power in our daily life activities is increasing quickly. Also, the cumulative growth of the human population accelerates the daily requirement of power. Therefore, to solve the problem of the energy crisis and fulfil the daily need of power, alternative energy sources become the most suitable solution to these problems. Among different types of alternative energy sources, nanogenerators have gained tremendous attention owing to their capability to harvest energy from environmental friendly mechanical sources and convert them into electrical energy. Therefore, the primary objectives of the research work are to develop self-powered energy harvesting devices with the help of piezoelectric and triboelectric effects and utilize them in electricity generation from environmentally available mechanical and biomechanical energy sources. Also, polymeric nanocomposites have been used in the development of these nanogenerators. To reduce environment pollution and maintain the fabrication cost, naturally available cotton pappus has been utilized in the fabrication procedure of a piezoelectric nanogenerator (PENG). The presence of the hydroxyl group and the amino group inside cotton pappus assist in the generation of stress-induced polarization and improve the piezoelectricity. Owing to these exceptional properties, cotton pappus has been incorporated into polydimethylsiloxane (PDMS) matrix and fabricated the polymeric nanocomposite, which has been further utilized in the designing process of PENG. Moreover, the capability of the fabricated PENG in harvesting biomechanical energy sources has been investigated by illuminating LEDs and charging capacitors. Besides this, the effect of the β-crystalline phase of electroactive polymers on the output performance of PENG has been monitored theoretically and experimentally. The formation of the β-crystalline phase inside the matrix of electroactive polymers (PVDF, PVDF-HFP, PVDF-TrFE) has been performed by

incorporating semiconducting materials for example C-dot, $MoTe_2$, $Bi_2Se_3$ etc. inside the polymer matrix. Furthermore, the sensitivity of the PENG has been utilized in harvesting energy from human blood flow and sensing objects with different masses. Alongside, some fabrication methods including solution casting, electrospinning etc are adapted to develop polymeric nanocomposites. The morphological, structural and electrical properties of these composites have been investigated with the support of FESM, XRD, FTIR, XPS, LCR meter, DSO etc.

Piezoelectric nanogenerators have some drawbacks including low sensitivity, difficulties in harnessing small-scale energies and moderate output performances. To solve these challenges, triboelectric effect has been utilized in the development of self-powered energy harvesting devices. To improve the output performance of the triboelectric nanogenerator (TENG), surface modification techniques have been performed in the designing of TENG. Along with this, 2D materials are used in the fabrication process of TENG to prevent the charge recombination process inside the device, which further results in better current density and output results. The utility of the TENG in tracking human physiological signals and detecting artificial finger movements is also monitored. To get a better sensitivity compared to PENG, another method, the piezo-tribo coupling effect has been utilized during the development of TENG, which assists in harnessing energy from biomechanical and small-scale energy sources and generates electrical energy.

Therefore, the developed self-powered piezoelectric and triboelectric nanogenerators will be impactful in green mechanical and biomechanical energy harvesting applications. Also, the outstanding sensitivity and energy-harvesting ability of the devices will become an essential asset in human health monitoring applications and human-machine interfaces.

# *Acknowledgements*

***" Research has shown over and over again that the more you acknowledge your past successes, the more confident you become in taking on and successfully accomplishing new ones "*** *by* ***Jack Canfield***

*One lovely rainy morning in August of 2013, I started my journey of higher studies at the world's most renowned and dreaming educational place, Jadavpur University. Starting from my bachelor's degree to my doctoral degree, the entire journey has been carried out under the shelter of this university, which is also my "second home" and spent my life's wonderful days here. Throughout these beautiful years, JU always stood with me and gifted me lots of memories, fame and trustworthy people. Today I am on the verge of completing my thesis work and want to grab the opportunity to convey my gratitude and love towards all the loveable people without them I would never have reached this stage.*

*First and foremost, I would like to express my truthful gratitude to my supervisor* ***Prof. Sukhen Das*** *for his valuable suggestions, guidance, and support throughout my doctoral journey. For me, the most learning thing from Prof. Das is that he never doubts his research scholar's ability and always gives them freedom in their research work. After attending the scientific events and competitions, Prof. Das shared his experiences and ideas, which has further helped me to refurnish my research idea and get better outcomes. Along with a good supervisor, Prof. Das is also a very good teacher. I was extremely fortunate to have him as my teacher during my B.Sc. and M.Sc. courses. Besides this, Prof. Das is a very kind-hearted and down-to-earth man. He always helps his students whenever they need any kind of assistance from him. He not only his university students but also helps other university students whenever they come to him for any type of assistance. I also get inspiration from his helping hand nature and think myself a fortunate person to have him as my supervisor and instructor throughout my doctoral journey.*

*I would like to extend my thankfulness to my co-supervisor* ***Dr. Ruma Basu*** *for her guidance, support, and mentorship throughout my research tenure. Her scientific ideas and research knowledge always helped me to find the solutions to my research problems. One thing I want to mention is that she always supported my research ideas and also told me "Debu, if everybody can do it, then why not we can do it". Alongside this, her eagerness to learn new ideas and student-friendly nature inspire me a lot. I feel myself the luckiest research scholar to have her as my co-supervisor and mentor during my research tenure.*

*I would take the opportunity to express my thanks to* ***Papiya Di (Prof. Papiya Nandy)*** *and* ***Soumya Da (Dr. Soumyaditya Sutradhar)*** *for their impactful advice and support, which have assisted me in empowering myself.*

*Since my B.Sc. days at JU, all of my respected professors have provided me with their unwavering support. I would specially thank to them. I would like to extend my gratitude to* ***Prof. Argha Deb, Prof. Partha Pratim Ray, Dr. Debasish Biswas, Dr. Sanjay Kumar, Dr. Kaustav Das, Dr. Abiral Tamang****. Without their valuable suggestions and blessings, I could not completed my journey.*

*The next person I want to acknowledge is my uncle* ***Mr. Sunil Kumar Sarkar.*** *Whenever I need any type of assistance regarding my education and other problems, he always stands with me like my father. His eagerness to learn new things and helping hand mentality inspired me. I also admired his decision-making ability and enjoyed his company and guidance. In addition to this, he always supported me and encouraged me to pursue this doctoral degree and get higher education. I am the happiest person to have you as my uncle as well as my guardian.*

*I would like to express my love and gratitude to my mentor* ***Nur Da (Dr. Nur Amin Hoque)****. He is the most decorated and scientifically updated researcher I ever met in my research journey. My research journey would never started until I met him. I have known him since my project time, where he inspired me why I should enter in research work. His research mentality and*

*responsibility towards lab work inspire me a lot. The thing which I have learnt throughout my research tenure is that don't believe in your luck, create your luck by hard work. Also, another important thing I have learned under his guidance is that if you love your work and workplace, then they will never let you go empty-handed. His positive attitude, hard-working mentality and kind-hearted nature encouraged me. I always enjoyed his guidance in my research journey. Any type of thanking will become small for this person. He is the one who embarked on my research from the ground up and provided me with guidance, without him, I could never have reached this position. He treated me like his younger brother rather than treating me like a student. Whenever I fall into any trouble in my research life or personal life, he stands up with me and solves the problems like his own problem. I am incredibly grateful for all that he has contributed to my life. I sincerely appreciate his courageous character, which has given me the willpower to rise to any obstacles in life and overcome them. Thank you Nur da for showing me the right path of my career. I am the most fortunate person to have you as my elder brother as well as my mentor of my research journey.*

*Next, I want to extend my thanks to the most important persons of my research journey* ***Prosenjit Da (Dr. Prosenjit Biswas****) and* ***Master Da (Mr. Md. Minarul Saikh)****. Prosenjit Da was the mentor of my project work and also taught me how to handle the different instruments. Dr. Biswas is the most decorated and down-to-earth person. His friendly nature and willing power encouraged me throughout my research journey. Another person whom I have known since my project work is Master Da. Mr. Md. Minarul Saikh is the most reserved and knowledgeable person in our lab. His problem-solving ability and deep knowledge of physics encouraged me a lot. Whenever I have faced any type of physics-related problems, I took his advice and suggestions. Also, we both loved to discuss physics-related problems in our research work. I feel lucky to have you both as my seniors.*

*I am extremely thankful from the bottom of my heart to my other lab seniors with whom I have spent various joyful moments of my research journey. Also, their valuable suggestions and support throughout these years assisted me in*

*running the research smoothly. I want to thank* ***Dr. Biswajoy Bagchi, Dr. Niranjan Bala, Dr. Pradip Thakur, Dr. Biplab Kumar Paul, Dr. Navonil Bose, Dr. Sumana Paul, Dr. Arpan Kool, Dr. Wahida Rahman, Dr. Dheeraj Mondal, Dr. Souravi Bardhan, Dr. Farha Khatun, Dr. Somtirtha Kool Banerjee, Dr. Swagata Roy, Dr. Bidhisha Ghosh, Dr. Tanumoy Debnath, Dr. Debopriya Bhattacharyya, Dr. Santanu Das, Dr. Anandalal Gayen, Dr. Debbithi Bera, Miss Satarupa Bhattacharya, Mr. Somen Biswas.***

*A special thanks go to my lab partner* ***Miss. Namrata Das****, without her assistance and support my doctoral journey remained incomplete. She is an outstanding and intellectual researcher. Her thinking ability and friendly nature encouraged me a lot. She always tried to develop new methods and innovate new things, which inspired me and encouraged my thinking ability. Besides, she has outstanding knowledge of English and has exceptional presentation ability. I always loved to attend her presentations and tried to adapt new styles of presenting work, which further helped me to refurnish my style of presentation. Also, she has assisted me in extending my vocabulary knowledge of English throughout these years. We always took an active part in different research-related discussions. Apart from my research journey, I have known her since my JU days, when she was my classmate and we also worked in the same group during our master degree's laboratory. The most notable thing is she always became happy with my success and never doubted my research capability. I always loved to share my research ideas with her because whenever I discussed with her, I got some new directions for my work, which also helped to publish our work in reputed journals. I feel myself fortunate one to have you as my lab partner throughout the research drive where we have also shared some joyful and funny moments.*

*I am extremely thankful to* ***Shubham Da (Dr. Shubham Roy)*** *and* ***Shilpa Di (Dr. Shilpa Maity)*** *for their valuable guidance, encouragement and support. Dr. Roy is an outstanding researcher with a versatile knowledge of instruments and software. His affection for research works inspired me. I always loved to take an active part in discussions with him, which helped to*

*empower knowledge. Thank you Shubham Da for supporting me and encouraging me throughout these years. Besides, I feel fortunate to have Dr. Maity as my senior as well as my elder sister during this journey. She is an independent, hard-working and kind-hearted woman. She always loved me like her younger brother. Her positive attitude and fighting spirit encouraged me throughout this period. Also, her mentality to accept any kind of situation inspired me.*

*I want to extend my thanks to my lab mates with whom I have spent these splendid years and also created some funny memories. Their immense assistance, support and love helped me to drive my research journey smoothly. I want to express my thanks to my seniors* ***Manisha Di, Sanghita Di, Madhuchhanda Di, Souvik Da and Saheli Di.*** *Also, I want to extend my love and cheer to* ***Dhananjoy, Tanmoy, Jhilik, Indrajit, Piyali, Anuja Choto Manisha, Suman, Sumana, Shriparna, Anwesha, Choto Anwesha, Aliva, Shubojit, Neelanjana, Jaba, Solanky****.*

*Besides my research works, I want to acknowledge a group of people with whom I have endured a couple of my greatest days of life. I would like to express my cheers to these special people.* ***Jyoti Da (Mr. Jyotipriya Roy)*** *is my roommate and senior who always helped me and supported me throughout this research journey. I have known him since my master's degree days at JU. His outstanding knowledge of Physics encouraged me and also he can feel that Physics. My knowledge of Physics has been earned with the assistance of this man. Also, his problem-solving ability and encouragement helped me to qualify for the UGC-NET exam. Without him, I could never qualify for this exam. He always treated me like his younger brother and supported me in my difficulties. I am very grateful for his guidance and moral support.*

***Dadabhai (Dr. Pratik Kumar Das)*** *always loved me and guided me like an elder brother. He is a decorated and knowledgeable researcher with a golden heart. His hard-working nature and friendly behaviour always inspired me. His calm attitude and never-giving-up mentality inspired me and also taught me how to face problems and find solutions. Besides, being a very good researcher, he is also a very good chef. I always enjoyed his company and his*

*delicious dishes. Thank you Dadabhai for encouraging me and standing with me during the whole period.*

***Raj (Mr. Kishalaya Das)*** *always supported me and encouraged me throughout my research tenure. He is my childhood friend and my closest one. His mentality to work hard and help other people always invigorated me. We always became happy with our success and felt sorrow for our failure. One thing I have learned from him that how to accept problems with smiling faces and solve it like your own problems. I am the luckiest person to have you as my friend.*

***Somdutta*** *always encouraged me and supported me throughout my doctoral journey. She is a kind-hearted and hard-working woman. Her positivity and passion towards work motivated me. Whenever I needed any time of help, she always stood with me and supported me during the period. Her trust, support and care assisted me in gaining success in my research career.*

*Throughout my research journey,* ***Mr. Arya Ray*** *and* ***Mr. Neelnisith Kamila*** *showed their support and encouragement. I have known Arya since my childhood days and have known Neel from my JU days. We trio are big fans of football. Their moral support and love inspired me to pursue a doctoral degree. Their presence in my JU days created lots of happy moments. We celebrated everyone's success like our own success. They always backed me in my difficulties and made my JU days memorable and happy. I want to express love to both of them from the bottom of my heart.*

*I want to extend my thanks to my classmates* ***Mr. Firoj Haque, Mr. Subhronil Pan, Mr. Anirban Dutta, Mr. Subhankar Singh, Mrs. Sreejita Mukherjee, Mr. Sourav Das, Mr. Shiladitya Sinha, Mr. Ion Santra*** *for their immense support and good-wish throughout my JU years. I am also expressing my gratitude to* ***Krittish Da (Dr. Krittish Roy), Jit Da (Mr. Jit Majumder) and Chitrak Da (Dr. Chitrak Bhadra).*** *Their valuable suggestions, guidance and support encouraged me to give my best in research work. Also, their trust and love throughout these years inspired me.*

*I would like to express my love and thanks to my school-life friends* ***Prodipta, Dipankar, Goswa, Ritonik, Puchan, Suvam, Dipanjan, Sayantan, Puchki, Titu, Ratna, Bibhas, Baidurya, Debu, Tanmoy and Riddhi****. Their love, trust and moral support helped me to flourish.*

*A special thanks goes to my childhood friends* ***Dr Saikat Mondol, Dr Soumyadip Mondal, Miss. Parthana Bain, Miss. Swarnali Biswas and Miss. Prakashita Bhattacharjee.*** *Their encouragement, blessing, love and positivity always assisted me in gaining success in my journey. I am very fortunate to have all of you as my friends and my well-wishers.*

*I want to convey my thanks to* ***Miss. Sunanda Banik, Mrs. Priyanka Banerjee and Puskar Da*** *for their love, caring and support throughout this journey.*

*I would like to take the opportunity to convey my heartfelt gratitude to* ***the employees of the Departmental Office of Physics*** *for their unwavering assistance whenever needed. I want to extend my thanks to* ***Monojit Da*** *of the Research Section and* ***the entire Ph.D. cell employees*** *for all of their assistance, which helped me to run my journey smoothly.*

*I am very thankful to the* ***University Grant Commission (UGC)****, Government of India for their financial support to carry out my research career. I want to extend my thanks to the* ***Department of Science and Technology (DST)****, Govt. of India for the instrumental facility provided throughout my doctoral period.*

*Finally, I would like to express my love to* ***my father (Mr. Asok Kumar Sarkar) and my mother (Mrs. Sarathi Sarkar),*** *without them I could not complete this journey. I am very fortunate to become their son. They are the building blocks of my career. Their blessings, love, and support have helped me to complete the journey of my doctoral degree. The journey of my educational life has been started by grabbing the finger of my father. His simplicity, down-to-earth mentality, and helping nature always inspired me a lot. I have learned a lot of things from my father including fighting spirit, problem-solving attitude, positivity, and most importantly, enjoying the success of others like your own*

*success, which helped me to drive my doctorate journey. Alongside, I admire my mother's love, support, and trust towards me. Without her support and care, my PhD journey will be incomplete. Her thinking ability, decision-making power, and hardworking behaviours have inspired me a lot. Apart from this, the supportive and belief in yourself natures of my parents along with their love, care, and blessings always gave me the strength to pursue the doctoral degree. Therefore, I want to dedicate my thesis to my parents.*

*Also, this journey would never be complete without the blessings and support of my aunt* ***Mrs. Niyati Mondal****, my maternal uncles* ***Mr. Manaranjan Mondal*** *and* ***Mr. Goutam Mondal****. I want to add special thanks to my other family members* ***Mrs. Namita Ckharaborty, Mrs. Jaba Sarkar, Mr. Pijush kumar Das, Mr. Santosh Das, Mrs. Chabi Rani Das, Mrs. Sukalpita Mondal, Mrs. Subhrashleta Mondal, Mr. Manas Das, Mr. Arun Kumar Sarkar, Mr. Barun Kumar Sarkar, Mr. Tapas Kumar Sarkar, Mr. Madhumoy Chakroborty, Mr. Abhijit Mahanta and Mrs. Tripti Sarkar.*** *Also the blessings of* ***my grandfather, grandmother*** *and* ***mamadada (Late Rabindranath Mahanta)*** *helped me to achieve my success and complete this doctoral journey. In the end, I want to dedicate my thesis to my beloved parents.*

***Debmalya Sarkar***

# *List of Publications*

1) **Debmalya Sarkar,** Namrata Das, Md Minarul Saikh, Prosenjit Biswas, Solanky Das, Sukhen Das, Nur Amin Hoque, Ruma Basu. Development of a sustainable and biodegradable sonchus asper cotton pappus based piezoelectric nanogenerator for instrument vibration and human body motion sensing with mechanical energy harvesting applications. ***ACS omega*** 2021, *6*, pp.28710-28717.

2) **Debmalya Sarkar,** Namrata Das, Md Minarul Saikh, Prosenjit Biswas, Shubham Roy, Sumana Paul, Nur Amin Hoque, Ruma Basu, Sukhen Das. High β-crystallinity comprising nitrogenous carbon dot/PVDF nanocomposite decorated self-powered and flexible piezoelectric nanogenerator for harvesting human movement mediated energy and sensing weights. ***Ceramics International*** 2023, *49*, pp.5466-5478.

3) **Debmalya Sarkar,** Namrata Das, Md Minarul Saikh, Shubham Roy, Sumana Paul, Nur Amin Hoque, Ruma Basu, Sukhen Das. Elevating the performance of nanoporous bismuth selenide incorporated arch-shaped triboelectric nanogenerator by implementing piezo-tribo coupling effect: Harvesting biomechanical energy and low scale energy sensing applications. ***Advanced Composites and Hybrid Materials*** 2023, *6*, p.232.

4) **Debmalya Sarkar,** Namrata Das, Souvik Sau, Ruma Basu, Sukhen Das. Micro-patterned $BaTiO_3$@ Ecoflex Nanocomposite Assisted Self-powered and Wearable Triboelectric Nanogenerator with Improved Charge Retention by 2D $MoTe_2$/PVDF Nanofibrous Layer. ***Journal of Materials Chemistry C*** 2024, *12*, pp. 984-1001.

## *Co-author Publications*

1) Namrata Das, **Debmalya Sarkar,** Md Minarul Saikh, Prosenjit Biswas, Sukhen Das, Nur Amin Hoque, Partha Pratim Ray. Piezoelectric activity assessment of size-dependent naturally acquired mud volcano clay nanoparticles assisted highly pressure sensitive nanogenerator for green mechanical energy harvesting and body motion sensing. ***Nano Energy*** 2022, *102*, p.107628.

2) Saheli Ghosh, Souravi Bardhan, Dhananjoy Mondal, **Debmalya Sarkar**, Jhilik Roy, Shubham Roy, Ruma Basu, Sukhen Das. Natural hematite-based self-poled piezo-responsive membrane for harvesting energy from water flow and catalytic removal of organic dye. ***Ceramics International*** 2023, *49*, pp.14710-14718.

3) Namrata Das, **Debmalya Sarkar,** Nitin Yadav, Asfak Ali, Sukhen Das, Partha Pratim Ray, Nur Amin Hoque. Development of a lead-free, high-frequency ultrasound transducer with broad bandwidth and enhanced pulse-echo response, employing β-$Ni(OH)_2$/PVDF-TrFE piezoelectric composite. ***Chemical Engineering Journal*** 2023, *475*, p.146322.

# *List of Conferences Attended*

1) Presenting poster entitled "Cotton Pappus Based Piezoelectric Nanogenrator and Touch-Sensor" in "**Anveshan 2019-2020, Student's Research Convention - East Zone**", organised by Association of Indian Universities (AIU), New Delhi held in February 2020 at Jadavpur University, Kolkata.

2) Attending a **DST-SERB Sponsored One Day Workshop on Material Synthesis & Characterization Techniques** organised by Department of Physics, Jadavpur University on February, 2020.

3) Presenting a poster entitled "Piezoelectric Nanogenerator Mediated Energy Harvesting" in the "**New Directions in Physical Sciences 2020 (NDPS-2020)** in February, 2020 at Jadavpur University, Kolkata.

4) Oral presentation entitled "Cotton Pappus Based Piezoelectric Nanogenrator and Touch-Sensor" in "**Anveshan 2019-2020, Student's Research Convention - East Zone**", organised by Association of Indian Universities (AIU), New Delhi held in February 2020 at Jadavpur University, Kolkata.

5) Presenting a poster entitled "Self-powered and light weight electronic skin (e-skin) based on ZnS@PDMS nanocomposite for human body movements detection" in the "**33$^{rd}$ AGM of MRSI and 4$^{th}$ Indian Material Conclave IUMRS-ICA 2022"** in December 2022 at IIT Jodhpur, India.

6) Presenting a poster entitled "3D Printer Assisted Cotton Pappus Embedded Polymeric Nanocomposite Based Wearable and Sustainable Triboelectric Nanogenerator" in the "**67$^{th}$ DAE Solid State Physics Symposium"** in December 2023 at Gitam University, India.

# Table of Contents

# Abbreviations

| | |
|---|---|
| *PVDF* | *Poly(vinylidene fluoride)* |
| *P(VDF-CTFE)* | *Poly(vinylidene fluoride-chloride trifluoride ethylene)* |
| *P(VDF-HFP)* | *Poly(vinylidene fluoride-co-hexafluoropropene)* |
| *P(VDF-TrFE)* | *Poly(vinylidene fluoride-Trifluoroethylene)* |
| *α, β, γ* | *Crystalline phases of PVDF* |
| *ac* | *Alternating current* |
| *SA* | *Sonchus asper* |
| $C_p$ | *Capacitance* |
| *PDMS* | *Polydimethylsiloxane* |
| $d_{33}$ | *Piezoelectric constant* |
| *DMF* | *Dimethyl formamide* |
| *DMSO* | *Dimethyl sulfoxide* |
| *DSC* | *Differential scanning calorimetry* |
| *f* | *Frequency* |
| *tan δ* | *Tangent loss* |
| *Cp* | *Capacitance* |
| *TTTT* | *All trans* |
| *FESEM* | *Field emission scanning electron microscopy* |
| *FTIR* | *Fourier transform infrared spectroscopy* |
| *TGA* | *Thermal gravimetric analysis* |
| *XRD* | *X-ray diffraction* |
| *XPS* | *X-ray photoelectron spectroscopy* |
| *DFT* | *Density functional theory* |
| *BTO* | *BaTiO3* |
| $I_{sc}$ | *Short circuit current* |
| *PENG* | *Piezoelectric nanogenerator* |
| *TENG* | *Triboelectric nanogenerator* |
| $V_{oc}$ | *Open circuit output voltage* |
| *wt%* | *Weight Percent* |

# *List of Figures*

## *Chapter 1*



## *Chapter 2*

## *Chapter 3*

## *Chapter 4*

## *Chapter 5*

# *List of Tables*

## *Chapter 1*



## *Chapter 2*



## *Chapter 3*



## *Chapter 4*



## *Chapter 5*



## *Chapter 6*

# Introduction

Chapter 1

## 1.1 Motivation

Nowadays, energy becomes the crucial part of our daily life's activities by fulfilling the all demands of today's life in every realm. Along with the increasing fashion of population, the requirement of energy also increases to meet everyone's demands. From the statistics of world energy, it has come to know that conventional energy is the key source of the energy which fulfills this energy demands. There are several sources of conventional energies including petroleum, fossils fuels like coal, natural gases, oil etc.[1, 2] Due to the steady rise in the energy demand, these non-renewable energy sources are limiting day by day. For this reason, alternative energy resources have come into light to solve the energy demand in the upcoming future. Moreover, the use of the non-renewable energy sources has some serious effect on the environment through the phenomenon of glaciers melting, global warming and other nature related problems. Thus, our environment is facing some serious issues for these conventional energy sources, which further can be fixed by introducing alternative energy resources.[3] The additional benefit of utilizing the alternative sources is that small amount of waste or neglected energy sources may have the potential to be transformed into efficient energy. To convert this waste energy into electricity, energy harvesting concept has been utilized which not only assists in developing the green energy but also environmental friendly and cost effective.[4] Thus, the energy harvester by utilizing the alternative energy resources has been attracted the researchers more in the era of Internet of Things (IoT). Along with the improvement of IoT, the demand of the energy harvesters is rising rapidly.[5] Moreover, the statistics regarding the demand of energy harvesting sensors in IoT reveals that over 50 billion energy harvesting sensors have already been used in the IoT and this number will reach up to 500 billion by the year of 2025.[6] Beside this, storage equipments including batteries or capacitors are required to power up these sensors. But, there have some drawbacks of using these storage equipments for example constrained capacity, regular charging requirements etc. Also, the containing of toxic substances like cobalt, lithium and hazardous electrolytes inside the batteries added the additional disadvantages of these energy storing gadgets and seriously polluted the environment at the time of disposal. The maintenance cost of these gadgets is also very expensive.[7-9] To keep these drawbacks in mind, researchers have concentrated on energy harvesters which can be utilized in IoT. The main benefit of using the energy harvester is that it has the potential to generate electricity for a long period until the ambient energy sources is exhausted. Additionally, they are nature friendly

compared to the conventional energy sources. In view of these advantages, the energy harvesters become a suitable candidate to be utilized as an alternative energy sources in the era of IoTs.[5] In the year of 2006, the first nanogenerator was developed by Wang et al. by using piezoelectric effect.[10] The aim of this novel work is to harvest mechanical energy. Moreover, the piezoelectric effect was first invented by Nobel Prize honored Pierre and Jacques Curie in the year of 1880.[11] After developing the piezoelectric nanogenerator, Prof. Wang and his group introduced triboelectric properties of the materials and utilized this effect to design nanogenerator, named as Triboelectric nanogenerator (TENG) in the year of 2012.[12-14] Owing to the capability of harvesting energy from living bodies including running, jogging, heart beating, stretching, bending etc. these PENGs and TENGs can be used in development of self-powered and wearable devices, sensors and actuators etc.[15-20]

In this present thesis, we have designed PENG, TENG and piezoelectric effect supported TENG and utilized them to harness mechanical and biomechanical energy resources.

## *1.2 Piezoelectric Nanogenerator*

It is an energy harvesting device, which has the capability to convert external mechanical energy sources into electrical energy with the help of piezoelectric effect. This energy harvesting device can generate power in the range of nanoWatt (nW) to mili Watt (mW).[21] This generated power can be used in powering up small and portable electronic gadgets.

### *1.2.1 Piezoelectric effect*

Piezoelectric effect is the phenomenon which is occurred due to the alteration in the polarization on the appliance of external pressure or stress. The term Piezoelectric is originated from the Greek word “Piezein” whose meaning is “electricity generating from pressure”. The piezoelectric effect was first discovered by Jacques and Pierre Curie in the year of 1880.[22-24] After one year, Hankel named this effect as “Piezoelectricity”.[25] The initial utilization of the piezoelectric effect was in First World War through developing an ultrasonic submarine detector. There are mainly two types of piezoelectric effect i.e. direct piezoelectric effect and inverse piezoelectric effect, shown in the figure 1.1. Direct piezoelectric effect means when a material is subjected to mechanical stress then polarization is induced across the material. The inverse polarization effect occurs during deformation of material after applying the external force.[26]

Moreover, the operating principle of piezoelectric energy harvester is based on the direct piezoelectric effect.

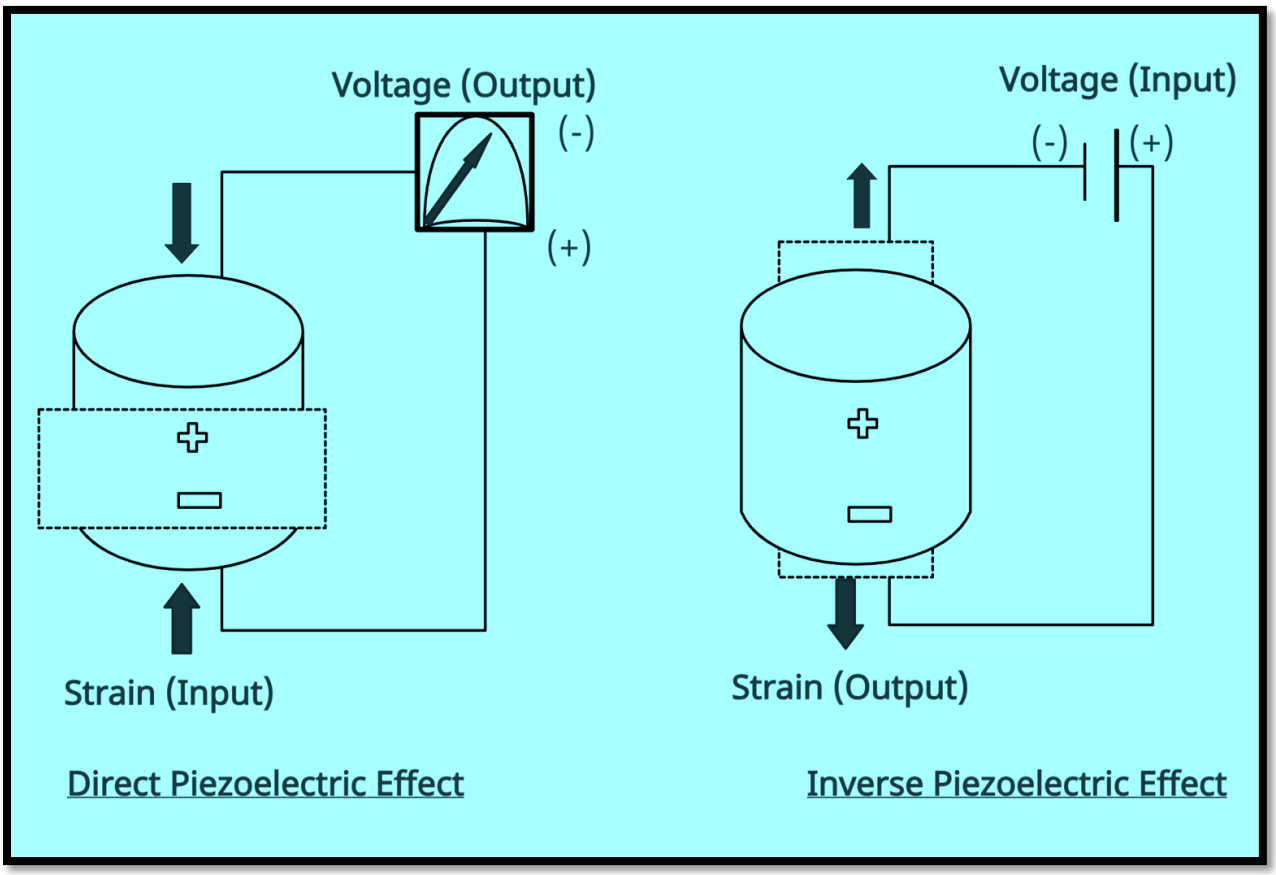


***Figure 1.1:*** *Schematic representation of direct and inverse piezoelectric effect. (Collected from internet)*

### *1.2.2 Mechanism*

The piezoelectric effect is interconnected to the formation of the dipole moment inside the solids. When an external stress or force is imposed on the materials, the polarization change takes place which may be occurred due to the orientation of the dipoles of the molecules or change in the alignment of dipoles. Moreover, the piezoelectricity depends on the following parameters which are also variable, i.e. symmetry of crystals, orientation of polarization and external applied stress. Generally, crystal exhibits charge balance which means that positive and negative charges are cancelled out each other along the rigid plane of the lattice. After applying external pressure on

the crystals, the balance of charge becomes disturbed which leads to induce charge carriers and develop electric current within the material. In case of inverse piezoelectric effect, the deployment of external field disrupts the crystal's neutral charge balance and results in modification of lattice structure. The formation of piezoelectric effect is better illustrated by using crystalline solid and ions array within the unit cell wherein the positive and negative charges remain the non-centrosymmetric inside the unit cell plane despite of applying any external force. Moreover, there are thirty two crystallographic classes, depending on the unit cell's symmetry and geometry. Among these thirty two classes, the number of non-centrosymmetric nature based classes is twenty one. Amidst all of classes, only one shows piezoelectricity. Due to the deficiency of the symmetry in the arrangement of ions, these crystalline solids generate net dipole moment which further helps in inducing piezoelectric effect.[27] This piezoelectric effect can be utilized to harness mechanical energy and convert them into electrical energy.

The underlying physics behind the generation of charges of PENG are described below. The electrical signal generated by PENG can be explained theoretically through Hooke's law[28]. The electrical behavior can be describes as

$$\boldsymbol{D = \varepsilon E} \quad \text{..... (1.1)}$$

Where, D represents the electric displacement, $\boldsymbol{\varepsilon}$ is the dielectric permittivity and E defines the strength of electric field. To identify the system, the linear elastic material can be written from Hooke's law as

$$\boldsymbol{S = sT} \quad \text{..... (1.2)}$$

Where, S defines the strain, s and T represent the compliance and stress of the system respectively. The combination of these two equations gives the piezoelectric strain-charge equations which are

$$\{\boldsymbol{D}\} = [\boldsymbol{\varepsilon^T}] + [\boldsymbol{d}]\{\boldsymbol{T}\} \quad \text{(Direct piezoelectric effect) ..... (1.3)}$$

$$\{\boldsymbol{S}\} = [\boldsymbol{s^E}]\{\boldsymbol{T}\} + [\boldsymbol{d^t}]\{\boldsymbol{E}\} \quad \text{(Inverse piezoelectric effect) ..... (1.4)}$$

Where, [d] defines the matrix of direct piezoelectric effect, [$d^t$] represents the matrix of inverse piezoelectric effect. The superscript T and E are the constant stress and electric field which are coming from the system. The term t elaborates the transposition of matrix.[28]

Therefore, piezoelectricity is a combination of stress and strain tensors, elastic and dielectric variables, and electric displacement and field vectors. Owing to the anisotropic behavior of the piezoelectric material, the relationship among stimulus and response relies upon the employed mechanical or electrical stimuli in the energy harvesting and sensing. In case of coordinate system, strain-charge equations will be[29]

$$D_i = \varepsilon_{ij}^{T} E_i + d_{iJ} T_J \quad \text{(Direct piezoelectric effect)} \tag{1.5}$$

$$S_I = S_{IJ}^{E} T_J + d_{Ii} E_i \quad \text{(Inverse piezoelectric effect)} \tag{1.6}$$

Where, $S_{IJ}^{E}$ defines the elastic compliance vector at a constant electric field, $\varepsilon_{ij}^{T}$ represents the dielectric permittivity tensor at constant stress. The notations: I and J index values are 1 to 6, whereas i and j can be 1 to 3. Along with this, D and E are 3X1 tensor which is related to the three coordinate axes X, Y and Z. Moreover, S and T are 6X1 tensor, demonstrating vertical stress or strain (indexing from 1 to 3), and shear stress or strain (indexing from 4 to 6). These equations give us the idea of the direction of stimuli.[30] Furthermore, the operating principal of PENG depends only on the direct piezoelectric effect. When external stress is applied on the piezoelectric material, the induced piezoelectric polarization charge is $\boldsymbol{\sigma}_P$ occurring at two ends of the piezoelectric materials. In this case, the induced charge is (t), flowing amidst the two electrodes. According to the Maxwell's equation, the displacement current ($J_D$) will be[31, 32]

$$J_D = \frac{\partial D}{\partial t} = \varepsilon_0 \frac{\partial E}{\partial t} + \frac{\partial P}{\partial t} \tag{1.7}$$

Where, P represents the polarization field. During the absence of external electric field and polarization field along the z axis, the displacement current will be

$$J_{DZ} = \frac{\partial P_Z}{\partial t} = \frac{\partial \sigma_P(z)}{\partial t} \tag{1.8}$$

Where, $\mathbf{D_Z = P_Z = \boldsymbol{\sigma}_P(z)}$**.** Also, the open circuit voltage of PENG will be

$$V_{OC} = k \frac{\sigma_P(z)}{\varepsilon} \tag{1.9}$$

Where, k stands for the thickness of the piezoelectric media. From these equations, we can see that output voltage has a dependency on the polarization charges which also follow the piezoelectric coefficient.[31, 33]

### *1.2.3 Piezoelectric materials*

The choice of the material is the crucial part of the designing PENG. Depending on the materials selection, output performance of PENG is varied. Piezoelectric materials are that kind of smart materials which can easily convert mechanical energy into electrical energy. There are several kind of piezoelectric materials for example natural and synthetic crystals lead based and lead free ceramics, naturally sustainable bio piezoelectric materials, electroactive polymers. Single crystals are generally composed of organized orientation of positive and negative ions which enhances the net dipole moment. The major utilized single crystals are quartz, lithium tantalate, langasite, gallium orthophosphate and lithium niobate.[34-37] Moreover, there have some drawbacks of utilizing these materials like high lost, difficult fabrication process etc. Also they have the tendency to loss piezoelectric effect under large electric filed. Piezoelectric ceramics are well known inorganic poly crystalline materials and consist of high piezoelectric coefficient and dielectric properties. The frequently used ceramics are lead zirconate titanate (PZT), barium titanate ($BaTiO_3$), zinc Oxide (ZnO), Potassium niobate ($KNbO_3$), sodium niobate ($NaNbO_3$), lead titanate ($PbTiO_3$), PZN-PT, zinc sulphite ($ZnSO_3$), PMN-PT, bismuth ferrite ($BiFeO_3$) etc.[10, 38-47] Among these piezoelectric ceramics lead based ceramics exhibit high dielectric properties, piezo coefficient value, but presence of lead restrict them their utilization in the field of biomedical applications. To overcome this problem, lead free piezoelectric ceramics has been introduced but their efficiency is not so good compared to lead based piezo ceramics. Apart from this, natural sustainable bio based materials has been utilized to design PENG. The main advantages of natural piezoelectric materials are environmental friendly behavior and low fabrication cost. Some traditional natural based piezoelectric materials are quartz, tendon, egg shell, sucrose, rochelle salt, silk, dentin, proteins, viruses, cellulose, chitins, enamel etc.[48-59]

### *1.2.4 Piezoelectric polymers*

Nowadays, the polymer based nanocomposite with various electroactive filler has been utilized widely due to their better optical, electrical and thermal properties. Among various available

polymers, Poly(vinylidene fluoride)(PVDF) consists of high piezoelectric coefficient values owing to the unique crystalline formation and structural orientations.[60-62] The co-polymers of PVDF including poly(vinylidene fluoride-co-hexafluoropropylene) (PVDF–HFP)[63,64], poly(vinylidene fluoride–trifluoroethylene–chlorofluoroethylene) (PVDF–TrFE–CFE), poly(vinylidene fluoride-co-trifluoroethylene) (PVDF–TrFE)[65-68] also exhibit very good piezoelectric properties. These polymers can be used to design flexible and environmental friendly PENG.

### *1.2.5 Poly(vinylidene fluoride) (PVDF)*

PVDF is a thermoplastic and semi-crystalline fluoro-polymer with various fascinating properties including light weighted and highly non-reactive. It is generally consist of 1,1-difluoroethene which is identified as vinylidene fluoride and abbreviated as VF2 or VDF. Compared to other fluropolymer, the presence of fluorine and hydrogen within PVDF are 59.4 wt% and 3 wt%. The density of PVDF is 1.78g/cm$^3$.Moreover, Dr. Heiji Kawai from Physical Research Laboratory of Kobayashi Institute, is the first scientist who was discovered the piezoelectric response of PVDF in the year of 1969. After that, various prestigious works on crystalline phases of PVDF have been done.[69-71]The chemical formula of PVDF is $(CH_2\text{-}CF_2)_n$. This semicrystalline polymer generally consists of five crystalline phases which are α, β, γ, δ and ε respectively.[72] Among them, β-crystalline phases is the most crystalline phase and also exhibits very good piezoelectricity and elasticity properties. Owing to these properties, the nucleation of β-crystalline phase has gained immense attention. Beside this, α-crystalline phase consists with monoclinic crystal structure and exhibits TGTG'(T-trans, G-gauche$^+$, G-gauche) dihedral conformation. This dihedral confirmation makes the α-phase non-polar in nature and does not exhibit any piezoelectricity. The β-crystalline phase is the most stable phase and crystal structure is orthorhombic. This β-phase consists of all TTTT conformation and leads to rise in piezoelectricity. Apart from this, the γ-phase exhibits TTTGTTG′ conformation which posses lower piezoelectricity value compared to β-crystalline phase of PVDF.[73-75]The schematic illustration of three phases of PVDF has been represented in the following figure 1.2. Furthermore, PVDF has three copolymers which are PVDF-HFP, PVDF-TrFE, PVDF-TrFE-CTFE.

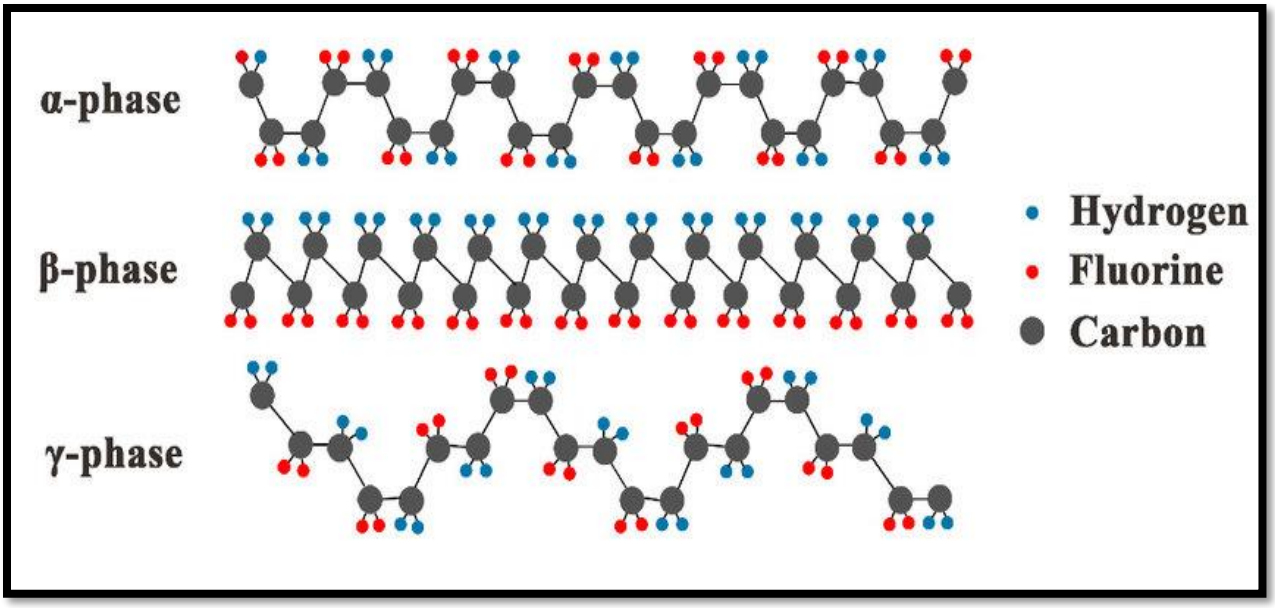


***Figure 1.2:*** *Crystalline phases of PVDF. (Collected from internet)*

PVDF-HFP is the low cost copolymer which is produced by incorporating the amorphous hexafluropropylene (HFP) into PVDF matrix.[76] Due to the existence of bulky $CF_3$ group, PVDF-HFP exhibits less crystallinity in comparison with pure PVDF. Moreover, PVDF-HFP consists of very good piezoelectric properties with $d_{33}$ value of 30 pC/N which helps in a potential candidate in piezoelectric and ferroelectric related applications.[77, 78] PVDF-TrFE is most effective copolymer of PVDF whose electroactive phase concentration is superior compared to PVDF. Due to inclusion of third fluoride to the TrFE monomer, the PVDF-TrFE copolymer results in all TTTT conformation and confirms the formation of ferroelectric β-phase. Additionally, PVDF-TrFE offers appealing piezoelectricity, excellent polarization value of 110 $mC/m^2$ and thermal stability.[79] Apart from these two copolymers, PVDF has another two copolymers named as PVDF-CTFE and PVDF-TrFE-CTFE. They are ferroelectric in nature and can be synthesized by incorporating required amount of CTFE into PVDF and PVDF-TrFE matrix. In comparison with pure PVDF, they exhibit outstanding dielectric and piezoelectric properties.[69, 80] The dielectric and piezoelectric values of PVDF and its copolymers have been depicted in the tabular format.

***Table 1.1:*** *Dielectric constant and piezoelectric coefficient of PVDF and its copolymers*

| *Polymer name* | *Dielectric constant* | *Piezoelectric coefficient* |
|---|---|---|
| *PVDF* | 6-12[69, 81, 82] | -24 to -34[69, 81] |
| *PVDF-HFP* | 11[69, 83] | -24[69, 85] |
| *PVDF-TrFE* | 18[69, 84] | -38[69, 86] |
| *PVDF-CTFE* | 13[69, 40] | -140[69, 80] |

### *1.2.6 Polydimethylsiloxane (PDMS)*

PDMS is a non-toxic, optically cleared and non-flammable silicon polymer. The chemical formula of PDMS is $CH_3[Si(CH_3)_2O]_nSi(CH_3)_3$, where n is the repeating polymer number.[87] Generally, it is a ferro or piezo-electret and used in sensing applications. Owing to heterogeneous structure, piezo-electret makes itself a potential candidate in sensing applications. This structure helps in the formation of regular or sporadic micro-cavities inside the polymer matrix. These cavities are further helped in developing of internal quasi-permanent macro-dipoles which further induces the piezoelectricity after applying external stress. Moreover, the piezoelectric coefficient of PDMS is 350 Pc/N which is very large compared to other polymers.[88]

### *1.2.7 Literature review on enhancement of β-phase and polymer based PENG*

The electroactive and polar β-crystalline phase of PVDF and its copolymers exhibits maximum piezoelectricity property which opens up the utilization of nanocomposite in the field of sensors and actuators, energy harvesters, water purification etc. Therefore, several techniques have been used to enhance the β-crystalline phase for example electrospinning, spin coating, solution casting and Langmuir-Blodgett. Among these, Solution casting technique is the upgraded

technique where incorporation of nano or micro fillers into the PVDF and its copolymers matrix is utilized. Among different type of fillers, ceramics filler like $BaTiO_3$[89], PZT[90] etc. are used to increase the energy storage and dielectric properties of the PVDF nanocomposites. Moreover, the self-poling property of PVDF that means no need of physical stretching are attained by incorporating metal nanoparticles like Fe, Pt, Ag etc.[91-93], metal based oxide nanoparticles like $TiO_2$, ZnO, $Fe_3O_4$, $SiO_2$ etc.[94-97], natural mineral nanoparticles like MMT, mud volcano clay etc.[20, 98], other nanofillers including graphene, carbon fibers, SWCNT, carbon black etc.[99-102]

From previous work, we can see that the β-phase nucleation of PVDF matrix was obtained by adding cerium(III)/yttrium(III) nitrate hexahydrate, which was reported by Thakur et al. The obtained maximum β-phase was 82.3% for 10 mass% cerium nitrate hexahydrate and 81.8% for 5 mass% yttrium nitrate hexahydrate loading.[73] Martins et al. reported that they obtained the maximum electroactive β-phase of 90% after incorporating the ferrite nanoparticles into PVDF matrix. The electroactive phase nucleation is depending on the electrostatic interaction between nanoparticles with negative charged surface and PVDF matrix with positive $CH_2$ dipole.[103] Moreover, the addition of natural mineral particles into polymer matrix also enhances the electroactive β-phase. Ghosh et al. used hematite natural particles to enhance the β-crystalline phase of PVDF matrix. They used simple solution casting method to fabricate the nanocomposite.[104] Das et al. reported the nucleation of electroactive β-phase of PVDF matrix by addition of mud volcano acquired clay nanoparticles. They got 84.8% β-phase for 1 wt% doping of clay nanoparticles. Moreover, they also used this nanocomposite to fabricate PENG, named as BPENG which exhibits the 125V output voltage and 7187μW/$cm^3$ power density. This fabricated BPENG has the capability to detect body movements and illuminate 40 no of LEDs.[20] Biswas et al. fabricated CTAB-MMT doped PVDF nanocomposite which shows maximum β-phase of 91%, colossal piezoelectric constant value of 62.5 pC/N and dielectric constant of 48. They utilized this nanocomposite to design PENG and photo power cell.[98] Not only mineral particles but non-conducting ceramic materials also gained immense attention to improve the β-phase of PVDF matrix. The incorporation of $BaTiO_3$ nanofillers into PVDF polymer leads to formation of electroactive β-phase (80%) which was observed by Mendes et al. This paper has been highlighted on the size and doping concentration of nanoparicles.[105] Gregorio et al. examined the effect of PZT and $BaTiO_3$ nanofillers on the dielectric properties and β-phase of PVDF matrix. They also came to a conclusion that the relative permittivity of nanocomposites

are increasing with doping concentration of fillers. This statement was well matched with theoretical calculated data.[106] Furthermore, several researchers have been used metal nanoparticles to improve the electroactive β-phase. For example, Biswas et al. embedded silver nanoparticles into PVDF and PVDF-HFP matrix by using in-situ chemical method. They have noticed that silver nanoparticles accelerate the formation of β-phase in crystallization of molten PVDF but in case of PVDF-HFP, they do not help in β-phase formation by restricting the mobility of chain.[107] Mandal et al. developed the thin film of palladium doped PVDF nanocomposite by using spin coating technique. They have explained the formation of β-phase well through dipole-surface charge model.[108] Santos et al. developed the electroactive β-phase of PVDF matrix by embedding copper nanowires by using precipitation technique through melt compression. The results indicated that the dielectric property is increased with doping percentage.[109] Mitra et al. reported the nucleation of electroactive phase of PVDF-HFP by incorporating $TiO_2$ nanoparticles by using solution casting technique. They also utilized the nanocomposite film to design the PENG and harvest the pressure from blood flow, different mechanical responses.[110] Furthermore, piezoelectric materials with optical properties have been used to investigate the optical properties of PVDF and its copolymers. Using the mechanoluminescence property of ZnS nanoparticles, Li et al. developed a ZnS/PVDF-HFP nanoconposite based flexible mechanoluminescent sensor which has the capability to convert mechanical energy into yellow, green and white light, visualized in bare eye.[111] He et al. embedded CuS into PVDF matrix to investigate absorption and dielectric properties. The results depicted that the nanocomposite exhibited colossal absorption and dielectric values owing to Debye dipolar relaxation, Maxwell-Wagner interfacial polarization and electron polarization.[112] Recently, bio based organic materials has been embedded into polymer matrix to enhance the β-phase. Tamang et al. developed DNA based PVDF nanocomposite where incorporation of DNA converts the non-polar α-phase into polar β-phase. They have used this nanocomposite to design PENG and examine the output performance.[113] The enhancement of electroactive β-phase of PVDF matrix by embedding cellulose nanofibers was reported by Fu et al. They have used electrospinning technique and get highest β-phase of 89.96% and also obtained excellent output results.[114] Hoque et al. extracted chitin nanofibers from Crab-shell and incorporated it to PVDF matrix to obtain the β-phase. This study exhibited that the maximum obtained β-phase is 81% which was further utilized to fabricate PENG and harness mechanical energy resources.[57] Along

with the nucleation of the β-phase, nanofillers embedded PVDF nanocomposites have been also used to develop self-powered and flexible PENGs. For example, Mao et al. fabricated a PENG by using mesoporous PVDF film. This device exhibits 11.1V output voltage and 9.8μA short circuit current respectively. Also it has the capability to convert surface oscillation into electrical energy.[115] Du et al. developed a PENG by using porous nofibers of PZT/PVDF composites which also exhibited nucleation of β-phase. To fabricate the fibers, the electrospinning method was used. This fiber was also utilized to fabricate PENG which exhibited the output voltage of 62V and power of 1366.9μW.[116] A highly flexible, non toxic and self powered sensor was fabricated by Bharti et al. by using $Bi_2WO_6$@PVDF-TrFE nanofiber mat. They obtained the output voltage of 205 V and short circuit current density of 11.91 mA $m^{-2}$ which was further used to power up electronic devices.[117] Moreover, 2D semiconducting materials are also used to design flexible PENG. Han et al. used 2D $MoS_2$ shell to fabricate the flexible power generator with the help of piezoelectric effect which can easily convert the finger tapping energy into electricity.[118] Lee et al. utilized the piezoelectric property of $WSe_2$ bilayers to develop the piezoelectric nanokgenerator.[119] Furthermore, Li et al. developed an electrode free PENG by using interfacial polarization effect consisted carbon black/PVDF-HFP nanocompoite. The obtained results are short circuit current of 0.66 μA, output voltage of 17.6 V and charge of 4.7 nC respectively.[120] Roy et al. reported 2D MOF embedded PVDF fibrous mat based flexible PENG which can successfully convert acoustic energy into electrical energy and detect human body movements.[121] Along with the PVDF and its copolymer, another piezoelectric polymer PDMS has been open up its utilization in developing PENG. For example, Zhou et al. designed PENGs with the help of carbon coated 0-D piezoceramic nanofillers embedded PDMS nanocomposites. This strategy helped them to obtain excellent peak power densities of 9.9 μW/$cm^2$, 45.4 μW/$cm^2$ and 59.8 μW/$cm^2$ for KNN@C, BT@C and PZT@C based PENGs.[122] Yoon et al. reported a stretchable and eco-friendly PENG depending on the heterostructure of zinc-aluminum layered double hydroxide nanosheets and ZnO, casting on the PDMS substrates. They elaborated the operating principle through flexoelectric and piezoelectric combine effect. This PENG generated power density of 2.7μW/$cm^2$ during finger tapping mode and harnessed biomechanical energies.[123] Veeralingam et al. fabricated flexible and semi-transparent lead free NiFe LDH:PDMS based PENG. The maximum output voltage of 53 V and current density of 0.79 μA $cm^{-2}$ was obtained by external pressure of 0.15 kgf. [124] Das et al.

reported a flexible and skin attachable PENG based on $ZnFe_2O_4$ (ZFO) reinforced PDMS nanocomposite. They used this device for monitoring patient different activities.[125]

From above discussion, we can see that the piezoelectric polymers based nanocomposites become most promising candidates in the area of energy harvester by using piezoelectric, triboelectric and pyroelectric effects, waste water and heavy metals detection, photo power cell, sensors and actuators, transducers, health monitoring units etc.

## *1.3 Triboelectric Nanogenerator (TENG)*

It is most promising energy harvesting device which has the ability to convert mechanical energy sources into electrical energy with the help of triboelectric effect and electrostatic induction.[126] In the year of 2012, Z. L. Wang and his group first fabricated the TENG with output power density of 3.67 $mW/m^2$.[127] After one year, they improved the power density of TENG by optimizing the variables like materials selection, surface properties, mode of operation etc. and obtained the maximum output power density of 313 $W/m^2$.[128] Moreover, the idea of triboelectric effect is first ever invented by Greece philosopher, Thales of Miletus who has discussed about the attraction of amber with other materials. The practical example of given phenomenon of Thales of Miletus is rubbing of pen with cotton or wool fabric. After rubbing, the pen can easily attract tiny strips of paper. From this rubbing effect, the word "tribo" is originated.[129] Generally, contact electrification assists in producing triboelectric effect. When two distinct materials are contacted with each other, then they become electrically charged and help in inducing the triboelectric effect. The occurrence of electrically charged of these materials is resulted from the transfer of ions, electrons or materials which arises from the application of friction or pressure. Moreover, adhesion, occurring due to the creation of chemical bonds, takes place on the surface of the materials at the time of contacting each other. This adhesion further helps in balancing the potential by transferring the charges from one material to other. After the separation of materials, some of the atoms will retain more electrons whereas other will release them. As a result, triboelectric charges are induced on the surface of the materials. The polarity of the different materials determines the direction of the flowing of electrons. With the help of this phenomenon, AC current is produced, which is further utilized in powering up the electronic devices by converting them into DC current through bridge rectifier.[126,130]

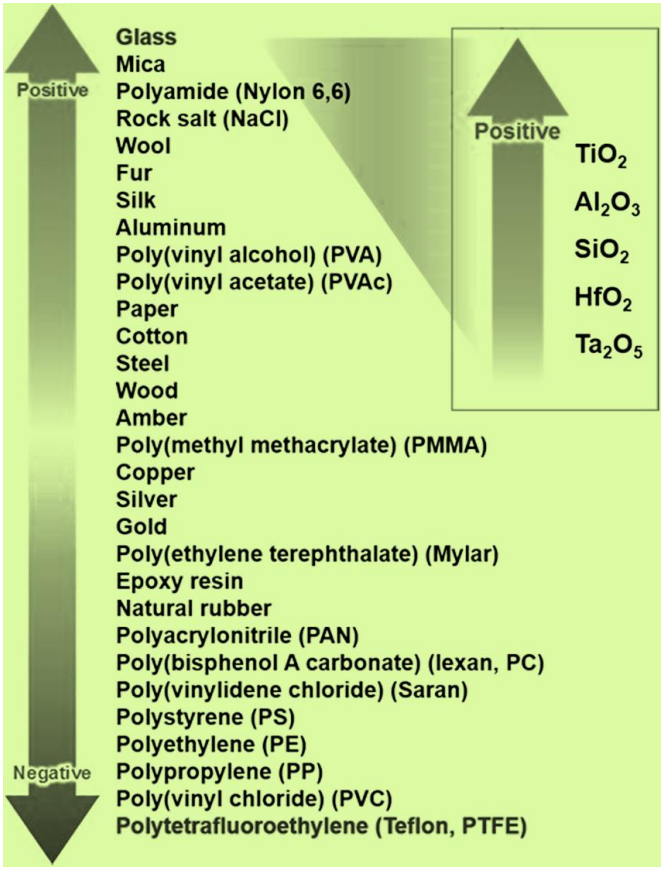


***Figure 1.3:*** *List of tribo-positive and tribo-negative materials. (Collected from internet)*

### *1.3.1 Theory of TENG*

TENG consists of two dielectric materials which are opposite to each other, shown in the figure 1.4. These two dielectric materials with relative dielectric constant of $\boldsymbol{\varepsilon}_{r1}$ and $\boldsymbol{\varepsilon}_{r2}$ are separated from a distance of x and induced surface charge densities of $+\boldsymbol{\sigma}$ and $-\boldsymbol{\sigma}$, resulting from contact electrification.[131] As a result, charges are flowed from one electrode (named as Metal 1) to other electrode (named as Metal 2) through external circuit and generated potential difference among the electrodes of TENG. The total potential differences of TENG will be[131]

$$V_{TENG} = -\frac{Q}{C(x)} + V_{OC}(x) \quad \text{..... (1.10)}$$

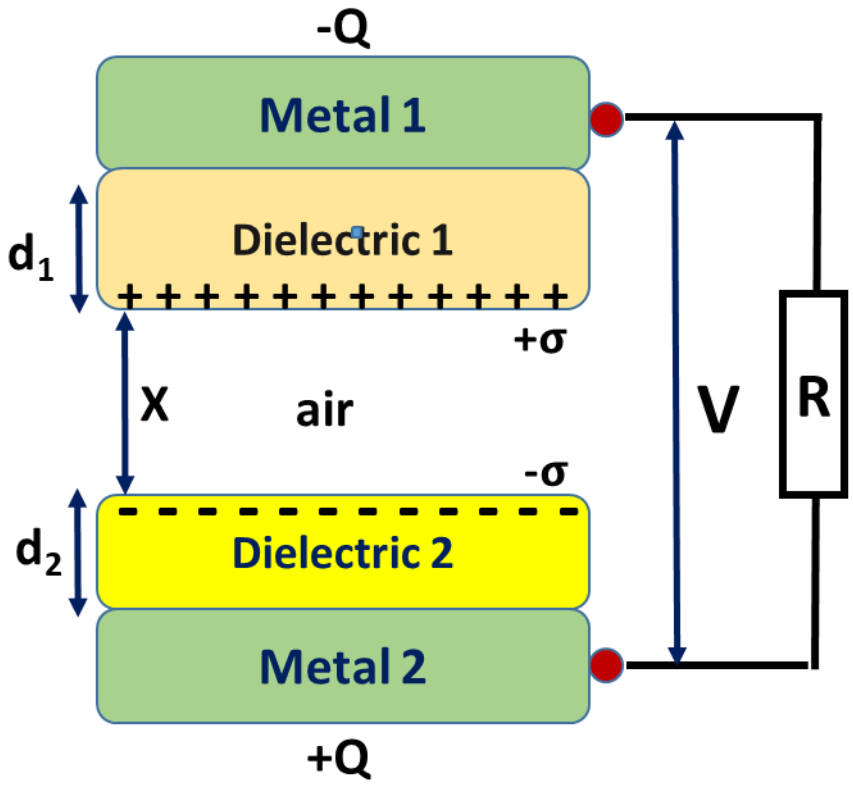


***Figure 1.4:*** *Basic structure of TENG.*

The second term of the above mentioned equation is raised by the tribo-charges of dielectric materials and also has the dependency on the distance between two dielectric materials. This second term is known as open-circuit voltage $V_{OC}(x)$. The first term is coming from the transferring of charges among the two electrodes of TENG. In the absence of tribo-charges, TENG behaves like a capacitor by inducing potential of $-\frac{Q}{C(x)}$ , where C defines the capacitance value, depending on the distance between materials. Moreover, the above stated equation is known as V-Q-x relationship, confirms the dependency of TENG on capacitance value. During the short-circuit situation, the transferred charges ($Q_{SC}$) nullify the generated tribo-charges. As a result, the equation will be[131]

$$0 = -\frac{Q_{SC}(x)}{C(x)} + V_{OC}(x)$$

$$Or,\ Q_{SC}(x) = C(x)V_{OC}(x) \quad \text{..... (1.11)}$$

With the utilization of this equation, there has a possibility to build up an equivalent circuit for TENG, comprised of two circuit components. The first is the capacitive component of circuit, denoting by C which is generated among the electrodes. The source of second component of the circuit is the separation of tribo-charges, shown with an ideal voltage source $V_{OC}(x)$. These two components build up the equivalent circuit, shown in the figure 1.5. Thus, TENG can be easily characterized by a small capacitor and voltage source that can be attached to the load in the circuit.

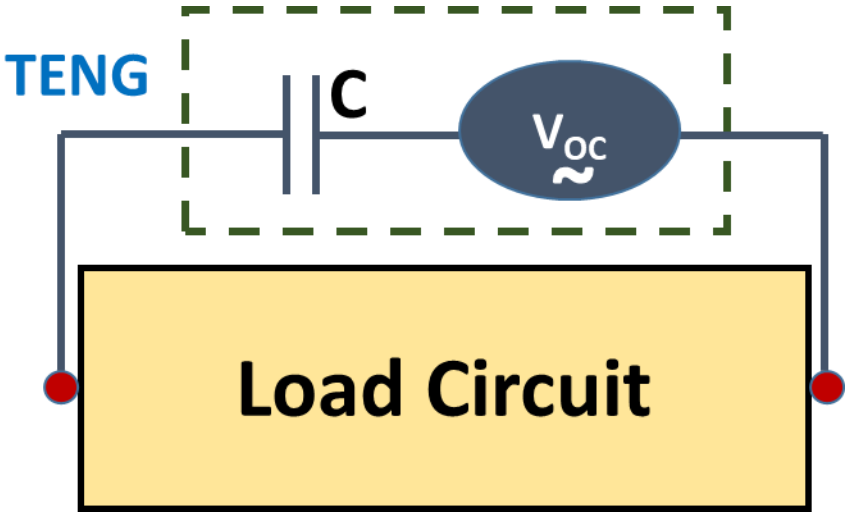


***Figure 1.5:*** *Basic equivalent circuit of TENG.*

To make the calculations simple and easy, resistive load can be used. Kirchhoff's law makes it possible to construct the following equation for whole system. The equation will be[132]

$$R.\frac{dQ}{dt} = -\frac{Q}{C(x)} + V_{OC}(x) \quad \text{..... (1.12)}$$

The above equation can be tackled with numerical analysis method such as Finite element method (FEM). Also, the behavior of TENG can be simulated by using software. To optimize the maximum power density of TENG, resistive load can be utilized. The output voltage (V) and

current (I) will need to be measured in series and parallel fashion on the load for achieving this. Both values are required to find out the instantaneous power density of TENG. The combination of Ohm's law and Joule's law gives us the expression of instantaneous power (P) of TENG, which will be[20]

$$\boldsymbol{P = V.I} \quad \text{..... (1.13)}$$

### *1.3.2 Operating modes of TENG*

There are four different modes of TENG which help in generating the output voltage. The four different operating modes are vertical contact-separation mode, lateral sliding mode, single electrode mode and free standing triboelectric layer mode respectively, explained in the following section.

#### *1.3.2.1 Vertical contact-separation mode*

The vertical contact-separation mode is the most primitive and fundamental mode of TENG by which power is generating through the contact separation of two opposite charged surfaces. Previously, we have discussed about the potential difference, resulting from two electrodes, consisting of thickness of $d_1$ and $d_2$. Thus, total amount of –Q charge and +Q charge are acquired on the top and bottom electrode respectively. The amount of stored charges on the surface of the dielectric 1 and dielectric 2 will be +$\boldsymbol{\sigma}$S and –$\boldsymbol{\sigma}$S. This type of phenomenon is known as dielectric-to-dielectric type mode. Apart from this, there is another type of phenomenon, known as conductor-to-dielectric mode, where one conductor replaces the one of dielectric material. This conductor serves as both electrode and triboelectric layer.[132] Conductor consists of both charges of dielectric 1 and metal 1, which is (+$\boldsymbol{\sigma}$S,-Q). Because of the larger dimension of electrodes in comparison with the distance between electrodes ($d_1$+ $d_2$+ x(t)), we are able to regard this as ideal capacitor with the expression of capacitance, which is $\boldsymbol{\varepsilon}$A/d. Thus, the voltage between electrodes will be $V_{OC} = \frac{Q}{C} = \frac{Q.d}{\varepsilon.A} = \frac{\sigma.d}{\varepsilon}$. This equation helps in deriving the following equations[131]

$$\boldsymbol{V_{OC} = \frac{\sigma x(t)}{\varepsilon_0}} \quad \text{..... (1.14)}$$

$$C = \frac{\varepsilon_0 S}{d_0 + x(t)} \quad \text{..... (1.15)}$$

$$d_0 = \frac{d_1}{\varepsilon_1} + \frac{d_2}{\varepsilon_2} \quad \text{..... (1.16)}$$

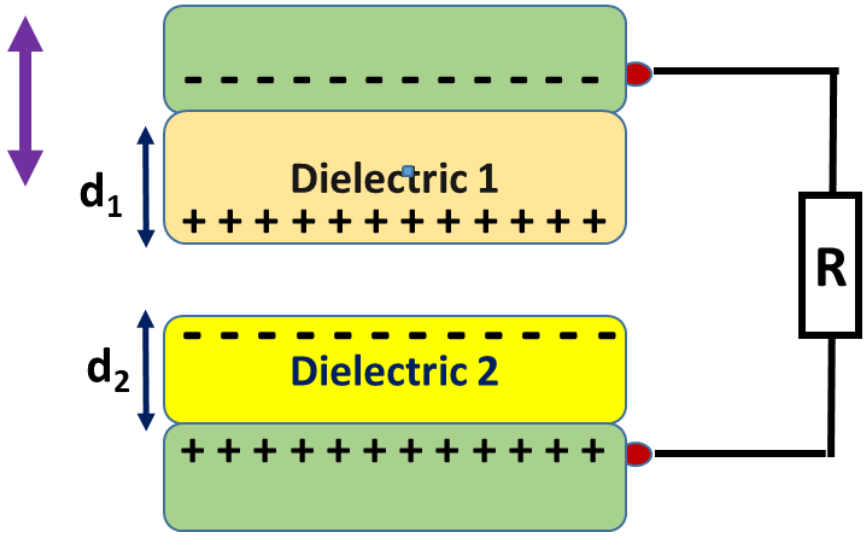


***Figure 1.6:*** *Schematic representation of the structure of vertical contact-separation mode.*

$$V_{TENG} = -\frac{Q(d_0 + x(t))}{\varepsilon_0 S} + \frac{\sigma x(t)}{\varepsilon_0} \quad \text{..... (1.17)}$$

The equation will be V-Q-x relation of vertical contact-separation mode of TENG. Moreover, the short-circuit charge will be

$$Q_{SC} = V_{OC} * C = \frac{S\sigma x(t)}{d_0 + x(t)} \quad \text{..... (1.18)}$$

In the above equations, S represents the contact area, $\boldsymbol{\sigma}$ defines the surface charge density of tribo materials, $d_0$ is the operative thickness of two dielectric layers and x(t) represents the separation amidst the two dielectric layers. Figure 1.6 shows the structure of vertical contact-separation mode.

Moreover, using contact-separation mode has been some advantages including high output power density, simple fabrication process, multilayered structure etc. For this, this method can be utilized in the wearable and self-powered electronics gadgets.

### *1.3.2.2 Lateral sliding mode*

Lateral sliding mode of TENG is similar to the contact-separation mode of TENG. Only one difference has in lateral sliding mode that is the direction of the relative separation among two tribo layers is parallel to surface of TENG. Moreover, the operating mode of lateral sliding TENG has been classified into two types, one is dielectric-to-dielectric and other is conductor-to-dielectric. From figure 1.7, it has been visualized that the equal distribution of positive and negative charges on the surface of two tribo layers is done after contacting. After sliding out the one tribo layer, a potential difference is occurred across the electrodes, which further increases with increasing the relative motion. As a result, current is generated throughout the external circuit. Similarly, currents are flowing back at the time of sliding in of tribo layer. Thus, the obtaining open-circuit voltage ($V_{OC}$) and short-circuit current ($I_{SC}$) of TENG in the lateral sliding mode will be[133]

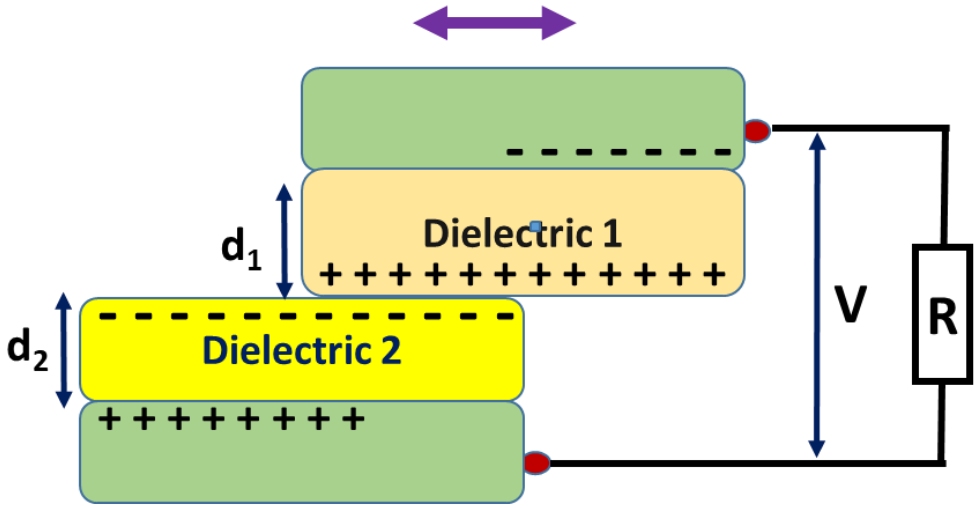


***Figure 1.7:*** *Schematic illustration of the structure of lateral sliding mode.*

$$V_{OC} = \frac{\sigma x(t) d_0}{\varepsilon_0 (l - x(t))} \quad \text{..... (1.19)}$$

$$I_{SC} = \sigma w v(t) \quad \text{..... (1.20)}$$

Where, **σ** represents the surface charge density of tribo materials, x(t) defines the relative separation among two tribo layers, $d_0$ is the operative thickness of tribo layers, l denotes the length of tribo layer in direction of motion, w is the width of the tribo layer perpendicular and v(t) defines the relative velocity between tribo layers.

Therefore, lateral sliding mode is very useful in packaging applications where separation gap is not needed.

### *1.3.2.3 Single electrode mode*

In this mode, only one electrode is required which acts as a primary electrode (PE).Ground is considered as a reference electrode (RE) in most of the cases. The operating principle of TENG within this single electrode mode can be organized into dielectric-to-dielectric and conductor-to-dielectric types. After getting contact, equal amount opposite charges are gathered on the surface of dielectric layer and PE. For this, potential drop generates among the PE and RE, helps in inducing current through the external circuit. When, the dielectric layer is returning to its previous stage, the inducing current will flow back by diminishing the potential drop in the external circuit.

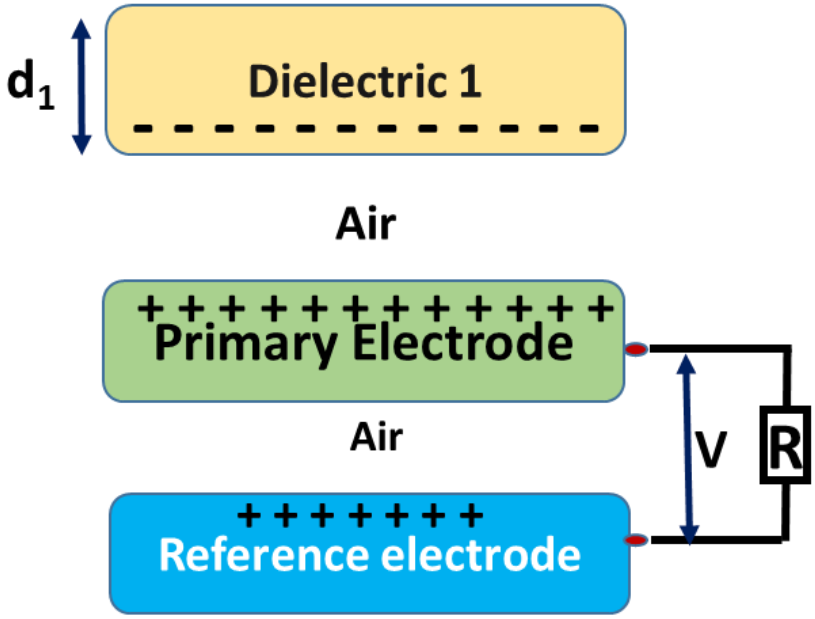


***Figure 1.8:*** *Structure of single electrode mode TENG.*

The obtained expression of open-circuit voltage ($V_{OC}$) and short-circuit charge ($Q_{SC}$) will be[134]

$$V_{OC} = \frac{\sigma w l C_2}{C_1C_2+C_2C_3+C_3C_1} \quad \text{..... (1.21)}$$

$$Q_{SC} = \frac{\sigma w l}{1-\frac{C_1(x)}{C_2(x)}} \quad \text{..... (1.22)}$$

Where, $\boldsymbol{\sigma}$ and w represent the surface charge density and thickness of dielectric layer, l defines the length of dielectric layer, $C_1$ is the capacitance value of dielectric layer to PE, $C_2$ represents the capacitance of dielectric layer to RE and $C_3$ stands for the capacitance value of PE to RE. The structure of single electrode mode has been illustrated in the figure 1.8.

Therefore, single electrode TENG can be used in biomedical application and health care units due to its easy fabrication process and freely movement of tribo layer.

#### *1.3.2.4 Free standing triboelectric layer mode*

In comparison to other three mode of TENG, the setup of the free standing triboelectric layer mode is little more complicated. The movement of tribo layer can be done vertically among the parallel two electrodes or laterally on the identical thin film. Moreover, dielectric-to-dielectric and conductor-to-dielectric are both appeared in the free standing mode of TENG. The operating mechanism of free standing TENG in the sliding more is depicted in the figure 1.9. After a single working cycle, adequately charged surfaces of tribo layer slide laterally.

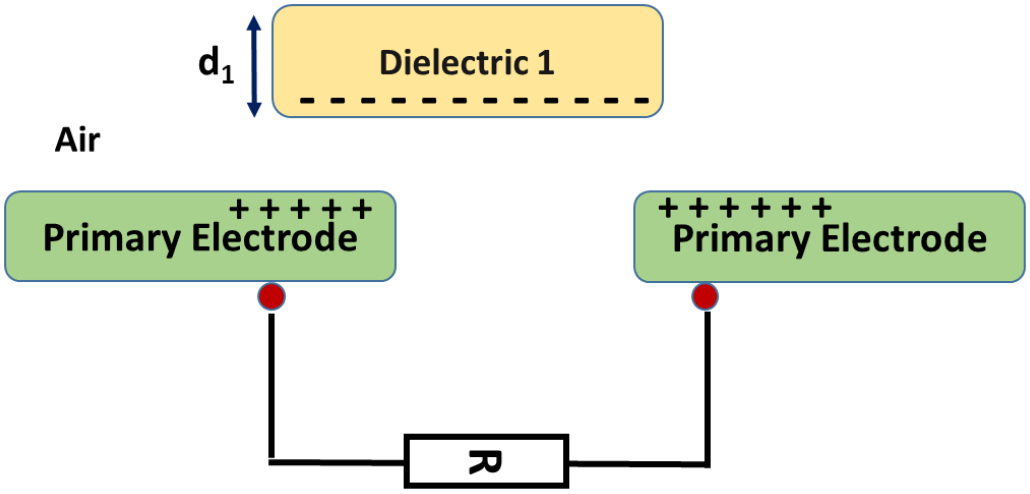


***Figure 1.9:*** *Schematic representation of the structure of free standing mode.*

Thus, two electrodes are charged in opposite directions. The potential difference among the two electrodes and generation of current through the external circuit are occurred, dependent upon the overlapping areas. It takes some serious effort to figure out the right formula for finding the overall capacitance value of TENG because the fringing effect outweighs the capacitance between both fully misaligned electrodes. The precise descriptions of open-circuit voltage and short-circuit current are therefore a bit difficult.[135] Moreover, there are some advantages of free standing triboelectric layer mode of TENG including high energy conversion ability, freely movement of tribo layer etc.

### *1.3.3 Literature review on TENG*

With the utilization of different operating modes of TENG, self-powered and wearable devices have been designed to harness mechanical energies, coming from different sources like wind, water, sound, vibration, and human body movements etc. and convert them into electricity. Moreover, TENG consists of numerous merits compared to other traditional techniques, including easy manufacturing process, high sensitivity with tremendous efficiency, cost-effectiveness and wide choice of materials etc. For this, it can be used in sustainable and green technologies. Additionally, the high conversion skill of biomechanical energy into electrical energy, the self-powered and wearable devices with tribo-effect has potential application in healthcare units. For example, Jao et al. developed textile based wearable sensors by using

contact-separation method of TENG to track gait phase and sense sweat and humidity. They modified the commercial fabric into multifunctional textile by using chitosan-glycerol film and fabricated the TENG, named as C-TENG which induced the current density of 10mA/$m^2$ throughout the humidity range.[136] Chiu et al. fabricated a smart glove by using nano-structured chitosan/ glycerol film and utilized it to detect different gestures. The operating mode of this glove depended on the vertical contact-separation mode. Here, chitosan/glycerol was used as positive layer and FEP film as negative layer. This fabricated wearable smart glove can be used in surgical unit.[137] To improve the output performance of wearable TENG, several techniques are applied. Cui et al. proposed a wearable TENG with porous nanocomposite by reinforcing $Na_2CO_3$ into PDMS matrix. The operating mode of this fabricated TENG was single-electrode mode. This fabricated nanogenerator exhibited 125V output voltage and 100μA short-circuit current. The potential application this nanogenerator was to detect human motions. This idea opened up a new application in self powered personal electronics.[138] A self-powered patch with single electrode based sliding mode TENG was reported by Yang et al. They utilized surface modified PTFE patch and Al electrode to develop the TENG, generated output voltage of 1100V and power density of 350Mw/$m^2$. This device has the versatility to sense displacement vector along with the mechanical energy. Thus, it can be utilized in touch pad applications.[139] Moreover, Shankaregowda et al. reported a graphite coating paper based electrode to fabricate the TENG. The hydrophobicity and flexibility of the electrode helped in harvesting mechanical energy arising from animal movements. Along with this, the graphite paper modified electrode based TENG successfully detected water and wind energy and converted them into electricity.[140] The energy conversion ability of TENG was improved by Zhang et al. through modifying the operating mode. They utilized the single electrode mode and free standing tribo layer mode to accelerate the efficiency of energy conversion. As a result, the dual mode TENG easily charged up different types of electrical storage equipments.[141] To optimize the performance of TENG, the modification of surface charge density and contact area are required. For example, Shao et al. prepared nanofibers by reinforcing $BaTiO_3$ into bacterial cellulose and utilized this nanofibers in designing the TENG. This nanofiber layer modified the dielectric property and surface structure, which resulted in the output voltage of 181V and short-circuit current of 21μA.[142] Venkatesan et al. accelerated the surface charge density of PVDF by electrospraying the PDMS-PVDF microbeads. This novel technique improved the output performance of TENG by inducing 305V

of output voltage and 124.3mW/m$^2$ of power density. The improvement of the output performance of the device successfully assisted in the employment of the device in portable electronic gadgets.[143] Also, Pandey et al. fabricated a nanofibrous tribo-positive layer by incorporating ZIF-8 into PAN and constructed TENG with it, named as PZ-TENG. This tribo-positive layer enhanced the effective surface area and resulted in better performance of TENG. For wirelessly monitoring human-machine interaction, this PZ-TENG was used as self-powered VLC system.[144] Another suitable way to improve the charge density of TENG is to prevent the charge combination process inside the device. For this, Wang et al. inserted the sulfonated cellulose nanofibrous layer during the fabrication of TENG. This nanofibrous layer restricted the charge recombination process and improved the dielectric property. The output performance of the fluronated nanofibers based TENG was utilized in wireless posture detection applications.[145] Also. Rana et al. fabricated a TENG with PVDF-TrFE/MXene nanofiber mat and investigated its utilization in controlling the smart home applications like fire alarms, smart doors, fans etc. The fabricated nanofiber mat assisted in formation of microcapacitor and boosted the output performance of TENG. Additionally, they examined the effect of fiber mat in output performance through theoretical modeling. The maximum power density of nanofiber mat based TENG was obtained with the value of 4.01W/m$^2$.[146] To keep in mind the stretchable and flexible properties of TENG, Zhao et al, developed all fibers based TENG with the help of PVDF and TPU nanofiber membrane and MWCNT based conductive layer. This all fiber based TENG with high stretchable property easily attached to the human skin and harvested biomechanical energy. The device induced maximum output voltage of 225V and current of 4.5μA.[147] Moreover, some researchers are utilized natural friendly and biodegradable materials during the fabrication process of TENG. This idea opens up the utilization of TENG in implantable applications and other health related problems. For example, Hao et al. utilized fully biodegradable natural wood to develop the TENG. This natural wood based TENG exhibited good output voltage of 220V and short-circuit current of 5.8μA, which assisted in powering up small electronic gadgets.[148] Khandelwal et al. improved the hydrophobicity of starch by incorporating the edible laver filler into it. This improvement of hybrophobicity assisted in the biodegradable nature of TENG. Also, the fabricated biodegradable TENG detected the biomechanical energy and power up electronic equipments.[149] Furthermore, Rani et al. collected the waste cigarette filters and utilized them in designing the TENG. To improve the performance of TENG, very small amount of CNT was

added with the cigarette filters. The fabricated device depicted the output voltage of 60V and power density of 110mW/m$^2$. Also, it can successfully detect the sound energy and convert it to electrical energy.[150] Shi et al. added a green fabrication technique of TENG and utilized it in self-powered wearable systems. This idea was executed by fish gelatin and micro-structured leaf. The micro-structure leaf helped in surface modification and improved the output performance. The micro-structured assisted fish gelatin based TENG induced maximum output voltage of 320V and short-circuit current of 0.80μA.[151] Xia et al. proposed a new tribo-positive material which is wool ball and developed a free floating TENG. The wool ball inspired TENG can harvest wind energy and generate output voltage of 462V and short-circuit current of 15.5μA.[152] Apart from the natural materials, self-healable hydrogels are developed to fabricate the TENG. Zhang et al. reported an ionic hydrogel based TENG to monitor the human-computer interactions and identify different objects through machine learning process. The hydrogel was prepared by polypropylene amine (PAM), sodium alginate (SA), tannic acid (TA) and MXene. The exhibited instantaneous power density of TENG was 52.24mW/m$^2$.[153] Rahman et al. reported ZIF-8 reinforcing stretchable and flexible hydrogel based electrode and designed the TENG with this electrode. The reinforcement of ZIF-8 in to hydrogel improved the output performance of TENG which exhibited maximum power density of 3.47W/m$^2$.[154] Luo et al. fabricated a MXene/PVA hydrogel based TENG. The incorporation of MXene promoted the conductivity and stretchability of hydrogel and generated the additional tribolectric effect. As a result, the hydrogel based TENG showed maximum output voltage of 230V.[155] Qin et al. reported a self-powered and flexible sweat sensor with the help of cellulose assisted conductive hydrogel. The conductive and self-healable hydrogel was prepared by polymerizing the cellulose with PANI and cross-linking with PVA/borax. This sweat sensor detected the Na, K, Ca ions in perspiration and transmitted the results wirelessly.[156] Zhang et al. developed a conductive hydrogel through PVA, graphite oxide, cotton paper and MXene. The as prepared hydrogel was further combined with PTFE to fabricate the TENG, which was utilized to monitor running posture and detect different strain. The obtained maximum voltage and short-circuit current was 229.85V and 10.36μA respectively.[157] Furthermore, the power density of the TENG has been improved by combining the triboeffect with other effect. For example, Singh et al. prepared ZnO-PVDF film based TENG where, ZnO-PVDF nanocomposite induced piezoelectric effect and triboelctric effect by combining with PTFE. This nanocomposite based piezo-tribo hybrid nanogenerator generated power density of

24.5μW/cm$^2$.[158] Karumuthil et al. proposed a energy hervester by using ZnO, grapheme oxide and MWCNT incorporated PDMS nanocomposite. The ferroelectric and piezoelectric properties of PDMS nanocomposite improved the output performance and assisted in detection of human footsteps.[159] Saquib et al. designed self-powered and bio-based nanogenerator by using porous tomato peel. The porous structure helped in enhancement of tribolectric charges. As a result, this green nanogenerator induced output voltage of 135 V and power density of 3750μW.[160] Zheng et al. reported core-shell resonator with the effect of piezo-tribo coupling effect, where $BaTiO_3$ served as core and porous PVDF-TrFE served as shell. This resonator behaved like an artificial cochlea.[161] Singh et al. improved the performance of TENG by combining the piezo-tribo effect. They utilized $MoS_2$-PVDF as piezoelectric layer and PDMS as tribo layer. They applied this device to harvest mechanical energy and generate electrical energy.[162] The tribolectrification between PVDF and PTFE was improved by Singh et al. through incorporating ZnO into PVDF matrix. The incorporation of ZnO enhanced the polarization effect and increased the output performance of TENG. The maximum obtained power density was 10.6μWcm$^{-2}$.[163] Chai et al. improved the output performance of TENG by combining the conduction of tribo materials and ferroelectricity. The ferroelectric layer optimized the power density of TENG from 0.11W/m$^2$ to 7.21W/m$^2$.[164] Suktep et al. designed a hybrid nanogenertor by utilizing piezo-tribo effect. The silk fibroin was utilized as tribo layer and gamma-glycine was served as piezoelectric material. The fabricated nanogenerator harvested output voltage of 81V and current of 121μA.[165]

The above discussions interprets the working principles and device designing process of TENG, selection of materials, techniques to improve the triboelectric charges, enhancement of output performance and applications in the various fields. Also, it emphasizes how TENG can easily scavenge mechanical energy sources coming from water, rain, wind, music playing, human body movements etc. Thus, TENG can be used in biomedical applications as biosensors, healthcare units, self-powered sensors like photodetectors, chemical sensor, humidity detector, sweat sensor etc.

## 1.4 Experimental Techniques

### 1.4.1 Fabrication process of thin films

The thesis showcases the simple fabrication process of polymer thin films by utilizing two well-known and simple process including solution casting method and electrospinning technique.

#### 1.4.1.1 Solution casting method

Solution casting method is a trouble-free and common procedure to fabricate the polymeric thin films. When the polymer and inorganic nanofillers are well dispersed and dissolved totally, then this technique will be employed. In solution casting method, the primary polymer (PVDF, PDMS, Ecoflex etc.) and the nanofillers are dispersed within the appropriate solvents including DMSO, DMF etc. with the help of mechanical forces coming from magnetic stirrer, water bath ultra-sonicator, electric force stirrer etc. After well dispersion of the polymer and nanofillers, the solution is casted on a clean and solid surfaced petri dices and transferred in a hot air oven at suitable temperature to obtain the required polymeric thin film. The procedure of solution casting has been represented schematically in the figure 1.10.

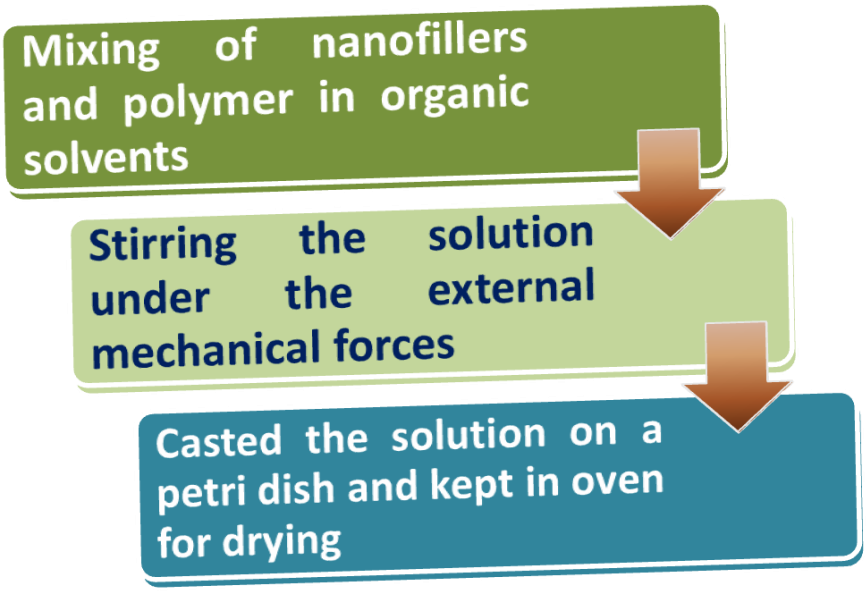


***Figure 1.10:*** *Flow chart of solution casting method.*

### 1.4.1.2 Electrospinning technique

The electrospinning technique is performed to fabricate the nanofibers. First of all, stock solution is prepared by dissolving required amount of polymer in solvent and acetone mixture and kept it under stirring condition. Thereafter, required amount of nanofillers are added in the mixture solution and placed it on the stirrer. In the next step, sonication has been performed to get the stock solution for the electrospinning process.

Thereafter, the stock solution has been loaded in syringe and performed the electrospinning process by adjusting some parameters including flow rate, distance between the needle of the syringe and the collector plate and high voltage. After completing the process, the nanofibers are acquired from the collector plate. The schematic of electrospinning process has been depicted in the figure 1.11.

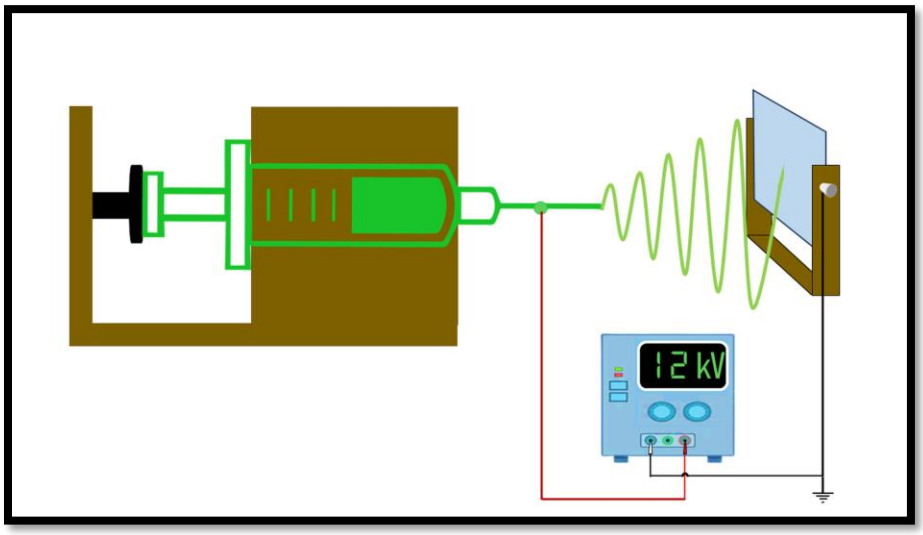


***Figure 1.11:*** *Schematic representation of electro-spinning process.*

### 1.4.2 Designing of self-powered devices

In this thesis, piezoelectric nanogenerator and tribelectric nanogenerator serve as self-powered and wearable devices. The fabrication process of these two nanogenerators is described below.

### 1.4.2.1 PENG fabrication

Firstly, the prepared composite thin film is taken and two aluminum electrodes with required thickness are attached on the both side of the composite film. Thereafter, two copper wires are

connected to the composite film to measure the electrical properties. In the next step, the copper wire connected aluminum electrode attaching composite film is encapsulated with polydimethylsiloxane (PDMS) (Sylgard 184, Dow Corning, ratio, 1:10) by submerging the whole system in PDMS gel. Then, the submerging system is placed in a vacuum oven for drying at $60^0$C for few minutes. After that, we get the fabricated PENG. Figure 1.12 represents the fabrication procedure of PENG schematically.

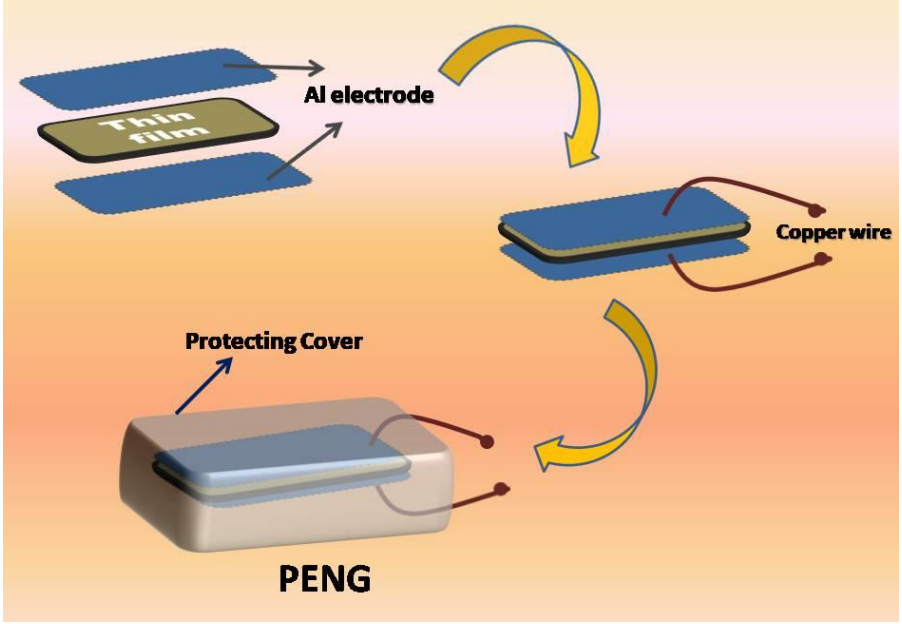


***Figure 1.12:*** *Schematic illustration of fabrication of PENG.*

### *1.4.2.2 Designing of TENG*

Generally, the fabricated TENG device consists of charge generating layer and charge collecting layer. Herein, PVA nanocomposite, human hand , Ecoflex and PDMS thin films have been used as charge generating layers and aluminium (Al) electrodes, carbon tape (thickness 41µm) as charge collecting layer. The fabrication of TENG consists of two parts i.e. positive and negative part. The positive tribo layer consists of PVA film, human hand and the negative layer consists of PDMS film and ecoflex. After successfully synthesized the positive and tribo layers, the electrodes are attached with the positive and negative layer of TENG. Then, protecting cover are utilized by maintaining ample air gap in the middle of the two parts of TENG (positive and negative parts). Lastly, two copper wires are connected with the electrodes to investigate the

output performance of fabricated TENG device. The designing of TENG has been illustrated in the figure 1.13.

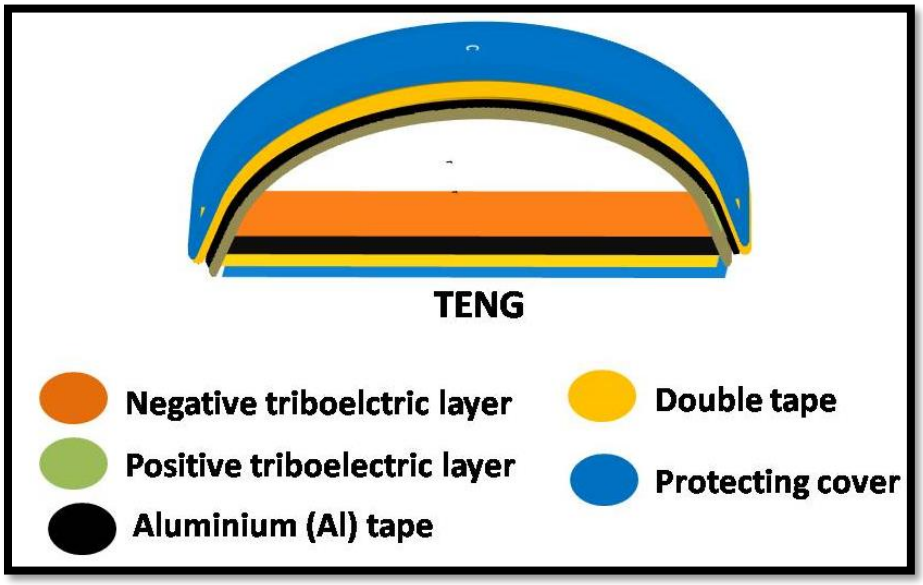


***Figure 1.13:*** *Schematic representation of the designing of TENG.*

## *1.5 Characterization Tools*

To acquire the structural, morphological and chemical information related to the synthesized nanomaterials and thin films, characterizations are the central part of any kind of research work, which not only give us the properties of the synthesized materials but also way out the direction of the research work. Herein, several scientific apparatus are used to investigate the structural, physical and chemical properties of synthesized nanoparticles and nanocomposites. The detailed descriptions regarding the scientific apparatus are stated below.

### *1.5.1 X-ray Diffractometer (XRD)*

The structural properties of synthesized nanomaterials and thin films have been examined by X-ray diffractometer (XRD; Model-D8, Bruker AXS Inc., Madison, WI). For Cu $K_\alpha$ (1.5406 Å) radiation, Germanium (002) monochromator has been used. The experimental results i.e. the diffraction patterns are visualized in θ - 2θ style. Also, the XRD of samples are performed under

40 kV voltage and 35 mA current respectively. Moreover, Bragg's equation is used to calculate the lattice spacing of the sample from measured diffraction angles.

$$2dSin\theta = n\lambda$$

Where, d defines the interplanar spacing, θ represents the glancing angle and d represents the wavelength of incident x-rays. The obtained diffraction patterns are utilized to study the structural properties of the synthesized samples.

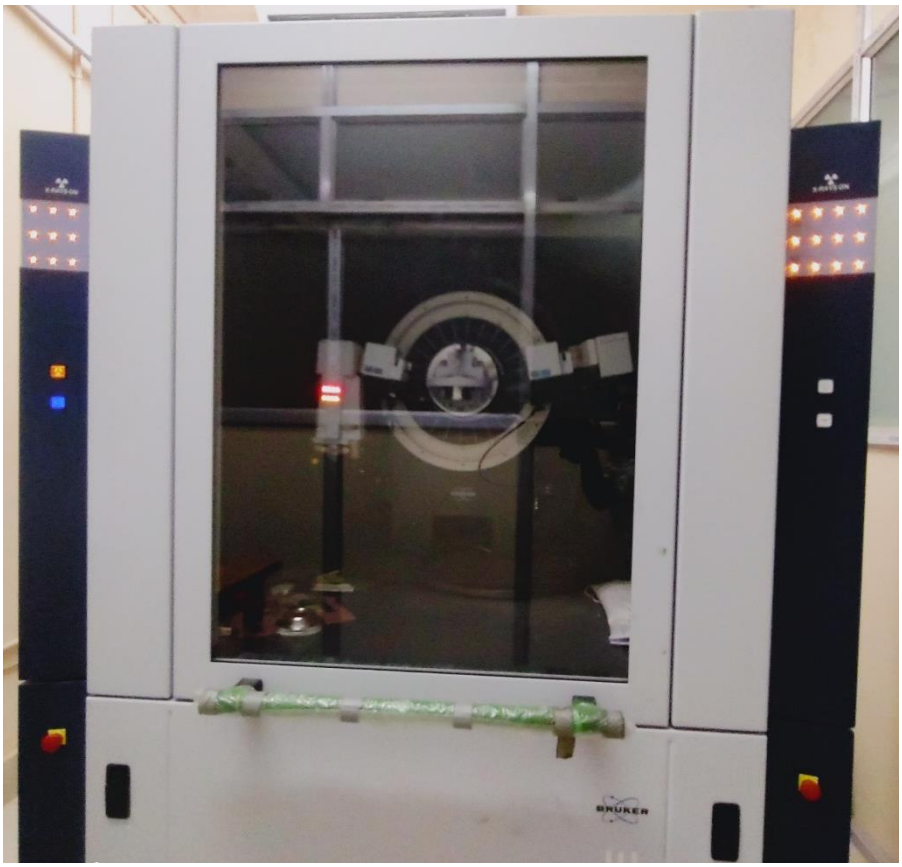

***Figure 1.14:*** *Digital image of X-ray Diffractometer (XRD).*

### *1.5.2 Fourier Transform Infrared (FTIR) Spectrometer*

FTIR is performed to find out the frequencies of absorbed energy and determine the presence of chemical bonds inside composite films. Moreover, the presence of electroactive crystalline phases inside pure PVDF and nanoparticles doped PVDF has been investigated by using FTIR

spectrometer (FTIR-8400S; Shimadzu). To carry out the experiment, the absorbance spectra of nanocomposites are varied from 400 $cm^{-1}$ to 4000 $cm^{-1}$ with high scan speed.

With the help of IR spectrum, the content of β-crystalline phase inside a composite film has been examined by using Lambert-Beer law

$$F(\beta) = \frac{A_\beta}{\left(\frac{K_\beta}{K_\alpha}\right)A_\alpha + A_\beta} \quad \text{..... (1.23)}$$

Where, $A_\alpha$ and $A_\beta$ represent the absorbance at 764 $cm^{-1}$ and 840 $cm^{-1}$ respectively. $K_\alpha$ and $K_\beta$ are the absorption coefficients at 764 and 840$cm^{-1}$ with carrying the value of $6.1 \times 10^4$ $cm^2mol^{-1}$ and $7.7 \times 10^4$ $cm^2mol^{-1}$ respectively.


***Figure 1.15:*** *Digital photograph of FTIR instrument.*

### *1.5.3 Field Emission Scanning Electron Microscope (FESEM)*

Field emission scanning electron microscope (FESEM) has been used to investigate the morphology and the microstructures of the synthesized materials and nanocomposites. Also, it gives us the idea of the surface of sample whether it is in micro scale or nano scale range. The FESEM images, which are included in this thesis, are captured by using FESEM; INSPECT F50. For capturing the better images of the surface of the sample, gold coating has been performed by using Q150T Turbo Pumped Sputter Coater.

***Figure 1.16:*** *Digital image of FESEM instrument.*

### *1.5.4 Energy Dispersive X-ray (EDX)*

EDX is performed to investigate the elemental composition of the material and determine the stoichiometry. Also, homogeneous distribution of nanoparticles inside the polymer matrix has been examined by EDX. In this thesis work, Zeiss Gemini SEM 500 is used to investigate the elemental composition of synthesized materials and examine the homogeneous distribution of materials inside the polymer.

### *1.5.5 Transmission Electron Microscopy (TEM)*

To acquire information regarding the topographical, morphological and chemical compositions of the samples, transmission electron microscopy (TEM; JEOL JEM F200) has been used. Also,

TEM gives us information of the homogeneous distribution of nanoparticles inside a PVDF matrix.

### *1.5.6 X-ray Photoelectron Spectroscopy (XPS)*

X-ray photoelectron spectroscopy (XPS) has been performed to investigate the chemical and electronic state of atom inside synthesized material. Also, it gives us the information regarding the surface groups of materials and nanocomposites. In this thesis, X-ray Photoelectron Spectroscopy (XPS) analysis of samples has been performed with an Omicron Multiprobe (Omicron Nanotechnology GmbH) photoelectron spectrometer fitted with an EA125 hemispherical analyzer and a monochromatized Al $K_\alpha$ ($h\nu$: 1486.6 eV) source.

### *1.5.7 LCR Meter*

LCR meter (IM 3536 LCR Meter) has been used to measure the dielectric properties, ac conductivity, tangent loss and capacitance value of nanocomposites with changing the range of frequency from 20 Hz to 2 MHz. Along with this, the ac voltage of 1 V at room temperature is maintained throughout the experiment. Moreover, the dielectric constant ($k$) and ac conductivity ($\sigma_{ac}$) of the nanocomposites have been calculated by using following equations respectively,

$$k = C.d / \varepsilon_0 A \quad \text{..... (1.24)}$$

$$\sigma_{ac} = 2\pi f \varepsilon_0 k \tan\delta \quad \text{..... (1.25)}$$

Where, C represents the capacitance value, d is the thickness of the nanocomposite, A is the area of the nanocomposite and $\varepsilon_0$ is the free space permittivity, whose value will be $8.854 \times 10^{-12}$ $F.m^{-1}$.

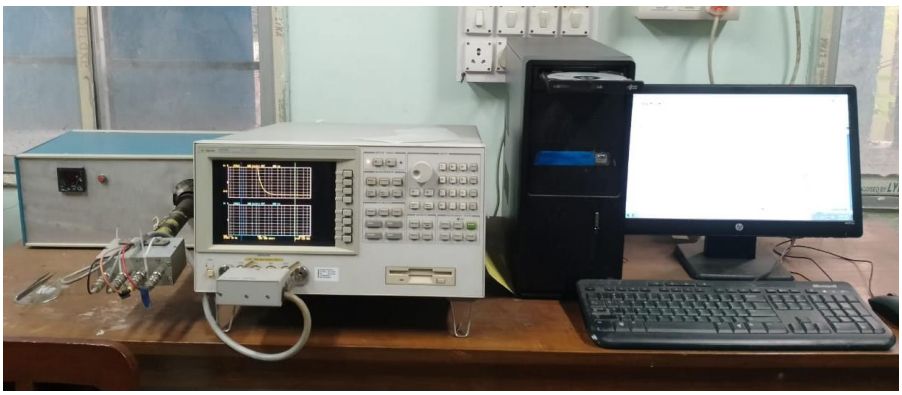

***Figure 1.17:*** *Digital snapshot of LCR meter.*

### *1.5.8 Thermal Gravimetric Analysis (TGA)*

To examine the temperature-dependent mass of the samples, thermal gravimetric analysis (TGA) has been performed by using TGA; TGA/SDTA851e, Mettler Toledo AG instrument.

***Figure 1.18:*** *Digital snapshot of TGA instrument.*

### *1.5.9 Surface Charge Analyzer*

The surface properties and distribution of pore size of synthesized nanoparticles have been investigated by using Automated Gas Sorption Analyzer, Autosorb iQ2, Quantachrome Instruments.

### *1.5.10 Universal Tensile Machine (UTM)*

Universal tensile machine (UTM) has been used to measure the tensile strength and Young's modulus of nanocomposites. To execute the measurement, the dimension of nanocomposites is kept at 1cm x 5cm. Also, strain rate of 5 mm/min is maintained throughout the measurement. Beside this, Tinius Olsen model: H50KS, UK model has been utilized in the UTM analysis.

### 1.5.11 Output Performance Analyzer

The open circuit voltage ($V_{OC}$) and short circuit current ($I_{SC}$) of the fabricated nanogenerator have been measured by digital storage oscilloscope (Keysight, Oscilloscope DSO-X 3012A) and Keysight, Electrometer B2985 under the application of mechanical energies.

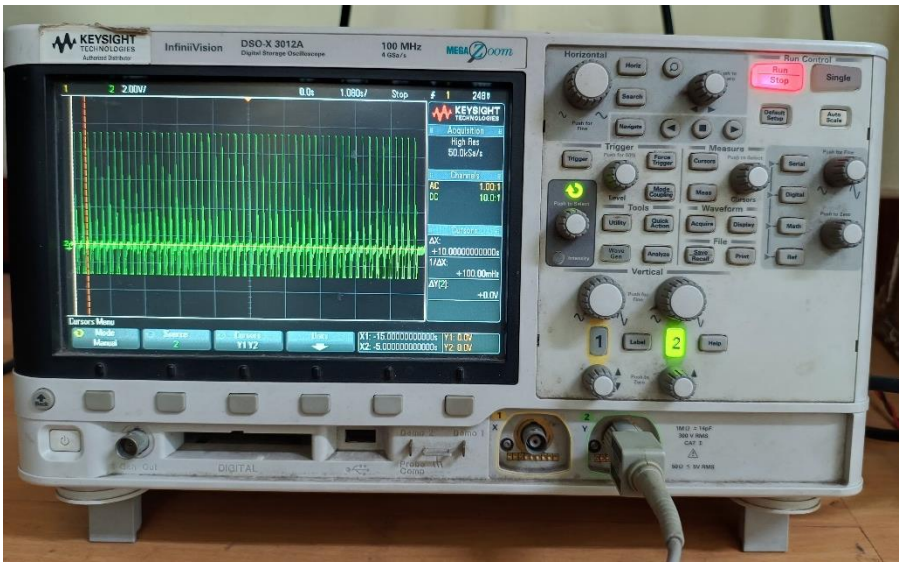


***Figure 1.19:*** *Digital image of digital storage oscilloscope (DSO).*

### 1.5.12 Wireless Communication system

The wireless communication system has been set up to monitor the output signal to our mobile or laptop, generated by the nanogenerator. For this, the device has been connected with the processing circuit to rectify the signal and then passed it to Arduino Uno. Thereafter, the signal has been transmitted to laptop or mobile through Bluetooth connection.

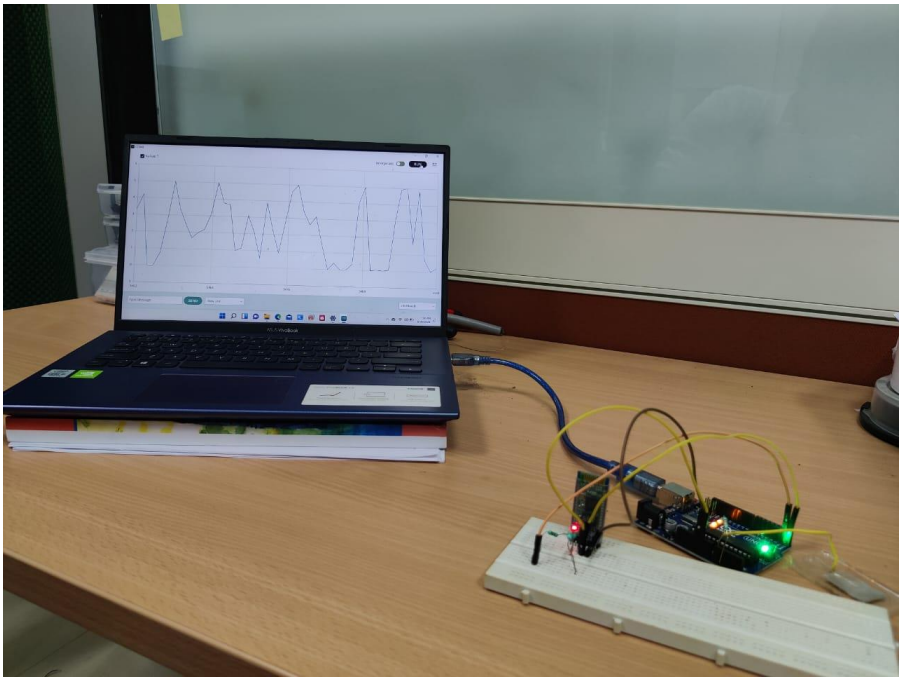

***Figure 1.20:*** *Pictorial representation of wireless communication system.*

## *1.6 Objectives*

With the increasing of global warming, conventional energy sources including coal, petroleum, natural gases etc. are limiting day by day. For this, human civilizations will face energy crisis in the upcoming days. Also, the demand of power in our daily life activities is elevating with the growing fashion of human population. Therefore, researchers are shifted their attention towards the alternative energy sources to solve these above mentioned problems. In comparison with other alternative energy sources, piezoelectric and triboelectric nanogenerators are the most promising and suitable choice, which has the ability to convert waste mechanical energy sources into electrical energy. Also, the self-powered property of these nanogenreators restricts the utilization of external power sources and makes the nanogenerators cost effective. Therefore, the primary objectives of this thesis work are to design the self-powered and wearable energy harvesting devices with the help of piezoelectric and triboelectric effect and utilize them in harvesting mechanical and biomechanical energy resources. To accomplish the objectives, natural piezoelectric material cotton pappus has been reinforced into PDMS polymer and fabricated the biocompatible and green piezoelectric nanogenerator, which has been further

utilized in electricity generation from mechanical and vibrational energy sources. Beside this, improvement of β-crystalline phase of PVDF polymer has been performed by incorporating the N-doped carbon dots and $Bi_2Se_3$. Also, we have utilized this β-crystalline phase in the designing process of piezoelectric nanogenerators. Thereafter, the capability of detecting different weights fallen on the device is also investigated. During the monitoring of output performance of PENGs, some problems including low sensitivity, lack of capability in detecting small scale energies, moderate output voltage and power density etc. are faced. For this, TENG has been introduced in this thesis work, which not only exhibits the colossal output voltage but also generates electricity from small scale energy sources. In fabrication of TENGs, PVA and human hand are used as positive triboelectric layer and PDMS and elecoflex are as negative tribolectric layers. Alongside, surface modification technique has been implemented in device designing process to improve the performance of the TENGs. Furthermore, 2D material ($MoTe_2$) has been used in charge recombination process inside the TENG, which reduces the charge loss inside the TENG and improve the output performance as well as sensitivity of the device. Also, piezo-tribo coupling effect has been used during the fabrication of TENG for elevating the output performance of the device. The utilization of these fabricated TENGs has been performed by monitoring the human physiological signals and detecting the artificial finger movements. Also, the realistic applications of PENGs and TENGs are investigated by charging capacitors and illuminating LEDs. Therefore, the high sensitivity and self-powered properties of fabricated energy harvesting devices open up the potential utilizations in the field of biomedical applications and human-machine interfaces.

## References

.


(1) Maduko, C. F.; Akuru, U. B. Future Trends on Global Energy Demand. ES4PG-2013 Conference Proceedings 2013, 217–223.

(2) Khan, K. A.; Hasan, M.; Islam, M. A.; Alim, M. A.; Asma, U.; Hassan, L.; Ali, M. H. A Study on Conventional Energy Sources for Power Production. Ijariie-Issn(O) 2018, 4, 214–228.

(3) Dresselhaus, M. S.; Thomas, I. . Dresselhaus. Nature 2001, 414, 332–337.

(4) De Marqui Junior, C.; Erturk, A.; Inman, D. J. An Electromechanical Finite Element Model for Piezoelectric Energy Harvester Plates. Journal of Sound and Vibration 2009, 327, 9–25.

(5) Dhar, A.; Kumar, N. S.; Khimani, M.; Al-Fatesh, A. S.; Ibrahim, A. A.; Fakeeha, A. H.; Bhadja, P.; Vekariya, R. L. Naturally Occurring Neem Gum: An Unprecedented Green Resource for Bioelectrochemical Flexible Energy Storage Device. International Journal of Energy Research 2020, 44, 913–924.

(6) Burhan, M.; Rehman, R. A.; Khan, B.; Kim, B. S. IoT Elements, Layered Architectures and Security Issues: A Comprehensive Survey. Sensors 2018, 18, 1–37.

(7) Shafique, K.; Khawaja, B. A.; Khurram, M. D.; Sibtain, S. M.; Siddiqui, Y.; Mustaqim, M.; Chattha, H. T.; Yang, X. Energy Harvesting Using a Low-Cost Rectenna for Internet of Things (IoT) Applications. IEEE Access 2018, 6, 30932–30941.

(8) Liu, L.; Shi, Q.; Ho, J. S.; Lee, C. Study of Thin Film Blue Energy Harvester Based on Triboelectric Nanogenerator and Seashore IoT Applications. Nano Energy 2019, 66, 104167.

(9) Yoon, S.; Carreon-Bautista, S.; Sanchez-Sinencio, E. An Area Efficient Thermal Energy Harvester with Reconfigurable Capacitor Charge Pump for IoT Applications. IEEE Transactions on Circuits and Systems II: Express Briefs 2018, 65, 1974–1978.

(10) Wang, Z. L.; Song, J. Piezoelectric Nanogenerators Based on Zinc Oxide Nanowire Arrays. Science 2006, 312, 242–246.

(11) Panda, P. K. Review: Environmental Friendly Lead-Free Piezoelectric Materials. Journal of Materials Science 2009, 44, 5049–5062.

(12) Fan, F. R.; Tian, Z. Q.; Lin Wang, Z. Flexible Triboelectric Generator. Nano Energy 2012, 1, 328–334.

(13) Hansen, B. J.; Liu, Y.; Yang, R.; Wang, Z. L. Hybrid Nanogenerator for Concurrently Harvesting Biomechanical and Biochemical Energy. ACS Nano 2010, 4, 3647–3652.

(14) Zheng, Q.; Shi, B.; Li, Z.; Wang, Z. L. Recent Progress on Piezoelectric and Triboelectric Energy Harvesters in Biomedical Systems. Advanced Science 2017, 4, 1–23.

(15) Chu, S.; Majumdar, A. Opportunities and Challenges for a Sustainable Energy Future. Nature 2012, 488, 294–303.

(16) Bai, P.; Zhu, G.; Lin, Z. H.; Jing, Q.; Chen, J.; Zhang, G.; Ma, J.; Wang, Z. L. Integrated Multilayered Triboelectric Nanogenerator for Harvesting Biomechanical Energy from Human Motions. ACS Nano 2013, 7, 3713–3719.

(17) Lou, Z.; Li, L.; Wang, L.; Shen, G. Recent Progress of Self-Powered Sensing Systems for Wearable Electronics. Small 2017, 13, 1–27.

(18) Jin, L.; Tao, J.; Bao, R.; Sun, L.; Pan, C. Self-Powered Real-Time Movement Monitoring Sensor Using Triboelectric Nanogenerator Technology. Scientific Reports 2017, 7, 1–6.

(19) Thakur, P.; Kool, A.; Hoque, N. A.; Bagchi, B.; Khatun, F.; Biswas, P.; Brahma, D.; Roy, S.; Banerjee, S.; Das, S. Superior Performances of in Situ Synthesized ZnO/PVDF Thin Film Based Self-Poled Piezoelectric Nanogenerator and Self-Charged Photo-Power Bank with High Durability. Nano Energy 2018, 44, 456–467.

(20) Das, N.; Sarkar, D.; Saikh, M. M.; Biswas, P.; Das, S.; Hoque, N. A.; Ray, P. P. Piezoelectric Activity Assessment of Size-Dependent Naturally Acquired Mud Volcano Clay Nanoparticles Assisted Highly Pressure Sensitive Nanogenerator for Green Mechanical Energy Harvesting and Body Motion Sensing. Nano Energy 2022, 102, 107628.

(21) Kim, W. G.; Kim, D. W.; Tcho, I. W.; Kim, J. K.; Kim, M. S.; Choi, Y. K. Triboelectric Nanogenerator: Structure, Mechanism, and Applications. ACS Nano 2021, 15, 258–287.

(22) Sáenz de Inestrillas, Á.; Camarena, F.; Bou Cabo, M.; Barreiro, J. M.; Reig, A. Design and Performance of a Metal-Shielded Piezoelectric Sensor. Sensors 2017, 17, 1–10.

(23) Hastings, G. W.; Mahmud, F. A. Electrical Effects in Bone. Journal of Biomedical Engineering 1988, 10, 515–521.

(24) Press, C.; Press, C. The Emergence of the Principle of Symmetry in Physics Author ( s ): SHAUL KATZIR Source : Historical Studies in the Physical and Biological Sciences. 2015, 35, 35–65.

(25) Elguero, J.; Alkorta, I. Polyhedra, Tiles and Graphene Defects: The Case of Tetraoctite. Mini-Reviews in Organic Chemistry 2022, 19, 138–145.

(26) Hoque, N. A.; Thakur, P.; Bala, N.; Kool, A.; Das, S.; Ray, P. P. Tunable Photoluminescence Emissions and Large Dielectric Constant of the Electroactive Poly(Vinylidene Fluoride–Hexafluoropropylene) Thin Films Modified with $SnO_2$ Nanoparticles . RSC Advances 2016, 6, 29931–29943.

(27) Mason, W. P. Piezoelectricity, Its History and Applications. Journal of the Acoustical Society of America 1981, 70, 1561–1566.

(28) Covaci, C.; Gontean, A. Piezoelectric Energy Harvesting Solutions: A Review. Sensors 2020, 20, 1–37.

(29) Ramadan, K. S.; Sameoto, D.; Evoy, S. A Review of Piezoelectric Polymers as Functional Materials for Electromechanical Transducers. Smart Materials and Structures 2014, 23 (3).

(30) Mishra, S.; Unnikrishnan, L.; Nayak, S. K.; Mohanty, S. Advances in Piezoelectric Polymer Composites for Energy Harvesting Applications: A Systematic Review. Macromolecular Materials and Engineering 2019, 304, 1–25.

(31) Chen, J.; Qiu, Q.; Han, Y.; Lau, D. Piezoelectric Materials for Sustainable Building Structures: Fundamentals and Applications. Renewable and Sustainable Energy Reviews 2019, 101, 14–25.

(32) Wang, Z. L. On Maxwell's Displacement Current for Energy and Sensors: The Origin of Nanogenerators. Materials Today 2017, 20, 74–82.

(33) Li, X.; Sun, M.; Wei, X.; Shan, C.; Chen, Q. 1D Piezoelectric Material Based Nanogenerators: Methods, Materials and Property Optimization. Nanomaterials 2018, 8 (4).

(34) Zaszczyńska, A.; Gradys, A.; Sajkiewicz, P. Progress in the Applications of Smart Piezoelectric Materials for Medical Devices. Polymers 2020, 12, 1–19.

(35) Luo, L.; Zhao, X.; Luo, H. Single Crystal PZN-PT, PMN-PT, PSN-PT and PIN-PT-Based Piezoelectric Materials. Advanced Piezoelectric Materials: Science and Technology 2010, 239–286.

(36) Mill, B. V.; Pisarevsky, Y. V. Langasite-Type Materials: From Discovery to Present State. Proceedings of the Annual IEEE International Frequency Control Symposium 2000, 133–144.

(37) Krempl, P.; Schjeinzer, G.; Wajlnofer, W. SENSORS ACTUiTORS A PHYSICAL Gallium Phosphate, GaP0 4 : A New Piezoelectric Crystal Material for High-Temperature Sensories. a 1997, 61, 361–363.

(38) Anton, S. R.; Sodano, H. A. A Review of Power Harvesting Using Piezoelectric Materials (2003-2006). Smart Materials and Structures 2007, 16 (3).

(39) Uchino, K. The Development of Piezoelectric Materials and the New Perspective; 2010.

(40) Maeder, M. D.; Damjanovic, D.; Setter, N. Lead Free Piezoelectric Materials. Journal of Electroceramics 2004, 13, 385–392.

(41) EGERTON, L.; DILLON, D. M. Piezoelectric and Dielectric Properties of Ceramics in the System Potassium—Sodium Niobate. Journal of the American Ceramic Society 1959, 42, 438–442.

(42) Xu, K.; Li, J.; Lv, X.; Wu, J.; Zhang, X.; Xiao, D.; Zhu, J. Superior Piezoelectric Properties in Potassium–Sodium Niobate Lead-Free Ceramics. Advanced Materials 2016, 28, 8519–8523.

(43) Damjanovic, D. Ferroelectric, Dielectric and Piezoelectric Properties of Ferroelectric Thin FIlms and Ceramics, D. Damjanovic, Rep. Prog. Physics, 1998.Pdf. Reports on Progress in Physics 1998, 61, 1267–1324.

(44) Kiat, J. M.; Kiat, J. M.; Uesu, Y.; Dkhil, B.; Matsuda, M.; Malibert, C.; Malibert, C.; Calvarin, G. Monoclinic Structure of Unpoled Morphotropic High Piezoelectric PMN-PT and PZN-PT Compounds. Physical Review B - Condensed Matter and Materials Physics 2002, 65, 641061–641064.

(45) Xu, S.; Yeh, Y. W.; Poirier, G.; McAlpine, M. C.; Register, R. A.; Yao, N. Flexible Piezoelectric PMN-PT Nanowire-Based Nanocomposite and Device. Nano Letters 2013, 13, 2393–2398.

(46) Choi, K. H.; Siddiqui, G. U.; Yang, B. su; Mustafa, M. Synthesis of $ZnSnO_3$ nanocubes and Thin Film Fabrication of ($ZnSnO_3$/PMMA) Composite through Electrospray Deposition. Journal of Materials Science: Materials in Electronics 2015, 26, 5690–5696.

(47) Sankar Ganesh, R.; Sharma, S. K.; Sankar, S.; Divyapriya, B.; Durgadevi, E.; Raji, P.; Ponnusamy, S.; Muthamizhchelvan, C.; Hayakawa, Y.; Kim, D. Y. Microstructure, Structural, Optical and Piezoelectric Properties of $BiFeO_3$ Nanopowder Synthesized from Sol-Gel. Current Applied Physics 2017, 17, 409–416.

(48) Bohuslav, M.; Hana, J.; Jiří, M.; Štěpán, J. Advanced Material-Technological Modelling of Complex Dynamic Thermomechanical Processes. Materials Science Forum 2010, 654–656, 1594–1597.

(49) Lemaire, E.; Moser, R.; Borsa, C. J.; Briand, D. Green Paper-Based Piezoelectronics for Sensors and Actuators. Sensors and Actuators, A: Physical 2016, 244, 285–291.

(50) Lemaire, E.; Ayela, C.; Atli, A. Eco-Friendly Materials for Large Area Piezoelectronics: Self-Oriented Rochelle Salt in Wood. Smart Materials and Structures 2018, 27 (2).

(51) Rajala, S.; Siponkoski, T.; Sarlin, E.; Mettänen, M.; Vuoriluoto, M.; Pammo, A.; Juuti, J.; Rojas, O. J.; Franssila, S.; Tuukkanen, S. Cellulose Nanofibril Film as a Piezoelectric Sensor Material. ACS Applied Materials and Interfaces 2016, 8, 15607–15614.

(52) Hoque, N. A.; Thakur, P.; Biswas, P.; Saikh, M. M.; Roy, S.; Bagchi, B.; Das, S.; Ray, P. P. Biowaste Crab Shell-Extracted Chitin Nanofiber-Based Superior Piezoelectric Nanogenerator. Journal of Materials Chemistry A 2018, 6, 13848–13858.

(53) Wu, J. Z.; Zhou, M. H.; Zhang, N. H. The Effect of Microscopic Attractive Interactions on Piezoelectric Coefficients of Nanoscale DNA Films and Its Resultant Mirocantilever-Based Biosensor Signals. Journal of Physics D: Applied Physics 2017, 50 (41).

(54) Xu, C.; Qu, T.; Zhang, X.; Qu, X.; Wang, N.; Zhang, Q.; Abdel-Magid, B.; Li, G. Enhanced Toughness and Thermal Conductivity for Epoxy Resin with a Core-Shell Structured Polyacrylic Modifier and Modified Boron Nitride. RSC Advances 2019, 9, 8654–8663.

(55) Liao, W. Q.; Tang, Y. Y.; Li, P. F.; You, Y. M.; Xiong, R. G. Competitive Halogen Bond

in the Molecular Ferroelectric with Large Piezoelectric Response. Journal of the American Chemical Society 2018, 140, 3975–3980.

(56) Zhang, J.; Chen, M.; Zhao, S.; Hu, S.; Shi, Z.; Cao, Y. ReliefF-Based EEG Sensor Selection Methods for Emotion Recognition. Sensors (Switzerland) 2016, 16, 1–15.

(57) García, Y.; Ruiz-Blanco, Y. B.; Marrero-Ponce, Y.; Sotomayor-Torres, C. M. Orthotropic Piezoelectricity in 2D Nanocellulose. Scientific Reports 2016, 6, 1–8.

(58) Alluri, N. R.; Saravanakumar, B.; Kim, S. J. Flexible, Hybrid Piezoelectric Film (BaTi(1-x)$ZrxO_3$)/PVDF Nanogenerator as a Self-Powered Fluid Velocity Sensor. ACS Applied Materials and Interfaces 2015, 7, 9831–9840.

(59) Reyes-Gasga, J.; Galindo-Mentle, M.; Brès, E.; Vargas-Becerril, N.; Orozco, E.; Rodríguez-Gómez, A.; García-García, R. Detection of the Piezoelectricity Effect in Nanocrystals from Human Teeth. Journal of Physics and Chemistry of Solids 2020, 136, 109140.

(60) Karan, S. K.; Maiti, S.; Paria, S.; Maitra, A.; Si, S. K.; Kim, J. K.; Khatua, B. B. A New Insight towards Eggshell Membrane as High Energy Conversion Efficient Bio-Piezoelectric Energy Harvester. Materials Today Energy 2018, 9, 114–125.

(61) Pi, Z.; Zhang, J.; Wen, C.; Zhang, Z. bin; Wu, D. Flexible Piezoelectric Nanogenerator Made of Poly(Vinylidenefluoride-Co-Trifluoroethylene) (PVDF-TrFE) Thin Film. Nano Energy 2014, 7, 33–41.

(62) Parangusan, H.; Ponnamma, D.; Al Ali Almaadeed, M. Flexible Tri-Layer Piezoelectric Nanogenerator Based on PVDF-HFP/Ni-Doped ZnO Nanocomposites. RSC Advances 2017, 7, 50156–50165.

(63) Parangusan, H.; Ponnamma, D.; Al-Maadeed, M. A. A. Stretchable Electrospun PVDF-HFP/Co-ZnO Nanofibers as Piezoelectric Nanogenerators. Scientific Reports 2018, 8, 1–11.

(64) Ramadoss, A.; Saravanakumar, B.; Lee, S. W.; Kim, Y. S.; Kim, S. J.; Wang, Z. L. Piezoelectric-Driven Self-Charging Supercapacitor Power Cell. ACS Nano 2015, 9, 4337–4345.

(65) Liu, Z. H.; Pan, C. T.; Lin, L. W.; Lai, H. W. Piezoelectric Properties of PVDF/MWCNT Nanofiber Using near-Field Electrospinning. Sensors and Actuators, A: Physical 2013, 193, 13–24.

(66) Serhan, M.; Sprowls, M.; Jackemeyer, D.; Long, M.; Perez, I. D.; Maret, W.; Tao, N.; Forzani, E. Total Iron Measurement in Human Serum with a Smartphone. AIChE Annual Meeting, Conference Proceedings 2019.

(67) Thakur, P.; Kool, A.; Hoque, N. A.; Bagchi, B.; Roy, S.; Sepay, N.; Das, S.; Nandy, P. Improving the Thermal Stability, Electroactive β Phase Crystallization and Dielectric Constant of NiO Nanoparticle/C-NiO Nanocomposite Embedded Flexible Poly(Vinylidene Fluoride) Thin Films. RSC Advances 2016, 6, 26288–26299.

(68) Roy, S.; Thakur, P.; Hoque, N. A.; Bagchi, B.; Sepay, N.; Khatun, F.; Kool, A.; Das, S. Electroactive and High Dielectric Folic Acid/PVDF Composite Film Rooted Simplistic Organic Photovoltaic Self-Charging Energy Storage Cell with Superior Energy Density and Storage Capability. ACS Applied Materials and Interfaces 2017, 9, 24198–24209.

(69) Thakur, P.; Kool, A.; Bagchi, B.; Hoque, N. A.; Das, S.; Nandy, P. Improvement of Electroactive β Phase Nucleation and Dielectric Properties of $WO_3 \cdot H_2O$ Nanoparticle Loaded Poly(Vinylidene Fluoride) Thin Films. RSC Advances 2015, 5, 62819–62827.

(70) Thakur, P.; Kool, A.; Bagchi, B.; Hoque, N. A.; Das, S.; Nandy, P. In Situ Synthesis of $Ni(OH)_2$ Nanobelt Modified Electroactive Poly(Vinylidene Fluoride) Thin Films: Remarkable Improvement in Dielectric Properties. Physical Chemistry Chemical Physics 2015, 17, 13082–13091.

(71) Koga, K.; Ohigashi, H. Piezoelectricity and Related Properties of Vinylidene Fluoride and Trifluoroethylene Copolymers. Journal of Applied Physics 1986, 59, 2142–2150.

(72) Pukada, E. History and Recent Progress in Piezoelectric Polymers. IEEE Transactions on Ultrasonics, Ferroelectrics, and Frequency Control 2000, 47, 1277–1290.

(73) Martins, P.; Lopes, A. C.; Lanceros-Mendez, S. Electroactive Phases of Poly(Vinylidene Fluoride): Determination, Processing and Applications. Progress in Polymer Science 2014, 39, 683–706.

(74) Bhavanasi, V.; Kumar, V.; Parida, K.; Wang, J.; Lee, P. S. Enhanced Piezoelectric Energy Harvesting Performance of Flexible PVDF-TrFE Bilayer Films with Graphene Oxide. ACS Applied Materials and Interfaces 2016, 8, 521–529.

(75) Lee, J. H.; Lee, K. Y.; Kumar, B.; Tien, N. T.; Lee, N. E.; Kim, S. W. Highly Sensitive Stretchable Transparent Piezoelectric Nanogenerators. Energy and Environmental Science 2013, 6, 169–175.

(76) Serhan, M.; Sprowls, M.; Jackemeyer, D.; Long, M.; Perez, I. D.; Maret, W.; Tao, N.; Forzani, E. Total Iron Measurement in Human Serum with a Smartphone. AIChE Annual Meeting, Conference Proceedings 2019.

(77) Roy, S.; Thakur, P.; Hoque, N. A.; Bagchi, B.; Sepay, N.; Khatun, F.; Kool, A.; Das, S. Electroactive and High Dielectric Folic Acid/PVDF Composite Film Rooted Simplistic Organic Photovoltaic Self-Charging Energy Storage Cell with Superior Energy Density and Storage Capability. ACS Applied Materials and Interfaces 2017, 9, 24198–24209.

(78) Thakur, P.; Kool, A.; Hoque, N. A.; Bagchi, B.; Roy, S.; Sepay, N.; Das, S.; Nandy, P. Improving the Thermal Stability, Electroactive β Phase Crystallization and Dielectric Constant of NiO Nanoparticle/C-NiO Nanocomposite Embedded Flexible Poly(Vinylidene Fluoride) Thin Films. RSC Advances 2016, 6, 26288–26299.

(79) Thakur, P.; Kool, A.; Bagchi, B.; Hoque, N. A.; Das, S.; Nandy, P. In Situ Synthesis of Ni(OH)2 Nanobelt Modified Electroactive Poly(Vinylidene Fluoride) Thin Films: Remarkable Improvement in Dielectric Properties. Physical Chemistry Chemical Physics

2015, 17, 13082–13091.

(80) Thakur, P.; Kool, A.; Bagchi, B.; Hoque, N. A.; Das, S.; Nandy, P. Improvement of Electroactive β Phase Nucleation and Dielectric Properties of WO3·H2O Nanoparticle Loaded Poly(Vinylidene Fluoride) Thin Films. RSC Advances 2015, 5, 62819–62827.

(81) Koga, K.; Ohigashi, H. Piezoelectricity and Related Properties of Vinylidene Fluoride and Trifluoroethylene Copolymers. Journal of Applied Physics 1986, 59, 2142–2150.

(82) Bhavanasi, V.; Kumar, V.; Parida, K.; Wang, J.; Lee, P. S. Enhanced Piezoelectric Energy Harvesting Performance of Flexible PVDF-TrFE Bilayer Films with Graphene Oxide. ACS Applied Materials and Interfaces 2016, 8, 521–529.

(83) Pukada, E. History and Recent Progress in Piezoelectric Polymers. IEEE Transactions on Ultrasonics, Ferroelectrics, and Frequency Control 2000, 47, 1277–1290.

(84) Martins, P.; Lopes, A. C.; Lanceros-Mendez, S. Electroactive Phases of Poly(Vinylidene Fluoride): Determination, Processing and Applications. Progress in Polymer Science 2014, 39, 683–706.

(85) Lee, J. H.; Lee, K. Y.; Kumar, B.; Tien, N. T.; Lee, N. E.; Kim, S. W. Highly Sensitive Stretchable Transparent Piezoelectric Nanogenerators. Energy and Environmental Science 2013, 6, 169–175.

(86) Kachroudi, A.; Basrour, S.; Rufer, L.; Sylvestre, A.; Jomni, F. Micro-Structured PDMS Piezoelectric Enhancement through Charging Conditions. Smart Materials and Structures 2016, 25 (10).

(87) Zaszczyńska, A.; Gradys, A.; Sajkiewicz, P. Progress in the Applications of Smart Piezoelectric Materials for Medical Devices. Polymers 2020, 12, 1–19.

(88) Lutkenhaus, J. L.; McEnnis, K.; Serghei, A.; Russell, T. P. Confinement Effects on Crystallization and Curie Transitions of Poly(Vinylidene Fluoride-Co-Trifluoroethylene). Macromolecules 2010, 43, 3844–3850.

(89) Wang, G.; Deng, Y.; Xiang, Y.; Guo, L. Fabrication of Radial ZnO Nanowire Clusters and Radial ZnO/PVDF Composites with Enhanced Dielectric Properties. Advanced Functional Materials 2008, 18, 2584–2592.

(90) Cao, X.; Ma, J.; Shi, X.; Ren, Z. Effect of $TiO_2$ Nanoparticle Size on the Performance of PVDF Membrane. Applied Surface Science 2006, 253, 2003–2010.

(91) Wang, Z.; Chen, X.; Li, K.; Bi, S.; Wu, C.; Chen, L. Preparation and Catalytic Property of PVDF Composite Membrane with Polymeric Spheres Decorated by Pd Nanoparticles in Membrane Pores. Journal of Membrane Science 2015, 496, 95–107.

(92) Wang, X.; Chen, C.; Liu, H.; Ma, J. Preparation and Characterization of PAA/PVDF Membrane-Immobilized Pd/Fe Nanoparticles for Dechlorination of Trichloroacetic Acid. Water Research 2008, 42, 4656–4664.

(93) Chen, X.; Wang, Z.; Bi, S.; Li, K.; Du, R.; Wu, C.; Chen, L. Combining Catalysis and Separation on a PVDF/Ag Composite Membrane Allows Timely Separation of Products during Reaction Process. Chemical Engineering Journal 2016, 295, 518–529.

(94) Wankhade, S. H.; Tiwari, S.; Gaur, A.; Maiti, P. PVDF–PZT Nanohybrid Based Nanogenerator for Energy Harvesting Applications. Energy Reports 2020, 6, 358–364.

(95) Shin, S. H.; Kim, Y. H.; Lee, M. H.; Jung, J. Y.; Nah, J. Hemispherically Aggregated BaTiO3 Nanoparticle Composite Thin Film for High-Performance Flexible Piezoelectric Nanogenerator. ACS Nano 2014, 8, 2766–2773.

(96) Mendes, S. F.; Costa, C. M.; Caparros, C.; Sencadas, V.; Lanceros-Méndez, S. Effect of Filler Size and Concentration on the Structure and Properties of Poly(Vinylidene Fluoride)/$BaTiO_3$ Nanocomposites. Journal of Materials Science 2012, 47, 1378–1388.

(97) Martins, P.; Costa, C. M.; Botelho, G.; Lanceros-Mendez, S.; Barandiaran, J. M.; Gutierrez, J. Dielectric and Magnetic Properties of Ferrite/Poly(Vinylidene Fluoride) Nanocomposites. Materials Chemistry and Physics 2012, 131, 698–705.

(98) Ghosh, S.; Bardhan, S.; Mondal, D.; Sarkar, D.; Roy, J.; Roy, S.; Basu, R.; Das, S. Natural Hematite-Based Self-Poled Piezo-Responsive Membrane for Harvesting Energy from Water Flow and Catalytic Removal of Organic Dye. Ceramics International 2023, 49, 14710–14718.

(99) Lund, A.; Gustafsson, C.; Bertilsson, H.; Rychwalski, R. W. Enhancement of β Phase Crystals Formation with the Use of Nanofillers in PVDF Films and Fibres. Composites Science and Technology 2011, 71, 222–229.

(100) Rani, P.; Ahamed, B.; Deshmukh, K. Dielectric and Electromagnetic Interference Shielding Properties of Zeolite 13X and Carbon Black Nanoparticles Based PVDF Nanocomposites. Journal of Applied Polymer Science 2021, 138, 1–10.

(101) Carabineiro, S. A. C.; Pereira, M. F. R.; Nunes-Pereira, J.; Silva, J.; Caparros, C.; Sencadas, V.; Lanceros-Méndez, S. The Effect of Nanotube Surface Oxidation on the Electrical Properties of Multiwall Carbon Nanotube/Poly(Vinylidene Fluoride) Composites. Journal of Materials Science 2012, 47, 8103–8111.

(102) Rahman, M. A.; Chung, G. S. Synthesis of PVDF-Graphene Nanocomposites and Their Properties. Journal of Alloys and Compounds 2013, 581, 724–730.

(103) Liang, H. Q.; Wu, Q. Y.; Wan, L. S.; Huang, X. J.; Xu, Z. K. Thermally Induced Phase Separation Followed by in Situ Sol-Gel Process: A Novel Method for PVDF/$SiO_2$ Hybrid Membranes. Journal of Membrane Science 2014, 465, 56–67.

(104) Biswas, P.; Hoque, N. A.; Thakur, P.; Saikh, M. M.; Roy, S.; Khatun, F.; Bagchi, B.; Das, S. Highly Efficient and Durable Piezoelectric Nanogenerator and Photo-Power Cell Based on CTAB Modified Montmorillonite Incorporated PVDF Film. ACS Sustainable Chemistry and Engineering 2019, 7, 4801–4813.

(105) Yang, Z.; Peng, H.; Wang, W.; Liu, T. Crystallization Behavior of Poly(ε-

Caprolactone)/Layered Double Hydroxide Nanocomposites. Journal of Applied Polymer Science 2010, 116, 2658–2667.

(106) Santos, J. P. F.; da Silva, A. B.; Arjmand, M.; Sundararaj, U.; Bretas, R. E. S. Nanofibers of Poly(Vinylidene Fluoride)/Copper Nanowire: Microstructural Analysis and Dielectric Behavior. European Polymer Journal 2018, 101, 46–55.

(107) Mandal, D.; Kim, K. J.; Lee, J. S. Simple Synthesis of Palladium Nanoparticles, β-Phase Formation, and the Control of Chain and Dipole Orientations in Palladium-Doped Poly(Vinylidene Fluoride) Thin Films. Langmuir 2012, 28, 10310–10317.

(108) Biswas, S.; Bhattacharya, S. Effect of Ag Nanoparticle Embedment on Electroactive Phase Nucleation of PVDF and PVDF-HFP under Non-Isothermal Condition: A Comparative Study. Thermochimica Acta 2017, 649, 69–81.

(109) Gregorio, R.; Cestari, M.; Bernardino, F. E. Dielectric Behaviour of Thin Films of β-PVDF/PZT and β-PVDF/$BaTiO_3$ Composites. Journal of Materials Science 1996, 31, 2925–2930.

(110) Mao, Y.; Zhao, P.; Mcconohy, G.; Yang, H.; Tong, Y.; Wang, X. Sponge-Like Piezoelectric Polymer Films for Scalable and Integratable Nanogenerators and Self-Powered Electronic Systems. 2014, 1–7.

(111) Fu, R.; Chen, S.; Lin, Y.; Zhang, S.; Jiang, J.; Li, Q.; Gu, Y. Crossmark. Materials Letters 2017, 187, 86–88.

(112) Tamang, A.; Ghosh, S. K.; Garain, S.; Alam, M.; Haeberle, J. DNA-Assisted β - Phase Nucleation and Alignment of Molecular Dipoles in PVDF Film: A Realization of Self-Poled Bioinspired Flexible Polymer Nanogenerator for Portable Electronic Devices. 2015.

(113) Online, V. A. Enhanced Wave Absorption of Nanocomposites Based on the Synthesized Complex Symmetrical CuS. 2013, 4685–4692.

(114) Li, H.; Zhang, Y.; Dai, H.; Tong, W.; Zhou, Y.; Zhao, J.; An, Q. A Self-Powered Porous ZnS/PVDF-HFP Mechanoluminescent Composite Film That Converts Human Movement into Eye-Readable Light. 2018, 5489–5495.

(115) Mitra, R.; Sheetal Priyadarshini, B.; Ramadoss, A.; Manju, U. Stretchable Polymer-Modulated PVDF-HFP/$TiO_2$ Nanoparticles-Based Piezoelectric Nanogenerators for Energy Harvesting and Sensing Applications. Materials Science and Engineering: B 2022, 286, 116029.

(116) Das, N. K.; Veeralingam, S.; Badhulika, S. Zinc Ferrite Nanoparticle-Based Wearable Piezoelectric Nanogenerators as Self-Powered Sensors to Monitor Human Motion. 2023.

(117) Veeralingam, S.; Gunasekaran, S. S.; Badhulika, S. MATERIALS CHEMISTRY FRONTIERS Bifunctional NiFe LDH as a Piezoelectric Nanogenerator and Asymmetric Pseudo-. 2022, 2297–2308.

(118) Sinha, C.; Mandal, D. Two-Dimensional MOF Modulated Fiber Nanogenerator for E Ff

Ective Acoustoelectric Conversion and Human Motion Detection. 2021.

(119) Yoon, C.; Ippili, S.; Jella, V.; Maria, A.; Jung, J.; Han, Y.; Yang, T.; Yoon, S.; Yoon, G. Nano Energy Synergistic Contribution of Flexoelectricity and Piezoelectricity towards a Stretchable Robust Nanogenerator for Wearable Electronics. Nano Energy 2022, 91, 106691.

(120) Zhou, Z.; Du, X.; Zhang, Z.; Luo, J.; Niu, S.; Shen, D. Nano Energy Interface Modulated 0-D Piezoceramic Nanoparticles / PDMS Based Piezoelectric Composites for Highly Efficient Energy Harvesting Application. Nano Energy 2021, 82, 105709.

(121) Li, Y.; Tong, W.; Yang, J.; Wang, Z.; Wang, D.; An, Q.; Zhang, Y. Electrode-Free Piezoelectric Nanogenerator Based on Carbon Black / Polyvinylidene Fluoride – Hexafluoropropylene Composite Achieved via Interface Polarization Effect. 2023, 457.

(122) Bharti, D. K.; Veeralingam, S.; Badhulika, S. Materials Horizons. 2022, 663–674.

(123) Lee, J.; Park, J. Y.; Cho, E. B.; Kim, T. Y.; Han, S. A.; Kim, T.; Liu, Y.; Kim, S. K.; Roh, C. J.; Yoon, H.; Ryu, H.; Seung, W.; Lee, J. S.; Lee, J.; Kim, S. Reliable Piezoelectricity in Bilayer WSe 2 for Piezoelectric Nanogenerators. 2017, 1606667, 1–7.

(124) Kyu, J.; Kim, S.; Jang, S.; Rang, Y.; Kim, S.; Chang, H.; Song, W.; Sook, S.; Lim, J.; An, K.; Myung, S. Nano Energy Tunable Piezoelectric Nanogenerators Using Fl Exoelectricity of Well-Ordered Hollow 2D $MoS_2$ Shells Arrays for Energy Harvesting. Nano Energy 2019, 61, 471–477.

(125) Du, X.; Zhou, Z.; Zhang, Z.; Yao, L. Porous , Multi-Layered Piezoelectric Composites Based on Highly Oriented PZT / PVDF Electrospinning Fibers for High-Performance Piezoelectric Nanogenerators. 2022, 11, 331–344.

(126) Wang, Z. L. Triboelectric Nanogenerators as New Energy Technology for Self-Powered Chemical Sensors. 2013,11, 9533–9557.

(127) Zi, Y.; Niu, S.; Wang, J.; Wen, Z.; Tang, W.; Wang, Z. L. The Performance of Triboelectric Nanogenerators. Nature Communications 2015.

(128) Niu, S.; Liu, Y.; Chen, X.; Wang, S.; Sheng, Y.; Lin, L.; Xie, Y.; Lin, Z. Theory of Freestanding Triboelectric- Layer-Based Nanogenerators. Nano Energy 2015, 12, 760–774.

(129) Niu, S.; Liu, Y.; Wang, S.; Lin, L.; Zhou, Y. S.; Hu, Y.; Wang, Z. L. Theoretical Investigation and Structural Optimization of Single-Electrode Triboelectric Nanogenerators. 2014, 3332–3340.

(130) Niu, S.; Liu, Y.; Wang, S.; Lin, L.; Zhou, Y. S.; Hu, Y.; Wang, Z. L. Theory of Sliding-Mode Triboelectric Nanogenerators. 2013, 6184–6193.

(131) Shafeek, S.; Luo, J. Nanogenerators for Self -Powered Sensors. 2016 5th International Conference on Electronic Devices, Systems and Applications (ICEDSA) 2016, 1–4.

(132) Niu, S.; Lin, Z. Theoretical Systems of Triboelectric Nanogenerators. Nano Energy 2015, 14, 161–192.

(133) Pan, S.; Zhang, Z. Fundamental Theories and Basic Principles of Triboelectric Effect : A Review. 2019, 7, 2–17.

(134) Iversen, P.; Lacks, D. J. Short Communication A Life of Its Own : The Tenuous Connection between Thales of Miletus and the Study of Electrostatic Charging. Journal of Electrostatics 2012, 70, 309–311.

(135) Zheng, L.; Lin, Z.; Cheng, G.; Wu, W.; Wen, X.; Lee, S.; Lin, Z. Silicon-Based Hybrid Cell for Harvesting Solar Energy and Raindrop Electrostatic Energy. Nano Energy 2014, 9, 291–300.

(136) Wang, N.; Yang, D.; Zhang, W.; Feng, M.; Li, Z.; Ye, E.; Loh, X. J.; Wang, D. Deep Trap Boosted Ultrahigh Triboelectric Charge Density in Nanofibrous Cellulose-Based Triboelectric Nanogenerators. 2023.

(137) Pandey, P.; Thapa, K.; Prasad, G.; Seo, M.; Hoon, K.; Kim, S.; Inn, J. Metal-Organic Frameworks-Based Triboelectric Nanogenerator Powered Visible Light Communication System for Wireless Human-Machine Interactions. Chemical Engineering Journal 2023, 452, 139209.

(138) Venkatesan, M.; Chandrasekar, J.; Liang, F.; Lin, W.; Chen, W.; Cho, C.; Chen, Y.; Lee, W.; Su, C.; Zhou, Y.; Lai, Y.; Kuo, C. Nano Energy Surface-Enhanced Fully Nanofiber-Based Self-Cleanable Ultraviolet Resistive Triboelectric Energy Harvester for Wearable Smart Garments. Nano Energy 2023, 113, 108556.

(139) Shao, Y.; Feng, C.; Deng, B.; Yin, B.; Yang, M. Nano Energy Facile Method to Enhance Output Performance of Bacterial Cellulose Nanofiber Based Triboelectric Nanogenerator by Controlling Micro-Nano Structure and Dielectric Constant. Nano Energy 2019, 62, 620–627.

(140) Zhang, Z.; Bai, Y.; Xu, L.; Zhao, M.; Shi, M.; Lin, Z. Nano Energy Triboelectric Nanogenerators with Simultaneous Outputs in Both Single-Electrode Mode and Freestanding-Triboelectric-Layer Mode. Nano Energy 2019, 66, 104169.

(141) Ankanahalli, S.; Farheen, R.; Muktar, S.; Bananakere, C.; Wang, J.; Guan, S. Nano Energy Single-Electrode Triboelectric Nanogenerator Based on Economical Graphite Coated Paper for Harvesting Waste Environmental Energy. Nano Energy 2019, 66, 104141.

(142) Yang, Y.; Zhang, H.; Chen, J.; Jing, Q.; Zhou, Y. S.; Wen, X.; Wang, Z. L. Single-Electrode-Based Sliding Triboelectric Nanogenerator for Self-Powered Displacement. 2013, 8, 7342–7351.

(143) Cui, C.; Wang, X.; Yi, Z.; Yang, B.; Wang, X.; Chen, X.; Liu, J. Flexible Single-Electrode Triboelectric Nanogenerator and Body Moving Sensor Based on Porous Na 2 $CO_3$ / Polydimethylsiloxane Film. 2018.

(144) Chiu, C.; Chen, S.; Pao, Y.; Huang, M.; Lin, Z. A Smart Glove with Integrated Triboelectric Nanogenerator for Self-Powered Gesture Recognition and Language Expression. Science and Technology of Advanced Materials 2019, 20, 964–971.

(145) Jao, Y.; Yang, P.; Chiu, C.; Lin, Y.; Chen, S. Nano Energy Full Paper A Textile-Based Triboelectric Nanogenerator with Humidity-Resistant Output Characteristic and Its Applications in Self-Powered Healthcare Sensors. Nano Energy 2018, 50, 513–520.

(146) Khandelwal, G.; Prashanth, N.; Joseph, M.; Alluri, N. R.; Kim, S. Enhancing Hydrophobicity of Starch for Biodegradable Material- Based Triboelectric Nanogenerators. 2021, 1–7.

(147) Hao, S.; Jiao, J.; Chen, Y.; Lin, Z.; Cao, X. Nano Energy Natural Wood-Based Triboelectric Nanogenerator as Self-Powered Sensing for Smart Homes and Floors. Nano Energy 2020, 75, 104957.

(148) Zhao, S.; Wang, J.; Du, X.; Wang, J.; Cao, R.; Yin, Y.; Zhang, X.; Yuan, Z.; Xing, Y.; Pui, D. Y. H.; Li, C. All-Nano Fi Ber-Based Ultralight Stretchable Triboelectric Nanogenerator for Self-Powered Wearable Electronics. 2018.

(149) Rana, S. M. S.; Rahman, M. T.; Salauddin, M.; Sharma, S.; Maharjan, P.; Bhatta, T.; Cho, H.; Park, C.; Park, J. Y. Electrospun PVDF-TrFE/MXene Nano Fi Ber Mat-Based Triboelectric Nanogenerator for Smart Home Appliances. 2021.

(150) Luo, X.; Zhu, L.; Wang, Y.; Li, J.; Nie, J.; Wang, Z. L. A Flexible Multifunctional Triboelectric Nanogenerator Based on MXene / PVA Hydrogel. 2021, 2104928, 1–9.

(151) Rahman, M. T.; Rahman, S.; Kumar, H.; Kim, K.; Kim, S. Metal-Organic Framework Reinforced Highly Stretchable and Durable Conductive Hydrogel-Based Triboelectric Nanogenerator for Biomotion Sensing and Wearable Human-Machine Interfaces. 2023, 2303471, 1–13.

(152) Zhang, H.; Zhang, D.; Wang, Z.; Xi, G.; Mao, R.; Ma, Y.; Wang, D.; Tang, M.; Xu, Z.; Luan, H. Ultrastretchable , Self-Healing Conductive Hydrogel-Based Triboelectric Nanogenerators for Human − Computer Interaction. 2023.

(153) Xia, K.; Xu, Z.; Hong, Y.; Wang, L. Materials Today Sustainability A Free- Fl Oating Structure Triboelectric Nanogenerator Based on Natural Wool Ball for Offshore Wind Turbine Environmental Monitoring. 2023, 24.

(154) Shi, X.; Wei, Y.; Yan, R.; Hu, L.; Zhi, J.; Tang, B.; Li, Y. Nano Energy Leaf Surface-Microstructure Inspired Fabrication of Fish Gelatin-Based Triboelectric Nanogenerator. Nano Energy 2023, 109, 108231.

(155) Mohana, G.; Wu, C.; Gebeyehu, K.; Umapathi, R.; Roi, C.; Jose, M. Nano Energy Acoustic-Electric Conversion and Triboelectric Properties of Nature-Driven CF-CNT Based Triboelectric Nanogenerator for Mechanical and Sound Energy Harvesting. Nano Energy 2023, 108, 108211.

(156) Saqib, Q. M.; Khan, M. U.; Song, H.; Chougale, M. Y.; Shaukat, R. A.; Kim, J.; Bae, J.;

Choi, M. J.; Kim, S. C.; Kwon, O.; Bermak, A. Natural Hierarchically Structured Highly Porous Tomato Peel Based Tribo- and Piezo-Electric Nanogenerator for Efficient Energy Harvesting. Advanced Sustainable Systems 2021, 5, 1–10.

(157) Cherumannil Karumuthil, S.; Rajeev, S. P.; Varghese, S. Piezo-Tribo Nanoenergy Harvester Using Hybrid Polydimethyl Siloxane Based Nanocomposite. Nano Energy 2017, 40, 487–494.

(158) Singh, H. H.; Khare, N. Flexible ZnO-PVDF/PTFE Based Piezo-Tribo Hybrid Nanogenerator. Nano Energy 2018, 51, 216–222.

(159) Sun, H.; Zhao, Y.; Wang, C.; Zhou, K.; Yan, C.; Zheng, G.; Huang, J.; Dai, K.; Liu, C.; Shen, C. Ultra-Stretchable, Durable and Conductive Hydrogel with Hybrid Double Network as High Performance Strain Sensor and Stretchable Triboelectric Nanogenerator. Nano Energy 2020, 76, 105035.

(160) Qin, Y.; Mo, J.; Liu, Y.; Zhang, S.; Wang, J.; Fu, Q.; Wang, S.; Nie, S. Stretchable Triboelectric Self-Powered Sweat Sensor Fabricated from Self-Healing Nanocellulose Hydrogels. 2022, 2201846, 1–10.

(161) Suktep, N.; Pongampai, S.; Pakawanit, P.; Noisak, J.; Bongkarn, T.; Charoonsuk, T.; Vittayakorn, N. Silk Fibroin/Amino Acid Hybrid Organic Piezoelectric-Triboelectric Nanogenerator. Integrated Ferroelectrics 2023, 238, 101–114.

(162) Chai, B.; Shi, K.; Zou, H.; Jiang, P.; Wu, Z.; Huang, X. Conductive Interlayer Modulated Ferroelectric Nanocomposites for High Performance Triboelectric Nanogenerator. Nano Energy 2022, 91, 106668.

(163) Singh, H. H.; Khare, N. Improved Performance of Ferroelectric Nanocomposite Flexible Film Based Triboelectric Nanogenerator by Controlling Surface Morphology, Polarizability, and Hydrophobicity. Energy 2019, 178, 765–771.

(164) Singh, V.; Singh, B. MoS2-PVDF/PDMS Based Flexible Hybrid Piezo-Triboelectric Nanogenerator for Harvesting Mechanical Energy. Journal of Alloys and Compounds 2023, 941, 168850.

(165) Zheng, J.; Yu, Z.; Wang, Y.; Fu, Y.; Chen, D.; Zhou, H. Acoustic Core-Shell Resonance Harvester for Application of Artificial Cochlea Based on the Piezo-Triboelectric Effect. ACS Nano 2021, 15, 17499–17507.

# Development of a Sustainable and Biodegradable Sonchus asper Cotton Pappus Based Piezoelectric Nanogenerator for Instrument Vibration and Human Body Motion Sensing with Mechanical Energy Harvesting Applications

Chapter 2

## 2.1 Introduction

To mitigate the utilization of conventional power sources such as firewood, fossils fuels etc., energy harvesting from existing natural systems has increased interest in the development of self-powered biocompatible and handheld electronic gadgets such as mobile phones, roll-up displays, implantable medical equipments, actuators, sensors, and portable electronic devices.[1–7] For low-energy devices, bio-based materials are become the most promising alternatives over regular rechargeable batteries.[8,9] Nowadays, piezoelectric nanogenerators (PENGs) and triboelectric nanogenerators (TENGs) have been identified as potential green energy harvesting devices, which can harvest electrical energy from various natural and artificial mechanical energy sources including human body movement, water flow, airflow, vibrations, and rotations.[5,10–23] The triboelectric nanogenerator (TENG) has been emerged as a newly evolved energy harvesting device for transforming mechanical energy into electrical power due to combine effect of contact electrification and electrostatic induction. Also, the high efficiency, low cost, easy availability, and eco-friendliness properties assist it in harnessing small mechanical energy and large-scale energy as well.[24,25]

Recently, PENGs have been attracted additional interest of scientists for their flexibility, mechanical durability, high performance, sensitivity, etc.[22,23,26] To upgrade PENGs, various piezoelectric ceramic and metal oxide materials such as ZnO, PMN−PT, (Na, K)-$NbO_3$, $BaTiO_3$, and PZT[27–30] have been used. Apart from the piezoelectric ceramic and metal oxide nanomaterials, certain polymers such as polyvinylidene fluoride (PVDF),[31] its copolymers with trifluoroethylen [P(VDF-TrFE)],[32] and poly(vinlyacetate) (PVAc)[33] also show high piezoelectric properties. Beside this, the above mentioned piezoelectric materials have some limitations because of their toxicity, high cost, non-biodegradability, and breakability, along with the lengthy and difficult synthesis process.[5] To address these problems, it is necessary to design devices using biodegradable, low-cost, and flexible materials for upcoming days. Therefore, amply available natural and nontoxic bio-piezoelectric materials have been attracted more interest in the development of eco-friendly smart devices.[34-40] Many bio-based PENGs, using a virus,[41] fish scale,[42] fish bladder,[43] cellulose,[44] paper-$BaTiO_3$-bacterial cellulose,[45] cellulose-$BaTiO_3$,[46] bio-waste crab shell,[6]and bio-waste onion skin[5] as piezoelectric materials, have been studied for harnessing green energy.

Recently, bio-waste material based PENGs have been reported with comparatively low output performances. For example, Maiti et al.[5] fabricates an onion skin based PENG that shows an output voltage of 18 V, short circuit of 166 nA, and instantaneous power density of 1.7 μW $cm^{-2}$. A fish scale based PENG with an output voltage of 10 V and a short circuit current of 51 nA has been reported by Ghosh and Mandal.[42] Owing to cost-effectiveness and recyclability, bio-waste materials have been attracted many researchers in energy harvesting applications. Thus, we have designed a simple and cost-effective bio-waste material based piezoelectric nanogenerator with high output performance, flexibility, high durability, and non-toxicity.

The environment-friendly Sonchus asper (SA) is the strongest natural polymer fiber.[47] SA is known to possess diuretic, refrigerant, sedative, and antiseptic properties and is mainly used in medical treatment.[48] Various chemical studies exposed the presence of ascorbic acid, carotenoids, and fatty acids in SA.[49] Also, the highly crystalline SA pappus forms stress-induced polarization and generates piezoelectricity.

In our study, a PDMS/SA microfiber thin film based piezoelectric nanogenerator (SPENG) has been fabricated for harvesting energy from a small amount of mechanical work such as walking, talking, bending, stretching, pulse vibration, and finger imparting. SA pappus is chosen as the key component of SPENG for its biocompatible, biodegradable, nontoxic, robust, sustainable, and renewable properties. The PDMS/SA pappus film based PENG, named SPENG, shows a maximum output voltage ($V_{OC}$) of 81.2 V and a short circuit current ($I_{SC}$) of 1.0 μA, with an instantaneous power density of 182.06 μW $cm^{-3}$ during continuous finger impartation. Moreover, the fabricated PENG has the capability of producing output voltage even in the case of low pressure of heart beats and pulses. The study indicates the prospect of the nanogenerator SPENG as a green and portable energy harvester to power up portable electronic devices. Furthermore, after proper improvisation, the fabricated nanogenerator may be used as an energy supply for pacemakers and other types of health care devices.

## *2.2 Materials and methods*

### *2.2.1 Purification of Sonchus asper (SA) Cotton Pappus*

Sonchus asper (SA) cotton pappus was collected from the Jadavpur University campus (Kolkata, India). Collected cotton fibers were washed with deionized water and dried at 100 °C for 4 h. The cotton was further purified by 100 mL of hydrogen peroxide (Merck India) and 100 mL of acetic acid (Alfa Aesar) at 80 °C for 24 h to eliminate the chemicals. Finally, the samples were washed several times with deionized water and dried overnight (15 h) at 100 °C.

### *2.2.2 Fabrication of Piezoelectric Nanogenerator*

The device has been fabricated by polydimethylsiloxane (PDMS), SA, aluminum electrodes, and copper wires. Two percent of SA pappus was mixed thoroughly with 2 g of PDMS (Sylgard 184, Dow Corning, ratio of 10:1) into a rectangular plastic mold with a dimension of 5 cm X 3 cm. To make the bubble-free composite, the solution was kept for 15 min under vacuum. After getting the bubble-free solution, the polymer composite was kept at 60 °C in a hot air oven for 15 min to get the polymer/SA fiber film (thickness 0.59 mm). Two aluminum electrodes (dimension 3.6 cm X 2.1 cm) both connected with 15 cm long copper wires were attached to the wide sides of the composite film. Finally, the assembly of the thin film along with the attached electrode was encapsulating the assembly with PDMS. Figure 2.1(a) shows the schematic representation of device (SPENG) fabrication procedures. The digital photograph of the PENG and its flexibility are represented in Figure 2.1(b) to (d).

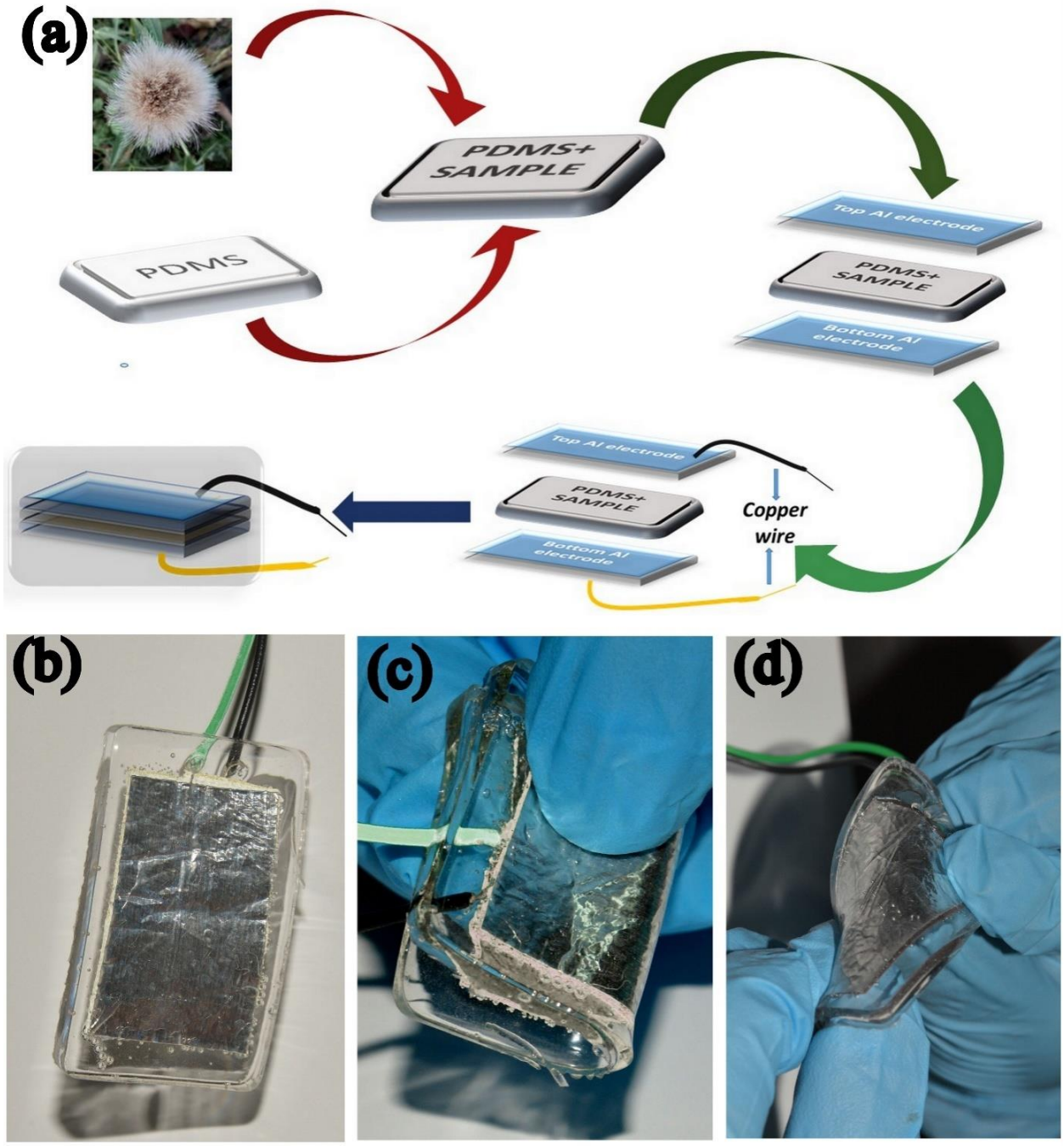


***Figure 2.1:*** *(a) Schematic representation of SPENG fabrication procedure, (b)-(d) digital photograph of SPENG and flexibility representation of the fabricated device.*

Moreover, the X-ray diffraction pattern and FESEM images of cotton pappus have been included in the figure 2.2. FESEM images are showing the fiber like morphology of SA cotton pappus in

the figure 2.2(a) and (b). The X-ray diffraction pattern confirms the peaks of SA cotton pappus at $2\theta = 13.3^0$, $22.5^0$ which is shown in the figure 2.2(c).

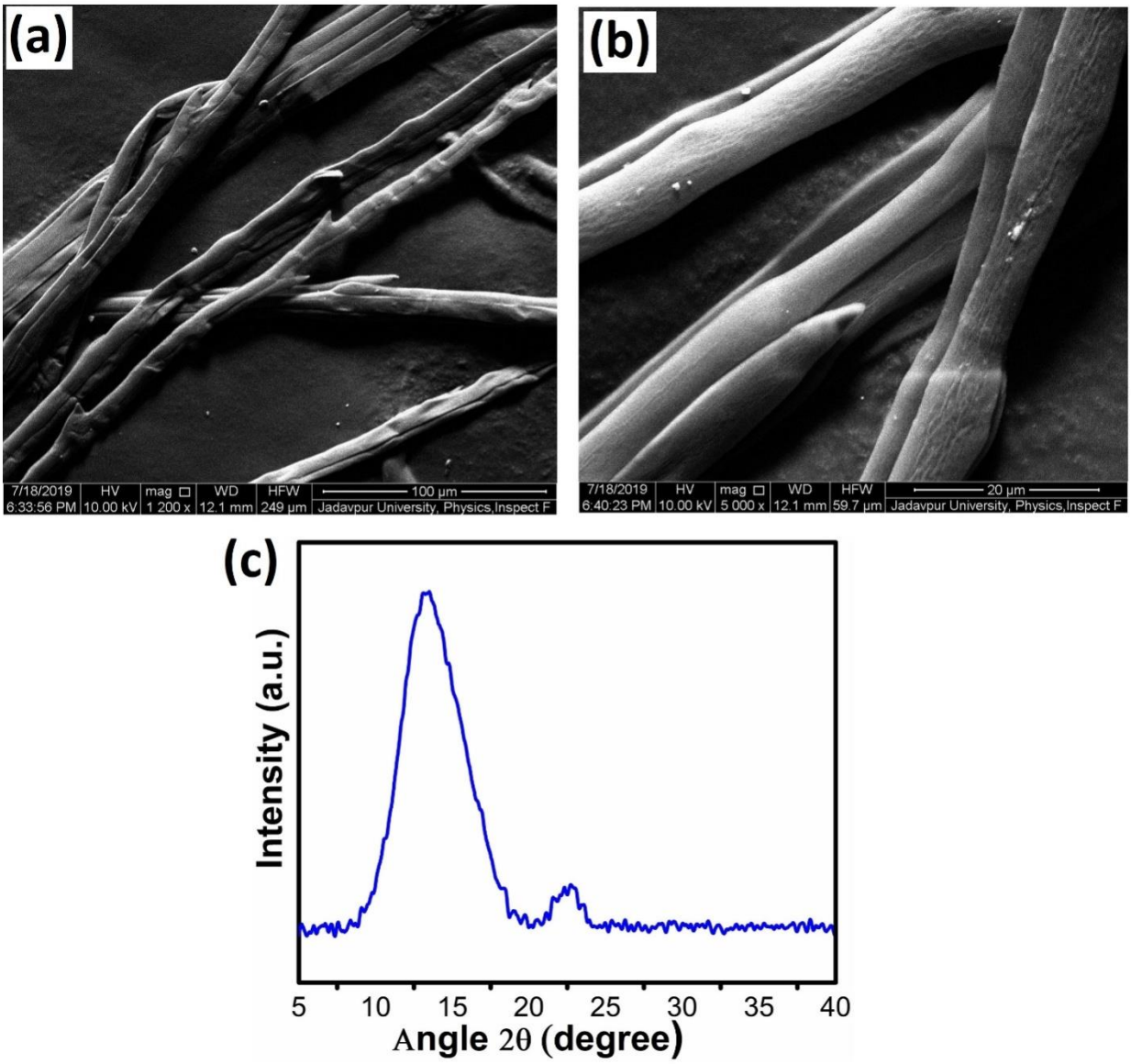


***Figure 2.2:*** *(a),(b) FESEM images of SA cotton pappus and (c) X-ray diffraction pattern of SA cotton pappus.*

## 2.3 Results and discussions

### 2.3.1 Output Performance

The open circuit output voltage ($V_{OC}$) and short circuit current ($I_{SC}$) generation through human finger imparting and releasing of axial force of ~ 13.5 N with ~ 5 to 6 Hz frequency are depicted in figure 2.3(a) and 2.3(b). Different output voltages have been generated by the SPENG depending on the application of various forces and frequencies. We have studied the voltage output performance of the SPENG by applying uniform force of 5 N under the variation of frequency ranging from 2 Hz to 10 Hz by using self-designed instrument (from Ocean college, Zhejiang University, PR China). With increasing frequency of the applied forces, the output performance ($V_{OC}$) increases gradually from ~ 7.5 V at 2 Hz to ~ 36 V at 10 Hz (Figure 2.3(c)).The output voltage of the SPENG is depended on the impedance and applied strain frequency. Even at low pressure finger impartation, the device shows high sensitivity. The maximum output voltage (observed by Keysight, Oscilloscope DSO-X 3012A) and short circuit current (recorded by Keysight, Electrometer B2985) of the SPENG are $V_{OC}$ ~ 81.2 V and $I_{SC}$ ~ 1.0µA respectively as shown in the Figures 2.3(a) and 2.3(b). It is evident from the figures that the values of both $V_{OC}$ and $I_{SC}$ are non-uniform in nature, which differs slightly for periodic pressing and releasing by finger. Such variation is raised due to the manual inconsistency of the applied strain on the energy scavenging devices during finger impartation. The enlarged view and working process of the nature of growth and decay of $V_{OC}$ for two successive cycles, generated by instrument impartation at 10 Hz frequency is shown in the figure 2.3(d). The highest positive peak is obtained when the strain has been applied. After withdrawal of the strain, the device recovers its original state and consequently negative peak appears. The output performance of SPENG is greater than any other previously reported such bio-materials-based devices, given in table form in Table 2.1.

***Table 2.1:*** *Comparing the output performance and power density of our fabricated PENG (SPENG) with the previously reported bio-based PENGs.*

| PENG based on Bio materials | Force | Short circuit current | Open circuit Voltage | Power density |
|---|---|---|---|---|
| ***Flexible ZnO–Cellulose Nanocomposite for Multisource Energy Conversion[57]*** | *Bath Sonication* | *1.25μA* | *0.08V* | *0.12μw/cm$^2$* |
| ***Flexible piezoelectric nanogenerators based on a fiber/ZnO nanowires/paper hybrid structure for energy harvesting[58]*** | *Not supplied* | *0.40-0.52 nA* | *17 mV* | *0.0002μW/cm$^2$* |
| ***Microfibre–nanowire hybrid structure for energy scavenging[59]*** | *Not supplied* | *4 nA* | *3mV* | *76mW/m$^2$* |
| ***Virus-based piezoelectric energy generation[60]*** | *34 N* | *6nA* | *0.4V* | *Not supplied* |
| ***Novel Piezoelectric Paper-Based Flexible Nanogenerators Composed of BaTiO3 Nanoparticles and Bacterial Cellulose[61]*** | *0.1 MPa* | *1.14μA* | *14V* | *0.64μW/cm$^2$* |
| ***High-performance bio-piezoelectric nanogenerator made with fish scale[62]*** | *0.17 MPa* | *1.5μA* | *4V* | |
| ***Enhanced electromechanical behavior of*** | *14 N* | *1.5μA* | *500mV* | *0.36μW/cm$^2$* |

| | | | | |
|---|---|---|---|---|
| ***cellulose film by zinc oxide nanocoating and its vibration energy harvesting[63]*** | | | | |
| ***Bioinspired piezoelectric nanogenerators based on vertically aligned phage nanopillars[64]*** | *30 N* | *9.5nA* | *140.8mV* | *0.3nW* |
| ***Efficient natural piezoelectric nanogenerator: Electricity generation from fish swim bladder[65]*** | *~1.4MPa* | *51nA* | *10V* | *0.23μW/cm$^2$* |
| ***Bio-waste onion skin as an innovative nature-driven piezoelectric material with high energy conversion efficiency[66]*** | *34 kPa* | *166nA* | *18V* | *1.7μW/cm$^2$* |
| ***Bio-assembled, piezoelectric prawn shell made selfpowered wearable sensor for noninvasive physiological signal monitoring[67]*** | *5.2 kPa* | *1nA* | *4V* | *0.041μW/cm$^2$* |
| ***Nature driven spider silk as high energy conversion efficient biopiezoelectric Nanogenerator[68]*** | | *0.68μA* | *21.3V* | *4.56μW/cm$^2$* |

| | | | | |
|---|---|---|---|---|
| ***A new insight towards eggshell membrane as high energy conversion efficient bio-piezoelectric energy harvester***[69] | *81.6kPa* | *1.45μA* | *26.4V* | *238.17μW/cm$^3$* |
| ***Biowaste crab shell-extracted chitin nanofiberbased superior piezoelectric nanogenerator***[70] | *27.5N* | *1.9μA* | *49V* | *6600μW/cm$^3$* |
| *$CsPbBr_3$ Perovskite Nanocrystals and pvdf based piezoelectric nanogenerator.*[71] | *Pressing* | *170 μAcm$^{-2}$* | *103V* | - |
| ***Silver-doped zinc oxide nanorods piezoelectric nanogenerator on cotton fabric.***[72] | *3 kgf* | *1.16 μA* | *2.28 V* | *1.45 mWcm$^{-2}$* |
| ***Piezoelectric PZT Thin Film Nanogenerator on Plastic Substrates.***[73] | *Periodical bending* | *150 μA·cm$^{-2}$* | *200V* | - |
| ***Our present work*** | ***13.5N*** | ***1.0μA*** | ***81.2V*** | ***182.06μW/cm$^3$*** |

The fabricated device has also been tested by bending and twisting and the output voltage performance is recorded. But no remarkable voltage generation is found, proposing that there has negligible triboelectric effect. Also switching polarity data have been taken and represented in figure 2.4. Recently Lee et al.[44] presents a virus-based PENG with an output voltage of ~ 0.4 V and current of ~ 4 nA, Ghosh et al.[46] designs a piezoelectric energy harvester with a fish swim bladder which shows output voltage of ~ 10 V. Maiti et al. also reports an output voltage ($V_{oc}$) of

18 V and a short circuit current of 166 nA in case of onion skin based PENG. Hoque et al.[6] also fabricates a bio-waste crab shell chitin nanofiber-based PENG with output voltage ~ 49 V and short circuit current ~ 1.9 μA. Therefore, the output performance of SA pappus based piezoelectric energy harvester (SPENG) is definitely better than previously reported similar bio-based devices.

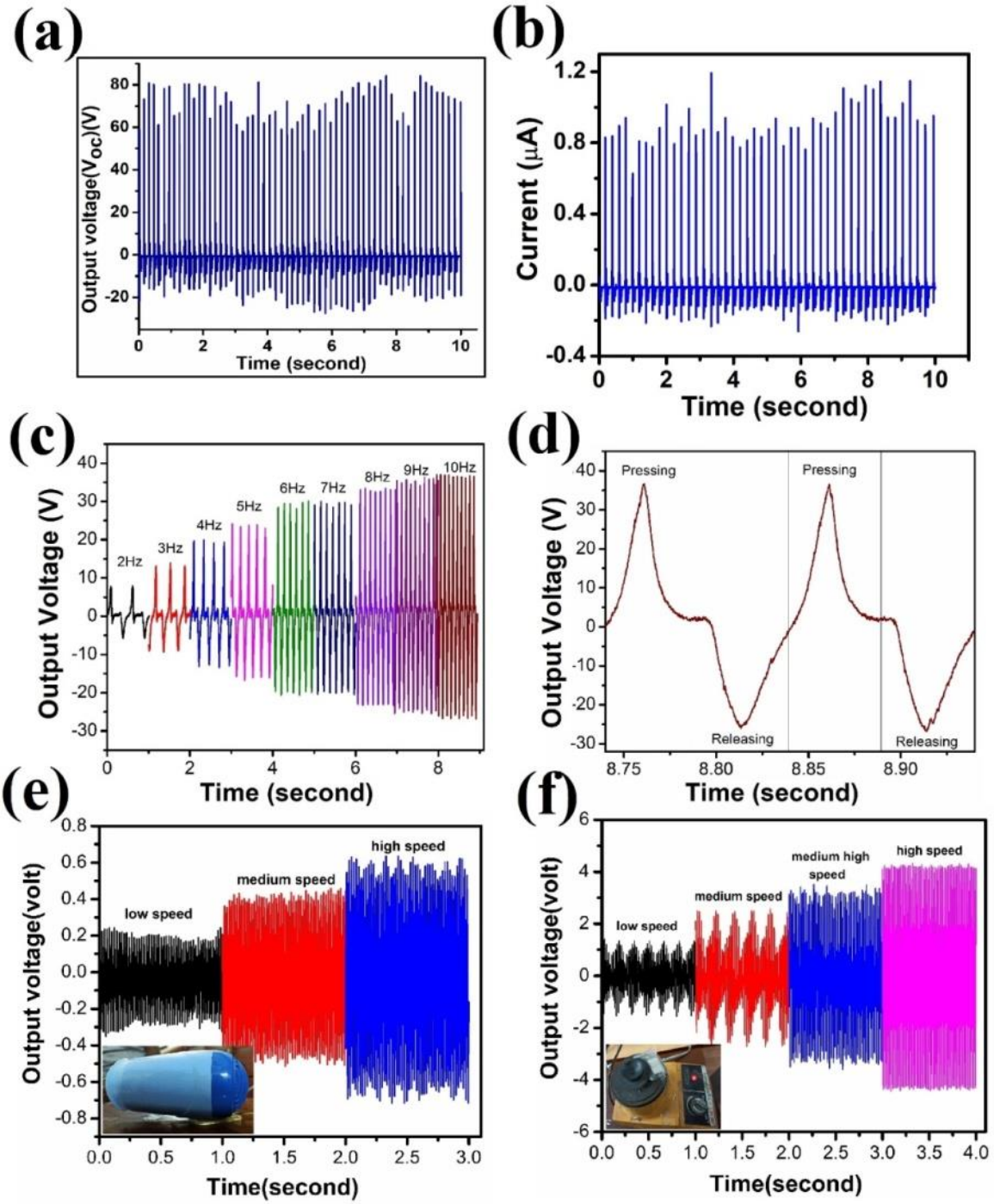


***Figure 2.3:*** *(a) Open circuit voltage ($V_{OC}$), (b) Short circuit current ($I_{SC}$) generated by human finger impartation at frequency ~5 to 6 Hz. (c) Frequency dependent $V_{OC}$. (d) Magnified view of $V_{OC}$ for 2 successive cycles corresponding to 10 Hz frequency under 5 N force. Voltage generation by using the vibration energy of (e) air drier and (f) vortex machine at different speeds.*

The SPENG also shows high power density ~182.06 μW/cm$^3$. The details of power density and external force calculation of fabricated SPENG are attached below.

$$Powerdensity = Power\ (IV)\ /\ operative\ volume\ of\ SPENG \quad \text{(2.1)}$$

For SA pappus based PENG, $I_{SC}$ = 1.0 μA and $V_{OC}$ = 81.2 V. Then calculated Power density using equation 2.1 will be 182.06 μW/cm$^3$.

The applied force on the SPENG by the finger impartation has been calculated by following two equations 2.2 and 2.3, which are depended on momentum and energy conservation law:

$$m.g.h = \frac{mv^2}{2} \quad \text{(2.2)}$$

$$(F - mg).\Delta t = mv \quad \text{(2.3)}$$

Where, m represents mass of the imparted object i.e. finger, v is the velocity of the object when it touches the PENG, h defines the falling height of the object, F is the applied force, g is the acceleration due to gravity, Δt represents the time duration between two successive positive or negative peak of the output voltage vs. time graph. In this work, m = 0.75 kg, v = 1.4 m/s, h = 0.10 m, and g = 9.8 m/s$^2$, Δt = 0.17 s. Thus, the external force by the finger impartation on SPENG will be F = 13.5 N.

Beside this, energy harvesting from different vibration energy of air drier and vortex machine in vibrating condition has also been tested. Placing the SPENG under air drier and operating the air drier at three different settings of low, medium, and high speed, SPENG produces $V_{OC}$ ~ 0.2 V, ~ 0.42 V and ~ 0.6 V respectively, shown in figure 2.3(e).When the device has been attached to a vortex machine body, then it shows remarkable voltage output like ~ 1.3 V, ~ 2.4 V, ~ 3.25 V and ~ 4.1 V depending on vortex rotating speed of low, medium, medium high and high speed respectively are presented in figure 2.3(f). All the above-mentioned experimental findings show that the SPENG can harvest electrical energy quite efficiently from any kind of mechanical energy generated by vibration.

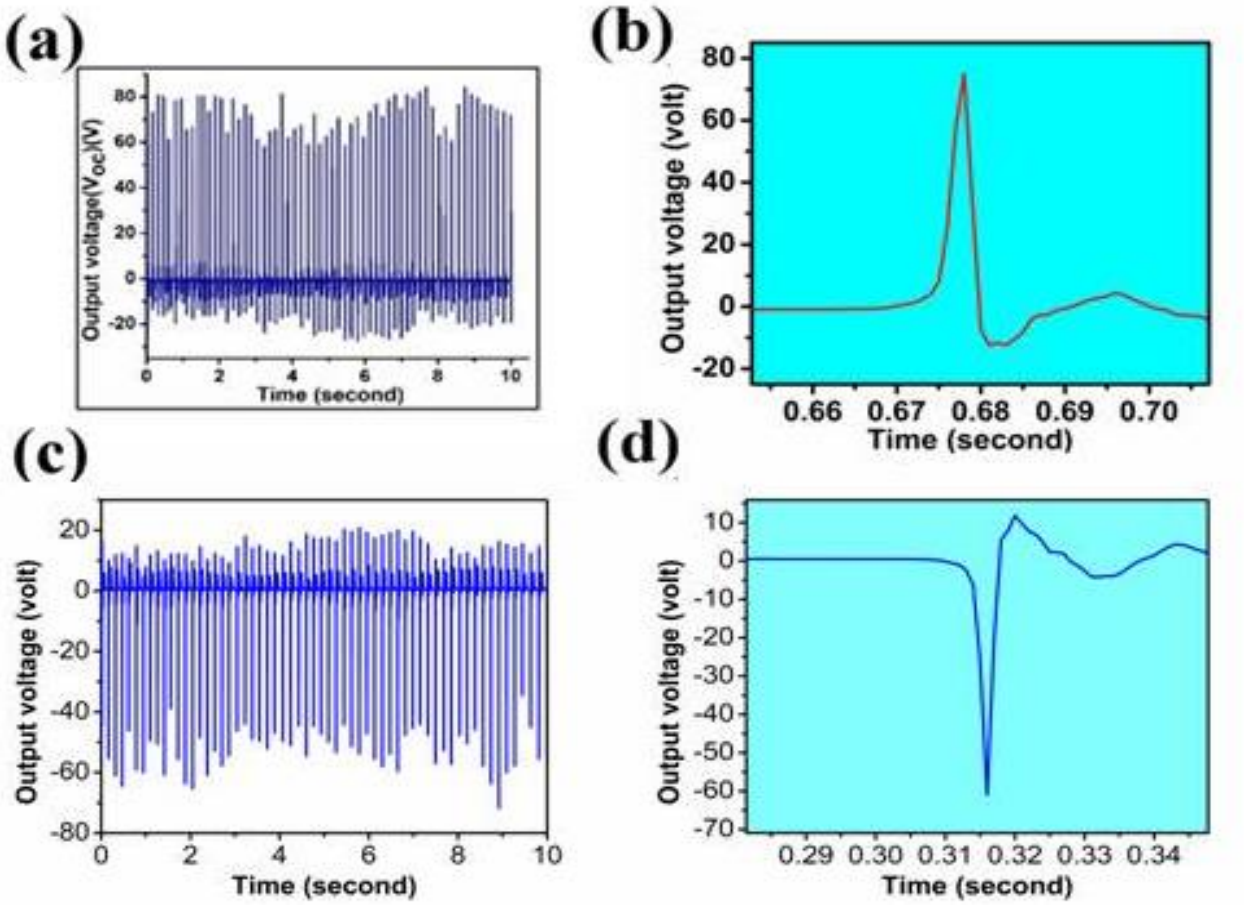


***Figure 2.4:*** *Output voltage switching polarity test (a) forward direction, (b) reverse direction, with magnifying views for both forward and reverse directions (b) and (d) respectively.*

### *2.3.2 Ultra-sensitivity of the SPENG under different body movements*

The fabricated SPENG is also capable of harvesting mechanical energy from the various body movements. Furthermore, the sensitivity of the fabricated device has been monitored by dropping balls of different masses from a height of 10 cm on the device surface, shown in figure 2.5(a) to (e). The output voltages are ~ 6V, ~ 10V, ~ 12V, ~ 15V, ~ 17V for dropping balls of masses 108.793 g, 35.214 g, 9.18 g, 59.34 g, and 15.01 g respectively. When balls are dropped on the device, different output voltages are induced depending on the masses of balls and the contact surface area. The ball having maximum mass shows low output voltage compared to the other balls, due to harder (low elastic properties than others ball) surface of bigger size ball. For this reason, different pressures are generated on the nanogenerator, which resulted in different output voltages.

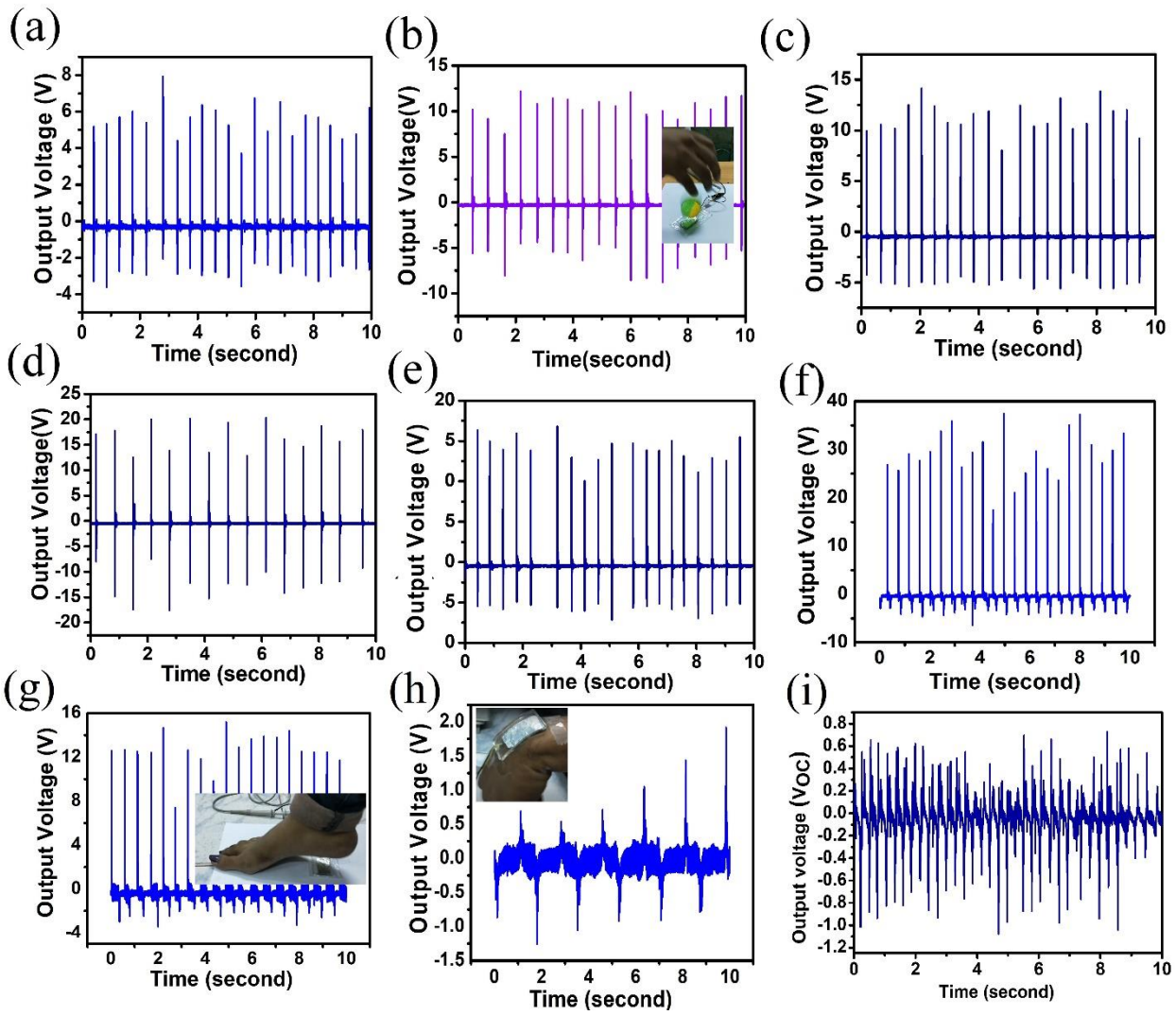


***Figure 2.5:*** *(a) to (e) Open circuit voltage generated by dropping balls of 108.793 g, 35.214 g, 9.18 g, 59.34 g, and 15.01 g on the device from a height of ~10 cm.(f) and (g) Output voltage generated by forefoot and heel pressing. (h) Wrist bending signal. (i) Light finger touching on SPENG.*

Figures 2.5(f) to (i) indicate that the self-powered flexible SPENG device is sensitive enough to utilize biomechanical energy from various body movements like heel and forefoot pressing, wrist up-down movement and just finger touch. High output voltages are obtained during forefoot pressing (~ 36 V) and heel pressing (~ 15 V) by attaching the device with foot and heel, depicted in figure 2.5(f) and (g). Generated output voltage during forefoot pressing is greater than that of

heel pressing. Possible reason behind this result may be the greater contact surface area for forefoot with device than heel with device surface. The maximum output voltage during wrist movement is ~ 1.9 V, as represented in figure 2.5(h), which also confirms the capability of the SPENG device in harvesting green energy from body movement. The sensitivity has been further checked by just touching the device with a finger, where $V_{OC}$ is ~ 0.65V (figure 2.5(i)). The results indicate that the fabricated SPENG is competent enough to detect even minute amount of pressure and convert the mechanical energy, caused by the application of pressure, into electrical energy. The output voltage of SPENG is recorded each month over the course of a year to check the stability of our device and results suggest that experimental device possesses almost same performances throughout the year. Thus, the fabricated SPENG is cost-effective, biocompatible, flexible and sustainable which, after proper improvisation, can charge biomedical devices by utilizing biological pressure from various body movement, muscle contraction/relaxation, and blood circulation.

Moreover, the experimental SPENG can be used to harness energy from a wide range of green bio-mechanical energy resources, by attaching the SPENG with running machines like treadmills, dancing floors, interior of shoes, wheels of the car etc. The produced electrical energy can also be used to switch on LEDs, LCD screens, and other different types of battery charging equipments.

### *2.3.3 Working Principle of fabricated SPENG*

The performances of SPENG can be explained with the help of synergetic effect of the electro activity. Most of the biomaterials such as cellulose, gelatin, chitin and collagen exhibit shear piezoelectricity due to their fibrous configuration. Such piezoelectric effect is due to internal rotation of polar atomic groups, which are interrelated with the asymmetric carbon atom[53,54]. SA pappus is composed of amide linkage, -OH groups, carbonyl groups, arranged in α-helical and β sheet structures. In the SA pappus, helical-α and β-sheets elastic structures of amino acids are connected strongly through intra and inter molecular H-bonding among themselves[55]. Due to high aspect ratio of SA pappus fibers in conjunction with strong hydrogen bonding energy and high binding energy, these fibers can be used undoubtedly as bio-piezo materials. The presence of amide and hydroxyl groups assists SA pappus to produce electric dipoles inside the fiber. These dipoles show a high piezoelectric response under applied external strain. Under

mechanical compression, highly crystalline SA pappus form stress-induced polarization and generate piezoelectricity. Thus, SA pappus is a promising piezoelectric material which has the capability to generate output voltage under applied mechanical compression.

The working principle of experimental device (SPENG) depends primarily on the changes in molecular structure of SA pappus under mechanical stress. Application of vertical pressure on the PENG, causes the movement of total polarization charge towards the electrodes, which acts as the key for the generation of piezoelectric potential across the two electrodes[56]. Thus, applied vertical force eventually initiate the accumulation of positive and negative charges separately on two electrodes and thus generates a positive voltage signal. The polarization charge increases with increasing magnitude of mechanical force and frequency of vibration. When the vertical strain is released, the collected charges on the electrodes move towards the reverse direction and hence a negative signal is produced. Due to the coincidence of negative signal and weak damped piezoelectric potential, we observe the first negative potential peak. Again, small a positive signal, indicated by second positive peak is observed due to assemblage of free charges at the electrodes. After returning to the original state, the accumulated electrons fall back again and giving a second negative peak. The second positive and negative signal peaks are occurred due to the damping effect of devices. Thus, a continuous pulse or application of an external force is the main source to obtain the output performances of PENG.

For the piezoelectric effect,

$\sigma_p(z)$ is the piezoelectric polarization charge density of PENG and $\sigma(x)$ is the free electron charge density in the electrode.

Considering the strain introduced by the applied compression, $\sigma(x)$ is a function of the thickness of the device (z). Now, for the mechanical force, the piezoelectric equation and constituter are given by

$$\boldsymbol{P_i} = (\boldsymbol{e})_{\boldsymbol{ijk}}(\boldsymbol{S})_{\boldsymbol{jk}} \quad \text{(2.4)}$$

$$\boldsymbol{T} = \boldsymbol{C^E S} - \boldsymbol{e^T E} \quad \text{(2.5)}$$

$$\boldsymbol{D} = \boldsymbol{eS} - \boldsymbol{\varepsilon E} \quad \text{(2.6)}$$

Where, $(e)_{ijk}$ denotes the piezoelectric third order tensor and S is the mechanical strain. $C^E$ and T are the elasticity tensor and stress tensor, $\varepsilon$ is the dielectric tensor.

Due to media polarization, the displacement current can be expressed as

$$J_{Di} = \frac{\partial P_i}{\partial t} \quad \text{..... (2.7)}$$

Equation 2.7 illustrates that the changing rate of the applied strain is proportional to the output current density of the PENG. The frequency dependent output performance of the device (shown in the Figure 2.3(c)) matches well with the equation 2.7.

### *2.3.4 Realistic application of SPENG*

The ability of fabricated SPENG to charge a 2.2 µF capacitor has been investigated by connecting the device with the capacitor through a simple bridge rectifier circuit (Figure 2.6(a) inset) and switching on the SPENG by periodic finger impartation at frequency ~ 5 -6 Hz. The exponential nature of the time-voltage curve during charging (figure 2.6(a)) of the capacitor indicates high energy storage capability. Using SPENG, the capacitor (2.2µF) is charged up to 3.2V within 16 seconds under periodic finger impartation. So, we can easily state that the charging efficiency of SPENG is higher than any other previously reported bio-waste based PENGs. Since the charging ability of SPENG is very high, it can be used as an alternative energy sources for portable or medical devices via capacitor charging. Figure 2.6(b) shows the competence of the SPENG to light up LEDs under continuous finger impartation. The power produced from SPENG can illuminate 39 blue LEDs, connected through a full wave bridge rectifier.

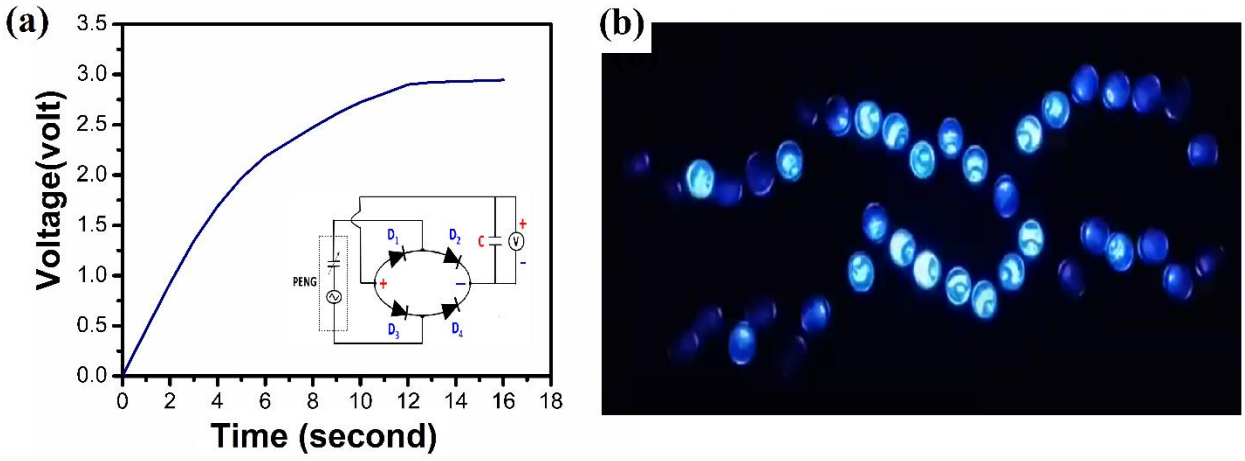


***Figure 2.6:*** *(a) Charging performance of 2.2 µF capacitor, inset circuit diagram for charging capacitor and LEDs light up and (b) snapshot in LEDs glowing condition.*

## 2.4 Conclusion:

The observations of the studies indicate that naturally and amply available fiber of Sonchus asper pappus, being piezoelectric in nature, may be successfully employed to develop a bio-inspired nanogenerator (SPENG). The fabricated SPENG performs quite efficiently to harvest waste energy from various mechanical and biomechanical movements. Electrical energy is produced by harnessing the mechanical energy from various living and nonliving sources. This biocompatible equipment is capable of generating high output voltage (Voc) of ~ 81.2 V and a short circuit current (Isc) of ~ 1.0 µA under periodic finger imparting and releasing (with axial force 13.5N) with an average frequency of 6 Hz. The calculated instant power density of the device is 182.06 $\mu Wcm^{-3}$. The fabricated SPENG shows remarkable response in exploiting vibration energy of vortex mixture (~ 6 V) and low force impact of 9.8 g ball falling from 10 cm height on the surface of SPENG (~15 V). The device is sensitive enough to respond on mere hand movement and finger touching on it. The realistic application of SPENG has been verified successfully through lighting up to 39 blue LEDs connected in series via finger impartation only and also by charging a capacitor (2.2µF) to 3.2V within a very short span time (16 second). All the results are reproducible and SPENG exhibits exceptional good mechanical stability with brilliant performances for a year indicating the excellent sustainability of the experimental device. The bio-piezoelectric material, SA pappus, collected from natural waste material, is a low cost, easily and amply available green energy material, which can be successfully utilized in several renewable energy applications. The flexible, biocompatible, and biodegradable SPENG, made of SA pappus, has the prospect to be used in different handy gadgets as an energy harvester, which can convert mechanical energy from different sources, easily available in the environment. After proper improvisation, the device may certainly be used in many in vivo applications as an energy harvester, which has been proven to be proficient enough to convert biomechanical energy, even when negligibly small, into usable form of electrical energy.

## References


1) Wang, Z. L.; Song, J. Piezoelectric Nanogenerators Based on Zinc Oxide Nanowire Arrays. Science 2006, 312, 242–246.
2) Qin, Y.; Wang, X.; Wang, Z, L. Microfibre–nanowire hybrid structure for energy scavenging. Nature 2008, 451, 809–813.
3) Yang, R.; Qin, Y.; Dai, L.; Wang, Z. L. Power generation with laterally packaged piezoelectric fine wires. Nature Nanotechnology 2009, 4, 34–39.
4) Mao, Y.; Zhao, P.; McConohy, G.; Yang, H.; Tong, Y.; Wang, X. Sponge-Like Piezoelectric Polymer Films for Scalable and Integratable Nanogenerators and Self-Powered Electronic Systems. Advanced Energy Materials 2014, 4, 1301624.
5) Maiti, S.; Karan, S. K.; Lee, J.; Mishra, A. K.; Khatua, B. B.; Kim, J. K. Bio-waste onion skin as an innovative nature-driven piezoelectric material with high energy conversion efficiency. Nano Energy 2017, 42, 282-293.
6) Hoque, N. A.; Thakur, P.; Biswas, P.; Saikh, M. M.; Roy, S.; Bagchi, B.; Das, S.; Ray, P. P. Biowaste crab shell-extracted chitin nanofiber-based superior piezoelectric nanogenerator. Journal of Materials Chemistry A 2018, 6, 13848-13858.
7) Hoque, N. A.; Thakur, P.; Roy, S.; Kool, A.; Bagchi, B.; Biswas, P.; Saikh, M. M.; Khatun, F.; Das, S.; Ray, P. P. $Er^{3+/}Fe^{3+}$ Stimulated Electroactive, Visible Light Emitting, and High Dielectric Flexible PVDF Film Based Piezoelectric Nanogenerators: A Simple and Superior Self-Powered Energy Harvester with Remarkable Power Density. ACS Applied Material Interfaces 2017, 9, 23048–23059.
8) Wang, Z. L. On Maxwell's displacement current for energy and sensors: the origin of nanogenerators. Materials Today 2017, 20, 74–82.
9) Wang, X.; Yang, B.; Liu, J.; Yang, C. A transparent and biocompatible single-friction-surface triboelectric and piezoelectric generator and body movement sensor. Journal of Materials Chemistry A 2017, 5, 1176–1183.
10) Shin, S. H.; Bae, Y. E.; Moon, H. K.; Kim, J.; Choi, S. H.; Kim, Y.; Yoon, H. J.; Lee, M. H.; Nah, J. Formation of Triboelectric Series via Atomic-Level Surface Functionalization for Triboelectric Energy Harvesting. ACS Nano 2017, 11, 6131–6138.

11) Han, M.; Zhang, X. S.; Meng, B.; Liu, W.; Tang, W.; Sun, X.; Wang, W.; Zhang, H. r-Shaped Hybrid Nanogenerator with Enhanced Piezoelectricity. ACS Nano 2013, 7, 8554–8560.

12) Chen, J.; Yang, J.; Guo, H.; Li, Z.; Zheng, L.; Su, Y.; Wen, Z.; Fan, X.; Wang, Z. L. Automatic Mode Transition Enabled Robust Triboelectric Nanogenerators. ACS Nano 2015, 9, 12334–12343.

13) Wang, X.; Yang, B.; Liu, J.; Zhu, Y.; Yang, C.; He, Q. A flexible triboelectric-piezoelectric hybrid nanogenerator based on P(VDF-TrFE) nanofibers and PDMS/MWCNT for wearable devices. Scientific Reports 2016, 6, 36409.

14) Xu, Q.; Wen, J.; Qin, Y. Development and outlook of high output piezoelectric nanogenerators. Nano Energy 2021, 86, 106080.

15) Hinchet, R.; Ghaffarinejad, A.; Lu, Y.; Hasani, J. Y.; Kim, S.-W.; Basset, P. Understanding and modeling of triboelectric-electret nanogenerator. Nano Energy 2018, 47, 401–409.

16) Su, H.; Wang, X.; Li, C.; Wang, Z.; Wu, Y.; Zhang, J.; Zhang, Y.; Zhao, C.; Wu, J.; Zheng, H. Enhanced energy harvesting ability of polydimethylsiloxane-BaTiO3-based flexible piezoelectric nanogenerator for tactile imitation application. Nano Energy 2021, 83, 105809.

17) Dong, K.; Wang, Y. C.; Deng, J.; Dai, Y.; Zhang, S. L.; Zou, H.; Gu, B.; Sun, B.; Wang, Z. L. A Highly Stretchable and Washable All-Yarn-Based Self-Charging Knitting Power Textile Composed of Fiber Triboelectric Nanogenerators and Supercapacitors. ACS Nano 2017, 11, 9490–9499.

18) Wang, Z. L.; Chen, J.; Lin, L. Progress in triboelectric nanogenerators as a new energy technology and self-powered sensors. Energy Environmental Science 2015, 8, 2250–2282.

19) Gu, L.; Liu, J.; Cui, N.; Xu, Q.; Du, T.; Zhang, L.; Wang, Z.; Long, C.; Qin, Y. Enhancing the current density of a piezoelectric nanogenerator using a three-dimensional intercalation electrode. Nature Communications 2020, 11, 1030.

20) Zhang, Y.; Wu, M.; Zhu, Q.; Wang, F.; Su, H.; Li, H.; Diao, C.; Zheng, H.; Wu, Y.; Wang, Z. L. Performance Enhancement of Flexible Piezoelectric Nanogenerator via

Doping and Rational 3D Structure Design For Self-Powered Mechanosensational System. Advanced Functional Materials 2019, 29, 1904259.

21) Erturun, U.; Eisape, A. A.; Kang, S. H.; West, J. E. Energy harvester using piezoelectric nanogenerator and electrostatic generator. Applied Physics Letters 2021, 118, 063902.
22) Karan, S. K.; Bera, R.; Paria, S.; Das, A. K.; Maiti, S.; Maitra, A.; Khatua, B. B. An Approach to Design Highly Durable Piezoelectric Nanogenerator Based on Self-Poled PVDF/AlO-rGO Flexible Nanocomposite with High Power Density and Energy Conversion Efficiency. Advanced Energy Materials 2016, 6, 1601016.
23) Shin, S.-H.; Kim, Y.-H.; Lee, M. H.; Jung, J.-Y.; Seol, J. H.; Nah, J. Lithium-Doped Zinc Oxide Nanowires–Polymer Composite for High Performance Flexible Piezoelectric Nanogenerator. ACS Nano 2014, 8, 10844–10850.
24) Maiti, S.; Karan, S. K.; Leea, J.; Mishra, A. K.; Khatua, B. B.; Kim, J. K. Bio-waste onion skin as an innovative nature-driven piezoelectric material with high energy conversion efficiency. Nano Energy 2017, 42, 282–293.
25) Pu, X.; Li, L.; Song, H.; Du, C.; Zhao, Z.; Jiang, C.; Cao, G.; Hu, W.; Wang, Z. L. A Self-Charging Power Unit by Integration of a Textile Triboelectric Nanogenerator and a Flexible Lithium-Ion Battery for Wearable Electronics. Advanced Materials 2015, 27, 2472–2478.
26) Wang, Z. L. Triboelectric Nanogenerators as New Energy Technology for Self-Powered Systems and as Active Mechanical and Chemical Sensors. ACS Nano 2013, 7, 9533.
27) Sun, C.; Shi, J.; Bayerl, D. J.; Wang, X. PVDF microbelts for harvesting energy from respiration. Energy & Environmental Science 2011, 4, 4508–4512.
28) Karan, S. K.; Bera, R.; Paria, S.; Das, A. K.; Maiti, S.; Maitra, A.; Khatua, B. B. An Approach to Design Highly Durable Piezoelectric Nanogenerator Based on Self-Poled PVDF/AlO-rGO Flexible Nanocomposite with High Power Density and Energy Conversion Efficiency. Advanced Energy Materials 2016, 6, 1601016.
29) Shin, S.-H.; Kim, Y.-H.; Lee, M. H.; Jung, J.-Y.; Seol, J. H.; Nah, J. Lithium-Doped Zinc Oxide Nanowires–Polymer Composite for High Performance Flexible Piezoelectric Nanogenerator. ACS Nano 2014, 8, 10844–10850.

30) Chung, S. Y.; Kim, S.; Lee, J.-H.; Kim, K.; Kim, S.-W.; Kang, C.-Y.; Yoon, S.-J.; Kim, Y. S. All-Solution-Processed Flexible Thin Film Piezoelectric Nanogenerator. Advanced Materials 2012, 24, 6022–6027.

31) Park, K. I.; Jeong, C. K.; Ryu, J.; Hwang, G. T.; Lee, K. J. Flexible and Large-Area Nanocomposite Generators Based on Lead Zirconate Titanate Particles and Carbon Nanotubes. Advanced Energy Materials 2013, 3, 1539–1544.

32) Yan, J.; Jeong, Y. G. High Performance Flexible Piezoelectric Nanogenerators based on BaTiO3 Nanofibers in Different Alignment Modes. ACS Applied Material Interfaces 2016, 8, 15700–15709.

33) Koka, A.; Sodano, H. A. A Low-Frequency Energy Harvester from Ultralong, Vertically Aligned BaTiO3 Nanowire Arrays. Advanced Energy Materials 2014, 4, 1301660.

34) Karan, S. K.; Mandal, D.; Khatua, B. B. Self-powered flexible Fe-doped RGO/PVDF nanocomposite: an excellent material for a piezoelectric energy harvester. Nanoscale 2015, 7, 10655–10666.

35) Whiter, R. A.; Narayan, V.; Kar-Narayan, S. A Scalable Nanogenerator Based on Self-Poled Piezoelectric Polymer Nanowires with High Energy Conversion Efficiency. Advanced Energy Materials 2014, 4, 1400519.

36) Paria, S.; Karan, S. K.; Bera, R.; Das, A. K.; Maitra, A.; Khatua, B. B. A Facile Approach To Develop a Highly Stretchable PVC/$ZnSnO_3$ Piezoelectric Nanogenerator with High Output Power Generation for Powering Portable Electronic Devices. Industrial & Engineering Chemistry Research 2016, 55, 10671–10680.

37) Kim, H.-J.; Kim, J.-H.; Jun, K.-W.; Kim, J.-H.; Seung, W.-C.; Kwon, O.-H.; Park, J.-Y.; Kim, S.-W.; Oh, I.-K. Silk Nanofiber-Networked Bio-Triboelectric Generator: Silk Bio-TEG. Advanced Energy Materials 2016, 6, 1502329.

38) Tollefson, J. Blue energy: after years in the doldrums, the quest to harvest energy from the oceans is gathering speed. Nature 2014, 508, 302.

39) Jiang, W.; Li, H.; Liu, Z.; Li, Z.; Tian, J.; Shi, B.; Zou, Y.; Ouyang, H.; Zhao, C.; Zhao, L.; Sun, R.; Zheng, H.; Fan, Y.; Wang, Z. L.; Li, Z. Fully Bioabsorbable Natural-Materials-Based Triboelectric Nanogenerators. Advanced Materials 2018, 30, 1801895.

40) Zheng, Q.; Zou, Y.; Zhang, Y.; Liu, Z.; Shi, B.; Wang, X.; Jin, Y.; Ouyang, H.; Li, Z.; Wang, Z. L. Biodegradable triboelectric nanogenerator as a life-time designed implantable power source. Science Advances 2016, 2, 1501478.

41) Chao, S.; Ouyang, H.; Jiang, D.; Fan, Y.; Li, Z. Triboelectric nanogenerator based on degradable materials. EcoMat 2021, 3, 12072.

42) Zhang, G.; Liao, Q.; Ma, M.; Zhang, Z.; Si, H.; Liu, S.; Zheng, X.; Dinga, Y.; Zhang, Y. A rationally designed output current measurement procedure and comprehensive understanding of the output characteristics for piezoelectric nanogenerators. Nano Energy 2016, 30, 180–186.

43) Shin, D.-M.; Han, H. J.; Kim, W.-G.; Kim, E.; Kim, C.; Hong, S. W.; Kim, H. K.; Oh, J.-W.; Hwang, Y.-H. Bioinspired piezoelectric nanogenerators based on vertically aligned phage nanopillars. Energy & Environmental Science 2015, 8, 3198–3203.

44) Lee, B. Y.; Zhang, J.; Zueger, C.; Chung, W.-J.; Yoo, S. Y.; Wang, E.; Meyer, J.; Ramesh, R.; Lee, S.-W. Virus-based piezoelectric energy generation. Nat. Nanotechnol. 2012, 7, 351–356.

45) Ghosh, S. K.; Mandal, D. High-performance bio-piezoelectric nanogenerator made with fish scale. Applied Physics Letters 2016, 109, 103701.

46) Ghosh, S. K.; Mandal, D. Efficient natural piezoelectric nanogenerator: Electricity generation from fish swim bladder. Nano Energy 2016, 28, 356–365.

47) Rajala, S.; Siponkoski, T.; Sarlin, E.; Mettänen, M.; Vuoriluoto, M.; Pammo, A.; Juuti, J.; Rojas, O. J.; Franssila, S.; Tuukkanen, S. Cellulose Nanofibril Film as a Piezoelectric Sensor Material. ACS Applied Material Interfaces 2016, 8, 15607–15614.

48) Zhang, G.; Liao, Q.; Zhang, Z.; Liang, Q.; Zhao, Y.; Zheng, X.; Zhang, Y. Novel Piezoelectric Paper-Based Flexible Nanogenerators Composed of $BaTiO_3$ Nanoparticles and Bacterial Cellulose. Advanced Science 2016, 3, 1500257.

49) Mahadeva, S. K.; Walus, K.; Stoeber, B. Piezoelectric Paper Fabricated via Nanostructured Barium Titanate Functionalization of Wood Cellulose Fibers. ACS Applied Materials & Interfaces 2014, 6, 7547–7553.

50) Khan, R. A.; Khan, M. R.; Sahreen, S.; Ahmed, M. Evaluation of phenolic contents and antioxidant activity of various solvent extracts of Sonchus asper (L.) Hill. Chemistry Central Journal 2012, 6, 1-7.

51) Khan, R. A.; Khan, M. R.; Sahreen, S.; Protective effect of Sonchus asper extracts against experimentally induced lung injuries in rats: A novel study. Experimental and Toxicologic Pathology 2012, 64, 725-731.

52) Afolayan, A. J.; Jimoh, F. O. Nutritional quality of some wild leafy vegetables in South Africa. Int. J. Food Sci. Nutr. 2008, 60, 424-431.

53) Roy, S.; Thakur, P.; Hoque, N. A.; Bagchi, B.; Sepay, N.; Khatun, F.; Kool, A.; Das, S. Electroactive and High Dielectric Folic Acid/PVDF Composite Film Rooted Simplistic Organic Photovoltaic Self-Charging Energy Storage Cell with Superior Energy Density and Storage Capability. ACS Applied Material Interfaces 2017, 9, 24198–24209.

54) Thakur, P.; Kool, A.; Bagchi, B.; Hoque, N. A.; Das, S.; Nandy, P. In situ synthesis of $Ni(OH)_2$ nanobelt modified electroactive poly(vinylidene fluoride) thin films: remarkable improvement in dielectric properties. RSC Advances 2015, 5, 28487.

55) Koka, A.; Sodano, H. A. A Low-Frequency Energy Harvester from Ultralong, Vertically Aligned BaTiO3 Nanowire Arrays. Advanced Energy Materials 2014, 4, 1301660.

56) Ding, R.; Zhang, X.; Chen, G.; Wang, H.; Kishor, R.; Xiao, J.; Gao, F.; Zeng, K.; Chen, X.; Sun, X. W.; Zheng, Y. High-performance piezoelectric nanogenerators composed of formamidinium lead halide perovskite nanoparticles and poly(vinylidene fluoride). Nano Energy 2017, 37, 126–135.

57) Kumar, A.; Gullapalli, H.; Balakrishnan, K.;-Mendez, A. B.; Vajtai, R.; Terrones, M.; Ajayan, P. M. Flexible ZnO-cellulose nanocomposite for multisource energy conversion. Small 2011, 7, 2173–2178.

58) Liao, Q.; Zhang, Z.; Zhang, X.; Mohr, M.; Zhang, Y.; Fecht, H.-J. Flexible piezoelectric nanogenerators based on a fiber/ZnO nanowires/paper hybrid structure for energy harvesting. Nano Research 2014, 7, 917–928.

59) Qin, Y.; Wang, X.; Wang, Z. L. Microfibre-nanowire hybrid structure for energy scavenging. Nature 2008, 451, 809-813.

60) Lee, B. Y.; Zhang, J.; Zueger, C.; Chung, W.-J.; Yoo, S. Y.; Wang, E.; Meyer, J.; Ramesh, R.; Lee, S. W. Virus-based piezoelectric energy generation. Nat. Nanotechnol. 2012, 7, 351-356.

61) Zhang, G.; Liao, Q.; Zhang, Z.; Liang, Q.; Zhao, Y.; Zheng, X.; Zhang, Y. Novel Piezoelectric Paper-Based Flexible Nanogenerators Composed of $BaTiO_3$ Nanoparticles and Bacterial Cellulose. Advanced Science 2016, 3, 1500257.

62) Ghosh, S. K.; Mandal, D. High-performance bio-piezoelectric nanogenerator made with fish scale. Applied Physics Letters 2016, 109, 103701- 05.

63) Mun, S.; Ko, H.-U.; Zhai, L.; Min, S.-K.; Kim, H.-C.; Kim, J. Enhanced electromechanical behavior of cellulose film by zinc oxide nanocoating and its vibration energy harvesting. Acta Materialia 2016, 114, 1-6.

64) Shin, D.-M.; Han, H. J.; Kim, W.-G.; Kim, E.; Kim, C.; Hong, S. W.; Kim, H. K.; Oh, J.-W.; Hwang, Y.-H. Bioinspired piezoelectric nanogenerators based on vertically aligned phage nanopillars. Energy & Environmental Science 2015, 8, 3198-3203.

65) Ghosh, S. K.; Mandal, D. Efficient natural piezoelectric nanogenerator: Electricity generation from fish swim bladder. Nano Energy 2016, 28, 356–365.

66) Maiti, S.; Karan, S. K.; Leea, J.; Mishra, A. K.; Khatua, B. B.; Kim, J. K. Bio-waste onion skin as an innovative nature-driven piezoelectric material with high energy conversion efficiency. Nano Energy 2017, 42, 282–293.

67) Ghosh, S. K.; Mandal, D. Bio-assembled, piezoelectric prawn shell made self-powered wearable sensor for non-invasive physiological signal monitoring. Applied Physics Letters 2017, 110, 123701.

68) Karan, S. K.; Maiti, S.; Kwonc, O.; Paria, S.; Maitra, A.; KumarSi, S.; Kim, Y.; Kim, J. K.; Khatua, B. B. Nature driven spider silk as high energy conversion efficient bio-piezoelectric nanogenerator. Nano Energy 2018, 49, 655–666.

69) Karan, S. K.; Maiti, S.; Paria, S.; Maitra, A.; Si, S. K.; Kim, J. K.; Khatua, B. B. A new insight towards eggshell membrane as high energy conversion efficient bio-piezoelectric energy harvester. Materials Today Energy 2018, 9, 114-125.

70) Hoque, N. A.; Thakur, P.; Biswas, P.; Saikh, M. M.; Roy, S.; Bagchi, B.; Das, S.; Ray, P. P. Biowaste crab shell-extracted chitin nanofiber-based superior piezoelectric nanogenerator. Journal of Materials Chemistry A 2018, 6, 13848-13858.

71) Chen, H.; Zhou, L.; Fang, Z.; Wang, S.; Yang, T.; Zhu, L.; Hou, X.; Wang, H.; Wang, Z. L. Piezoelectric Nanogenerator Based on In Situ Growth All-Inorganic CsPbBr3

Perovskite Nanocrystals in PVDF Fibers with Long-Term Stability. Advanced Functional Materials 2021, 31, 2011073.

72) Rafique, S.; Kasi, A. K.; Kasi, J. K.; Aminullah.; Bokhari, M.; Shakoor, Z. Fabrication of silver-doped zinc oxide nanorods piezoelectric nanogenerator on cotton fabric to utilize and optimize the charging system. Nanomaterials and Nanotechnology 2020, 10, 1-12.

73) Park, K.-Il.; Son, J. H.; Hwang, G.-T.; Jeong, C. K.; Ryu, J.; Koo, M.; Choi, I.; Lee, S. H.; Byun, M.; Wang, Z. L.; Lee, K. J. Highly-Efficient, Flexible Piezoelectric PZT Thin Film Nanogenerator on Plastic Substrates. Advanced Materials 2014, 26, 2514-2520.

# High β-crystallinity comprising Nitrogenous carbon dot/PVDF nanocomposite decorated self-powered and flexible piezoelectric nanogenerator for harvesting human movement mediated energy and sensing weights

*Chapter 3*

## 3.1 Introduction

The global energy crisis is increasing rapidly with the speedy development of the worldwide economy.[1-3] In addition, with the continuous growth of human civilization, non-renewable energy resources such as coal, petroleum, natural gas, fossil fuels, firewood, etc., are limiting day by day.[4-5] As a result, renewable energy sources have become the only option to solve this energy crisis by generating electricity.[6-10] To address this problem, several renewable energy resources, such as solar energy, mechanical motion, tidal energy, thermal energy, biomass energy, etc., which are easily available in nature, are utilized to obtain the useable form of energy.[11-16] Among them, mechanical energy is available quite effortlessly in our daily activities. Several researchers have reported that mechanical energies involved in everyday human movement activities, like walking, running, talking, etc., can be used in electrical energy generation.[17-19] Thus, piezoelectric nanogenerators (PENG) have attracted great interest in generating electrical energy from various mechanical energy sources by using different piezoelectric materials.[20-22] For the development of PENG, several piezoelectric nanomaterials and ceramics such as ZnO, PZT, $BaTiO_3$, PMN-PT, $ZnSnO_3$, (Na, K)-$NbO_3$ have been used widely. Versatile use of these materials has been limited due to their heavy weight and non-flexible nature.[21-25] In search to resolve the difficulty, polymers have appeared as the most promising material to design lightweight, flexible, cost-effective, and eco-friendly PENGs.[20,26]

Recently, different types of piezoelectric materials like quantum dots, perovskite materials, oxide materials, biomaterials, etc., have been used to design the active layer of various optoelectronic devices, for example, light-emitting diodes (LEDs), solar cells, photodetectors and piezoelectric energy harvester. Among them, quantum dots have attracted immense interest in developing PENGs because of their high surface-to-volume ratio and very high electrical activity. So, quantum dots and polymer matrix-based nanocomposites have been fabricated to enhance the piezoelectric properties. These nanocomposites are used as piezoelectric layer for fabricating PENGs.[27-29] Cai et al. reported carbon black /graphene and PVDF-based films for harvesting energy.[30] Alam et al. investigated $TiO_2$/ PVDF-HFP nanofiber-based nanogenerator to harvest acoustic energy.[31] A triboelectric nanogenerator for harvesting energy and a gesture sensing application was reported by Chen et al.[32(a)]. PVDF and its copolymers have been used in energy harvesting applications as the materials are eco-friendly, electroactive, hydrophobic, of low cost

and flexible.[30] With this in mind, we have fabricated Carbon dot incorporated PVDF nanocomposites to investigate the optical properties of nanocomposites and enhance the piezoelectric worth of the PENG. Polyvinylidene fluoride (PVDF) is a highly non-reactive, thermoplastic, semi-crystalline fluoropolymer. Depending on the bond orientation of $–CH_2$ and $–CF_2$ dipoles, it consists of five crystalline polymorphic phases namely α, β, γ, δ and ε.[20] Among them, α, β and γ are the most common phases of PVDF. Here non-polar α crystalline phase (TGTG′ dihedral conformation) is obtained directly through the melting process. Having all-trans (TTTT) conformation, the β crystalline phase is the polar and most crucial phase of PVDF, exhibiting the highest piezoelectric, pyroelectric, ferroelectric, and dielectric properties compared to other phases of PVDF.[33-35] The γ crystalline phase shows average piezoelectric properties due to its TTTGTTG′ conformation.[36,37] Thus, a simple and cost-effective method is required to develop the electroactive β crystalline phase nucleation of PVDF to optimize their applications in diverse fields. "Poling" is the traditional procedure for nucleating the β crystalline phase in PVDF. Apart from these processes, self-poled electroactive PVDF can be achieved easily by incorporating nano/micro-fillers such as metal oxide, nanoparticles of metals and metal salts, carbon nanotube, ceramic nanoparticles, clays, and organic molecule, etc.[33-38] Nowadays, a single device with various applications has attracted immense interest in research and industry.[39-42] Thus, the orientation of polar β-phase of PVDF and optical absorption property of carbon dot play an essential role in making a composite, possessing diverse properties. We can use this composite to design a mechanical energy harvester and a photodetector as well.[43]

Carbon dots (CDs) are quasi-spherical nanoparticles having diameters of less than 10nm. These CDs, a new member of the nanocarbon family was discovered in 2004. Besides being eco-friendly, the CDs possess many fold advantages such as good solubility, biocompatibility, conductivity, light bleaching property etc. The main advantage of using Carbon dots is that they have excellent photoluminescence properties, the reason behind their outstanding performance in biological sensing, fluorescence labeling, chemical sensing, and light-emitting diodes.[44,46] CDs can be treated as a shell-core material. The central carbon core is a $sp^2$-$sp^3$ hybrid crystal or formless. The spherical shell has some defects and surface functional groups, like amino group (-$NH_2$), carboxyl group (-COOH), hydroxyl group (-OH), sulfonic group (-$HSO_3$), carbonyl group (C=O), epoxy (-CH(O)CH-) and cyano (-CN) group, etc. With these functional groups, CDs exhibit excellent dispersion in solvents and take active parts in bonding with different

materials.[45(a)] Herein, we have used nitrogen (N) into carbon dots which enhance the performance of CDs in above said applications. Nitrogen doping helps carbon to attribute new physical and chemical properties. Beside this, the doping of N into CDs reduces the work function of CDs and stimulates in delocalization of charge. Additionally, doping nitrogen also enhances the charge transferability of CDs and also increases the number of surface defects in CD, which henceforth helps in escalating the piezo effect of PVDF.[45(b)] Owing to these advantages, we have selected nitrogen as a primary doping material into CDs.

In the present work, we have designed a nitrogen-doped Carbon dots (N-CDs) incorporated self-poled piezoelectric PVDF (PCD) film based piezoelectric nanogenerator (PPNCD) for harnessing various forms of mechanical and biomechanical energy such as talking, walking, finger impartation and so forth and converting them into electrical energy. Carbon dots are selected as the main component for fabricating nanocomposites and energy harvesters due to their biocompatibility, eco-friendliness, solubility, chemical stability, and excellent photoluminescence properties. Besides this, larger surface area and surface defects of Carbon dots facilitates the formation of β phase in the PVDF polymer matrix. The large surface area and rich surface defects of CDs generate the active points, having induced mass potential and help in formation of β-phase within PVDF matrix. Furthermore, the rich surface defects in the shell of CDs encourage in chemical bond formation between filler and substrate and make interface bond stronger.[48] Different characterization techniques have investigated the effects of N-CDs in PVDF polymer. The exceptional diverse properties of CDs encouraged researchers to explore the possibility of the material in several fields of application such as sensing and bioimaging, photocatalysis, light-emitting diode, electrocatalysis, and solar cells.[20] The experimental PCD film-based PENG (PPNCD) shows elevated output performance with an instantaneous power density of 1979.87$\mu Wcm^{-3}$ under periodic finger impartation. The sensitivity of the device has been investigated by dropping different balls on the upper surface. The β-crystalline phase of PCD nanocomposites have been examined by X-ray diffraction pattern and FTIR spectra. Furthermore, the density functional theory (DFT) calculations are used to find out the geometrical and electrical properties of the β-crystalline phase. In addition, the fabricated PPNCD can generate output voltages from various body movements like touching, bending, heartbeats and pulses, heel pressing etc. Our study indicates the prospect of the piezoelectric

nanogenerator PPNCD as green and handy energy harvester to power up various electronic devices quite easily and as wearable sensor to detect different weights.

## 3.2 Experimental section

### 3.2.1 Preparation of Nitrogen doped Carbon dots (N-CDs)

Nitrogen doped CDs were prepared by a modified report as reported previously by Dong et al. (J. Mater. Chem. C, 2014, 2, 7477). All reagents were used without further purification. Ethanolamine and hydrogen peroxide aqueous solution (30% hydrogen peroxide) were of analytical grade and purchased from Merck. De-ionized water was thoroughly used in the synthesis process. In a typical synthesis procedure, 3ml of ethanolamine and 4.5ml of hydrogen peroxide were taken in a 200ml beaker. The beaker was then placed in an oil bath at a temperature of 200℃ for 30min. During this synthesis procedure, the color of the solution changes from bright yellow to dark brown. The obtained gel was diluted with appropriate amount of dimethylsulfoxide (DMSO) for further use.

### 3.2.2 Synthesis of Carbon dots incorporated PVDF composite (PCD) Nanocomposites

N-CDs/PVDF-based nanocomposites were prepared with the help of a simple solution casting method. At first, 250 mg of PVDF (Sigma-Aldrich, Germany; Mw: 180 000 GPC; Mn:71 000) was mixed with the required amount of dimethylsulfoxide (DMSO) (Merck) and kept at 60 °C on a magnetic stirrer to get a clear solution. The required amount of N-CDs (1, 1.75, 2.5, 5, 10 mass percent) were added with the clear solution and kept on a magnetic stirrer for 14h under the same conditions. After that, the prepared solutions were cast on clean and dust-free Petri dishes and dried at 80°C in the oven to obtain the composite PCD nanocomposites. Table 3.1 describes the amount of N-CDs, DMSO and PVDF used to prepare the samples, with their respective names.

***Table 3.1:*** *Samples name for different concentrated N-CDs and solvents added with PVDF*

| *Samples name* | *DMSO (in ml)* | *PVDF (mg)* | *N-CDs( in ml)* |
|---|---|---|---|
| ***Pure PVDF*** | *5* | *250* | *0* |
| ***PCD1*** | *4.95* | *250* | *0.05* |
| ***PCD1.75*** | *4.9125* | *250* | *0.0875* |
| ***PCD2.5*** | *4.875* | *250* | *0.125* |
| ***PCD5*** | *4.75* | *250* | *0.25* |
| ***PCD10*** | *4.50* | *250* | *0.5* |

### *3.2.3 Fabrication of device*

At first, PCD nanocomposite was taken with dimensions of 2.4cm X 1.8 cm X 46μm. Then two aluminum electrodes with a thickness of 40μm were pasted on both sides of the PCD film, and two copper wires were connected from both sides of the nanocomposite to measure the output performance of the nanogenerators. After that, the nanocomposite containing the electrodes and wires was *encapsulated* with the polydimethylsiloxane (PDMS) (Sylgard 184, Dow Corning, ratio of 1:10) and kept for 15min in a vacuum to remove the bubbles from the mixture. After removing the bubbles, the device was put in the oven at $60^0$C for drying. The dimension of the fabricated device (PPNCD) was 5cm X 3 cm X 0.3 cm. The procedure is shown in figure 3.1 (a).

## *3.3 Characterizations*

The microstructure, surface morphology, different phase behavior, and thermal properties of nanocomposites are examined by field emission scanning microscopy (FESEM; INSPECT F50), Transmission electron microscope (UHR-FEG TEM, JEM-2100F, Jeol, Japan), Fourier transform infrared (FTIR) spectroscopy (FTIR-8400S; Shimadzu), X-ray diffraction (XRD; Model-D8, Bruker AXS Inc., Madison, WI), thermal gravimetric analysis (TGA;

TGA/SDTA851e, Mettler Toledo AG) and differential scanning calorimeter (DSC-60, Shimadzu, Singapore) respectively. Furthermore, X-ray Photoelectron Spectroscopy (XPS) analysis has been performed with an Omicron Multiprobe (Omicron Nanotechnology GmbH) photoelectron spectrometer fitted with an EA125 hemispherical analyzer and a monochromatized Al $K_\alpha$ ($h\nu$: 1486.6 eV) source.

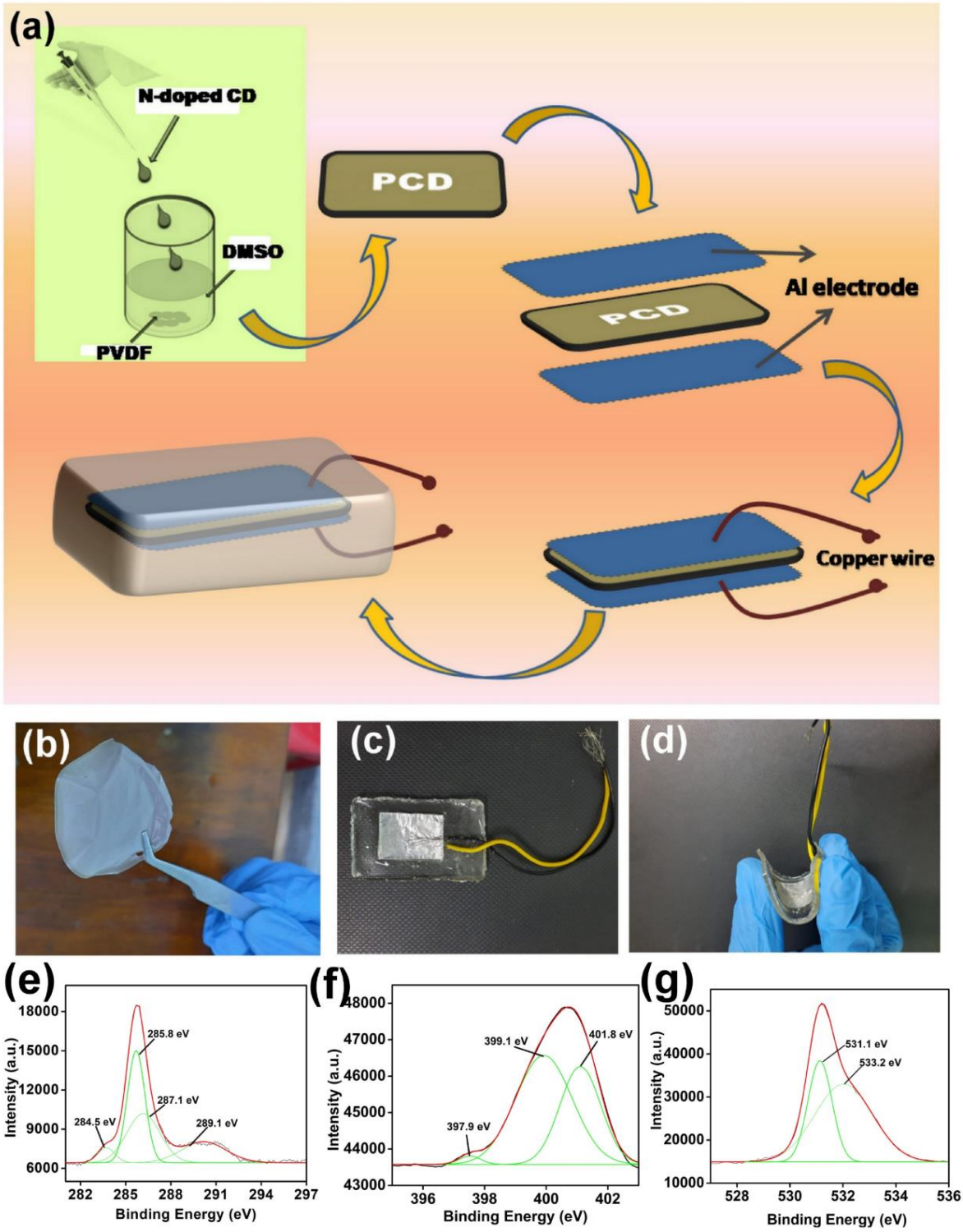


***Figure 3.1:*** *(a) Graphical representation of the fabricated PPNCD device. (b) A digital snapshot of PCD nanocomposite. (c) and (d) Digital image and flexibility show of designed PPNCD device. XPS peaks of (e) C1s, (f) N1s and (g) O1s.*

## 3.4 Results and discussion

### 3.4.1 Structural analysis of N-CDs and PCD nanocomposites

The TEM image of N-CDs interprets that the dispersion of synthesized N-CDs is uniform. As a result, no agglomeration takes place. Moreover, the diameter of the N-CDs is calculated from TEM image, which is 2.5nm. Figure 3.2 exhibits the TEM image of N-CDs.

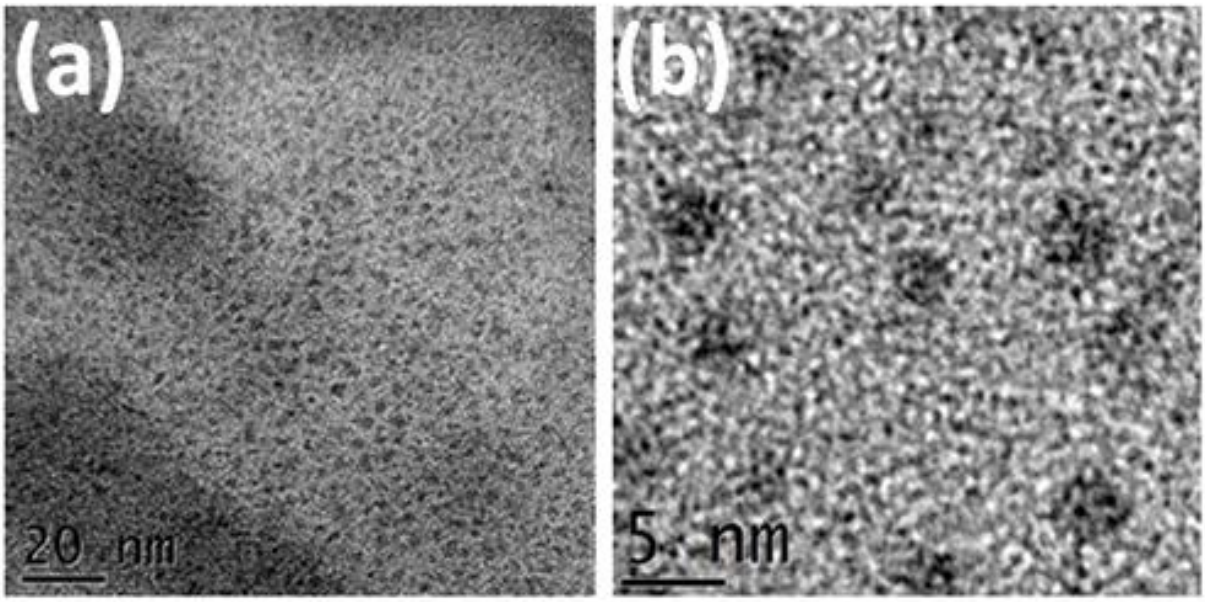


***Figure 3.2:*** *(a) and (b) TEM images of N-doped C-dots.*

Furthermore, X-ray photoelectron spectroscopy (XPS) analysis is performed to analyze the state of doping and investigate the surface groups of N doping CDs. Figure 3.1(e) to (g) shows the data of XPS analysis of N-doped CDs and the results of XPS analysis confirm that N-CD consists of carbon, nitrogen and oxygen. Figure 3.1(e) elaborates that C1s spectrum mainly consists of four peaks which are observed at 284.5eV, 285.8eV, 287.1eV, and 289.1eV. The peak at 284.5eV confirms the presence of graphitic structure ($sp^2C–sp^2C$).[45(b)] Moreover, the observing peaks at 285.8eV, 287.1eV, and 289.1eV binding energy validate the presence of C=N, C–N and C–O bonds respectively.[32(b)] From figure 3.1(f), we can see that N1s consist of three peaks. Among them, the peaks at 397.9eV and 399.1eV confirm the presence of pyridinic groups.[45(b)] Beside this, a peak at 401.8eV is observed which attributes to N-O bonds. Furthermore, O1s spectrum discloses the presence of C=O and $sp^2C–OH$ bonds at binding

energy of 531.1eV and 533.2eV respectively, which shown in the figure 3.1(g).The peak at binding energy of 533.2eV also indicates the presence of the cyclic ether containing groups (C=C–O–C, C–O–C).[45(b)] Thus, XPS analysis indicates the states of N doping in CDs.

FESEM micrographs depicting the surface morphology and microstructure of nanocomposites of pure PVDF and N-CDs incorporated composites are shown in figure 3.3. Surface images of N-CDs doped PVDF nanocomposites indicate the formation of spherulites. The diameter of the spherulites is near about 5μm, which confirms the nucleationof the electroactive β-phase. In the case of pure PVDF nanocomposite, the diameter of spherulites is nearly 40μm, which confirms the presence of non-polar α-phase.[33]

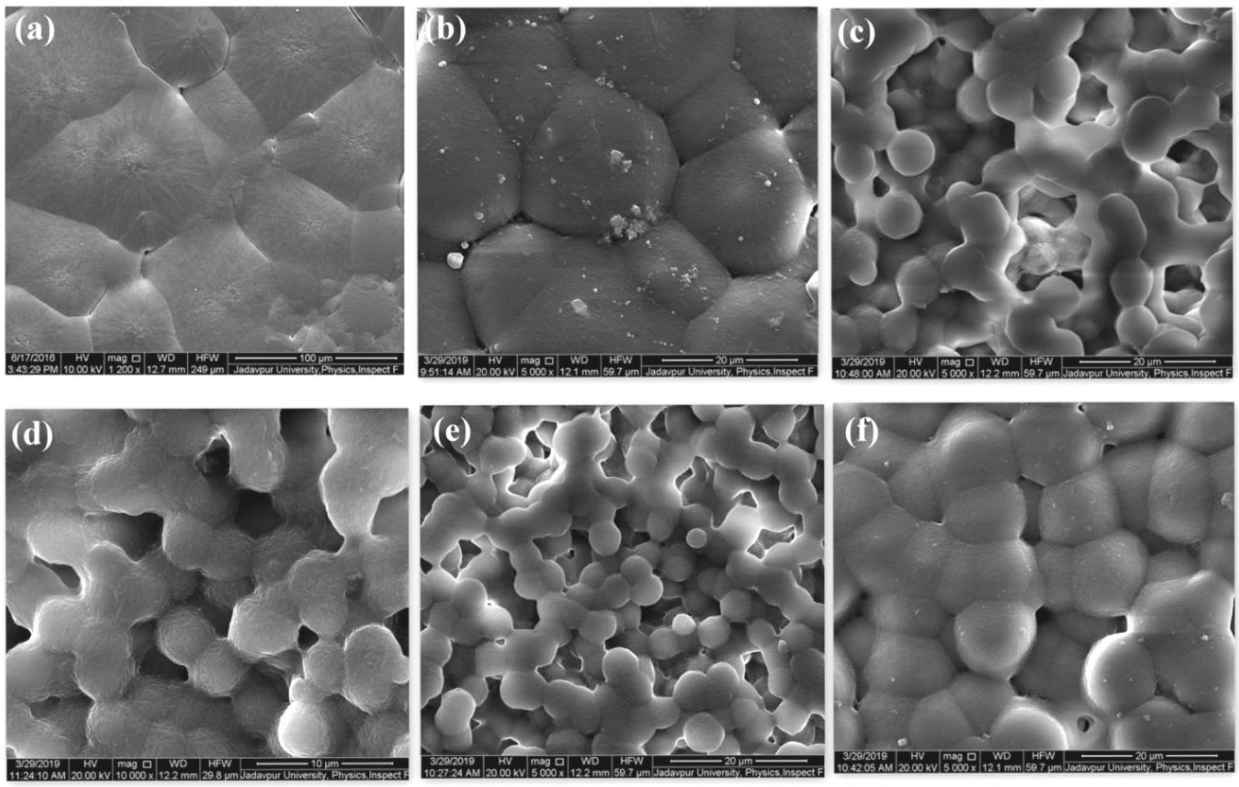


***Figure 3.3:*** *FESEM pictures of (a) pure PVDF and (b)-(f) different concentrated N-CDs loaded PVDF nanocomposites.*

### *3.4.2 Electroactive β- phase analysis*

The FTIR spectra and XRD patterns help in investigating the phase behavior of pure PVDF nanocomposite, and N-CDs loaded PVDF (PCD) films. The X-ray diffraction study confirms electroactive β-phase formation into the PVDF matrix. The XRD pattern of pure PVDF film and N-CDs loaded PVDF (PCD) films are shown in figure 3.4(a). In the case of pure PVDF nanocomposite, we get peaks at 2θ = 17.6° (100), 18.3° (020), 19.9° (021), and26.6° ((201), (310)) which indicate the presence of non-polar α-phase. A minute peak at 2θ =38.3° is observed in the XRD pattern of pure PVDF nanocomposite due to the reflection from either the (002) plane or the (211) plane where (002) plane corresponds to α- phase and (211) plane corresponds to γ-phase.[31,32(a)] This issue has been solved by FTIR analysis of pure PVDF nanocomposite. With addition of N-CDs into the PVDF matrix, all XRD peaks corresponding to α and γ phases vanish. Only one distinctive peak at 2θ = 20.6 ((110),(200)) has a substantial rise, which confirms the nucleation of electroactive β-phase in PCD nanocomposites.[36] A closer scrutiny of the XRD patterns indicates maximum intensity of diffraction peak at 2θ =20.6 for 2.5 mass percent loading of N-CD into PVDF matrix (PCD 2.5), confirming more electroactive β-phase crystallization in these PCD films. The amounts of α-phase and β-phase content are estimated by the ratio between $I_{20.6}$ and $I_{18.3,}$ as shown in figure 3.4(b). This figure shows that for PCD 2.5, we get a maximum ratio which is 3.537. Figure 3.4(c) and 3(d) describe the FTIR spectra of pure PVDF and N-CDs incorporated PVDF (PCD) films in the range of 400 to 1100$cm^{-1}$. The FTIR spectrum of pure PVDF indicates the absorbance peaks of non-polar α-phases at 487$cm^{-1}$ ($CF_2$ waging), 531$cm^{-1}$ ($CF_2$ bending), 616 and 764$cm^{-1}$ ($CF_2$ bending and skeletal bending), and 796 and 976$cm^{-1}$ ($CH_2$ rocking). A small peak is observed in the FTIR spectrum of pure PVDF nanocomposite at 840$cm^{-1}$ due to $CH_2$ rocking, $CF_2$ stretching, and skeletal C−C stretching, which indicates the presence of β- phase though there is an absence of absorbance band of γ-phase at 1234$cm^{-1}$. However, in the case of the PCD nanocomposites, all absorbance peaks of non-polar α-phase vanish entirely. Only the absorbance peaks at 445$cm^{-1}$ ($CF_2$ rocking and $CH_2$ rocking), 479$cm^{-1}$ ($CF_2$ deformation), 510 $cm^{-1}$ ($CF_2$ stretching), 600 $cm^{-1}$ ($CF_2$ wagging), and 840 $cm^{-1}$ are raised prominently. The presence of peaks at 445, 510, and 840$cm^{-1}$ bands in the FTIR spectra is certainly the signature of nucleation of electroactive β-phases in the N-CDs doped PVDF nanocomposites.[36] Therefore, due to the catalytic effect of

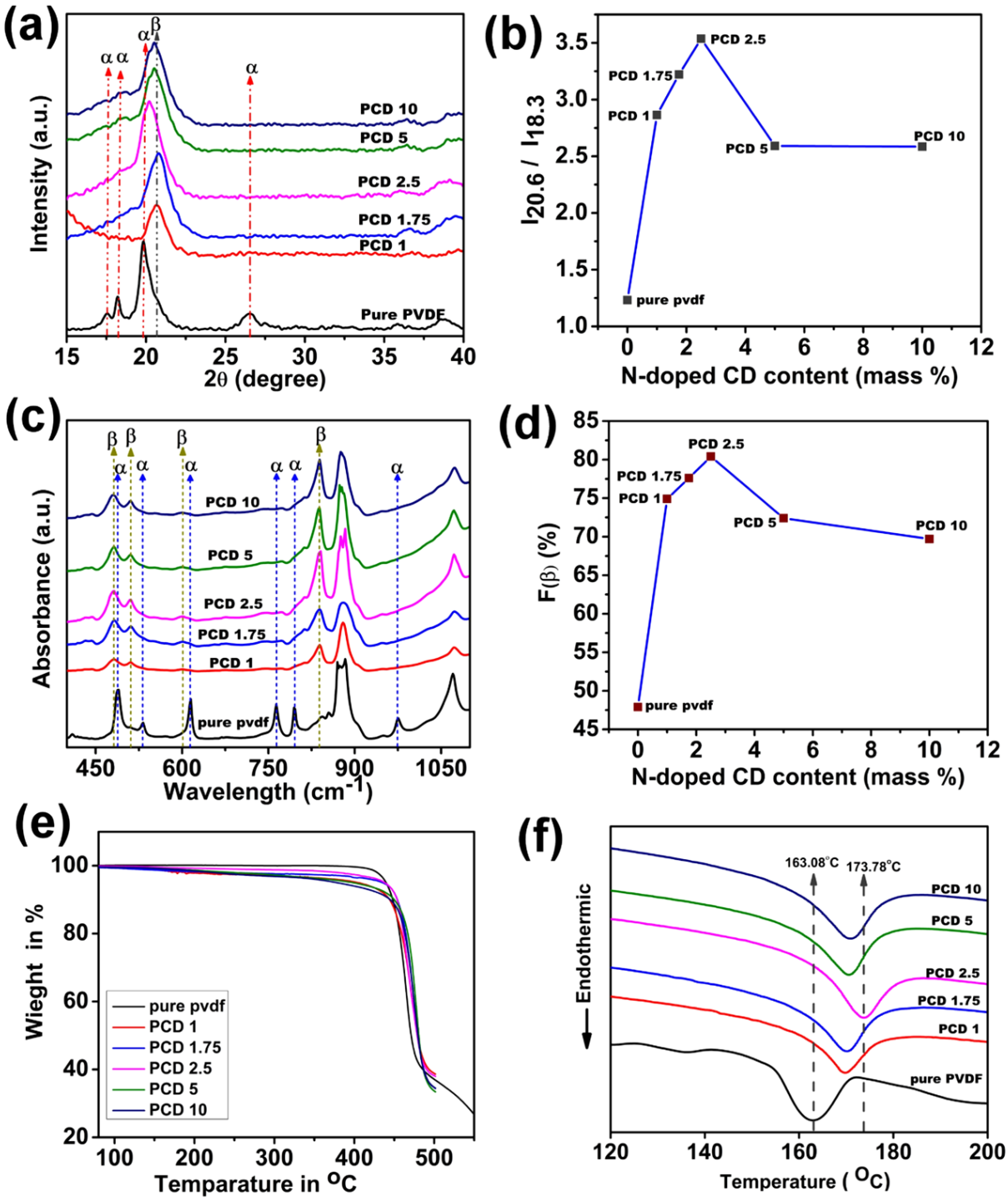


***Figure 3.4:*** *(a) XRD pattern of pure PVDF and N-CDs incorporated PCD nanocomposites (PCD 1, PCD 1.75, PCD 2.5, PCD 5 and PCD10). (b) $I_{20.5}$ / $I_{18.3}$ ratio of measured samples from XRD pattern. (c) FTIR spectra of pure PVDF and PCD nanocomposites. (d) Content of β-phase*

*of measured samples. (e) TGA analysis and (f) DSC thermograph of pure PVDF and N-CDs doped PCD nanocomposites.*

N-CDs in the PVDF matrix, β-phases are mainly nucleated in the composite samples. Closer inspection of the FTIR spectra of the composite nanocomposites reveals that the intensity of the absorbance bands of β-phase is seemed to be maximized for PCD 2.5 (figure 3.4(c)). These results are in agreement with the XRD data (figure 3.4(a)). In order to estimate the amount of β phase present in the PCD nanocomposites, we have calculated the fraction of electroactive β-phase content (F(β)) with the help of The Lambert−Beer law:[37]

$$\boldsymbol{F(\beta) = \frac{A_\beta}{\left(\frac{K_\beta}{K_\alpha}\right)A_\alpha + A_\beta}} \qquad \text{…………} (3.1)$$

Where, $A_\alpha$ = absorbance at 764cm$^{-1}$, $A_\beta$ = absorbance at 840 cm$^{-1}$, $K_\alpha$ = 6.1 X 104cm$^2$ mol$^{-1}$(absorption coefficients at 764cm$^{-1}$), $K_\beta$ = 7.7 X 104cm$^2$ mol$^{-1}$(absorption coefficients at 840cm$^{-1}$).The equation 3.1 gives us an idea about the amount of β phase present in the PCD nanocomposites and this assessment is very important as better β phase nucleation leads to better piezoelectric property. The fraction of β-phase increases with the doping concentration of N-CDs and attains a maximum value for 2.5 mass percent (F(β) ≈ 80.4%), which is shown in figure 3.4(d). The β-phase content increases with the doping concentration of CDs and attains a maximum F(β) value (80.4%) for 2.5% doping. The reason behind this is the interaction between dopant and polymer matrix. Generally, at lower doping concentrations, the interfacial area among the dopant and polymer remains low. As we are increasing the doping concentration, interfacial area also increases by improving the dopant-polymer interaction. As a result, number of chains aligning with all trans (TTTT) conformation inside the PVDF matrix increases which helps in increase in β-phase content.[32(c)] In case of 2.5% CDs, maximum dispersion and distribution properties of CDs in the PVDF matrix take place. As a result, the most intimate interaction occurs among the dopant (CDs) and PVDF matrix and we get the highest number of all trans (TTTT) conformation aligning chains inside the PVDF matrix. On further increasing the mass% on CDs in PVDF agglomeration takes place which results in reduction in the interfacial surfaces between CD and PVDF matrix leading to a decrement in β-phase content. The

electrostatic interaction takes place between negative charge surface of CDs and positive -$CH_2$ group of PVDF, which helps in formation of β-phase.

### *3.4.3 Thermal analysis*

The thermal strength of the PCD nanocomposites has been examined by the TGA thermograph shown in the figure 3.4(e). The study is performed by placing the nanocomposites under a nitrogen atmosphere within the temperature range of 30°C to 500°C with the heating rate at 10°C/min. From the figure 3.4(e), it can be noticed that a very small amount of weight loss takes place between the temperature of 350°C to 450°C in case of PCD nanocomposites, which is trivial compared to pure PVDF nanocomposite. After crossing the temperature of 450°C, a gradual shift of degradation temperature of PCD nanocomposites is observed. The TGA thermograph also exhibits that after completing the 50% weight loss, we get the different degradation temperature for different doping concentration based PCD nanocomposites, which is higher in comparison with the degradation temperature of pure PVDF nanocomposite at the same weight loss. For example, in case of pure PVDF nanocomposite the degradation temperature at 50% weight loss is 466°C, whereas, the degradation temperature for PCD 2.5 nanocomposite at same weight loss is 480°C. The homogeneous dispersion of N-doped CD into polymer matrix and interfacial strength between N-doped CD and PVDF are the key factors for getting such higher degradation temperature of PCD nanocomposites.[20] Thus, the TGA thermograph and above said discussion indicate that PCD films have higher thermal stability than pure PVDF nanocomposite.

The crystallization behaviors and melting temperature of PCD nanocomposites has been investigated by differential scanning calorimetry (DSC) analyzer. The formation of β-crystalline phase of PCD nanocomposites is also confirmed by DSC analysis. Figure 3.4(f) represents the melting temperatures and crystallization behaviors of pure PVDF and N-doped CD incorporated PVDF (PCD) nanocomposites. From DSC thermographs, the melting temperature ($T_m$) of pure PVDF is 163.08°C, which confirms the presence of the non polar α-crystalline phase inside the nanocomposite.[20] Whereas, in case of PCD nanocomposites, noticeable shift in melting temperature are observed, which are higher in comparison to pure PVDF. Among all nanocomposites, PCD 2.5 exhibits better melting temperature ($T_m$) with the value of 173.78°C. Therefore, the shifting of melting temperature confirms the transformation of α-crystalline phase

(TGTG conformation) to β-crystalline phase (TTTT conformation) of PVDF. Thus, the experimental investigations confirm that N-doped CD is a very good nucleating agent and plays an important role in β-crystalline phase formation. This statement is commensurate with previously described XRD and FTIR results.

### *3.4.4 Phase transformation of PVDF*

The incorporation of CDs into PVDF leads to phase transformation of PVDF by changing the α-phase into β-phase, which is also confirmed by XRD, FTIR and TGA analysis. When CDs are incorporated into PVDF matrix, the interaction between negatively charged surface of CDs and positive -$CH_2$dipoles of polymer takes place, making the CDs as nucleation sites for β-phase formation. As a result, the non polar α- phase nucleates into polar β-phase. Due to this strong electrostatic interaction, the PVDF chains get aligned on the surface of CDs which leads to the formation of all trans (TTTT) electroactive β-phase in the polymer matrix.[55] The schematic of electrostatic interaction between negative charge surface of CDs and positive -$CH_2$ group of PVDF has been represented schematically in the figure 3.5.

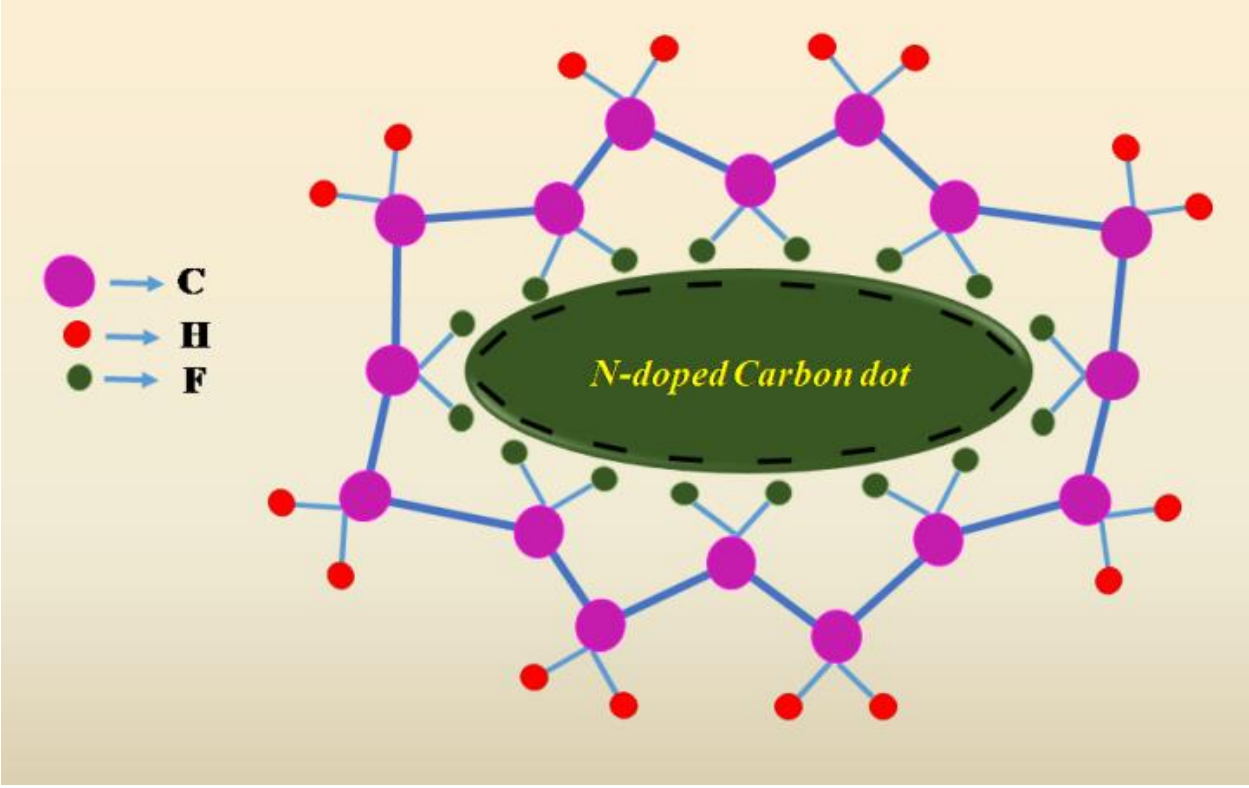


***Figure 3.5:*** *Schematic representation of electrostatic interaction.*

### *3.4.5 Theoretical estimation (DFT) of the formation of electroactive β-phase*

The results obtained from the basic characterizations such as XRD and FTIR shows the formation of β phase with increasing dopant (N-CD) concentrations. Thus, density functional calculations have been performed to obtain the structural and electrical characteristics of the sample. Herein, the DFT study has been implemented using Orca v.1.2 program. The hybrid Becke, 3-parameter, Lee-Yang-Parr (B3LYP) functional has been used along with 6-31G* basis set and RIJCOSX auxiliary basis function to accommodate atoms like C, H and F. The molecular models of both α and β-phases were prepared in Avogadro v.1.2.0 software program. Initially, the geometries and frequencies were optimized of both the models and no imaginary frequency were found, which ensures the validity of the structures.

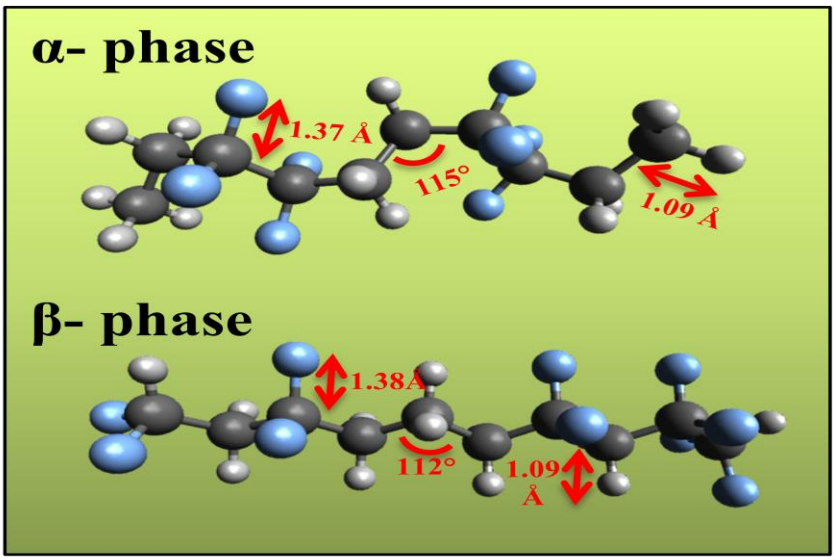


***Figure 3.6:*** *Geometry optimized structures of α and β-phases of PVDF showing bond angle and bond lengths.*

It is observed that the randomized orientation of C and F in α-PVDF radically polarized into the β-phase, which causes a significant change in dihedral C-C-C angle (mentioned in figure 3.6). Almost all F and H have been rotated to the either side of C-C chain, which not only polarizes the model but also minimizes the single point energy of the β-PVDF. Such energy minimization in β-PVDF stabilizes its structure. Moreover, the electrical properties have been estimated theoretically using DFT, which shows significant changes in both dipole moment and isotropic

polarizability. A detailed comparison of electrical properties of α and β-phases of PVDF have been depicted in table 3.2. Such an augmented polarizability and dipole moment is desirable in piezoelectric materials.

***Table 3.2:*** *Comparison of the electrical properties between α and β-phases of PVDF*

| | *Energy (joule)* | *Dipole moment (debye)* | *Quadrupole moment (a.u.)* | *Polarizability (a.u.)* |
|---|---|---|---|---|
| *α phase of PVDF film* | *-5.1* | *0.37* | *73.74* | *106.62* |
| *β-phase of PVDF film* | *-6.04* | *3.68* | *86.06* | *108.54* |

### *3.4.6 Working mechanism of PPNCD*

The fabricated piezoelectric nanogenerator (PPNCD) generates appreciable voltage from mechanical energy generated through continuous finger impartation. The synergistic effect of the dipoles, which are present in PVDF i.e. electroactive β-phases and nitrogen doped carbon dots (N-CDs), may explain the possible working mechanism of PPNCD. The presence of N-CDs molecules in the composite matrix triggers the electroactive β-phase formation with the help of strong electrostatic interactions between the water molecules of N-CDs and the negative $–CF_2$ dipoles of the PVDF matrix during the formation of hydrogen bonds. When an external mechanical force is applied on the PPNCD under periodic finger imparting, a secondary potential is generated in the N-CDs molecules, which arrange the PVDF dipoles in the direction of the applied mechanical force, thus promoting stress-associated polarization. When a vertical mechanical compression is given on the PPNCD, a positive potential at the top electrode and a negative potential at the bottom one have been produced due to formation of self-polarization

induced by the deformation of the crystalline structure of the N-CDs doped PVDF nanocomposite (PCD 2.5). The potential difference between the two electrodes along with self-polarization, regulates the flow of electrons from one electrode to another through an external load. The piezoelectric potential abruptly diminishes after the quick release of the compressive force. The electrons gathered at the bottom electrode flow back to the other electrode via the external circuit, ensuing in an opposite electrical output.[37] This process is repeated in the PPNCD under continuous compression and relaxation consecutively to obtain the output electric signals from the piezoelectric energy harvesting device. Figure 3.7 describes the voltage generation mechanism of the PPNCD device. Furthermore, the working principle of PPNCD device can be illustrated with the help of Maxwell's equations. In electrodynamics, Maxwell's equations remain constant with local invariance which can be expressed in the equation form

$$\boldsymbol{\nabla}.\vec{\boldsymbol{J}} + \frac{\boldsymbol{\partial}}{\boldsymbol{\partial t}}(\boldsymbol{\nabla}.\vec{\boldsymbol{D}}) = \mathbf{0} \quad \textit{(3.2)}$$

$$\textbf{Or, } \frac{\boldsymbol{\partial \rho}}{\boldsymbol{\partial t}} + \boldsymbol{\nabla}.\vec{\boldsymbol{J}} = \mathbf{0} \quad \textit{(3.3)}$$

This equation is called continuity equation. Where, **J** and **ρ** are the total current density and total charge density.

The charge density can be defined as

$$\boldsymbol{\rho} = \boldsymbol{\rho_f} + \boldsymbol{\rho_b} \quad \textit{(3.4)}$$

Where, $\rho_f$ = free charges and $\rho_b$ = bound charges.

The current density can be expressed as

$$\boldsymbol{J} = \boldsymbol{J_f} + \boldsymbol{J_b} \quad \textit{(3.5)}$$

Where, $J_f$ = free currents and $J_b$ = bound currents.

In case of dielectric materials, the auxiliary fields take active part in dipole formation, can be defined as

$$\boldsymbol{D(r,t)} = \boldsymbol{\epsilon_0 E(r,t)} + \boldsymbol{P(r,t)} \quad \textit{(3.6)}$$

$$\boldsymbol{H(r,t)} = \frac{\boldsymbol{B(r,t)}}{\boldsymbol{\mu_0}} + \boldsymbol{M(r,t)} \quad \textit{(3.7)}$$

Where, D = displacement field; $\epsilon_0$ = permittivity of free space; E = electric field; P = polarization; H = magnetic field; $\mu_0$ = permeability of free space; B = magnetic induction; M = magnetization.

In our present work, Maxwell's equations in matter can be utilized to describe the working principle. Considering the free charges and current, the Maxwell's equations will be

$\boldsymbol{\nabla}.\vec{\boldsymbol{D}} = \boldsymbol{\rho_f}$ (Gauss's Law of electrostatics)……... *(3.8)*

$\boldsymbol{\nabla}.\vec{\boldsymbol{H}} = \mathbf{0}$ (Gauss's law magnetostatics)……... *(3.9)*

$\boldsymbol{\nabla x}\vec{\boldsymbol{E}} = -\frac{\boldsymbol{\partial}\vec{\boldsymbol{B}}}{\boldsymbol{\partial t}}$ (Faraday's law)…….. *(3.10)*

$\boldsymbol{\nabla x}\vec{\boldsymbol{H}} = \vec{\boldsymbol{J}}_{\boldsymbol{f}} + \frac{\boldsymbol{\partial}\vec{\boldsymbol{D}}}{\boldsymbol{\partial t}}$ (Ampere's circuital law with correction)……. *(3.11)*

Where, $\vec{E}$ = electric field, $\vec{D}$ = displacement electric field, $\vec{B}$ = magnetic induction, $\vec{H}$ = magnetic field, $\rho_f$ = volume charge density of free electron, $\vec{J}_f$ = current density due to free electron flow.

From electrodynamics, with the help of following equations, we get the displacement current for an electric field and polarization current for an electric polarization respectively.

$\boldsymbol{J} = \boldsymbol{\epsilon_0}\frac{\partial \mathbf{E}}{\partial \mathbf{t}}$ …… *(3.12)*

$\boldsymbol{J_P} = \frac{\partial \mathbf{P}}{\partial \mathbf{t}}$ ……... *(3.13)*

Thus, in case of linear isotropic medium, the second term of Maxwell's fourth equation (equation 3.11) represents the total displacement current ($\vec{J}_D$).

$\vec{\boldsymbol{J}}_{\boldsymbol{D}} = \frac{\boldsymbol{\partial}\vec{\boldsymbol{D}}}{\boldsymbol{\partial t}} = \boldsymbol{\epsilon_0}\frac{\boldsymbol{\partial}\vec{\boldsymbol{E}}}{\boldsymbol{\partial t}} + \frac{\boldsymbol{\partial}\vec{\boldsymbol{P}}}{\boldsymbol{\partial t}}$ …… *(3.14)*

There, the total displacement current is a time-dependent term and depends on the electric field and electric polarization of the dielectric medium. The first term of equation (xiv) helps in enhancement of output performance of wireless system like radio, RADAR, Wi-Fi etc. and the second term enhances the piezoelectric effect by increasing the value of P, depends on the applied force or strain. Applying mechanical strain on a linear isotropic material, the piezoelectric equations will be[37]

$$\vec{P}_i = (e)_{ijk}\left(\vec{S}\right)_{jk} \quad \text{(3.15)}$$

$$\vec{T} = C_E\vec{S} - e^T\vec{E} \quad \text{(3.16)}$$

$$\vec{D} = e\vec{S} - k\vec{E} \quad \text{(3.17)}$$

Where, $\vec{S}$ = mechanical strain, $(e)_{ijk}$ = piezoelectric third order tensor, $\vec{T}$ = stress tensor, $C_E$ = elasticity tensor, k = dielectric tensor.

The displacement current of a linear polarizing medium is

$$\vec{J}_{Di} = \frac{\partial \vec{P}_i}{\partial t} \quad \text{(3.18)}$$

So, the equation 3.18 concludes that the piezoelectric effect and output current density is directly proportional to the rate of change of applied force or strain. Therefore, the attaining output value of PPNCD by applying force matches with the theoretical equations.

In absent of external field E on dielectric medium, displacement current is only depend on the polarization (from equation 3.18 ). Taking the polarization along the z direction, we can write that

$$D_z = P_z = \sigma_P(z) \quad \text{(3.19)}$$

Where, $\sigma_P(z)$ = piezoelectric polarization surface charges density of the material.

Then, the displace current term along z direction will be

$$J_{DZ} = \frac{\partial P_z}{\partial t} = \frac{\partial \sigma_p(z)}{\partial t} \quad \text{(3.20)}$$

The above equation clearly explains the reason of getting high output performance of PPNCD device.

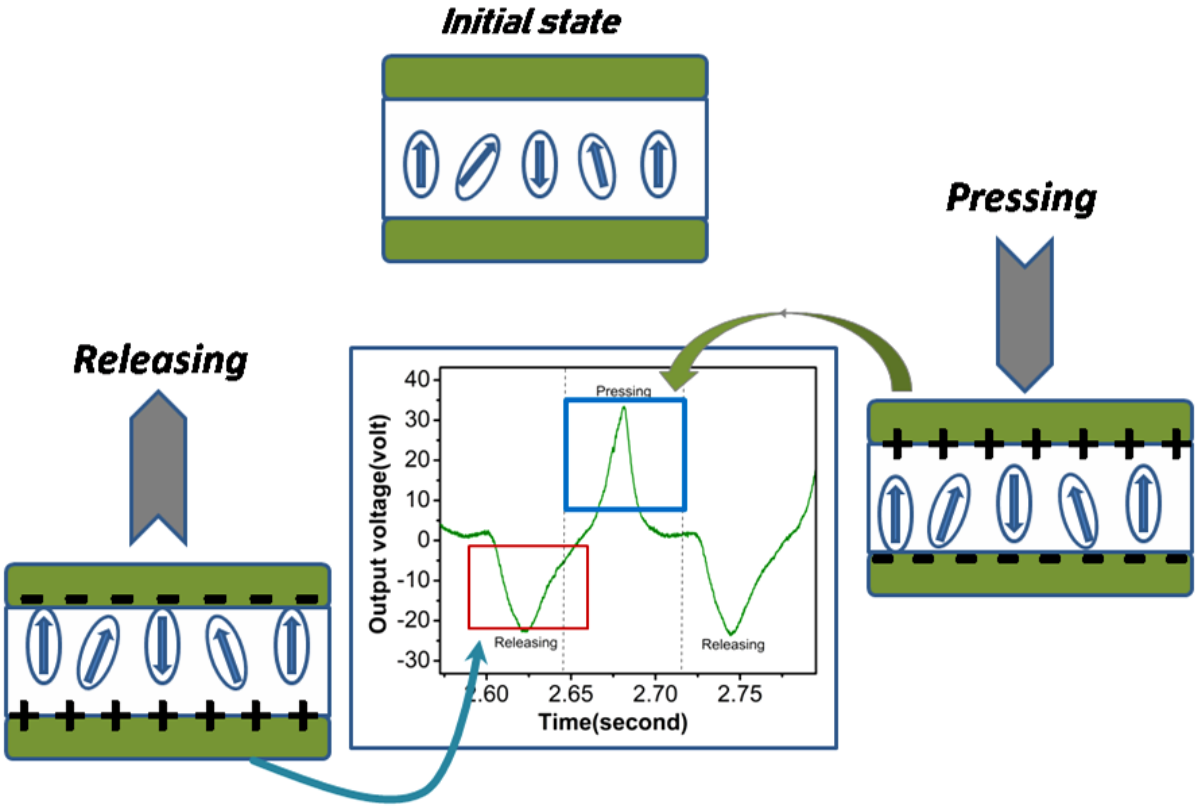


***Figure 3.7:*** *Possible voltage generation mechanism of our fabricated device.*

### *3.4.7 Output performances of PPNCD nanogenerators*

The fabrication process of the device (PPNCD) is shown schematically in figure 3.1(a). A digital snapshot of the fabricated device is displayed in figure 3.1(c) and the flexibility of the device is shown in figure 3.1(d). In the present work, we have designed a piezoelectric energy harvesting device (PPNCD) with the help of N-CDs/ PVDF (PCD) film and PDMS. Figure 3.8(a) shows the output voltage vs. time graph. The output voltage is generated by continuous finger imparting and releasing an axial pressure of 12.3N. The current vs. time output feature of fabricated PPNCD is depicted in figure 3.8(b). Maximum output voltage and current have been obtained at the frequency of 6 Hz. The output performance of the nanogenerator is high during finger impartation. The output voltage (measured by Keysight, Oscilloscope DSO-X 3012A) and the short circuit current (observed by Keysight, Electrometer B2985) of PPNCD are $V_{OC}$ ~80V and $I_{SC}$ ~ 1.4µA respectively (figure 3.8(a) and (b)). The difference in the peaks values of the output voltage and current during periodic pressing and releasing is basically owing to the inconsistency of the given strain on the piezoelectric energy harvester during manual finger impartation. While

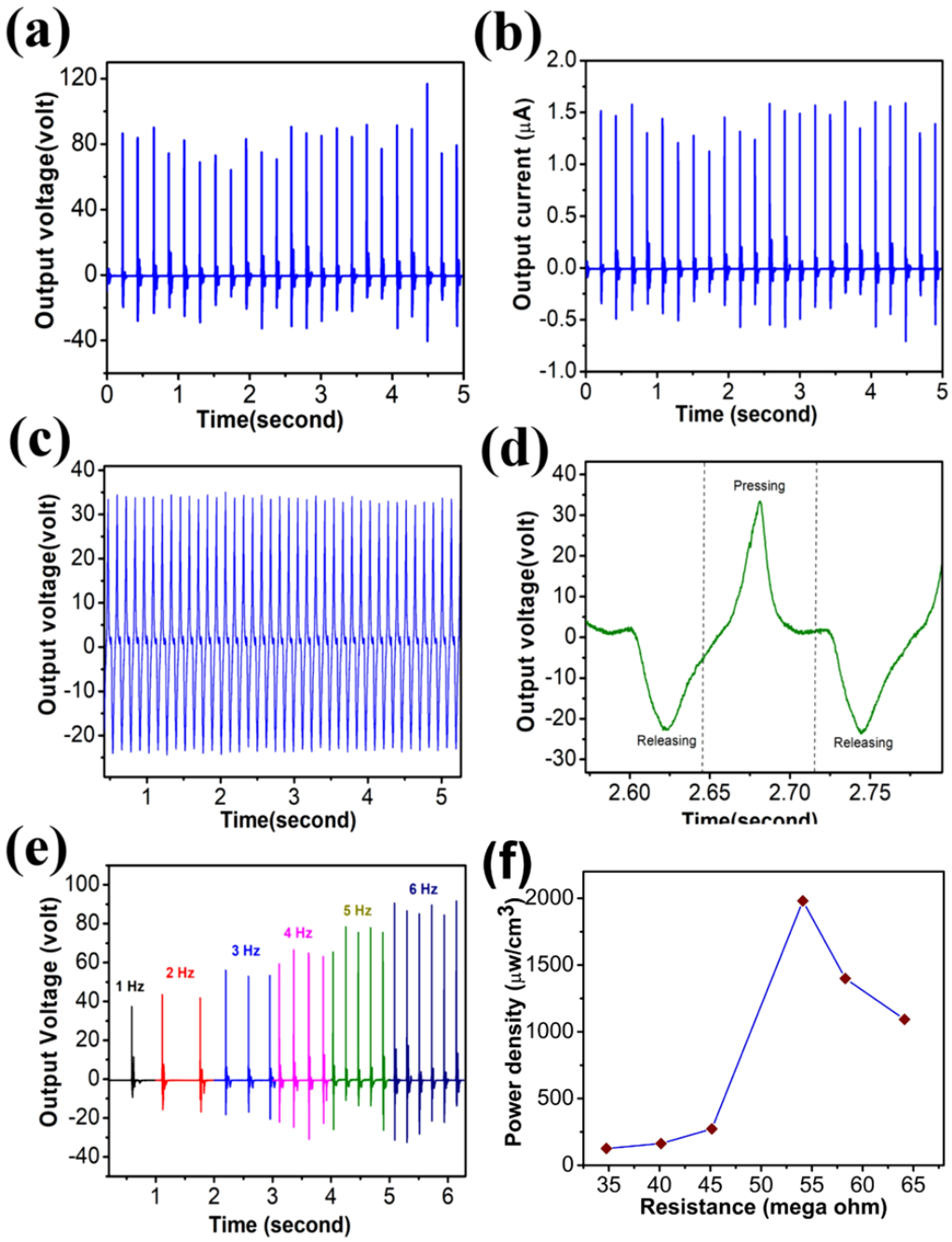


***Figure 3.8:*** *(a) Open circuit voltage ($V_{OC}$) and (b) short circuit current ($I_{SC}$) of fabricated PPNCD device under periodic finger impartation at frequency 6 Hz. (c) Output voltage generation and (d) enlarged view of $V_{OC}$ under 5N force at 6Hz frequency. (e) Frequency dependent output voltage generated by human finger impartation. (f) Power density for various load resistances.*

recording the data of output voltage vs. time graph of PPNCD device on the application of force by hand, we have tried to maintain uniformity as much as possible. Since the applied force is not machine operated, some human error occurs during the process and every cycle does not obtain the exact force.[17]This discrepancy in the applied force led to the asymmetric peaks in the output voltage vs. time graph. Another reason for this asymmetry in voltage output is that the time period for every cycle of applied force is not exactly the same. This again is due to human error as mentioned earlier. The magnified view of $V_{OC}$ is shown in figure 3.8(d). When strain is applied to the device, the positive peaks appear and negative peaks appear when the device comes back to its original form after recovering the strain. Subsequent small peaks have been obtained due to the damping effect of the N-CDs/PVDF nanocomposite. Compared to the pure PVDF-based piezoelectric nanogenerators[20], the output performance of PPNCD is higher, which indicates that the presence of N-CDs in the PVDF matrix significantly increases the output performances of PPNCD. The piezoelectric co-efficient of the PCD nanocomposite is calculated from the following equation

$$\boldsymbol{d_{33} = \frac{Q}{F}} \quad \text{..... (3.21)}$$

Where $d_{33}$ is the piezoelectric co-efficient, Q is the charge which is generated by applied force and F is the applied force of 12.3N. Again, the charge is calculated using the equation

$$\boldsymbol{Q = \int I_{sc}\, dt} \quad \text{..... (3.22)}$$

Where, $I_{SC}$ is the short circuit current.[47] The value of Q is 359pC which is calculated from short circuit current vs. time plot. Putting the value of Q and F in the $d_{33}$ equation, we get the final value of piezoelectric co-efficient ($d_{33}$) of the PCD nanocomposite, which is 29pC/N. This value confirms the presence of the polar β-crystalline phase and electret dipoles in the PCD nanocomposite. The efficient power density is calculated from the equation

$$\boldsymbol{P = \frac{V^2}{R_L \times v}} \quad \text{..... (3.23)}$$

Where, V is the output voltage, $R_L$ is the load resistance, and v is the volume (surface area X thickness). The fabricated PPNCD device can produce an excellent peak power density of 1979.87μWcm$^{-3}$ at 57 MΩ loads (figure 3.8(f)). The reasons behind such high power density are as follows

i) The strain encouraged piezoelectric potential generated by the N-CDs and the self-poled PVDF polymer under continuous finger tapping force (~12.3N) to reinforce each other.

ii) The continuous finger tapping helps in generating the additional strain which in turn encourages spontaneous polarization and resultant dipole formation, leading to the charge separation and accumulation of charges at the edge sites of piezoelectric N-CDs and PVDF polymer.

The voltage generation record during twisting and bending of the device shows no significant output, which confirms the absence of a triboelectric effect in this particular case. Figure 3.8(e) shows the frequency-dependent (1Hz to 6Hz) output performance of the device, obtained by continuous finger impartation. The output voltage increases gradually as the frequency of finger impartation on PPNCD increases. The output performance of our fabricated device depends on the impedance and the applied strain frequency. The impedance and the applied strain frequency of PPNCD are inversely proportional to each other[20]. Furthermore, the output performance of PPNCD device has been compared with previously reported carbon doped piezoelectric nanogenerator (Table 3.3) which confirms the better performance of the fabricated device.

***Table 3.3:*** *Comparison of the output performance of PPNCD device with the formerly reported carbon based PENG.*

| *Carbon based PENG* | *Force* | *$V_{OC}$* | *$I_{SC}$* | *Power density* |
|---|---|---|---|---|
| ***Investigating the role of carbon nanotubes(CNTs) In the piezoelectric performance of a PVDF/KNNbased electrospun nanogenerator[49]*** | *Finger tapping* | *23.24 V* | *9 µA* | *52.29µW/cm$^2$* |

| | | | | |
|---|---|---|---|---|
| ***Humidity Sustainable Hydrophobic Poly(vinylidene fluoride)-Carbon Nanotubes Foam Based Piezoelectric Nanogenerator[50]*** | *0.25 N* | *12 V* | *30 nA/cm$^2$* | |
| ***PVDF Nanofibers with Embedded Polyaniline−Graphitic Carbon Nitride Nanosheet Composites for Piezoelectric Energy Conversion[51]*** | *Punching mode* | *30 V* | *3.7 µA* | *14.7 µW/cm$^2$* |
| ***Flexible Interconnected Cu-Ni Nanoalloys Decorated Carbon Nanotube-Poly(vinylidene fluoride) Piezoelectric Nanogenerator[52]*** | | *12 V* | *0.3 µA/cm$^2$* | *204 µW/cm$^3$* |
| ***Boosting piezoelectric and triboelectric effects of PVDF nanofiber through carbon-coated piezoelectric nanoparticles for highly sensitive wearable sensors[53]*** | *14.7 N* | *40 V* | | |
| ***Development of a carbon nanofiber-attached flexible piezoelectric nanocomposite towards self-powered wearable devices[54]*** | *Bending* | *0.62 V* | | |
| *Our present work* | ***12.3 N*** | ***80V*** | ***1.4 µA*** | ***1979.87µWcm$^{-3}$*** |

### *3.4.8 Weight sensing performance of PPNCD*

Excellent response has been observed while checking the sensitivity of PPNCD by dropping various rubber balls of different masses from a height of 10 cm on the top surface of the device, as shown in figure 3.9(a) to (e).By dropping rubber balls of masses 108.79g, 35.22g, 59.35g, 9.18g, and 15.04g, the observed output voltages are 7V, 9V, 10V, 11V, and 13V.The reason for getting different output voltages depends on the different masses and contact areas of balls with surface of the film. In case of 108.79g mass contained rubber ball, we get low output voltage in comparison with other mass contained rubber balls. The reason behind this is the harder surface, larger size and low elastic properties of 108.79g mass contained ball than other balls. Besides this, we have investigated the capability and sensitivity of the device with some Indian coins which are of different weights but of nearly the same size. The coins are released from a height of 10cm on the upper surface of PPNCD. When a coin falls on the device, N-CDs and PVDF move toward each other, and we get output voltage. Due to the different masses of Indian coins (1 rupee, 2 rupee, 5 rupee, and 10 rupee), we get different output voltages which are shown in figure 3.9(f). The graph describes that with the increasing masses of Indian coins, the output voltage also increases. The sensitivity performance of PPNCD device has been depicted in the figure 3.9(g) and 3.9(h).

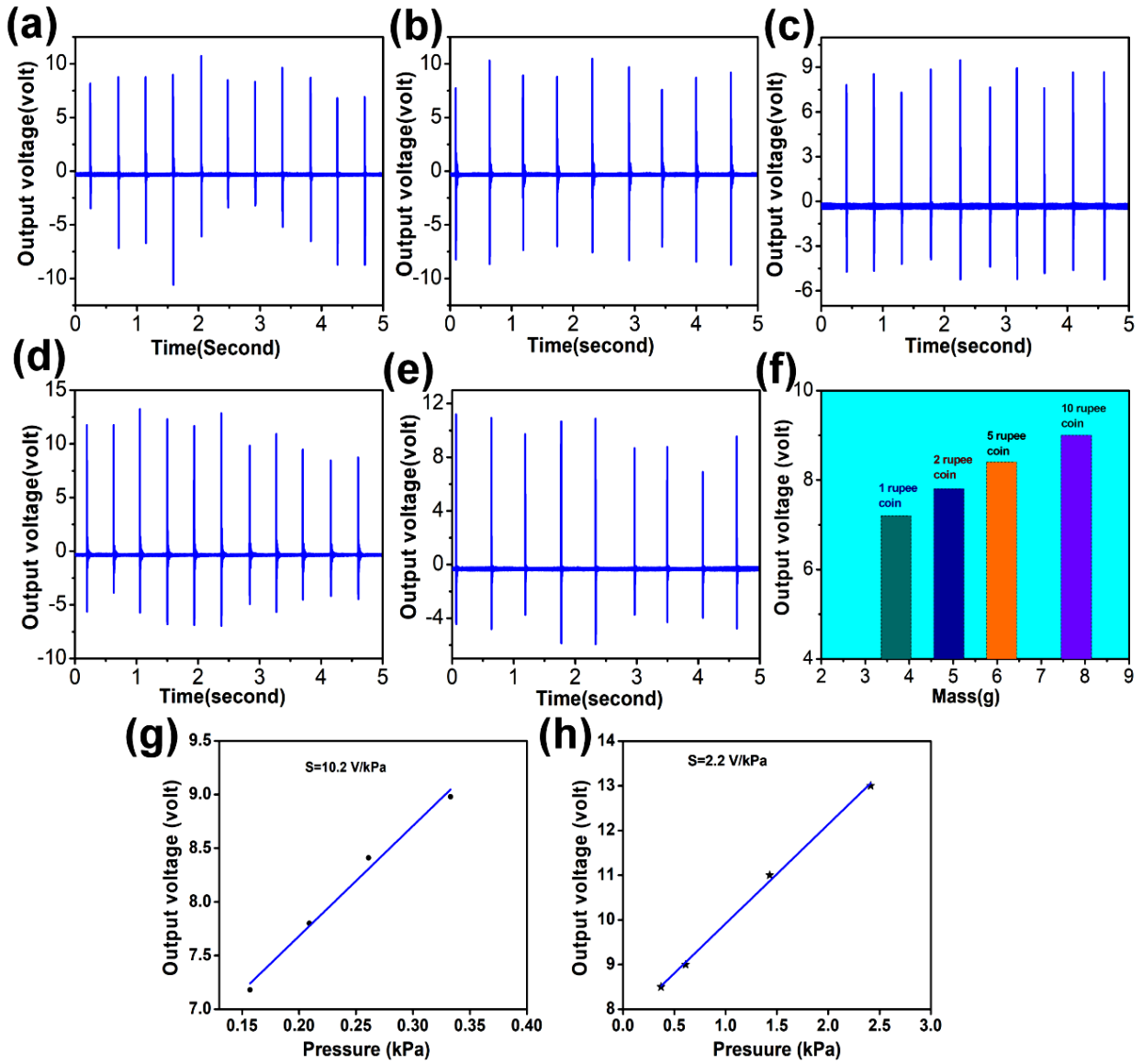


***Figure 3.9:*** *(a)-(e) Output voltage generated by falling different masses (108.9g, 35.22g, 59.35g, 9.18g, and 15.04g) of rubber balls on PPNCD device. (f) Response of the device by dropping different masses of Indian coins on the upper part from 10 cm height. The sensitivity of the PPNCD device performed with respect to stress, employed by (g) falling coins and (h) dropping different masses of rubber balls.*

These two graphs describe that output voltage of fabricated device increases by increasing the external pressure and maintain the linear relationship between output voltage and pressure. The sensitivity of the device has been measured by the following equation

$$S = \Delta V / \Delta P \quad \text{..... (3.24)}$$

Where, ΔV and ΔP are the change in the output voltage and applied external pressure.[47] The sensitivity of PPNCD device is found to be 10.2V/kPa up to the external pressure region of 0.36kPa, which is generated by falling different masses coins, shown in the figure 3.9(g). Furthermore, rubber balls having different masses have been dropped on the device from a fixed height of 10cm to check the sensitivity of the device in the higher pressure region. The PPNCD device generates different output voltages at different external pressures and also maintains the linearity pattern between the output voltage and pressure, shown in the figure 3.9(h). The sensitivity of the device in this region (0.5 to 3kPa) is 2.2V/kPa which is very low compared to the sensitivity of the low range pressure region (less than 0.5kPa). Theoretical bounds of the effective strain in the N-doped carbon dots are responsible for this phenomenon in the higher pressure region (> 0.5kPa).[47] Beside this, our device can detect very low pressure of 0.15kPa. The coin and rubber balls dropping experiments give us the sensitivity value and the range of sensitivity of the fabricated device. Along with this, these experiments also describe the capability of the self-powered device to detect the both low and high range pressure. Thus, the PPNCD device can be used as a dedicated weight sensor as well.

### *3.4.9 Voltage generation from human body movements*

The PPNCD device has generated the output voltage from body movements such as foot pressing, heel pressing, pulse cycle, wrist up-down etc. Outstanding output performance has been obtained by attaching the PPNCD device with foot and heel, shown in figure 3.10(a) and 3.10(b). During foot pressing and heel pressing, the generated output voltages are 32V and 12V, respectively, indicating that the fabricated device generates higher voltage during foot pressing due to increase in contact area with the PPNCD device. Figure 3.10(e) displays the output performance during wrist up-down movement. From this graph, we can see that when the wrist is up, the device is sensitive enough to generate nearly 0.62V and when the wrist is down then, the generated output voltage is near about 0.29V, which confirms the capability of the device in

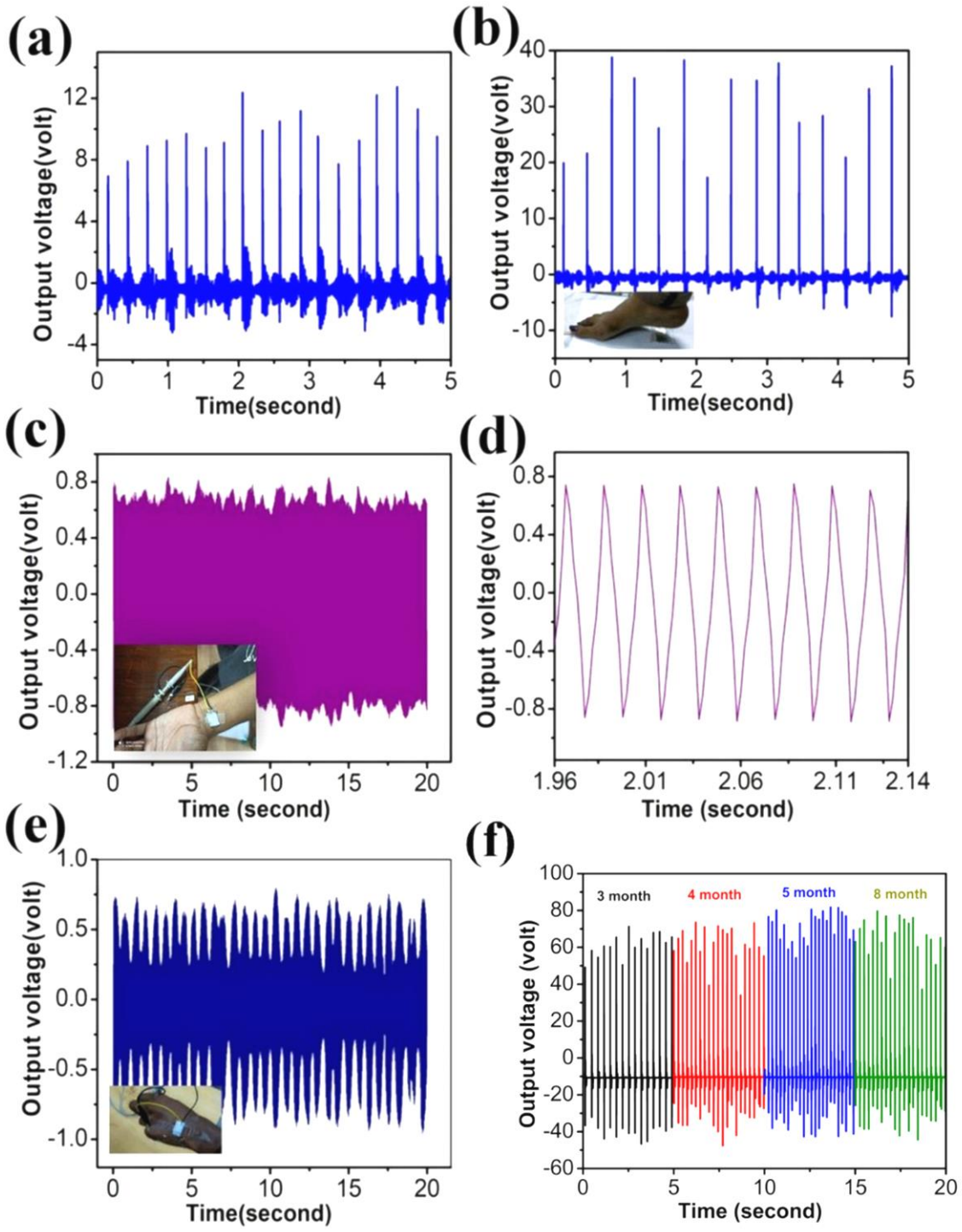


***Figure 3.10:*** *Open circuit voltage generated by (a) forefeet tapping, and (b) heel pressing. (c) and (d) Pulse sensing and magnified view of peaks generated from heartbeats by attaching our PPNCD device to the wrist artery. (e) Voltage generation from wrist up-down. (f) Durability test of PPNCD device.*

harvesting green energy effortlessly. The sensitivity is further verified by attaching the device to wrist artery. Figure 3.10(c) shows the output voltage generated from the pulse wave. During the heartbeat, blood flows through our body, including the wrist, and creates pressure. Systolic pressure and diastolic pressure are the central part of the pulse wave. Systolic pressure gives thepeak, and diastolic pressure gives the trough of the pulse wave. The devised nanogenerator responses quite efficiently to the pulse pressure (occurs due to alternation of systolic and diastolic pressure) during blood flow. The device can detect this pressure and generates voltage, shown in figure 3.10(d). Thus, PPNCD is suitable for sensing pulse waves. The stability and durability of the fabricated PPNCD has been studied for the eight months, and the device continues to produce almost the same output voltage during the whole time period as shown in figure 3.10(f).

### *3.4.10 Commercial LED and capacitor charging ability of PPNCD*

The energy conversion ability of the fabricated PENG (PPNCD) is performed by charging a capacitor and lighting up commercial LEDs. A 2.2µF capacitor has been charged by connecting the PPNCD through a bridge rectifier under continuous finger impartation. The exponential fashion of the capacitor charging graph explains that the device can charge a 2.2µF capacitor, as shown in figure 3.11(a).Our fabricated device PPNCD can charge a 2.2µF capacitor up to 3.2V within 14seconds. As the device involves very short duration to charge a capacitor, it can be used as an alternative energy source for portable or medical devices. Another important aspect of the device is that it light up commercially available transparent LEDs under periodic finger impartation, as shown in figure 3.11(c) and (d). The power produced from PPNCD can light up to 15 blue LEDs or 15 white LEDs by connecting them in series connection through a full-wave bridge rectifier.

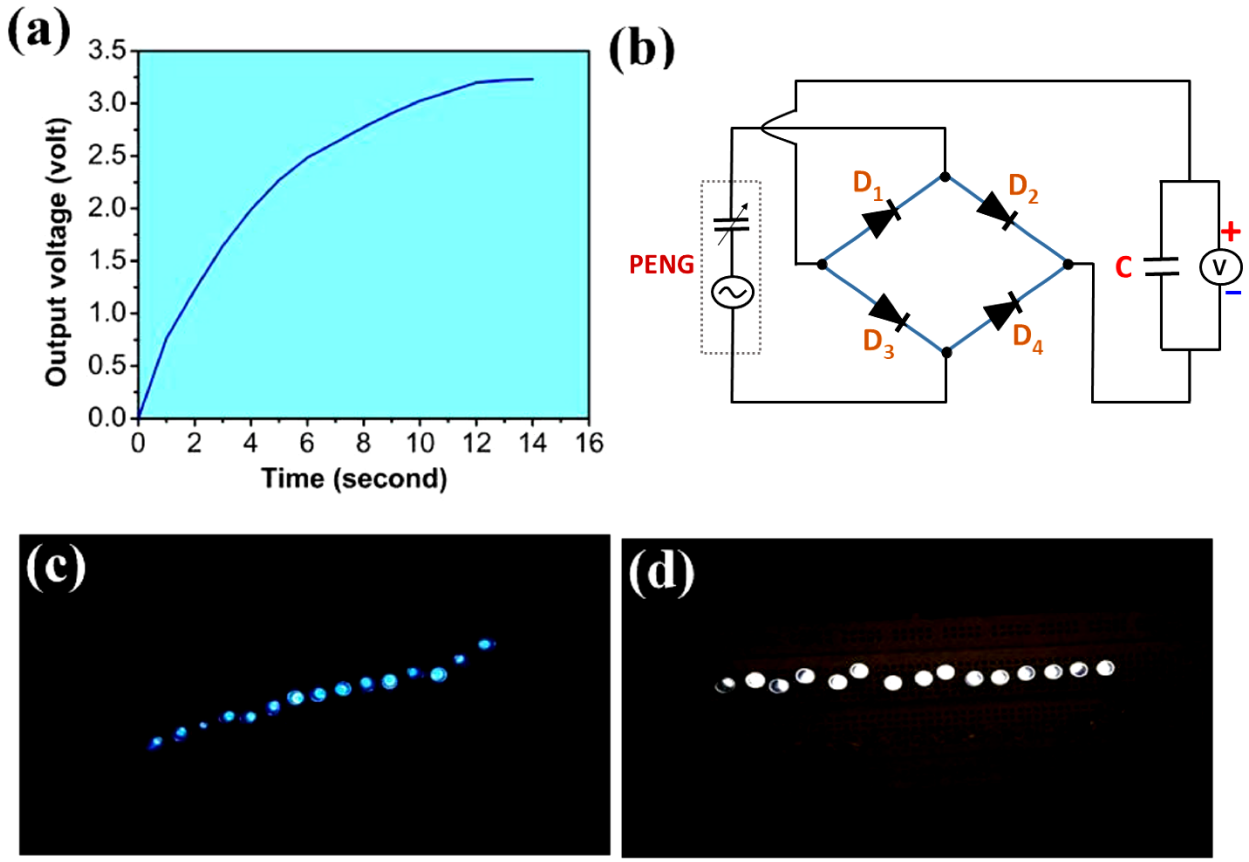


***Figure 3.11:*** *(a) A 2.2μF capacitor charging by PPNCD device. (b) Circuit draw of charging a capacitor and lighting up LEDs. Digital photographs of (c) blue and (d) white LEDs under shining conditions.*

From the previous investigations, we can see that the device fabricated in our laboratory is very sensitive and flexible and can be used as a flexible energy harvester and weight sensor which can generate electricity via various body movements and dropping different weights. Furthermore, PPNCD device can be employed to light up LED, charge capacitor, etc.

## *3.5 Conclusion*

The present work describes the fabrication and action of N-CDs/PVDF nanocomposite-based PENG (PPNCD) in harvesting electrical energy from various mechanical energy sources. The PENG is competent enough to convert mechanical energies of pulse wave and simple body movements into electrical energy with high values of $V_{OC}$ and $I_{SC}$. The impact generated by dropping balls or coins on the PENG have been utilized quite efficient to produce electrical

energy. The self-powered tiny device produces excellent output voltage ($V_{OC}$ ~ 80V) and a short circuit current ($I_{SC}$ ~1.4μA) under periodic finger impartation (~12.3N) with an average of 6Hz frequency. The instant power density of PPNCD is 1979.87μWcm$^{-3}$. Moreover, the highest β-crystalline phase content (F(β) ~ 80.4%) PCD nanocomposite evaluates the piezoelectric co-efficient ($d_{33}$) value of 29pC/N. The density functional theory (DFT) calculations have been performed to investigate the electrical properties of the β-crystalline phase. In addition with this, the PCD nanocomposite assisted wearable sensor has the capability to sense the external pressure at very low region (up to 0.5kPa) along with the sensitivity of 10.2V/kPa. The additional significance of the PPNCD has been established by charging a 2.2 μF capacitor up to 3.2V in a short period (14 seconds) and by illuminating 15 blue or 15 white transparent LEDs, connected in series. The apparatus shows outstanding long-term mechanical stability and reproducibility for near about a year. The N-CDs incorporated PVDF composite nanocomposites can be used for multipurpose applications, like mechanical energy harvester, weight sensor, pulse sensor, and thus may be employed in multi-faced fields such as optoelectronic, biomedical, and energy technologies after suitable improvisation.

## References


1) Ren, X.; Fan, H.; Wang, C.; Ma, J.; Li, H.; Zhang, M.; Lei, S.; Wang, W. Wind energy harvester based on coaxial rotatory freestanding triboelectric nanogenerators for self-powered water splitting. Nano energy 2018, 50, 562-70.
2) Cao, X.; Zhang, M.; Huang, J.; Jiang, T.; Zou, J.; Wang, N.; Wang, Z. Inductor-Free Wireless Energy Delivery via Maxwell's Displacement Current from an Electrodeless Triboelectric Nanogenerator. Advanced materials 2018, 30, 1704077.
3) Qian, Y.; Du, J.; Kang, D. J. Enhanced electrochemical performance of porous Co-doped $TiO_2$ nanomaterials prepared by a solvothermal method. Microporous Mesoporous Mater 2019, 273, 148–155.
4) Wu, C.; Ding, W.; Liu, R.; Wang, J.; Wang, A. C.; Wang, J.; Li, S.; Zi, Y.; Wang, Z. L. Keystroke dynamics enabled authentication and identification using triboelectric nanogenerator array. Materials Today 2018, 21, 216–222.
5) Chen, X.; Guo, H.; Wu, H.; Chen, H.; Song, Y.; Su, Z.; Zhang, H. Hybrid generator based on freestanding magnet as all-direction in-plane energy harvester and vibration sensor. Nano Energy 2018, 49, 51–58.
6) Meng, K.; Chen, J.; Li, X.; Wu, Y.; Fan, W.; Zhou, Z.; He, Q.; Wang, X.; Fan, X.; Zhang, Y.; Yang, J.; Wang, Z. L. Flexible weaving constructed self-powered pressure sensor enabling continuous diagnosis of cardiovascular disease and measurement of Cuffless blood pressure. Advanced Functional Materials 2019, 5, 1806388.
7) Wang, Y.; Zhu, L.; Feng, Y.; Wang, Z.; Wang, Z. L. Comprehensive pyro-phototronic effect enhanced ultraviolet detector with ZnO/Ag Schottky junction. Advanced Functional Materials 2019, 29, 1807111.
8) Chen, J.; Tang, W.; Han, K.; Xu, L.; Chen, B.; Jiang, T.; Wang, Z. L. Bladeless-turbine-based triboelectric nanogenerator for fluid energy harvesting and self-powered fluid gauge. Advanced Materials Technologies 2019, 4, 1800560.
9) Pu, X.; Guo, H.; Tang, Q.; Chen, J.; Feng, L.; Liu, G.; Wang, X.; Xi, Y.; Hu, C.; Wang, Z. L. Rotation sensing and gesture control of a robot joint via triboelectric quantization sensor. Nano Energy 2018, 54, 453–460.

10) Wu, H.; Su, Z.; Shi, M.; Miao, L.; Song, Y.; Chen, H.; Han, M.; Zhang, H. Self-powered noncontact electronic skin for motion sensing. Advanced Functional Materials 2018, 28, 1704641.
11) Gu, L.; Cui, N.; Cheng, L.; Xu, Q.; Bai, S.; Yuan, M.; Wu, W.; Liu,J.; Zhao, Y.; Ma, F.; Qin, Y.; Wang, Z. L. Flexible Fiber Nanogenerator with 209 V Output Voltage Directly Powers a Light-Emitting Diode. Nano Letters 2013, 13, 91-94.
12) Liu, J.; Cui, N.; Gu, L.; Chen, X.; Bai, S.; Zheng, Y.; Hu, C.; Qin, Y. A Three-Dimensional Integrated Nanogenerator for Effectively Harvesting Sound Energy from the Environment. Nanoscale 2016, 8, 938-4944.
13) Chen, J.; Yang, J.; Guo, H.; Li, Z.; Zheng, L.; Su, Y.; Wen, Z.; Fan,X.; Wang, Z. L. Automatic Mode Transition Enabled Robust Triboelectric Nanogenerators. ACS Nano 2015, 9, 12334-12343.
14) Yang, W.; Chen, J.; Zhu, G.; Yang, J.; Bai, P.; Su, Y. J.; Jing, Q. S.; Cao, X.; Wang, Z. L. Harvesting Energy from the Natural Vibration of Human Walking. ACS Nano 2013, 7, 11317-11324.
15) Yang, J.; Chen, J.; Liu, Y.; Yang, W.; Su, Y.; Wang, Z. L. Triboelectrification-Based Organic Film Nanogenerator for Acoustic Energy Harvesting and Self-Powered Active Acoustic Sensing. ACS Nano 2014, 8, 2649-2657.
16) Zhu, D.; Tudor, M. J.; Beeby, S. P. Strategies for Increasing the Operating Frequency Range of Vibration Energy Harvesters. Measurement Science and Technology 2010, 21, 022001.
17) Sarkar, D.; Das, N.; Saikh, M. M.; Biswas, P.; Das, S.; Das, S.; Hoque, N. A.; Basu, R. Development of a Sustainable and Biodegradable Sonchus asper Cotton Pappus Based Piezoelectric Nanogenerator for Instrument Vibration and Human Body Motion Sensing with Mechanical Energy Harvesting Applications. ACS Omega 2021, 6, 28710-28717.
18) Zhao, J.; Li, F.; Wang, Z.; Dong, P.; Xia, G.; Wang, K. Flexible PVDF nanogenerator-driven motion sensors for human body motion energy tracking and monitoring. Journal of Materials Science: Materials in Electronics 2021, 32, 14715–14727.
19) Hajra, S.; Sahu, M.; Oh, D.; Kim, H. J. Lead-free and flexible piezoelectric nanogenerator based on CaBi4Ti4O15 Aurivillius oxides/ PDMS composites for efficient biomechanical energy harvesting. Ceramics International 2021, 47, 15695-15702.

20) Song, S.; Zheng, Z.; Bi, Y.; Lv, X.; Sun, S. Improving the electroactive phase, thermal and dielectric properties of PVDF/graphene oxide composites by using methyl methacrylate-co-glycidyl methacrylate copolymers as compatibilizer. Journal of Materials Science 2019, 54, 3832–3846.

21) Wu, J. M.; Chen, K.-H.; Zhang, Y.; Wang, Z. L. A self-powered piezotronic strain sensor based on single $ZnSnO_3$ microbelts. Rsc Advances 2013, 3, 25184-25189,

22) Park, K. I.; Son, J. H.; Hwang, G. T.; Jeong, C. K.; Ryu, J.; Koo, M.; Choi, I.; Lee, S. H.; Byun, M.; Wang, Z. L. Highly-efficient, flexible piezoelectric PZT nanocomposite nanogenerator on plastic substrates. Advanced materials 2014, 26, 2514-2520,

23) Lin, Z.-H.; Yang, Y.; Wu, J. M.; Liu, Y.; Zhang, F.; Wang, Z. L. $BaTiO_3$ nanotubes-based flexible and transparent nanogenerators. The journal of physical chemistry letters 2012, 3, 3599-3604,

24) Xu, S.; Yeh, Y.-w.; Poirier, G.; McAlpine, M. C.; Register, R. A.; Yao, N. Flexible piezoelectric PMN–PT nanowire-based nanocomposite and device. Nano letters 2013, 13, 2393-2398.

25) Kang, H. B.; Chang, J.; Koh, K.; Lin, L.; Cho, Y. S. High quality Mn-doped (Na, K) $NbO_3$ nanofibers for flexible piezoelectric nanogenerators. ACS applied materials &interfaces 2014, 6, 10576-10582

26) Chang, C.; Tran, V. H.; Wang, J.; Fuh, Y.-K.; Lin, L. Direct-write piezoelectric polymeric nanogenerator with high energy conversion efficiency. Nano letters 2010, 10, 726-731.

27) Ding, R.; Zhang, X.; Chen, G.; Wang, H.; Kishor, R.; Xiao, J.; Gao, F.; Zeng, K.; Chen, X.; Wei Sun, X.; Zheng, Y. High-performance piezoelectric nanogenerators composed of formamidinium lead halide perovskite nanoparticles and poly(vinylidene fluoride). Nano Energy 2017, 37, 126–135.

28) Ippili, S.; Jella, V.; Eom, J. H.; Kim, J.; Hong, S.; Choi, J. S.; Tran, V. D.; Hieu, N. V.; Kim, Y. J.; Kim, H. J.; Yoon, S. G. An eco-friendly flexible piezoelectric energy harvesterthat delivers high output performance is based on lead-free $MASnI_3$ films and $MASnI_3$-PVDF composite films. Nano Energy 2019, 57, 911–923.

29) Jella, V.; Ippili, S.; Eom, J.; Choi, J.; Yoon, S. Enhanced output performance of a flexible piezoelectric energy harvester based on stable $MAPbI_3$-PVDF composite films. Nano Energy 2018, 53, 46–56.

30) Cai, J.; Hu, N.; Wu, L.; et al. Preparing carbon black/graphene/PVDF-HFP hybrid composite films of high piezoelectricity for energy harvesting technology. Composites Part A: Applied Science and Manufacturing 2019, 121, 223-231.

31) Alam, M.; Sultana, A.; Mondol, D. Biomechanical and acoustic energy harvesting from $TiO_2$ nanoparticle modulated PVDF-HFP nanofiber made high performance nanogenerator. ACS Applied Energy Materials 2018, 1, 3103-3112.

32) (a) Chen, X.; Song, Y.; Chen, H.; Zhang, J.; Zhang, H. An Ultrathin Stretchable Triboelectric Nanogenerator with Coplanar Electrode forEnergy Harvesting and Gesture Sensing. Journal of Materials Chemistry A 2017, 5, 12361-12368.

33) (b) Yan, X.; Xu, T.; Chen, G.; Yang, S.; Liu, H.; Xue, Q. Preparation and characterization of electrochemically deposited carbon nitride films on silicon substrate. Journal of Physics D: Applied Physics 2004, 37, 907-13.

34) (c) Kar, E.; Bose, N.; Dutta, B,; Mukherjee, N.; Mukherjee, S. MWCNT@$SiO_2$ Heterogeneous Nanofiller-Based Polymer Composites: A Single Key to the High-Performance Piezoelectric Nanogenerator and X-band Microwave Shield. ACS Applied Nano Materials 2018, 1, 4005-18.

35) Thakur, P.; Kool, A.; Bagchi, B.; Hoque, N. A.; Das, S.; Nandy, P. The Role of Cerium(III)/Yttrium(III) Nitrate Hexahydrate Salts on Electroactive ß-phase Nucleation and Dielectric Properties of Poly(vinylidene fluoride) Nanocomposites. RSC Advances 2015, 5, 28487-28496.

36) Saikh, M. M.; Hoque, N. A.; Biswas, P.; Rahman, W.; Das, N.; Das, S; Thakur, P. Self-Polarized $ZrO_2$/Poly(vinylidene fluoride-*co*-hexafluoropropylene) Nanocomposite-Based Piezoelectric Nanogenerator and Single-Electrode Triboelectric Nanogenerator for Sustainable Energy Harvesting from Human Movements. Physica status solidi (a) 2021, 218, 2000695.

37) Zhang, Y.; Wang, Y.; Deng, Y.; Li, M.; Bai, J. Enhanced Dielectric Properties of Ferroelectric Polymer Composites Induced by Metal-Semiconductor Zn-ZnO Core-Shell Structure. ACS Applied Materials & Interfaces 2012, 4, 65-68.

38) Thakur, P.; Kool, A.; Bagchi, B.; Hoque, N. A.; Das, S.; Nandy, P. In Situ Synthesis of $Ni(OH)_2$ Nanobelt Modified Electroactive Poly(vinylidene fluoride) Nanocomposites: Remarkable Improvement in Dielectric Properties. Physical Chemistry Chemical Physics 2015, 17, 13082-13091.

39) Das, N.; Sarkar, D.; Saikh, M. M.; Biswas, P.; Das, S.; Hoque, N. A.; Ray, P. P. Piezoelectric activity assessment of size-dependent naturally acquired mud volcano clay nanoparticles assisted highly pressure sensitive nanogenerator for green mechanical energy harvesting and body motion sensing. Nano Energy 2022, 102, 107628.

40) Pal, K.; Kang, D. J.; Zhang, Z. X.; Kim, J. K. Synergistic Effects of Zirconia-Coated Carbon Nanotube on Crystalline Structure of Polyvinylidene Fluoride Nanocomposites: Electrical Properties andFlame-Retardant Behaviour. Langmuir 2010, 26, 3609-3614.

41) Xu, C.; Wang, Z. L. Compact Hybrid Cell Based on a Convoluted Nanowire Structure for Harvesting Solar and Mechanical Energy. Advanced Materials 2011, 23, 873-877.

42) Yang, Y.; Zhang, H.; Liu, Y.; Lin, Z.-H.; Lee, S.; Lin, Z.; Wong, C. P.; Wang, Z. L. Silicon-Based Hybrid Energy Cell for Self-Powered Electrodegradation and Personal Electronics. ACS Nano 2013, 7, 2808-2813.

43) Yoon, G. C.; Shin, K.-S.; Gupta, M. K.; Lee, K. Y.; Lee, J.-H.; Wang, Z. L.; Kim, S.-W. High-Performance Hybrid Cell Based on an Organic Photovoltaic Device and a Direct Current Piezoelectric Nanogenerator. Nano Energy 2015, 12, 547-555.

44) Li, P.; Zhang, Z. Self-powered 2D material-based PH sensor and photodetector driven by monolayer MoSe2 piezoelectric nanogenerator. ACS Applied Materials & Interfaces 2020, 12, 58132-58139.

45) 43.Sultana, A.; Sadhukhan, P.; Alam, M.; Das, S.; Middya,T. R.; Mandal, D. Organo-Lead Halide Perovskite Induced Electroactive ß-Phase in Porous PVDF Films: An Excellent Material for Photoactive Piezoelectric Energy Harvester and Photodetector. ACS Applied Materials & Interfaces 2018, 10, 4121-4130.

46) Lim, S. Y.; Shen, W.; Gao, Z. Carbon quantum dots and their applications. Chemical Society Reviews 2015. 44, 362-381.

47) (a) Begum, S.; Ullah, H.; Kausar, A.; Siddiq, M.; Aleem, M. A. Epoxy functionalized multi - walled carbon nanotubes/polyvinylidene fluoride nanocomposites: Microstructure,

morphology, thermal, piezoelectricity and conductivity investigations. Polymer Composites 2019, 40, E776–E794.

48) (b) Dong, X.; Su, Y.; Geng, H.; Li, Z.; Yang, C.; Li, X.; Zhang, Y. Fast one-step synthesis of N-doped carbon dots by pyrolyzing ethanolamine. Journal of Materials Chemistry C 2014, 36, 7477-81.

49) Zhang, X.; Jiang, M.; Niu, N.; Chen, Z.; Li, S.; Liu, S.; Li. J. Natural-product-derived carbon dots: from natural products to functional materials. Chem. Sus. Chem. 2018, 11, 11-24.

50) Roy, K.; Jana, S.; Ghosh, S. K.; Mahanty, B.; Mallick, Z.; Sarkar, S.; Sinha, C.; Mandal, D. Three-dimensional MOF-assisted self-polarized ferroelectret: an effective autopowered remote healthcare monitoring approach. Langmuir 2020, 36, 11477-11489.

51) Huang, p.; Xu, S.; Zhong, W.; Fu, H.; Luo, Y.; Xiao, Z.; Zhang, M. Carbon quantum dots inducing formation of β phase in PVDF-HFP to improve the piezoelectric performance. Sensors and Actuators A: Physical 2021, 330,112880.

52) Bairagi, S.; Ali, S. W. Investigating the role of carbon nanotubes (CNTs) in the piezoelectric performance of a PVDF/KNN-based electrospun nanogenerator. Soft Matter 2020, 20, 4876-86.

53) Badatya, S.; Bharti, D. K.; Sathish, N.; Srivastava, A. K.; Gupta, M. K. Humidity sustainable hydrophobic poly (vinylidene fluoride)-carbon nanotubes foam based piezoelectric nanogenerator. ACS Applied Materials & Interfaces 2021, 23, 27245-54.

54) Khalifa, M.; Anandhan, S. PVDF nanofibers with embedded polyaniline–graphitic carbon nitride nanosheet composites for piezoelectric energy conversion. ACS Applied Nano Materials 2019, 11, 7328-39.

55) Badatya, S.; Kumar, A.; Srivastava, A. K.; Gupta, M. K. Flexible Interconnected Cu-Ni Nanoalloys Decorated Carbon Nanotube-Poly (vinylidene fluoride) Piezoelectric Nanogenerator. Advanced Materials Technologies 2022, 2101281.

56) Li, X.; Ji, D.; Yu, B.; Ghosh, R.; He, J.; Qin, X.; Ramakrishna, S. Boosting piezoelectric and triboelectric effects of PVDF nanofiber through carbon-coated piezoelectric nanoparticles for highly sensitive wearable sensors. Chemical Engineering Journal 2021, 426, 130345.

57) Panwar, L, S.; Panwar, V. Development of a carbon nanofiber-attached flexible piezoelectric nanocomposite towards self-powered wearable devices. Materials Today: Proceedings 2022, 62, 6804-6808.

58) Kar, E.; Bose, N.; Dutta, B.; Mukherjee, N.; Mukherjee, S. MWCNT@$SiO_2$ Heterogeneous Nanofiller-Based Polymer Composites: A Single Key to the High-Performance Piezoelectric Nanogenerator and X-band Microwave Shield. ACS Applied Nano Materials 2018, 1, 4005-18.

# 3D Printer Assisted Cotton Pappus Embedded Polymeric Nanocomposite Based Wearable and Sustainable Triboelectric Nanogenerator

*Chapter 4*

## 4.1 Introduction

With the fastest development of internet of things (IoT), the self-powered and wearable electronic devices attract the researchers and human being more due to its user friendly behavior and numerous utilization in the field of human-machine interaction and health monitoring unit.[1,2] But, these wearable devices for example mobile phones, actuators, in-vivo medical gadgets etc. have some drawbacks like large dimension, regular requirement of charging, eco-friendliness etc. For resolving these issues, natural available material based wearable and eco-friendly energy harvesting device is required.[3-6]

In comparison with other energy harvesting devices, triboelectric nanogenerator (TENG) is the most used and newly developed energy harvester which can easily convert mechanical energy into electrical energy. The additional advantages of utilizing the TENG are high efficiency, cost effectiveness, environmental friendly and harnessing both large and small scale energies, which not only helps in fulfill the power demand of human society but also resolves the drawbacks of conventional energy storage devices.[7,8] Thus, the aim of the current work is to design a TENG by using natural available materials and harvesting the biomechanical energies arises from human body movements. Also, surface modification technique has been used to improve the output performance of the device.[9]Among other natural available materials, cotton pappus is the sturdiest environmental friendly polymeric fiber. It has sedative, antiseptic and diuretic properties and exhibits high crystallinity and high aspect ratio.[10] Moreover, the presence of hydroxyl group, amide linkage, α-helix and β-sheet structured amino acid inside the cotton pappus assists in inducing the polarization which directly affects in output of TENG.[6]

In this work, we have fabricated a eco-friendly, flexible and wearable TENG (CPTNG) by using 3D printer assisted cotton pappus incorporated PDMS nanocomposite (CPD). The device exhibits the output voltage of 201V under axial pressure of 12N. The instantaneous power density of the fabricated CPTNG is 1.02W/m$^2$ at $10^7\Omega$. Moreover, the device is affixed with different parts of human body and generated electricity during the movement of these parts. Also, the transmission of generated signal of CPTNG device during finger bending is monitored through ARDUINO. The realistic application of the device has been investigated by lighting up 95 no of blue LEDs. Thus, the fabricated device can be used as biomechanical energy harvester.

## 4.2 Experimental Section

### 4.2.1 Purification of cotton pappus

Firstly, the cotton pappus was assembled from the premises of Jadavpur University. Thereafter, the assembled pappus were cleaned with DI water and placed in a vacuum oven to dry at $100^0$C. For eliminating the chemicals, further purification was performed by using hydrogen peroxide (Merck India) and acetic acid (Alfa Aesar). After removing the chemicals from the body of pappus, the samples were rinsed with DI water for several times and kept in a vacuum oven at $100^0$C for overnight.

### 4.2.2 Fabrication of CPD nanocomposite and CPTNG device

To fabricate the nanocomposite, a simple solution casting technique was used. First of all, 1g of PDMS (Sylgard 184, Dow Corning) and required amount of curing agent in the ratio of 10:1 was measured in a petri dish and mixed very well. Thereafter, 1wt% of purified cotton pappus was added in the previous mixing solution and poured the sample loaded mixing solution into 3D printed rectangular mold. In the next step, this 3D printed mold was placed in a vacuum desiccator for few minutes to make the solution bubble free. After that, the bubble free solution loaded 3D printed mold was transferred in a hot air oven to dry the solution at $60^0$C for 20min. Finally, we get the CPD nanocomposite with thickness of 1.5 mm.

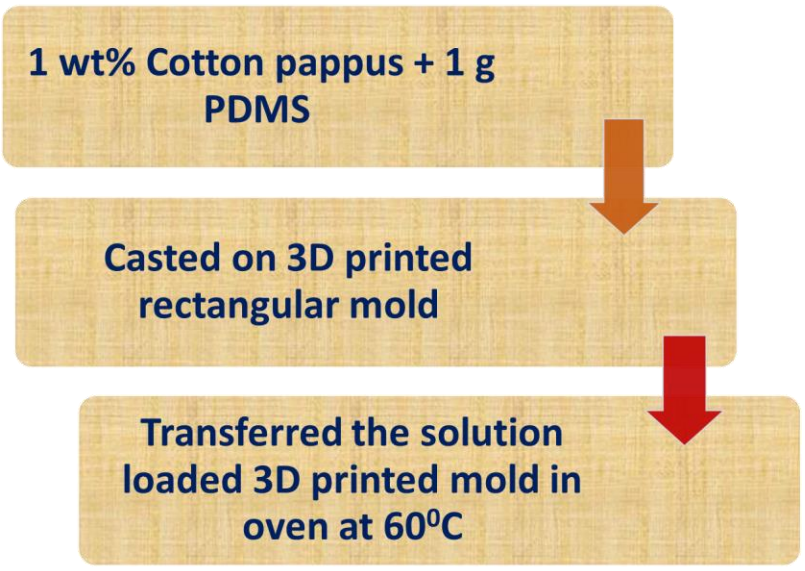


***Figure 4.1:*** *Schematic illustration of fabrication procedure of CPD nanocomposite*

The step by step fabrication technique of CPD nanocomposite has been illustrated in the figure 4.1. Also, the digital snapshot of the fabricated nanocomposite has been depicted in the figure 4.2 (a).

To fabricate the CPTNG device, CPD nanocomposite, conductive cloth and copper wire were used. At first, the cotton pappus loaded PDMS solution were casted on the 3D printed mold and then performed vacuum technique by using desiccator. Thereafter, the a 2cm X 2cm conductive cloth were placed on the upper side of the mold and kept the whole system in a hot air oven at $60^0$C for 30min. After that, the conductive cloth attached CPD nanocomposite was peeled off from the mold and connected with a copper wire by using silver paste. Finally, we get the CPTNG device with thickness of 1.75mm. The schematic representation of designed CPTNG device has been shown in the figure 4.2 (b).

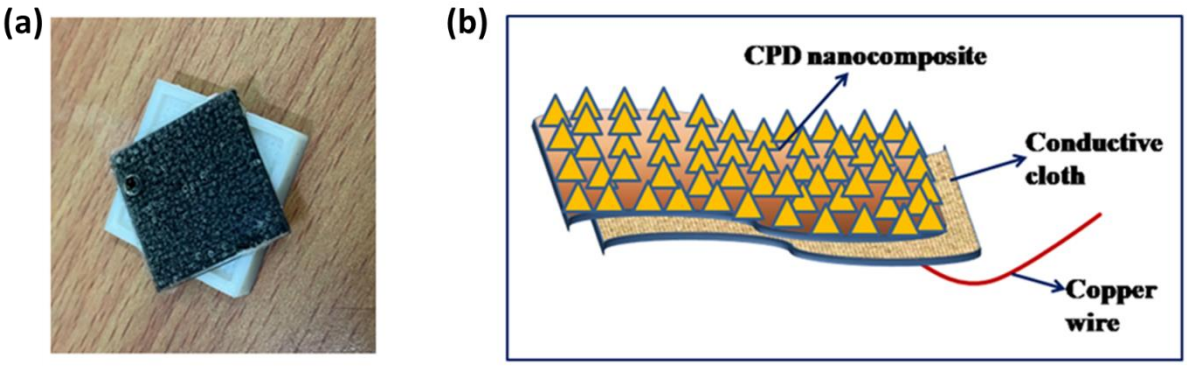


***Figure 4.2:*** *(a) Digital image of 3D printer assisted CPD nanocomposite, (b) schematic depiction of fabricated CPTNG device.*

## *4.3 Working Mechanism of CPTNG*

The operating principal of generating electrical signals of CPTNG device is depended on the combine effects of contact-triboelectrification and electrostatic induction. During the generation of electrical energy, CPD nanocomposite and human hand serve as tribo-negative and tribo-positive layer respectively and conductive cloth has been utilized as charge collecting layer or electrode layer. Once human hand contacts with CPD nanocomposite, the negative triboelectric charges are generated on the surface of CPD nanocomposite owing to the negative tribopolarity, whereas, the human hand contains positive triboelectric charges, depicted in the figure 4.3 (i). In

the next step, the CPD nanocomposite and human hand are separated from each other, which lead to conductive cloth to acquire electrostatic charges to counterbalance the triboelectric chargrs. As a result, electrons are flowing from conductive cloth to ground state across the external load for maintaining the potential difference among the ground and electrode layer, shown in the figure 4.3 (ii). These flows of electrons are continued until the human hand is completely detached from the CPD nanocomposite (figure 4.3 (iii)). Whenever, human hand are started to get in touch with CPD nanocomposite again, the induced electrostatic charges within the conductive cloth are started to decrease. As a result, electrons are flowed back from ground state to conductive cloth and this electron flowing is carried on until the human hand is completely contacted with the CPD nanocomposite again, shown in the figure 4.3 (iv).

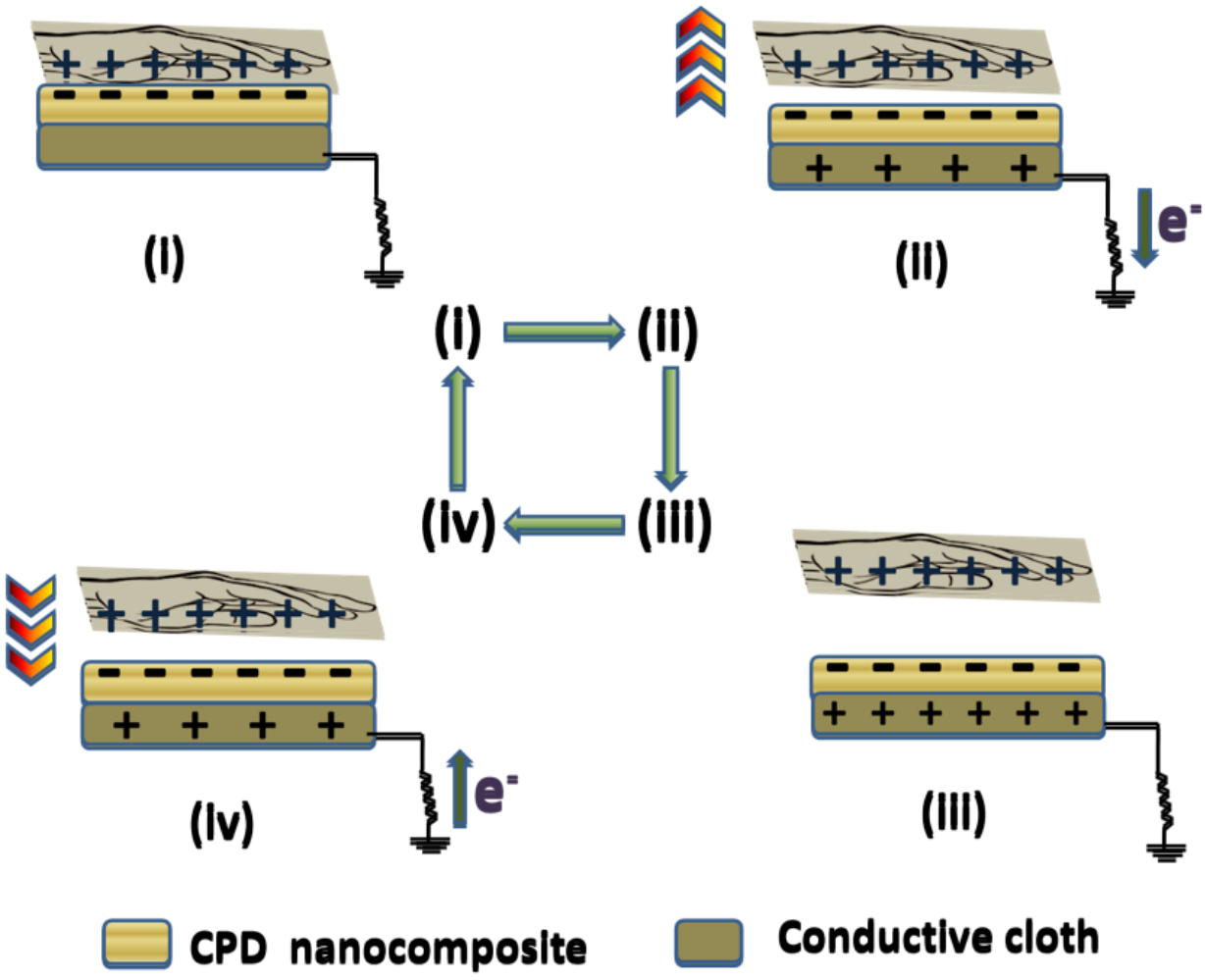


***Figure 4.3:*** *Operating mechanism of CPTNG device.*

Therefore, this periodic contact-separation mode assists CPTNG device to generate alternative current continuously.

## 4.4 Characterizations techniques

The surface morphology of cotton pappus was examined by field emission scanning electron microscopy (FESEM; INSPECT F50). The structural analysis of CPD nanocomposite was investigated by X-ray diffraction (XRD; Model-D8, Bruker AXS Inc., Madison, WI). The electrical performance of CPTNG device was measured by Digital Storage Oscilloscope (RTB2002).

## 4.5 Results and discussions

The morphological property of the surface of the cotton pappus has been depicted in the figure 4.4(a), where the fibrous structure of the sample is shown clearly. The average thickness of these fibers is 6.18µm. So, we have incorporated these fibrous pappus into PDMS to get the nanocomposite. Figure 4.4(b) confirms the presence of cotton pappus inside the CPD nanocomposite which clearly indicates the successful incorporation of fibrous pappus inside the PDMS matrix. The structural analysis of fabricated CPD nanocomposite has been examined by XRD spectrum, shown in the figure 4.4(c). The observable diffraction peaks of the nanocomposite are situated at $2\theta=12.8^0$, $22.5^0$, $34.1^0$. The sharp peak at $2\theta=12.8^0$ is raised due to the presence of PDMS inside the nanocomposite. Compared to the characteristic peak of pure PDMS, a slight shifting of this sharp peak at $12.8^0$ of CPD composite is noticed which is occurred due to presence of cotton pappus. Moreover, the other two crystalline peaks are observed at $22.5^0$

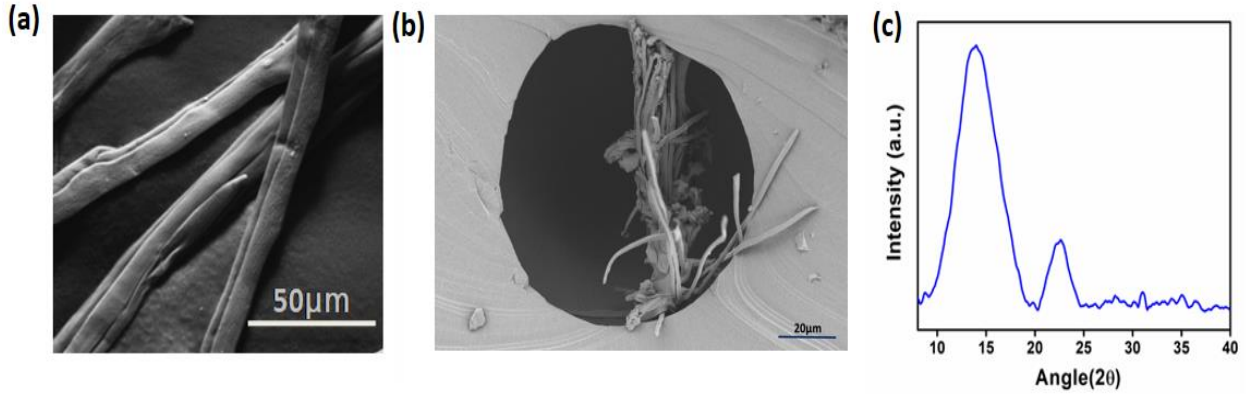


***Figure 4.4:*** *(a) Fiber like structure of cotton pappus, (b) FESEM image of CPD nanocomposite, (c) X-ray diffraction peaks of CPD nanocomposite.*

(002) and $34.1^0$ (023, 040) which occurs due to the effect of cellulose inside the fibers and confirms the presence of sample inside the nanocomposite.[12]

After successfully characterized CPD nanocomposite, we have utilized it to fabricate the CPTNG device.

The output performances of the fabricated TENG have been measured by connecting it to DSO. The CPTNG device exhibits 201V output voltage under periodic finger tapping condition (axial pressure of 12N). Figure 4.5(a) represents the output voltage vs. time graph. Furthermore, the power density of fabricated device has been measured by utilizing the following equation

$$\mathbf{P} = \frac{\mathbf{V^2}}{\mathbf{R_L \times A}} \quad \text{..... } (4.1)$$

Where, V denotes the output voltage of the CPTNG device, $R_L$ is the value of load resistance and A represents the area of the device.[11] The obtained maximum power density of the device is $1.02 W/m^2$, depicted in the figure 4.5(b). The basic operating principal of the device depends on the dual effect of tribo-electrification and electrostatic induction.

***Table 4.1:*** *Output performance of CPTNG device*

| | ***Output voltage*** | ***Applied pressure*** | ***Power density*** |
|---|---|---|---|
| ***CPTNG device*** | ***201 V*** | ***12 N*** | ***1.02 W/m²*** |

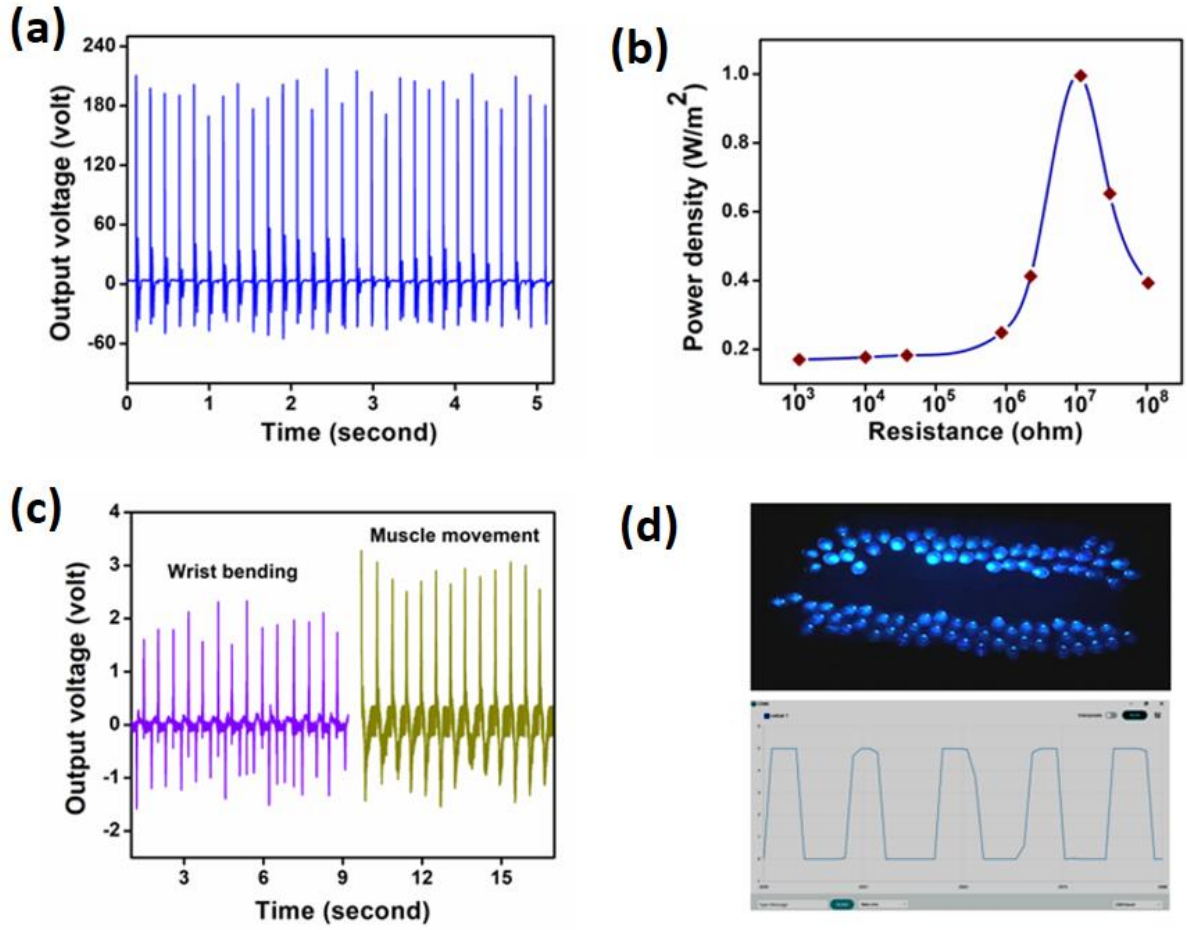


***Figure 4.5:*** *(a) Generating output voltage and (b) power density of CPTNG device under axial pressure of 12N, (c) voltage generation by fabricated device from wrist bending and muscle movements, (d) lighting up 95 no of blue LEDs and transmission of signal through ARDUINO during finger bending condition.*

Moreover, the CPTNG device has been affixed with wrist and muscle of the human body and monitored the output performance (figure 4.5(c)). During wrist up-down, the device exhibits 1.8V output voltage which is generated due to the skin deformation and pressure of the joint of the wrist. Also, the device can detect successfully the movement of muscle and exhibit 2.8V output voltage. The realistic application of CPTNG device is observed by connecting the blue LEDs in series combination through the bridge rectifier. The result shows that the device can illuminate 95 no of LEDs (figure 4.5(d)). The transmission of the signal during finger movement has been visualized in the figure 4.5(d) by using ARDUINO set up.

## 4.6 Conclusion

In summary, a wearable and self-powered CPTNG device has been fabricated by using cotton pappus loaded CPD nanocomposite and investigated the output performance. The device shows outstanding output voltage of 201V and power density of 1.02W/$m^2$ under continuous finger tapping condition. To create the surface roughness and increase the output results of the device, 3D printed mold has been employed. Moreover, the capability of the CPTNG device to convert the mechanical energies has been monitored by wrist and elbow bending movements and LEDs illumination .Also, the transmission of the signals are observed by using ARDUINO. Therefore, CPTNG device could be a promising candidate in health monitoring system.

## References


1) Rana, S. S.; Halim, M. A.; Kabir, M. H. Design and implementation of a security improvement framework of Zigbee network for intelligent monitoring in IoT platform. Applied Sciences 2018, 8, 2305.
2) H. Wu, Y. Huang, F. Xu, Y. Duan and Z. Yin, Advanced materials **28**, 9881-919 (2016).
3) Wang, Z. L.; Song, J. Piezoelectric nanogenerators based on zinc oxide nanowire arrays. Science 2006, 312, 242-246.
4) Yang, R..; Qin, Y.; Dai, L.; Wang, Z. L. Power generation with laterally packaged piezoelectric fine wires. Nature nanotechnology 2009, 4, 34-39.
5) Maiti, S.; Karan, S. K.; Lee, J.; Mishra, A. K.; Khatua, B. B.; Kim, J. K. Bio-waste onion skin as an innovative nature-driven piezoelectric material with high energy conversion efficiency. Nano Energy 2017, 42, 282-293.
6) Sarkar, D.; Das, N.; Saikh, M. M.; Biswas, P.; Das, S.; Das, S.; Hoque, N. A. Basu, R. Development of a sustainable and biodegradable sonchus asper cotton pappus based piezoelectric nanogenerator for instrument vibration and human body motion sensing with mechanical energy harvesting applications. ACS omega 2021. 6, 28710-28717.
7) Xie, Y.; Ma, Q. Yue, B.; Chen, X.; Jin, Y.; Qi, H.; Hu, Y.; Yu, W.; Dong, X.; Jiang, H. Triboelectric nanogenerator based on flexible Janus nanofiber membrane with simultaneous high charge generation and charge capturing abilities. Chemical Engineering Journal 2023, 452, 139393.
8) Rahman, M. T.; Rana, S. S.; Salauddin, M.; Zahed, M. A.; Lee, S.; Yoon, E. S. Park, J. Y. Silicone-incorporated nanoporous cobalt oxide and MXene nanocomposite-coated stretchable fabric for wearable triboelectric nanogenerator and self-powered sensing applications. Nano Energy 2022, 100, 107454.
9) Liu, Y.; Fu, Q.; Mo, J.; Lu, Y.; Cai, C.; Luo, B; Nie, S. Chemically tailored molecular surface modification of cellulose nanofibrils for manipulating the charge density of triboelectric nanogenerators. Nano Energy 2021, 89, 106369.
10) Khan, R. A.; Khan, M. R.; Sahreen, S. Protective effect of Sonchus asper extracts against experimentally induced lung injuries in rats: a novel study. Experimental and Toxicologic Pathology 2012, 64, 725-731.

11) Sarkar, D.; Das, N.; Saikh, M. M.; Biswas, P.; Roy, S.; Paul, S.; Hoque, N. A.; Basu, R.; Das, S. High β-crystallinity comprising nitrogenous carbon dot/PVDF nanocomposite decorated self-powered and flexible piezoelectric nanogenerator for harvesting human movement mediated energy and sensing weights. Ceramics International 2023, 49, 5466-5478.

12) Andra, S.; Balu, S. K.; Jeevanandam, J.; Muthalagu, M.; Danquah, M. K. Surface cationization of cellulose to enhance durable antibacterial finish in phytosynthesized silver nanoparticle treated cotton fabric. Cellulose 2021, 28, 5895-910.

# Micro-patterned $BaTiO_3$@Ecoflex Nanocomposite Assisted Self-powered and Wearable Triboelectric Nanogenerator with Improved Charge Retention by 2D $MoTe_2$/PVDF Nanofibrous Layer

*Chapter 5*

## 5.1 Introduction

In the era of internet of things, flexible, self-powered and skin attachable wearable electronic devices have gained tremendous attention due to their versatile utilizations in the field of robotics technology, human-machine interfaces, biomedical application and healthcare units.[1-5] The main advantages of using these skin attachable wearable devices are the detection and monitoring ability of different physical parameters like pressure, strain, sensitivity, temperature etc. Along with this, these skin attachable devices also have the capability to detect multiple stimuli at a single time.[6-8] Moreover, there have been some limitations in the use of conventional energy storage equipments like daily charging requirements, large dimension etc. which restricts in long term use and also unable to match the required power demand. To overcome these issues and fulfill the power demand, self-powered and wearable energy harvesting devices have been utilized.[9] Among different types of energy harvesting devices, triboelectric nanogenerator (TENG) is the most suitable and promising candidate in energy harvesting techniques by converting the waste mechanical energy into electrical energy. Generally, fabrication of TENG depends on four basic components i.e. charge generating layer, charge trapping layer, electrode layer and charge storage layer.[10] Among them, charge generating layer and charge trapping layer play important roles to improve the output performance of TENG. However, the working performance of TENG depends on the coupling effect of generated triboelectric charges and induced electrostatic charges. Although, several techniques have been used to improve the power of TENG by inducing more triboelectrification in the charge generating layer, for example, selecting triboelectric materials from triboelectric series, chemical modification, using micro structured materials etc.[11-12] Along with this, the utilization of functional substances with nanomaterials is a new technique to improve the power of TENG.[10] Rajagopalan et al. introduces a quasi-equilibrium state (made of nylon and aluminium oxide) which helps in better contact electrification process and exhibits high output performance of fabricated TENG.[13] Moreover, Li et al. used $BaTiO_3$/polyimide nanocomposite to enhance the output performance of TENG.[14] But charge recombination takes place in the above mentioned reported studies which diminish the surface charge density and gives us low output performance of TENG. Generally, when charge generating layer and electrode layer get in contact with each other, then electrostatic potential is generated between them. As a result, due to the electric field, the surface charges of charge generating layer drift easily towards the electrode layer and combine with the opposite charges

which is induced on the electrode layer.[15] For this reason, charge recombination happens between the generating and electrode layer. This charge recombination directly affects the output performance of TENG by reducing the surface charge density. To overcome this problem, an intermediate layer has been placed between the charge collecting layer and electrode layer[16]. This intermediate layer not only traps the electrons but also enhances the output performance of TENG. Recently, polymer nanocomposite by incorporating 2D materials proves itself a potential candidate as intermediate layer by preventing charge recombination and enhancing the performance of TENG.[17] Moreover, 2D materials like MXene, reduced graphene oxide (rGO), transition metal dichalcogenaides (TMD), black phosphorous etc. consist of large surface area which accelerates in more charge accumulation and results in better output performance.[18] Along with the intermediate layer, surface modification also plays an important role to improve the performance of the TENG. Few pioneer works are reported on surface modification process which includes Lee et al.[19] introduces $C_{60}$ functionalized polyimide based TENG and Jae Park et al.[20] fabricates cation functionalized nanogenerator to enhance the output performance. But there are some drawbacks of utilizing these processes such as air breakdown, high cost fabrication process, low durability etc.[9] Thus, surface modification is required. In this work, our aim is to modify the surface, design a charge generating and intermediate or trapping layer. To fulfill this aim, nanocomposite has been introduced. The benefits of using nanocomposites in TENG are they consist of large surface area and controllable morphology, the fabrication process is very simple.[21-23] Moreover, the introduction of functional substances into nanocomposite helps in surface modification and increases the surface potential which directly enhances the triboelectric charges.[10] Additionally, the large phase interaction between inorganic additives and polymer chains inside the nanocomposite improves the trapping ability of materials and prevents the charge recombination.[24-26]

2D materials specially transition metal dichalcogenides (TMDs) consists of excellent physical and structural properties such as high in-plane conductivity, strong spin–orbit coupling, large magneto-resistance, large surface area, thermal stability, porosity etc.[27-30] Owing to these properties, 2D TMDs have broaden its utilization in versatile application like energy storage and conversion, catalysis, hydrogen evolution, waste water purifications etc.[31-34] Amidst all 2D TMDs, molybdenum ditelluride ($MoTe_2$) is one of the compelling and barely explored material. It has semimetallic property and topological electronic states.[35-37] Moreover, $MoTe_2$ can be

synthesized in both semimetallic (1T') and semiconducting (2H) phase as the energy gap between these two phases is very minimal (near about 40meV). Also layer structured, semiconducting $MoTe_2$ exhibits direct band gap 1.1eV.[37,38-39] These properties make it a potential choice in the field of electrical and optical applications.[40] Moreover, the excellent structural property, large surface area, high-in-plane conductivity and large spin-orbital coupling of $MoTe_2$ assist in creating the conducting channel inside the nanocomposite and promoting the charge transportation. This further helps in enhancing the trapping depth and restricting the recombination of triboelectric charges and induced charges.[34,40] Furthermore, by applying external force, the inversion symmetry in odd layer of $MoTe_2$ is broken which helps in inducing polarization inside the material.[41-43] Thus incorporating this material in polymer matrix improves in inducing more polarization and enhances the trapping ability of material.[36,43]

In the present work, we have designed a wearable, flexible and skin attachable triboelectric nanogenerator (EPMTNG) by using charge generating layer, charge trapping layer and carbon tape. Here, the $BaTiO_3$ (BTO) incorporated Ecoflex nanocomposite (EBTO) with micro-pattern serves as charge generating layer. Moreover, the incorporation of BTO nanoparticles increases the surface potential and induces more triboelectric charges which further helps in enhancement of output performance of the device. But, charge recombination occurs between EBTO layer and carbon tape which results in low output performance. To overcome this problem, 2D $MoTe_2$ (MT) incorporated PVDF nanofibers (PM5) has been inserted between EBTO layer and carbon tape. The PM5 nanofibers not only serve as an intermediate trapping layer but also prevent the charge recombination process. This leads to then increment of the output performance of the device. The presence of intermediate trapping layer in the fabricated device is further established by using theoretically simulated model. Moreover, our fabricated EPMTNG device generates outstanding output voltage of 319V and power density of $2.9W/m^2$ under periodic finger impartation. Owing to high sensitivity at low pressure region, the fabricated device easily detects different human physiological signals. These physiological signals include wrist bending, elbow movements, blood flow, vocal cord movement etc. Moreover, the device has the ability to monitor the robotic gestures. Also, the practical utilization of the device is monitored by capacitor charging and LEDs illuminating performance. Therefore, the EPMTNG can be used in health care monitoring and different robotics applications.

## 5.2 Experimental section

### 5.2.1 Synthesis method of $BaTiO_3$ (BTO)

The nanoparticles were synthesized by simple hydrothermal process. At first, 2g Barium hydroxide salt was measured and dissolved it in 100mL double distilled water. Thereafter, 0.5g Titanium dioxide salt was added with the solution and placed it on a magnetic stirrer for 2h to dissolve the salts totally. In the next step, the solution was transferred in a hydrothermal setup and placed it in a vacuum oven at 160$^o$C for 4h. After that the hydrothermal set up was cooled down and centrifugation process was performed. Thereafter, the collected product after centrifugation was dried in a vacuum oven for 12h at 60$^o$C. In the final step, the synthesized powders were heat treated in air at 500$^o$C for 1h.

### 5.2.2 Synthesis method of 2D $MoTe_2$ (MT) nanoparticles

Firstly, 1.088g Sodium molybdate dehydrate, 1.148g metal Tellurium powder and 0.255g Sodium borohydride were mixed with 60mL double distilled water at room temperature under continuous stirring condition. After that, the mixture was poured in a hydrothermal set up and performed the hydrothermal process at 200$^0$C for 30h. Thereafter, the samples were collected and cleaned thoroughly with distilled water and acetone. Then the cleaned sample was dried at 60$^0$C to obtain the MT nanoparticles.

### 5.2.3 Fabrication of micro-patterned $BaTiO_3$@Ecoflex nanocomposite

The nanocomposite was fabricated by applying simple solution casting method. At first, 1g of Ecoflex-A and 1g of Ecoflex-B were measured in a Petri dish and the two solutions were mixed very well for 10minutes. After mixing the two solutions, 0.5 wt% $BaTiO_3$ (BTO) was added in the mixed solution and stirred at 500rpm thoroughly for 5 minutes. Thereafter, the final solution was casted on a 3D printed rectangular mould to create roughness on the surface. After that, the rectangular mould was kept in room temperature (25$^0$C) for 9h to cure the solution. After curing the solution, sample was peeled off carefully and we finally get the $BaTiO_3$ incorporated Ecoflex nanocomposite with micro-patterned surface and named as EBTO. Figure 5.1(a) represents the schematic illustration of fabrication process of EBTO nanocomposite.

### 5.2.4 Formation of $MoTe_2$ (MT) incorporated PVDF nanofibers

The electrospinning technique was utilized to fabricate the nanofibers. First of all, stock solution was prepared by dissolving 12wt% PVDF in 6ml DMF and 4ml acetone mixture and kept under stirring condition (400rpm) for 3h at $60^0$C. Thereafter, required amount (1, 5, 10wt%) of synthesized $MoTe_2$ naoparticles was added to the prepared PVDF, DMF and acetone solution and placed it on the stirrer for another 3h at same temperature ($60^0$C). Moreover, the addition of nanoparticles transformed the transparent colour of the solution into blackish colour. In the next step, the blackish coloured solution was sonicated for 15minutes and we get the stock solution which was used in the electrospinning process.

A 10ml syringe with a diameter of 8mm was taken and filled with prepared stock solutions. Thereafter, the stock solution loaded syringe was placed in a syringe pump and performed the electrospinning process by adjusting some parameters including temperature ($25^0$C) and humidity (40%). To extract the solution by pump, the flow rate was adjusted at 0.4ml/hour. Moreover, the distance between the needle of the syringe and the collector plate (Al foil) was maintained at 14cm throughout the fabrication process of the nanofibers. Along with this, the nanofibers were fabricated at 12kV high voltage condition and extracted from the collector plate (Al foil). To recognize the nanoparticles incorporated nanofibers, we have named 5wt% $MoTe_2$ loaded nanofibers as PM5.The fabrication process of nanofibers has been depicted in the figure 5.1(b).

### 5.2.5 Fabrication of EPMTNG device

Our fabricated triboelectric nanogenerator (EPMTNG) is made up of three layers which are charge generating layer, charge trapping layer and charge collecting layer. Here, $BaTiO_3$@ Ecoflex nanocomposite serves as charge generating layer. For charge trapping layer, we have selected $MoTe_2$ incorporated PVDF nanofibers. Carbon tape has been used as charge collecting layer. At first, nanofibers were prepared and affixed to carbon tape. Thereafter, $BaTiO_3$ incorporated Ecoflex solution was casted on the other side of nanofiber. Then, 3D printed plate was attached on the upper surface of the $BaTiO_3$@Ecoflex layer and kept the whole system at room temperature ($25^0$C) for 9h to dry the Ecoflex solution. After completing the drying process, the 3D printed plate was peeled off from the upper surface of Ecoflex layer and copper wire was connected between carbon tape and nanofibers for investigating the electrical performance. The

dimension of the fabricated EPMTNG device is 4.4cm X 2.5cm. Figure 5.1(c) exhibits the graphical representation of fabricated device.

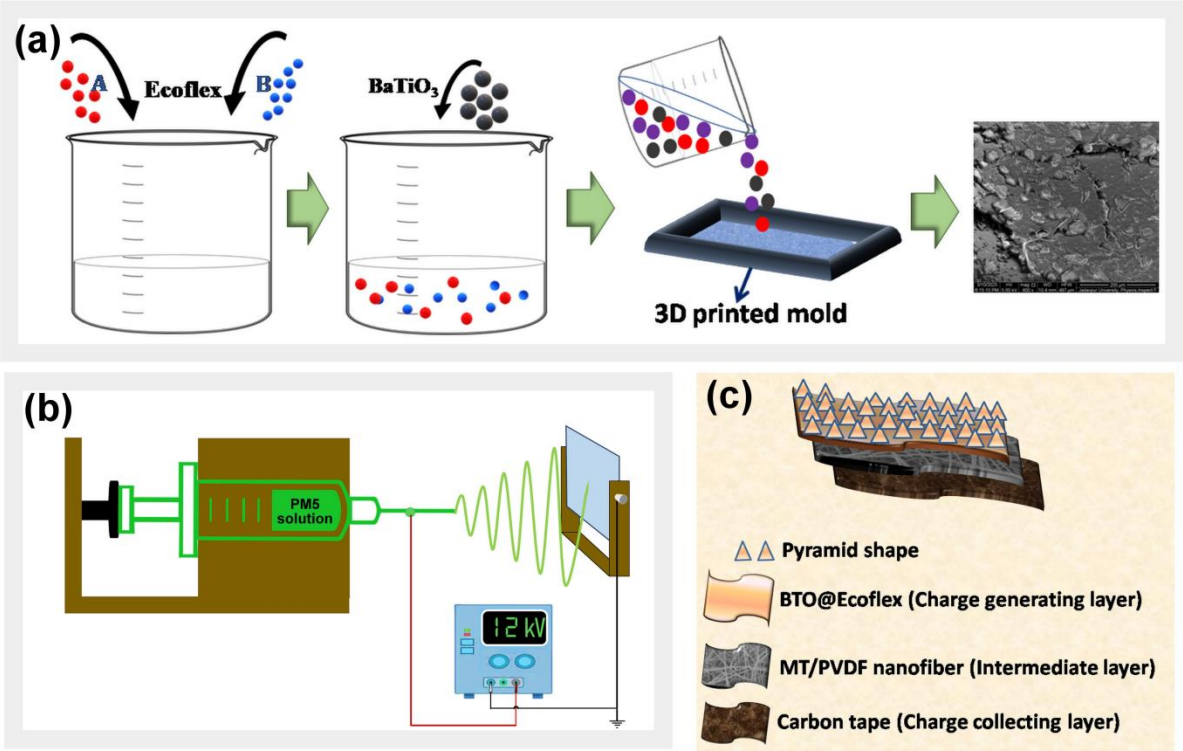


***Figure 5.1:*** *Graphical representation of the fabrication process of (a) micro-patterned EBTO nanocomposite and (b) PM5 nanofiber. (c) The designing of fabricated EPMTNG device.*

## *5.3 Characterization techniques*

The structural and morphological properties of the synthesized nanopartices and fabricated nanocomposites are examined by X-ray diffraction (XRD; Model-D8, Bruker AXS Inc., Madison, WI) and field emission scanning electron microscopy (FESEM; INSPECT F50). The EDS spectra and elemental colour mapping of charge generating and intermediate layer are performed by Zeiss Gemini SEM 500.The eletroactive phase formation of intermediate layer is investigated by Fourier transform infrared (FTIR) spectroscopy (FTIR-8400S; Shimadzu). The electrical properties of charge generating and intermediate layer are investigated by digital LCR meter (Agilent, E4980A). The output performance of the EPMTNG device is investigated by Digital Oscilloscope (RTB2002).

## 5.4 Results and discussion

The structural and morphological properties of charge generating layer and charge trapping layer have been analyzed by X-ray diffraction peaks, FTIR spectrums and FESEM images.

### 5.4.1 Charge generating layer

BTO incorporated Ecoflex (EBTO) nanocomposite represents the charge generating layer. The synthesis procedure of BTO nanoparticles is elaborated in the section 5.2.1. The characteristic XRD peaks at $2\theta = 22.2^0$, $31.1^0$, $38.8^0$, $45.5^0$, $56.1^0$, $65.7^0$, $70.3^0$, $74.7^0$ confirm formation of BTO nanoparticles.[14] The FESEM image exhibits the spherulities microstructure of nanoparticles. The XRD peaks and FESEM image of BTO nanoparticles have been shown in the figure 5.2(a) and 5.2(b). Moreover, the crystalline size (D) of nanoparticle has been calculated from XRD peaks by using the Scherrer formula, which will be

$$\boldsymbol{D = \frac{k\lambda}{\beta cos\theta}} \quad \text{..... (5.1)}$$

Where, λ represents the wavelength of X-ray, β is the full width at half maximum (FWHM) of peaks, k is the crystalline shape constant whose value is 0.9. The calculated average crystalline size of BTO nanoparticle is 9.4nm.

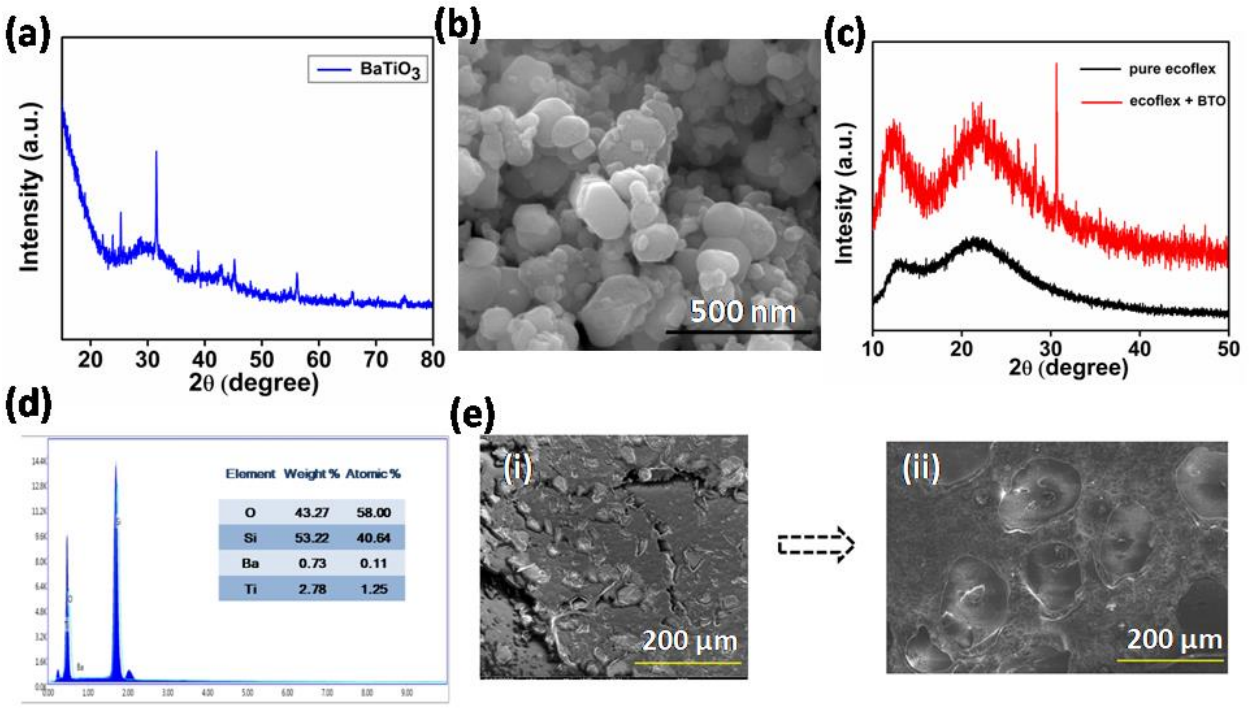


***Figure 5.2:*** *(a) Diffraction peaks and (b) surface morphology of BTO nanoparticles. (c) The X-ray diffraction peaks of pure Ecoflex and EBTO nanocomposite. (d) Energy dispersive spectra of EBTO nanocomposite. (e) Surface roughness of EBTO nanocomposite after 10000 cycles.*

The table 5.1 related to this calculation has been inserted below. Thus, we have incorporated BTO nanoparticle into Ecoflex polymer and named the nanocomposite as EBTO and investigated the structural and morphological properties. Figure 5.2(c) shows the XRD peaks of pure Ecoflex and EBTO nanocomposite. In case of pure Ecoflex, the characteristic peaks at $12.7^0$, $21.6^0$ is observed whereas in case of EBTO nanocomposite, an additional characteristic peak at $30.8^0$ has been noticed which occurs due to the BTO nanoparticles and also confirms the presence of BTO in the EBTO nanocomposite.[14,18] The surface morphology of EBTO nanocomposite has been investigated by FESEM image. First figure of figure 5.2(e) exhibits the morphology of nanocomposite. Furthermore, EDS spectra are performed to verify the atomic weight percentage and distribution of elements inside the nanocomposite. Figure 5.2(d) reveals the atomic weight percentage of individual elements Silicone (Si), Barium (Ba), Titanium (Ti) and Oxygen (O) which are present in the fabricated EBTO nanocomposite. This confirms the homogeneous distribution of these elements inside the nanocomposite and concludes the successful fabrication of EBTO nanocomposite. Furthermore, FESEM image has been captured

to investigate the surface roughness of the device after 10000 cycles (figure 5.2(e)). From the images, it have been visualized that the micro-patterns of the EBTO layer remain almost same after 10000 cycles and no such damage has been observed.

***Table 5.1:*** *Crystalline size and other parameters of BTO nanoparticles*

| ***Peak position (2θ)*** | ***FWHM (β)*** | ***Crystalline size (D) in nm*** | ***Microstrain*** | ***Dislocation density (δ) in $nm^{-2}$*** |
|---|---|---|---|---|
| *23.38841* | *8.975* | *9.039199306* | *0.1891968* | *0.012238835* |
| *29.43656* | *5.564* | *14.76242074* | *0.0924203* | *0.004588649* |
| *36.8923* | *11.85* | *7.067140747* | *0.1550151* | *0.020022233* |
| *43.21281* | *5.422* | *15.75927335* | *0.0597336* | *0.004026499* |
| *47.83022* | *8.824* | *9.848576431* | *0.0868228* | *0.010309867* |
| *56.23773* | *16.859* | *5.342795575* | *0.1376589* | *0.035031835* |
| *66.46394* | *10.397* | *9.134872987* | *0.0692414* | *0.011983812* |
| *77.39912* | *22.904* | *4.444335604* | *0.1247444* | *0.05062748* |

### *5.4.2 Charge trapping layer*

The charge trapping layer consists of MT nanoparticles incorporated PVDF nanofibers. The details synthesis method of MT nanoparticles has been elaborated in the supporting information file. The XRD peaks of MT nanoparticles are depicted in the figure 5.3(a). The observable

diffraction peaks at $23^0$, $27.5^0$, $40.4^0$, $49.6^0$, and $56.9^0$ are well matched with JCPDS file no. 01-073-1650. Some additional peaks at $38.1^0$, $43.2^0$ and $45.8^0$ attributes due to weaker Te rings and also matches with JCPDS file no 01-079-0736.[30] Thus, the XRD peaks confirm that synthesized nanoaprticles are $MoTe_2$ (MT). The crystalline size of the synthesized nanoparticles has been measured by Scherrer equation. The average crystalline size of MT nanoparticles is 30.2nm.

The surface morphology of MT nanoparticles has been investigated by FESEM image, shown in the figure 5.3(b). From FESEM image, we can observe the layered structure of MT nanoparticles which also confirms that the synthesized nanoparicles have 2D structure. Furthermore, we have incorporated this 2D MoTe2 nanoparticle into PVDF matrix and fabricated the PM5 nanofibers. The structural properties of PM5 nabofiber have been examined through XRD and FTIR

***Table 5.2:*** *Crystalline size and other structural parameters of MT nanoparticles*

| **Peak position (2θ)** | **FWHM (β)** | **Crystalline size (D) in nm** | **Microstrain** | **Dislocation density (δ) in $nm^{-2}$** |
|---|---|---|---|---|
| 27.48546 | 0.28717 | 28.47936409 | 0.0051235 | 0.001232933 |
| 38.21063 | 0.32076 | 26.2108107 | 0.0040405 | 0.00145559 |
| 40.36877 | 0.38304 | 22.09715331 | 0.0045464 | 0.002047988 |
| 45.85212 | 0.12221 | 50.58050087 | 0.0012608 | 0.00039087 |
| 49.57632 | 0.24608 | 35.55968099 | 0.002325 | 0.000790832 |

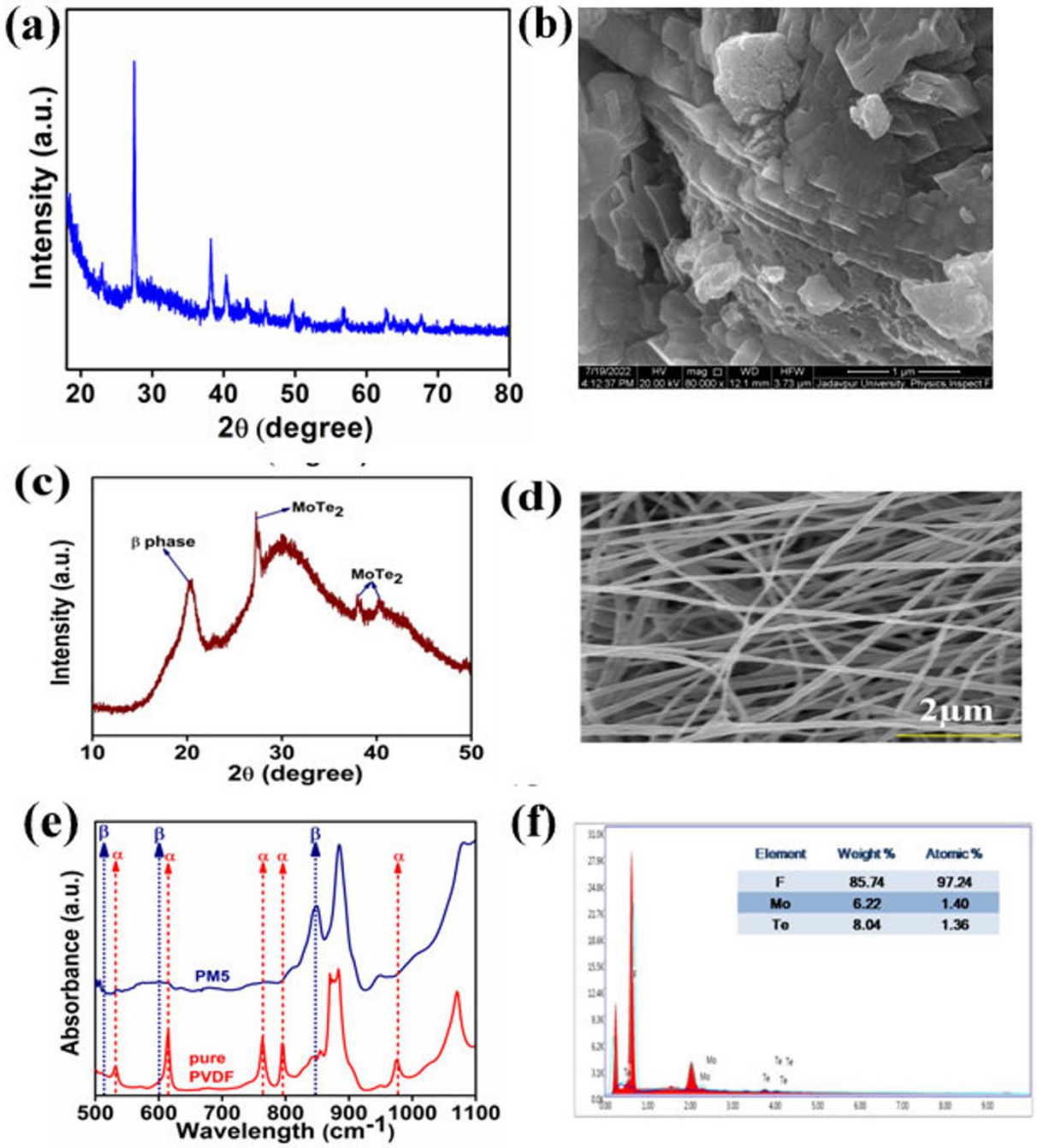


***Figure 5.3:*** *(a) XRD peaks and (b) FESEM image of MT nanoparticles. (c) The characteristic diffraction peaks and (d) FESEM image of PM5 nanofibers. (e) FTIR analysis of pure PVDF and PM5 nanofibers. (f) ) Energy dispersive spectra of PM5 fibers.*

spectra. Figure 5.3(c) represents the diffraction peaks of the nanofibers where, the characteristic peaks obtain at $20.3^0$, $27.3^0$, $38.1^0$ and $40.4^0$. Among them the last three peaks attributes due to the presence of MT nanoparicles within the nanofibers. The first characteristic peak at $20.3^0$ arises due to the nucleation of β-crystalline phase within the PM5 nanofibers and also denotes the crystalline plane (110) and (200). The formation of this β-phase is occurred due to electrostatic interaction between MT nanoparticles and PVDF matrix which helps in conversion of α-crystalline phase to β-crystalline phase. The nucleation of β-phase inside the PM5 nanofibers is further confirmed by FTIR analysis, depicted in the figure 5.3(e). From literature review, the absorbance peaks of pure PVDF at 487cm$^{-1}$ (due to $CF_2$ wagging), 531cm$^{-1}$ (due to $CF_2$ bending), 616 and 764cm$^{-1}$ (due to $CF_2$ and skeletal bending), 796 and 976cm$^{-1}$ (due to $CH_2$ rocking) are observed which is clearly indicating the presence of non polar α-crystalline phase. Whereas, the incorporating of MT nanopaerticles into PVDF matrix disappear the non-polar α-phase and get rise in β-crystalline phase. From figure 5.3(e), the observable absorption peaks at 445cm$^{-1}$ ($CF_2$ and $CH_2$ rocking), 479cm$^{-1}$ ($CF_2$ deformation), 510cm$^{-1}$ ($CF_2$ stretching), 600cm$^{-1}$ ($CF_2$ wagging), and 840cm$^{-1}$ ($CH_2$ rocking, $CF_2$ and skeletal C–C stretching) clearly point out the presence of polar electro-active β-phase. This β-crystalline phase of PM5 nanofibers improves the polarization effect and enhances the dielectric property. Moreover, the amount of β-phase content inside the nanofiber has been calculated by using Lambert-beer law,

$$\boldsymbol{F(\beta)} = \frac{\boldsymbol{A_\beta}}{\left(\frac{\boldsymbol{K_\beta}}{\boldsymbol{K_\alpha}}\right)\boldsymbol{A_\alpha}+\boldsymbol{A_\beta}} \quad \ldots\ldots (5.2)$$

Where, F(β) is the fraction of β-crystalline phase content, $A_\alpha$ and $A_\beta$ are the absorbance at 764cm$^{-1}$ and 840cm$^{-1}$ respectively. $K_\alpha$ and $K_\beta$ are the absorption coefficients at 764 and 840cm$^{-1}$ whose values are $6.1 \times 10^4$cm$^2$mol$^{-1}$ and $7.7 \times 10^4$cm$^2$mol$^{-1}$ respectively.[45(b),47] So, the calculated F(β) value of PM5 nanofibers is 93%. The surface morphology of the PM5 has been investigated by FESEM image which indicates the nanofibrous morphology, depicted in the figure 5.3(d). Also, the EDS spectrum has been performed to examine the atomic weight percentage inside the nanofibers. Figure 5.3(f) represents the atomic weight percentage of nanofibers where the presence of Fluorine (F), Molybdenum (Mo) and Tellurium (Te) is confirmed the homogeneous distribution of these elements within the nanofibers.

### *5.4.3 Working mechanism of EPMTNG device*

The schematic illustration of working mechanism of fabricated EPMTNG device and influence of trapping layer on output performance has been depicted in the figure 5.4(a) and (b). The EPMTNG device is designed with three layers i.e. charge generating layer, charge trapping layer and charge collecting layer. In this present work, EBTO nanocomposite, PM5 nanofiber and carbon tape serve as charge generating, charge trapping and charge collecting layer respectively. The combined effect of tribo-electrification and electrostatic induction plays an important role in operating mechanism of EPMTNG device. When human hand gets into contact with charge generating layer (EBTO), EBTO layer generates negative triboelctric charges due to negative tribopolarity. On the contrary, human hand induces positive triboelectric charges as shown in step (i) of figure 5.4(a). In the next step, relative separation between human hand and EBTO layer takes place. As a result, electrostatic charges are generated on the charge collecting layer (carbon tape) to balance the triboelectric charges. Thus, a potential difference develops between the ground and carbon tape which further helps in flowing of electrons from carbon tape to ground through external load, depicted in step (ii) of figure 5.4(a). These electrons are continuing their flow until the EPMTNG device is separated completely (step (iii) of figure 5.4(a)). After completing the separation, the human hand starts to come close to EBTO layer again and results in decrease of positive electrostatic charges which are generated on the charge collecting layer (carbon tape). Thus, electrons return from ground to carbon tape and this flow continues until the human hand is fully contacted with EBTO layer again, shown in step (iv) of figure 5.4(a). With the help of this contact separation procedure, EPMTNG device generates output signal periodically.[9]

Generally, triboelectric nanogenerator (TENG) consists of four representative layers, which are charge generating layer, charge trapping layer, charge collecting layer and charge storage layer. During triboelectrification, the charge generating layer induces the triboelectric charges, which can drift easily due to the effect of the driving force of electric field and combines with the opposite induced charges, generated in the charge collection layer. As a result, huge charge loss takes place, which reduces the surface charge density of TENG and diminishes the output performance of nanogenerator.[10] To overcome the significant issue of charge loss and improve the performance of TENG, a charge trapping layer has been introduced in the intermediate of charge generating layer and charge collection layer. The trapping layer restricts in combination

of triboelectric charges and opposite induced charges and enhances the output performance of nanogenerator by increasing the surface charge density. For this reason, we have introduced intermediate trapping layer (PM5) in the designing process of EPMTNG device. The effect of intermediate trapping layer on the output performance of EPMTNG device has been elaborated

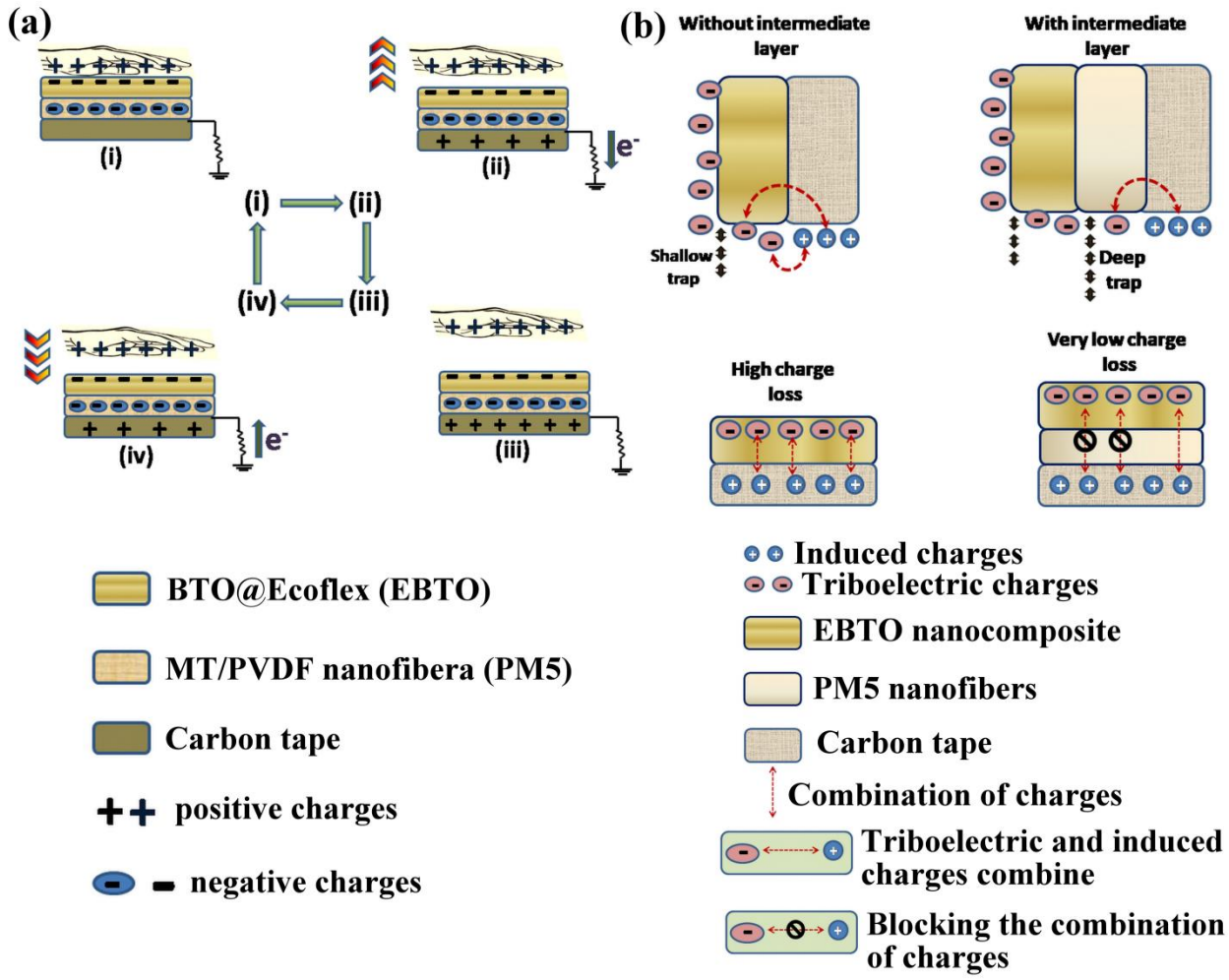


***Figure 5.4:*** *(a) Working mechanism of the EPMTNG. (b) Graphical representation of the presence of trapping layer (PM5 nanofibers) on the output performance.*

schematically in the figure 5.4(b). In the absence of charge trapping layer, the generated triboelectric charges of the EBTO layer get captured inside the trap sites. This helps in accumulation of induced positive charges in the carbon tape which results in the formation of electric field among EBTO layer and carbon tape. As the charge trapping ability of EBTO layer

is very low, the triboelectric charges which are trapped in the shallow trap of EBTO layer easily drift to the carbon tape in the presence of weak electric field and combine with induced charges easily. As a result, huge charge loss takes place which further results in low output performance. To improve the output performance and reduce the charge loss, an intermediate trapping layer (PM5 nanofiber) has been inserted between EBTO layer and carbon tape. When PM5 layer has been introduced in EPMTNG device, the phase interfaces between $MoTe_2$ and PVDF matrix serves as efficient trap sites for rapidly accumulating triboelectric charges. These trap networks retain the negative triboelectric charges while hindering the charges to drift from the EBTO layer (charge generating layer) to carbon tape (charge collecting layer), leading to decrease in the neutralization of negative tribo-charges and positive induced charges. Moreover, the addition of $MoTe_2$ into polymer matrix generates the induced charges under the application of external field, owing to the excellent aspect ratio and high conducting properties of the nanoparticles and increases the Coulomb force, which results in enhancement of polarization effect. This polarization effect arranges more capturing networks and then traps the triboelectric charges steadily by using the deep traps. Furthermore, the $MoTe_2$ nanoparticles strengthen the trapping depth of triboelectric charges by creating the conducting channels inside the PM5 layer and help in capturing more charges. Thus, the charges which are trapped in deep traps depart slowly from the trapping sites and extend the charge residence time, resulting in decrement of charge loss through reducing the charge recombination process. Therefore, the incorporation of PM5 layer in EPMTNG assists in accumulation of more triboelectric charges on the surface of EBTO layer and enhances the output performance of the device through increasing the surface charge density.[10,25] The following equations help in establishing the idea of insertion of PM5 layer in EPMTNG device, which will be[16,60]

$$\boldsymbol{\varepsilon_r} = \frac{\boldsymbol{d_{film} C_0}}{\boldsymbol{A\,\varepsilon_0}} \quad \textit{(5.3)}$$

$$\boldsymbol{P} = \boldsymbol{\varepsilon_0(\varepsilon_r - 1)E} \quad \textit{(5.4)}$$

$$\boldsymbol{\sigma} = \frac{\boldsymbol{V\varepsilon_0\varepsilon_r}}{\boldsymbol{d}} \quad \textit{(5.5)}$$

$$\boldsymbol{V_{OC}} = \frac{\boldsymbol{\sigma x(t)}}{\boldsymbol{\varepsilon_0}} \quad \textit{(5.6)}$$

Where, $\boldsymbol{\varepsilon}_r$ defines the relative permittivity, $d_{film}$ stands for the thickness of EBTO nanocomposite and PM5 layer, $C_0$ is the highest capacitance value, A defines the area of the EBTO nanocomposite and PM5 layer, $\boldsymbol{\varepsilon}_0$ represents the free space permittivity, P represents the

polarization at electric field, E defines the electric field, $\boldsymbol{\sigma}$ is the surface charge density, V represents the surface potential, d is the thickness of the device, $V_{oc}$ defines the output voltage of the fabricated device and x(t) is the separation distance. With the addition of PM5 layer, the capacitance value of the device increases which helps in enlarging the relative permittivity from equation (5.3). Thus, the higher relative permittivity assists in strengthening the polarization effect under the application of electric field, illustrated in the equation (5.4) and captures more triboelectric charges. Owing to this high permittivity and polarization effect, the PM5 layer reduces the charge loss and enhances the surface charge density of the device from equation (5.5). As a result, the enhancement of the surface charge density improves the output voltage of EPMTNG device, described from equation (5.6).

### *5.4.4 Theoretical investigation of the effect of PM5 fibers on EPMTNG*

The effect of intermediate trapping layer (PM5 fibers) on the output performance of EPMTNG has been investigated theoretically by using finite element analysis. Also a simulation model using numerical analysis through python has been prepared for the comparison of surface potential and output performance of TENG, with respect to the presence and absence of intermediate layer. For this, a fundamental numerical modeling has been prepared and analyzed it by using Python 3.9 libraries on Jupyter lab framework. Moreover, some libraries including NumPy and Pandas have been used in Python to analysis the numerical functions and data configurations. NumPy helps in numerical operations including multidimensional array and matrix, elemental operations etc. and Panda assists in analyzing the organized and structured data-frame. After successfully simulated the data in Python, Matplotlib library have been utilized to plot the excepted graph by using the simulated data points. In the absence of intermediate trapping layer (PM5), the V-Q-x relation of conductor to dielectric type triboelectric nanogenerator will be[16,57]

$$\boldsymbol{V = -\frac{Q}{S\varepsilon_0}\left(d_0 + x(t)\right) + \frac{\sigma x(t)}{\varepsilon_0}} \quad \text{..... (5.7)}$$

Where, $\boldsymbol{d_0 = \frac{d_{EBTO}}{\varepsilon_{r_{EBTO}}}}$

In the above equation (5.7), Q is the amount of charge transferred; S defines the area of EPMTNG; $\boldsymbol{\varepsilon}_0$ represents the free space permittivity; $d_{EBTO}$ is the thickness of charge generating layer (EBTO nanocomposite); $\boldsymbol{\varepsilon}_{rEBTO}$ represents the relative permittivity of EBTO

nanocomposite; x(t) is the distance between two triboelectric surfaces; $\boldsymbol{\sigma}$ defines the surface charge density. For open-circuit condition, Q=0 that means no charge transfer process will occur. Therefore, the open-circuit voltage will be[58]

$$\boldsymbol{V_{OC} = \frac{\sigma x(t)}{\varepsilon_0}} \quad \text{..... (5.8)}$$

During the presence of intermediate layer (PM5) within EPMTNG device, V-Q-x relationship will be[57]

$$\boldsymbol{V = -\frac{Q}{S\varepsilon_0}\left(d_0 + x(t)\right) + \frac{\sigma x(t)}{\varepsilon_0}} \quad \text{..... (5.9)}$$

Where, $d_0$ will be sum of the EBTO layer and PM5 layer. That means, $\boldsymbol{d_0 = \frac{d_{EBTO}}{\varepsilon_{r_{EBTO}}} + \frac{d_{PM5}}{\varepsilon_{r_{PM5}}}}$. To simplify the calculations, some assumptions are taken which are (a) the distribution of charges on the surface of triboelectric layers is uniform, (b) triboelectric charges are only staying on the contact surfaces,(c) measured surface charge density is linearly related to the surface potential, (d) the applying force on the device for all cases is same, (e) thickness of EBTO nanocomposite and PM5 layer are assumed to be 1mm and 256µm respectively. The highest capacitance value is considered to be utilized in calculation. Area of the EBTO nanocomposite and PM5 layer are 1.1cm$^2$ and 1.4cm$^2$ respectively. The surface charge density of TENG with PM5 layer and without PM5 layer is assumed to be 3.5 X $10^{-4}$C/m$^2$ and 1.3 X $10^{-4}$C/m$^2$ respectively.

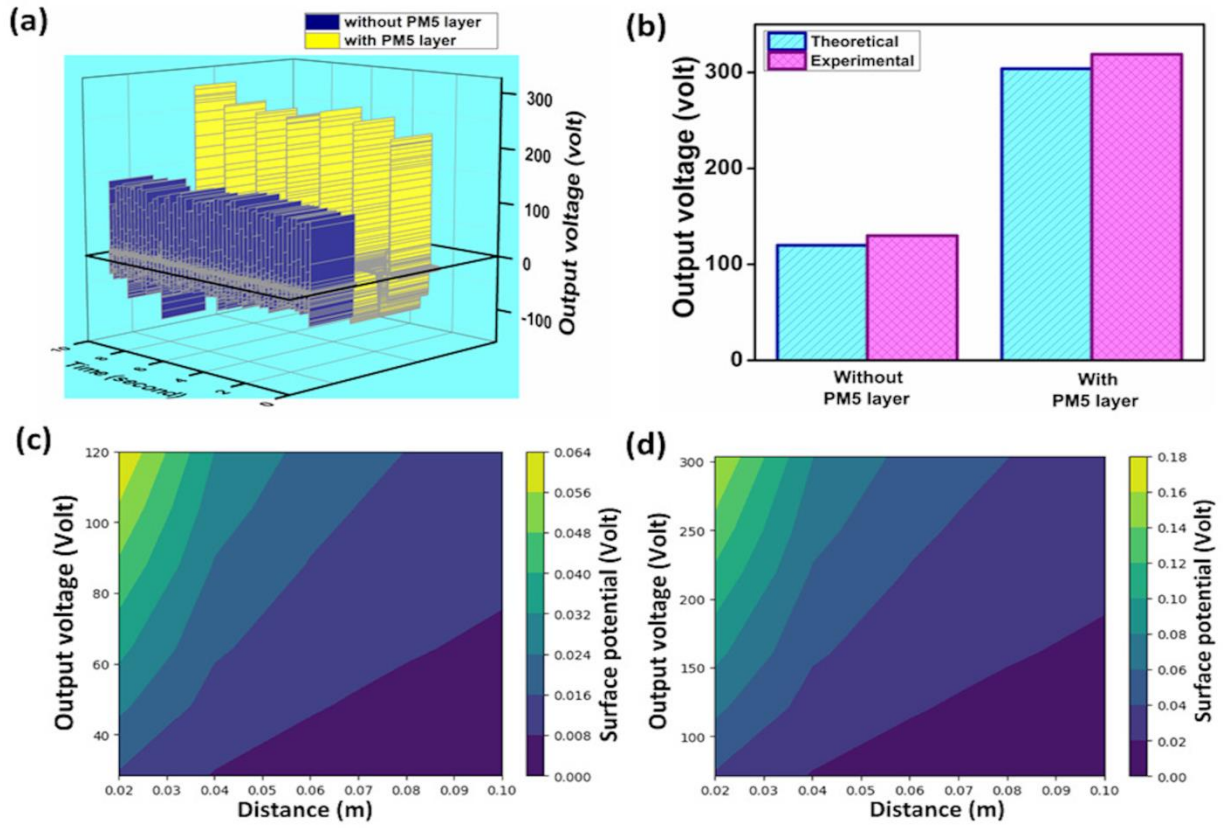


***Figure 5.5:*** *(a) Theoretical assessment of the effect of PM5 layer on the output performance of EPMTNG. (b) Comparison of theoretically and experimentally obtained output voltage. Contour plot of surface potential during the (c) absence of PM5 layer and (d) presence of PM5 layer.*

First of all, we have calculated the relative permittivity ($\boldsymbol{\varepsilon}_r$) of EBTO nanocomposite and PM5 layer. As we know that high permittivity based layer increases the surface charge of density by inducing more polarization. The $\boldsymbol{\varepsilon}_r$ has been measured by using the equation[57]

$$\boldsymbol{\varepsilon_r} = \frac{\boldsymbol{d_{film} C_0}}{\boldsymbol{A\, \varepsilon_0}} \quad \text{..... (5.10)}$$

Here, $d_{film}$ stands for the thickness of EBTO nanocomposite and PM5 layer, $C_0$ is the highest capacitance value, A defines the area of the EBTO nanocomposite and PM5 layer and $\boldsymbol{\varepsilon}_0$ represents the free space permittivity. Thus, the calculated relative permittivity values of EBTO nanocomposite and PM5 layer are 7 and 23 respectively.

Therefore, the high permittivity value of PM5 layer assists in inducing more polarization effect and enhances the surface charge density of EPMTNG device. In the presence of PM5 layer, the induced high surface charge density increases the output voltage of the device. The estimated

output voltage of EPMTNG device from finite element analysis is 304V. In the absence of PM5 layer, the estimated voltage is 120V, shown in the figure 5.5(a). Additionally, a diagram has been presented to investigate the theoretically and experimentally obtained output voltage with the absence and presence of PM5 intermediate layer, shown in the figure 5.5(b). Moreover, the changes in relative permittivity, the value of $d_0$ also changes for both cases (with and without PM5 layer). Along with this, the amount of charge transfer (Q) is both cases also varied with the surface charge density as charge transfer is dependent on the surface charge density and contact area. In order to investigate the effect of PM5 layer, the surface potential has been calculated theoretically by using the equation:[18]

$$\boldsymbol{V = \frac{\sigma * d_0}{\varepsilon_0 * \varepsilon_r}} \quad \text{..... (5.11)}$$

Where, $\sigma$ defines the surface charge density, $d_0$ represents the thickness of layer, $\varepsilon_0$ is the permittivity of free space and $\varepsilon_r$ is the relative permittivity. The estimated results from simulation describe that TENG with PM5 layer consists of surface potential of 0.18V, which is higher than the TENG without PM5 layer (surface potential of 0.064V). Also, the variation of surface potential with the different distances between human hand and device has been mapped in both cases. The simulated data of surface potential in both cases are represented in the figure 5.5(c) and 5.5(d). The possible reasons behind the enhancement of surface charge density, surface potential and output voltage during the presence of intermediate trapping layer are

(i) Prevention of electrons decay with positive induced charges

(ii) Capturing more residual charges in trap sites of PM5 layer

(iii) Reinforcing the polarization effect through trapping more charges and improving the conductivity. This further restricts the charge loss by preventing charge recombination and enhances the surface potential.

As a result, output performance of EPMTNG is increased. Thus, the theoretical model clearly indicates the prominent advantages due to the presence of intermediate layer in fabricated device and establishes our proposed concept.

### *5.4.5 Output performance and electrical properties of EPMTNG device*

The three layers of the device not only increase the output performance but also make the device flexible and user friendly. Furthermore, the output performance of EPMTNG device has been investigated by connecting the wire of device with DSO. The wearable and flexible device

exhibits 319V output voltage under continuous finger tapping condition with generated axial pressure of 12N. Moreover, the influence of intermediate layer is also observed. With the help of intermediate layer, the EPMTNG device exhibits 319V output voltage whereas the device generates only 130V output voltage in the absence of charge trapping layer (Figure 5.6(a)). The reason behind such high output is the influence of trapping layer by capturing more charges within the trapping sites and increasing the charge storage ability of the device. From, Coulomb's law, we can see that the electric field (E) among triboelectric ($Q_t$) and induced charges ($Q_e$) is varying inversely to the square of the distance(r) between triboelectric charges and induced charges, i.e.

$$\boldsymbol{E} = \frac{\boldsymbol{K_e Q_t Q_e}}{\boldsymbol{r^2}} \quad \text{..... (5.12)}$$

Where $K_e$ represents the Coulomb's constant.

When the intermediate trapping layer is absent, the small amount of charges is trapped at high electric field. Thereafter, these trapped charges drift easily and combines with induced charges as drift velocity (u) depends on the electric field, which will be[17]

$$\boldsymbol{u} = \mu\boldsymbol{E} \quad \text{..... (5.13)}$$

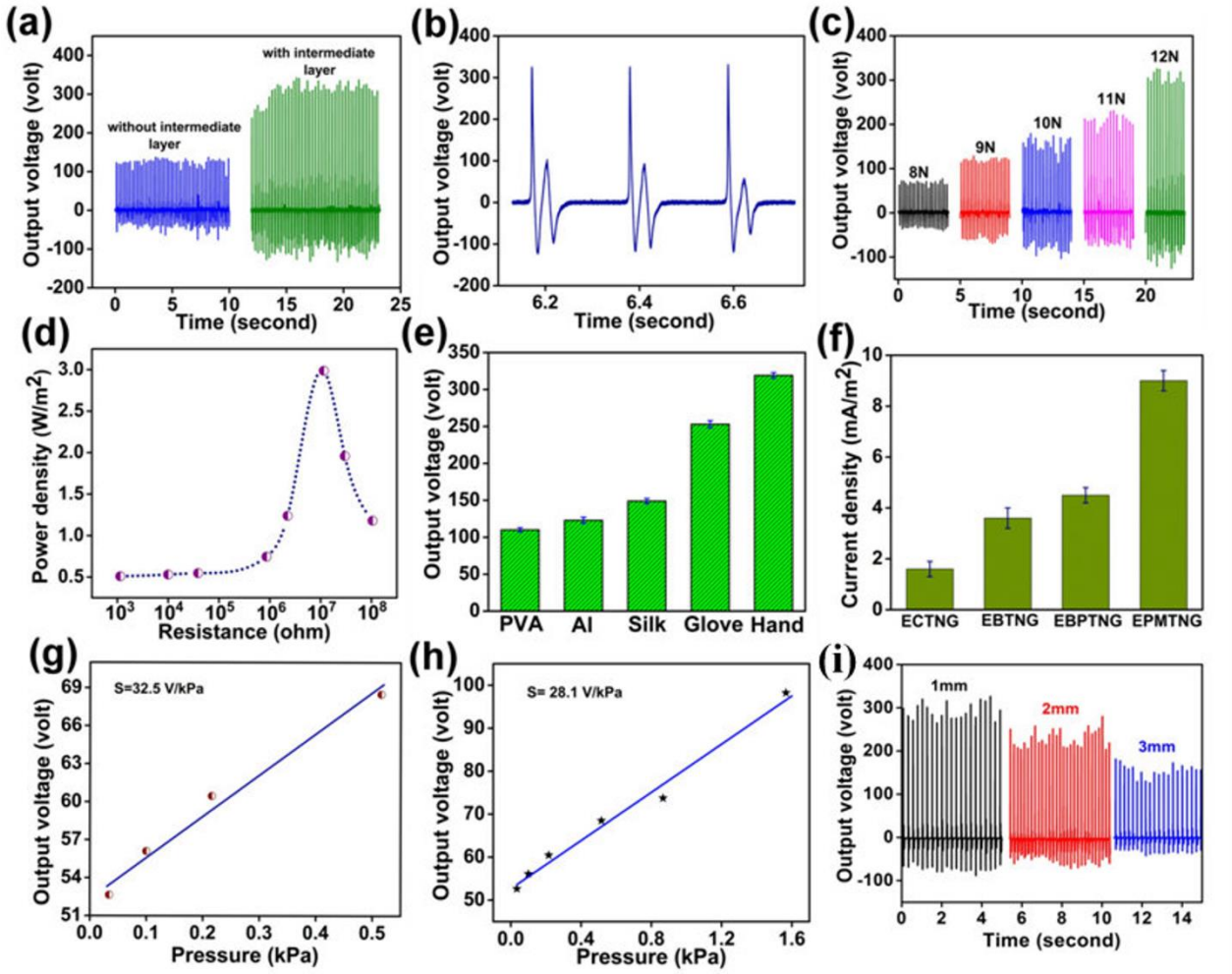


***Figure 5.6:*** *(a) Output voltage of the EPMTNG device under periodic finger tapping (12N). (b) Magnified view of generated output voltage of the device during same axial pressure. (c) Force dependent output voltage of EPMTNG. (d) Instantaneous power density with the variation of external load resistance. (e) Obtaining the output voltage by different tribo positive materials. (f) Measuring the current densities of four devices: ECTNG, EBTNG, EBPTNG and EPMTNG. Sensitivity of EPMTNG at (g) low pressure region (up to 0.5kPa) and (h) high pressure (> 0.5kPa) region. (i) Output voltage of EPMTNG device at different thickness of EBTO nanocomposite.*

That means, high electric field induces high drift velocity which helps in more charge recombination process and induces low output result. Whereas, the presence of charge trapping layer increases the distance (r) between charges and induces weak electric field which reduces

the drift velocity of charges and prevents in charge recombination. As a result, EPMTNG device generates such high output voltage in presence of intermediate layer (PM5). Moreover, the enlarged view of generated output voltage has been depicted in the figure 5.6(b) where positive peak appears at the time of applying strain on the EPMTNG device and negative peak induces after recovering the strain. The influence of applied force on the output performance of device has been monitored by applying different force on the device, shown in the figure 5.6(c). As we increase the applied force, the output voltage also increases. The possible reason behind this is that with the increase of force, the contact between the two triboelectric layers also increase which helps in more charge generation.[52] In order to explore the load capacity of our fabricated device, the multiple valued load resistances have been used. The EPMTNG device exhibits different instantaneous power density with the variation of load resistance changing from $10^3$ to $10^8\Omega$ (figure 5.6(d)).The power density of the device has been calculated by using

$$\boldsymbol{P = \frac{V^2}{R_L \times A}} \quad \text{..... (5.14)}$$

Where, V represents the output voltage of the EPMTNG device, $R_L$ defines the value of load resistance and A is the surface area of the EPMTNG device (4.4 X 2.5cm$^2$).[47] The obtained maximum power density is 2.9W/m$^2$ at $10^7\Omega$. Furthermore, the thickness of charge generating layer (EBTO nanocomposite) effects in the output performance of triboelectric nanogenerator. As we increase the thickness of EBTO nanocomposite, output voltage also decreases. The maximum voltage is obtained for 1mm thickness, depicted in the figure 5.6(i). The reason behind this behavior is that the surface charge density reduces with the increasing of thickness of EBTO which results in lowering the output voltage. The equation which validates this reason, will be

$$\boldsymbol{\sigma = \frac{V \varepsilon_o \varepsilon_r}{d}} \quad \text{..... (5.15)}$$

Where, V describes the surface potential of EBTO nanocomposite, $\varepsilon_0$ represents the dielectric constant of air and $\varepsilon_r$ represents the dielectric constant of nanocomposite, $\boldsymbol{\sigma}$ defines the surface charge density of nanocomposite and d is the thickness of EBTO nanocomposite.[18]Thus, it is clearly visible that increasing thickness of nanocomposite decreases the surface charge density which results in low output voltage as

$$\boldsymbol{V_{OC} = {\sigma A}/{2C_o}} \quad \text{..... (5.16)}$$

where, $V_{OC}$ is the output voltage of EPMTNG device, $\boldsymbol{\sigma}$ is the surface potential and A is the surface area of EBTO nanocomposite , $C_o$ defines the capacitance of device.[56]

While measuring the output voltage of the device for more than one set of values, we get different results. This incident also happens in case of measuring the current density. The possible reasons behind the changes of the results are the presence of errors arising from external mechanical force, contact area, contact speed, frequency etc.[59] Another leading factor of inducing the errors is the separation distance between the two triboelctric layers. When separation distance is deviated from its optimal value, the charge transfer between electrodes also changes. As a result, we get different output results for same device. Also, the contact area of the EPMTNG device is another source of error. Error in contact area results in fluctuations in charge density and gives us inaccurate output value. Whenever, we measure the output voltage and current density for different case of fabricated TENGs, some deviations are observed due to the above mentioned sources of errors. To improve the reliability, error bar has been included. Moreover, the material selection of positive layer of EPMTNG device plays a significant role in the output performance. To demonstrate the excellent output performance of fabricated device, its output result has been measured by using different positive materials like PVA, aluminum sheet, silk, nitrile glove and human hand, shown in the figure 5.6(e). The measured output voltages using different positive materials like PVA, aluminium sheet, silk, nitrile glove and human hand are 110 ± 2.9V, 123 ± 4.2V, 149 ± 3.5V, 253 ± 4.8V and 318 ± 3.9V respectively. The findings indicate that the performance of triboelectric nanogenerator is greatly impacted by the active layer materials and the human hand generates maximum output voltage than other positive materials as it is an extremely positive triboelectric material.[9] For this reason, we have selected human hand as positive layer in this present work. Furthermore, the current density of the EPMTNG has been measured. Also, the influence of trapping layer in the current density has been examined. We have prepared four devices (i) Ecoflex and carbon tape based TENG, named as ECTNG, (ii) BTO incorporated Ecoflex nanocomposite and carbon tape based TENG, named as EBTNG, (iii) EBTO layer, PVDF layer and carbon tape based TENG, named as EBPTNG and (iv) EBTO layer and MT incorporated PVDF nanofiber (charge trapping layer) based EPMTNG. The measured current density of these devices is shown in the figure 5.6(f). The measured current densities of these four devices are 1.6 ± 0.2, 3.6 ± 0.4, 4.5 ± 0.3, 9 ± 0.4mA/m$^2$ respectively. This result indicates that the presence of intermediate trapping layer improves the current density of TENG compared to other devices. Generally, in the absence of charge trapping layer, some charges of EBTNG device are captured in the shallow trap of BTO layer. Thereafter,

these charges drift easily and combine with positive charges of carbon tape which results in low surface charge density. Moreover, the presence of MT nanoparticles within the intermediate layer reinforces the polarization effect and prevents in charge recombination. This increases charge density and enhances the current density of EPMTNG. This can be mathematically expressed as

$$J_D = \sigma_T \frac{dH}{dt} \frac{\frac{d\varepsilon_0}{\varepsilon}}{dt(\frac{d\varepsilon_0}{\varepsilon}+z)(\frac{d\varepsilon_0}{\varepsilon}+z)} + \frac{d\sigma_T}{dt} \frac{H}{(\frac{d\varepsilon_0}{\varepsilon}+z)} \quad \text{..... (5.17)}$$

Where, $J_D$ represents the current density and H represents the function of time which is associating with the contact frequency. This equation confirms that the current density is directly proportional to the charge density.[18] Thus, we get maximum current density in case of EPMTNG device compared to other devices. Also, the sensitivity of the fabricated EPMTNG device has been measured by falling different masses objects on the device. The equation helped in calculates the sensitivity of the device will be

$$S = {\Delta V}/{\Delta P} \quad \text{..... (5.18)}$$

Where, S is the sensitivity of the device, ΔV is the change in the obtained output voltage and ΔP defines the change in applied pressure.[47]The sensitivity of the device at low pressure region (up to 0.5kPa) is 32.5V/kPa, shown in the figure 5.6(g). In the higher pressure region (> 0.5kPa), the sensitivity value of the device is 28.1V/kPa, shown in the figure 5.6(h).

Furthermore, the stability performance of EPMTNG device has been performed over 10000 cycles under the applied mechanical force by human hand. Figure 5.7(a) exhibits the stability performance of the device, resulting that the device maintains near about the same output voltage throughout the whole time period and no such degradation of output voltage is observed after 10000 cycles. These results confirm the long-term stability of the EPMTNG device. The durability test of EPMTNG device has been performed under the application of mechanical force by hand. The device exhibits near about 314V output voltages at 5Hz frequency. The durability test has been conducted for a consecutive 12days and the results interpret that EPMTNG device generates near about same output voltage throughout the whole time period and maintains over 98% of initial output voltage, shown in the figure 5.7(b). Therefore, the results indicate that the EPMTNG device has exceptional durability and is suitable for long-term practical applications.

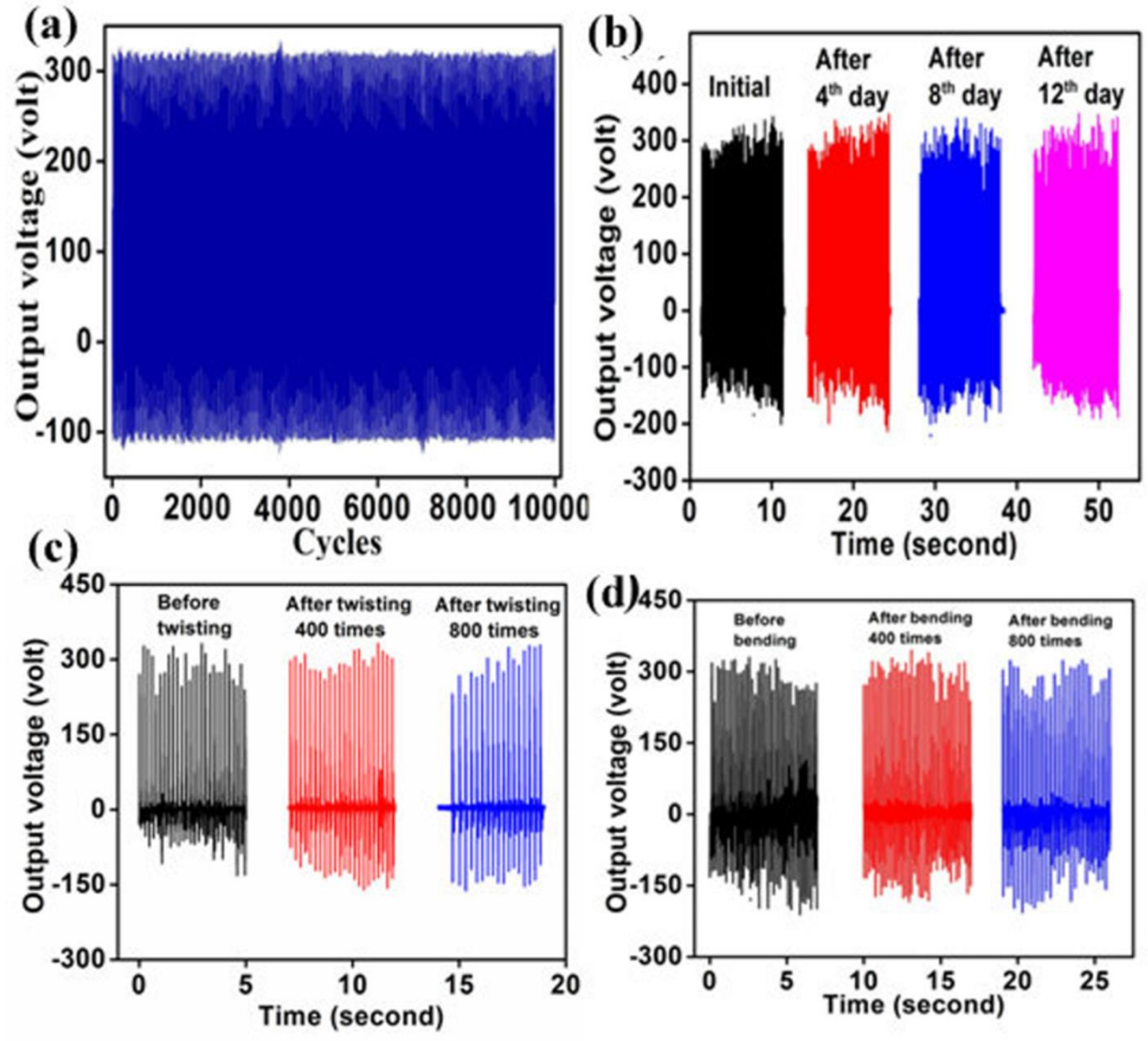


***Figure 5.7:*** *(a) Stability and (b) durability performance of EPMTNG device. (c) Twisting performance of the fabricated device. (d) Measuring the robustness of the fabricated device by bending it over 800 times.*

To observe the robustness of the device, bending and twisting tests have been examined. Figure 5.7(d) shows the bending performance of the EPMTNG device. After bending over 400 times, the device exhibits near about same output voltage compared to its initial value and maintains 99% of initial value. Thereafter, the device has been bend again more 400 times and has been maintained 98% of initial value. The results of the bending test indicate the very good robustness

of the device. Moreover, the twisting performance of the device has been observed in the figure 5.7(c). After twisting the device over 400 times, the device generates almost same output voltage and maintains 98% of its initial value. To investigate the high robustness of the device, we have twisted it 400 times more and obtained nearly same output voltage, maintaining the 97% of initial value. Therefore, the bending and twisting test of the device exhibit the outstanding robustness behavior of the EPMTNG device.

### 5.4.6 Electrical properties of EPMTNG device

The electrical properties of the different layers of the fabricated EPMTNG device have been examined by dielectric measurement. To enhance the surface charge density and improve the output performance of the device, dielectric parameters play a significant role. In this present work, we have prepared three systems, one is EBTO layer, PM5 nanofiber and dual layer (combining EBTO and PM5) by attaching the copper electrode on the both side of each system and measured the dielectric parameters (for measurement of the prepared three systems) through LCR meter by varying the frequency range from 10Hz to 1MHz. Figure 5.8(a) exhibits the dielectric constant value of three systems by varying the frequencies. Relative dielectric constant can be expressed as

$$\boldsymbol{\varepsilon} = \boldsymbol{\varepsilon'} + \mathbf{j}\, \boldsymbol{\varepsilon''} \quad \ldots\ldots \quad (5.19)$$

Where, $\varepsilon'$ is the real part and $\varepsilon''$ is the imaginary part of relative dielectric constant. The imaginary part contributes in energy dissipation inside the dielectric material, whereas the real part indicates the energy storage capacity of dielectric substance. The real part of dielectric constant can be calculated by using this mathematical equation

$$\boldsymbol{\varepsilon'} = \frac{\mathbf{C\,d}}{\boldsymbol{\varepsilon_0}\mathbf{A}} \quad \ldots\ldots \quad (5.20)$$

Where, C represents the capacitance value of respective system; $\varepsilon_0$ is free space permittivity whose value is $8.85 \times 10^{-12}$ F/m; d is the thickness and A is the area of respective systems. For EBTO layer, the maximum dielectric constant is found to be 11 at 10Hz frequency which is very high compared to the dielectric constant (~ 3) of pure ecoflex. The reasons behind getting high value of dielectric constant are the formation of macroscopic dipole and microcapacitor network.[44] Moreover, the presence of oxygen (O) inside the BTO nanoparticles and hydrogen (H) inside the ecoflex polymer helps in dipole formation, whereas the microcapacitors are induced between nearest fillers (BTO nanoparticles). Each single microcapacitor contributes to

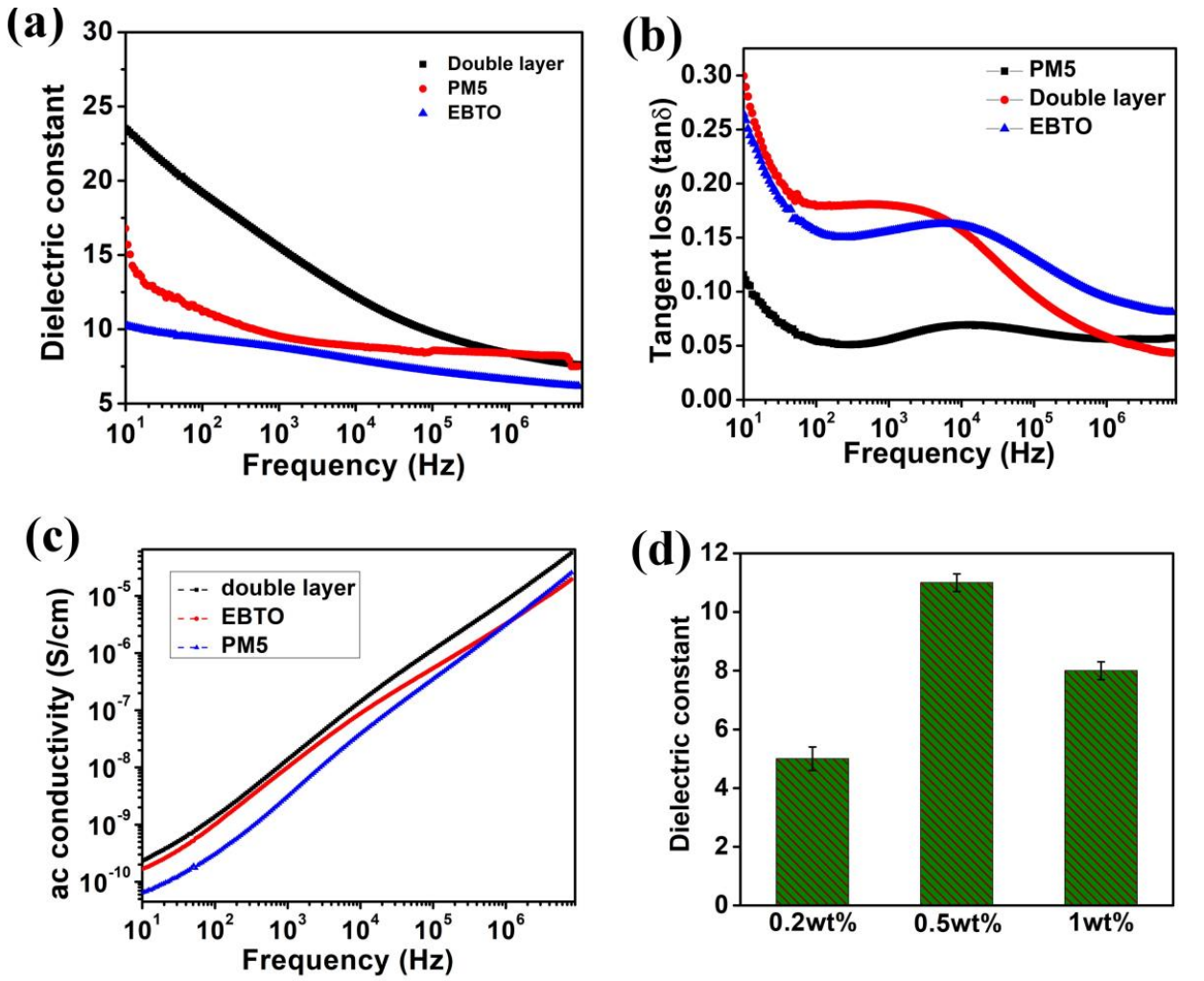


***Figure 5.8:*** *(a) Dielectric constant and (b) tangent loss of EBTO nanocomposite, PM5 nanofibers and dual layer. (c) Measured ac conductivity of three layers by varying frequencies. (d) Dielectric constant of EBTO layer at different weight percentage loading of BTO nanoparticles.*

build microcapacitor network which further leads to high dielectric value.[18] Thus, EBTO layer shows maximum dielectric value at 0.5wt% of BTO. At higher doping concentration (1wt%), dielectric value of nanocomposite reduces due to the attainment of the percolation limit.[9] After reaching the percolation threshold, the interaction between fillers triggers the leakage current to increase. Additionally, the BTO nanoparticle sets up a network of conductive molecules within the polymer matrix, which results in shifting from non-Ohmic to Ohomic conduction.[18] Due to these possible reasons, the dielectric value decreases at higher concentration of BTO, depicted in

figure 5.8(d). For PM5 nanofiber layer, the obtained maximum dielectric constant is found to be 16 at 10Hz frequency. Thereafter, dielectric constant reduces gradually with the increasing in frequency value. This phenomenon is attributed due to the Maxwell-Wagner interfacial polarization, which occurs while the carriers of free charge accumulate at high resistive grain edge. In details, within the PM5 nanofiber layer, the edges of insulated grains separate the conducting grains, which facilitate in trapping of free charge carriers and induce dipoles through the grain during their hopping.[45] For this reason, we get such high value of dielectric constant. Additionally, a fast decrement of dielectric value at high frequency zone has been observed as dipole orientation polarization and electronic displacement polarization are unable to survive with the frequency variation.[46] In case of double layer, the maximum dielectric constant is found to be 23 at 10Hz frequency which is relatively high compared to EBTO layer. The possible reason behind this increment in dielectric value is the addition of intermediate layer, which traps more residual charges in trapping sites. Moreover, the incorporation of MT nanoparticles into PVDF matrix reinforces the polarization effect of dual layer and enhances the number of charge carriers which improves the dielectric property.[18]

Along with the dielectric value, tangent loss and ac conductivity of three systems have been observed and shown in the figure 5.8(b) and figure 5.8(c). The EBTO layer, PM5 layer and dual layer exhibit low tangent loss. From figure 5.8(b), low tangent loss value is observed at low frequency region, whereas increment of loss value at higher frequency region is visualized. The possible reason behind this phenomenon is the thermal agitation of the dipoles.[45] Thus, the high dielectric value with low tangent loss of EBTO layer, PM5 fiber and double layer confirms that the EPMTNG device consists of good storage capacity.

### *5.4.7 Robotic gesture detection*

Owing to have high sensitivity, low thickness and flexibility, the wearable EPMTNG device has been utilized in robotic gesture detection. Firstly, the device is affixed with a hollow cylindrical object and the different responses of pressure which is generated by the full bending of each fingers of an artificial wooded hand, was monitored. Figure 5.9(a) to (e) represents the digital snapshots of the device being pressed by the five fingers (index, middle, ring, middle and thumb). For continuous pressing and releasing of artificial hand fingers, we get individual output responses of each finger, shown in the figure 5.9(f). Along with this, the positive peaks and the

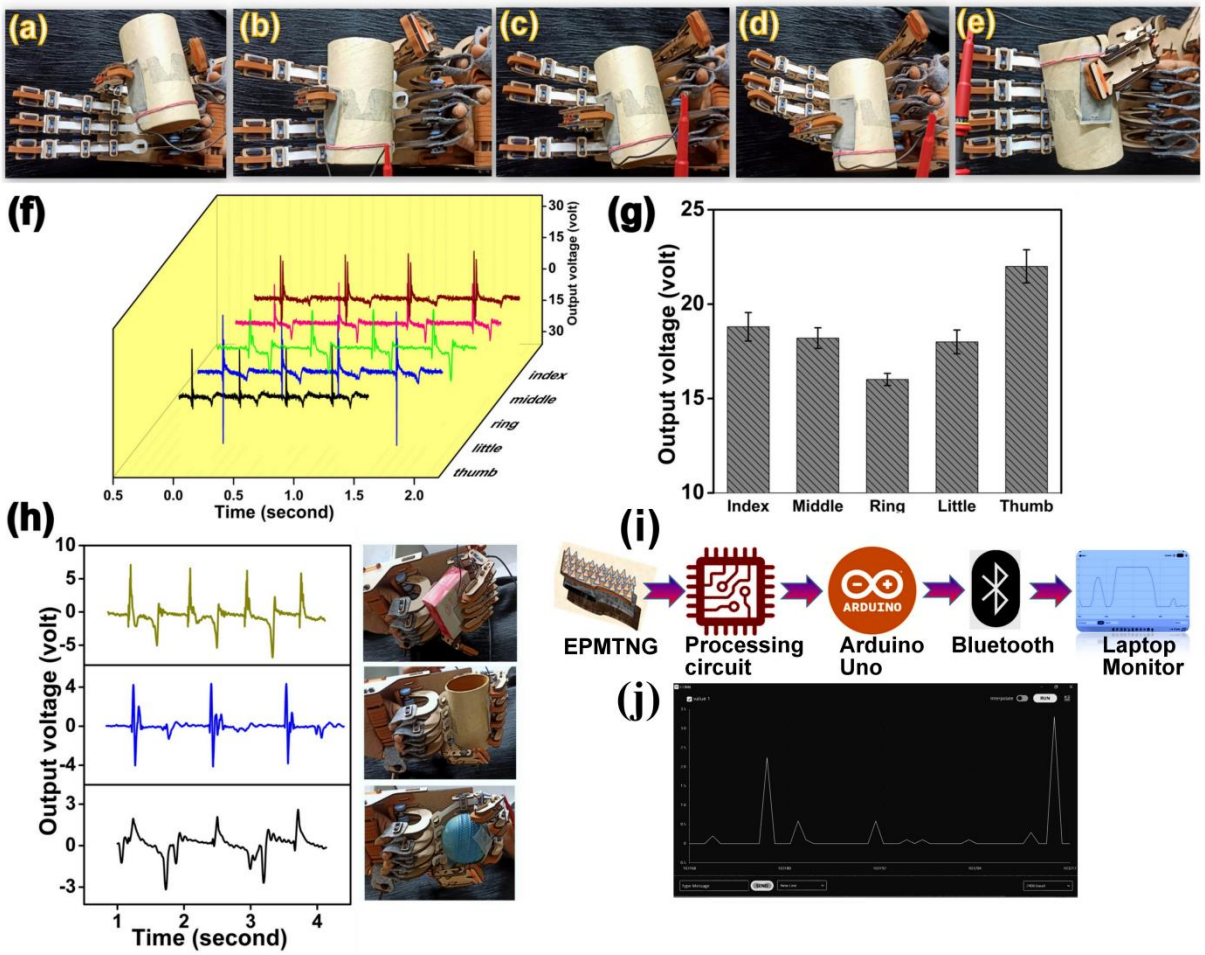


***Figure 5.9:*** *(a) to (e) Digital snapshots and (f) output responses of five artificial fingers (index, middle, ring, middle and thumb) at touching condition of device. (g) Obtaining the output voltage during each finger movement. (h) Output responses and digital image of gripping different objects (rectangular box, hollow cylinder and rubber ball). (i) Schematic illustration of wireless connection of transmitted signal. (j) Displaying the transmitted signal on laptop monitor during artificial finger bending.*

negative peaks of generated output responses are also observed which are attributed due to the pressing and releasing effect of fingers. As the generated forces of the fingers on the EPMTNG device are different, thus the obtained output voltages of each finger movement are also different. During artificial finger bending, the generated error values are also included with the obtained output voltages of each finger movement (figure 5.9(g)). Therefore, index, middle,

thumb fingers generate 19 ± 0.7V, 18 ± 0.5V, 22 ± 0.8V and ring, little fingers exhibit 16 ± 0.3V, 17 ± 0.6V output voltage respectively. Thus, the flexible and wearable device can be utilized in robotic surgery and human-machine interfaces applications.[53] Furthermore, the sensing ability of device opens up a new path of utilization in the field of soft robotic application. The utilization of the device in soft robotic application has been investigated by gripping different shaped objects. First of all, three differently shaped objects are selected which are a rectangular box, a hollow cylindrical object and a rubber ball. Thereafter, the device is attached with these respective objects and monitored the responses during gripping condition. When the objects are gripped, the device generates positive peaks and negative peaks occur at the time of releasing the object, shown in the figure 5.9(h). Also, each differently shaped object generates different output response during gripping and releasing condition due to different contact area. Therefore, the rectangular box generates high output voltage compared to other objects as the higher curvature induces superior contact area which leads to high output result.[54]Thus, the gripping ability and object distinguishable capability makes EPMTNG device a suitable candidate in soft robotic applications. Additionally, a wireless system has been introduced to monitor the bending movements of robotics finger by transmitting the generated signal to a laptop through Arduino Uno Bluetooth system. Figure 5.9(i) demonstrates the wireless connection of the transmitted signal. During bending of finger, the EPMTNG device generates the output signal which passes through low pass filter and rectifier module contained processing circuit for rectifying the signal. After getting rectified, the signal has been sent to Arduino Uno and also transferred wirelessly to laptop via Bluetooth system. The rectified signals during bending motion are clearly displayed in the laptop monitor, shown in the figure 5.9(j).

### *5.4.8 Tracking different human physiological signals*

The different body portions of human body exhibits various characteristics of physiological signal. Owing to high sensitivity, stretchability, flexibility and skin compatibility properties, EPMTNG device can be used as self-powered human physiological signal detector. These properties can have advance implication in multiple areas for example human machine interface, analysis of the performance in different sporting activity, medical rehabilitation etc.[9] To track the physiological signals, we have attached EPMTNG device to the different parts of human body like wrist, neck, throat, and elbow. As the device has high sensitivity in low pressure region

(32.5V/kPa up to 0.5kPa) so it can successfully detect the blood flow of human body. When we are attaching the EPMTNG device on wrist pulse, the device exhibits quite high output voltage (near about 0.7V), generated from blood flow, shown in the figure 5.10(a). Systolic and diastolic are the two main components of blood pressure, which provide the peak and dip of the pulse wave during blood flow.[47]

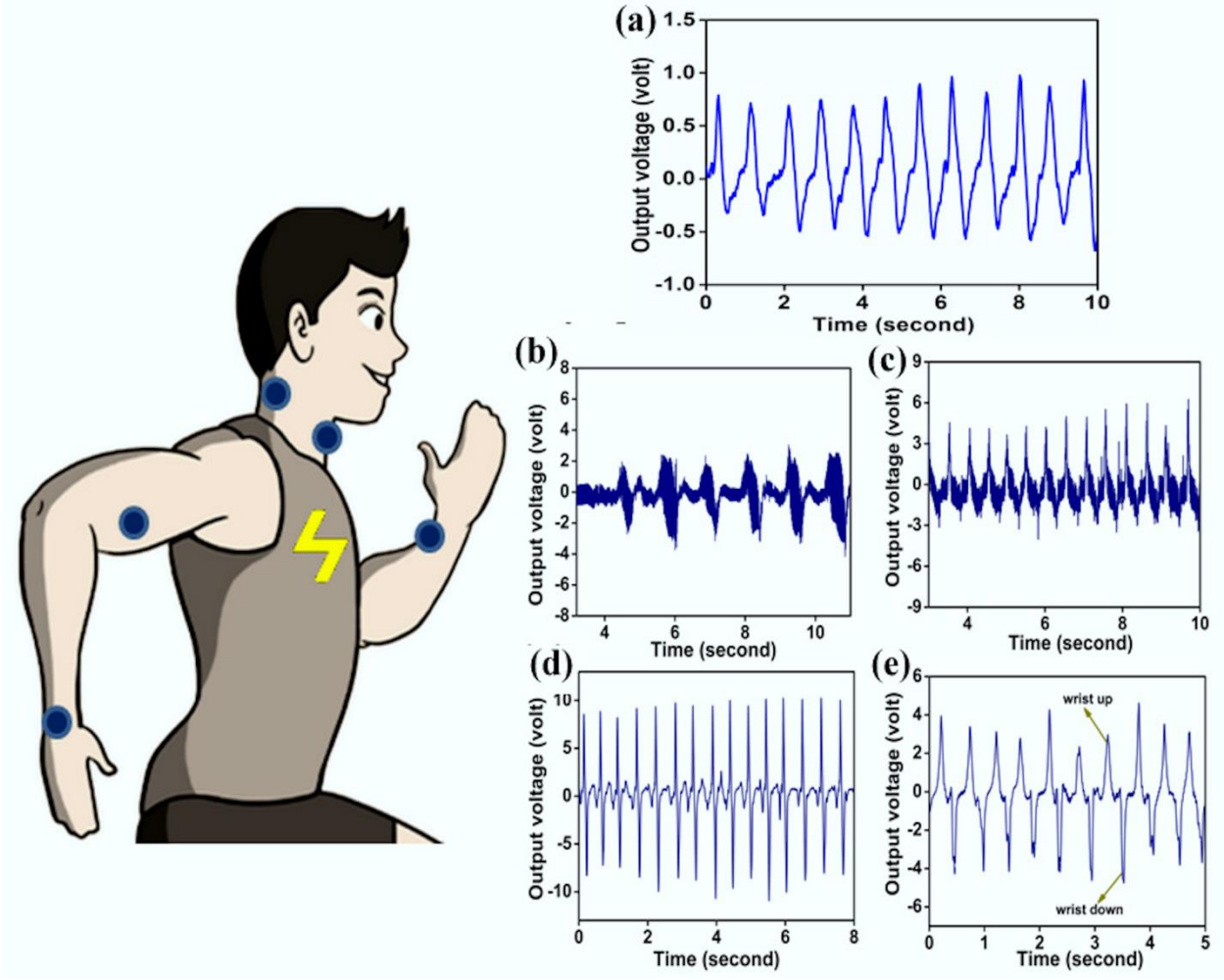


***Figure 5.10:*** *Generating the output voltage from (a) blood flow by fabricated EPMTNG device. Tracking the human physiological signals generated by the wearable device during (b) coughing, (c) neck movement, (d) flexion and extension of elbow and (e) wrist up down.*

Therefore, the fabricated device promptly detects the alternation of systolic and diastolic pressure and generates output signal. From the following figure, it has been clearly visualized that the EPMTNG device successfully detects 12 pulse beats in 10 seconds. That means, the total number of pulse beats detected by our device in 60 seconds will be 72. This value is well matched with the normal pulse rate of a healthy person in 60 seconds. Thus, the EPMTNG device may be useful in the clinical identification of hypertension and heart related health problems.[48] Moreover, the capability of EPMTNG device towards sensing thoracic pressure, generated by the vibration of vocal cord at the time of coughing, has been monitored.

The result exhibits that the fabricated device can detect every action of coughing (made up with opening burst, noisy airflow and closing of glottis) and generate output voltage in every action, which is near about 2V. The detection of coughing action depicts in the figure 5.10(b). Therefore, the EPMTNG device can be utilized to track the airflow process during coughing action and diagnosis the diseases related to the coughing like bronchitis, asthma etc.[49,50] Moreover, the neck movement of human body is also detected by the EPMTNG device. The device successfully detects continuous up and down motion of head and generates the output signal. During neck movement, the generated output voltage is near about 5V (figure 5.10(c)). The device was further affixed with synovial joints like elbow and wrist to monitor the generated physiological signal. In case of elbow movement, the EPMTNG device can promptly detect the flexion and extension of elbow and convert this generated stress into electrical signal, shown in the figure 5.10(d).[51] Additionally, the sensing ability of device towards the wrist movement has been investigated. The EPMTNG device is expanded and emits rising and falling voltage signal as the wrist bending continuously occurs from outward to inward (figure 5.10(e)). This response is generated due to the combine effect of wrist joint pressure and skin deformation.[52] Therefore, the fabricated device may be helpful in the area of sports like monitoring athlete movement and other sporting activity. All these results confirm the potential utilization of EPMTNG device towards the broad futuristic application in healthcare unit and self-evaluation of health.

### 5.4.9 Realistic approach of fabricated EPMTNG device

To investigate the energy conversion ability and practical utilization of EPMTNG device in our daily life, the LEDs illumination and capacitor charging have been performed. The LEDs are illuminated under periodic finger pressing condition by connecting them into series arrangement

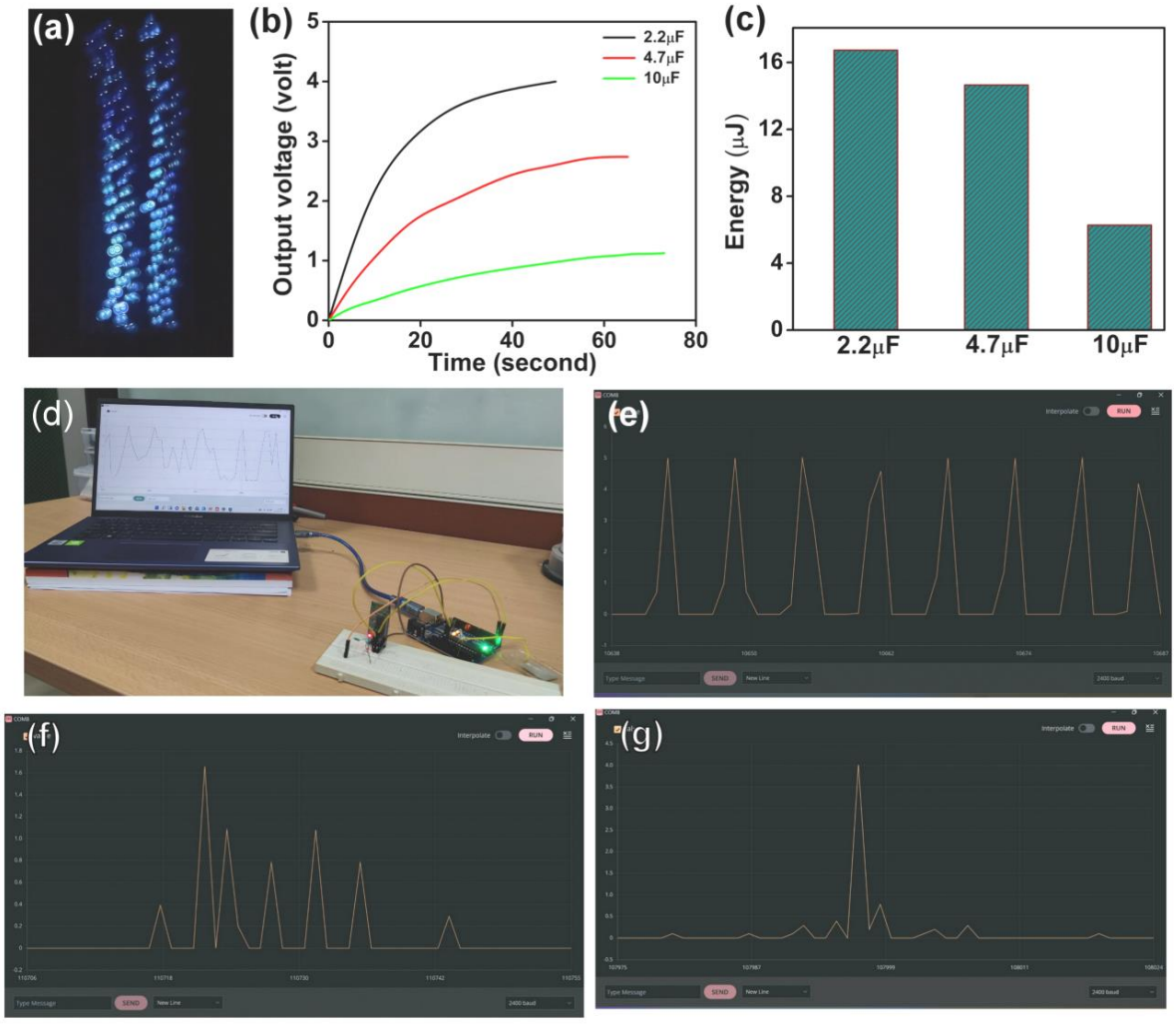


***Figure 5.11:*** *(a) Digital image of illuminating blue LEDs under periodic finger pressing. (b) Charging of capacitors by EPMTNG device. (c) Storing of energies into three capacitors. (d) Pictorial representation of wireless connection. Transmitting the generated signals wirelessly during (e) single finger tapping, (f) vocal cord vibration, (g) glottis movement.*

with the help of bridge rectifier. Figure 5.11(a) represents the pictorial image of lighting up of blue LEDs. This figure also depicts the capability of illuminating 140 no of blue LEDs of

EPMTNG device under periodic finger impartation. Furthermore, the fabricated device is wired with bridge rectifier to charge up the capacitors under continuous finger pressing. Figure 5.11(b) exhibits the capacitor charging curve which clearly indicates that EPMTNG device is capable of charging 2.2μF, 4.7μF and 10μF capacitor up to 3.9V, 2.5V and 1.1V within 75second.Additionally, the capacitor charging curves illustrates how the saturation voltage gradually reduces with the capacitance value increases. Moreover, the accumulation of energy inside the capacitors during the charging process has been calculated by using

$$\boldsymbol{E = \frac{1}{2}CV^2} \quad \text{..... (5.21)}$$

Where, E defines the accumulated energy, C describes the capacitance value and V defines the voltage on the capacitor. The total amount of energy gathered in the 2.2μF, 4.7μF and 10μF capacitors are 16.7μJ, 14.6μJ and 6.2μJ respectively, depicted in the figure 5.11(c). Thus, portable electronic appliances can be charged by using this EPMTNG device which has very good energy conversion and energy storage ability. Along with the capacitor charging and LEDs illuminating, wireless transmission of the generated signal from fabricated device has been visualized. First of all, the device is connected with the processing circuit to rectify the signal and then passed it to Arduino Uno, which is further transmitted the signal in laptop through Bluetooth connection. The digital snapshot of wireless connection is represented in the figure 5.11(d). The wireless transmission of signals, generated from single finger tapping, coughing and speaking conditions are also monitored. Figure 5.11(e) exhibits the transmitted signals wirelessly during single finger tapping. The vocal cord vibration and glottis movements are also monitored. Figure 5.11(f) depicts the generated signals from the vocal cord vibration of female person at the time of speaking some words. Each and every vibration is successfully displayed on the monitor of the laptop through waveforms. Moreover, the wireless transmission of signals, induced from glottis movement during single coughing has been visualized in the figure 5.11(g).

## *5.5 Conclusion*

The current work expresses the fabrication process and output performance of wearable and flexible EPMTNG device. The designing of the device is made of micro-patterned $BaTiO_3$@Ecoflex (EBTO) nanocomposite, 2D layered $MoTe_2$ incorporated PVDF nanofibers (PM5) and carbon tape. The idea behind the utilization of surface modification of EBTO nanocomposite is to create the surface area and improve the surface potential. The micro-

patterned structure creates the surface roughness on EBTO nanocomposite and assists in increment of effective contact area between human hand and EBTO layer. Therefore, more triboelectric charges are induced on the surface of EBTO layer and human hand. As a result, potential difference increases during triboelectrification process. This potential difference further helps in enhancing the output performance of EPMTNG device. Furthermore, a charge trapping layer (PM5 nanofiber) has been introduced between EBTO nanocomposite and carbon tape to prevent the charge recombination process and enhance the output performance of fabricated device. The idea behind the addition of charge trapping layer in the designing of EPMTNG has been established theoretically by using finite element simulation model where the value of theoretically calculated surface potential and output voltage in the presence of PM5 layer, are clearly indicated the validation of proposed concept. Under continuous finger pressing (12N) condition, the self-powered and flexible device generates the output voltage of 319V and current density of 9mA/$m^2$ respectively. Also, the device exhibits very good power density of 2.9W/$m^2$ at $10^7\Omega$ under the same axial pressure. Moreover, the effect of PM5 nanofibers in the electrical property of the device has been investigated by dielectric measurements. The incorporation of 2D $MoTe_2$ nanoparticles into PVDF matrix increases the β-crystalline phase and reinforces the polarization effect by inducing more charge carriers inside the polymer matrix. This β-phase nucleation and polarization reinforcement help in the improvement of the dielectric property of the device. In addition to this, the wearable EPMTNG device has high sensitivity (32.5V/kPa) at low pressure region of up to 0.5kPa. This high sensitivity value helps in the tracking of different human physiological signals and transmitting these signals wirelessly to laptop. The additional significance of the device is the detection of robotic gestures. Furthermore, the realistic utilization of fabricated device is monitored by illuminating LEDs and charging different capacitors. Thus, the self-powered and wearable EPMTNG device can be used in multidimensional applications including monitoring sporting activity, speech therapy, medical rehabilitation etc. Also, the device has the potential utilization in the field of robotic surgery and soft robotics applications. Therefore, the fabricated device may be useful in health care unit and human machine interfaces.

## References


1) Chen, C.; Chen, L.; Wu, Z.; Guo, H.; Yu, W.; Du, Z.; Wang, Z. L. 3D double-faced interlock fabric triboelectric nanogenerator for bio-motion energy harvesting and as self-powered stretching and 3D tactile sensors. Materials Today 2020, 32, 84-93.
2) Rana, S. S.; Halim, M. A.; Kabir, M. H. Design and implementation of a security improvement framework of Zigbee network for intelligent monitoring in IoT platform. Applied Sciences 2018, 8, 2305.
3) Zhang, D.; Yang, Z.; Li, P.; Pang, M.; Xue, Q. Flexible self-powered high-performance ammonia sensor based on Au-decorated $MoSe_2$ nanoflowers driven by single layer $MoS_2$-flake piezoelectric nanogenerator. Nano Energy 2019, 65, 103974.
4) Wang, D.; Zhang, D.; Guo, J.; Hu, Y.; Yang, Y.; Sun, T.; Zhang, H.; Liu, X. Multifunctional poly (vinyl alcohol)/Ag nanofibers-based triboelectric nanogenerator for self-powered MXene/tungsten oxide nanohybrid $NO_2$ gas sensor. Nano Energy 2021, 89, 106410.
5) Wu, H.; Huang, Y.; Xu, F.; Duan, Y.; Yin, Z. Energy harvesters for wearable and stretchable electronics: from flexibility to stretchability. Advanced materials 2016, 28, 9881-919.
6) Hua, Q.; Sun, J.; Liu, H.; Bao, R.; Yu, R.; Zhai, J.; Pan, C.; Wang, Z. L. Skin-inspired highly stretchable and conformable matrix networks for multifunctional sensing. Nature communications 2018, 9, 244.
7) Zhang, C.; Liu, S.; Huang, X.; Guo, W.; Li, Y.; Wu, H. A stretchable dual-mode sensor array for multifunctional robotic electronic skin. Nano Energy 2019, 62, 164-70.
8) Bu, T.; Xiao, T.; Yang, Z.; Liu, G.; Fu, X.; Nie, J.; Guo, T.; Pang, Y.; Zhao, J.; Xi, F.; Zhang, C. Stretchable triboelectric–photonic smart skin for tactile and gesture sensing. Advanced Materials 2018, 30, 1800066.
9) Rahman, M. T.; Rana, S. S.; Salauddin, M.; Zahed, M. A.; Lee, S.; Yoon, E. S.; Park, J. Y. Silicone-incorporated nanoporous cobalt oxide and MXene nanocomposite-coated stretchable fabric for wearable triboelectric nanogenerator and self-powered sensing applications. Nano Energy 2022, 100, 107454.

10) Xie, Y.; Ma, Q.; Yue, B.; Chen, X.; Jin, Y.; Qi, H.; Hu, Y.; Yu, W.; Dong, X.; Jiang, H. Triboelectric nanogenerator based on flexible Janus nanofiber membrane with simultaneous high charge generation and charge capturing abilities. Chemical Engineering Journal 2023, 452, 139393.
11) Jiang, H.; Lei, H.; Wen, Z.; Shi, J.; Bao, D.; Chen, C.; Jiang, J.; Guan, Q.; Sun, X.; Lee, S. T. Charge-trapping-blocking layer for enhanced triboelectric nanogenerators. Nano Energy 2020, 75, 105011.
12) Chai, B.; Shi, K.; Zou, H.; Jiang, P.; Wu, Z.; Huang, X. Conductive interlayer modulated ferroelectric nanocomposites for high performance triboelectric nanogenerator. Nano Energy 2022, 91, 106668.
13) Rajagopalan, P.; Huang, S.; Shi, L.; Kuang, H.; Jin, H.; Dong, S.; Shi, W.; Wang, X.; Luo, J. Novel insights from the ultra-thin film, strain-modulated dynamic triboelectric characterizations. Nano Energy 2021, 80,105560.
14) Li, Z.; Wang, X.; Hu, Y.; Li, L.; Wang, C. Triboelectric properties of BaTiO3/polyimide nanocomposite film. Applied Surface Science 2022, 572, 151391.
15) Cui, N.; Gu, L.; Lei, Y.; Liu, J.; Qin, Y.; Ma, X.; Hao, Y.; Wang, Z. L. Dynamic behavior of the triboelectric charges and structural optimization of the friction layer for a triboelectric nanogenerator. ACS nano 2016, 10, 6131-8.
16) Xie, X.; Chen, X.; Zhao, C.; Liu, Y.; Sun, X.; Zhao, C.; Wen, Z. Intermediate layer for enhanced triboelectric nanogenerator. Nano Energy 2021, 79, 105439.
17) Kim, D. W.; Lee, J. H.; You, I.; Kim, J. K.; Jeong, U. Adding a stretchable deep-trap interlayer for high-performance stretchable triboelectric nanogenerators. Nano Energy. 2018, 50, 192-200.
18) Shrestha, K.; Sharma, S.; Pradhan, G. B.; Bhatta, T.; Maharjan, P.; Rana, S. S.; Lee, S.; Seonu, S.; Shin, Y.; Park, J. Y. A Siloxene/Ecoflex Nanocomposite-Based Triboelectric Nanogenerator with Enhanced Charge Retention by $MoS_2$/LIG for Self-Powered Touchless Sensor Applications. Advanced Functional Materials 2022, 32, 2113005.
19) Lee, J. W.; Jung, S.; Jo, J.; Han, G. H.; Lee, D. M.; Oh, J.; Hwang, H. J.; Choi, D.; Kim, S. W.; Lee, J. H.; Yang, C. Sustainable highly charged $C_{60}$-functionalized polyimide in a non-contact mode triboelectric nanogenerator. Energy & Environmental Science 2021, 14, 1004-15.

20) Rana, S. S.; Rahman, M. T.; Sharma, S.; Salauddin, M.; Yoon, S. H.; Park, C.; Maharjan, P.; Bhatta, T.; Park, J. Y. Cation functionalized nylon composite nanofibrous mat as a highly positive friction layer for robust, high output triboelectric nanogenerators and self-powered sensors. Nano Energy 2021, 88, 106300.

21) Li, Y.; Zheng, C.; Liu, S.; Huang, L.; Fang, T.; Li, J. X.; Xu, F.; Li, F. Smart glove integrated with tunable MWNTs/PDMS fibers made of a one-step extrusion method for finger dexterity, gesture, and temperature recognition. ACS applied materials & interfaces 2020, 12, 23764-73.

22) Kim, W. G.; Kim, D. W.; Tcho, I. W.; Kim, J. K.; Kim, M. S.; Choi, Y. K. Triboelectric nanogenerator: Structure, mechanism, and applications. Acs Nano 2021, 15, 258-87.

23) Qin, Z.; Chen, X.; Yin, Y.; Ma, G.; Jia, Y.; Deng, J.; Pan, K. Flexible januselectrospun nanofiber films for wearable triboelectric nanogenerator. Advanced Materials Technologies 2020, 5, 1900859.

24) Tayyab, M.; Wang, J.; Wang, J.; Maksutoglu, M.; Yu, H.; Sun, G.; Yildiz, F.; Eginligil, M.; Huang, W. Enhanced output in polyvinylidene fluoride nanofibers based triboelectric nanogenerator by using printer ink as nano-fillers. Nano Energy 2020, 77, 105178.

25) Jiang, H.; Lei, H.; Wen, Z.; Shi, J.; Bao, D.; Chen, C.; Jiang, J.; Guan, Q.; Sun, X.; Lee, S. T. Charge-trapping-blocking layer for enhanced triboelectric nanogenerators. Nano Energy 2020, 75, 105011.

26) Kim, D. W.; Lee, J. H.; You, I.; Kim, J. K.; Jeong, U. Adding a stretchable deep-trap interlayer for high-performance stretchable triboelectric nanogenerators. Nano Energy 2018, 50, 192-200.

27) Cui, J.; Li, P.; Zhou, J.; He, W. Y.; Huang, X.; Yi, J.; Fan, J.; Ji, Z.; Jing, X.; Qu, F.; Cheng, Z. G. Transport evidence of asymmetric spin–orbit coupling in few-layer superconducting 1T d-$MoTe_2$. Nature communications 2019, 10, 2044.

28) Hao, S.; Zeng, J.; Xu, T.; Cong, X.; Wang, C.; Wu, C.; Wang, Y.; Liu, X.; Cao, T.; Su, G.; Jia, L. Low-temperature eutectic synthesis of $PtTe_2$ with Weak antilocalization and controlled layer thinning. Advanced Functional Materials 2018, 28, 1803746.

29) Lee, S.; Jang, J.; Kim, S. I.; Jung, S. G.; Kim, J.; Cho, S.; Kim, S. W.; Rhee, J. Y.; Park, K. S.; Park, T. Origin of extremely large magnetoresistance in the candidate type-II Weyl semimetal $MoTe_{2-x}$. Scientific reports 2018, 8, 13937.

30) Bhat, K. S.; Nagaraja, H. S. Performance evaluation of molybdenum dichalcogenide ($MoX_2$; X= S, Se, Te) nanostructures for hydrogen evolution reaction. International Journal of Hydrogen Energy 2019, 44, 17878-86.

31) Yang, X.; Han, J.; Yu, J.; Chen, Y.; Zhang, H.; Ding, M.; Jia, C.; Sun, J.; Sun, Q.; Wang, Z. L. Versatile triboiontronic transistor via proton conductor. ACS nano 2020, 14, 8668-77.

32) Lan, L.; Yao, Y.; Ping, J.; Ying, Y. Ultrathin transition-metal dichalcogenide nanosheet-based colorimetric sensor for sensitive and label-free detection of DNA. Sensors and Actuators B: Chemical 2019, 290, 565-72.

33) Gao, G.; Yu, J.; Yang, X.; Pang, Y.; Zhao, J.; Pan, C.; Sun, Q.; Wang, Z. L. Triboiontronic transistor of $MoS_2$. Advanced Materials 2019, 31, 1806905.

34) Liu, Y.; Ping, J.; Ying, Y. Recent progress in 2D-nanomaterial-based triboelectric nanogenerators. Advanced Functional Materials 2021, 31, 2009994.

35) Pradhan, N. R.; Rhodes, D.; Feng, S.; Xin, Y.; Memaran, S.; Moon, B. H.; Terrones, H.; Terrones, M.; Balicas, L. Field-effect transistors based on few-layered α-$MoTe_2$. ACS nano 2014, 8, 5911-20.

36) Bera, A.; Kundu, M.; Das, B.; Kalimuddin, S.; Bera, S.; Roy, D. S.; Pradhan, S. K.; Naskar, S.; De, S. K.; Das, B.; Mondal, M. Emergence of electric field-induced conducting states in single-crystalline $MoTe_2$ nanoflakes and its application in memristive devices. Applied Surface Science 2023, 610, 155409.

37) Keum, D. H.; Cho, S.; Kim, J. H.; Choe, D. H.; Sung, H. J.; Kan, M.; Kang, H.; Hwang, J. Y.; Kim, S. W.; Yang, H.; Chang, K. J. Bandgap opening in few-layered monoclinic $MoTe_2$. Nature Physics 2015, 11, 482-6.

38) Ruppert, C.; Aslan, B.; Heinz, T. F. Optical properties and band gap of single-and few-layer $MoTe_2$ crystals. Nano letters 2014, 14, 6231-6.

39) Duerloo, K. A.; Li, Y.; Reed, E. J. Structural phase transitions in two-dimensional Mo-and W-dichalcogenide monolayers. Nature communications 2014, 5, 4214.

40) Huang, J. H.; Deng, K. Y.; Liu, P. S.; Wu, C. T.; Chou, C. T.; Chang, W. H.; Lee, Y. J.; Hou, T. H. Large-area 2D layered $MoTe_2$ by physical vapor deposition and solid-phase crystallization in a tellurium-free atmosphere. Advanced Materials Interfaces 2017, 4, 1700157.

41) Seol, D.; Kim, S.; Jang, W. S.; Jin, Y.; Kang, S.; Kim, S.; Won, D.; Lee, C.; Kim, Y. M.; Lee, J.; Yang, H. Selective patterning of out-of-plane piezoelectricity in $MoTe_2$ via focused ion beam. Nano Energy 2021, 79, 105451.

42) Wang, L.; Liu, S.; Feng, X.; Zhang, C.; Zhu, L.; Zhai, J.; Qin, Y.; Wang, Z. L. Flexoelectronics of centrosymmetric semiconductors. Nature Nanotechnology 2020, 15, 661-7.

43) Chen, Y.; Tian, Z.; Wang, X.; Ran, N.; Wang, C.; Cui, A.; Lu, H.; Zhang, M.; Xue, Z.; Mei, Y.; Chu, P. K. 2D Transition Metal Dichalcogenide with Increased Entropy for Piezoelectric Electronics. Advanced Materials 2022, 34, 2201630.

44) Zhang, L.; Shan, X.; Bass, P.; Tong, Y.; Rolin, T. D.; Hill, C. W.; Brewer, J. C.; Tucker, D. S.; Cheng, Z. Y. Process and microstructure to achieve ultra-high dielectric constant in ceramic-polymer composites. Scientific reports 2016, 6, 35763.

45) (a) Roy, S.;Bardhan, S.; Pal, K.; Ghosh, S.; Mandal, P.; Das, S.; Das, S. Crystallinity mediated variation in optical and electrical properties of hydrothermally synthesized boehmite (γ-AlOOH) nanoparticles. Journal of Alloys and Compounds 2018, 763, 749-758.

46) (b) Das, N.; Sarkar, D.; Saikh, M. M.; Biswas, P.; Das, S.; Hoque, N. A.; Ray, P. P. Piezoelectric activity assessment of size-dependent naturally acquired mud volcano clay nanoparticles assisted highly pressure sensitive nanogenerator for green mechanical energy harvesting and body motion sensing. Nano Energy 2022, 102, 107628.

47) Das, S.; Das, S.; Sutradhar, S. Effect of $Gd^{3+}$ and $Al^{3+}$ on optical and dielectricproperties of ZnO nanoparticle prepared by two step hydrothermal method. Ceramics International 2017, 43, 6932e6941.

48) Sarkar, D.; Das, N.; Saikh, M. M.; Biswas, P.; Roy, S.; Paul, S.; Hoque, N. A.; Basu, R.; Das, S. High β-crystallinity comprising nitrogenous carbon dot/PVDF nanocomposite decorated self-powered and flexible piezoelectric nanogenerator for harvesting human movement mediated energy and sensing weights. Ceramics International 2023, 49, 5466-5478.

49) Park, D. Y.; Joe, D. J.; Kim, D. H.; Park, H.; Han, J. H.; Jeong, C. K.; Park, H.; Park, J. G.; Joung, B.; Lee, K. J. Self-Powered Real-Time Arterial Pulse Monitoring Using Ultrathin Epidermal Piezoelectric Sensors. Adv. Mater. 2017, 29, 1702308.

50) Roy, K.; Ghosh, S. K.; Sultana, A.; Garain, S.; Xie, M.; Bowen, C. R.; Henkel, K.; Schmeiβer, D.; Mandal D. A self-powered wearable pressure sensor and pyroelectric breathing sensor based on GO interfaced PVDF nanofibers. ACS Applied Nano Materials 2019, 2, 2013-25.

51) Nicholls, B.; Ang, C. S.; Efstratiou, C.; Lee, Y.; Yeo, W.-H. In Swallowing Detection for Game Control: Using Skin-Like Electronics to Support People with Dysphagia., 2017 IEEE International Conference on Pervasive Computing and Communications Workshops (PerCom Workshops), IEEE, Kona, Hawaii, U.S.A., March 13−17, 2017,

52) Tee, B. C.; Wang, C.; Allen, R.; Bao, Z. An Electrically and Mechanically Self-Healing Composite with Pressure- and Flexion-Sensitive Properties for Electronic Skin Applications. Nature Nanotechnology 2012, 7, 825−832.

53) He, M.; Du, W.; Feng, Y.; Li, S.; Wang, W.; Zhang, X.; Yu, A.; Wan, L.; Zhai, J. Flexible and stretchable triboelectric nanogenerator fabric for biomechanical energy harvesting and self-powered dual-mode human motion monitoring. Nano Energy 2021, 86, 106058.

54) Ghosh, S. K.; Kim, J.; Kim, M. P.; Na, S.; Cho, J.; Kim, J. J.; Ko, H. Ferroelectricity-Coupled 2D-MXene-Based Hierarchically Designed High-Performance Stretchable Triboelectric Nanogenerator. ACS nano 2022, 16, 11415-27.

55) Jin, T.; Sun, Z.; Li, L.; Zhang, Q.; Zhu, M.; Zhang, Z.; Yuan, G.; Chen, T.; Tian, Y.; Hou, X.; Lee, C. Triboelectric nanogenerator sensors for soft robotics aiming at digital twin applications. Nature communications 2020, 11, 5381.

56) Shen, X.; Han, W.; Jiang, Y.; Ding, Q.; Li, X.; Zhao, X.; Li, Z. Punching pores on cellulose fiber paper as the spacer of triboelectric nanogenerator for monitoring human motion. Energy Reports 2020, 6, 2851-60.

57) Yi, F.; Lin, L.; Niu, S.; Yang, P. K.; Wang, Z.; Chen, J.; Zhou, Y.; Zi, Y.; Wang, J.; Liao, Q.; Zhang, Y. Stretchable-rubber-based triboelectric nanogenerator and its application as self-powered body motion sensors. Advanced Functional Materials 2015, 25, 3688-96.

58) Park, H. W.; Huynh, N. D.; Kim, W.; Lee, C.; Nam, Y.; Lee, S.; Chung, K. B.; Choi, D. Electron blocking layer-based interfacial design for highly-enhanced triboelectric nanogenerators. Nano Energy 2018, 50, 9-15.

59) Paria, S.; Bera, R.; Karan, S. K.; Maitra, A.; Das, A. K.; Si, S. K.; Halder, L.; Bera, A.; Khatua, B. B. Insight into cigarette wrapper and electroactive polymer based efficient TENG as biomechanical energy harvester for smart electronic applications. ACS Applied Energy Materials. 2018, 1, 4963-75.

60) Hong, D.; Choi, Y. M.; Jeong, J. Test bed for contact-mode triboelectric nanogenerator. Review of Scientific Instruments 2018, 89.

# Elevating the performance of nanoporous Bismuth Selenide incorporated arch-shaped triboelectric nanogenerator by implementing piezo-tribo coupling effect: Harvesting biomechanical energy and low scale energy sensing applications

*Chapter 6*

## 6.1 Introduction

With the fastest expansion of recent science and technology, Internet of things (IoTs) makes human life easier and enjoyable.[1] As a result, the usage of conventional energy storage tools like sodium ion batteries, rigid batteries, lithium-ion batteries, supercapacitors etc. which have immense dimensions and regular charging requirements, seems to be limited.[2-5] Therefore, alternative energy sources and equipments which help us to charge up the sensors and devices have gained immense attentions among the researches in the last few years.[6-7] Triboelectric nanogenerator (TENG) is chosen as the suitable candidate of alternative energy sources which can power up the previously mentioned devices easily due to its conversion ability of naturally available mechanical energies like water wave energy, wind energy, biomechanical energy, vibrational energy, low scale mechanical energy and rotational energy into electrical energies.[8-10, 14] The triboelectric phenomenon was first proposed by Wang et al. in 2012 and published a standard list of triboelectric materials to give us the idea about their effective pairing. Moreover, the working principle of TENG is based on electrostatic induction and tribo-electrification.[10] Generally, TENG has four working modes. Among them, contact-separation (CS) mode is most preferable one due to its charge generating, simple fabrication process and high output performance.[10] Therefore, selection of triboelectric materials plays an important role in improving the charge generation and fabrication of TENG. To design the layered structure and improve the charge generation of TENG device, polymers are utilized due to their high charge affinity, high dipole moment, flexibility and durability.[11-13] Till now, the reported negative triboelectric polymers are poly(tetrafluoroethylene) (PTFE), poly(vinyldene fluoride) (PVDF), poly(dimethyl siloxane) (PDMS), polyimide (PI), poly(vinyl chloride) (PVC), poly propylene (PP) etc. and reported positive polymers are thermoplastic polyurethane (TPU), poly(vinyl alcohol) (PVA), poly(3-hydroxybutyrate-co-3-hydroxyvalerate)(PHBV) etc.[10, 15] In this present work, PDMS and PVA have been used as tribo-negative and tribo-positive material.

Moreover, there are so many advantages of using TENG such as light weight, flexibility, durability, simple fabrication process, cost effectiveness and robustness.[11, 12, 29] Recently, few pioneers works have been done by utilizing the effect of TENG. For example, Lin et al. developed an active bacterial anti-adhesion strategy to remove the bacteria from the surfaces of materials which was driven by TENG.[16] Jia et al. proposed the electron transfer mechanism

among the metal and $SiO_2$ composites by using first principal study. This idea is very helpful in selection of dielectric layer for TENG.[17] Moreover, Zhang et al. proposed a new strategy to combat the environmental pollution by using cellulose instead of traditional polymers and utilized it to design nanogenerators.[18] Additionally, Ghafari et al. developed PVDF nanogenerator for harvesting low range frequencies and converting them into electricity.[19] To improve the performance of TENG and keep the properties like flexibility, durability etc. intact, researchers have given the efforts to hybridize the triboelectric effect with other effect.[22] For example, Han et al. fabricated triboelectric-electromagnetic nanogenerator,[20] Wei et al. designed an energy harvester using the combine effect of Curie effect, triboelectric effect and electrostatic induction effect,[21] Jirayupat et al. fabricated a hybrid nanogenerator by using piezo-tribo combine effect.[22] Although several work has been done on hybrid nanogenerator but very few work has been reported on nanocomposite based piezo-tribo coupling effect. Although, the working mechanisms of triboelectricity and piezoelectricity are different, their electrical stimuli generation process never overlaps with each other.[30(a)] Thus, combining the piezoelectric effect with triboelectricity into a single device not only enhances electron transfer but also generates extra charges, which results in better output. Moreover, the alignment of dipoles of piezoelectric materials within nanocomposite film plays an important role to obtain better output performance by generating maximum piezopotential.[22] In this study, piezoelectric layer based TENG has been designed with the help of nanoporous $Bi_2Se_3$ and PVDF polymer based nanocomposite thin film, PDMS thin layer and PVA thin film. To improve the output performance of the fabricated TENG, doping technique has been used. PVDF is a semi-crystalline, electro-active, fluro polymer. It consists of five crystalline phases such as α, β, γ, δ, ε. Among them β phase is more crystalline and polar due to its all-trans conformation and also exhibits very good piezoelectric and ferroelectric properties.[30(b)] Owing to these properties, PVDF has broaden its utilization in various fields of application. For example, Cheng et al. fabricated porous PVDF-Ni/PE-CNTs composite foam through melt extrusion and batch foaming methods which exhibited very good hydrophobic, EMI shielding and optical-electrical-thermal properties.[23] Gao et al. modified the surface of CNTs through silanization and fluorosilanization combine methods and utilized the modified CNTs to prepare hydrophobic electrospun membrane by mixing with PVDF matrix. This membrane was further utilized in direct contact memebrane distillation applications.[24] Furthermore, Wu et al. improved the thermal conductivity and dielectric properties of PVDF

matrix by embedding BN-$SiO_2$@MWCNT into PVDF and proposed the utilization of the nanocomposite in the field of microelectronic packaging.[25] Sharafkhani et al. fabricated a high performance piezoelectric sensor by using well-orientated CNTs contained PVDF nanofibers.[26] Moreover, Li et al. developed piezoelectric sensor with the help of PVDF-HFP/ZnO nanofibers to track sporting workout of players and monitor their activities wirelessly.[27] Liu et al. fabricated PVDF/PAN membrane with 83.4% β content through electrospinning method. This electrospun membrane was further utilized as piezoelectric energy harvester and sodium-ion battery separator.[28] Beside this, several approaches were taken to synthesize the dipole aligned β phase by using annealing and post stretching or doping with fillers. Here, $Bi_2Se_3$ nanograins have been reinforced into PVDF matrix to enhance the percentage of crystallinity of β phase because of the dipole-dipole interaction between the hydrogen atom of the PVDF matrix and electronegative atom of the co-polymer. The induced β phase gives high polarizability, electro-active and dielectric properties which enhances the output performance of TENG.[31]

Topological insulators (TI) are a new class of quantum matter, consisting of bulk gap and reversible time symmetry protected relativistic Dirac fermions on the surface. In the bulk states, these materials are electrically insulating but can carry out the electricity in the surface states because of the topologically covered electronic edge. Thus, TIs are used directly in thermoelectric devices, superconductors, photoelectronic sensors etc.[32-34] Compared to other TIs, bismuth selenide ($Bi_2Se_3$) has gained huge attention among the researchers owing to has the topological surface states. $Bi_2Se_3$ has sole characteristics such as high surface mobility, small band gap near about 0.35eV, excellent electrical conductivity and photoconductivity.[35-39] The small band gap property helps $Bi_2Se_3$ in light absorption over the wide wavelength range. The sturdy topological structures helps bismuth selenide to maintain the stability in ambient or unkind environment.[40] Inside the crystal structure of this TI, five covalent bonded atomic planes Se–Bi–Se–Bi–Se make the planar quintuple layers and these weakly bonded quintuple layers are piled along c axis through Van der Waals interactions. Owing to this specific structure and topological surface states, $Bi_2Se_3$ makes itself a potential candidate in the area of electrochemical energy storage system and also borrows the distinctive physical properties and electronic structure.[41-44] For these reasons, $Bi_2Se_3$ has been selected as primary doping element and also utilized in device fabrication process.

In this current work, arch shaped and self-powered piezoelectric thin film with bismuth selenide based triboelectric nanogenerator, named as PBTNG has been designed to harness different types of mechanical energies like heel and feet pressing, hand impartation, single finger tapping, pulse vibration, keypad striking etc. and convert them into electrical energy. The $Bi_2Se_3$ nanoparticles have been chosen as doping material owing to the topological surface, distinctive physical properties, and electronic structure. The piezoelectric thin film based PBTNG device exhibits very good output voltage ($V_{OC}$) of 171.8 V with maximum power density of 2.03 $Wm^{-2}$ under continuous finger impartation. Moreover, the PBTNG device has the capability to illuminate LEDs through heel pressing and periodic finger impartation. Beside this, the device is sensible enough to catch small scale mechanical energies and convert them into electrical energy easily. These valuable investigations are indicating that PBTNG is a green and wearable energy harvester which can be used to power up portable electronic devices used in daily life.

## *6.2 Experimental section*

### *6.2.1 Synthesis procedure of $Bi_2Se_3$ nanoparticle*

0.03g Selenium powder was dissolved in 60mL Ethylene glycol and placed the solution on a magnetic stirrer for few minutes. Thereafter, 0.03g bismuth nitrate salt was added with the solution and kept on stirrer until it dissolved totally. After that the final solution was transferred into a 80mL hydrothermal setup and kept it inside a oven at $160^0$C for 10h.In the next step, the product was washed with distilled water and acetone for several times through centrifugation at 8000 rpm for 15 minutes. After completing the centrifugation process, the final product was accumulated and kept in a vacuum oven at $60^0$C for 12h.

### *6.2.2 Synthesis of PDMS and PVA thin films*

At first, 2 g of polydimethylsiloxane (PDMS) (Sylgard 184, Dow Corning, ratio of 1:10) was taken in a rectangular mold and mixed the solution very well with binder. Thereafter, the mixture was kept in a vacuum desiccator for 15 min to make the mixture bubble free. After completing the vacuum process, the bubble free mixture was placed in a hot air oven at $60^o$C for 15 min to obtain the thin film. Finally, we get the PDMS thin film of thickness 0.61mm.

The thin film of PVA was synthesized by using simple solution casting method. The required amount of PVA (20% of solvent) was mixed with distilled water and kept the solution on magnetic stirrer at 60$^{o}$C for 12 h to get homogeneous mixture. Thereafter, the solution was casted in a clean Petri dish and placed in a hot air oven at 80$^{o}$C to obtain the PVA thin film of thickness 51µm.

### *6.2.3 Fabrication of $Bi_2Se_3$ assisted PVDF (PBi) piezoelectric nanocomposite*

The simple solution technique was used to fabricate the $Bi_2Se_3$ doped PVDF nanocomposite (PBi) thin films. Firstly, 250 mg of PVDF (Sigma-Aldrich, Germany;Mw: 180 000 GPC; Mn:71 000) was mixed with 5mL of dimethylsulfoxide (DMSO) (Merck) and placed them on magnetic stirrer at 60$^{o}$C to obtain the clear solution. After obtaining the clear solution, $Bi_2Se_3$ (1, 2.5 and 5 mass %)were added with them and kept the total solutions on the magnetic stirrer at 60$^{o}$C for 14 h. Thereafter, the mixtures were casted in dust free and clean Petri dishes and placed in a vacuum oven to dry at 80$^{o}$C. After completing the drying process, we finally get the nanocomposite thin films which are named as PBi1, PBi2.5, PBi5 according to the 1, 2.5 and 5 mass % of $Bi_2Se_3$. Figure 6.1(a) and 6.1(b) represent the fabrication process of PBi thin film schematically and digital picture of fabricated thin film.

### *6.2.4 Designing of piezoelectric layer based triboelectric nanognerator (PBTNG)*

The fabricated PBTNG device consists of three layers i.e. charge generating layer, piezoelectric layer and charge collecting layer. Herein, PVA and PDMS thin films has been used as charge generating layers, PBi thin film as piezoelectric layer and aluminium (Al) electrodes ( thickness 41 µm) as charge collecting layer. The fabrication procedure of PBi thin film, PVA film and PDMS film has been elaborated in the supporting information file. PBTNG consists of two parts i.e. positive and negative part. The positive part consists of PVA film and Al electrode, and the negative part consists of PDMS film, Al electrode and PBi thin film. Thereafter, the positive part (PVA film and electrode attached together) was affixed with double tape to the upper part of the arch-shaped protective foam cover. Then, the negative part (PDMS layer, electrode and PBi filmattached together) was affixed to the lower part of the protective cover, maintaining ample air gap in the middle of the two parts. Two copper wires were joined with the electrodes to

investigate the output performance of fabricated PBTNG device. Figure 6.1(c) exhibits the design of fabricated PBTNG device graphically.

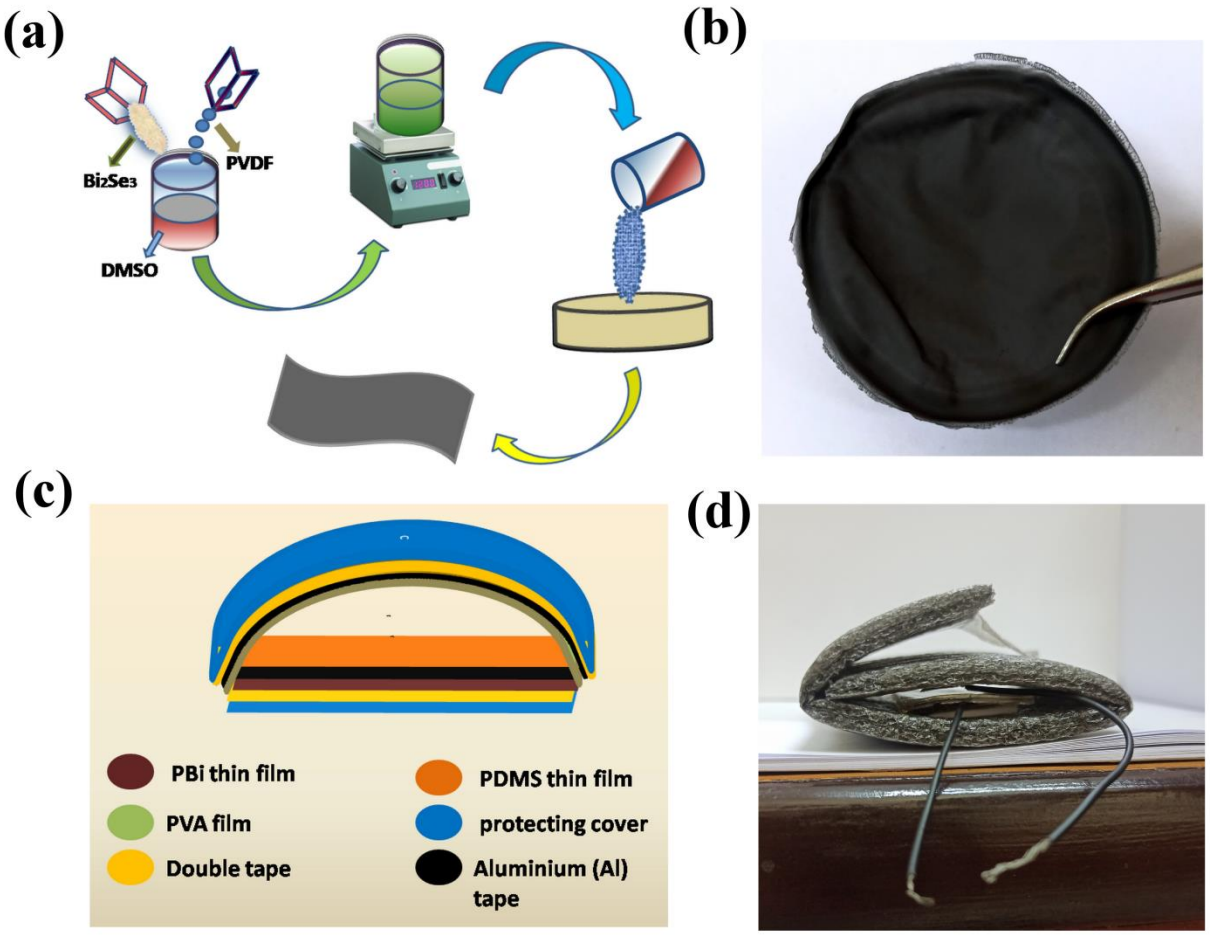


***Figure 6.1:*** *(a) Schematic representation of the fabrication process of PBi nanocomposite. (b) Snapshot of the piezoelectric thin (PBi) film. (c) Graphical illustration of designed PBTNG device. (e) Digital photograph of arch like shape of PBTNG.*

## 6.3 Characterization techniques

The crystallographic structures and surface morphologies of the synthesized nanopartices and fabricated thin films are investigated by X-ray diffraction (XRD; Model-D8, Bruker AXS Inc., Madison, WI), field emission scanning electron microscopy (FESEM; INSPECT F50) and transmission electron microscopy (TEM; JEOL JEM F200). The elemental mapping of thin film has been performed by using Zeiss Gemini SEM 500. The elemental analysis of PBi nanocomposite was done by X-ray photoelectron spectroscopy (XPS) (Model: PHI5000VERSAPROBE III, Make ULVAC-PHI, Inc., Japan).The different phase performance and thermal behaviors of thin films are examined by Fourier transform infrared (FTIR) spectroscopy (FTIR-8400S; Shimadzu) and thermal gravimetric analysis (TGA; TGA/SDTA851e, Mettler Toledo AG). The mechanical properties of thin film have been measured by Universal Testing Machine (Tinius Olsen model: H50KS, UK). The electrical properties of the thin film are investigated by IM 3536 LCR Meter. The surface properties of synthesized $Bi_2Se_3$ nanoparticles have been examined using Automated Gas Sorption Analyzer, Autosorb iQ2, Quantachrome Instruments.

## 6.4 Results and discussion

### 6.4.1 Experimental analysis of nanoporous $Bi_2Se_3$

#### 6.4.1.1 Structural and morphological analysis of $Bi_2Se_3$

The crystalline peaks and surface morphology of the nanoparticle have been investigated by XRD analysis and FESEM micrographs. The crystalline peaks at 25.02$^o$ (101), 29.23$^o$ (015), 40.22$^o$ (101), 43.52$^o$ (110), 47.72$^o$ (116) and 53.35$^o$ (205) confirm the formation of $Bi_2Se_3$ nanosized (33 nm) particles, shown in the figure 6.2(a). These identical peaks match with the JCPDS file no 33-0214. Furthermore, the refinement of XRD peaks of $Bi_2Se_3$ was performed by using Rietveld-based software package MAUD v2.8 to investigate the micro-structural and crystallographic parameters. Initially, standard Caglioti PV functions were deployed to refine the detector and diffractometer. During this cycle, instrumental broadening was also rectified. The experimental diffraction peaks were refined by employing a regular crystallographic information

file (.cif) of bismuth selenide (COD file no. 1530736). To achieve better fitting outcomes, a number of micro-structural parameters including crystal size, unit cell dimension were optimized. The texture analyses were also performed to obtain adequate fitting results. The low value of the global reliability parameters such as $R_{WP}$ and $R_P$ are suggesting the consistency of refinements. The refinement of parameters was performed up to fifteen cycles and corresponding results are depicted in the Table 6.1.Figure 6.2(a) shows the experimental and refined X-ray crystalline peaks of $Bi_2Se_3$ nanoparticles. Furthermore, the computed.cif files of $Bi_2Se_3$ have been visualized with the help of VESTA 3.5.7 software which confirms the rhombohedral structure of bismuth selenide, shown in the figure 6.2(c). The rhombohedral structure consists of three quintuple layers (QL) which are weakly bound to each other through Van der Waals force. Each QL have five atomic planes along with the atomic order of $Se_1$-Bi-$Se_2$-Bi-$Se_1$ where, $Se_1$ & $Se_2$ denotes the nonequivalent layers.[48] Moreover, the polyhedral species has been observed with bond length and bond angle, depicted at figure 6.2(d). The bond length between Bi-$Se_1$ and Bi-$Se_2$ is 2.97 Å and 2.73Å and the dihedral angle between $Se_1$-Bi-$Se_2$ is 86.26°.

***Table 6.1:*** *Refinement parameters of $Bi_2Se_3$ nanoparticle*

| *Parameters* | *$Bi_2Se_3$* |
|---|---|
| *a (Å)* | *9.8600* |
| *b(Å)* | *9.86578* |
| *c(Å)* | *9.86578* |
| *α (°)* | *24.2300* |
| *β(°)* | *24.2340* |
| *γ (°)* | *24.2340* |
| *V (Å$^3$)* | *142.1871* |
| *$\chi^2$* | *1.8659* |
| *$R_p$ (%)* | *8.7887* |
| *$R_{wp}$ (%)* | *12.0082* |

The surface morphology of nanoparticle has been examined by FESEM image (figure 6.2(b)). The FESEM image describes that the synthesized nanoparticles are porous and some gaps are seen to restrict the formation of uniform structure. This is the reason we get tube or grain-like structure of the nanoparticle.

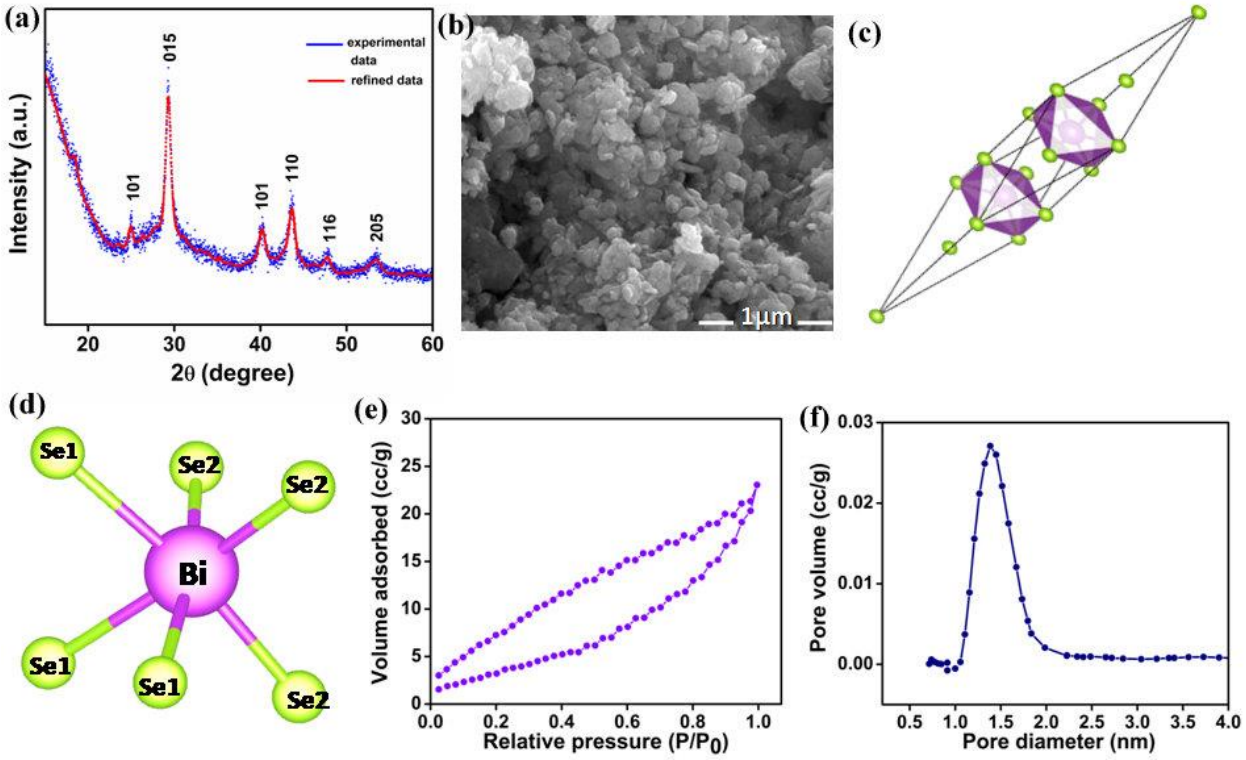


***Figure 6.2:*** *(a) Crystalline peaks and (b) FESEM image of synthesized $Bi_2Se_3$ nanoparticles. (c) Rhombohedral structure and (d) polyhedral species of synthesized nanoparticles. (e) $N_2$ adsorption/desorption isotherm and (f) pore size distribution of $Bi_2Se_3$ nanoparticles.*

### 6.4.1.2 Surface properties of $Bi_2Se_3$ nanoparticles

Brunnauer–Emmett–Teller (BET) experiment is performed to investigate the surface area and pore size of the synthesized $Bi_2Se_3$ nanoparticles. The surface properties of synthesized $Bi_2Se_3$ nanoparticles have been examined by Nitrogen adsorption/desorption isotherm. Figure 6.2(e) shows the adsorption/desorption isotherm of $Bi_2Se_3$ nanoparticles which indicates that the isotherm is type II. Throughout the adsorption process, at first the single molecular layer adsorption takes place at low pressure thereafter multi molecular layer adsorption occurs at higher pressure.[6] Figure 6.2(e) also indicates that the obtained hysteresis loop of the synthesized $Bi_2Se_3$ nanoparticles is well matched with H3 loop which confirms the presence of slit-shaped pores inside the $Bi_2Se_3$ nanoparticles.[6] From BET analysis, surface area of $Bi_2Se_3$ nanoparticles is measured which is 16.07 $m^2/g$. Moreover, the pore size and pore volume of the synthesized nanoparticles have been obtained from the desorption part of the adsorption/desorption isotherm. Figure 6.2(b) depicts the pore size distribution of $Bi_2Se_3$ nanoparticles. The obtained pore size of the $Bi_2Se_3$ nanoparticles is 2.64 nm and pore volume is 0.031 $cm^3/g$.

### 6.4.2 Theoretical analysis of nanoporous $Bi_2Se_3$

Density functional theory (DFT) study is performed on the samples to investigate the electronic band structure, density of state (DOS) by using both localized and de-localized methods. On one hand, the DFT calculation over $Bi_2Se_3$ was conducted by using Quantum Espresso software employing a local density approximation functional having cut-off wave function energy of 50 Ry. Moreover, the band structures were calculated by using a similar theoretical level employing a Γ-centered k-point having a width of 9x9x9 mesh.

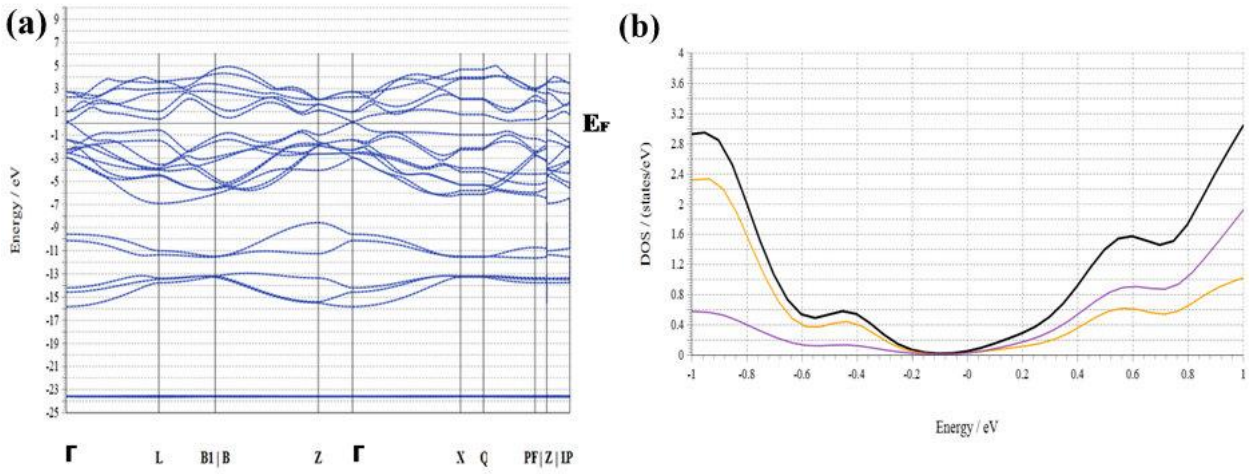


***Figure 6.3:*** *(a) Electronic band structure and (b) density of states (DOS) calculation of $Bi_2Se_3$ nanoparticles.*

The electronic band structure gives us the idea about the surface states of $Bi_2Se_3$. The surface states is represented by the electronic bands which are located around Fermi energy level ($E_F$) at the centre of Brillouin zone, i.e. Γ-point. It is observed that both the conduction band minima and valence band maxima share the single valley nature.[35, 48] Moreover, the momentum of both these bands matches with each other elucidating a direct band gap nature of the $Bi_2Se_3$ nanoparticle. A very small gap (~ 0.1 eV) exists between the conduction band minima and valence band maxima resulting in a semi-conductive nature of the sample, shown in the figure 6.3(a). It is evident that the Dirac cone is situated inside the band gap. Along with the band structure calculation; DOS has been examined to elucidate the dirac cone within the band gap. From the electronic band structure, the surface states are located at Fermi level which confirms the presence of the Dirac cone within the band gap. The dependency of momentum of electrons on energy is linear. As the surface states present within the energy gap, the DOS near the Fermi energy level should be linear. [48] Figure 6.3(b) confirms that the DOS maintains the linearity near Fermi level. According to Mohyedinet al. the electronic band gap radically decreases with the increasing number of quintuple layers (QL) of $Bi_2Se_3$. They also validated the fact that such an increment in QLs can cause higher polarizability in the sample.[44] Herein, the synthesized $Bi_2Se_3$ nanoparticles have five QLs, which could also enhance the polarizability of the sample. In order to achieve a

promising piezoelectric material the dopant (herein $Bi_2Se_3$) should have a promising polarizability. Thus, studying electronic band structure and DOS help in predicting the applicability of the material in this domain.

### *6.4.3 Experimental analysis of PBi nanocomposite films*

#### *6.4.3.1 Morphological analysis of PBi thin films*

The microstructure and surface morphology of the $Bi_2Se_3$ incorporated PVDF composite thin (PBi) films are examined by FESEM images, shown in the figure 6.4(a) to (d). The closer inspections of the FESEM images of the composite thin films are indicating the formation of the spherulites. The diameter of the spherulites of PBi thin films is near about 10µm which confirms the presence of the electroactive β-crystalline phase. Whereas, the diameter of the pure PVDF thin film is 50µm which indicates the presence of the non-polar α-crystalline phase.[31] Moreover, the presence of $Bi_2Se_3$ nanoparticle inside the polymer matrix has been shown in the figure 6.4(e). The homogeneous surface of PBi 2.5 confirms the well dispersion of $Bi_2Se_3$ porous nanoparticles into PVDF matrix. The Van der Waals interaction between $Bi_2Se_3$ porous nanoparticles and PVDF matrix is responsible for this well dispersion.[26] Along with the high resolution SEM image, elemental mapping have been provided to confirm the homogeneous dispersion of $Bi_2Se_3$ nanoparticles into PVDF matrix, shown in the figure 6.4(f) to (h).

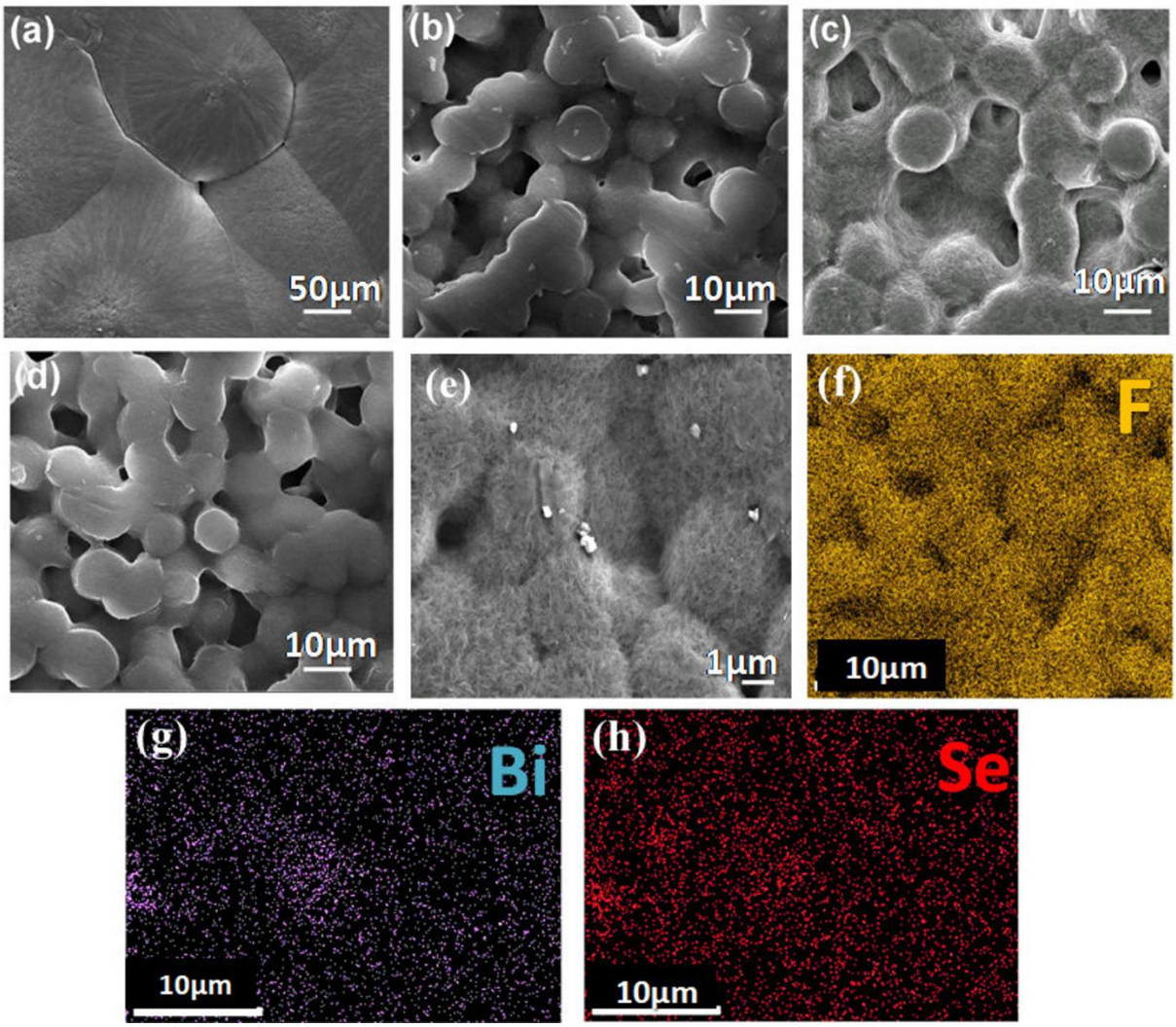


***Figure 6.4:*** *FESEM images of (a) pure PVDF thin film and (b)-(d) $Bi_2Se_3$ incorporated PVDF thin (PBi) films. (e) Confirming the presence of $Bi_2Se_3$ nanoparticles within the PBi composite film. Elemental mapping images of (f) fluorine (F), (g) bismuth (Bi) and (h) selenium (Se).*

The presence of incorporated $Bi_2Se_3$ nanoparticles within the composite film has been clearly observed in the figure 6.4(e) and no agglomeration takes place. These results are clearly indicating the uniform and homogeneous dispersion of synthesized $Bi_2Se_3$ nanoparticles within PVDF matrix.

### 6.4.3.2 Mechanical properties of PBi thin film

The stress vs. strain curve and Young's modulus of $Bi_2Se_3$ incorporated PVDF thin film represents the mechanical properties. The mechanical properties of thin film have been measured by Universal Testing Machine with strain rate of 5 mm/min. The dimension of the thin film was 50 mm x 15 mm and thickness was 0.122 mm to execute the measurement. The stress vs. strain curve of the thin film has been depicted in the figure 6.5(a). The maximum tensile strength of the thin film is 15 MPa and Young's modulus is 881 $N/mm^2$. This result infers the higher mechanical stability of thin film in comparison with pure PVDF whose Young's modulus is 700 $N/mm^2$. Moreover, the improvement of tensile strength is attributed due to tough interfacial interaction between the $Bi_2Se_3$ nanoparticle and PVDF matrix.[56] The increment in Young's modulus of thin film compared to pure PVDF is attained because of the interaction among the $Bi_2Se_3$ and PVDF matrix which restrict in the mobility of molecular chains of polymer. Along with this, the polar groups of the thin film enhance the friction amidst the molecules at the time of their continuous movements and make the mobility of molecular chain much harder.[57] As a result, the thin film shows better stiffness and Young's modulus than pure PVDF.

### 6.4.3.3 Electroactive β-crystalline phase analysis of PBi thin films

The formation of electroactive β-crystalline phase in $Bi_2Se_3$ nanoparticle loaded PVDF thin (PBi) films have been investigated by X-ray diffraction patterns. Figure 6.5(b) demonstrates the XRD pattern of pure PVDF thin film and PBi thin films. For pure PVDF thin film, the characteristic peaks are observed at 2θ= 17.6° (100), 18.3° (020), 19.9° (021), and 26.6° ((201), (310)) confirming the existence of non-polar α-crystalline phase. At 2θ=38.3°, a tiny peak is also noticed in the XRD pattern of the pure PVDF thin film. The reason behind this is the reflection from either (002) plane (representing the α-crystalline phase) or (211) plane (representing the γ-crystalline phase).[31, 47, 53] This matter has been resolved by the FTIR spectra of the pure PVDF thin film. When $Bi_2Se_3$ nanoparticles are added into PVDF polymer matrix, all characteristic XRD peaks of the α-crystalline phase disappears. Only one diffraction peak at 2θ= 20.4°(110),(200) has extensive rise, confirming the formation of electroactive β-crystalline phase in PBi thin films.[31, 53] The closer inspection of XRD graph shows that with the increasing mass % of $Bi_2Se_3$ intensity of β-crystalline phase at 20.4° also increases and maximizes for 2.5 mass % loading $Bi_2Se_3$. Thus, PBi 2.5 exhibits maximum β-crystalline phase compared to other PBi thin

films. The intensity ratio between 20.4° and 18.3° has been calculated to check the presence of α and β-crystalline phase in pure PVDF thin film and PBi thin films. The maximum $I_{20.4}/ I_{18.3}$ value is obtained for PBi 2.5 which is 1.65, shown in the figure 6.5(c).

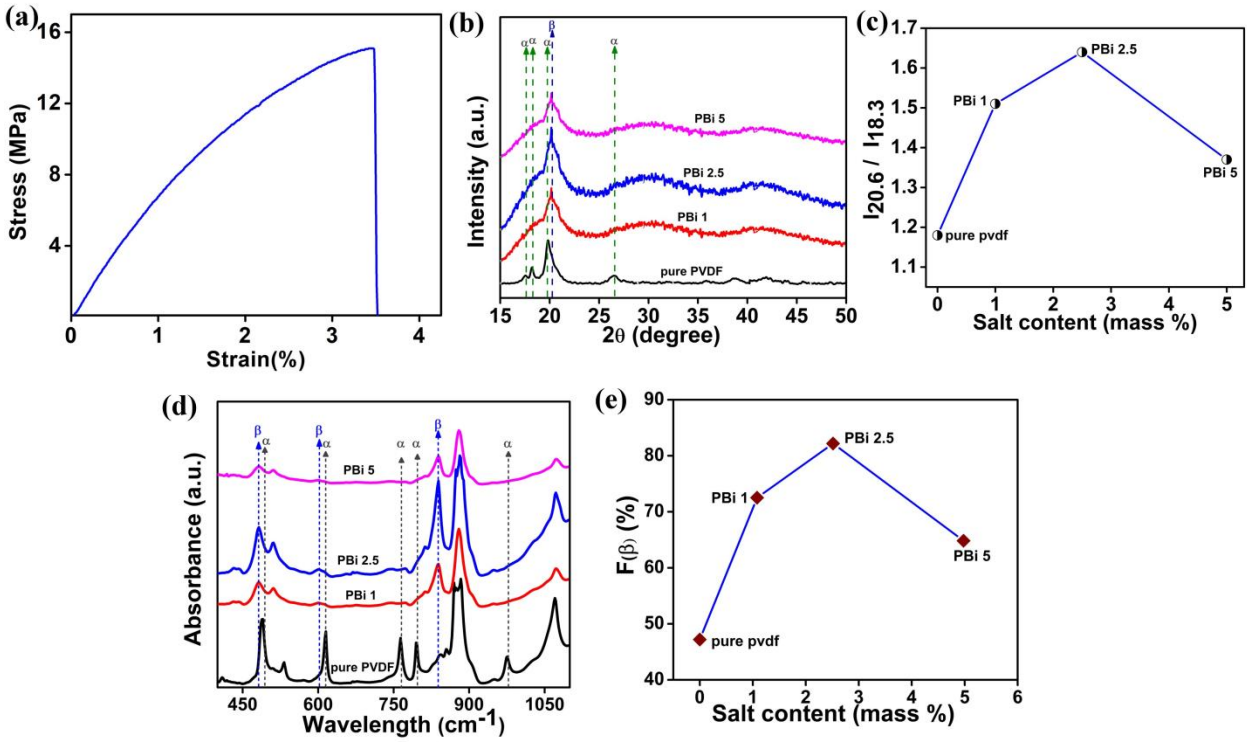


***Figure 6.5:*** *(a) Stress vs. strain curve of PBi 2.5 thin film. (b) X-ray diffraction peaks and (c) $I_{20.4}/ I_{18.3}$ ratio of pure PVDF thin film and $Bi_2Se_3$ doped PVDF thin films (PBi 1, PBi 2.5, PBi 5). (d) FTIR spectrum and (e) F(β) value of pure PVDF thin film and PBi thin films.*

The electroactive β-crystalline phase formation has been further examined by FTIR spectra analysis. Figure 6.5(d) illustrates the FTIR spectrum of pure PVDF thin film and $Bi_2Se_3$ loaded PVDF thin (PBi) films in the region of 400 to 1100 $cm^{-1}$. In case of pure PVDF thin film, the absorbance peaks at 487$cm^{-1}$ ($CF_2$ waging), 531 $cm^{-1}$ ($CF_2$ bending), 616 and 764$cm^{-1}$ ($CF_2$ bending and skeletal bending), and 796 and 976$cm^{-1}$ ($CH_2$ rocking) stipulating the presence of

the non polar α-crystalline phase. At 840cm$^{-1}$ ($CH_2$ rocking, $CF_2$ stretching, and skeletal C−C stretching), a small absorbance peak is also observed in the IR spectrum of pure PVDF thin films. The presence of β and β+γ crystalline phases may be the reason behind getting this peak. But no characteristic peak at 1234cm$^{-1}$ is present, which is the main absorbance peak for γ-crystalline phase in the FTIR spectra of pure PVDF. For this reason, the absorbance peak at 840cm$^{-1}$ confirms the presence of the β phase, occurring due to the all TTTT conformation in polymer chain of pure PVDF film. After doping with $Bi_2Se_3$ nanoparticles into PVDF matrix, all characteristic absorbance peaks which are representing the non polar α-crystalline phase disappeared and absorbance peaks at 445 cm$^{-1}$ ($CF_2$ rocking and $CH_2$ rocking), 479 cm$^{-1}$ ($CF_2$ deformation), 510 cm$^{-1}$ ($CF_2$ stretching), 600 cm$^{-1}$ ($CF_2$ wagging), and 840 cm$^{-1}$ appeared which confirms the nucleation of the electroactive β-crystalline phase in PBi thin films.[31, 53] Thus, β-crystalline phase has mainly nucleated in the composite thin films due to the catalytic effect of $Bi_2Se_3$ nanoparticles in the PVDF polymer matrix. The closer investigation of FTIR spectra of PBi thin films discloses that for PBi 2.5, the intensity of absorbance spectra becomes maximum which is matched with the XRD data. Furthermore, the fraction of electroactive β-crystalline phase (F(β)) has been calculated for estimating the amount of β-crystalline phase available in the PBi thin films by using the Lambert−Beer law [31]

$$\boldsymbol{F(\beta)} = \frac{\boldsymbol{A_\beta}}{\left(\frac{\boldsymbol{K_\beta}}{\boldsymbol{K_\alpha}}\right)\boldsymbol{A_\alpha}+\boldsymbol{A_\beta}} \quad \text{..... (6.1)}$$

Where, $A_\alpha$ = absorbance at 764 cm$^{-1}$, $A_\beta$ = absorbance at 840 cm$^{-1}$,$K_\beta$ = 7.7 × 104 cm$^2$ mol$^{-1}$ (absorption coefficients at 840 cm$^{-1}$), $K_\alpha$ = 6.1 × 104 cm$^2$ mol$^{-1}$ (absorption coefficients at 764 cm$^{-1}$).This equation is very helpful as it gives the idea about the amount of β-crystalline phase available in PBi thin films and a better formation of the β-crystalline phase gives better piezoelectric property. Compared to other PBi thin films, PBi 2.5 exhibits the maximum F(β) value which is 82.1%, shown in the figure 6.5(e).

### *6.4.3.4 Elemental analysis of PBi nanocomposite*

The X-ray photoelectron spectroscopy (XPS) analysis of the nanocomposite PBi 2.5 is shown in figure 6.6(a). The XPS spectra revealed that the C-1s peak is observed at a binding energy of 285 eV in the $Bi_2Se_3$/PVDF nanocomposite, corresponding to carbon atoms present in the sample.

The presence of carbon atoms bonded with fluorine was evident from the peak observed at approximately 292 eV, which is a characteristic of the -$CF_2$- group. Additionally, a peak observed at 286.5 eV indicated the presence of carbon atoms bonded with hydrogen in the form of -$CH_2$- bonds. The F-1s peak observed at a binding energy of 690 eV confirmed the presence of fluorine atoms in the sample, which is also present in the PVDF polymer. [33, 54] From figure 6.6 (b), the core level spectra of Bi-4f is observed in the binding energy range of 155 to 168 eV. The deconvoluted spectra of Bi-4f also show two major peaks centered at 157.6 eV and 162.9 eV, which represent the two various spin-orbits coupled 4f components ($4f_{7/2}$ and $4f_{5/2}$ respectively) in bismuth. Similarly, deconvoluted spectra of Se-3d display two major peaks centered at 53.3 eV and 54.1 eV corresponding to the spin-orbit coupled 3d components $3d_{5/2}$ and $3d_{3/2}$ respectively. In brief, the core level spectra of Se-3d lie in the binding energy range of 50 eV to 57 eV as can be seen in figure 6.6(c).

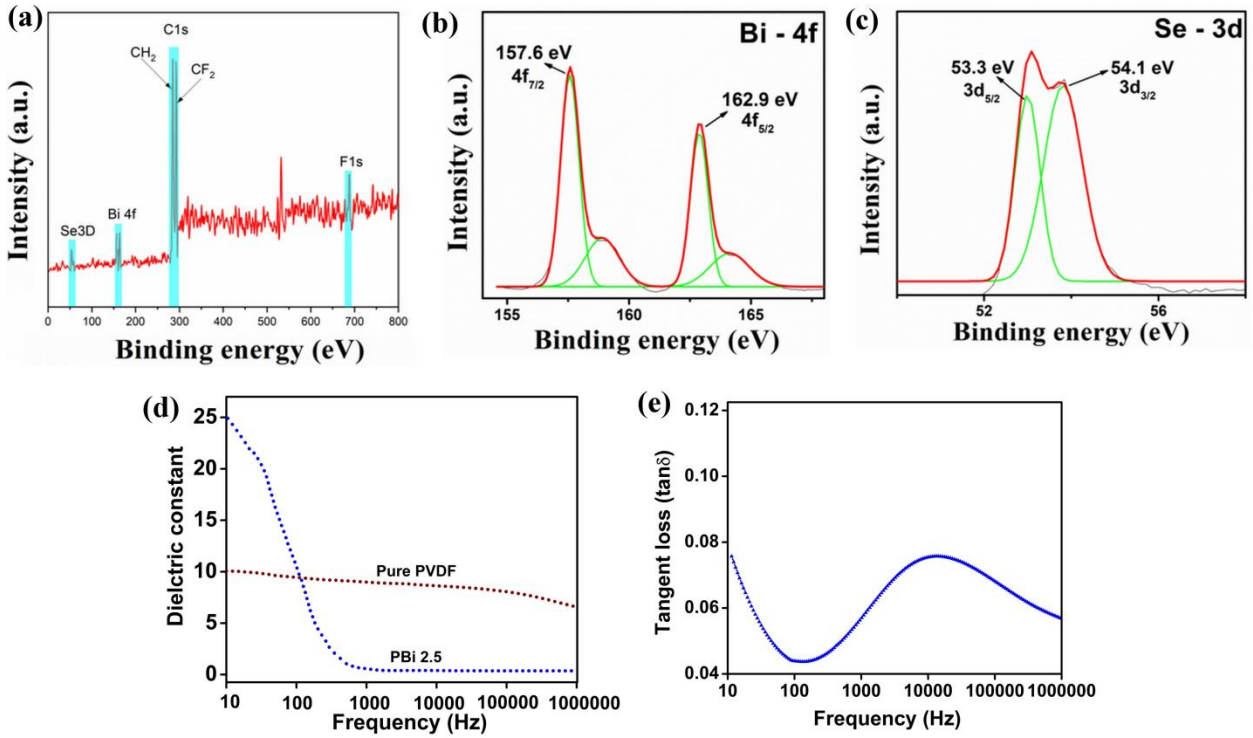


***Figure 6.6:*** *(a) XPS analysis of the PBi 2.5 nanocomposite. Core level spectra of (b) Bi-4f in the binding energy range of 155 to 168 eV and (c) Se-3d in the binding energy range of 50 eV to 57 eV. (d) Dielectric constant of pure PVDF film and PBi 2.5 film. (e) Tangent loss of PBi 2.5 film.*

These spectra thus confirmed the presence of bismuth and selenium in the nanocomposite. Overall, the XPS analysis provided evidence for the presence of the expected elements and bonding in the $Bi_2Se_3$/PVDF thin film.[33] The peaks observed in the survey scan and core-level spectra offered valuable information about the elemental composition and bonding in the sample PBi 2.5.

### *6.4.3.5 Electrical properties of composite film*

The electrical properties of PBi 2.5 thin film has been investigated by dielectric measurement. The dielectric properties of thin film depend on various parameters like applied external electric field, grain structure, chemical composition etc. Relative dielectric constant ($\varepsilon = \varepsilon' + j\,\varepsilon''$) describes the dielectric response. In the expression of relative dielectric constant, $\varepsilon'$ and $\varepsilon''$ exhibit the real part and imaginary part of $\varepsilon$. The real part gives the idea about the energy storage capacity of the dielectric material, caused by polarization and the imaginary part helps in energy dissipation within the material. The mathematical formula which can be used to calculate the real part of the dielectric constant, expressed as [49]

$$\boldsymbol{\varepsilon' = \frac{C*d}{\varepsilon_0*A}} \quad \text{..... } (6.2)$$

Where, C is value of capacitance of the PBi film, d and A are thickness and area of the silver coated PBi film and $\varepsilon_0$ is permittivity of the free space permittivity with value of $8.85 \times 10^{-12}$ F/m. The real part of the dielectric constant of the PBi 2.5 thin film has been observed by varying the external electric field frequency from 10 Hz to 1MHz. The maximum dielectric constant of this thin film is found at 10Hz frequency with the value of 25 which is higher than the dielectric constant of pure PVDF film (the value is 10 at 10 Hz frequency), shown in the figure 6.6(d). The value of the dielectric constant is decreasing steadily with the increasing frequencies. The behavior of the dielectric constant vs. frequency graph can be represented by Maxwell-Wagner interfacial polarization phenomenon.[49] When the free charge carriers gather at the grain boundary which has high resistivity, the interfacial polarization takes place. In brief, inside the dielectric thin film, the boundaries of insulated grain separate the conducting grains which help in the trapping of free charge carriers and generate dipoles through the grain at the time of their hopping. Furthermore, a constant loss in the value of dielectric constant due to the gradually decrement of the average dipole moment per unit volume, is

observed. In the high frequency region, a rapid decrement of dielectric value has been seen as electronic displacement polarization and dipole orientation polarization cannot survive with the variation of the external electric field frequency.[50] The tangent loss (tanδ) vs. frequency graph (figure 6.6(e)) also supports the dielectric value of PBi thin film. At the low frequency region, low tangent loss has been visualized. If the value of frequency increases, the tangent loss value also increases at higher order frequency range. This phenomenon can occur due to the thermal agitation of the dipoles, occurring due to their orientations. As a result, the dipoles are unable to follow the variation of the applying external electric field and exhibit high loss at higher range of frequency.[49] Thus, the PBi 2.5 thin film exhibits high dielectric constant value along with low tangent loss, so this thin film could have good storage capacity.

### *6.4.4 Theoretical investigation of structural and electrical properties of PBi nanocomposite*

The structural and electrical properties of the PBi 2.5 film were found out with the help of density functional theory. Herein, the DFT calculation has been employed by using the Orca v.1.2 program. The hybrid Becke, 3-parameter, Lee-Yang-Parr (B3LYP) functional along with the def 2 functional associated with 6-31G* basis set and RIJCOSX auxiliary basis function has been used for assigning the atoms like C, H and F. The molecular models of PVDF monomer and α, β-crystalline phases were drawn by Avogadro v.1.2.0 software program. The frequencies and geometries of all models were optimized and no imaginary frequency was observed, which confirms the proposed models. These optimized structures also consist of lowest amount of self consistent field energy. The mechanism of attachment of $Bi_2Se_3$ ions on PVDF polymer has been investigated. Figure 6.7(a) and 6.7(b) show the top and side view of $Bi_2Se_3$ ions and PVDF polymer interaction. These two images exhibit that PVDF monomer places itself parallel to the plane of nanoparticles. Initially, the PVDF monomer is placed near about 3Å distance from the $Bi_2Se_3$ plane and it maintained the parallel distance from plane of the nanoparticle. Then, the DFT study was performed to optimize the geometrical structure and monitor the interaction between monomer and nanoparticle atoms. After the DFT calculation, a chemical interaction occurred between the PVDF monomer and $Bi_2Se_3$ plane as the bond length between C and Bi is shifted from 3Å to 5Å, shown in the figure 6.7(c) and thus the bond lengths between H-Se and F-Se also changes, shown in the figure 6.7(b). It is observed that the Se atom is attracted by the neighboring H atom, which results in a significant reduction in the distance between H-Se

(2.686Å) atoms. Conversely, the distance between F-Se (3.336Å) slightly increased in order to minimize the surface energy of the composite. Such interaction between $Bi_2Se_3$ and PVDF plays an important role to attach $Bi_2Se_3$ with PVDF, which has also been validated by XRD and FTIR results. In reality, $Bi_2Se_3$ nanoparticle posses negative surface charge, [38] which is responsible to attract the H-moiety of the PVDF to form a strong attachment between $Bi_2Se_3$-PVDF.

Moreover, the electrical properties of the β-crystalline phase has been investigated by 6-31G*basis set.

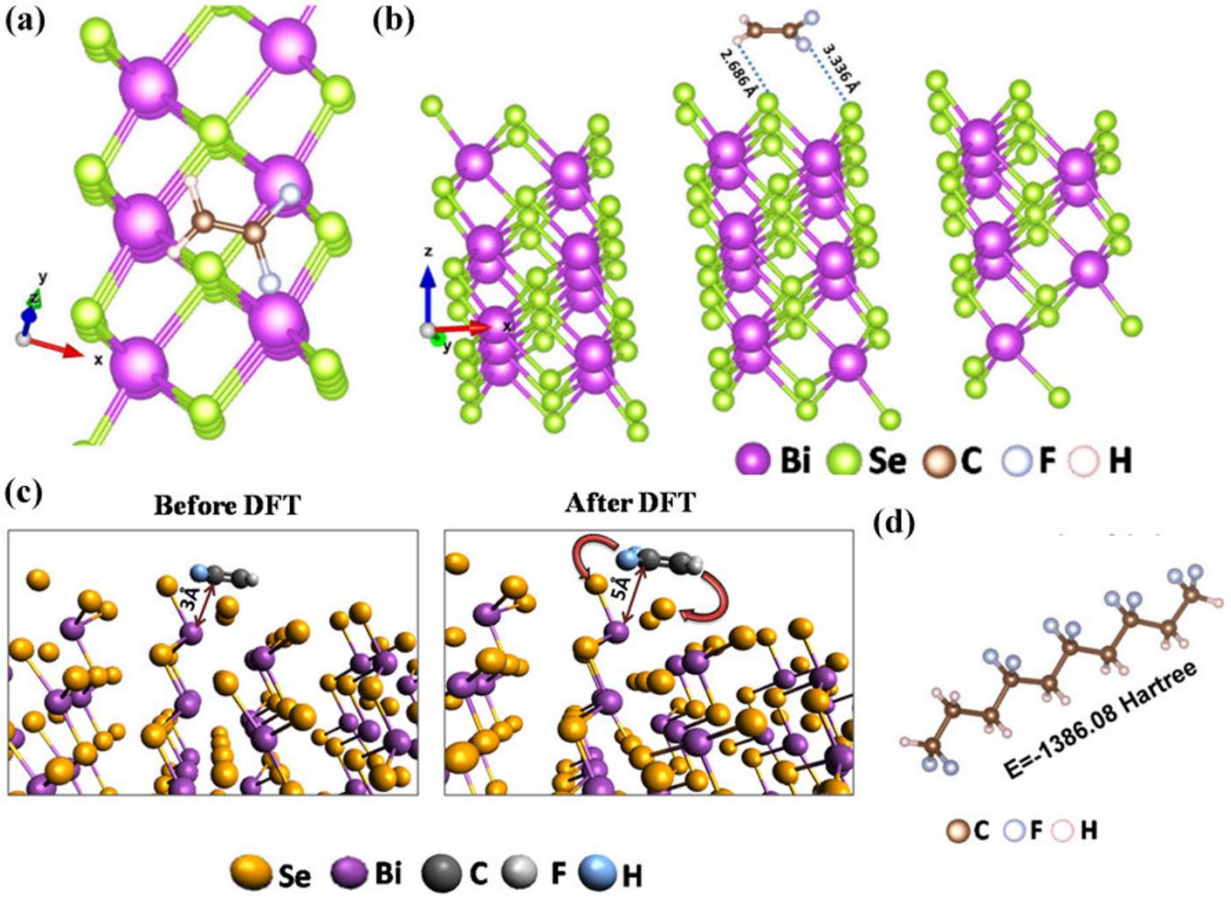


***Figure 6.7:*** *Optimized geometrical structures acquired from DFT (a) top view of $Bi_2Se_3$ and PVDF interaction, (b) side view of $Bi_2Se_3$ and PVDF interaction with bond lengths. (c) Pictorial representation of bond length shifting occurred between C and Bi before and after DFT. (d) β-crystalline phase of PBi 2.5 nanocomposite with total energy.*

From the geometrical structures of α and β-phases, it is noticed that the irregular orientation of C atom and F atom in α-PVDF got completely polarized into the β-phase of PVDF. That is the reason, a significant change in the C-C-C dihedral angle ($114^0$) has been observed. The F and H atoms are rotated alongside of C-C chain and helped the model to polarize and

minimize the single point energy of β-phase (figure 6.7(d)). The electrical properties of β-phase have been calculated theoretically, which describes that both isotropic polarizability and dipole moment of β-phase increases compared to the value of α-phase. Due to this, the higher dielectric constant value of PBi thin film is obtained compared to pure PVDF film experimentally. The comparison of electrical properties between α and β-phases of PVDF have been investigated in the table 6.2.

***Table 6.2:*** *Comparison of electrical properties between α and β-phase of PVDF*

| *Phase of PVDF* | *Energy (hartree)* | *Dipole moment (debye)* | *Quadrupole moment (a.u.)* | *Polarizability (a.u.)* |
|---|---|---|---|---|
| ***α phase*** | *-1187.68* | *0.37* | *73.74* | *106.62* |
| ***β-phase*** | *-1386.08* | *5.07* | *82.16* | *108.41* |

### *6.4.5 Working mechanism of PBTNG device*

Figure 6.8 describes the working mechanism of PBTNG device. The working principle of fabricated triboelectric nanogenerator depends on the coupling effect of triboelectrification and piezoelectric effect during contact separation (CS) mode. In CS mode, PBTNG consists of two parts i.e. positive and negative part. The positive part consists of PVA film and Al electrode, and

the negative part consists of PDMS film, Al electrode and PBi thin film. According to the triboelectric series, the PVA and PDMS film acquire positive and negative triboelectric charges respectively. When these two films get contacted with each other, the PDMS film gains electrons from PVA film. The electron transfer capability depends on their position in the triboelectric series. The working mechanism of PBTNG is elaborated in four stages.

***Stage 1:*** In the original state, the triboelectric layers are separated from each other. Thus, the PBTNG device remains electrically neutral condition and also free of charges, shown in the figure 6.8(i).When an external force is applied on the PBTNG device, the PVA and PDMS film come close to each other from the original state. As a result, the positive and negative triboelectric charges are produced in the PVA and PDMS films respectively, shown in the figure 6.8(ii). In this stage, the piezoelectric layer (PBi thin film) remains same and no deformation takes place under applied external force.

***Stage 2*****:** Under external force, the deformation of the piezoelectric layer (PBi film) takes place and the dipoles of the piezoelectric film are aligned along the direction of the applied external force. Under the deformation, the electric dipoles of the nanocomposite get properly oriented and help in the changing of polarization inside the piezoelectric nanocomposite. As a result, equal amount of positive and negative piezoelectric charges is induced on the top and bottom electrodes respectively. Thus, electron flow occurs from top electrode to bottom electrode during this deformation process. The above said phenomenon is depicted schematically in the figure 6.8(iii).

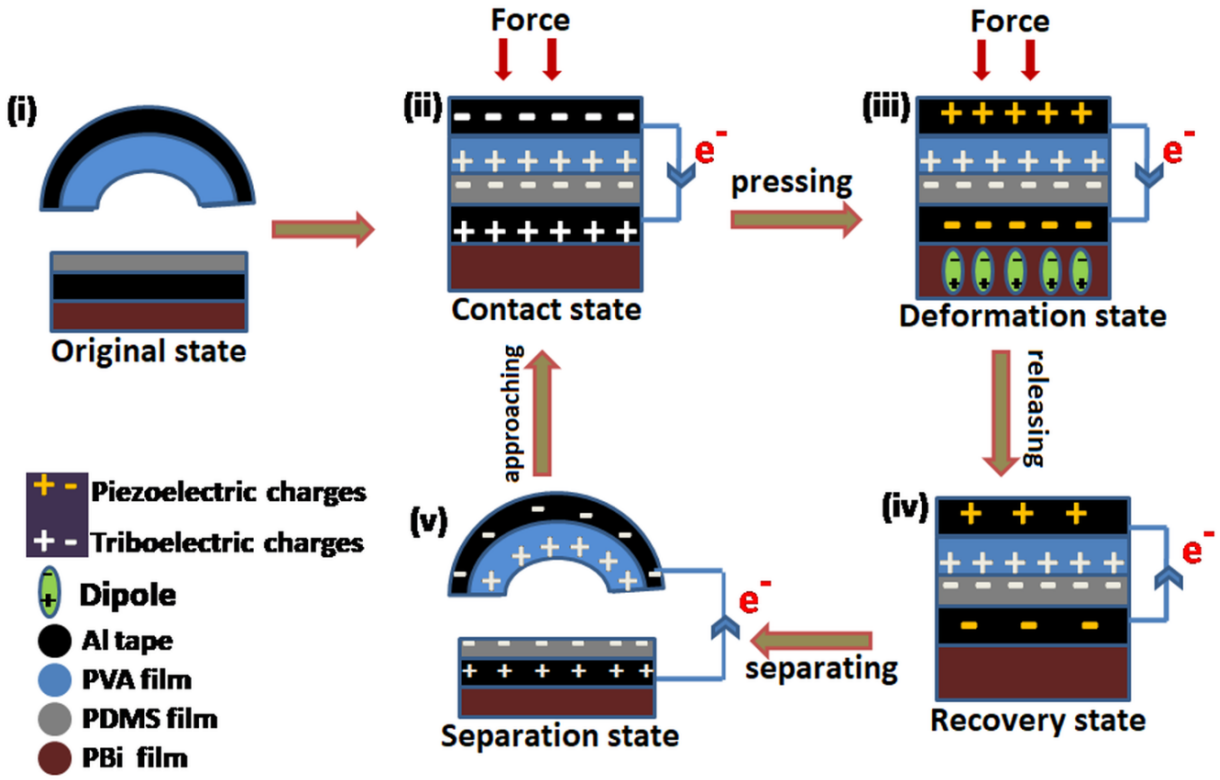


***Figure 6.8:*** *Mechanism of the voltage generation of fabricated PBTNG device.*

***Stage 3:*** When the external force starts to decrease, the contact between the positive and negative layer remains intact and the polarization of the piezoelectric thin film starts to recover. As a result electrons flow from bottom to top electrode until the polarization is fully recovered, shown in the figure 6.8(iv).

***Stage 4:*** After the recovery of polarization, the piezoelectric potential gets balanced and only the triboelectric charges gather on the surface of positive and negative triboelectric layer. On further decrement of external force, separation between the positive and negative triboelectric layer takes place. As a result, the electrons flow from bottom to top aluminum electrode, shown in the figure 6.8(v).On further application of external force on PBTNG device again, the two charge generating layers start to come close to each other. As a result, the electrons flow between

electrodes and it returns to figure 2(ii) and the cyclic process continues. Thus, the flow of electrons between the two electrodes generate alternative electric signal.

The above said detailed description of the mechanism of PBTNG device confirms that both the triboelectrification and piezoelectricity process takes active part to complete a full cycle. Therefore, the coupling effect of triboelectrification and piezoelectric effect is responsible for the improvement of the output performance of the device. The basic mechanism of triboelectric nanogenerator (TENG) can be elaborated by Maxwell's equations. Wang, the founder of TENG has introduced the surface polarization ($P_S$) term in the displacement vector (D) equation: [53]

$$\boldsymbol{D = \varepsilon_0 E + P + P_S} \quad \text{..... (6.3)}$$

Where, $P_S$ defines the polarization induced by electrostatic triboelectric and piezoelectric effect. P is the electric field encouraged medium polarization.

After adding surface polarization term in displacement vector, the Maxwell displacement current[31] will be

$$\boldsymbol{J_D = \frac{\partial D}{\partial t} = \varepsilon \frac{\partial E}{\partial t} + \frac{\partial P_S}{\partial t}} \quad \text{..... (6.4)}$$

Where, E is the electric field and ε is the permittivity of the medium.[31]

The first term in displacement current equation gives the idea of the electromagnetic wave which has been utilized in various wireless systems and the second term represents the contribution of the displacement current in the energy and sensors systems.[46, 52, 53]

### *6.4.6 Investigation of output performances of the fabricated PBTNG device*

The output performance of PBTNG device is shown in the figure 6.9. The output voltage vs. time graph of fabricated device is displayed in the figure 6.9(a). Figure 6.9(b) describes the short circuit current vs. time graph of PBTNG device. The generation of the output voltage and short circuit current are performed by periodic finger pressing and releasing, with axial pressure of 11.7 N. The fabricated energy harvesting device (PBTNG) attains maximum output voltage at 5Hz frequency. The generated output voltage (recorded by the Keysight, Oscilloscope DSO-X 3012A) and the short circuit current (measured by the Keithley DAQ6510) of PBTNG device are

$V_{OC}$ ~171.8 V and $I_{SC}$ ~ 11.7 µA respectively, shown in the figure 6.9(a) and 6.9(b). The non uniform pattern of the peak values of $V_{OC}$ under periodic finger imparting and releasing are obtained due to the inconsistent strain applied on the energy harvesting device at the time of the manual finger impartation. Figure 6.9(d) displays the single peak of the output voltage. This figure describes the appearance of the positive peak when the strain is applied on the device and after recovering the strain, the device returns to its original state then eventually a negative peak appears. The output performance of the PBTNG device is further verified at different frequency range of 1to 6 Hz under periodic finger impartation. The frequency dependent output performance graph of PBTNG device is shown in the figure 6.9(c). The maximum output voltage (~ 171.8 V) is obtained at 5 Hz frequency which is near about two times higher than the obtained highest output voltage (~ 89.6 V) at 1 Hz frequency. The output voltage of PBTNG device can be calculated with the help of the following equations [55]

$$\boldsymbol{V_{oc}} = \frac{\boldsymbol{\sigma * x(t)}}{\boldsymbol{\varepsilon_0}} \quad \text{..... (6.5)}$$

$$\boldsymbol{x(t) = v * t \ (t < \frac{x_{max}}{v})} \quad \text{..... (6.6)}$$

Where, $V_{OC}$ = output voltage; σ= charge density of the surface; x(t) = distance b/w two positive and negative triboelectric layers; $\varepsilon_o$= vacuum permittivity; ν = average velocity; $x_{max}$ = maximum distance between triboelectric layers.

With the increase of the frequencies, the velocity of the applied force also increases. Thus, the output voltage of PBTNG device increases with the increase of frequencies and gradually rises up to 5 Hz. Thereafter, the output voltage decreases by increasing the frequency. The reason behind this is obtaining very small compression cycle at very high range frequencies. Therefore, the PBTNG device cannot come back to its original state completely. For this reason, the x(t) value and $V_{OC}$ value are reduced with increasing frequency from 5 Hz. The load capacity of fabricated device is investigated by varying the different external loads. The PBTNG device generates different instantaneous power density by varying the resistance value of the resistors from $10^3$ Ω to $10^9$ Ω. Figure 6.9(e) exhibits the power density vs. resistance graph. The power density is calculated from the following equation: [53]

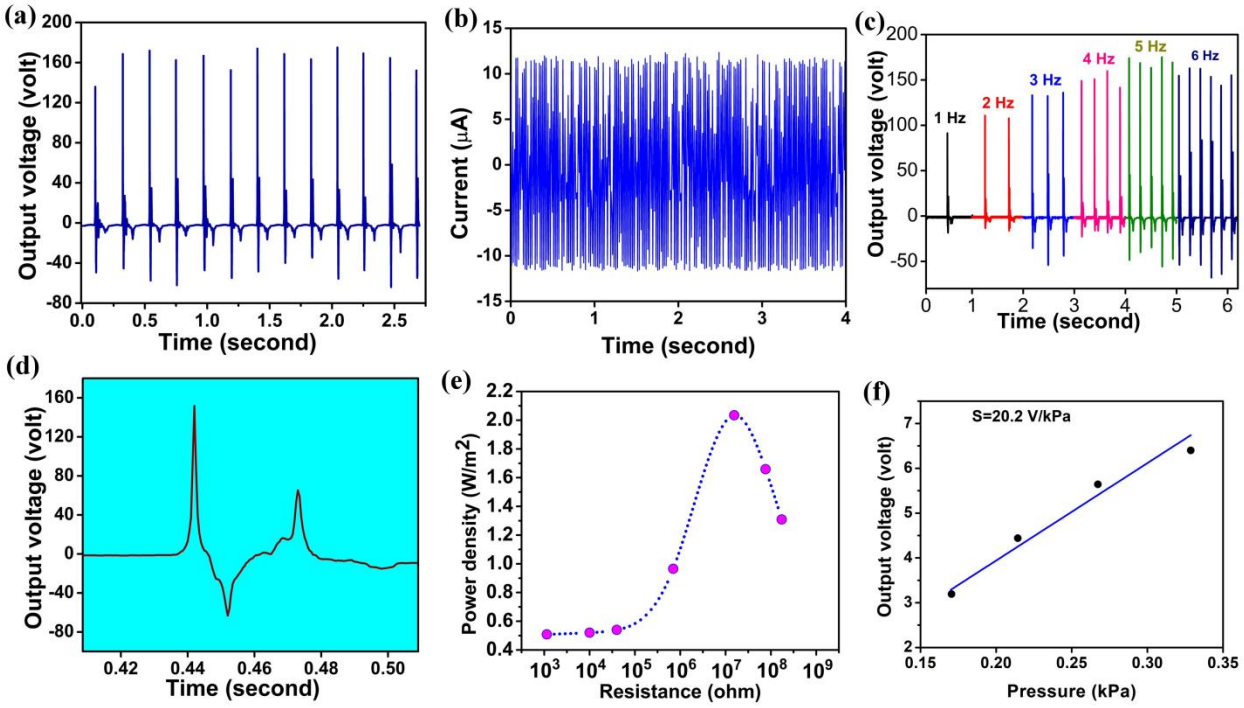


***Figure 6.9:*** *(a) Output voltage and (b) short circuit current of the designed PBTNG device during the periodic finger tapping. (c) Frequency dependent output voltage. (d) Magnified sight of generated output voltage at 5Hz frequency. (e) Power density by varying different load resistances. (f) Sensitivity of PBTNG device.*

$$\boldsymbol{P} = \frac{\boldsymbol{V^2}}{\boldsymbol{R_L \times A}} \quad \text{..... (6.7)}$$

Where, V is the output voltage of the PBTNG device, $R_L$ is the load resistance and A is the effective surface area of the PBTNG device. In this present work, the effective surface area (A) of the device is (0.022 x 0.011) $m^2$.

The maximum generated power density of PBTNG device is 2.03 $W/m^2$ at $10^7$ Ω. Additionally, the sensitivity of PBTNG device has been calculated by using the following equation [47]

$$\boldsymbol{S} = \boldsymbol{\Delta V / \Delta P} \quad \text{..... (6.8)}$$

Where, ΔV and ΔP represents the change in the output voltage and externally applied pressure. The sensitivity of PBTNG device is 20.2 V/kPa up to the pressure region of 0.5 kPa, which is generated by dropping coins on the surface of the device, shown in the figure 6.9(f).

### *6.4.7 Electricity generation from different body movements*

The fabricated device (PBTNG) has the capability to detect different body movements and convert them into electrical energy directly, shown in figure 6.10. PBTNG device can produce output voltage easily from different body movements like heel and foot pressing, single finger tapping etc. Figure 6.10(b) and 6.10(e) show the excellent output performance of device when attached it with heel and foot. At the time of heel and foot pressing, the observable output voltages are 52 V and 15 V. These results describe that the generated output voltage is higher during heel pressing compared to the foot pressing. The contact area of heel or foot with the device is responsible for this phenomenon i.e. higher contact area with the PBTNG device leads to higher output voltage. As a result, heel pressing gives us higher voltage than feet pressing. The output performance of the PBTNG has been also performed under the single finger tapping. The generated output voltage during single finger tapping is 40V which has been shown in the figure 6.10(a). The sensitivity of the single electrode bismuth selenide based triboelectric nanogenerator

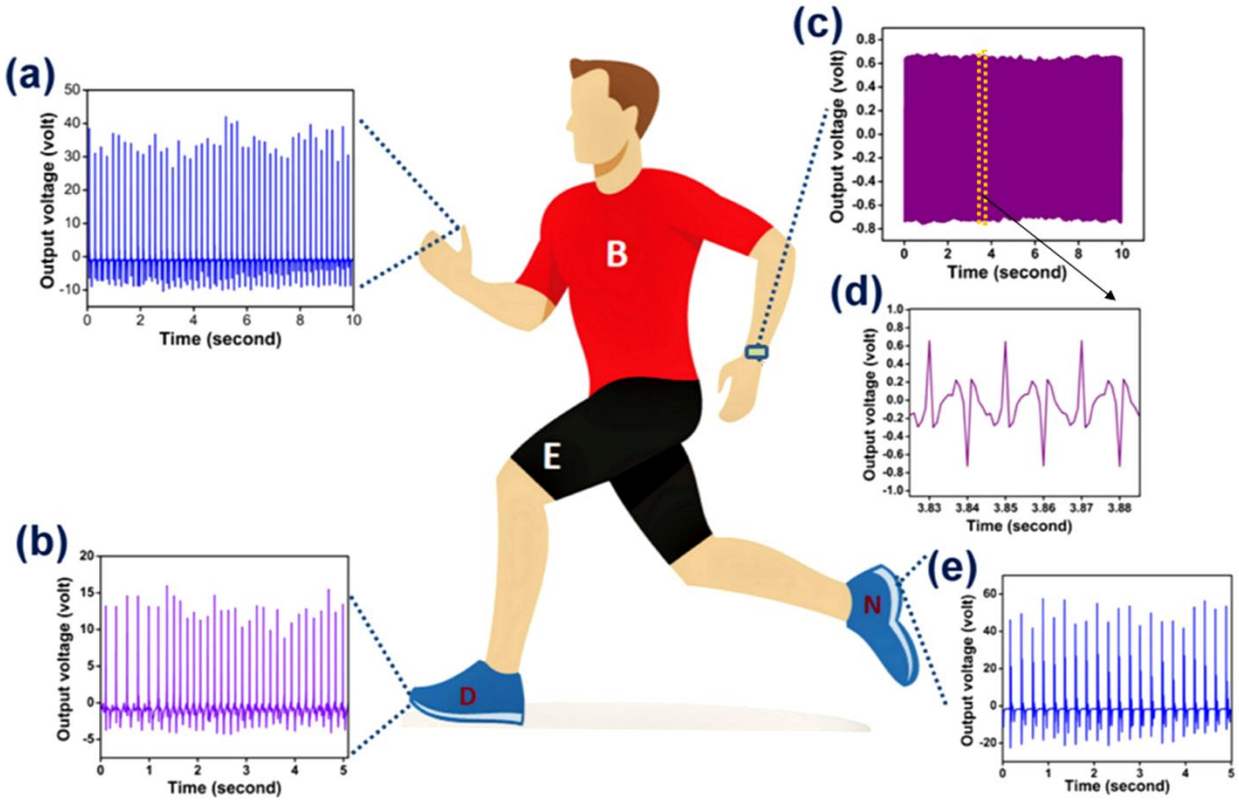


***Figure 6.10:*** *Output voltage produced by PBTNG device from (a) single finger tapping, (b) feet tapping and (e) heel pressing. (c) Monitoring the heart beating of human body by attaching SBTNG device on the wrist. (d) Enlarged view of the generated peaks during heartbeat.*

(SBTNG) (consisting of PBi thin film, Al electrode and PDMS film) is checked by dropping coins on the upper surface and it shows high sensitivity value of 20.2 V/kPa at low pressure region (less than 0.5 kPa. When SBTNG device is attached with the wrist, it shows very good output voltage, shown in the figure 6.10(c). The magnified view of this graph describes that after touching with wrist, the SBTNG device detects the blood pressure of human body. This pressure is divided into two parts one is systolic pressure and another is diastolic pressure. During the blood flow, the systolic pressure and the diastolic pressure provide the peak and the drain of the pulse wave.[53] The SBTNG device detects this pulse pressure which is arising from the alternation of the systolic and diastolic pressure, quickly and generates output voltage, shown in

the figure 6.10(d). Thus, fabricated device is very much sensitive and can be used in various medical equipments.

### *6.4.8 Generation of electrical signals from low frequency range energy resources*

SBTNG device has the capability to perceive another low range mechanical energy which is generated during writing some words on the upper surface of the device. A paper sheet has been placed on the surface of the device and wrote some English letters on it, the SBTNG can harvest the mechanical energy from this writing process and generate some electrical energy, displayed in the output voltage vs. time graph in the figure 6.11(c) which describes that the SBTNG devices shows output voltage near about 0.5V at the time of writing condition.

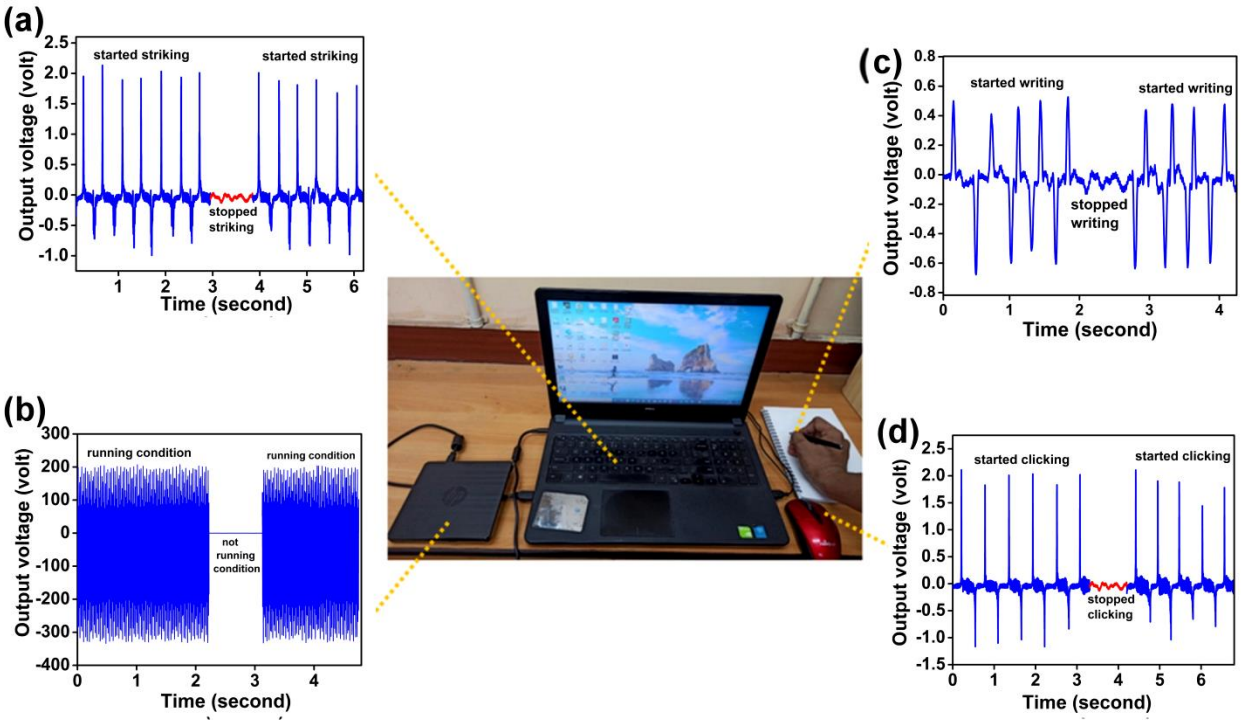


***Figure 6.11:*** *Catching small or low range mechanical energies with the help of SBTNG device from (a) Striking space bar of keyboard, (b) External CD drive on running condition, (c) Writing on device, (d) Mouse clicking.*

During stopped writing condition, no peak is observed in the figure 6.11(c).Thus, SBTNG can be used as self-powered handwriting pad to identify signature. Moreover, the negative part of PBTNG device is attached with the space bar of the keyboard to catch the mechanical energy during keystroke. At the time of striking the space bar, each keystroke generates huge amount of mechanical energy and the device successfully coverts them into electrical energy easily. The generated output voltage of

SBTNG device during keystroke is 2V as shown in the figure 6.11(a). Hence, SBTNG can be utilized as the self powered keyboards, keystroke speed recorder sensor etc. External CD drive gives the vibrational energy at very low frequency range during running condition and fabricated SBTNG device is highly sensitive and quite efficient to recognize this vibrational energy. During running condition, it can easily covert this vibrational energy into electrical energy and generate output voltage near about 200mV. Figure 6.11(b) shows the output voltage vs. time graph of the CD drive at running conditions. Beside this, the fabricated SBTNG device has the ability to covert mechanical energy into electrical energy which is arising by clicking the mouse continuously. The generated output voltage is 1.8V during mouse clicking condition which is shown in the figure 6.11(d).

### *6.4.9 Realistic applications of PBTNG nanogenerator*

The realistic applications of piezoelectric thin film based triboelectric nanogenerator (PBTNG) have been investigated by charging capacitors and illuminating blue light-emitting diodes (LEDs). The PBTNG device is connected with bridge rectifier to charge the capacitors under periodic finger impartation. Figure 6.12(a) illustrates the capacitor charging graph which shows that the fabricated device has the capability to charge 1μF, 2.2μF and 4.7μF capacitors up to 3.97 V, 2.20V, and 1.19 V within 60s. Along with this, figure 6.12(a) also describes that with the increasing value of capacitance the saturation voltage decreases gradually. Furthermore, the energy storage capacity of three capacitors has been measured. The energy (E) accumulated into the capacitors can be calculated by the following equation: [51]

$$\boldsymbol{E = \frac{1}{2} CV^2} \quad \text{..... } \textit{(6.9)}$$

Where, C= Capacitance value of the capacitor and V= voltage on the capacitor.

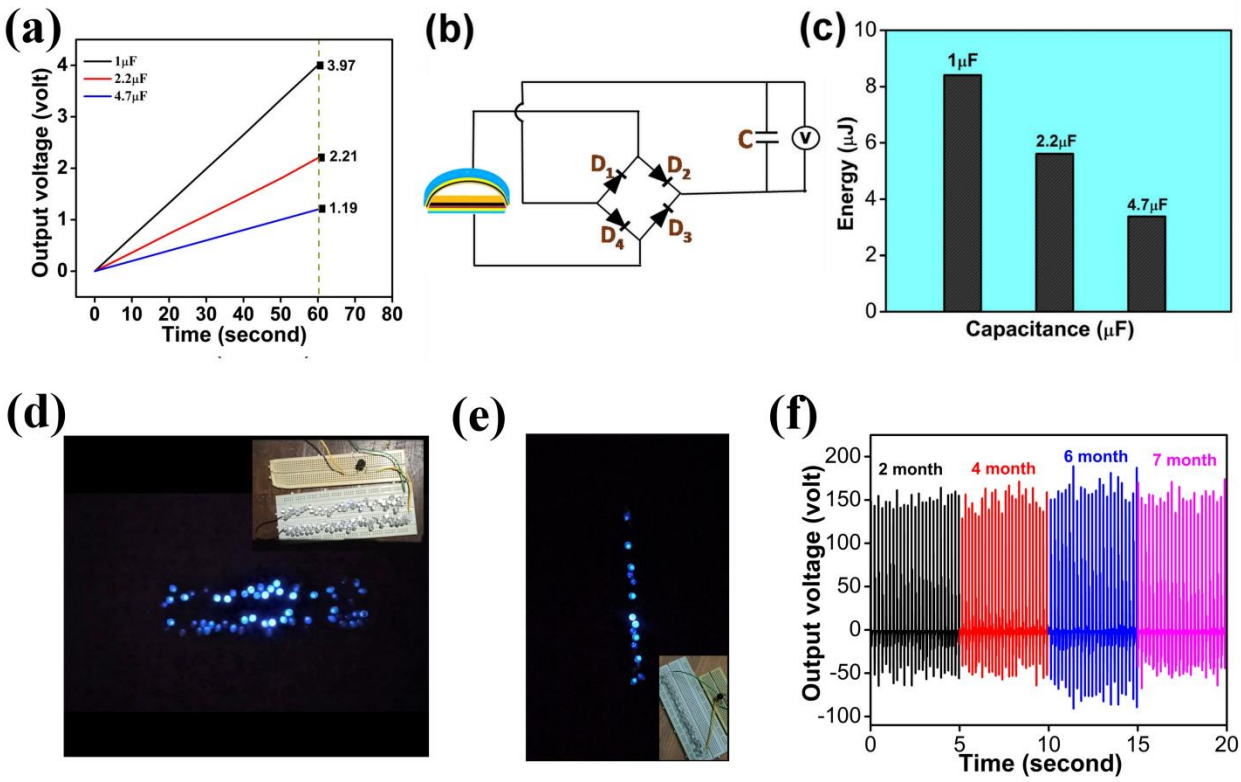


***Figure 6.12:*** *(a) Charging of capacitors by fabricated PBTNG device. (b) Circuit diagram of capacitor charging and illuminating of LEDs. (c) Accumulation of energies into the capacitors. Snapshots of blue LEDs lighting up by (d) periodic finger impartation and (e) heel pressing. (f) Durability performance of PBTNG device.*

The amount of the energy accumulated in the three capacitors (1, 2.2 and 4.7μF) is shown in the figure 6.12(c).The closer inspections of the figure 6.12(c) describe that the capacitor having smaller capacitance value has larger energy storage capacity which means, 1μF capacitor can accumulate larger amount of energy compared to the other two capacitors (2.2 and 4.7μF). The amount of energy accumulated in the 1, 2.2 and 4.7 μF are 7.88, 5.32 and 3.32 μJ respectively. Thus, PBTNG device can be utilized to power up portable electronic gadgets. Apart from this, the fabricated device also has the potential to charge up transparent blue light emitting diodes (LEDs) under continuous finger impartation and heel pressing. The power generated from the PBTNG device can illuminate 84 blue LEDs under the periodic finger impartation and 30 blue LEDs under the heel pressing by connecting them in the series combination through a bridge rectifier, shown in the figure 6.12(d) and 6.12(e). The durability of fabricated PBTNG has been

investigated for seven months and the device exhibits near about same output voltage throughout the whole time period, shown in the figure 6.12(f).

## 6.5 Conclusion

In this present work, the arch shaped, self-powered and wearable piezoelectric thin film with bismuth selenide based triboelectric nanogenerator, named as PBTNG has been fabricated with the help of nanoporous $Bi_2Se_3$ and PVDF based piezoelectric thin (PBi) film, PVA thin film, PDMS and aluminium electrodes. The coupling effect between piezoelectricity and triboelectricity enhances the output performances of fabricated triboelectric nanogenerator. The PBTNG device converts different forms of mechanical energy into electrical energy easily. The single electrode bismuth selenide based triboelectric nanogenerator, named as SBTNG exhibits high sensitivity (20.2 V/kPa) at low pressure region (<0.5 kPa) which helps SBTNG to catch the small biomechanical energy, generated by various body movements and convert them into electrical energy. Besides, the extra advantage of using this SBTNG device is that it can harness electrical energy from small scale range energy sources like keypad tapping, mouse clicking, writing on device, vibration of external CD drive at running mode etc. and each and every case shows very good output performance. The wearable and self-powered PBTNG device generates outstanding output voltage ($V_{OC}$) which is near about 171.8 V and short circuit current ($I_{SC}$) near about 11.7μAat 5 Hz frequency under continuous finger impartation (near about 11.7 N).The maximum power density produced by PBTNG device is 2.03 $W/m^2$ at $10^7\Omega$. The PBTNG device also produces very good output voltage during heel pressing which has been utilized to illuminate 30 numbers of blue LEDs. The realistic importance of PBTNG device has been examined by charging three different capacitors within a short time span and lighting up 84 numbers of blue LEDs under periodic finger impartation. The device exhibits long term durability for seven month by generating almost the same output performance throughout this period. The piezoelectric thin film with bismuth selenide based triboelectric nanogenerator (PBTNG) can be used in various versatile applications like weight sensor, mechanical and biomechanical energy harvester, blood flow sensor etc. Furthermore, the device can be utilized as self-powered handwriting identifier, keystroke sensor and recorder, vibrational energy sensor etc.

## References


1) Jiang, D.; Lian, M.; Xu, M.; Sun, Q.; Xu, B. B.; Thabet, H. K.; El-Bahy, S. M.; Ibrahim, M. M.; Huang, M.; Guo, Z. Advances in triboelectric nanogenerator technology—Applications in self-powered sensors, Internet of things, biomedicine, and blue energy. Advanced Composites and Hybrid Materials 2023, 6, 57.
2) Li, D.; Hu, J.; Wang, C.; Guo, L.; Zhou, J.; Metal-organic framework-induced edge-riched growth of layered $Bi_2Se_3$ towards ultrafast Na-ion storage. Journal of Power Sources 2023, 555, 232387.
3) Li, D.; Liu, H.; Liu, H.; Chen, Y.; Wang, C.; Guo, L. A $NiCoSe_x$/CG heterostructure with strong interfacial interaction showing rapid diffusion kinetics as a flexible anode for high-rate sodium storage. Dalton Trans 2023, 52, 5192-201.
4) Yuan, G.; Wan, T.; BaQais, A.; Mu, Y.; Cui, D.; Amin, M. A.; Li, X.; Xu, B. B.; Zhu, X.; Algadi, H.; Li, H. Boron and fluorine Co-doped laser-induced graphene towards high-performance micro-supercapacitors. Carbon 2023, 212, 118101.
5) Lin, Z.; Li, X.; Zhang, H.; Xu, B. B.; Wasnik, P.; Li, H.; Singh, M. V.; Ma, Y.; Li, T.; Guo, Z. Research progress of MXenes and layered double hydroxides for supercapacitors. Inorganic Chemistry Frontiers 2023, 10, 4358-4392.
6) Karthik, A.; Chiniwar, D. S.; Das, M.; Prabhu, P.; Mulimani, P. A.; Samanth, K.; Naik, N. Electric Propulsion for Fixed Wing Aircrafts–A Review on Classifications, Designs, and Challenges. Engineered Science 2021, 16, 129-45.
7) Li, T.; Wei, H.; Zhang, Y.; Wan, T.; Cui, D.; Zhao, S.; Zhang, T.; Ji, Y.; Algadi, H.; Guo, Z.; Chu, L. Sodium alginate reinforced polyacrylamide/xanthan gum double network ionic hydrogels for stress sensing and self-powered wearable device applications. Carbohydrate Polymers 2023, 309, 120678.
8) Akram, W.; Chen, Q.; Xia, G.; Fang, J. A review of single electrode triboelectric nanogenerators. Nano Energy 2022, 106, 108043.
9) He, J.; Cao, S.; Zhang, H. Cylinder-based hybrid rotary nanogenerator for harvesting rotational energy from axles and self-powered tire pressure monitoring. Energy Science and Engineering 2020, 8, 291-9.

10) Zou, H.; Zhang, Y.; Guo, L.; Wang, P.; He, X.; Dai, G.; Zheng, H.; Chen, C.; Wang, A. C.; Xu, C.; Wang, Z. L. Quantifying the triboelectric series. Nature Communications 2019, 10, 1427.
11) Shawon, S. M.; Sun, A. X.; Vega, V. S.; Chowdhury, B. D.; Tran, P.; Carballo, Z. D.; Tolentino, J. A.; Li, J.; Rafaqut, M. S.; Danti, S.; Uddin, M. J. Piezo-tribo dual effect hybrid nanogenerators for health monitoring. Nano Energy 2021, 82, 105691.
12) Lopez, D.; Chowdhury, A. R.; Abdullah, A. M.; Sadaf, M. U.; Martinez, I.; Choudhury, B. D.; Danti, S.; Ellison, C. J.; Lozano, K.; Uddin, M. J. Polymer based triboelectric nanogenerator for cost-effective green energy generation and implementation of surface-charge engineering. Energy Technology 2021, 9, 2001088.
13) Bhatta, T.; Maharjan, P.; Cho, H.; Park, C.; Yoon, S. H.; Sharma, S.; Salauddin, M.; Rahman, M. T.; Rana, S. S.; Park, J. Y. High-performance triboelectric nanogenerator based on MXene functionalized polyvinylidene fluoride composite nanofibers. Nano Energy 2021, 81, 105670.
14) Wei, X.; Wang, B.; Wu, Z.; Wang, Z. L. Open-Environment Tactile Sensing System: Towards Simple and Efficient Material Identification. Advanced Materials 2022, 34, 2203073.
15) He, W.; Fu, X.; Zhang, D.; Zhang, Q.; Zhuo, K.; Yuan, Z.; Ma, R. Recent progress of flexible/wearable self-charging power units based on triboelectric nanogenerators. Nano Energy 2021, 84, 105880.
16) Lin, J.; Li, J.; Feng, S.; Gu, C.; Li, H.; Lu, H.; Hu, F.; Pan, D.; Xu, B. B.; Guo, Z. An active bacterial anti-adhesion strategy based on directional transportation of bacterial droplets driven by triboelectric nanogenerators. Nano Research 2023, 16, 1052-63.
17) Jia, B.; Lei, M.; Zou, Y.; Qin, G.; Zhang, C.; Han, L.; Zhang, Q.; Lu, P. The electron transfer mechanism between metal and silicon oxide composites for triboelectric nanogenerators. Advanced Composites and Hybrid Materials 2022, 5, 3223-31.
18) Zhang, M.; Du, H.; Liu, K.; Nie, S.; Xu, T.; Zhang, X.; Si, C. Fabrication and applications of cellulose-based nanogenerators. Advanced Composites and Hybrid Materials 2021, 4, 865–884.

19) Ghafari, E.; Nantung, T.; Lu, N. An Efficient Polyvinylidene Fluoride (PVDF) Nanogenerator for Energy Harvesting in Low Frequency Range. ES Materials and Manufacturing 2019, 5, 72-77.

20) Han, C.; Cao, Z.; Yuan, Z.; Zhang, Z.; Huo, X.; Zhang, L. A.; Wu, Z.; Wang, Z. L. Hybrid Triboelectric-Electromagnetic Nanogenerator with a Double-Sided Fluff and Double Halbach Array for Wave Energy Harvesting. Advanced Functional Materials 2022, 32, 2205011.

21) Wei, X.; Zhao, Z.; Wang, L.; Jin, X.; Yuan, Z.; Wu, Z.; Wang, Z. L. Energy conversion system based on Curie effect and triboelectric nanogenerator for low-grade heat energy harvesting. Nano Energy 2022, 91, 106652.

22) Jirayupat, C.; Wongwiriyapan, W.; Kasamechonchung, P.; Wutikhun, T.; Tantisantisom, K.; Rayanasukha, Y.; Jiemsakul, T.; Tansarawiput, C.; Liangruksa, M.; Khanchaitit, P.; Horprathum, M. Piezoelectric-induced triboelectric hybrid nanogenerators based on the ZnO nanowire layer decorated on the Au/polydimethylsiloxane–Al structure for enhanced triboelectric performance. ACS Applied Materials and Interfaces 2018, 10, 6433-40.

23) Cheng, H.; Lu, Z.; Gao, Q.; Zuo, Y.; Liu, X.; Guo, Z.; Liu, C.; Shen, C. PVDF-Ni/PE-CNTs composite foams with co-continuous structure for electromagnetic interference shielding and photo-electro-thermal properties. Engineered Science 2021, 16, 331-40.

24) 24.Gao, C.; Deng, W.; Pan, F.; Feng, X.; Li, Y. Superhydrophobicelectrospun PVDF membranes with silanization and fluorosilanization co-functionalized CNTs for improved direct contact membrane distillation. Engineered Science 2020, 9, 35-43.

25) Wu, Z.; Wang, X.; Annamareddy, S. H.; Gao, S.; Xu, Q.; Algadi, H.; Sridhar, D.;Wasnik, P.; Xu, B. B.; Weng, L.; Guo, Z. Dielectric Properties and Thermal Conductivity of Polyvinylidene Fluoride Synergistically Enhanced with Silica@ Multi-walled Carbon Nanotubes and Boron Nitride. ES Materials and Manufacturing 2023, 22, 847.

26) Sharafkhani, S.; Kokabi, M. Enhanced sensing performance of polyvinylidene fluoride nanofibers containing preferred oriented carbon nanotubes. Advanced Composites and Hybrid Materials 2022, 5, 3081-93.

27) Li, G.Y.; Li, J.; Li, Z.J.; Zhang, Y.P.; Zhang, X.; Wang, Z.J.; Han, W.P.; Sun, B.; Long, Y.Z.; Zhang, H.D. Hierarchical PVDF-HFP/ZnO composite nanofiber–based highly

sensitive piezoelectric sensor for wireless workout monitoring. Advanced Composites and Hybrid Materials 2022, 5, 766-75.

28) Liu, Z.; Li, G.; Qin, Q.; Mi, L.; Li, G.; Zheng, G.; Liu, C.; Li, Q.; Liu, X. Electrospun PVDF/PAN membrane for pressure sensor and sodium-ion battery separator. Advanced Composite and Hybrid Materials 2021, 4, 1215-25.

29) Li, R.; Wei, X.; Shi, Y.; Yuan, Z.; Wang, B.; Xu, J.; Wang, L.; Wu, Z.; Wang, Z.L. Low-grade heat energy harvesting system based on the shape memory effect and hybrid triboelectric-electromagnetic nanogenerator. Nano Energy 2022, 96, 107106.

30) Suo, G.; Yu, Y.; Zhang, Z.; Wang, S.; Zhao, P.; Li, J.; Wang, X. Piezoelectric and triboelectric dual effects in mechanical-energy harvesting using $BaTiO_3$/polydimethylsiloxane composite film. ACS Applied Materials and Interfaces 2016, 8, 34335-41.

31) Das, N.; Sarkar, D.; Saikh, M. M.; Biswas, P.; Das, S.; Hoque, N. A.; Ray, P. P. Piezoelectric activity assessment of size-dependent naturally acquired mud volcano clay nanoparticles assisted highly pressure sensitive nanogenerator for green mechanical energy harvesting and body motion sensing. Nano Energy 2022, 102, 107628.

32) Hong, M.; Chasapis, T. C.; Chen, Z. G.; Yang, L.; Kanatzidis, M. G.; Snyder, G. J.; Zou, J. n-type $Bi_2Te_{3-x}Se_x$nanoplates with enhanced thermoelectric efficiency driven by wide-frequency phonon scatterings and synergistic carrier scatterings. ACS Nano 2016, 10, 4719-27.

33) Gautam ,S.; Aggarwal, V.; Singh, B.; Awana, V. P.; Ganesan, R.; Kushvaha, S. S. Signature of weak-antilocalization in sputtered topological insulator $Bi_2Se_3$ thin films with varying thickness. Scientific Reports 2022, 12, 9770.

34) Sun, H.; Jiang, T.; Zang, Y.; Zhen, X.; Gong, Y.; Yan, Y.; Xu, Z.; Liu, Y.; Fang, L.; He, K. Broadband ultrafast photovoltaic detectors based on large-scale topological insulator $Sb_2Te_3$/STO heterostructures. Nanoscale 2017, 9, 9325-32.

35) Mishra, S. K.; Satpathy, S.; Jepsen, O.; (1997) Electronic structure and thermoelectric properties of bismuth telluride and bismuth selenide. Journal of Physics: Condensed Matter 1997, 9, 461.

36) Yan, Y.; Wang, L. X.; Yu, D. P.; Liao, Z.M. Large magnetoresistance in high mobility topological insulator $Bi_2Se_3$. Applied Physics Letters 2013, 103, 033106.

37) Yang, W. J.; Lee, C. W.; Kim, D. S.; Kim, H. S.; Kim, J. H.; Choi, H. Y.; Choi, Y. J.; Kim, J. H.; Park, K.; Cho, M. H. Tuning of topological Dirac states via modification of van der Waals gap in strained ultrathin $Bi_2Se_3$ films. The Journal of Physical Chemistry C 2018, 122, 23739-48.

38) Mishra, V.; Baranwal, V.; Mishra, R. K.; Sharma, S.; Paul, B.; Pandey, A. C. Immunotoxicological impact and biodistribution assessment of bismuth selenide ($Bi_2Se_3$) nanoparticles following intratracheal instillation in mice. Scientific Reports 2017, 7, 18032.

39) Sharma, A.; Bhattacharyya, B.; Srivastava, A. K.; Senguttuvan, T. D.; Husale, S.; (2016) High performance broadband photodetector using fabricated nanowires of bismuth selenide. Scientific Reports 2016, 6, 19138.

40) Zhang, H.; Zhang, X.; Liu, C.; Lee, S. T.; Jie, J. High-responsivity, high-detectivity, ultrafast topological insulator $Bi_2Se_3$/silicon heterostructure broadband photodetectors. ACS Nano 2016, 10, 5113-22.

41) Tang, H.; Liang, D.; Qiu, R. L.; Gao, X. P. Two-dimensional transport-induced linear magneto-resistance in topological insulator $Bi_2Se_3$ nanoribbons. ACS Nano 2011, 5, 7510-6.

42) Zhang, H.; Liu, C. X.; Qi, X. L.; Dai, X.; Fang, Z.; Zhang, S. C. Topological insulators in $Bi_2Se_3$, $Bi_2Te_3$ and $Sb_2Te_3$ with a single Dirac cone on the surface. Nature Physics 2009, 5, 438-42.

43) Li, C. H.; Van, 'T.; Erve, O. M.; Robinson, J. T.; Liu, Y.; Li, L.; Jonker, B. T. (2014) Electrical detection of charge-current-induced spin polarization due to spin-momentum locking in $Bi_2Se_3$. Nature Nanotechnology 2014, 9, 218-24.

44) Mohyedin, M. Z.; Taib, M. F.; Malik, N. A.; Alam, N. N.; Mustaffa, M.; Ali, A. M.; Hassan, O. H.; Haq, B. U.; Yahya, M. Z. First-principles calculations of electronic and optical properties of orthorhombic $Bi_2Se_3$nano thin film. Computational Condensed Matter 2022, 30, e00618.

45) Wang, Z. L. On Maxwell's displacement current for energy and sensors: the origin of nanogenerators. Materials Today 2017, 20, 74-82.

46) He, J.; Qian, S.; Niu, X.; Zhang, N.; Qian, J.; Hou, X.; Mu, J.; Geng, W.; Chou, X. Piezoelectric-enhanced triboelectric nanogenerator fabric for biomechanical energy harvesting. Nano Energy 2019, 64, 103933.

47) Chen, X.; Song, Y.; Chen, H.; Zhang, J.; Zhang, H. (2017) An ultrathin stretchable triboelectric nanogenerator with coplanar electrode for energy harvesting and gesture sensing. Journal of Materials Chemistry A 2017, 5, 12361-8.

48) Ajeel, F. N.; Mohammed, M. H.; Abd, Ali RA (2017) Topological Insulators in Bi2Se3 Family Nanostructured Thin Films: Study Topological Nature and Surface states. University of Thi-Qar Journal 12:40_50-.

49) Roy, S.; Bardhan, S.; Pal, K.; Ghosh, S.; Mandal, P.; Das,S.; Das, S. Crystallinity mediated variation in optical and electrical properties of hydrothermally synthesized boehmite (γ-AlOOH) nanoparticles. Journal of Alloys and Compounds, 2018, 763,749-58.

50) Das, S.; Das, S.; Sutradhar, S. Effect of $Gd^{3+}$ and $Al^{3+}$ on optical and dielectric properties of ZnO nanoparticle prepared by two-step hydrothermal method. Ceramics International 2017, 43, 6932-41

51) Zheng, F.; Zhou, Y.; Hu, S.; Li, R.; Wang, Z. L.; Wu, Z. A. Hybridized Triboelectric-Electromagnetic Nanogenerator as a Power Supply of Monitoring Sensors for the Ventilation System. Advanced Energy Materials 2022, 12, 2201966.

52) Guo, Y.; Zhang, X. S.; Wang, Y.; Gong, W.; Zhang, Q.; Wang, H.; Brugger, J. All-fiber hybrid piezoelectric-enhanced triboelectric nanogenerator for wearable gesture monitoring. Nano Energy 2018, 48, 152-60.

53) Sarkar, D.; Das, N.; Saikh, M. M.; Biswas, P.; Roy, S.; Paul, S.; Hoque, N. A.; Basu, R.; Das, S. High β-crystallinity comprising nitrogenous carbon dot/PVDF nanocomposite decorated self-powered and flexible piezoelectric nanogenerator for harvesting human movement mediated energy and sensing weights. Ceramics International 2023, 49, 5466-78.

54) Gupta, V.; Kumar, A.; Mondal, B.; Babu, A.; Ranpariya, S.; Sinha, D. K.; Mandal, D. Machine Learning-Aided All-Organic Air-Permeable Piezoelectric Nanogenerator. ACS Sustainable Chemistry and Engineering 2023, 11, 6173-82.

55) Jalili, M. A.; Khosroshahi, Z.; Kheirabadi, N. R.; Karimzadeh, F.; Enayati, M. H. Green triboelectricnanogenerator based on waste polymers for electrophoretic deposition of titania nanoparticles. Nano Energy 2021, 90, 106581.

56) Primadona, I.; Dara, F.; Syampurwadi, A.; Nasir, M. Nanocomposites of polyvinylidene fluoride copolymer-functionalized carbon nanotubes prepared by electrospinning method. IOP Conference Series: Earth and Environmental Science 2020, 483, 012045.

57) Chu, R.; Weng, L.; Guan, L.; Liu, J.; Zhang, X.; Wu, Z. Preparation and properties comparison of ZIF-67/PVDF and SiCNWs/PVDF composites for energy storage. Journal of Materials Science: Materials in Electronics 2023, 34, 347.

# Conclusion

*Chapter 7*

## 7. Conclusion

With the fastest developments of human civilization, fossils fuels are limiting day by day. Therefore, human society will face some serious energy crisis in the upcoming days. From different literature review, it has been came to know that the fossils fuels will run out near about one hundred and fifty years. Alongside the growing fashion of human population increases the daily power requirements of human body. To fulfill the power demand of human society and resolves the problem of energy crisis, researches are looking forward towards the utilization of alternative energy sources. Among different types of alternative sources, renewable energy is the most suitable and easily available energy sources in our environment, which is easily available in our nature and also a never ending energy sources. Therefore, utilization these renewable sources in our daily life activities not only resolve the power demand of the human society but also gives us the alternative of fossils fuels. There are several renewable sources are available in our nature for example wind energy, water wave, solar energy, mechanical energy etc. Amidst of all renewable sources, mechanical energy is the most abundant energy sources and also environmental friendly. Therefore, my primary objectives is to develop self-powered energy harvesting devices and utilize them in generating electrical energy through harvesting mechanical energy sources by using piezoelectric and triboelectric effects.

***In chapter 2,*** naturally available Sonchus asper (SA) pappus has been employed to fabricate a bio-inspired nanogenerator which is named as SPENG. The efficiency of the fabricated SPENG is investigated by harnessing the mechanical energy arising from various living and nonliving sources. Moreover, the amide and hydroxyl groups of SA pappus assist in producing electric dipoles inside the fiber under the application of external strain. For this, SA pappus forms stress-induced polarization and generates piezoelectricity. As a result, the fabricated SPENG device exhibits high output voltage (Voc) of ~ 81.2 V and a short circuit current (Isc) of ~ 1.0 µA under axial force of 13.5N. The instant power density of the device has been calculated, which is 182.06 $\mu Wcm^{-3}$. Beside this, the SPENG shows remarkable response in exploiting vibration energy of vortex mixture (~ 6 V). Also, it responses proficiently when different masses objects are fallen on the surface of the device from 10 cm. Moreover, the sensitivity of the device has been utilized to harvest biomechanical energy from various body movements like heel and forefoot pressing, wrist up-down movement and just finger touch. Each and every case, the

device exhibits very good output results. Furthermore, the realistic application of SPENG has been verified by successfully lighting up to 39 blue LEDs connected in series via finger impartation only and also by charging a capacitor (2.2μF) to 3.2V within a very short span time (16 second). All the results are reproducible and SPENG has outstanding mechanical stability with brilliant performances for a year. Therefore, the self-powered and flexible SPENG can be used to harness energy from a wide range of green bio-mechanical energy resources including treadmills, dancing floors, interior of shoes, wheels of the car etc. and generated electrical energy which can be used to switch on LEDs, LCD screens, and other different types of battery charging equipments.

***In chapter 3,*** N doped carbon dots (N-CDs) have been incorporated into PVDF matrix to form the electroactive β-crystalline phase confirming by XRD, FTIR and FESEM analysis. Also, TEM and XPS analysis of N-CDs are performed to investigate the homogenous dispersion and the surface groups of synthesized nanoparticles. The incorporation of N-CDs into PVDF matrix nucleates the formation of β-crystalline phase and exhibits the maximum F(β) value of 80.4% for 2.5 wt% loading of N-CDs. Moreover, the presence of N-CDs inside PVDF matrix strengthens the thermal property of PCD nanocomposite and improves the piezoelectric co-efficient ($d_{33}$) value, which is 29 pC/N. The density functional theory (DFT) calculations have been carried out to investigate the electrical properties of the β-crystalline phase. After successfully characterized the PCD nanocomposite, we have utilized it in development of a self-powered and flexible piezoelectric nanogenerator, named as PPNCD and generated electricity from various mechanical energy sources. Under 12.3 N forces, the PPNCD generates maximum output voltage of 80 V and short circuit current of 1.4μA. The instant power density of PPNCD is 1979.87$\mu Wcm^{-3}$. Beside this, the sensitivity of the device has been measured in both low and high pressure region from 0.1 to 3 kPa and the obtaining results indicate that the device has very good sensitivity with the value of 10.2 V/kPa. This impressive sensitivity of PPNCD assists in harvesting electrical energy from pulse wave and other human body movements. Also, the device has the ability to induce electrical energy from the impact of different masses objects falling from a fixed height on the device. Along with this, PPNCD has the potential to charge a 2.2 μF capacitor up to 3.2V in a short period (14 seconds) and light up 15 blue and 15 white transparent LEDs by connecting them in series. Therefore, the significant sensitivity and energy harvesting ability of PPNCD open up its utilization in multipurpose applications including

mechanical energy harvester, weight sensor, and pulse sensor so that it can be employed in optoelectronic, biomedical, and energy technologies.

***In chapter 4,*** we have fabricated 3D printer assisted cotton pappus embedded CPD nanocomposite which is further used in designing of self-powered and wearable TENG (CPTNG). The reason behind the utilization of 3D printed mold is to enhance the output performance of the device by inducing more surface potential. Moreover, the high aspect ratio and presence of chemical groups of cotton pappus directly improves the output results of CPTNG device by generating more polarization. Thus, the fabricated self-powered and wearable CPTNG depicts outstanding output performance of 201V output voltage and 1.02W/$m^2$ power density under 12N axial pressure. Additionally, the environmental friendly and flexible properties of the device expand its utilization in the field of biomechanical energy harvester by harnessing the energy during wrist up-down and muscle movements and converting them into electrical energy. The energy conversion ability of the device has been monitored by lighting up 95 no of blue LEDs. Furthermore, the transmission of signal come out from finger bending movement is also monitored by using ARDUINO UNO setup. Thus, the CPTNG device may be helpful in future health monitoring unit.

***In chapter 5,*** self-powered and flexible triboelectric nanogenerator (EPMTNG) has been designed with charge generating layer using micro-patterned $BaTiO_3$@Ecoflex (EBTO) nanocomposite, nanofibrous trapping layer with 2D $MoTe_2$ and carbon tape as charge collecting layer. The utilization of micro-patterned surface assists in creation of surface roughness of EBTO layer and increases the effective contact area among human hand and EBTO layer, which results in the enhancement of output performance of the device by increasing the potential difference during triboelectrification process. Along with the enhancement of output performance of the device, charge recombination takes place between charge generating layer and charge collecting layer resulting in the decrement of output performance of the device by lowering the surface charge density. To overcome this problem, an intermediate nanofibrous trapping layer by incorporating 2D $MoTe_2$ into PVDF matrix (PM5) has been introduced in the device designing process. The introduction of PM5 trapping layer restricts the triboelectric charges to combine with the opposite induced charges and increases the surface charge density, which further results in enhancement of output performance. Moreover, the incorporation of 2D $MoTe_2$ nanoparticles

reinforces the polarization effect by accumulating more charge carriers and improves electrical conductivity of the device. Besides, the fabricated EPMTNG device exhibits output voltage of 319V and current density of 9mA/$m^2$ under the axial pressure of 12N. The generated maximum power density of the device is 2.9W/$m^2$ at $10^7\Omega$. A theoretical simulation model using finite element analysis has been prepared to validate the idea of incorporation of intermediate trapping layer (PM5 nanofibers). Beside this, EPMTNG shows very good sensitivity of 32.5V/kPa at low pressure region of up to 0.5kPa helping in the detection of human physiological signals arising from blood flow, neck movement, elbow movement and glottis movement. The additional significance of the EPMTNG device is the detection of robotic gestures. Along with this, a wireless communication setup has been established to monitor the signals of human physiological activities and artificial finger movements. The realistic applications of the device have been investigated by illuminating 140 no of blue LEDs and charging capacitors. Therefore, the self-powered and flexible EPMTNG can be used in multidimensional applications including monitoring sporting activity, speech therapy, medical rehabilitation, robotic surgery, soft robotic applications etc.

***In chapter 6,*** an arch shaped and self-powered triboelectric nanogenerator has been developed with the help of piezoelectric thin film, tribo-positive and tribo-negative layers and aluminium electrodes and named the nanogenerator as PBTNG. The idea behind the addition of piezoelectric layer in the development of the device is to elevate the output performance and sensitivity of the device. To fabricate the piezoelectric thin film (PBi), nanoporous bismuth selenide ($Bi_2Se_3$) has been incorporated into PVDF matrix, which further helps in the nucleation of β-crystalline phase and improves the piezoelectric property. Furthermore, density functional theory (DFT) has been performed to investigate the electrical properties including polarizability and dipole moment of PBi thin film and the interaction between $Bi_2Se_3$ and PVDF matrix. Also, DFT has been carried out to investigate the electrical band gap and density of states of $Bi_2Se_3$ nanoparticles. Beside this, the working principal of the fabricated PBTNG device depends on the coupling effect of piezoelectricity and triboelectricity by which PBTNG exhibits outstanding output voltage of 171.8V and short circuit current of 11.7μA under periodic finger impartation. The maximum power density generated by the PBTNG device is 2.03 W/$m^2$ at $10^7\Omega$. The utilization of the device in our daily life activities has been monitored by illuminating 84 numbers of blue LEDs and charging three different capacitors under periodic finger tapping

conditions. Also, the device has the capability to convert the mechanical energy generated during heel pressing into electrical energy and illuminate 30 numbers of blue LEDs at the same heel pressing condition. Beside this, the sensitivity of the PBTNG has been measured by falling Indian coins and dropping different mass containing balls on the surface of the device. The obtaining high sensitivity value of 20.2 V/kPa at low pressure region (<0.5 kPa) assists in detecting different body movements like heel pressing, feet tapping, blood flow, single finger tapping etc. and converts them into electricity. Also, the sensitivity of the device extends its utilization in harnessing small scale energies coming from keypad tapping, mouse clicking, writing on device, vibration of external CD drive at running mode etc. Moreover, the PBTNG exhibits long term durability for seven month by generating almost the same output performance throughout the time period. Therefore, the valuable investigations and results are indicating that PBTNG is a green and wearable energy harvester and can be used to power up portable electronic devices used in daily life.

# Publications

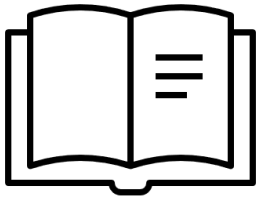

ACS OMEGA

http://pubs.acs.org/journal/acsodf

Article

# Development of a Sustainable and Biodegradable *Sonchus asper* Cotton Pappus Based Piezoelectric Nanogenerator for Instrument Vibration and Human Body Motion Sensing with Mechanical Energy Harvesting Applications

Debmalya Sarkar, Namrata Das, Md. Minarul Saikh, Prosenjit Biswas, Solanky Das, Sukhen Das,* Nur Amin Hoque,* and Ruma Basu*

Cite This: *ACS Omega* 2021, 6, 28710−28717

Read Online

ACCESS | Metrics & More | Article Recommendations | Supporting Information

**ABSTRACT:** Energy harvesting from natural resources has gained much attention due to the huge increase in the demand for portable electronic devices and the shortage of conventional energy resources in general. In the present work, the fabrication and realistic applications of a piezoelectric nanogenerator (PENG) using polydimethylsiloxane (PDMS) and the abundantly available, environment-friendly natural fiber *Sonchus asper* (SA) have been discussed. The biocompatible, low-cost SA fibers were flexible enough and showed high piezoelectric properties as active materials in the study. The SA pappus based piezoelectric nanogenerator demonstrated its ability to convert the harvested biomechanical energy into electrical energy from the various mechanical energy sources available in our environment. The SA pappus/PDMS thin film based piezoelectric nanogenerator (SPENG) fabricated in the laboratory showed colossal output performances (open circuit output voltage, $V_{OC}$ ∼81.2 V; short circuit current, $I_{SC}$ ∼1.0 $\mu$A) by continuous finger impartation. Uniform output performance was also obtained by the application of uniform force on the devices (e.g., ∼42 V for 5 N force at 10 Hz frequency). The SPENG was capable to charge a 2.2 $\mu$F capacitor to 3.2 V within a short time span (16 s) under continuous finger impartation and illuminate 39 commercial high-power blue LEDs that were connected in series. Thus, the fabricated SPENG can be used as a green and portable energy source to power up portable electronic devices. Apart from this, the SPENG may also be used as a self-powered energy supply for pacemakers or different types of health care units if properly improvised.



## INTRODUCTION

To reduce the use of conventional power sources such as fossils fuels, firewood, etc., energy harvesting from living natural systems has attracted more interest in the development of self-powered biocompatible and portable electronic gadgets such as mobile phones, implantable medical appliances, roll-up displays, actuators, sensors, and wearable electronic devices.[1−7] For low-energy devices, bio-based materials are considered to be suitable alternatives over regular rechargeable batteries.[8,9] Nowadays, piezoelectric nanogenerators (PENGs) and triboelectric nanogenerators (TENGs) have been identified as promising green energy harvesting devices. These PENGs and TENGs can harvest electrical energy from various natural and artificial mechanical energy sources (such as human body movement, water flow, airflow, vibrations, and rotations) via piezoelectric and triboelectric effects.[5,10−23]

The triboelectric nanogenerator (TENG) has emerged as a newly evolved energy harvesting device for transforming mechanical energy into electrical power due to the couple effect of contact electrification and electrostatic induction. Due to its high efficiency, low cost, easy availability, and eco-friendliness, TENG is applicable in harnessing small mechanical energy and large-scale energy as well.[24,25]

Recently, PENGs have attracted additional interest of scientists due to their flexibility, mechanical durability, high performance, sensitivity, etc.[22,23,26] To upgrade PENGs, various piezoelectric ceramic and metal oxide materials such as ZnO, PMN−PT, (Na, K)-$NbO_3$, $BaTiO_3$, and PZT[27−30] have been used. Apart from the piezoelectric ceramic and

Received: June 28, 2021
Accepted: September 10, 2021
Published: October 25, 2021

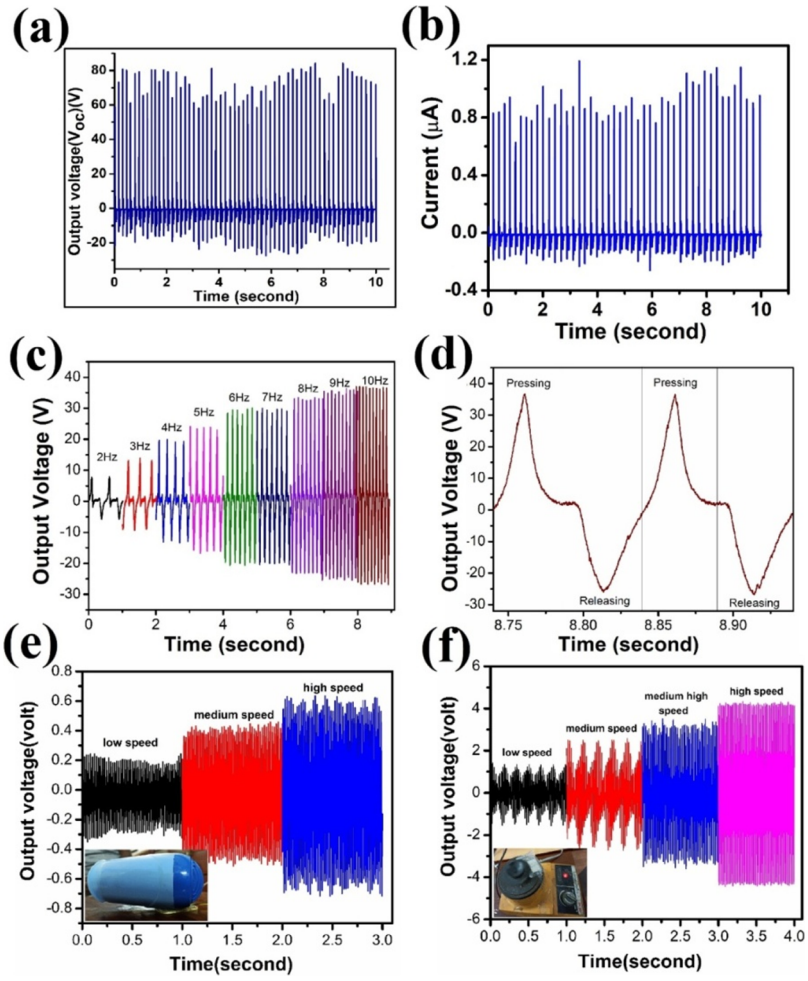


**Figure 1.** (a) Open circuit voltage ($V_{OC}$) and (b) short circuit current ($I_{SC}$) generated by human finger impartation at a frequency of ∼5 to 6 Hz. (c) Frequency-dependent $V_{OC}$. (d) Magnified view of $V_{OC}$ for two successive cycles corresponding to 10 Hz frequency under 5 N force. Voltage generation by using the vibration energy of an (e) air drier and (f) vortex machine at different speeds.

metal oxide nanomaterials, certain polymers such as polyvinylidene fluoride (PVDF),[31] its copolymers with trifluoroethylene [P(VDF-TrFE)],[32] and poly(vinlyacetate) (PVAc)[33] also show high piezoelectric properties. The announced materials have some limitations because of their toxicity, high cost, nonbiodegradability, and breakability, along with the lengthy and difficult synthesis process.[5] To address these problems, it is necessary to design devices using biodegradable, low-cost, and flexible materials for upcoming days. Therefore, amply available natural and nontoxic bio-piezoelectric materials have attracted more interest in the development of eco-friendly smart devices.[34−40] Many bio-based PENGs, using a virus,[41] fish scale,[42] fish bladder,[43] cellulose,[44] paper-$BaTiO_3$-bacterial cellulose,[45] cellulose-$BaTiO_3$,[46] biowaste crab shell,[6] and biowaste onion skin[5] as piezoelectric materials, have been studied for harnessing green energy.

Recently, biowaste material based PENGs have been reported with comparatively low output performances. Maiti et al.[5] described their study on an onion skin based PENG that showed an output voltage of ∼18 V, short circuit of ∼166 nA, and instantaneous power density of ∼1.7 $\mu$W cm$^{-2}$. A fish scale based PENG with an output voltage of 10 V and a short circuit current of 51 nA was reported by Ghosh and Mandal.[42] Due to their cost-effectiveness and recyclability, biowaste materials have attracted many researchers for harvesting electrical energy. Thus, we have designed a simple and cost-effective biowaste material based piezoelectric nanogenerator with high output performance, flexibility, high durability, and nontoxicity.

The environment-friendly *Sonchus asper* (SA) is the strongest natural polymer fiber.[47] SA is known to possess diuretic, refrigerant, sedative, and antiseptic properties and is mainly used in medical treatment.[48] Various chemical studies exposed the presence of ascorbic acid, carotenoids, and fatty acids in SA.[49] Also, the highly crystalline SA pappus forms stress-induced polarization and generates piezoelectricity.

In our study, we fabricated a PDMS/SA microfiber thin film based piezoelectric nanogenerator (SPENG) for harvesting energy from a small amount of mechanical work such as walking, talking, bending, stretching, pulse vibration, and finger imparting. SA pappus was chosen as the key component of SPENG as it is not only an abundantly available biowaste material but biocompatible, biodegradable, nontoxic, robust, sustainable, and renewable also. The PDMS/SA pappus film based PENG, named SPENG, showed a maximum output voltage ($V_{OC}$) of 81.2 V and a short circuit current ($I_{SC}$) of 1.0 $\mu$A, with an instantaneous power density of 182.06 $\mu$W cm$^{-3}$ during continuous finger impartation. Moreover, the fabricated PENG was capable of producing output voltage even in the case of low pressure of heart beats and pulses. The study


https://doi.org/10.1021/acsomega.1c03374
ACS Omega 2021, 6, 28710−28717

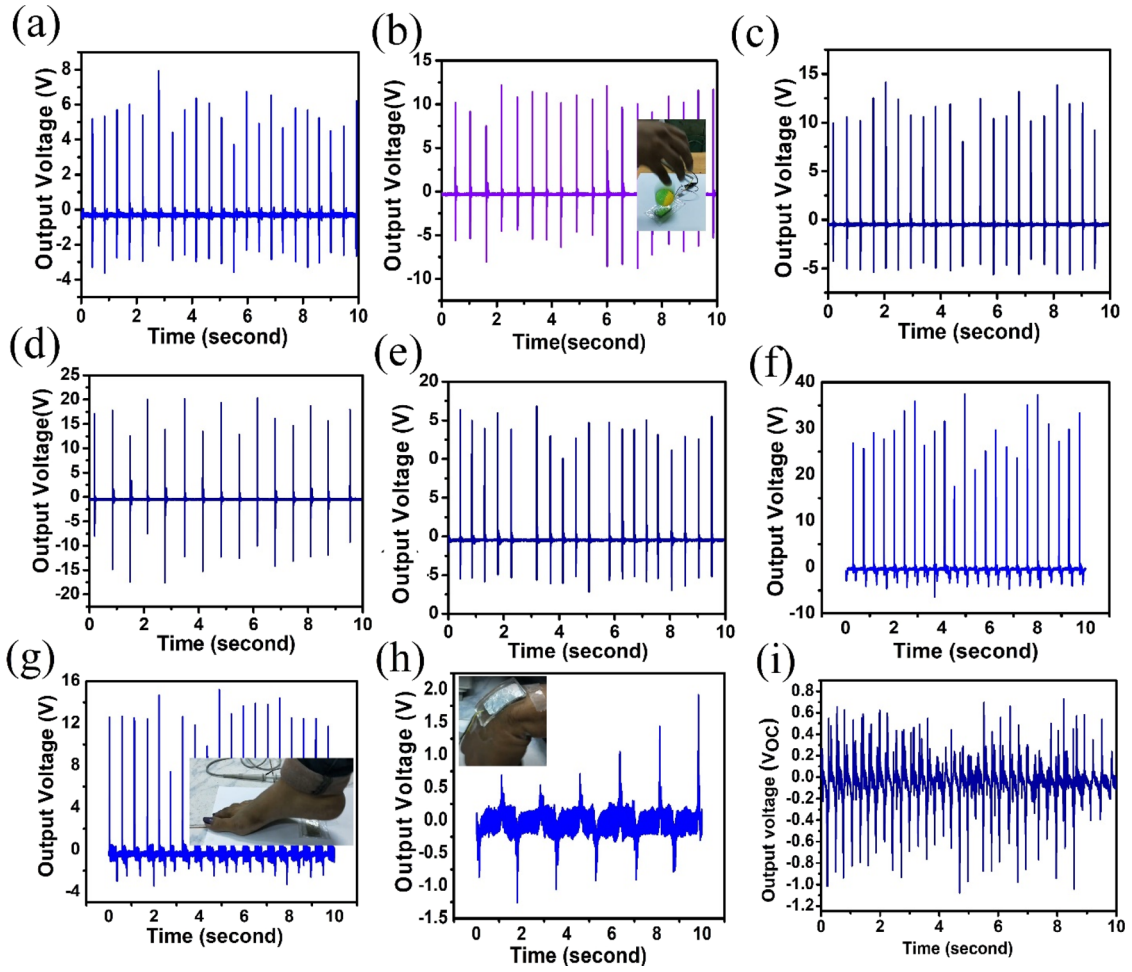


**Figure 2.** (a–e) Open circuit voltage generated by dropping balls of 108.793, 35.214, 9.18, 59.34, and 15.01 g on the device from a height of ∼10 cm. (f and g) Output voltage generated by forefoot and heel pressing. (h) Wrist bending signal. (i) Light finger touching on SPENG.

indicated the prospect of the nanogenerator SPENG as a green and portable energy harvester to power up portable electronic devices. Furthermore, after proper improvisation, the fabricated nanogenerator might be used as an energy supply for pacemakers and other types of health care devices.

## RESULTS AND DISCUSSIONS

**Output Performance.** The open circuit output voltage ($V_{OC}$) and short circuit current ($I_{SC}$) generation through human finger imparting and releasing of an axial force of ∼13.5 N with ∼5 to 6 Hz frequency is depicted in Figure 1a,b. Different output voltages were generated by the SPENG depending on the application of various forces and frequencies. We studied the voltage output performance of the SPENG by applying a uniform force of 5 N under varied frequencies ranging from 2 to 10 Hz by using a self-designed instrument (from Ocean College, Zhejiang University, PR China).

With increasing frequency of the applied forces, the output performance ($V_{OC}$) increased gradually from ∼7.5 V at 2 Hz to ∼36 V at 10 Hz (Figure 1c). The output voltage of the SPENG depended on the impedance and applied strain frequency. Even at low-pressure finger impartation, the device showed high sensitivity. The maximum output voltage (observed by Keysight, Oscilloscope DSO-X 3012A) and short circuit current (recorded by Keysight, Electrometer B2985) of the SPENG were $V_{OC}$ ∼81.2 V and $I_{SC}$ ∼1.0 $\mu$A, respectively, as shown in Figure 2a,b. It is evident from the figures that the values of both $V_{OC}$ and $I_{SC}$ were non-uniform, which differed slightly for periodic pressing and releasing by finger.

Such variation was due to the manual inconsistency of the applied strain on the energy scavenging devices during finger impartation. The enlarged view and working process of the nature of growth and decay of $V_{OC}$ for two successive cycles, generated by instrument impartation at 10 Hz frequency, are shown in the Figure 1d. The highest positive peak was obtained when the strain was applied. After withdrawal of the strain, the device recovered its original state, and consequently, the negative peak appeared. The output performance of SPENG is greater than that of any other previously reported biomaterial-based devices, given in table form in the Supporting Information (Table S1). The fabricated device was also tested by bending and twisting and the output voltage performance was recorded, but no remarkable voltage generation was found, proposing that there was negligible triboelectric effect. Also, switching polarity data have been taken and represented in Figure S2 in the Supporting Information. Recently, Lee et al.[41] presented a virus-based PENG with an output voltage of ∼0.4 V and current of ∼4 nA. Ghosh and Mandal[43] reported a piezoelectric energy harvester derived from a fish swim bladder with an output voltage of ∼10 V. Maiti et al. also reported an output voltage ($V_{OC}$) of 18 V and a short circuit current of 166 nA in the case of an onion


https://doi.org/10.1021/acsomega.1c03374
ACS Omega 2021, 6, 28710−28717

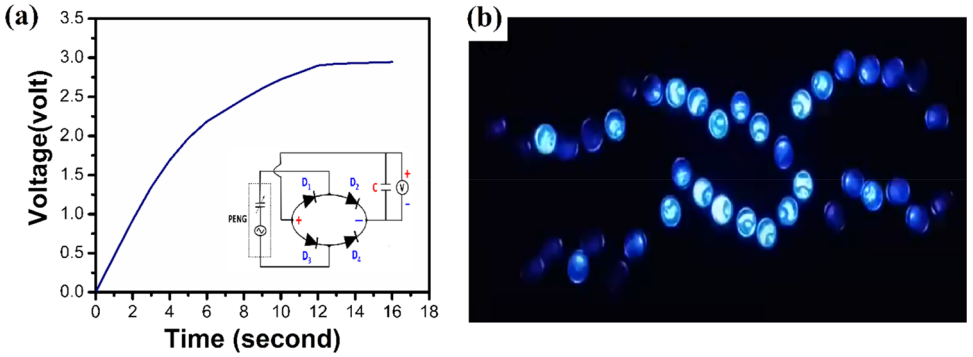


**Figure 3.** (a) Charging performance of the 2.2 $\mu$F capacitor; inset: circuit diagram for the charging capacitor and LEDs light up and (b) snapshot of LEDs in glowing condition.

skin based PENG. Hoque et al.[6] also fabricated a biowaste crab shell chitin nanofiber-based PENG with an output voltage ∼49 V and a short circuit current ∼1.9 $\mu$A. Thus, the output performance of the SA pappus based piezoelectric energy harvester, SPENG, was definitely better than that of previously reported similar bio-based devices. The SPENG also showed a high power density of ∼182.06 $\mu$W cm$^{-3}$. The details of power density and external force calculation of the fabricated SPENG are in the Supporting Information section.

Energy harvesting from different vibration energies of an air drier and vortex machine in vibrating condition was also tested. Placing the SPENG under the air drier and operating the air drier at three different settings of low, medium, and high speed, SPENG produced $V_{OC}$ ∼0.2, ∼0.42, and ∼0.6 V, respectively, as shown in Figure 1e.When attached to a vortex machine body, the SPENG showed remarkable voltage output of ∼1.3, ∼2.4, ∼3.25, and ∼4.1 V depending on the vortex rotating speed of low, medium, medium high, and high speed, respectively, as presented in Figure 1f. All the above-mentioned experimental findings show that the SPENG can harvest electrical energy quite efficiently from any kind of mechanical energy generated by vibration.

**Ultrasensitivity of the SPENG under Different Body Movements.** The fabricated SPENG was also capable of harvesting mechanical energy from the various body movements. Furthermore, the sensitivity of the fabricated device was tested by dropping balls of different masses from a height of 10 cm on the device surface, shown in Figure 2a−e. The output voltages were ∼6, ∼10, ∼12, ∼15, and ∼17 V for dropping balls of masses 108.793, 35.214, 9.18, 59.34, and 15.01 g, respectively. When balls were dropped on the device, different output voltages were produced depending on the masses of balls and the contact surface area. The ball with the maximum mass showed a low output voltage compared to the other balls due to the harder (lower elastic properties than other balls) surface of the bigger-size ball. For this reason, different pressures were generated on the nanogenerator, which resulted in different output voltages.

Figure 3f−i indicates that the self-powered flexible SPENG device was sensitive enough to utilize biomechanical energy from various body movements like heel and forefoot pressing, wrist up−down movement, and just finger touch. High output voltages were obtained during forefoot pressing (∼36 V) and heel pressing (∼15 V) by attaching the device to the foot and heel, depicted in Figure 2f−g. The generated output voltage during forefoot pressing was greater than that during heel pressing. A possible reason behind this result may be the greater contact surface area for the forefoot with device than the heel with device surface. The maximum output voltage during wrist movement is ∼1.9 V, as represented in Figure 2h, which also confirms the capability of the SPENG device in harvesting green energy from body movement. The sensitivity was further checked by just touching the device with a finger, where $V_{OC}$ was ∼0.65 V (Figure 2i). The results indicate that the fabricated SPENG is competent enough to detect even a minute amount of pressure and convert the mechanical energy, caused by the application of pressure, into electrical energy. The output voltage was recorded each month over the course of a year to check the stability of our device, and results suggested that the experimental device possessed almost the same performances throughout the year. Thus, the fabricated SPENG is cost-effective, biocompatible, flexible, and sustainable, which, after proper improvisation, can charge biomedical devices by utilizing the biological pressure from various body movements, muscle contraction/relaxation, and blood circulation.

Moreover, the experimental SPENG can be used to harness energy from a wide range of green biomechanical energy resources by attaching the SPENG to running machines like treadmills, dancing floors, interior of shoes, wheels of cars, etc. The electrical energy produced can also be used to switch on LEDs, LCD screens, and other different types of battery charging equipment.

**Working Principle of the Fabricated SPENG.** The performances of SPENG can be explained with the help of the synergetic effect of the electro activity. Most of the biomaterials such as cellulose, gelatin, chitin, and collagen exhibit shear piezoelectricity due to their fibrous configuration. Such piezoelectric effect is due to the internal rotation of polar atomic groups, which are interrelated with the asymmetric carbon atom.[50,51] SA pappus is composed of an amide linkage, −OH groups, and carbonyl groups arranged in $\alpha$-helical and $\beta$-sheet structures. In the SA pappus, $\alpha$-helical and $\beta$-sheet elastic structures of amino acids are connected strongly through intra- and intermolecular H-bonding among themselves.[30] Due to the high aspect ratio of SA pappus fibers in conjunction with the strong hydrogen bonding energy and high binding energy, these fibers can be used undoubtedly as bio-piezo materials. The presence of amide and hydroxyl groups assists SA pappus to produce electric dipoles inside the fiber. These dipoles show a high piezoelectric response under applied external strain. Under mechanical compression, highly crystalline SA pappus forms stress-induced polarization and generates piezoelectricity. Thus, SA pappus is a promising piezoelectric material


https://doi.org/10.1021/acsomega.1c03374
ACS Omega 2021, 6, 28710−28717

that has the capability to generate output voltage under applied mechanical compression.

The working principle of the experimental device (SPENG) depends primarily on the changes in the molecular structure of SA pappus under mechanical stress. Application of vertical pressure on the PENG causes the movement of total polarization charge toward the electrodes, which acts as the key for the generation of piezoelectric potential across the two electrodes.[52] Thus, the applied vertical force eventually initiates the accumulation of positive and negative charges separately on two electrodes and thus generates a positive voltage signal. The polarization charge increases with increasing magnitude of mechanical force and frequency of vibration. When the vertical strain is released, the collected charges on the electrodes move toward the reverse direction, and hence, a negative signal is produced. Due to the coincidence of the negative signal and weak damped piezoelectric potential, we observe the first negative potential peak. Again, a small positive signal, indicated by the second positive peak, is observed due to the assemblage of free charges at the electrodes. After returning to the original state, the accumulated electrons fall back again and give a second negative peak. The second positive and negative signal peaks occur due to the damping effect of devices. Thus, a continuous pulse or the application of an external force is the main source to obtain the output performances of PENG.

For the piezoelectric effect, $\sigma_p(z)$ = piezoelectric polarization charge density of PENG and $\sigma(x)$ = free electron charge density in the electrode.

Considering the strain introduced by the applied compression, $\sigma(x)$ is a function of the thickness of the device ($z$). Now, for the mechanical force, the piezoelectric equation and constituter are given by:

$$P_i = (e)_{ijk}(S)_{jk} \tag{1}$$

$$T = C^E S - e^T E \tag{2}$$

$$D = \varepsilon S - \varepsilon E \tag{3}$$

where $(e)_{ijk}$ denotes the piezoelectric third-order tensor and $S$ is the mechanical strain. $C^E$ and $T$ are the elasticity tensor and stress tensor, and $\varepsilon$ is the dielectric tensor.

Due to media polarization, the displacement current can be expressed as follows:

$$J_{Di} = \frac{\partial Pi}{\partial t} \tag{4}$$

Equation 4 illustrates that the changing rate of the applied strain is proportional to the output current density of the PENG. The frequency dependence of output performance of the device (shown in the Figure 1c) matches well with eq 4.

**Realistic Application of SPENG.** The ability of the fabricated SPENG to charge a 2.2 $\mu$F capacitor was investigated by connecting the device with the capacitor through a simple bridge rectifier circuit (Figure 3a inset) and switching on the SPENG by periodic finger impartation at a frequency ∼5−6 Hz. The exponential nature of the time−voltage curve during the charging (Figure 3a) of the capacitor indicated a high energy storage capability. Using SPENG, the capacitor (2.2 $\mu$F) was charged up to 3.2 V within 16 s under periodic finger impartation. So, we can easily state that the charging efficiency of SPENG is higher than that of any other previously reported biowaste-based PENGs. Since the charging ability of SPENG is very high, it can be used as an alternative energy source for portable or medical devices via capacitor charging. Figure 3b shows the competence of the SPENG to light up LEDs under continuous finger impartation. The power produced from SPENG can illuminate 39 blue LEDs connected through a full wave bridge rectifier. The video is in the Supporting Information (Video S1).

## CONCLUSIONS

The observations of the studies indicated that the naturally and amply available fiber of *Sonchus asper* pappus, being piezoelectric in nature, might be successfully employed to develop a bio-inspired nanogenerator (SPENG). The fabricated SPENG performed quite efficiently to harvest waste energy from various mechanical and biomechanical movements. Electrical energy was produced by harnessing the mechanical energy from various living and nonliving sources. This biocompatible equipment was capable of generating a high output voltage ($V_{OC}$) of ∼81.2 V and a short circuit current ($I_{SC}$) of ∼1.0 $\mu$A under periodic finger imparting and releasing (with an axial force of 13.5 N) with an average frequency of 6 Hz. The calculated instant power density of the device was 182.06 $\mu$W cm$^{-3}$. The fabricated SPENG showed remarkable response in exploiting the vibration energy of the vortex mixture (∼6 V) and low force impact of the 9.8 g ball falling from 10 cm height on the surface of SPENG (∼15 V). The device was sensitive enough to respond to mere hand movement and finger touching on it. The realistic application of SPENG was verified by successfully lighting up to 39 blue LEDs connected in series via finger impartation only and also by charging a capacitor (2.2 $\mu$F) to 3.2 V within a very short span time (16 s). All the results were reproducible, and SPENG showed an exceptionally good mechanical stability with brilliant performances for a year that indicated the excellent sustainability of the experimental device.

The bio-piezoelectric material, SA pappus, collected from natural waste material is a low-cost and easily and amply available green energy material, which can be successfully utilized in several renewable energy applications. The flexible, biocompatible, and biodegradable SPENG, made of SA pappus, has the prospect to be used in different handy gadgets as an energy harvester, which can convert mechanical energy from different sources easily available in the environment. After proper improvisation, the device may certainly be used in many in vivo applications as an energy harvester, which has been proven to be proficient enough to convert biomechanical energy, even when negligibly small, into a usable form of electrical energy.

## MATERIALS AND METHODS

***Sonchus asper* (SA) Cotton Pappus Purification.** *Sonchus asper* (SA) cotton pappus was collected from the Jadavpur University campus (Kolkata, India). Collected cotton fibers were washed with deionized water and dried at 100 °C for 4 h. The cotton was further purified by 100 mL of hydrogen peroxide (Merck India) and 100 mL of acetic acid (Alfa Aesar) at 80 °C for 24 h to eliminate the chemicals. Finally, the samples were washed several times with deionized water and dried overnight (15 h) at 100 °C.

**Piezoelectric Nanogenerator Fabrication.** The device was fabricated by polydimethylsiloxane (PDMS), SA, aluminum electrodes, and copper wires. Two percent of SA pappus



https://doi.org/10.1021/acsomega.1c03374
ACS Omega 2021, 6, 28710−28717

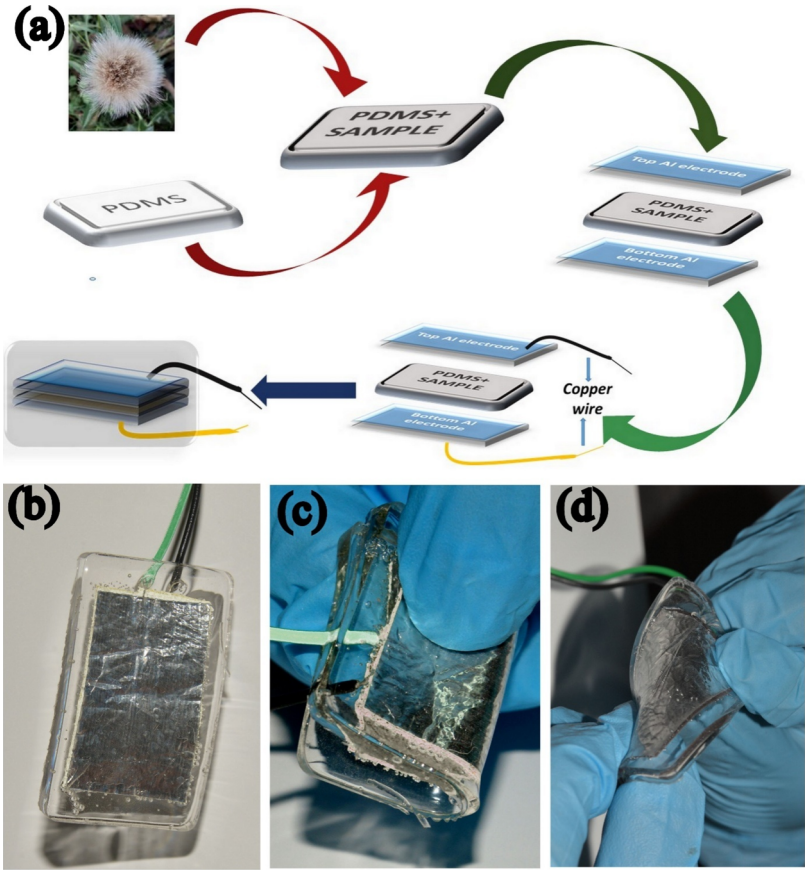


**Figure 4.** (a) Schematic representation of the SPENG fabrication procedure. (b–d) Digital photograph of SPENG and flexibility representation of the fabricated device.

was mixed thoroughly with 2 g of PDMS (Sylgard 184, Dow Corning, ratio of 10:1) into a rectangular plastic mold with a dimension of 5 × 3 cm. To make the bubble-free composite, the solution was kept for 15 min under vacuum. After getting the bubble-free solution, the polymer composite was kept at 60 °C in a hot air oven for 15 min to get the polymer/SA fiber film (thickness 0.59 mm). Two aluminum electrodes (dimension 3.6 × 2.1 cm) both connected with 15 cm long copper wires were attached to the wide sides of the composite film. Finally, the assembly of the thin film along with the attached electrode was encapsulating the assembly with PDMS. Figure 4a shows the schematic representation of device (SPENG) fabrication procedures. The digital photograph of the PENG and its flexibility are represented in Figure 4b–d. The X-ray diffraction pattern and FESEM images of cotton pappus have been included in the Supporting Information Section S1.

## ■ ASSOCIATED CONTENT

### Supporting Information

The Supporting Information is available free of charge at https://pubs.acs.org/doi/10.1021/acsomega.1c03374.

FESEMimages and the X-ray diffraction pattern of the SA cotton pappus (Figure S1); output voltage switching polarity test (Figure S2); and comparison of output performance and power density of our fabricated PENG (SPENG) with the previously reported bio-based PENGs (Table S1) (PDF)

Video of illuminating 39 blue LEDs with the help of SPENG (MP4)

## ■ AUTHOR INFORMATION


### Corresponding Authors

**Sukhen Das** − *Department of Physics, Jadavpur University, Kolkata, West Bengal 700032, India;* orcid.org/0000-0001-8372-3076; Phone: 9433091337; Email: sdasphysics@gmail.com

**Nur Amin Hoque** − *Department of Marine Information Technology, Ocean College, Zhejiang University, Zhoushan 316021, PR China; Department of Physics, IISER Mohali, Sahibzada Ajit Singh Nagar, Punjab 140306, India;* orcid.org/0000-0003-1133-018X; Phone: +919836964481; Email: nuramin03@gmail.com

**Ruma Basu** − *Department of Physics, Jogamaya Devi College, Kolkata, West Bengal 700026, India;* Phone: +919433115930; Email: ruma.b1959@gmail.com

### Authors

**Debmalya Sarkar** − *Department of Physics, Jadavpur University, Kolkata, West Bengal 700032, India*

**Namrata Das** − *Department of Physics, Jadavpur University, Kolkata, West Bengal 700032, India*

**Md. Minarul Saikh** − *Department of Physics, Jadavpur University, Kolkata, West Bengal 700032, India; General Degree College at Pedong, Kalimpong, West Bengal 734311, India*

**Prosenjit Biswas** − *Department of Physics, Kalimpong College, Kalimpong, West Bengal 734301, India*




https://doi.org/10.1021/acsomega.1c03374
ACS Omega 2021, 6, 28710−28717

**Solanky Das** − *Department of Physics, Jadavpur University, Kolkata, West Bengal 700032, India*

Complete contact information is available at: https://pubs.acs.org/10.1021/acsomega.1c03374

### Notes

The authors declare no competing financial interest.

## ■ ACKNOWLEDGMENTS

The authors appreciate the financial assistance from the University Grant Commission (UGC), Government of India; FIST; and the PURSE program of DST, Government of India.

## ■ REFERENCES

(1) Wang, Z. L.; Song, J. Piezoelectric Nanogenerators Based on Zinc Oxide Nanowire Arrays. *Science* **2006**, *312*, 242−246.
(2) Qin, Y.; Wang, X.; Wang, Z. L. Microfibre−nanowire hybrid structure for energy scavenging. *Nature* **2008**, *451*, 809−813.
(3) Yang, R.; Qin, Y.; Dai, L.; Wang, Z. L. Power generation with laterally packaged piezoelectric fine wires. *Nat. Nanotechnol.* **2009**, *4*, 34−39.
(4) Mao, Y.; Zhao, P.; McConohy, G.; Yang, H.; Tong, Y.; Wang, X. Sponge-Like Piezoelectric Polymer Films for Scalable and Integratable Nanogenerators and Self-Powered Electronic Systems. *Adv. Energy Mater.* **2014**, *4*, 1301624.
(5) Maiti, S.; Karan, S. K.; Lee, J.; Mishra, A. K.; Khatua, B. B.; Kim, J. K. Bio-waste onion skin as an innovative nature-driven piezoelectric material with high energy conversion efficiency. *Nano Energy* **2017**, *42*, 282−293.
(6) Hoque, N. A.; Thakur, P.; Biswas, P.; Saikh, M. M.; Roy, S.; Bagchi, B.; Das, S.; Ray, P. P. Biowaste crab shell-extracted chitin nanofiber-based superior piezoelectric nanogenerator. *J. Mater. Chem. A* **2018**, *6*, 13848−13858.
(7) Hoque, N. A.; Thakur, P.; Roy, S.; Kool, A.; Bagchi, B.; Biswas, P.; Saikh, M. M.; Khatun, F.; Das, S.; Ray, P. P. $Er^{3+}/Fe^{3+}$ Stimulated Electroactive, Visible Light Emitting, and High Dielectric Flexible PVDF Film Based Piezoelectric Nanogenerators: A Simple and Superior Self-Powered Energy Harvester with Remarkable Power Density. *ACS Appl. Mater. Interfaces* **2017**, *9*, 23048−23059.
(8) Wang, Z. L. On Maxwell's displacement current for energy and sensors: the origin of nanogenerators. *Mater. Today* **2017**, *20*, 74−82.
(9) Wang, X.; Yang, B.; Liu, J.; Yang, C. A transparent and biocompatible single-friction-surface triboelectric and piezoelectric generator and body movement sensor. *J. Mater. Chem. A* **2017**, *5*, 1176−1183.
(10) Shin, S. H.; Bae, Y. E.; Moon, H. K.; Kim, J.; Choi, S. H.; Kim, Y.; Yoon, H. J.; Lee, M. H.; Nah, J. Formation of Triboelectric Series via Atomic-Level Surface Functionalization for Triboelectric Energy Harvesting. *ACS Nano* **2017**, *11*, 6131−6138.
(11) Han, M.; Zhang, X. S.; Meng, B.; Liu, W.; Tang, W.; Sun, X.; Wang, W.; Zhang, H. r-Shaped Hybrid Nanogenerator with Enhanced Piezoelectricity. *ACS Nano* **2013**, *7*, 8554−8560.
(12) Chen, J.; Yang, J.; Guo, H.; Li, Z.; Zheng, L.; Su, Y.; Wen, Z.; Fan, X.; Wang, Z. L. Automatic Mode Transition Enabled Robust Triboelectric Nanogenerators. *ACS Nano* **2015**, *9*, 12334−12343.
(13) Wang, X.; Yang, B.; Liu, J.; Zhu, Y.; Yang, C.; He, Q. A flexible triboelectric-piezoelectric hybrid nanogenerator based on P(VDF-TrFE) nanofibers and PDMS/MWCNT for wearable devices. *Sci. Rep.* **2016**, *6*, 36409.
(14) Xu, Q.; Wen, J.; Qin, Y. Development and outlook of high output piezoelectric nanogenerators. *Nano Energy* **2021**, *86*, 106080.
(15) Hinchet, R.; Ghaffarinejad, A.; Lu, Y.; Hasani, J. Y.; Kim, S.-W.; Basset, P. Understanding and modeling of triboelectric-electret nanogenerator. *Nano Energy* **2018**, *47*, 401−409.
(16) Su, H.; Wang, X.; Li, C.; Wang, Z.; Wu, Y.; Zhang, J.; Zhang, Y.; Zhao, C.; Wu, J.; Zheng, H. Enhanced energy harvesting ability of polydimethylsiloxane-BaTiO3-based flexible piezoelectric nanogenerator for tactile imitation application. *Nano Energy* **2021**, *83*, 105809.
(17) Dong, K.; Wang, Y. C.; Deng, J.; Dai, Y.; Zhang, S. L.; Zou, H.; Gu, B.; Sun, B.; Wang, Z. L. A Highly Stretchable and Washable All-Yarn-Based Self-Charging Knitting Power Textile Composed of Fiber Triboelectric Nanogenerators and Supercapacitors. *ACS Nano* **2017**, *11*, 9490−9499.
(18) Wang, Z. L.; Chen, J.; Lin, L. Progress in triboelectric nanogenerators as a new energy technology and self-powered sensors. *Energy Environ. Sci.* **2015**, *8*, 2250−2282.
(19) Gu, L.; Liu, J.; Cui, N.; Xu, Q.; Du, T.; Zhang, L.; Wang, Z.; Long, C.; Qin, Y. Enhancing the current density of a piezoelectric nanogenerator using a three-dimensional intercalation electrode. *Nat. Commun.* **2020**, *11*, 1030.
(20) Zhang, Y.; Wu, M.; Zhu, Q.; Wang, F.; Su, H.; Li, H.; Diao, C.; Zheng, H.; Wu, Y.; Wang, Z. L. Performance Enhancement of Flexible Piezoelectric Nanogenerator via Doping and Rational 3D Structure Design For Self-Powered Mechanosensational System. *Adv. Funct. Mater.* **2019**, *29*, 1904259.
(21) Erturun, U.; Eisape, A. A.; Kang, S. H.; West, J. E. Energy harvester using piezoelectric nanogenerator and electrostatic generator. *Appl. Phys. Lett.* **2021**, *118*, No. 063902.
(22) Karan, S. K.; Bera, R.; Paria, S.; Das, A. K.; Maiti, S.; Maitra, A.; Khatua, B. B. An Approach to Design Highly Durable Piezoelectric Nanogenerator Based on Self-Poled PVDF/AlO-rGO Flexible Nanocomposite with High Power Density and Energy Conversion Efficiency. *Adv. Energy Mater.* **2016**, *6*, 1601016.
(23) Shin, S.-H.; Kim, Y.-H.; Lee, M. H.; Jung, J.-Y.; Seol, J. H.; Nah, J. Lithium-Doped Zinc Oxide Nanowires−Polymer Composite for High Performance Flexible Piezoelectric Nanogenerator. *ACS Nano* **2014**, *8*, 10844−10850.
(24) Pu, X.; Li, L.; Song, H.; Du, C.; Zhao, Z.; Jiang, C.; Cao, G.; Hu, W.; Wang, Z. L. A Self-Charging Power Unit by Integration of a Textile Triboelectric Nanogenerator and a Flexible Lithium-Ion Battery for Wearable Electronics. *Adv. Mater.* **2015**, *27*, 2472−2478.
(25) Wang, Z. L. Triboelectric Nanogenerators as New Energy Technology for Self-Powered Systems and as Active Mechanical and Chemical Sensors. *ACS Nano* **2013**, *7*, 9533.
(26) Sun, C.; Shi, J.; Bayerl, D. J.; Wang, X. PVDF microbelts for harvesting energy from respiration. *Energy Environ. Sci.* **2011**, *4*, 4508−4512.
(27) Chung, S. Y.; Kim, S.; Lee, J.-H.; Kim, K.; Kim, S.-W.; Kang, C.-Y.; Yoon, S.-J.; Kim, Y. S. All-Solution-Processed Flexible Thin Film Piezoelectric Nanogenerator. *Adv. Mater.* **2012**, *24*, 6022−6027.
(28) Park, K. I.; Jeong, C. K.; Ryu, J.; Hwang, G. T.; Lee, K. J. Flexible and Large-Area Nanocomposite Generators Based on Lead Zirconate Titanate Particles and Carbon Nanotubes. *Adv. Energy Mater.* **2013**, *3*, 1539−1544.
(29) Yan, J.; Jeong, Y. G. High Performance Flexible Piezoelectric Nanogenerators based on $BaTiO_3$ Nanofibers in Different Alignment Modes. *ACS Appl. Mater. Interfaces* **2016**, *8*, 15700−15709.
(30) Koka, A.; Sodano, H. A. A Low-Frequency Energy Harvester from Ultralong, Vertically Aligned $BaTiO_3$ Nanowire Arrays. *Adv. Energy Mater.* **2014**, *4*, 1301660.
(31) Karan, S. K.; Mandal, D.; Khatua, B. B. Self-powered flexible Fe-doped RGO/PVDF nanocomposite: an excellent material for a piezoelectric energy harvester. *Nanoscale* **2015**, *7*, 10655−10666.
(32) Whiter, R. A.; Narayan, V.; Kar-Narayan, S. A Scalable Nanogenerator Based on Self-Poled Piezoelectric Polymer Nanowires with High Energy Conversion Efficiency. *Adv. Energy Mater.* **2014**, *4*, 1400519.
(33) Paria, S.; Karan, S. K.; Bera, R.; Das, A. K.; Maitra, A.; Khatua, B. B. A Facile Approach To Develop a Highly Stretchable PVC/ZnSnO3 Piezoelectric Nanogenerator with High Output Power Generation for Powering Portable Electronic Devices. *Ind. Eng. Chem. Res.* **2016**, *55*, 10671−10680.
(34) Kim, H.-J.; Kim, J.-H.; Jun, K.-W.; Kim, J.-H.; Seung, W.-C.; Kwon, O.-H.; Park, J.-Y.; Kim, S.-W.; Oh, I.-K. Silk Nanofiber-

Networked Bio-Triboelectric Generator: Silk Bio-TEG. *Adv. Energy Mater.* **2016**, *6*, 1502329.
(35) Tollefson, J. Blue energy: after years in the doldrums, the quest to harvest energy from the oceans is gathering speed. *Nature* **2014**, *508*, 302.
(36) Jiang, W.; Li, H.; Liu, Z.; Li, Z.; Tian, J.; Shi, B.; Zou, Y.; Ouyang, H.; Zhao, C.; Zhao, L.; Sun, R.; Zheng, H.; Fan, Y.; Wang, Z. L.; Li, Z. Fully Bioabsorbable Natural-Materials-Based Triboelectric Nanogenerators. *Adv. Mater.* **2018**, *30*, 1801895.
(37) Zheng, Q.; Zou, Y.; Zhang, Y.; Liu, Z.; Shi, B.; Wang, X.; Jin, Y.; Ouyang, H.; Li, Z.; Wang, Z. L. Biodegradable triboelectric nanogenerator as a life-time designed implantable power source. *Sci. Adv.* **2016**, *2*, e1501478.
(38) Chao, S.; Ouyang, H.; Jiang, D.; Fan, Y.; Li, Z. Triboelectric nanogenerator based on degradable materials. *EcoMat* **2021**, *3*, 12072.
(39) Zhang, G.; Liao, Q.; Ma, M.; Zhang, Z.; Si, H.; Liu, S.; Zheng, X.; Dinga, Y.; Zhang, Y. A rationally designed output current measurement procedure and comprehensive understanding of the output characteristics for piezoelectric nanogenerators. *Nano Energy* **2016**, *30*, 180−186.
(40) Shin, D.-M.; Han, H. J.; Kim, W.-G.; Kim, E.; Kim, C.; Hong, S. W.; Kim, H. K.; Oh, J.-W.; Hwang, Y.-H. Bioinspired piezoelectric nanogenerators based on vertically aligned phage nanopillars. *Energy Environ. Sci.* **2015**, *8*, 3198−3203.
(41) Lee, B. Y.; Zhang, J.; Zueger, C.; Chung, W.-J.; Yoo, S. Y.; Wang, E.; Meyer, J.; Ramesh, R.; Lee, S.-W. Virus-based piezoelectric energy generation. *Nat. Nanotechnol.* **2012**, *7*, 351−356.
(42) Ghosh, S. K.; Mandal, D. High-performance bio-piezoelectric nanogenerator made with fish scale. *Appl. Phys. Lett.* **2016**, *109*, 103701.
(43) Ghosh, S. K.; Mandal, D. Efficient natural piezoelectric nanogenerator: Electricity generation from fish swim bladder. *Nano Energy* **2016**, *28*, 356−365.
(44) Rajala, S.; Siponkoski, T.; Sarlin, E.; Mettänen, M.; Vuoriluoto, M.; Pammo, A.; Juuti, J.; Rojas, O. J.; Franssila, S.; Tuukkanen, S. Cellulose Nanofibril Film as a Piezoelectric Sensor Material. *ACS Appl. Mater. Interfaces* **2016**, *8*, 15607−15614.
(45) Zhang, G.; Liao, Q.; Zhang, Z.; Liang, Q.; Zhao, Y.; Zheng, X.; Zhang, Y. Novel Piezoelectric Paper-Based Flexible Nanogenerators Composed of $BaTiO_3$ Nanoparticles and Bacterial Cellulose. *Adv. Sci.* **2016**, *3*, 1500257.
(46) Mahadeva, S. K.; Walus, K.; Stoeber, B. Piezoelectric Paper Fabricated via Nanostructured Barium Titanate Functionalization of Wood Cellulose Fibers. *ACS Appl. Mater. Interfaces* **2014**, *6*, 7547−7553.
(47) Khan, R. A.; Khan, M. R.; Sahreen, S.; Ahmed, M. Evaluation of phenolic contents and antioxidant activity of various solvent extracts of Sonchus asper (L.) Hill. *Chem. Cent. J.* **2012**, *6*, 12−17.
(48) Khan, R. A.; Khan, M. R.; Sahreen, S. Protective effect of Sonchus asper extracts against experimentally induced lung injuries in rats: A novel study. *Exp. Toxicol. Pathol.* **2012**, *64*, 725−731.
(49) Afolayan, A. J.; Jimoh, F. O. Nutritional quality of some wild leafy vegetables in South Africa. *Int. J. Food Sci. Nutr.* **2009**, *60*, 424−431.
(50) Roy, S.; Thakur, P.; Hoque, N. A.; Bagchi, B.; Sepay, N.; Khatun, F.; Kool, A.; Das, S. Electroactive and High Dielectric Folic Acid/PVDF Composite Film Rooted Simplistic Organic Photovoltaic Self-Charging Energy Storage Cell with Superior Energy Density and Storage Capability. *ACS Appl. Mater. Interfaces* **2017**, *9*, 24198−24209.
(51) Thakur, P.; Kool, A.; Bagchi, B.; Hoque, N. A.; Das, S.; Nandy, P. In situ synthesis of $Ni(OH)_2$ nanobelt modified electroactive poly(vinylidene fluoride) thin films: remarkable improvement in dielectric properties. *RSC Adv.* **2015**, *5*, 28487.
(52) Ding, R.; Zhang, X.; Chen, G.; Wang, H.; Kishor, R.; Xiao, J.; Gao, F.; Zeng, K.; Chen, X.; Sun, X. W.; Zheng, Y. High-performance piezoelectric nanogenerators composed of formamidinium lead halide perovskite nanoparticles and poly(vinylidene fluoride). *Nano Energy* **2017**, *37*, 126−135.


https://doi.org/10.1021/acsomega.1c03374
*ACS Omega* 2021, 6, 28710−28717

Ceramics International 49 (2023) 5466–5478

Contents lists available at ScienceDirect

Ceramics International

journal homepage: www.elsevier.com/locate/ceramint

# High β-crystallinity comprising nitrogenous carbon dot/PVDF nanocomposite decorated self-powered and flexible piezoelectric nanogenerator for harvesting human movement mediated energy and sensing weights

Debmalya Sarkar [a], Namrata Das [a], Md Minarul Saikh [a,b], Prosenjit Biswas [c], Shubham Roy [a], Sumana Paul [d], Nur Amin Hoque [e,*], Ruma Basu [f,**], Sukhen Das [a,***]

[a] Department of Physics, Jadavpur University, Kolkata, 700032, West Bengal, India
[b] Government General Degree College at Pedong, Kalimpong, 734311, West Bengal, India
[c] Department of Physics, Kalimpong College, Kalimpong, 734301, West Bengal, India
[d] Department of Physics, Indian Institute of Technology Guwahati, Guwahati, 781039, India
[e] Department of Physics, IISER Mohali, Sahibzada Ajit Singh Nagar, Punjab, 140306, India
[f] Department of Physics, Jogamaya Devi College, Kolkata, 700026, West Bengal, India

ARTICLE INFO

*Keywords:*
Nitrogen doped C-dot
Density functional theory
Piezoelectricity
Human movement-mediated energy harvester
Weight sensor

ABSTRACT

This work reports a flexible and wearable nanocomposite made of nitrogen doped carbon dot (N-CD) modified PVDF (PCD) nanocomposite assisted piezoelectric device (PPNCD) that can harvest different forms of mechanical energy and convert them into electrical energy. The efficacy of this device is dependent upon its 'sandwiched' structure made of PCD nanocomposite wrapped with aluminum electrodes on both sides. Herein, N-doped CD has been incorporated into PVDF matrix for obtaining maximum β-crystalline phase (F(β) ~ 80.4%), which is confirmed by XRD, FTIR and DSC analysis. The polarizability of the PCD nanocomposite has a great contribution to the total output performance of the device. The polarizability of the film has been measured by using a standard density functional approach. The piezoelectric coefficient ($d_{33}$) has also been calculated, which is found to be 29 pC/N. Such augmented electrical parameters and enhanced piezoelectric coefficient are further utilized to fabricate the PPNCD device, which is capable to detect human body movements efficiently and can act as a weight sensor with a sensitivity of 10.2 V/kPa (up to 0.5 kPa). Moreover, this device provides a power density of 1979.87μWcm$^{-3}$ and exhibits an exceptional output performance ($V_{OC}$ ~ 80V) under periodic finger impartations in comparison to other carbon based piezoelectric nanogenerators. The PPNCD device can illuminate 15 blue/white LEDs and charge a 2.2 μF capacitor within a few seconds under continuous finger impartations. Such a multifunctional device could be a promising candidate for both healthcare monitoring systems and their power supplies.

## 1. Introduction

The global energy crisis is increasing rapidly with the speedy development of the worldwide economy [1–3].In addition, with the continuous growth of human civilization, non-renewable energy resources such as coal, petroleum, natural gas, fossil fuels, firewood, etc., are limiting day by day [4,5]. As a result, renewable energy sources have become the only option to solve this energy crisis by generating electricity [6–10]. To address this problem, several renewable energy resources, such as solar energy, mechanical motion, tidal energy, thermal energy, biomass energy, etc., which are easily available in nature, are utilized to obtain the useable form of energy [11–16]. Among them, mechanical energy is available quite effortlessly in our daily activities. Several researchers have reported that mechanical energies involved in

* Corresponding author.
** Corresponding author.
*** Corresponding author.
*E-mail addresses:* nuramin03@gmail.com (N.A. Hoque), ruma.b1959@gmail.com (R. Basu), sdasphysics@gmail.com (S. Das).

https://doi.org/10.1016/j.ceramint.2022.10.070
Received 12 September 2022; Received in revised form 29 September 2022; Accepted 6 October 2022
Available online 10 October 2022

everyday human movement activities, like walking, running, talking, etc., can be used in electrical energy generation1 [7–19]. Thus, piezoelectric nanogenerators (PENG) have attracted great interest in generating electrical energy from various mechanical energy sources by using different piezoelectric materials [20–22]. For the development of PENG, several piezoelectric nanomaterials and ceramics such as ZnO, PZT, $BaTiO_3$, PMN-PT, $ZnSnO_3$, (Na, K)–$NbO_3$ have been used widely. Versatile use of these materials has been limited due to their heavy weight and non-flexible nature [21–25]. In search to resolve the difficulty, polymers have appeared as the most promising material to design lightweight, flexible, cost-effective, and eco-friendly PENGs [20,26].

Recently, different types of piezoelectric materials like quantum dots, perovskite materials, oxide materials, biomaterials, etc., have been used to design the active layer of various optoelectronic devices, for example, light-emitting diodes (LEDs), solar cells, photodetectors and piezoelectric energy harvester. Among them, quantum dots have attracted immense interest in developing PENGs because of their high surface-to-volume ratio and very high electrical activity. So, quantum dots and polymer matrix-based nanocomposites have been fabricated to enhance the piezoelectric properties. These nanocomposites are used as piezoelectric layer for fabricating PENGs [27–29]. Cai et al. reported carbon black/graphene and PVDF-based films for harvesting energy [30].Alam et al. investigated $TiO_2$/PVDF-HFP nanofiber-based nanogenerator to harvest acoustic energy [31]. A triboelectric nanogenerator for harvesting energy and a gesture sensing application was reported by Chen et al.[32a]. PVDF and its copolymers have been used in energy harvesting applications as the materials are eco-friendly, electroactive, hydrophobic, of low cost and flexible [30]. With this in mind, we have fabricated Carbon dot incorporated PVDF nanocomposites to investigate the optical properties of nanocomposites and enhance the piezoelectric worth of the PENG.

Polyvinylidene fluoride (PVDF) is a highly non-reactive, thermoplastic, semi-crystalline fluoropolymer. Depending on the bond orientation of $–CH_2$ and $–CF_2$ dipoles, it consists of five crystalline polymorphic phases namely α, β, γ, δ and ε [20]. Among them, α, β and γ are the most common phases of PVDF. Here non-polar α crystalline phase (TGTG' dihedral conformation) is obtained directly through the melting process. Having all-trans (TTTT) conformation, the β crystalline phase is the polar and most crucial phase of PVDF, exhibiting the highest piezoelectric, pyroelectric, ferroelectric, and dielectric properties compared to other phases of PVDF [33–35]. The γ crystalline phase shows average piezoelectric properties due to its TTTGTTG' conformation [36,37]. Thus, a simple and cost-effective method is required to develop the electroactive β crystalline phase nucleation of PVDF to optimize their applications in diverse fields. "Poling" is the traditional procedure for nucleating the β crystalline phase in PVDF. Apart from these processes, self-poled electroactive PVDF can be achieved easily by incorporating nano/micro-fillers such as metal oxide, nanoparticles of metals and metal salts, carbon nanotube, ceramic nanoparticles, clays, and organic molecule, etc.[33-38]Nowadays, a single device with various applications has attracted immense interest in research and industry [39–42]. Thus, the orientation of polar β-phase of PVDF and optical absorption property of carbon dot play an essential role in making a composite, possessing diverse properties. We can use this composite to design a mechanical energy harvester and a photodetector as well [43].

Carbon dots (CDs) are quasi-spherical nanoparticles having diameters of less than 10nm. These CDs, a new member of the nanocarbon family was discovered in 2004. Besides being eco-friendly, the CDs possess many fold advantages such as good solubility, biocompatibility, conductivity, light bleaching property etc. The main advantage of using Carbon dots is that they have excellent photoluminescence properties, the reason behind their outstanding performance in biological sensing, fluorescence labeling, chemical sensing, and light-emitting diodes [44, 46]. CDs can be treated as a shell-core material. The central carbon core is a $sp^2$-$sp^3$ hybrid crystal or formless. The spherical shell has some defects and surface functional groups, like amino group (-$NH_2$), carboxyl group (-COOH), hydroxyl group (-OH), sulfonic group (-$HSO_3$), carbonyl group (C═O), epoxy (–CH(O)CH–) and cyano (-CN) group, etc. With these functional groups, CDs exhibit excellent dispersion in solvents and take active parts in bonding with different materials.[(45a)] Herein, we have used nitrogen (N) into carbon dots which enhance the performance of CDs in above said applications. Nitrogen doping helps carbon to attribute new physical and chemical properties. Beside this, the doping of N into CDs reduces the work function of CDs and stimulates in delocalization of charge. Additionally, doping nitrogen also enhances the charge transferability of CDs and also increases the number of surface defects in CD, which henceforth helps in escalating the piezo effect of PVDF.[(45b)] Owing to these advantages, we have selected nitrogen as a primary doping material into CDs.

In the present work, we designed a nitrogen-doped Carbon dots(N-CDs) incorporated self-poled piezoelectric PVDF (PCD) film based piezoelectric nanogenerator (PPNCD) for harnessing various forms of mechanical and biomechanical energy such as talking, walking, finger impartation and so forth and converting them into electrical energy. Carbon dots are selected as the main component for fabricating nanocomposites and energy harvesters due to their biocompatibility, eco-friendliness, solubility, chemical stability, and excellent photoluminescence properties. Besides this, larger surface area and surface defects of Carbon dots facilitates the formation of β phase in the PVDF polymer matrix. The large surface area and rich surface defects of CDs generate the active points, having induced mass potential and help in formation of β-phase within PVDF matrix. Furthermore, the rich surface defects in the shell of CDs encourage in chemical bond formation between filler and substrate and make interface bond stronger [48]. Different characterization techniques have investigated the effects of N-CDs in PVDF polymer. The exceptional diverse properties of CDs encouraged researchers to explore the possibility of the material in several fields of application such as sensing and bioimaging, photocatalysis, light-emitting diode, electrocatalysis, and solar cells [20].

The experimental PCD film-based PENG (PPNCD) shows elevated output performance with an instantaneous power density of 1979.87μ$Wcm^{-3}$ under periodic finger impartation. The sensitivity of the device has been investigated by dropping different balls on the upper surface. The β-crystalline phase of PCD nanocomposites have been examined by X-ray diffraction pattern and FTIR spectra. Furthermore, the density functional theory (DFT) calculations are used to find out the geometrical and electrical properties of the β-crystalline phase. In addition, the fabricated PPNCD can generate output voltages from various body movements like touching, bending, heartbeats and pulses, heel pressing etc. Our study indicates the prospect of the piezoelectric nanogenerator PPNCD as green and handy energy harvester to power up various electronic devices quite easily and as wearable sensor to detect different weights.

## 2. Experimental section

### 2.1. Synthesis of carbon dots incorporated PVDF composite (PCD) nanocomposites

N-CDs/PVDF-based nanocomposites were prepared with the help of a simple solution casting method. At first, 250 mg of PVDF (Sigma-Aldrich, Germany; Mw: 180 000 GPC; Mn:71 000) was mixed with the required amount of dimethyl sulfoxide (DMSO) (Merck) and kept at 60 °C on a magnetic stirrer to get a clear solution. The required amount of N-CDs (1, 1.75, 2.5, 5, 10 mass percent) were added with the clear solution and kept on a magnetic stirrer for 14 h under the same conditions. After that, the prepared solutions were cast on clean and dust-free Petri dishes and dried at 80 °C in the oven to obtain the composite PCD nanocomposites. Table 1 describes the amount of N-CDs, DMSO and PVDF used to prepare the samples, with their respective names.

**Table 1**
Samples name for different concentrated N-CDs and solvents added with PVDF.

| Samples name | DMSO(in ml) | PVDF(mg) | N-CDs(in ml) |
|---|---|---|---|
| Pure PVDF | 5 | 250 | 0 |
| PCD1 | 4.95 | 250 | 0.05 |
| PCD1.75 | 4.9125 | 250 | 0.0875 |
| PCD2.5 | 4.875 | 250 | 0.125 |
| PCD5 | 4.75 | 250 | 0.25 |
| PCD10 | 4.50 | 250 | 0.5 |

### 2.2. Fabrication of device

At first, PCD nanocomposite was taken with dimensions of 2.4 cm× 1.8 cm × 46μm. Then two aluminum electrodes with a thickness of 40 μm were pasted on both sides of the PCD film, and two copper wires were connected from both sides of the nanocomposite to measure the output performance of the nanogenerators. After that, the nanocomposite containing the electrodes and wires was encapsulated with the polydimethylsiloxane (PDMS) (Sylgard 184, Dow Corning, ratio of 1:10) and kept for 15 min in a vacuum to remove the bubbles from the mixture. After removing the bubbles, the device was put in the oven at 60$^{O}$C for drying. The dimension of the fabricated device (PPNCD) was 5cm × 3 cm × 0.3 cm. The procedure is shown in Fig. 1(a).

## 3. Results and discussion

The microstructure, surface morphology, different phase behavior, and thermal properties of nanocomposites are examined by field emission scanning microscopy (FESEM; INSPECT F50), Transmission electron microscope (UHR-FEG TEM, JEM-2100F, Jeol, Japan), Fourier transform infrared (FTIR) spectroscopy (FTIR-8400S; Shimadzu), X-ray diffraction (XRD; Model-D8, Bruker AXS Inc., Madison, WI), thermal gravimetric analysis (TGA; TGA/SDTA851e, Mettler Toledo AG) and differential scanning calorimeter (DSC-60, Shimadzu, Singapore) respectively. Furthermore, X-ray Photoelectron Spectroscopy (XPS) analysis has been performed with an Omicron Multiprobe (Omicron Nanotechnology GmbH) photoelectron spectrometer fitted with an EA125 hemispherical analyzer and a monochromatized Al $K_{\alpha}$ (hν: 1486.6 eV) source.

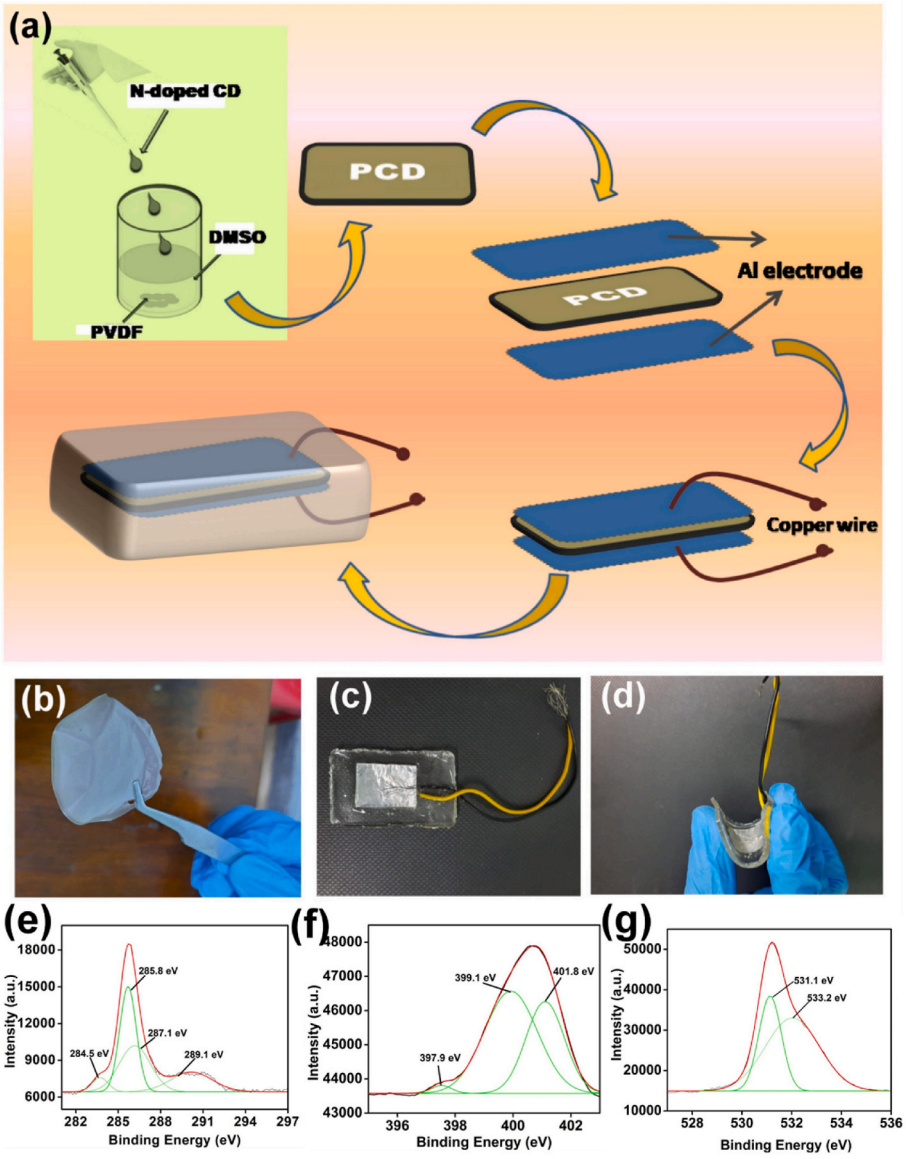


**Fig. 1.** (a) Graphical representation of the fabricated PPNCD device. (b) A digital snapshot of PCD nanocomposite. (c, d) Digital image and flexibility show of designed PPNCD device. XPS peaks of (e) C1s, (f) N1s and (g) O1s.

### 3.1. Structural analysis of N-CDs and PCD nanocomposites

The TEM image of N-CDs interprets that the dispersion of synthesized N-CDs is uniform. As a result, no agglomeration takes place. Moreover, the diameter of the N-CDs is calculated from TEM image, which is 2.5 nm. Fig. S1(b) exhibits the TEM image of N-CDs. Furthermore, X-ray photoelectron spectroscopy (XPS) analysis is performed to analyze the state of doping and investigate the surface groups of N doping CDs. Figure shows the data of XPS analysis of N-doped CDs and the results of XPS analysis confirm that N-CD consists of carbon, nitrogen and oxygen. Fig. 1(e) elaborates that C1s spectrum mainly consists of four peaks which are observed at 284.5 eV, 285.8 eV, 287.1 eV, and 289.1 eV. The peak at 284.5 eV confirms the presence of graphitic structure ($sp^2C$–$sp^2C$) [45b]. Moreover, the observing peaks at 285.8 eV, 287.1 eV, and 289.1 eV binding energy validate the presence of C═N, C–N and C–O bonds respectively [32b]. From Fig. 1(f), we can see that N1s consist of three peaks. Among them, the peaks at 397.9 and 399.1 eV confirm the presence of pyridinic groups [45b]. Beside this, a peak at 401.8 eV is observed which attributes to N–O bonds. Furthermore, O1s spectrum discloses the presence of C═O and $sp^2$C–OH bonds at binding energy of 531.1 eV and 533.2 eV respectively, which shown in Fig. 1(g). The peak at binding energy of 533.2 eV also indicates the presence of the cyclic ether containing groups (C═C–O–C, C–O–C).[45(b)] Thus, XPS analysis indicates the states of N doping in CDs.

FESEM micrographs depicting the surface morphology and microstructure of nanocomposites of pure PVDF and N-CDs incorporated composites are shown in Fig. 2. Surface images of N-CDs doped PVDF nanocomposites indicate the formation of spherulites. The diameter of the spherulites is near about 5μm, which confirms the nucleationof the electroactive β-phase. In the case of pure PVDF nanocomposite, the diameter of spherulites is nearly 40μm, which confirms the presence of non-polar α-phase [33].

### 3.2. Electroactive β-phase analysis

The FTIR spectra and XRD patterns help in investigating the phase behavior of pure PVDF nanocomposite, and N-CDs loaded PVDF (PCD) films. Fig. 3(c) and (d) describe the FTIR spectra of pure PVDF and N-CDs incorporated PVDF (PCD) films in the range of 400–1100 $cm^{-1}$. The FTIR spectrum of pure PVDF indicates the absorbance peaks of non-polar α-phases at 487$cm^{-1}$ ($CF_2$ waging), 531 $cm^{-1}$ ($CF_2$ bending), 616 and 764 $cm^{-1}$ ($CF_2$ bending and skeletal bending), and 796 and 976 $cm^{-1}$ ($CH_2$ rocking). A small peak is observed in the FTIR spectrum of pure PVDF nanocomposite at 840 $cm^{-1}$ due to $CH_2$ rocking, $CF_2$ stretching, and skeletal C–C stretching, which indicates the presence of β-phase though there is an absence of absorbance band of γ-phase at 1234$cm^{-1}$. However, in the case of the PCD nanocomposites, all absorbance peaks of non-polar α-phase vanish entirely. Only the absorbance peaks at 445 $cm^{-1}$ ($CF_2$ rocking and $CH_2$ rocking), 479 $cm^{-1}$ ($CF_2$ deformation), 510 $cm^{-1}$ ($CF_2$ stretching), 600 $cm^{-1}$ ($CF_2$ wagging), and 840 $cm^{-1}$ are raised prominently. The presence of peaks at 445, 510, and 840 $cm^{-1}$ bands in the FTIR spectra is certainly the signature of nucleation of electroactive β-phases in the N-CDs doped PVDF nanocomposites [36]. Therefore, due to the catalytic effect of N-CDs in the PVDF matrix, β-phases are mainly nucleated in the composite samples. Closer inspection of the FTIR spectra of the composite nanocomposites reveals that the intensity of the absorbance bands of β-phase is seemed to be maximized for PCD 2.5 (Fig. 3(c)). These results are in agreement with the XRD data (Fig. 3(a)). In order to estimate the amount of β phase present in the PCD nanocomposites, we have calculated the fraction of electroactive β-phase content (F(β)) with the help of The Lambert−Beer law:

$$F(\beta) = \frac{A_\beta}{\left(\frac{K_\beta}{K_\alpha}\right)A_\alpha + A_\beta} \quad \text{(i)}$$

Where.

$A_\alpha$ = absorbance at 764 $cm^{-1}$.

$A_\beta$ = absorbance at 840 $cm^{-1}$,

$K_\beta = 7.7 \times 104$ $cm^2$ $mol^{-1}$(absorption coefficients at 840 $cm^{-1}$)

$K_\alpha = 6.1 \times 104$ $cm^2$ $mol^{-1}$(absorption coefficients at 764 $cm^{-1}$) [37].

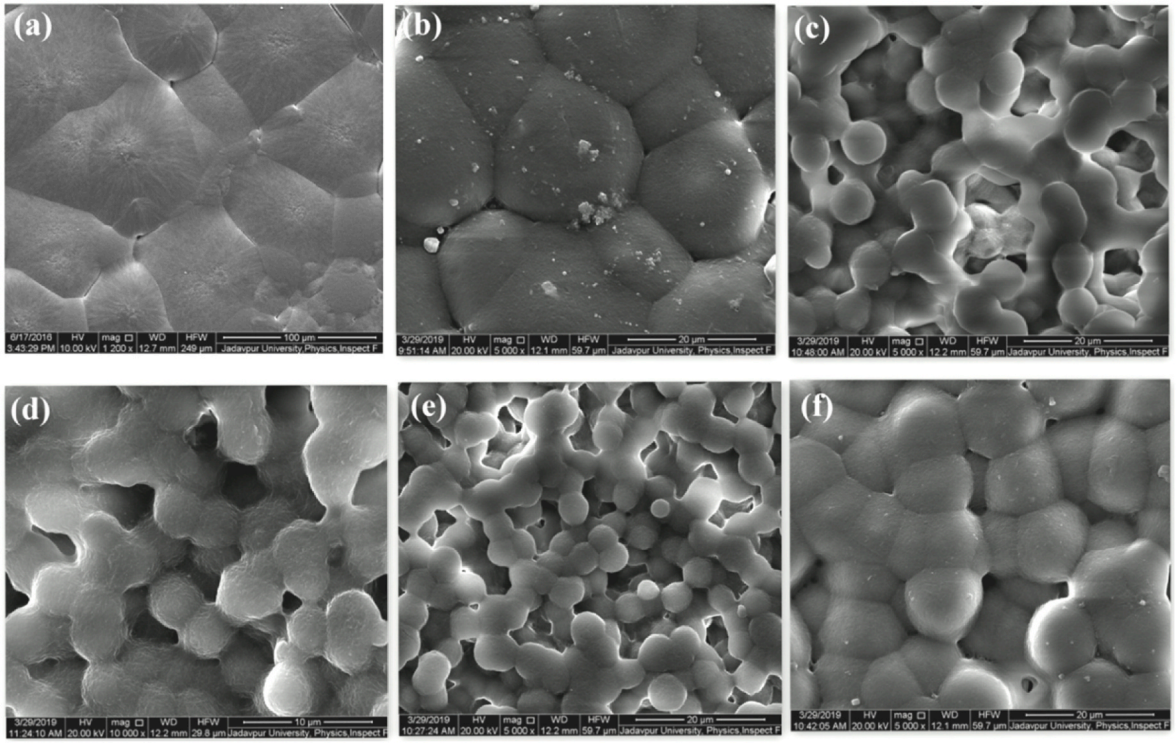


**Fig. 2.** FESEM pictures of (a) pure PVDF and (b)–(f) and different concentrated N-CDs loaded PVDF nanocomposites.

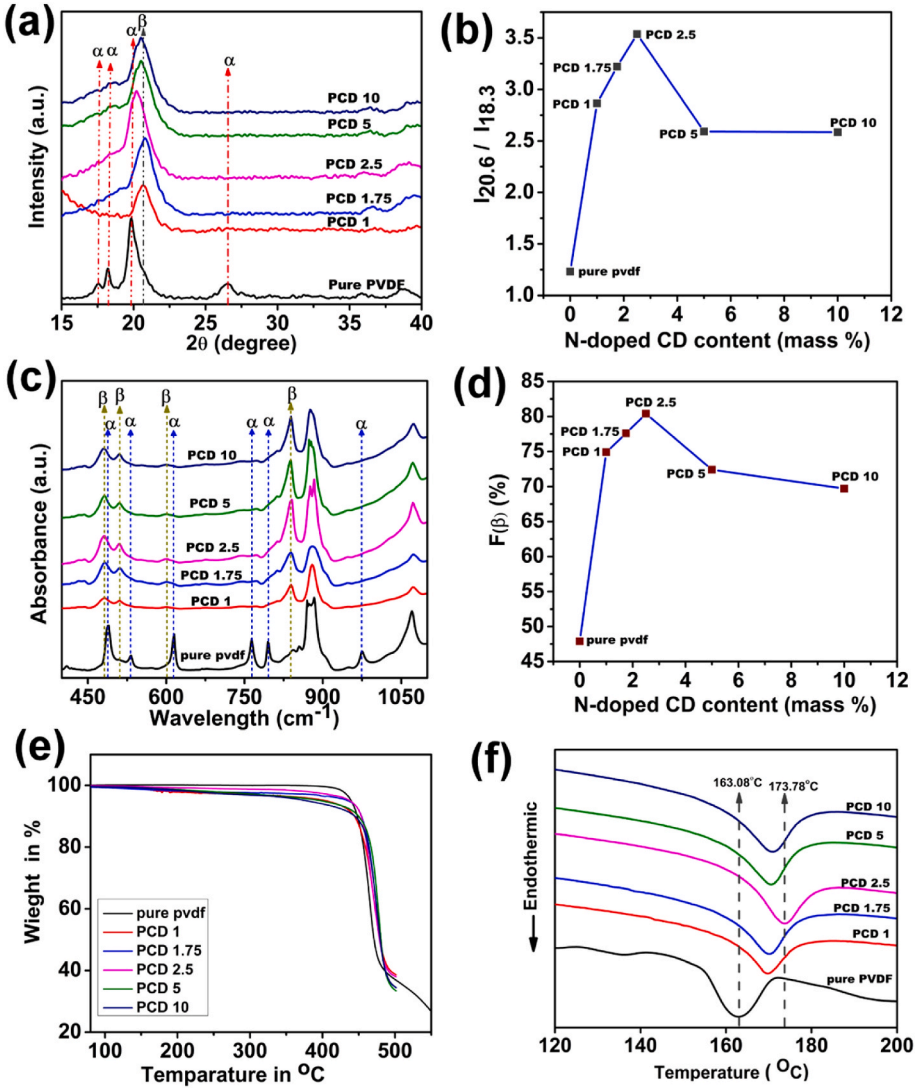


**Fig. 3.** (a) XRD pattern of pure PVDF and N-CDs incorporated PCD nanocomposites (PCD 1, PCD 1.75, PCD 2.5, PCD 5 and PCD10). (b) $I_{20.5}/I_{18.3}$ ratio of measured samples from XRD pattern. (c) FTIR spectra of pure PVDF and PCD nanocomposites. (d) Content of β-phase of measured samples. (e) TGA analysis and (f) DSC thermograph of pure PVDF and N-CDs doped PCD nanocomposites.

This equation gives us an idea about the amount of β phase present in the PCD nanocomposites and this assessment is very important as better β phase nucleation leads to better piezoelectric property. The fraction of β-phase increases with the doping concentration of N-CDs and attains a maximum value for 2.5 mass percent (F(β) ≈ 80.4%), which is shown in Fig. 3(d).

The β-phase content increases with the doping concentration of CDs and attains a maximum F(β) value (80.4%) for 2.5% doping. The reason behind this is the interaction between dopant and polymer matrix. Generally, at lower doping concentrations, the interfacial area among the dopant and polymer remains low. As we are increasing the doping concentration, interfacial area also increases by improving the dopant-polymer interaction. As a result, number of chains aligning with all trans (TTTT) conformation inside the PVDF matrix increases which helps in increase in β-phase content [32c]. In case of 2.5% CDs, maximum dispersion and distribution properties of CDs in the PVDF matrix take place. As a result, the most intimate interaction occurs among the dopant (CDs) and PVDF matrix and we get the highest number of all trans (TTTT) conformation aligning chains inside the PVDF matrix. On further increasing the mass% on CDs in PVDF agglomeration takes place which results in reduction in the interfacial surfaces between CD and PVDF matrix leading to a decrement in β-phase content. The electrostatic interaction takes place between negative charge surface of CDs and positive $-CH_2$ group of PVDF, which helps in formation of β-phase as can be seen in Fig. S2. Additionally, the explanation of phase transformation of PVDF has been discussed in the supporting information file.

The X-ray diffraction study also confirms electroactive β-phase formation into the PVDF matrix. The XRD pattern of pure PVDF film and N-CDs loaded PVDF (PCD) films are shown in Fig. 3(a). In the case of pure PVDF nanocomposite, we get peaks at 2θ = 17.6° (100), 18.3° (020), 19.9° (021), and26.6° ((201), (310)) which indicate the presence of non-polar α-phase. A minute peak at 2θ = 38.3° is observed in the XRD pattern of pure PVDF nanocomposite due to the reflection from either the (002) plane or the (211) plane where (002) plane corresponds to α-phase and (211) plane corresponds to γ-phase [31,32a]. This issue has been solved by FTIR analysis of pure PVDF nanocomposite. With addition of N-CDs into the PVDF matrix, all XRD peaks corresponding to α and γ phases vanish. Only one distinctive peak at 2θ = 20.6 ((110), (200)) has a substantial rise, which confirms the nucleation of electroactive β-phase in PCD nanocomposites [36].

A closer scrutiny of the XRD patterns indicates maximum intensity of diffraction peak at 2θ = 20.6 for 2.5 mass percent loading of N-CD into PVDF matrix (PCD 2.5), confirming more electroactive β-phase

crystallization in these PCD films. The amounts of α-phase and β-phase content are estimated by the ratio between $I_{20.6}$ and $I_{18.3,}$ as shown in Fig. 3(b). This fig. shows that for PCD 2.5, we get a maximum ratio which is 3.537.

### 3.3. Thermal analysis

The thermal strength of the PCD nanocomposites has been examined by the TGA thermograph shown in Fig. 3(e). The study is performed by placing the nanocomposites under a nitrogen atmosphere within the temperature range of 30 °C–500 °C with the heating rate at 10 °C/min. From Fig. 3(e), it can be noticed that a very small amount of weight loss takes place between the temperature of 350 °C–450 °C in case of PCD nanocomposites, which is trivial compared to pure PVDF nanocomposite. After crossing the temperature of 450 °C, a gradual shift of degradation temperature of PCD nanocomposites is observed. The TGA thermograph also exhibits that after completing the 50% weight loss, we get the different degradation temperature for different doping concentration based PCD nanocomposites, which is higher in comparison with the degradation temperature of pure PVDF nanocomposite at the same weight loss. For example, in case of pure PVDF nanocomposite the degradation temperature at 50% weight loss is 466 °C, whereas, the degradation temperature for PCD 2.5 nanocomposite at same weight loss is 480 °C. The homogeneous dispersion of N-doped CD into polymer matrix and interfacial strength between N-doped CD and PVDF are the key factors for getting such higher degradation temperature of PCD nanocomposites [20]. Thus, the TGA thermograph and above said discussion indicate that PCD films have higher thermal stability than pure PVDF nanocomposite.

The crystallization behaviors and melting temperature of PCD nanocomposites has been investigated by differential scanning calorimetry (DSC) analyzer. The formation of β-crystalline phase of PCD nanocomposites is also confirmed by DSC analysis. Fig. 3 (f) represents the melting temperatures and crystallization behaviors of pure PVDF and N-doped CD incorporated PVDF (PCD) nanocomposites. From DSC thermographs, the melting temperature ($T_m$) of pure PVDF is 163.08 °C, which confirms the presence of the non polar α-crystalline phase inside the nanocomposite [20]. Whereas, in case of PCD nanocomposites, noticeable shift in melting temperature are observed, which are higher in comparison to pure PVDF. Among all nanocomposites, PCD 2.5 exhibits better melting temperature ($T_m$) with the value of 173.78 °C. Therefore, the shifting of melting temperature confirms the transformation of α-crystalline phase (TGTG conformation) to β-crystalline phase (TTTT conformation) of PVDF. Thus, the experimental investigations confirm that N-doped CD is a very good nucleating agent and plays an important role in β-crystalline phase formation. This statement is commensurate with previously described XRD and FTIR results.

### 3.4. Theoretical estimation (DFT) of the formation of electroactive β-phase

The results obtained from the basic characterizations such as XRD and FTIR shows the formation of β phase with increasing dopant (N-CD) concentrations. Thus, density functional calculations have been performed to obtain the structural and electrical characteristics of the sample. Herein, the DFT study has been implemented using Orca v.1.2 program. The hybrid Becke, 3-parameter, Lee-Yang-Parr (B3LYP) functional has been used along with 6–31G* basis set and RIJCOSX auxiliary basis function to accommodate atoms like C, H and F. The molecular models of both α and β-phases were prepared in Avogadro v.1.2.0 software program. Initially, the geometries and frequencies were optimized of both the models and no imaginary frequency were found, which ensures the validity of the structures.

It is observed that the randomized orientation of C and F in α-PVDF radically polarized into the β-phase, which causes a significant change in dihedral C–C–C angle (mentioned in Fig. 4). Almost all F and H have been rotated to the either side of C–C chain, which not only polarizes the model but also minimizes the single point energy of the β-PVDF. Such energy minimization in β-PVDF stabilizes its structure.

Moreover, the electrical properties have been estimated theoretically using DFT, which shows significant changes in both dipole moment and isotropic polarizability. A detailed comparison of electrical properties of α and β-phases of PVDF have been depicted in Table 2. Such an augmented polarizability and dipole moment is desirable in piezoelectric materials.

## 4. Working mechanism of PPNCD

The fabricated piezoelectric nanogenerator (PPNCD) generates appreciable voltage from mechanical energy generated through continuous finger impartation. The synergistic effect of the dipoles, which are present in PVDF i.e. electroactive β-phases and nitrogen doped carbon dots (N-CDs), may explain the possible working mechanism of PPNCD. The presence of N-CDs molecules in the composite matrix triggers the electroactive β-phase formation with the help of strong electrostatic interactions between the water molecules of N-CDs and the negative $–CF_2$ dipoles of the PVDF matrix during the formation of hydrogen bonds. When an external mechanical force is applied on the PPNCD under periodic finger imparting, a secondary potential is generated in the N-CDs molecules, which arrange the PVDF dipoles in the direction of the applied mechanical force, thus promoting stress-associated polarization. When a vertical mechanical compression is given on the PPNCD, a positive potential at the top electrode and a negative potential at the bottom one have been produced due to formation of self-polarization induced by the deformation of the crystalline structure of the N-CDs doped PVDF nanocomposite (PCD 2.5). The potential difference between the two electrodes along with self-polarization, regulates the flow of electrons from one electrode to another through an external load. The piezoelectric potential abruptly diminishes after the quick release of the compressive force. The electrons gathered at the bottom electrode flow back to the other electrode via the external circuit, ensuing in an opposite electrical output [37]. This process is repeated in the PPNCD under continuous compression and relaxation consecutively to obtain the output electric signals from the piezoelectric energy harvesting device. Fig. 5 describes the voltage generation mechanism of the PPNCD device. Furthermore, the working principle of PPNCD device can be illustrated with the help of Maxwell's equations. In electrodynamics, Maxwell's equations remain constant with local invariance which can be expressed in the equation form

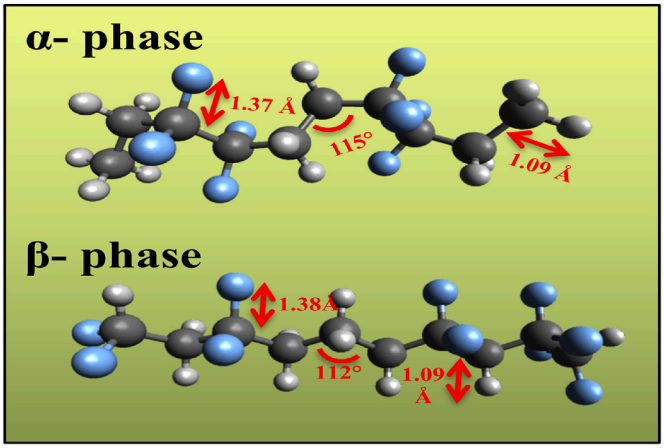


**Fig. 4.** Geometry optimized structures of α and β-phases of PVDF showing bond angle and bond lengths.

**Table 2**
Comparison of the electrical properties between α and β-phases of PVDF.

| | Energy (joule) | Dipole moment (debye) | Quadrupole moment (a.u.) | Polarizability (a.u.) |
|---|---|---|---|---|
| **α phase of PVDF film** | −5.1 | 0.37 | 73.74 | 106.62 |
| **β-phase of PVDF film** | −6.04 | 3.68 | 86.06 | 108.54 |

$$\nabla.\vec{\mathbf{J}} + \frac{\partial}{\partial \mathbf{t}}\left(\nabla.\vec{\mathbf{D}}\right) = 0 \quad \text{(ii)}$$

$$\frac{\partial \boldsymbol{\rho}}{\partial \mathbf{t}} + \nabla.\vec{\boldsymbol{J}} = 0 \quad \text{(iii)}$$

This equation is called continuity equation. Where, **J** and **ρ** are the total current density and total charge density.

The charge density can be defined as

$$\rho = \rho_f + \rho_b \quad \text{(iv)}$$

Where, $\rho_f$ = free charges and $\rho_b$ = bound charges.

The current density can be expressed as

$$J = J_f + J_b \quad \text{(v)}$$

Where, $J_f$ = free currents and $J_b$ = bound currents.

In case of dielectric materials, the auxiliary fields take active part in dipole formation, can be defined as

$$D(r,t) = \varepsilon_0 \boldsymbol{E}(\boldsymbol{r},\boldsymbol{t}) + \boldsymbol{P}(\boldsymbol{r},\boldsymbol{t}) \quad \text{(vi)}$$

$$H(r,t) = \frac{\mathbf{B}(\mathbf{r},\mathbf{t})}{\boldsymbol{\mu_0}} - M(r,t) \quad \text{(vii)}$$

Where, D = displacement field; $\varepsilon_0$ = permittivity of free space; E = electric field; P = polarization; H = magnetic field; $\mu_0$ = permeability of free space; B = magnetic induction; M = magnetization.

In our present work, Maxwell's equations in matter can be utilized to describe the working principle. Considering the free charges and current, the Maxwell's equations will be

$$\nabla.\vec{\mathbf{D}} = \boldsymbol{\rho_r}(\text{Gauss'sLawofelectrostatics}) \quad \text{(viii)}$$

$$\nabla.\vec{\mathbf{H}} = \mathbf{0}(\text{Gauss'slaw magnetostatics}) \quad \text{(ix)}$$

$$\nabla\,\mathbf{x}\vec{\mathbf{E}} = -\frac{\partial \vec{\mathbf{B}}}{\partial \mathbf{t}}(\text{Faraday's law}) \quad \text{(x)}$$

$$\nabla\mathbf{x}\vec{\mathbf{H}} = \vec{\mathbf{J}}_\mathbf{f} + \frac{\partial \vec{\mathbf{D}}}{\partial \mathbf{t}}(\text{Ampere's circuital law with correction}) \quad \text{(xi)}$$

Where, $\vec{E}$ = electric field, $\vec{D}$ = displacement electric field, $\vec{B}$ = magnetic induction, $\vec{H}$ = magnetic field, $\rho_f$ = volume charge density of free electron, $\vec{J}_f$ = current density due to free electron flow.

From electrodynamics, with the help of following equations, we get the displacement current for an electric field and polarization current for an electric polarization respectively.

$$J_{=}\boldsymbol{\varepsilon_0}\frac{\partial \mathbf{E}}{\partial \mathbf{t}} \quad \text{(xii)}$$

$$Jp = \frac{\partial \mathbf{P}}{\partial \mathbf{t}} \quad \text{(xiii)}$$

Thus, in case of linear isotropic medium, the second term of Maxwell's fourth equation (equation (xi)) represents the total displacement current ($\vec{j}_D$).

$$\vec{\mathbf{j}}_\mathbf{D} = \frac{\partial \vec{\mathbf{D}}}{\partial \mathbf{t}} = \boldsymbol{\varepsilon_0}\frac{\partial \vec{\mathbf{E}}}{\partial \mathbf{t}} + \frac{\partial \vec{\mathbf{P}}}{\partial \mathbf{t}} \quad \text{(xiv)}$$

There, the total displacement current is a time-dependent term and depends on the electric field and electric polarization of the dielectric medium. The first term of equation (xiv) helps in enhancement of output performance of wireless system like radio, RADAR, Wi-Fi etc. and the second term enhances the piezoelectric effect by increasing the value of P, depends on the applied force or strain. Applying mechanical strain on a linear isotropic material, the piezoelectric equations will be [37].

$$\vec{\mathbf{P}}_\mathbf{i} = (\mathbf{e})_{\mathbf{ijk}}\left(\vec{\mathbf{S}}\right)_{\mathbf{jk}} \quad \text{(xv)}$$

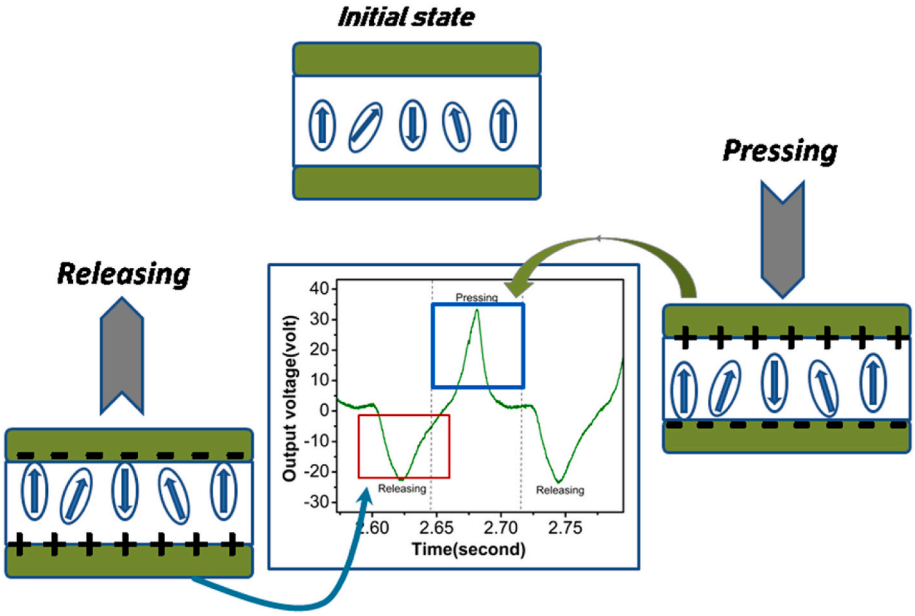


**Fig. 5.** Possible voltage generation mechanism of our fabricated device.

$$\vec{T} = C_E \vec{S} - e^T \vec{E} \quad \text{(xvi)}$$

$$\vec{D} = e\vec{S} - k\vec{E} \quad \text{(xvii)}$$

Where, $\vec{S}$ = mechanical strain, $(e)_{ijk}$ = piezoelectric third order tensor, $\vec{T}$ = stress tensor, $C_E$ = elasticity tensor, k = dielectric tensor.

The displacement current of a linear polarizing medium is

$$\vec{J}_{Di} = \frac{\partial \vec{P}_i}{\partial t} \quad \text{(xviii)}$$

So, the equation (xviii) concludes that the piezoelectric effect and output current density is directly proportional to the rate of change of applied force or strain. Therefore, the attaining output value of PPNCD by applying force matches with the theoretical equations.

In absent of external field E on dielectric medium, displacement current is only depend on the polarization (from equation (xviii)). Taking the polarization along the z direction, we can write that

$$D_z = P_z = \sigma_P(z) \quad \text{(xix)}$$

Where, $\sigma_P(z)$ = piezoelectric polarization surface charges density of the material.

Then, the displace current term along z direction will be

$$J_{DZ} = \frac{\partial P_z}{\partial t} = \frac{\partial \sigma_p(z)}{\partial t} \quad \text{(xx)}$$

The above equation clearly explains the reason of getting high output performance of PPNCD device.

## 5. Output performances of PPNCD nanogenerators

The fabrication process of the device (PPNCD) is shown schematically in Fig. 1(a). A digital snapshot of the fabricated device is displayed in Fig. 1(c) and the flexibility of the device is shown in Fig. 1(d). In the present work, we have designed a piezoelectric energy harvesting device (PPNCD) with the help of N-CDs/PVDF (PCD) film and PDMS. Fig. 6(a)

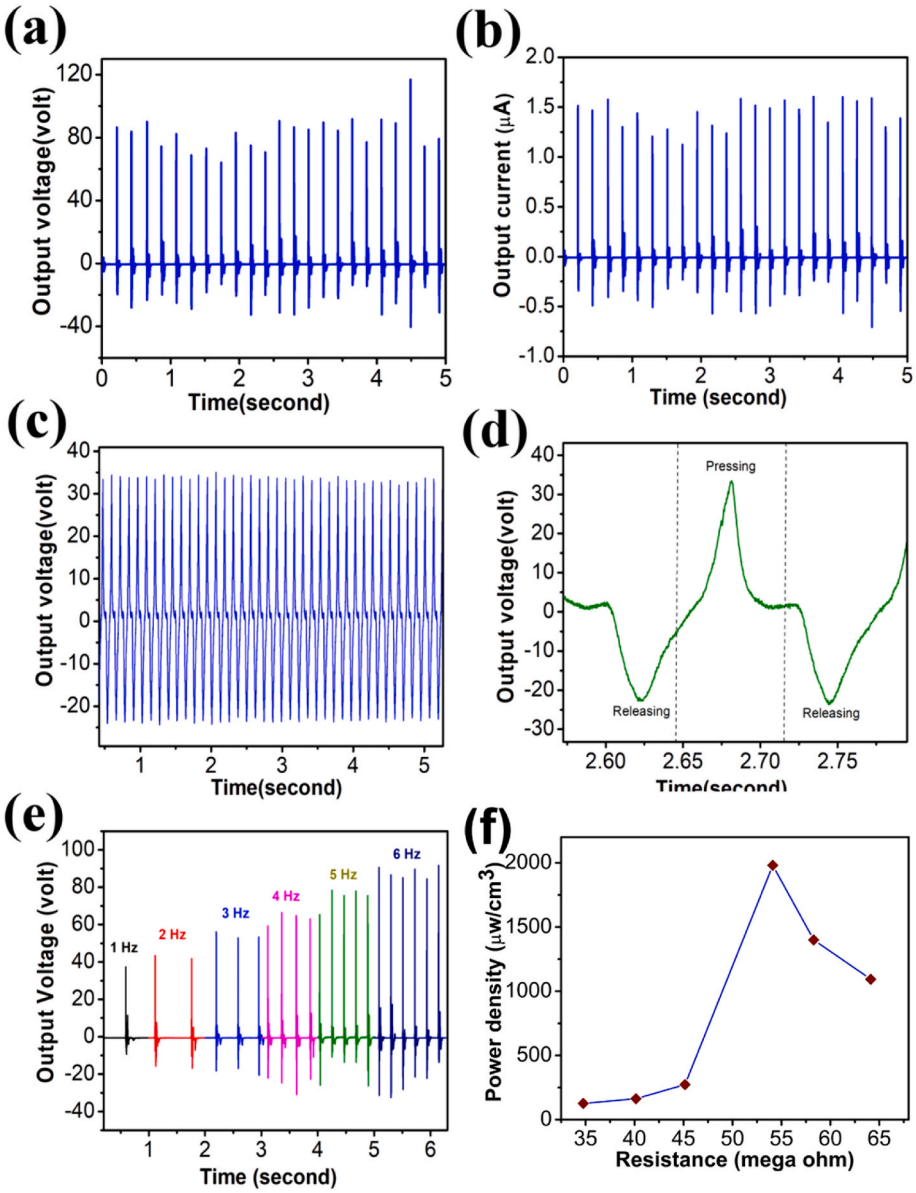


**Fig. 6.** (a) Open circuit voltage ($V_{OC}$) and (b) short circuit current ($I_{SC}$) of fabricated PPNCD device under periodic finger impartation at frequency 6 Hz. (c) Output voltage generation and (d) enlarged view of $V_{OC}$ under 5N force at 6Hz frequency. (e) Frequency dependent output voltage generated by human finger impartation. (f) Power density for various load resistances.

shows the output voltage vs. time graph. The output voltage is generated by continuous finger imparting and releasing an axial pressure of 12.3 N. The current vs. time output feature of fabricated PPNCD is depicted in Fig. 6(b). Maximum output voltage and current have been obtained at the frequency of 6 Hz. The output performance of the nanogenerator is high during finger impartation. The output voltage (measured by Keysight, Oscilloscope DSO-X 3012A) and the short circuit current (observed by Keysight, Electrometer B2985) of PPNCD are $V_{oc}$ ~80 V and $I_{sc}$ ~ 1.4μA respectively (Fig. 6(a) and (b)). The difference in the peaks values of the output voltage and current during periodic pressing and releasing is basically owing to the inconsistency of the given strain on the piezoelectric energy harvester during manual finger impartation. While recording the data of output voltage vs. time graph of PPNCD device on the application of force by hand, we have tried to maintain uniformity as much as possible. Since the applied force is not machine operated, some human error occurs during the process and every cycle does not obtain the exact force [17]. This discrepancy in the applied force led to the asymmetric peaks in the output voltage vs. time graph. Another reason for this asymmetry in voltage output is that the time period for every cycle of applied force is not exactly the same. This again is due to human error as mentioned earlier. The magnified view of $V_{oc}$ is shown in Fig. 6(d). When strain is applied to the device, the positive peaks appear and negative peaks appear when the device comes back to its original form after recovering the strain. Subsequent small peaks have been obtained due to the damping effect of the N-CDs/PVDF nanocomposite. Compared to the pure PVDF-based piezoelectric nanogenerators [20], the output performance of PPNCD is higher, which indicates that the presence of N-CDs in the PVDF matrix significantly increases the output performances of PPNCD. The piezoelectric co-efficient of the PCD nanocomposite is calculated from the following equation $d_{33} = \frac{Q}{F}$ ..... (xxi).

Where $d_{33}$ is the piezoelectric co-efficient, Q is the charge which is generated by applied force and F is the applied force of 12.3 N. Again, the charge is calculated using the equation

$$Q = \int I_{sc} dt \tag{xxii}$$

Where, $I_{SC}$ is the short circuit current [47]. The value of Q is 359 pC which is calculated from short circuit current vs. time plot. Putting the value of Q and F in the $d_{33}$ equation, we get the final value of piezoelectric co-efficient ($d_{33}$) of the PCD nanocomposite, which is 29 pC/N. This value confirms the presence of the polar β-crystalline phase and electret dipoles in the PCD nanocomposite. The efficient power density is calculated from the equation

$$P = \frac{V^2}{R_L \times v} \tag{xxiii}$$

Where, V is the output voltage, $R_L$ is the load resistance, and v is the volume (surface area × thickness). The fabricated PPNCD device can produce an excellent peak power density of 1979.87 $\mu Wcm^{-3}$at 57 MΩ loads (Fig. 6(f)). The reasons behind such high power density are as follows.

i) The strain encouraged piezoelectric potential generated by the N-CDs and the self-poled PVDF polymer under continuous finger tapping force (~12.3 N) to reinforce each other.
ii) The continuous finger tapping helps in generating the additional strain which in turn encourages spontaneous polarization and resultant dipole formation, leading to the charge separation and accumulation of charges at the edge sites of piezoelectric N-CDs and PVDF polymer.

The voltage generation record during twisting and bending of the device shows no significant output, which confirms the absence of a triboelectric effect in this particular case. Fig. 6(e) shows the frequency-dependent (1 Hz–6 Hz) output performance of the device, obtained by continuous finger impartation. The output voltage increases gradually as the frequency of finger impartation on PPNCD increases. The output performance of our fabricated device depends on the impedance and the applied strain frequency. The impedance and the applied strain frequency of PPNCD are inversely proportional to each other [20]. Furthermore, the output performance of PPNCD device has been compared with previously reported carbon doped piezoelectric nanogenerator (Table S2) which confirms the better performance of the fabricated device.

### 5.1. Weight sensing performance of PPNCD

Excellent response has been observed while checking the sensitivity of PPNCD by dropping various rubber balls of different masses from a height of 10 cm on the top surface of the device, as shown in Fig. 7(a)-(e). By dropping rubber balls of masses 108.79g, 35.22g, 59.35g, 9.18g, and 15.04g, the observed output voltages are 7V, 9V, 10V, 11V, and 13V.The reason for getting different output voltages depends on the different masses and contact areas of balls with surface of the film. In case of 108.79g mass contained rubber ball, we get low output voltage in comparison with other mass contained rubber balls. The reason behind this is the harder surface, larger size and low elastic properties of 108.79g mass contained ball than other balls. Besides this, we have investigated the capability and sensitivity of the device with some Indian coins which are of different weights but of nearly the same size. The coins are released from a height of 10 cm on the upper surface of PPNCD. When a coin falls on the device, N-CDs and PVDF move toward each other, and we get output voltage. Due to the different masses of Indian coins (1 rupee,2 rupee, 5 rupee, and 10 rupee), we get different output voltages which are shown in Fig. 7(f).The graph describes that with the increasing masses of Indian coins, the output voltage also increases. The sensitivity performance of PPNCD device has been depicted in Fig. 7(g) and (h). These two graphs describe that output voltage of fabricated device increases by increasing the external pressure and maintain the linear relationship between output voltage and pressure. The sensitivity of the device has been measured by the following equation

$$S = \Delta V / \Delta P \tag{xxiv}$$

Where, ΔV and ΔP are the change in the output voltage and applied external pressure [47]. The sensitivity of PPNCD device is found to be 10.2 V/kPa up to the external pressure region of 0.36 kPa, which is generated by falling different masses coins, shown in Fig. 7(g). Furthermore, rubber balls having different masses have been

dropped on the device from a fixed height of 10 cm to check the sensitivity of the device in the higher pressure region. The PPNCD device generates different output voltages at different external pressures and also maintains the linearity pattern between the output voltage and pressure, shown in Fig. 7(h). The sensitivity of the device in this region (0.5–3 kPa) is 2.2 V/kPa which is very low compared to the sensitivity of the low range pressure region (less than 0.5 kPa). Theoretical bounds of the effective strain in the N-doped carbon dots are responsible for this phenomenon in the higher pressure region (>0.5 kPa) [47]. Beside this, our device can detect very low pressure of 0.15 kPa. The coin and rubber balls dropping experiments give us the sensitivity value and the range of sensitivity of the fabricated device. Along with this, these experiments also describe the capability of the self-powered device to detect the both low and high range pressure. Thus, the PPNCD device can be used as a dedicated weight sensor as well.

### 5.2. Voltage generation from human body movements

The PPNCD device has generated the output voltage from body movements such as foot pressing, heel pressing, pulse cycle, wrist up-down etc. Outstanding output performance has been obtained by

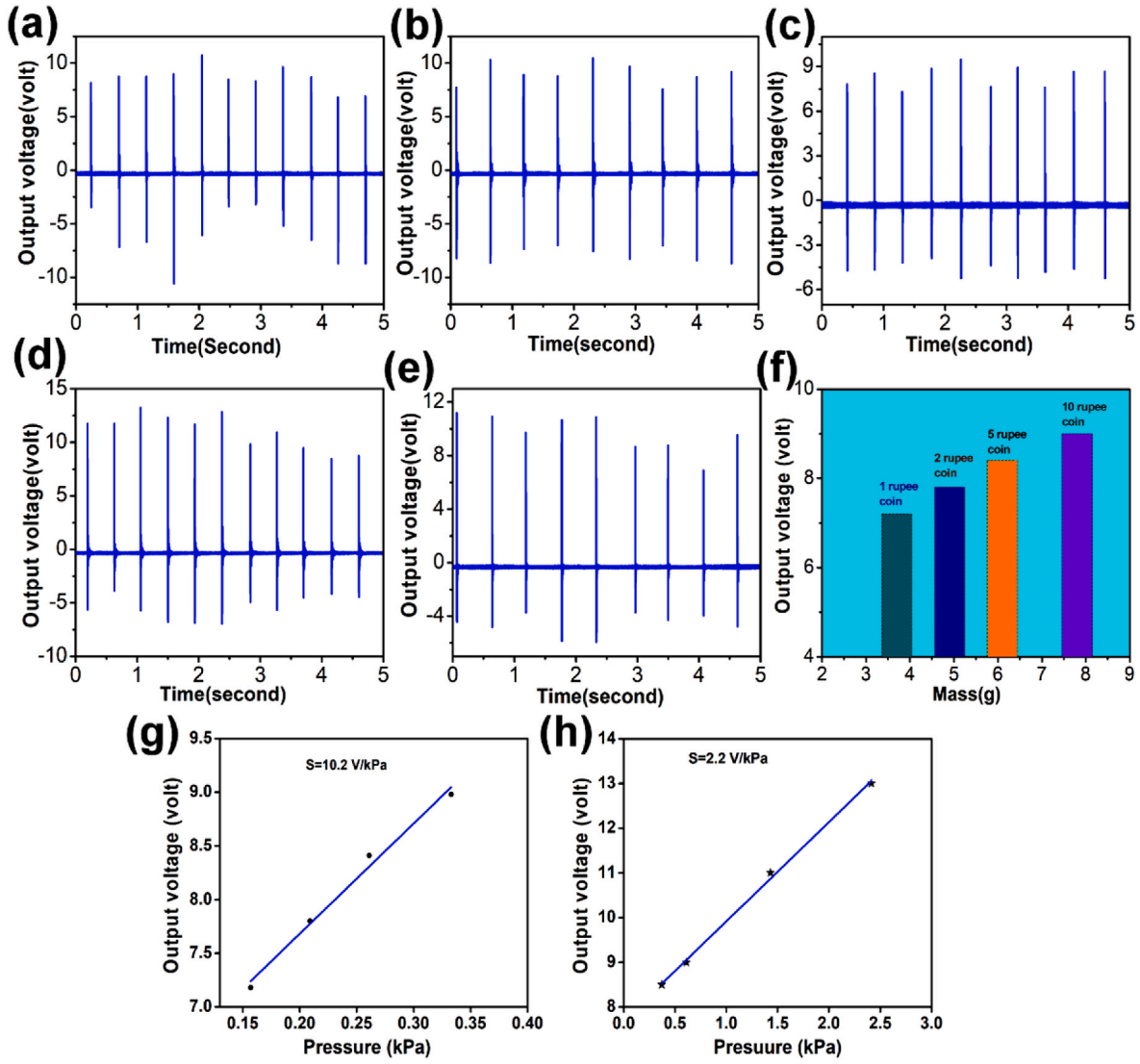


**Fig. 7.** (a)–(e) Output voltage generated by falling different masses (108.9g, 35.22g, 59.35g, 9.18g, and 15.04g) of rubber balls on PPNCD device. (f) Response of the device by dropping different masses of Indian coins on the upper part from 10 cm height. The sensitivity of the PPNCD device performed with respect to stress, employed by (g) falling coins and (h) dropping different masses of rubber balls.

attaching the PPNCD device with foot and heel, shown in Fig. 8(a) and (b). During foot pressing and heel pressing, the generated output voltages are 32V and 12V, respectively, indicating that the fabricated device generates higher voltage during foot pressing due to increase in contact area with the PPNCD device. Fig. 8(e) displays the output performance during wrist up-down movement. From this graph, we can see that when the wrist is up, the device is sensitive enough to generate nearly 0.62V and when the wrist is down then, the generated output voltage is near about 0.29V, which confirms the capability of the device in harvesting green energy effortlessly. The sensitivity is further verified by attaching the device to wrist artery. Fig. 8(c) shows the output voltage generated from the pulse wave. During the heartbeat, blood flows through our body, including the wrist, and creates pressure.

Systolic pressure and diastolic pressure are the central part of the pulse wave. Systolic pressure gives the peak, and diastolic pressure gives the trough of the pulse wave. The devised nanogenerator responses quite efficiently to the pulse pressure (occurs due to alternation of systolic and diastolic pressure) during blood flow. The device can detect this pressure and generates voltage, shown in Fig. 8(d). Thus, PPNCD is suitable for sensing pulse waves. The stability and durability of the fabricated PPNCD has been studied for the eight months, and the device continues to produce almost the same output voltage during the whole time period as shown in Fig. 8 (f).

### 5.3. Commercial LED and capacitor charging ability of PPNCD

The energy conversion ability of the fabricated PENG (PPNCD) is performed by charging a capacitor and lighting up commercial LEDs. A 2.2μF capacitor has been charged by connecting the PPNCD through a bridge rectifier under continuous finger impartation. The exponential fashion of the capacitor charging graph explains that the device can charge a 2.2μF capacitor, as shown in Fig. 9(a).Our fabricated device PPNCD can charge a 2.2μF capacitor up to 3.2 V within 14 s. As the device involves very short duration to charge a capacitor, it can be used as an alternative energy source for portable or medical devices. Another important aspect of the device

is that it light up commercially available transparent LEDs under periodic finger impartation, as shown in Fig. 9(c) and (d). The power produced from PPNCD can light up to 15 blue LEDs (shown in supporting video VS1) or 15 white LEDs (shown in supporting video VS2) by connecting them in series connection through a full-wave bridge rectifier.

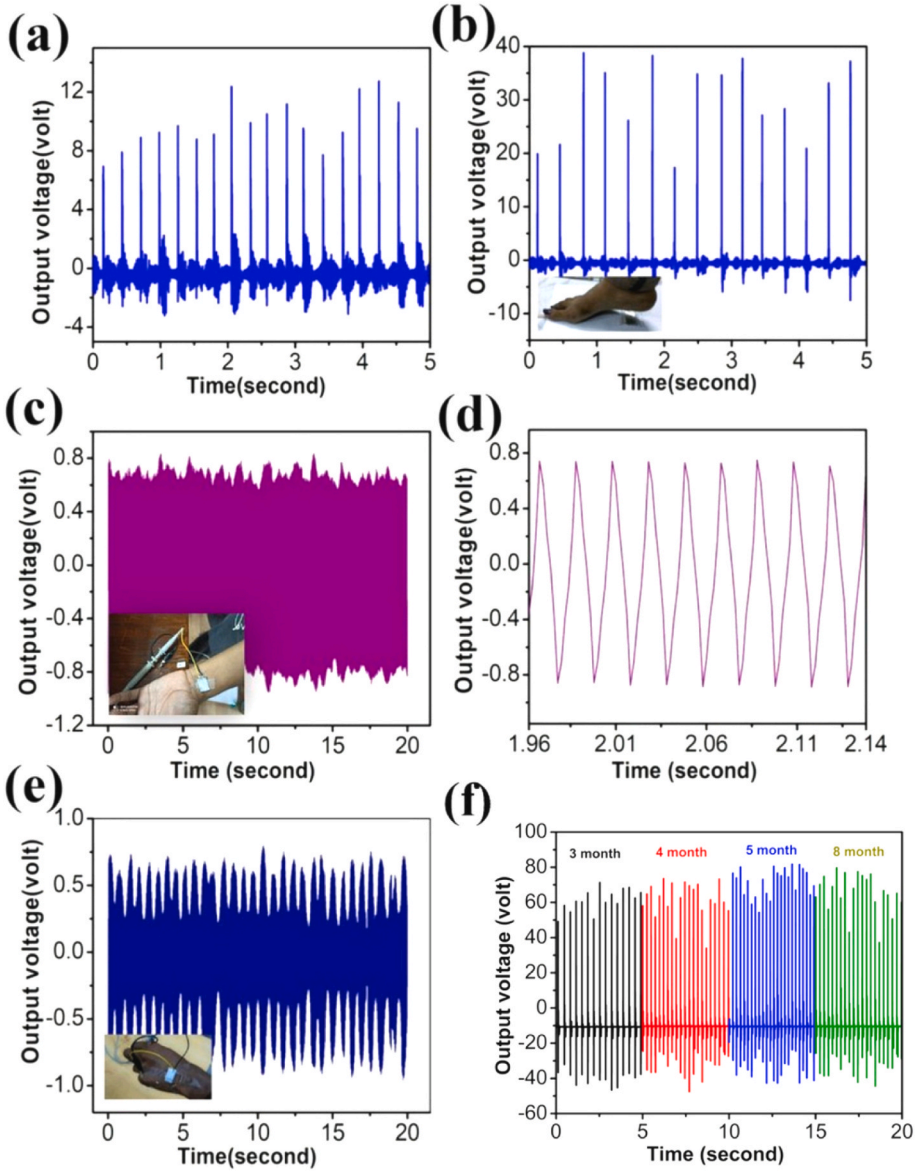


**Fig. 8.** Open circuit voltage generated by (a) forefeet tapping, and (b) heel pressing. (c) and (d) Pulse sensing and magnified view of peaks generated from heartbeats by attaching our PPNCD device to the wrist artery. (e) Voltage generation from wrist up-down. (f) Durability test of PPNCD device.

Supplementary video related to this article can be found at https://doi.org/10.1016/j.ceramint.2022.10.070

From the previous investigations, we can see that the device fabricated in our laboratory is very sensitive and flexible and can be used as a flexible energy harvester and weight sensor which can generate electricity via various body movements and dropping different weights. Furthermore, PPNCD device can be employed to light up LED, charge capacitor, etc.

## 6. Conclusion

The present work describes the fabrication and action of N-CDs/PVDF nanocomposite-based PENG (PPNCD) in harvesting electrical energy from various mechanical energy sources. The PENG is competent enough to convert mechanical energies of pulse wave and simple body movements into electrical energy with high values of $V_{OC}$ and $I_{SC}$. The impact generated by dropping balls or coins on the PENG have been utilized quite efficient to produce electrical energy. The self-powered tiny device produces excellent output voltage ($V_{OC}$ ~ 80 V) and a short circuit current ($I_{SC}$ ~1.4 μA) under periodic finger impartation (~12.3 N) with an average of 6 Hz frequency. The instant power density of PPNCD is 1979.87μWcm$^{-3}$. Moreover, the highest β-crystalline phase content (F(β) ~ 80.4%) PCD nanocomposite evaluates the piezoelectric co-efficient ($d_{33}$) value of 29 pC/N. The density functional theory (DFT) calculations have been performed to investigate the electrical properties of the β-crystalline phase. In addition with this, the PCD nanocomposite assisted wearable sensor has the capability to sense the external pressure at very low region (up to 0.5 kPa) along with the sensitivity of 10.2 V/kPa. The additional significance of the PPNCD has been established by charging a 2.2 μF capacitor up to 3.2 V in a short period (14 s) and by illuminating 15 blue or 15 white transparent LEDs, connected in series. The apparatus shows outstanding long-term mechanical stability and reproducibility for near about a year. The N-CDs incorporated PVDF composite nanocomposites can be used for multipurpose applications, like mechanical energy harvester, weight sensor, pulse sensor, and thus may be employed in multi-faced fields such as optoelectronic, biomedical, and energy technologies after suitable improvisation.

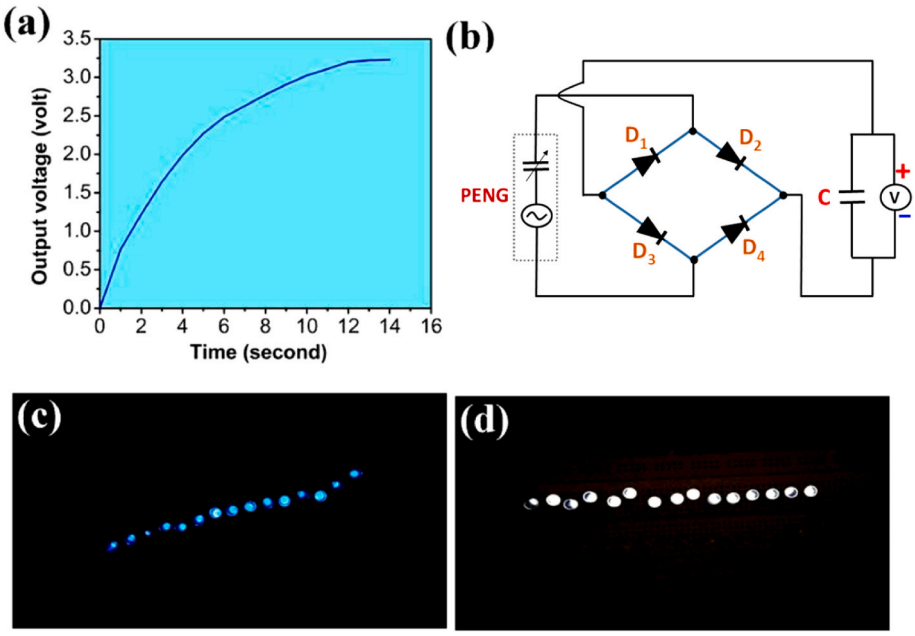


**Fig. 9.** (a) A 2.2μF capacitor charging by PPNCD device. (b) Circuit draw of charging a capacitor and lighting up LEDs. Digital photographs of (c) blue and (d) white LEDs under shining conditions

## Author agreement statement

This article is original, neither the manuscript nor any parts of its content has been published before nor submitted to another journal. It is not currently being considered for publication elsewhere. All the authors have read the paper and agree with its submission.

## Credit author statement

Debmalya Sarkar: writing original draft, designing, conceptualization, data acquisition, manuscript preparation, Namrata Das: data acquisition, conceptualization, Md. Minarul Saikh: visualization, Prosenjit Biswas: visualization, Shubham Roy: computation, Sumana Paul: methodology, Nur Amin Hoque: supervision, editing, Ruma Basu: supervision, editing, Sukhen Das: supervision, editing.

## Funding

The financial assistances for the successful completion of our work are mentioned below:

Debmalya Sarkar: University Grants Commission, Govt. of India (Grant No.1413/(CSIR-UGC NET DEC.2018)).

Namrata Das: University Grants Commission, Govt. of India (Grant No.191620153244).

Md. Minarul Saikh: No funding.

Prosenjit Biswas: No funding.

Shubham Roy: Swami Vivekananda Merit-Cum-Means Scholarship (Grant No.WBP191577101345).

Sumana Paul: Science and Research Board, Govt. of India (Grant No. PDF/2019/001498).

Nur Amin Hoque: ICMR (Grant No.ICMR-17-0130).

Ruma Basu: No funding.

Sukhen Das: SERB, Govt. of India (Grant no: EEQ/2018/000747).

## Declaration of competing interest

The authors declare that they have no known competing financial interests or personal relationships that could have appeared to influence the work reported in this paper.

## Acknowledgments

We are very thankful to the FIST and PURSE program of the Department of Science and Technology (DST), Government of India, for their instrumental assistance.

## Appendix A. Supplementary data

Supplementary data to this article can be found online at https://doi.org/10.1016/j.ceramint.2022.10.070.

## References

[1] X. Ren, H. Fan, C. Wang, J. Ma, H. Li, M. Zhang, S. Lei, W. Wang, Wind energy harvester based on coaxial rotatory freestanding triboelectric nanogenerators for self-powered water splitting, Nano Energy 50 (2018) 562–570.

[2] Cao, X.; Zhang, M.; Huang, J.; Jiang, T.; Zou, J.; Wang, N.; Wang, Z. Inductor-free wireless energy delivery via maxwell's displacement current from an electrodeless triboelectric nanogenerator. Advanced materials2018,30, 1704077.

[3] Y. Qian, J. Du, D.J. Kang, Enhanced electrochemical performance of porous Co-doped TiO2 nanomaterials prepared by a solvothermal method, Microporous Mesoporous Mater. 273 (2019) 148–155.

[4] C. Wu, W. Ding, R. Liu, J. Wang, A.C. Wang, J. Wang, S. Li, Y. Zi, Z.L. Wang, Keystroke dynamics enabled authentication and identification using triboelectric nanogenerator array, Mater. Today 21 (2018) 216–222.

[5] X. Chen, H. Guo, H. Wu, H. Chen, Y. Song, Z. Su, H. Zhang, Hybrid generator based on freestanding magnet as all-direction in-plane energy harvester and vibration sensor, Nano Energy 49 (2018) 51–58.

[6] K. Meng, J. Chen, X. Li, Y. Wu, W. Fan, Z. Zhou, Q. He, X. Wang, X. Fan, Y. Zhang, J. Yang, Z.L. Wang, Flexible weaving constructed self-powered pressure sensor enabling continuous diagnosis of cardiovascular disease and measurement of Cuffless blood pressure, Adv. Funct. Mater. 5 (2019), 1806388.

[7] Y. Wang, L. Zhu, Y. Feng, Z. Wang, Z.L. Wang, Comprehensive pyro-phototronic effect enhanced ultraviolet detector with ZnO/Ag Schottky junction, Adv. Funct. Mater. 29 (2019), 1807111.

[8] J. Chen, W. Tang, K. Han, L. Xu, B. Chen, T. Jiang, Z.L. Wang, Bladeless-turbine-based triboelectric nanogenerator for fluid energy harvesting and self-powered fluid gauge, Adv. Mater. Technol. 4 (2019), 1800560.

[9] X. Pu, H. Guo, Q. Tang, J. Chen, L. Feng, G. Liu, X. Wang, Y. Xi, C. Hu, Z.L. Wang, Rotation sensing and gesture control of a robot joint via triboelectric quantization sensor, Nano Energy 54 (2018) 453–460.

[10] H. Wu, Z. Su, M. Shi, L. Miao, Y. Song, H. Chen, M. Han, H. Zhang, Self-powered noncontact electronic skin for motion sensing, Adv. Funct. Mater. 28 (2018), 1704641.

[11] L. Gu, N. Cui, L. Cheng, Q. Xu, S. Bai, M. Yuan, W. Wu, J. Liu, Y. Zhao, F. Ma, Y. Qin, Z.L. Wang, Flexible fiber nanogenerator with 209 V output voltage directly powers a light-emitting diode, Nano Lett. 13 (2013) 91–94.

[12] J. Liu, N. Cui, L. Gu, X. Chen, S. Bai, Y. Zheng, C. Hu, Y. Qin, A three-dimensional integrated nanogenerator for effectively harvesting sound energy from the environment, Nanoscale 8 (2016) 4938–4944.
[13] J. Chen, J. Yang, H. Guo, Z. Li, L. Zheng, Y. Su, Z. Wen, X. Fan, Z.L. Wang, Automatic mode transition enabled robust triboelectric nanogenerators, ACS Nano 9 (2015) 12334–12343.
[14] W. Yang, J. Chen, G. Zhu, J. Yang, P. Bai, Y.J. Su, Q.S. Jing, X. Cao, Z.L. Wang, Harvesting energy from the natural vibration of human walking, ACS Nano 7 (2013) 11317–11324.
[15] J. Yang, J. Chen, Y. Liu, W. Yang, Y. Su, Z.L. Wang, Triboelectrification-based organic film nanogenerator for acoustic energy harvesting and self-powered active acoustic sensing, ACS Nano 8 (2014) 2649–2657.
[16] D. Zhu, M.J. Tudor, S.P. Beeby, Strategies for increasing the operating frequency range of vibration energy harvesters, Meas. Sci. Technol. 21 (2010), 022001.
[17] D. Sarkar, N. Das, M.M. Saikh, P. Biswas, S. Das, S. Das, N.A. Hoque, R. Basu, Development of a sustainable and biodegradable Sonchus asper cotton pappus based piezoelectric nanogenerator for instrument vibration and human body motion sensing with mechanical energy harvesting applications, ACS Omega 6 (2021) 28710–28717.
[18] J. Zhao, F. Li, Z. Wang, P. Dong, G. Xia, K. Wang, Flexible PVDF nanogenerator-driven motion sensors for human body motion energy tracking and monitoring, J. Mater. Sci. Mater. Electron. 32 (2021) 14715–14727.
[19] S. Hajra, M. Sahu, D. Oh, H.J. Kim, Lead-free and flexible piezoelectric nanogenerator based on CaBi4Ti4O15 Aurivillius oxides/PDMS composites for efficient biomechanical energy harvesting, Ceram. Int. 47 (2021) 15695–15702.
[20] S. Song, Z. Zheng, Y. Bi, X. Lv, S. Sun, Improving the electroactive phase, thermal and dielectric properties of PVDF/graphene oxide composites by using methyl methacrylate-co-glycidyl methacrylate copolymers as compatibilizer, J. Mater. Sci. 54 (2019) 3832–3846.
[21] J.M. Wu, K.-H. Chen, Y. Zhang, Z.L. Wang, A self-powered piezotronic strain sensor based on single ZnSnO3 microbelts, RSC Adv. 3 (2013) 25184–25189.
[22] K.I. Park, J.H. Son, G.T. Hwang, C.K. Jeong, J. Ryu, M. Koo, I. Choi, S.H. Lee, M. Byun, Z.L. Wang, Highly-efficient, flexible piezoelectric PZT nanocompositenanogenerator on plastic substrates, Adv. Mater. 26 (2014) 2514–2520.
[23] Z.-H. Lin, Y. Yang, J.M. Wu, Y. Liu, F. Zhang, Z.L. Wang, BaTiO3 nanotubes-based flexible and transparent nanogenerators, The journal of physical chemistryletters 3 (2012) 3599–3604.
[24] S. Xu, Y.-w. Yeh, G. Poirier, M.C. McAlpine, R.A. Register, N. Yao, Flexible piezoelectric PMN–PT nanowire-based nanocomposite and device, Nano Lett. 13 (2013) 2393–2398.
[25] H.B. Kang, J. Chang, K. Koh, L. Lin, Y.S. Cho, High quality Mn-doped (Na, K) NbO3 nanofibers for flexible piezoelectric nanogenerators, ACS applied materials &interfaces 6 (2014) 10576–10582.
[26] C. Chang, V.H. Tran, J. Wang, Y.-K. Fuh, L. Lin, Direct-write piezoelectric polymeric nanogenerator with high energy conversion efficiency, Nano Lett. 10 (2010) 726–731.
[27] R. Ding, X. Zhang, G. Chen, H. Wang, R. Kishor, J. Xiao, F. Gao, K. Zeng, X. Chen, X. Wei Sun, Y. Zheng, High-performance piezoelectric nanogenerators composed offormamidinium lead halide perovskite nanoparticles and poly(vinylidene fluoride), Nano Energy 37 (2017) 126–135.
[28] S. Ippili, V. Jella, J.H. Eom, J. Kim, S. Hong, J.S. Choi, V.D. Tran, N.V. Hieu, Y. J. Kim, H.J. Kim, S.G. Yoon, An eco-friendly flexible piezoelectric energy harvesterthat delivers high output performance is based on lead-free MASnI3 films andMASnI3-PVDF composite films, Nano Energy 57 (2019) 911–923.
[29] V. Jella, S. Ippili, J. Eom, J. Choi, S. Yoon, Enhanced output performance of a flexible piezoelectric energy harvester based on stable MAPbI3-PVDF compositefilms, Nano Energy 53 (2018) 46–56.
[30] J. Cai, N. Hu, L. Wu, et al., Preparing carbon black/graphene/PVDF-HFP hybrid composite films of high piezoelectricity for energy harvesting technology, Composites Part A: Applied Science andManufacturing 121 (2019) 223–231.
[31] M. Alam, A. Sultana, D. Mondol, Biomechanical and acoustic energy harvesting from TiO2 nanoparticle modulated PVDF-HFP nanofiber made high performance nanogenerator, ACS Appl. Energy Mater. 1 (2018) 3103–3112.
[32] (a) X. Chen, Y. Song, H. Chen, J. Zhang, H. Zhang, An ultrathin stretchable triboelectric nanogenerator with coplanar electrode forEnergy harvesting and gesture sensing, J. Mater. Chem. 5 (2017) 12361–12368;
(b) X. Yan, T. Xu, G. Chen, S. Yang, H. Liu, Q. Xue, Preparation and characterization of electrochemically deposited carbon nitride films on silicon substrate, J. Phys. Appl. Phys. 37 (2004) 907–913;
(c) E. Kar, N. Bose, B. Dutta, N. Mukherjee, S. Mukherjee, MWCNT@SiO2 heterogeneous nanofiller-based polymer composites: a single key to the high-performance piezoelectric nanogenerator and X-band microwave shield, ACS Appl. Nano Mater. 1 (2018) 4005–4018.
[33] P. Thakur, A. Kool, B. Bagchi, N.A. Hoque, S. Das, P. Nandy, The role of cerium (III)/Yttrium(III) nitrate hexahydrate salts on electroactive ß-phase nucleation and dielectric properties ofPoly(vinylidene fluoride) nanocomposites, RSC Adv. 5 (2015) 28487–28496.
[34] M.M. Saikh, N.A. Hoque, P. Biswas, W. Rahman, N. Das, S. Das, P. Thakur, Self-polarized $ZrO_2$/Poly(vinylidene fluoride-*co*-hexafluoropropylene) nanocomposite-based piezoelectric nanogenerator and single-electrode triboelectric nanogenerator for sustainable energy harvesting from human movements, Phys. Status Solidi A 218 (2021), 2000695.
[35] Y. Zhang, Y. Wang, Y. Deng, M. Li, J. Bai, Enhanced dielectric properties of ferroelectric polymer composites induced by metal-semiconductor Zn-ZnO core-shell structure, ACS Appl. Mater. Interfaces 4 (2012) 65–68.
[36] P. Thakur, A. Kool, B. Bagchi, N.A. Hoque, S. Das, P. Nandy, In situ synthesis of Ni (OH)2 nanobelt modified electroactive poly(vinylidene fluoride) nanocomposites: remarkable improvement in dielectric properties, Phys. Chem. Chem. Phys. 17 (2015) 13082–13091.
[37] N. Das, D. Sarkar, M.M. Saikh, P. Biswas, S. Das, N.A. Hoque, P.P. Ray, Piezoelectric activity assessment of size-dependent naturally acquired mud volcano clay nanoparticles assisted highly pressure sensitive nanogenerator for green mechanical energy harvesting and body motion sensing, Nano Energy 102 (2022), 107628.
[38] K. Pal, D.J. Kang, Z.X. Zhang, J.K. Kim, Synergistic effects of zirconia-coated carbon nanotube on crystalline structure of polyvinylidene fluoride nanocomposites: electrical properties andFlame-retardant behaviour, Langmuir 26 (2010) 3609–3614.
[39] C. Xu, Z.L. Wang, Compact hybrid cell based on a convoluted nanowire structure for harvesting solar and mechanical energy, Adv. Mater. 23 (2011) 873–877.
[40] Y. Yang, H. Zhang, Y. Liu, Z.-H. Lin, S. Lee, Z. Lin, C.P. Wong, Z.L. Wang, Silicon-based hybrid energy cell for self-powered electrodegradation and personal electronics, ACS Nano 7 (2013) 2808–2813.
[41] G.C. Yoon, K.-S. Shin, M.K. Gupta, K.Y. Lee, J.-H. Lee, Z.L. Wang, S.-W. Kim, High-performance hybrid cell based on an organic photovoltaic device and a direct current PiezoelectricNanogenerator, Nano Energy 12 (2015) 547–555.
[42] P. Li, Z. Zhang, Self-powered 2D material-based PH sensor and photodetector driven by monolayer MoSe2 piezoelectric nanogenerator, ACS Appl. Mater. Interfaces 12 (2020) 58132–58139.
[43] A. Sultana, P. Sadhukhan, M. Alam, S. Das, T.R. Middya, D. Mandal, Organo-Lead halide perovskite induced electroactive ß-phase in porous PVDF films: an excellent material for PhotoactivePiezoelectric energy harvester and photodetector, ACS Appl. Mater. Interfaces 10 (2018) 4121–4130.
[44] S.Y. Lim, W. Shen, Z. Gao, Carbon quantum dots and their applications, Chem. Soc. Rev. 44 (2015) 362–381.
[45] (a) S. Begum, H. Ullah, A. Kausar, M. Siddiq, M.A. Aleem, Epoxy functionalized multi - walled carbon nanotubes/polyvinylidene fluoride nanocomposites: microstructure, morphology, thermal,piezoelectricity and conductivity investigations, Polym. Compos. 40 (2019) E776–E794;
(b) X. Dong, Y. Su, H. Geng, Z. Li, C. Yang, X. Li, Y. Zhang, Fast one-step synthesis of N-doped carbon dots by pyrolyzing ethanolamine, J. Mater. Chem. C 36 (2014) 7477–7481.
[46] X. Zhang, M. Jiang, N. Niu, Z. Chen, S. Li, S. Liu, J. Li, Natural-product-derived carbon dots: from natural products tofunctional materials, ChemSusChem 11 (2018) 11–24.
[47] K. Roy, S. Jana, S.K. Ghosh, B. Mahanty, Z. Mallick, S. Sarkar, C. Sinha, D. Mandal, Three-dimensional MOF-assisted self-polarized ferroelectret: an effective autopowered remote healthcare monitoring approach, Langmuir 36 (2020) 11477–11489.
[48] P. Huang, S. Xu, W. Zhong, H. Fu, Y. Luo, Z. Xiao, M. Zhang, Carbon quantum dots inducing formation of β phase in PVDF-HFP to improve the piezoelectric performance, Sensor Actuator Phys. 330 (2021), 112880.

Advanced Composites and Hybrid Materials (2023) 6:232
https://doi.org/10.1007/s42114-023-00807-0

RESEARCH

# Elevating the performance of nanoporous bismuth selenide incorporated arch-shaped triboelectric nanogenerator by implementing piezo-tribo coupling effect: harvesting biomechanical energy and low scale energy sensing applications

**Debmalya Sarkar[1] · Namrata Das[1] · Md. Minarul Saikh[1,2] · Shubham Roy[1,6] · Sumana Paul[3] · Nur Amin Hoque[4] · Ruma Basu[5] · Sukhen Das[1]**

Received: 27 September 2022 / Revised: 2 October 2023 / Accepted: 2 December 2023 / Published online: 15 December 2023


## Abstract

With the increasing demand of environmental friendly and unlimited power supplies, the use of triboelectric nanogenerator (TENG) also increases due to its high mechanical energy to electrical energy conversion ability. Herein, an arch shaped, self-powered, and wearable piezoelectric thin film with bismuth selenide based triboelectric nanogenerator, named as PBTNG, is fabricated with the help of nanoporous bismuth selenide ($Bi_2Se_3$) incorporated poly(vinyldene fluoride) (PVDF) composite piezoelectric thin film (PBi). The mechanism of the PBTNG device is induced by piezo-tribo coupling effect. Furthermore, the surface area and distribution of pore size of $Bi_2Se_3$ have been measured from Brunnauer–Emmett–Teller (BET) analysis and also described by basal spacing, which helps in increment of β-crystalline phase of the thin film. The density functional theory (DFT) has been performed to find out the electrical band gap and density of states of $Bi_2Se_3$ nanoparticles. The interaction of nanoparticle with PVDF monomer and electrical properties of β-phase has been investigated with DFT calculations as well. The fabricated triboelectric device exhibits outstanding output performance with a maximum power density of 2.03 $Wm^{-2}$ under continuous finger impartation and can illuminate light-emitting diodes (LEDs) under heel pressing and periodic finger tapping. Additionally, the wearable PBTNG device traps the biomechanical energy from different body movements like heel pressing, feet tapping, blood flow, single finger tapping, etc., and converts them into electrical energy easily. Furthermore, single electrode bismuth selenide based triboelectric nanogenerator, named as SBTNG exhibits high sensitivity value (20.2 V/kPa) at low pressure region (< 0.5 kPa) which helps in electricity generation from small scale mechanical energies such as writing on the device, mouse clicking, keyboard striking, external CD drive running, etc. Thus, self-powered and wearable energy harvester can be used in daily life as a substitute of batteries.

**Keywords** Nanoporous $Bi_2Se_3$ · Piezoelectric thin film · Coupling effect induced triboelectric nanogenerator · Harvesting small scale energies · Sensing body movements

✉ Nur Amin Hoque
nuramin03@gmail.com

✉ Ruma Basu
ruma.b1959@gmail.com

✉ Sukhen Das
sdasphysics@gmail.com

[1] Department of Physics, Jadavpur University, Kolkata 700032, West Bengal, India

[2] Government General Degree College at Pedong, Kalimpong-734311, West Bengal, India

[3] Department of Physics, Indian Institute of Technology Guwahati, Guwahati 781039, India

[4] SAIS Department, Indian Association for the Cultivation of Science, Kolkata 700032, India

[5] Department of Physics, Jogamaya Devi College, Kolkata 700026, West Bengal, India

[6] School of Science and Shenzhen Key Laboratory of Flexible Printed Electronics Technology, Harbin Institute of Technology, Shenzhen 518055, China

## 1 Introduction

With the fastest expansion of recent science and technology, internet of things (IoTs) makes human life easier and enjoyable [1]. As a result, the usage of conventional energy storage tools like sodium ion batteries, rigid batteries, lithium-ion batteries, supercapacitors, etc., which have immense dimensions and regular charging requirements, seems to be limited [2–5]. Therefore, alternative energy sources and equipment which help us to charge up the sensors and devices have gained immense attentions among the researches in the last few years [6, 7].

Triboelectric nanogenerator (TENG) is chosen as the suitable candidate of alternative energy sources which can power up the previously mentioned devices easily due to its conversion ability of naturally available mechanical energies like water wave energy, wind energy, biomechanical energy, vibrational energy, low scale mechanical energy, and rotational energy into electrical energies [8–11]. The triboelectric phenomenon was first proposed by Wang et al. in 2012 and published a standard list of triboelectric materials to give us the idea about their effective pairing. Moreover, the working principle of TENG is based on electrostatic induction and tribo-electrification [10]. Generally, TENG has four working modes. Among them, contact-separation (CS) mode is most preferable one due to its charge generating, simple fabrication process, and high output performance [10]. Therefore, selection of triboelectric materials plays an important role in improving the charge generation and fabrication of TENG. To design the layered structure and improve the charge generation of TENG device, polymers are utilized due to their high charge affinity, high dipole moment, flexibility, and durability [12–14]. Until now, the reported negative triboelectric polymers are poly(tetrafluoroethylene) (PTFE), poly(vinyldene fluoride) (PVDF), poly(dimethyl siloxane) (PDMS), polyimide (PI), poly(vinyl chloride) (PVC), poly propylene (PP), etc., and reported positive polymers are thermoplastic polyurethane (TPU), poly(vinyl alcohol) (PVA), poly(3-hydroxybutyrate-co-3-hydroxyvalerate) (PHBV), etc. [10, 15]. In this present work, PDMS and PVA have been used as tribo-negative and tribo-positive material.

Moreover, there are so many advantages of using TENG such as light weight, flexibility, durability, simple fabrication process, cost effectiveness, and robustness [12, 13, 16]. Recently, few pioneers works have been done by utilizing the effect of TENG. For example, Lin et al. developed an active bacterial anti-adhesion strategy to remove the bacteria from the surfaces of materials which were driven by TENG [17]. Jia et al. proposed the electron transfer mechanism among the metal and $SiO_2$ composites by using first principle study. This idea is very helpful in selection of dielectric layer for TENG [18]. Moreover, Zhang et al. proposed a new strategy to combat the environmental pollution by using cellulose instead of traditional polymers and utilized it to design nanogenerators [19]. Additionally, Ghafari et al. developed PVDF nanogenerator for harvesting low range frequencies and converting them into electricity [20]. To improve the performance of TENG and keep the properties like flexibility, durability, etc. intact, researchers have given the efforts to hybridize the triboelectric effect with other effect [21]. For example, Han et al. fabricated triboelectric-electromagnetic nanogenerator [22]; Wei et al. designed an energy harvester using the combine effect of Curie effect, triboelectric effect, and electrostatic induction effect [23]; Jirayupat et al. fabricated a hybrid nanogenerator by using piezo-tribo combine effect [21]. Although several work has been done on hybrid nanogenerator but very few work has been reported on nanocomposite-based piezo-tribo coupling effect. Although the working mechanisms of triboelectricity and piezoelectricity are different, their electrical stimuli generation process never overlaps with each other [24]. Thus, combining the piezoelectric effect with triboelectricity into a single device not only enhances electron transfer but also generates extra charges, which results in better output. Moreover, the alignment of dipoles of piezoelectric materials within nanocomposite film plays an important role to obtain better output performance by generating maximum piezopotential [21]. In this study, piezoelectric layer based TENG has been designed with the help of nanoporous $Bi_2Se_3$ and PVDF polymer based nanocomposite thin film, PDMS thin layer, and PVA thin film. To improve the output performance of the fabricated TENG, doping technique has been used. PVDF is a semi-crystalline, electro-active, fluro polymer. It consists of five crystalline phases such as α, β, γ, δ, and ε. Among them β phase is more crystalline and polar due to its all-trans conformation and also exhibits very good piezoelectric and ferroelectric properties [24]. Owing to these properties, PVDF has broaden its utilization in various fields of application. For example, Cheng et al. fabricated porous PVDF-Ni/PE-CNT composite foam through melt extrusion and batch foaming methods which exhibited very good hydrophobic, EMI shielding, and optical-electrical-thermal properties [25]. Gao et al. modified the surface of CNTs through silanization and fluorosilanization combine methods and utilized the modified CNTs to prepare hydrophobic electrospun membrane by mixing with PVDF matrix. This membrane was further utilized in direct contact membrane distillation applications [26]. Furthermore, Wu et al. improved the thermal conductivity and dielectric properties of PVDF matrix by embedding BN-$SiO_2$@MWCNT into PVDF and proposed the utilization of the nanocomposite in the

field of microelectronic packaging [27]. Sharafkhani et al. fabricated a high performance piezoelectric sensor by using well-orientated CNT-contained PVDF nanofibers [28]. Moreover, Li et al. developed piezoelectric sensor with the help of PVDF-HFP/ZnO nanofibers to track sporting workout of players and monitor their activities wirelessly [29]. Liu et al. fabricated PVDF/PAN membrane with 83.4% β content through electrospinning method. This electrospun membrane was further utilized as piezoelectric energy harvester and sodium-ion battery separator [30]. Beside this, several approaches were taken to synthesize the dipole-aligned β phase by using annealing and post stretching or doping with fillers. Here, $Bi_2Se_3$ nanograins have been reinforced into PVDF matrix to enhance the percentage of crystallinity of β phase because of the dipole–dipole interaction between the hydrogen atom of the PVDF matrix and electronegative atom of the co-polymer. The induced β phase gives high polarizability, and electroactive and dielectric properties which enhances the output performance of TENG [31].

Topological insulators (TI) are a new class of quantum matter, consisting of bulk gap and reversible time symmetry protected relativistic Dirac fermions on the surface. In the bulk states, these materials are electrically insulating but can carry out the electricity in the surface states because of the topologically covered electronic edge. Thus, TIs are used directly in thermoelectric devices, superconductors, photoelectronic sensors, etc. [32–34]. Compared to other TIs, bismuth selenide ($Bi_2Se_3$) has gained huge attention among the researchers owing to the topological surface states. $Bi_2Se_3$ has sole characteristics such as high surface mobility, small band gap near about 0.35 eV, excellent electrical conductivity, and photoconductivity [35–39]. The small band gap property helps $Bi_2Se_3$ in light absorption over the wide wavelength range. The sturdy topological structures help bismuth selenide to maintain the stability in ambient or unkind environment [40]. Inside the crystal structure of this TI, five covalent bonded atomic planes Se–Bi–Se–Bi–Se make the planar quintuple layers, and these weakly bonded quintuple layers are piled along *c* axis through Van der Waals interactions. Owing to this specific structure and topological surface states, $Bi_2Se_3$ makes itself a potential candidate in the area of electrochemical energy storage system and also borrows the distinctive physical properties and electronic structure [41–44]. For these reasons, $Bi_2Se_3$ has been selected as primary doping element and also utilized in device fabrication process.

In this current work, arch-shaped and self-powered piezoelectric thin film with bismuth selenide based triboelectric nanogenerator, named as PBTNG, has been designed to harness different types of mechanical energies like heel and feet pressing, hand impartation, single finger tapping, pulse vibration, keypad striking, etc., and convert them into electrical energy. The $Bi_2Se_3$ nanoparticles have been chosen as doping material owing to the topological surface, distinctive physical properties, and electronic structure. The piezoelectric thin film based PBTNG device exhibits very good output voltage ($V_{OC}$) of 171.8 V with maximum power density of 2.03 $Wm^{-2}$ under continuous finger impartation. Moreover, the PBTNG device has the capability to illuminate LEDs through heel pressing and periodic finger impartation. Beside this, the device is sensible enough to catch small scale mechanical energies and convert them into electrical energy easily. These valuable investigations are indicating that PBTNG is a green and wearable energy harvester which can be used to power up portable electronic devices used in daily life.

## 2 Fabrication of piezoelectric thin film with bismuth selenide based triboelectric nanogenerator (PBTNG)

The fabricated PBTNG device consists of three layers, i.e., charge generating layer, piezoelectric layer and charge collecting layer. Herein, PVA and PDMS thin films have been used as charge generating layers, PBi thin film as piezoelectric layer and aluminum (Al) electrodes (thickness 41 μm) as charge collecting layer. The fabrication procedure of PBi thin film, PVA film and PDMS film has been elaborated in the supporting information file. PBTNG consists of two parts, i.e. positive and negative parts. The positive part consists of PVA film and Al electrode, and the negative part consists of PDMS film, Al electrode and PBi thin film. Thereafter, the positive part (PVA film and electrode attached together) was affixed with double tape to the upper part of the arch-shaped protective foam cover. Then, the negative part (PDMS layer, electrode, and PBi film attached together) was affixed to the lower part of the protective cover, maintaining ample air gap in the middle of the two parts. Two copper wires were joined with the electrodes to investigate the output performance of fabricated PBTNG device. Figure 1(c) exhibits the design of fabricated PBTNG device graphically.

## 3 Working mechanism of PBTNG device

Figure 2 describes the working mechanism of PBTNG device. The working principle of fabricated triboelectric nanogenerator depends on the coupling effect of triboelectrification and piezoelectric effect during contact separation (CS) mode. In CS mode, PBTNG consists of two parts, i.e. positive and negative parts. The positive part consists of PVA film and Al electrode, and the negative part consists of PDMS film, Al electrode and PBi thin film. According to the triboelectric series, the PVA and PDMS film acquire positive

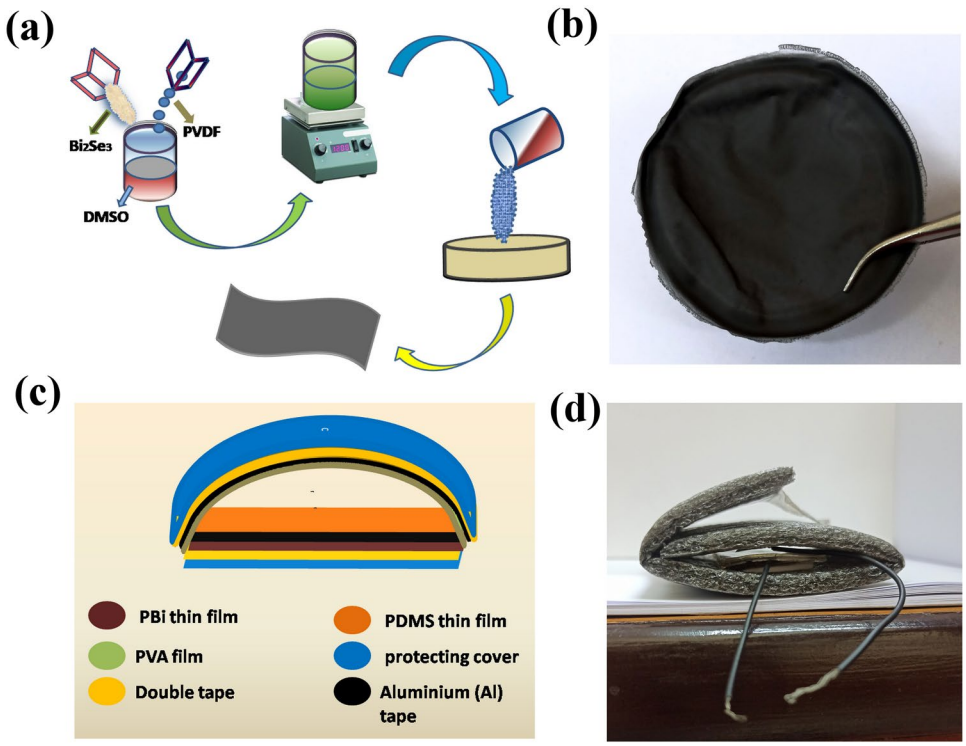


**Fig. 1** **a** Schematic demonstration of the fabrication process of PBi thin film. **b** Snapshot of the piezoelectric thin (PBi) film. **c** Graphical illustration of designed PBTNG device. **e** Digital photographs of arch-like shape of PBTNG device

and negative triboelectric charges respectively. When these two films get contacted with each other, the PDMS film gains electrons from PVA film. The electron transfer capability depends on their position in the triboelectric series. The working mechanism of PBTNG is elaborated in four stages.

Stage 1: In the original state, the triboelectric layers are separated from each other. Thus, the PBTNG device remains electrically neutral condition and also free of charges, shown in Fig. 2(i). When an external force is applied on the PBTNG device, the PVA and PDMS film come close to each other from the original state. As a result, the positive and negative triboelectric charges are produced in the PVA and PDMS films respectively, shown in Fig. 2(ii). In this stage, the piezoelectric layer (PBi thin film) remains same and no deformation takes place under applied external force.

Stage 2: Under external force, the deformation of the piezoelectric layer (PBi film) takes place and the dipoles of

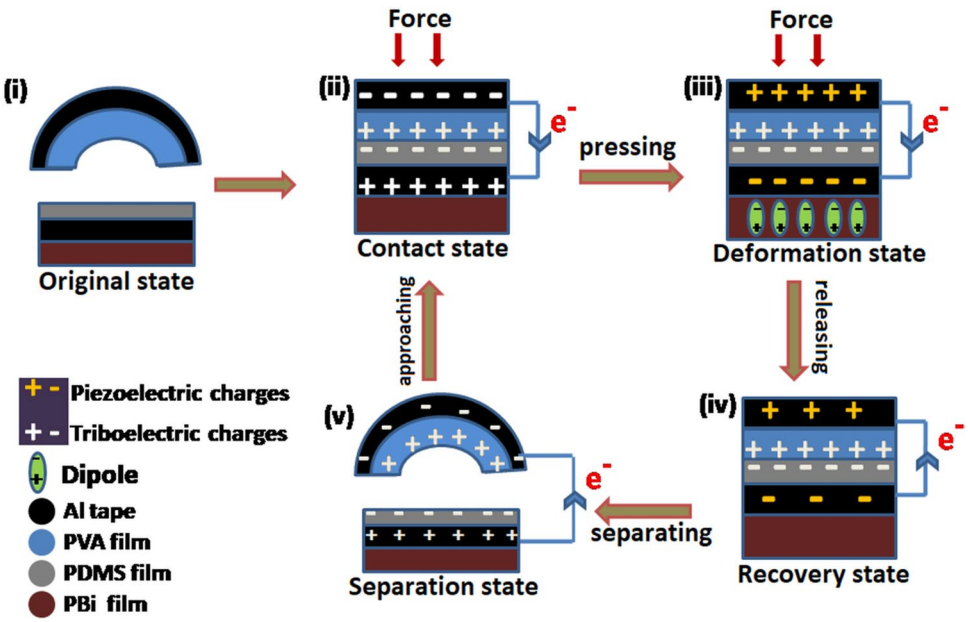


**Fig. 2** Mechanism of the voltage generation of fabricated PBTNG device

the piezoelectric film are aligned along the direction of the applied external force. Under the deformation, the electric dipoles of the nanocomposite get properly oriented and help in the changing of polarization inside the piezoelectric nanocomposite. As a result, equal amount of positive and negative piezoelectric charges is induced on the top and bottom electrodes respectively. Thus, electron flow occurs from top electrode to bottom electrode during this deformation process. The above-said phenomenon is depicted schematically in Fig. 2(iii).

Stage 3: When the external force starts to decrease, the contact between the positive and negative layers remains intact and the polarization of the piezoelectric thin film starts to recover. As a result electrons flow from bottom to top electrode until the polarization is fully recovered, shown in Fig. 2(iv).

Stage 4: After the recovery of polarization, the piezoelectric potential gets balanced and only the triboelectric charges gather on the surface of positive and negative triboelectric layers. On further decrement of external force, separation between the positive and negative triboelectric layers takes place. As a result, the electrons flow from bottom to top aluminum electrode, shown in Fig. 2(v). On further application of external force on PBTNG device again, the two charge generating layers start to come close to each other. As a result, the electrons flow between electrodes and it returns to Fig. 2(ii) and the cyclic process continues. Thus, the flow of electrons between the two electrodes generates alternative electric signal. The above said detailed description of the mechanism of PBTNG device confirms that both the triboelectrification and piezoelectricity process takes active part to complete a full cycle. Therefore, the coupling effect of triboelectrification and piezoelectric effect is responsible for the improvement of the output performance of the device.

The basic mechanism of triboelectric nanogenerator (TENG) can be elaborated by Maxwell's equations. Wang, the founder of TENG, has introduced the surface polarization ($P_S$) term in the displacement vector ($D$) equation: [45]

$$\boldsymbol{D} = \boldsymbol{\varepsilon}_0 \boldsymbol{E} + \boldsymbol{P} + \boldsymbol{Ps} \tag{1}$$

where $P_S$ is the polarization which is induced by electrostatic triboelectric and piezoelectric effect and $P$ is the electric field–encouraged medium polarization.

After adding surface polarization term in displacement vector, the Maxwell displacement current [31] will be

$$\boldsymbol{J}_D = \frac{\partial \boldsymbol{D}}{\partial t} = \boldsymbol{\varepsilon} \frac{\partial \boldsymbol{E}}{\partial t} + \frac{\partial \boldsymbol{P}_S}{\partial t} \tag{2}$$

where $E$ is the electric field and $\varepsilon$ is the permittivity of the medium [31].

The first term in displacement current equation gives the idea of the electromagnetic wave which has been utilized in various wireless systems and the second term represents the contribution of the displacement current in the energy and sensors systems [45–48].

## 4 Result and discussions

The crystallographic structures and surface morphologies of the synthesized nanoparticles and fabricated thin films are investigated by X-ray diffraction (XRD; Model-D8, Bruker AXS Inc., Madison, WI), field emission scanning electron microscopy (FESEM; INSPECT F50), and transmission electron microscopy (TEM; JEOL JEM F200). The elemental mapping of thin film has been performed by using Zeiss Gemini SEM 500. The elemental analysis of PBi nanocomposite was done by X-ray photoelectron spectroscopy (XPS) (model: PHI5000VERSAPROBE III, Make ULVAC-PHI, Inc., Japan). The different phase performance and thermal behaviors of thin films are examined by Fourier transform infrared (FTIR) spectroscopy (FTIR-8400S; Shimadzu) and thermal gravimetric analysis (TGA; TGA/SDTA851e, Mettler Toledo AG). The mechanical properties of thin film have been measured by Universal Testing Machine (Tinius Olsen model: H50KS, UK). The electrical properties of the thin film are investigated by IM 3536 LCR Meter. The surface properties of synthesized $Bi_2Se_3$ nanoparticles have been examined using automated gas sorption analyzer (Autosorb iQ2, Quantachrome Instruments).

### 4.1 Experimental and computational structural analysis of nanoporous $Bi_2Se_3$

The detailed synthesis procedure of $Bi_2Se_3$ nanoparticle has been described in the supporting information file. The crystalline peaks and surface morphology of the nanoparticle have been investigated by XRD analysis and FESEM micrographs. The crystalline peaks at 25.02° (101), 29.23° (015), 40.22° (101), 43.52° (110), 47.72° (116), and 53.35° (205) confirm the formation of $Bi_2Se_3$ nanosized (33 nm) particles. These identical peaks match with the JCPDS file no 33–0214. Furthermore, the refinement of XRD peaks of $Bi_2Se_3$ was performed by using Rietveld-based software package MAUD v2.8 to investigate the micro-structural and crystallographic parameters. Initially, standard Caglioti PV functions were deployed to refine the detector and diffractometer. During this cycle, instrumental broadening was also rectified. The experimental diffraction peaks were refined by employing a regular crystallographic information file (.cif) of bismuth selenide (COD file no. 1530736). To achieve better fitting outcomes, a number of micro-structural parameters including crystal size and unit cell dimension were optimized. The texture analyses

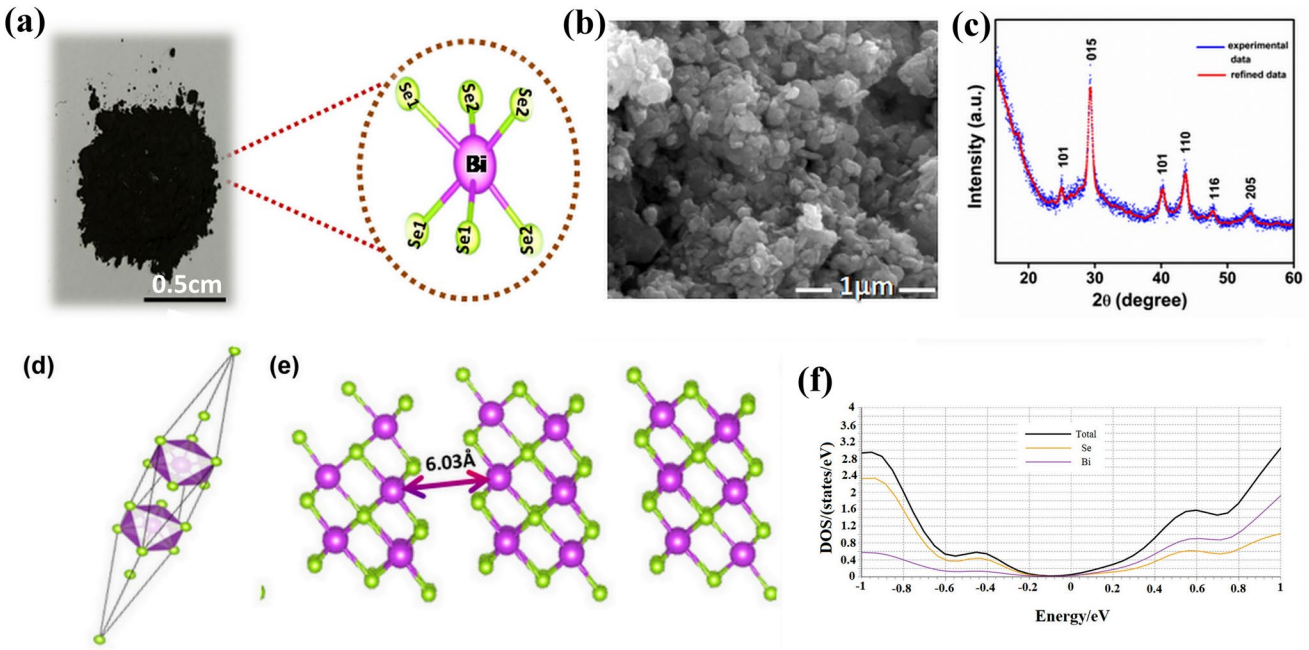


**Fig. 3** **a** Optical image of $Bi_2Se_3$ and polyhedral species of $Bi_2Se_3$ from Rietveld refinement. **b** FESEM image and **c** crystalline peaks of synthesized nanoparticle. **d** Rhombohedral structure, **e** basal spacing, and **f** density of state (DOS) calculation of $Bi_2Se_3$ nanoparticle

were also performed to obtain adequate fitting results. The low values of the global reliability parameters such as $R_{WP}$ and $R_P$ are suggesting the consistency of refinements. The refinement of parameters was performed up to 15 cycles and corresponding results are depicted in the Table S1. Figure 3(c) shows the experimental and refined X-ray crystalline peaks of $Bi_2Se_3$ nanoparticles. The surface morphology of nanoparticle has been examined by FESEM image (Fig. 3(b)). The FESEM image describes that the synthesized nanoparticles are porous and some gaps are seen to restrict the formation of uniform structure. This is the reason we get tube or grain-like structure of the nanoparticle.

From BET analysis, surface area of $Bi_2Se_3$ nanoparticles is measured which is 16.07 $m^2/g$. From the desorption part of the adsorption/desorption isotherm, the obtained pore size of the $Bi_2Se_3$ nanoparticles is 2.64 nm and pore volume is 0.031 $cm^3/g$. The obtained hysteresis loop and the pore size distribution of the synthesized $Bi_2Se_3$ nanoparticles are given in the supporting file, Fig. S7. The porosity is further confirmed by basal spacing whose value is found to be 6.03 Å (Fig. 3(e)) which infers the high porosity value of synthesized nanoparticle. Furthermore, the computed.cif files of $Bi_2Se_3$ have been visualized with the help of VESTA 3.5.7 software which confirms the rhombohedral structure of bismuth selenide, shown in Fig. 3(d). The rhombohedral structure consists of three quintuple layers (QL) which are weakly bound to each other through Van der Waals force.

Each QL have five atomic planes along with the atomic order of $Se_1$–Bi–$Se_2$–Bi–$Se_1$ where, $Se_1$ and $Se_2$ denote the nonequivalent layers [49]. Moreover, the polyhedral species has been observed with bond length and bond angle, depicted in Fig. 3(a). The bond lengths between Bi–$Se_1$ and Bi–$Se_2$ are 2.97 Å and 2.73 Å and the dihedral angle between $Se_1$–Bi–$Se_2$ is 86.26°.

Furthermore, density functional theory (DFT) study is performed on the samples to investigate the electronic band structure and density of state (DOS) by using both localized and de-localized methods. On one hand, the DFT calculation over $Bi_2Se_3$ was conducted by using Quantum Espresso software employing a local density approximation functional having cut-off wave function energy of 50 Ry. Moreover, the band structures were calculated by using a similar theoretical level employing a Γ-centered k-point having a width of 9×9×9 mesh.

The electronic band structure gives us the idea about the surface states of $Bi_2Se_3$. The surface states are represented by the electronic bands which are located around Fermi energy level ($E_F$) at the center of Brillouin zone, i.e. Γ-point. It is observed that both the conduction band minima and valence band maxima share the single valley nature [35, 49]. Moreover, the momentum of both these bands matches with each other, elucidating a direct band gap nature of the $Bi_2Se_3$ nanoparticle. A very small gap (~0.1 eV) exists between the conduction band minima and valence band maxima, resulting in a semi-conductive nature of the sample, shown in the Fig. S3(c).

It is evident that the Dirac cone is situated inside the band gap. Along with the band structure calculation, DOS has been examined to elucidate the Dirac cone within the band gap. From the electronic band structure, the surface states are located at Fermi level which confirms the presence of the Dirac cone within the band gap. The dependency of momentum of electrons on energy is linear. As the surface states present within the energy gap, the DOS near the Fermi energy level should be linear [49]. Figure 3(f) confirms that the DOS maintains the linearity near Fermi level.

According to Mohyedin et al., the electronic band gap radically decreases with the increasing number of quintuple layers (QL) of $Bi_2Se_3$. They also validated the fact that such an increment in QLs can cause higher polarizability in the sample [44]. Herein, the synthesized $Bi_2Se_3$ nanoparticles have five QLs, which could also enhance the polarizability of the sample. In order to achieve a promising piezoelectric material, the dopant (herein $Bi_2Se_3$) should have a promising polarizability. Thus, studying electronic band structure and DOS helps in predicting the applicability of the material in this domain.

## 4.2 Surface morphological analysis of composite thin films

The microstructure and surface morphology of the $Bi_2Se_3$ incorporated PVDF composite thin (PBi) films are examined by FESEM images, which are shown in Fig. S1. The closer inspections of the FESEM images of the composite thin films are indicating the formation of the spherulites. The diameter of the spherulites of PBi thin films is near about 5 µm which confirms the presence of the electroactive β-crystalline phase, whereas the diameter of the pure PVDF thin film is 40 µm which indicates the presence of the non-polar α-crystalline phase [31]. The surface structure and topography of $Bi_2Se_3$ incorporated PVDF thin film have also been investigated by TEM images. Figure 4(a) depicts the TEM images of PBi 2.5 film where homogeneous surface of PBi 2.5 composite is clearly visible. Moreover, the presence of $Bi_2Se_3$ nanoparticle inside the polymer matrix is shown in Fig. 4(b). The homogeneous surface of PBi 2.5 confirms the well dispersion of $Bi_2Se_3$ porous nanoparticles into PVDF matrix. The Van der Waals interaction between $Bi_2Se_3$ porous nanoparticles and PVDF matrix is

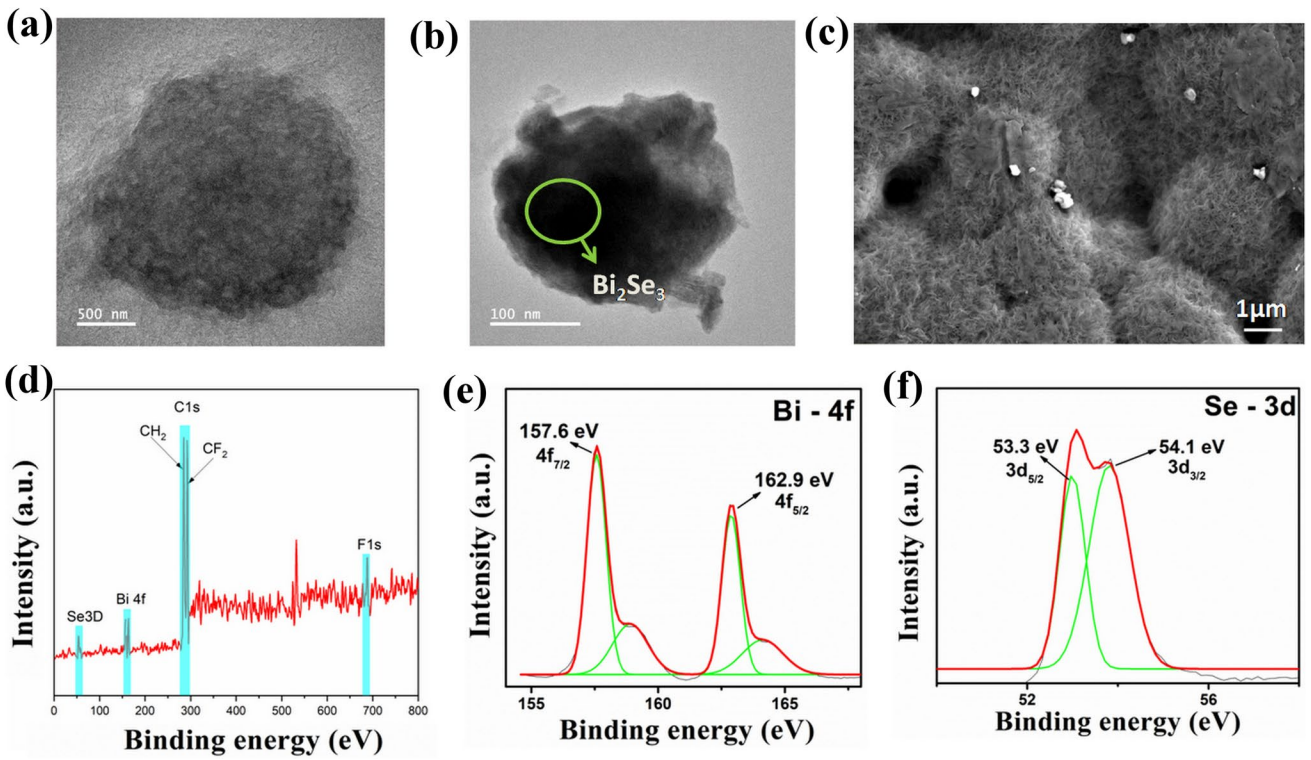


**Fig. 4** **a** TEM images of PBi 2.5 film. **b** TEM image showing the presence of $Bi_2Se_3$ nanoparticle inside the polymer matrix. **c** High-resolution SEM image confirming the presence of $Bi_2Se_3$ nanoparticle within the composite film. **d** XPS analysis of the nanocomposite PBi 2.5. **e** Core level spectra of Bi-4f in the binding energy range of 155 to 168 eV. **f** Core level spectra of Se-3d in the binding energy range of 50 eV to 57 eV

responsible for this well dispersion [28]. Along with this, the high-resolution SEM images with elemental mapping have been provided to confirm the homogeneous dispersion of $Bi_2Se_3$ nanoparticles into PVDF matrix, shown in the supporting information file. The presence of incorporated $Bi_2Se_3$ nanoparticles within the composite film has been clearly observed in Fig. 4(c) and no agglomeration takes place. These results are clearly indicating the uniform and homogeneous dispersion of synthesized $Bi_2Se_3$ nanoparticles within PVDF matrix. Moreover, the synthesis procedure of composite film is described in the supporting information file.

### 4.3 Elemental analysis of PBi nanocomposite (X-ray photoelectron spectroscopy)

The X-ray photoelectron spectroscopy (XPS) analysis of the nanocomposite PBi 2.5 is shown in Fig. 4(d). The XPS spectra revealed that the C-1s peak is observed at a binding energy of 285 eV in the $Bi_2Se_3$/PVDF nanocomposite, corresponding to carbon atoms present in the sample. The presence of carbon atoms bonded with fluorine was evident from the peak observed at approximately 292 eV, which is a characteristic of the $–CF_2–$ group. Additionally, a peak observed at 286.5 eV indicated the presence of carbon atoms bonded with hydrogen in the form of $–CH_2–$ bonds. The F-1s peak observed at a binding energy of 690 eV confirmed the presence of fluorine atoms in the sample, which is also present in the PVDF polymer [33, 50]. From Fig. 4 (e), the core level spectra of Bi-4f is observed in the binding energy range of 155 to 168 eV. The deconvoluted spectra of Bi-4f also show two major peaks centered at 157.6 eV and 162.9 eV, which represent the two various spin–orbit-coupled 4f components ($4f_{7/2}$ and $4f_{5/2}$ respectively) in bismuth. Similarly, deconvoluted spectra of Se-3d display two major peaks centered at 53.3 eV and 54.1 eV corresponding to the spin–orbit coupled 3d components $3d_{5/2}$ and $3d_{3/2}$ respectively. In brief, the core level spectra of Se-3d lie in the binding energy range of 50 eV to 57 eV as can be seen in Fig. 4(f). These spectra thus confirmed the presence of bismuth and selenium in the nanocomposite. Overall, the XPS analysis provided evidence for the presence of the expected elements and bonding in the $Bi_2Se_3$/PVDF thin film [33]. The peaks observed in the survey scan and core-level spectra offered valuable information about the elemental composition and bonding in the sample PBi 2.5.

### 4.4 Electroactive β-crystalline phase analysis of PBi thin films

The formation of electroactive β-crystalline phase in $Bi_2Se_3$ nanoparticle loaded PVDF thin (PBi) films has been investigated by X-ray diffraction patterns. Figure 5(a) demonstrates the XRD pattern of pure PVDF thin film and PBi thin films. For pure PVDF thin film, the characteristic peaks are observed at $2\theta = 17.6°$ (100), 18.3° (020), 19.9° (021), and 26.6° ((201), (310)) confirming the existence of non-polar α-crystalline phase. At $2\theta = 38.3°$, a tiny peak is also noticed in the XRD pattern of the pure PVDF thin film. The reason behind this is the reflection from either (002) plane (representing the α-crystalline phase) or (211) plane (representing the γ-crystalline phase) [31, 45, 51]. This matter has been resolved by the FTIR spectra of the pure PVDF thin film. When $Bi_2Se_3$ nanoparticles are added into PVDF polymer matrix, all characteristic XRD peaks of the α-crystalline phase disappear. Only one diffraction peak at $2\theta = 20.4°$ (110), (200) has extensive rise, confirming the formation of electroactive β-crystalline phase in PBi thin films [31, 45]. The closer inspection of XRD graph shows that the increasing mass % of $Bi_2Se_3$ intensity of β-crystalline phase at 20.4° also increases and maximizes for 2.5 mass % loading $Bi_2Se_3$. Thus, PBi 2.5 exhibits maximum β-crystalline phase compared to other PBi thin films. The intensity ratio between 20.4° and 18.3° has been calculated to check the presence of α- and β-crystalline phases in pure PVDF thin film and PBi thin films. The maximum $I_{20.4}/I_{18.3}$ value is obtained for PBi 2.5 which is 1.65, shown in Fig. S2(b).

The electroactive β-crystalline phase formation has been further examined by FTIR spectra analysis. Figure 5(b) illustrates the FTIR spectrum of pure PVDF thin film and $Bi_2Se_3$ loaded PVDF thin (PBi) films in the region of 400 to 1100 $cm^{-1}$. In case of pure PVDF thin film, the absorbance peaks at 487 $cm^{-1}$ ($CF_2$ waging), 531 $cm^{-1}$ ($CF_2$ bending), 616 and 764 $cm^{-1}$ ($CF_2$ bending and skeletal bending), and 796 and 976 $cm^{-1}$ ($CH_2$ rocking), stipulating the presence of the non-polar α-crystalline phase. At 840 $cm^{-1}$ ($CH_2$ rocking, $CF_2$ stretching, and skeletal $C-C$ stretching), a small absorbance peak is also observed in the IR spectrum of pure PVDF thin films. The presence of β and β + γ crystalline phases may be the reason behind getting this peak. But no characteristic peak at 1234 $cm^{-1}$ is present, which is the main absorbance peak for γ-crystalline phase in the FTIR spectra of pure PVDF. For this reason, the absorbance peak at 840 $cm^{-1}$ confirms the presence of the β phase, occurring due to the TTTT conformation in polymer chain of pure PVDF film. After doping with $Bi_2Se_3$ nanoparticles into PVDF matrix, all characteristic absorbance peaks which are representing the non-polar α-crystalline phase disappeared and absorbance peaks at 445 $cm^{-1}$ ($CF_2$ rocking and $CH_2$ rocking), 479 $cm^{-1}$ ($CF_2$ deformation), 510 $cm^{-1}$ ($CF_2$ stretching), 600 $cm^{-1}$ ($CF_2$ wagging), and 840 $cm^{-1}$ appeared, which confirms the nucleation of the electroactive β-crystalline phase in PBi thin films [31, 45]. Thus, β-crystalline phase has mainly nucleated in the composite thin films due to the catalytic effect of $Bi_2Se_3$ nanoparticles in the PVDF

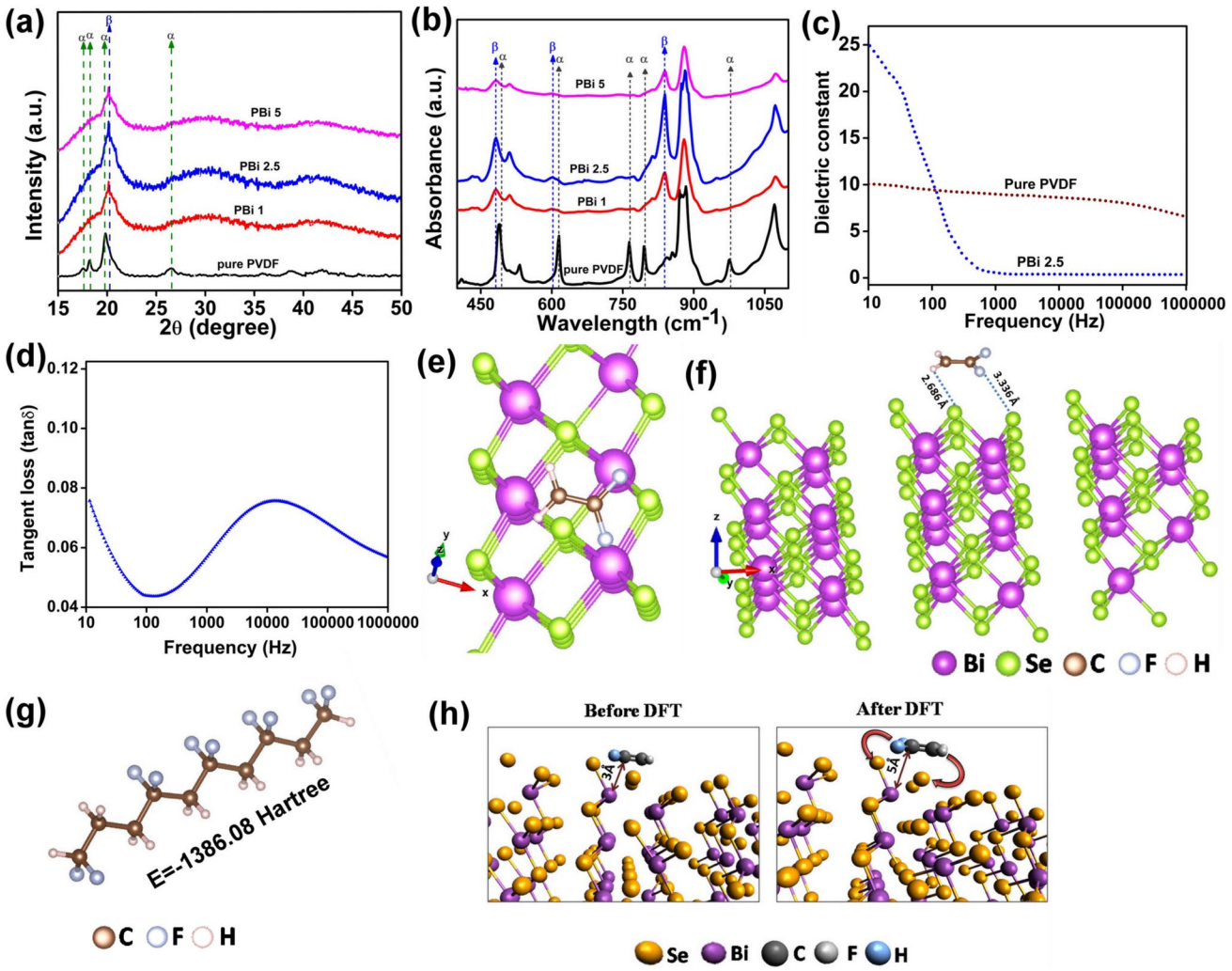


**Fig. 5** **a** X-ray diffraction peaks of pure PVDF thin film and $Bi_2Se_3$ doped PVDF thin films (PBi 1, PBi 2.5, PBi 5). **b** FTIR spectrum of pure PVDF thin film and PBi thin films. **c** Dielectric constant of pure PVDF film and PBi 2.5 film. **d** Tangent loss of PBi 2.5 film. Optimized geometrical structures acquired from DFT **e** top view of $Bi_2Se_3$ and PVDF interaction, **f** side view of $Bi_2Se_3$ and PVDF interaction with bond lengths, **g** β-crystalline phase of PVDF with total energy. **h** Pictorial representation of bond length shifting occurred between C and Bi before and after DFT

polymer matrix. The closer investigation of FTIR spectra of PBi thin films discloses that for PBi 2.5, the intensity of absorbance spectra becomes maximum which is matched with the XRD data. Furthermore, the fraction of electroactive β-crystalline phase ($F(\beta)$) has been calculated for estimating the amount of β-crystalline phase available in the PBi thin films by using the Lambert – Beer law [31].

$$F(\beta) = \frac{A_\beta}{\left(\frac{K_\beta}{K_\alpha}\right)A_\alpha + A_\beta} \tag{3}$$

where $A_\alpha$ = absorbance at 764 $cm^{-1}$, $A_\beta$ = absorbance at 840 $cm^{-1}$, $K_\beta = 7.7 \times 104$ $cm^2$ $mol^{-1}$ (absorption coefficients at 840 $cm^{-1}$), and $K_\alpha = 6.1 \times 104$ $cm^2$ $mol^{-1}$ (absorption coefficients at 764 $cm^{-1}$). This equation is very helpful as it gives the idea about the amount of β-crystalline phase available in PBi thin films and a better formation of the β-crystalline phase gives better piezoelectric property. Compared to other PBi thin films, PBi 2.5 exhibits the maximum $F(\beta)$ value which is 82.1%, shown in Fig. S2(a).

Furthermore, the structural and electrical properties of the PBi 2.5 film were found out with the help of density functional theory. Herein, the DFT calculation has been employed by using the Orca v.1.2 program. The hybrid Becke, 3-parameter, and Lee–Yang–Parr (B3LYP) functional along with the def 2 functional associated with 6-31G* basis set and RIJCOSX auxiliary basis function have been used for assigning the atoms like C, H, and F. The molecular

models of PVDF monomer and α, β-crystalline phases were drawn by Avogadro v.1.2.0 software program. The frequencies and geometries of all models were optimized and no imaginary frequency was observed, which confirms the proposed models. These optimized structures also consist of lowest amount of self-consistent field energy. The mechanism of attachment of $Bi_2Se_3$ ions on PVDF polymer has been investigated. Figure 5(e) and (f) shows the top and side views of $Bi_2Se_3$ ions and PVDF polymer interaction. These two images exhibit that PVDF monomer places itself parallel to the plane of nanoparticles. Initially, the PVDF monomer is placed near about 3 Å distance from the $Bi_2Se_3$ plane and it maintained the parallel distance from plane of the nanoparticle. Then, the DFT study was performed to optimize the geometrical structure and monitor the interaction between monomer and nanoparticle atoms. After the DFT calculation, a chemical interaction occurred between the PVDF monomer and $Bi_2Se_3$ plane as the bond length between C and Bi is shifted from 3 to 5 Å, shown in Fig. 5(h), and thus the bond lengths between H–Se and F–Se also change, shown in Fig. 5(f). It is observed that the Se atom is attracted by the neighboring H atom, which results in a significant reduction in the distance between H–Se (2.686 Å) atoms. Conversely, the distance between F–Se (3.336 Å) slightly increased in order to minimize the surface energy of the composite. Such interaction between $Bi_2Se_3$ and PVDF plays an important role to attach $Bi_2Se_3$ with PVDF, which has also been validated by XRD and FTIR results. In reality, $Bi_2Se_3$ nanoparticle possesses negative surface charge, [38] which is responsible to attract the H-moiety of the PVDF to form a strong attachment between $Bi_2Se_3$-PVDF.

Moreover, the electrical properties of the β-crystalline phase have been investigated by 6-31G* basis set. From the geometrical structures of α and β-phases, it is noticed that the irregular orientation of C atom and F atom in α-PVDF got completely polarized into the β-phase of PVDF. That is the reason a significant change in the C–C–C dihedral angle (114°) has been observed. The F and H atoms are rotated alongside of C–C chain and helped the model to polarize and minimize the single point energy of β-phase (Fig. 5(g)). The electrical properties of β-phase have been calculated theoretically, which describes that both isotropic polarizability and dipole moment of β-phase increase compared to the value of α-phase. Due to this, the higher dielectric constant value of PBi thin film is obtained compared to pure PVDF film experimentally (Fig. 5(c)). The comparison of electrical properties between α and β phases of PVDF has been investigated in Table S2.

The mechanical properties of PBi thin film have been measured by a universal testing machine with strain rate of 5 mm/min. The maximum tensile strength of the thin film is 15 MPa and Young's modulus is 881 $N/mm^2$. This result infers the higher mechanical stability of thin film in comparison with pure PVDF whose Young's modulus is 700 $N/mm^2$. The detailed description regarding the mechanical stability of the thin film has been elaborated in the supporting information file.

### 4.5 Electrical properties of composite film

The electrical properties of PBi 2.5 thin film have been investigated by dielectric measurement. The dielectric properties of thin film depend on various parameters like applied external electric field, grain structure, chemical composition, etc. Relative dielectric constant ($\varepsilon = \varepsilon' + j\,\varepsilon''$) describes the dielectric response. In the expression of relative dielectric constant, $\varepsilon'$ and $\varepsilon''$ exhibit the real part and imaginary parts of $\varepsilon$. The real part gives the idea about the energy storage capacity of the dielectric material caused by polarization and the imaginary part helps in energy dissipation within the material. The mathematical formula which can be used to calculate the real part of the dielectric constant is expressed as [52].

$$\varepsilon' = \frac{C*d}{\varepsilon_0*A} \tag{4}$$

where $C$ is value of capacitance of the PBi film, $d$ and $A$ are thickness and area of the silver coated PBi film, and $\varepsilon_0$ is permittivity of the free space permittivity with value of $8.85 \times 10^{-12}$ F/m. The real part of the dielectric constant of the PBi 2.5 thin film has been observed by varying the external electric field frequency from 10 Hz to 1 MHz. The maximum dielectric constant of this thin film is found at 10 Hz frequency with the value of 25 which is higher than the dielectric constant of pure PVDF film (the value is 10 at 10 Hz frequency), shown in Fig. 5(c). The value of the dielectric constant is decreasing steadily with the increasing frequencies. The behavior of the dielectric constant vs. frequency graph can be represented by Maxwell–Wagner interfacial polarization phenomenon [52]. When the free charge carriers gather at the grain boundary which has high resistivity, the interfacial polarization takes place. In brief, inside the dielectric thin film, the boundaries of insulated grain separate the conducting grains which help in the trapping of free charge carriers and generate dipoles through the grain at the time of their hopping. Furthermore, a constant loss in the value of dielectric constant due to the gradual decrement of the average dipole moment per unit volume is observed. In the high frequency region, a rapid decrement of dielectric value has been seen as electronic displacement polarization and dipole orientation polarization cannot survive with the variation of the external electric field frequency [53]. The tangent loss ($\tan\delta$) vs. frequency graph (Fig. 5(d)) also supports the dielectric value of PBi thin film. At the low frequency region, low tangent loss has been visualized. If the value of frequency increases, the tangent loss

value also increases at higher order frequency range. This phenomenon can occur due to the thermal agitation of the dipoles, occurring due to their orientations. As a result, the dipoles are unable to follow the variation of the applying external electric field and exhibit high loss at higher range of frequency [52]. Thus, the PBi 2.5 thin film exhibits high dielectric constant value along with low tangent loss, so this thin film could have good storage capacity.

## 5 Analysis of output performances of the fabricated PBTNG device

The schematic representations of the fabricated piezoelectric thin film (PBi) and device (PBTNG) are demonstrated in Fig. 1(a) and (c). The optical images of PBi thin film and PBTNG device are shown in Fig. 1(b) and (d). Figure 1(d) exhibits the arch like shape of fabricated PBTNG device. The output performance of PBTNG device is shown in Fig. 6. The output voltage vs. time graph of fabricated device is displayed in Fig. 6(a). Figure 6(b, c) describes the short circuit current vs. time graph of PBTNG device. The generation of the output voltage and short circuit current is performed by periodic finger pressing and releasing, with axial pressure of 11.7 N. The fabricated energy harvesting device (PBTNG) attains maximum output voltage at 5 Hz frequency. The generated output voltage (recorded by the Keysight, Oscilloscope DSO-X 3012A) and the short circuit current (measured by the Keithley DAQ6510) of PBTNG device are $V_{OC}$ ~ 171.8 V and $I_{SC}$ ~ 11.7 μA, respectively, shown in Fig. 6(a) and (b). The non-uniform patterns of the peak values of $V_{OC}$ under periodic finger imparting and releasing are obtained due

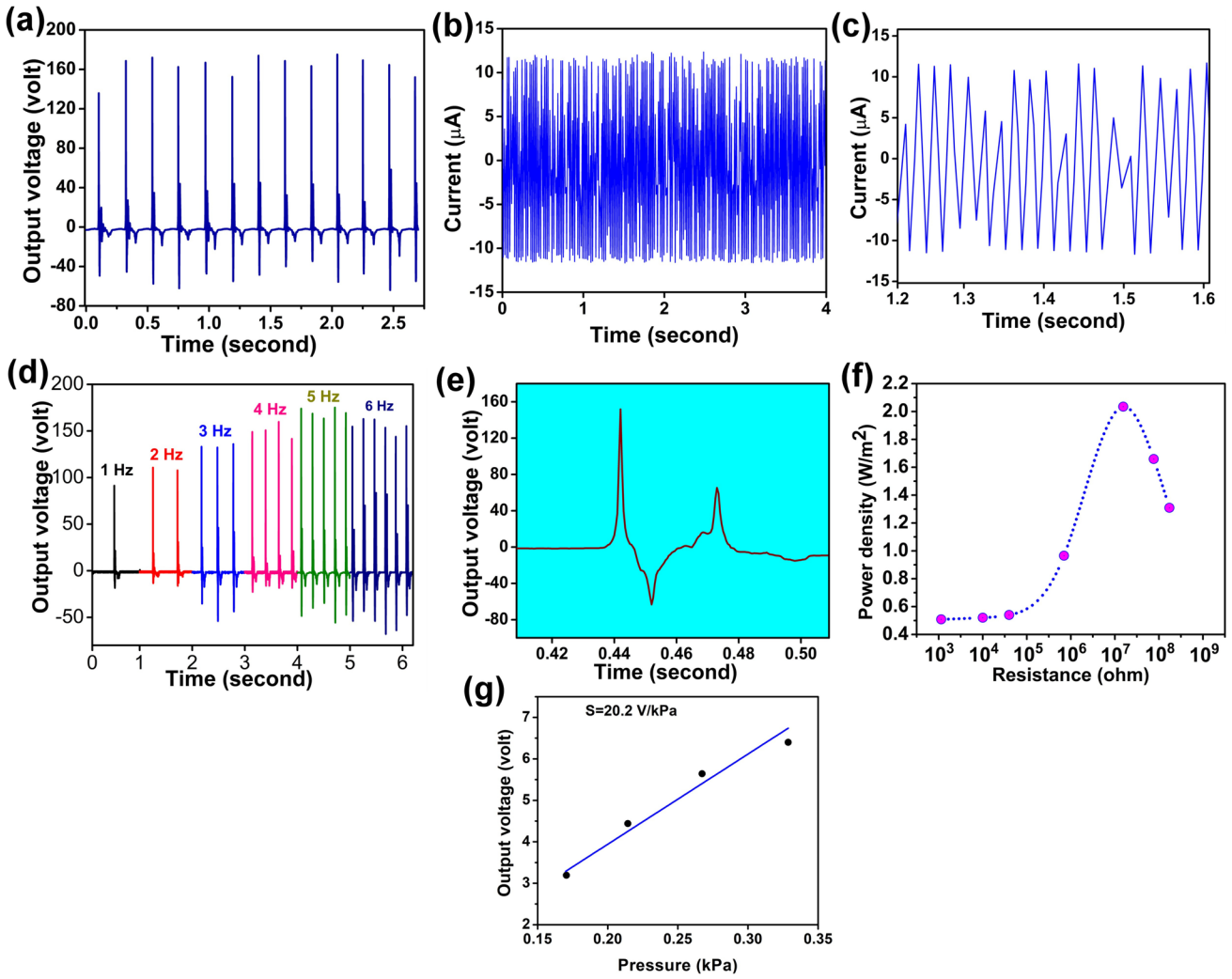


**Fig. 6** **a** Output voltage and **b** short circuit current of the designed PBTNG device during the periodic finger tapping. **c** The magnified view of short circuit current graph. **d** Frequency dependent output voltage. **e** Magnified sight of generated output voltage at 5 Hz frequency. **f** Power density by varying different load resistances. **g** Sensitivity of PBTNG device

to the inconsistent strain applied on the energy harvesting device at the time of the manual finger impartation. Figure 6(e) displays the single peak of the output voltage. This figure describes the appearance of the positive peak when the strain is applied on the device and after recovering the strain, the device returns to its original state, then eventually a negative peak appears. The output performance of the PBTNG device is further verified at different frequency ranges of 1 to 6 Hz under periodic finger impartation. The frequency dependent output performance graph of PBTNG device is shown in Fig. 6(d). The maximum output voltage (~171.8 V) is obtained at 5 Hz frequency which is near about two times higher than the obtained highest output voltage (~89.6 V) at 1 Hz frequency. The output voltage of PBTNG device can be calculated with the help of the following equations [54]:

$$V_{oc} = \frac{\sigma * x(t)}{\varepsilon_0} \tag{5}$$

$$x(t) = v * t(t < \frac{x_{max}}{v}) \tag{6}$$

where $V_{OC}$ = output voltage; $\sigma$ = charge density of the surface; $x(t)$ = distance b/w two positive and negative triboelectric layers; $\varepsilon_o$ = vacuum permittivity; $\nu$ = average velocity; $x_{max}$ = maximum distance between triboelectric layers. With the increase of the frequencies, the velocity of the applied force also increases. Thus, the output voltage of PBTNG device increases with the increase of frequencies and gradually rises up to 5 Hz. Thereafter, the output voltage decreases by increasing the frequency. The reason behind this is obtaining very small compression cycle at very high-range frequencies. Therefore, the PBTNG device cannot come back to its original state completely. For this reason, the $x(t)$ value and $V_{OC}$ value are reduced with increasing frequency from 5 Hz.

The load capacity of fabricated device is investigated by varying the different external loads. The PBTNG device generates different instantaneous power densities by varying the resistance value of the resistors from $10^3$ to $10^9$ Ω. Figure 6(f) exhibits the power density vs. resistance graph. The power density is calculated from the following equation [45]:

$$P = \frac{V^2}{R_L \times A} \tag{7}$$

where $V$ is the output voltage of the PBTNG device, $R_L$ is the load resistance, and $A$ is the effective surface area of the PBTNG device. In this present work, the effective surface area ($A$) of the device is $0.022 \times 0.011$ m$^2$. The maximum generated power density of PBTNG device is 2.03 W/m$^2$ at $10^7$ Ω. Comparing the output performance of the PTNG (piezoelectric thin (PBi) film is absent) with PBTNG device, the fabricated device (PBTNG) exhibits higher output voltage which confirms the effective contribution of the piezoelectric thin film, shown in Fig. S6(a). Additionally, the sensitivity of PBTNG device has been calculated by using the following equation [51]:

$$S = \Delta V / \Delta P \tag{8}$$

where $\Delta V$ and $\Delta P$ represent the changes in the output voltage and externally applied pressure. The sensitivity of PBTNG device is 4.1 V/kPa up to the pressure region of 4.7 kPa, which is generated by dropping various masses rubber balls, shown in Fig. 6(g).

### 5.1 Electricity generation from different body movements and low frequency range mechanical energy resources

The fabricated device (PBTNG) has the capability to detect different body movements and small range mechanical energy and convert them into electrical energy directly, shown in Figs. 7 and 8. PBTNG device can produce output voltage easily from different body movements like heel and foot pressing, single finger tapping, etc. Figure 7(b) and (e) shows the excellent output performance of device when attached it with heel and foot. At the time of heel and foot pressing, the observable output voltages are 52 V and 15 V. These results describe that the generated output voltage is higher during heel pressing compared to the foot pressing. The contact area of heel or foot with the device is responsible for this phenomenon, i.e., higher contact area with the PBTNG device leads to higher output voltage. As a result, heel pressing gives us higher voltage than feet pressing. The output performance of the PBTNG has been also performed under the single finger tapping. The generated output voltage during single finger tapping is 40 V, which is shown in Fig. 7(a). The sensitivity of the single-electrode bismuth selenide–based triboelectric nanogenerator (SBTNG) (consisting of PBi thin film, Al electrode and PDMS film) is checked by dropping coins on the upper surface, and it shows high sensitivity value of 20.2 V/kPa at low pressure region (less than 0.5 kPa), shown in Fig. S6(b). This sensitivity value helps SBTNG device in harvesting low frequency range of mechanical energy sources like touching, keypad typing, writing, running external CD drive, etc. When SBTNG device is attached with the wrist, it shows very good output voltage, shown in Fig. 7(c). The magnified view of this graph describes that after touching with wrist, the SBTNG device detects the blood pressure of human body. This pressure is divided into two parts: one is systolic pressure and another is diastolic pressure. During the blood flow, the systolic pressure and the diastolic pressure provide the peak and the drain of the pulse wave [45].

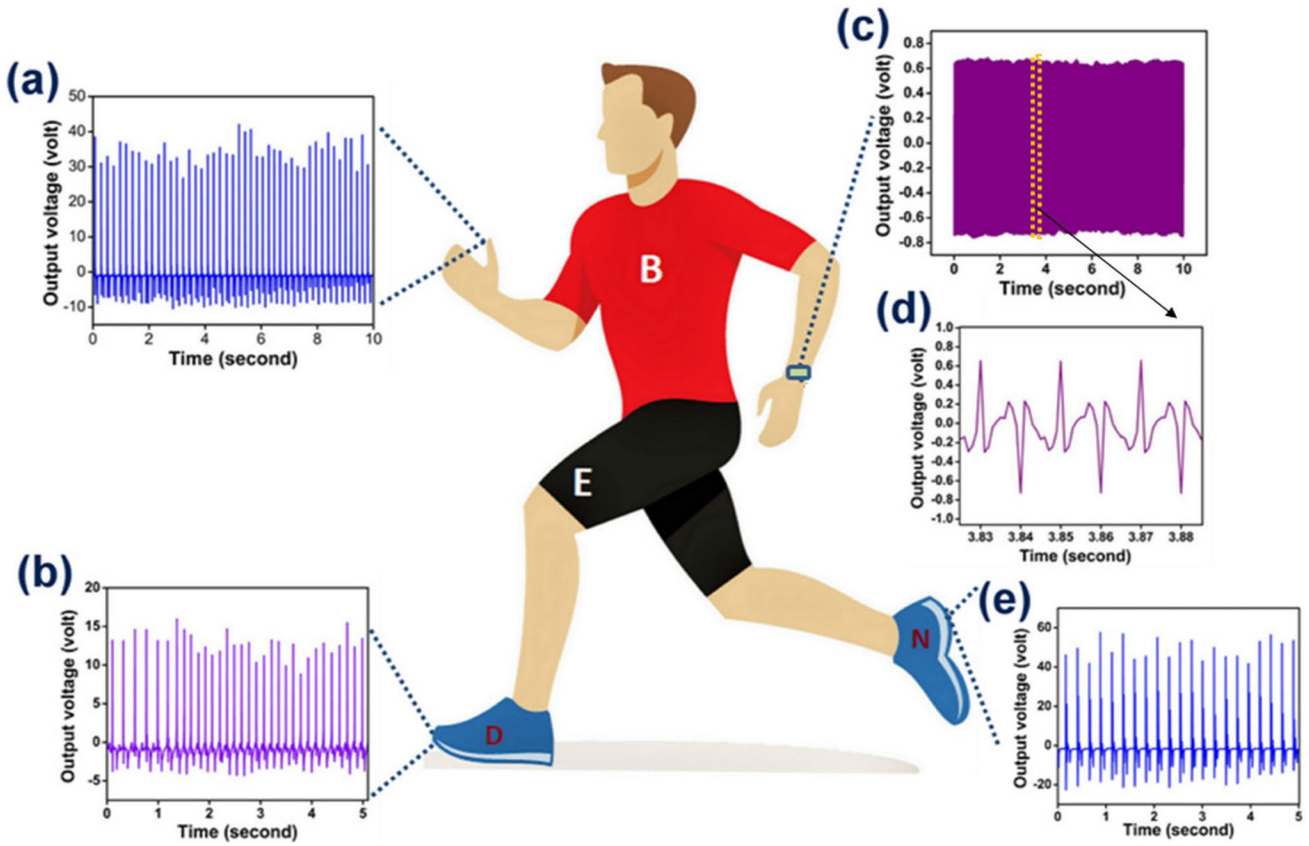


**Fig. 7** Output voltage produced by PBTNG device from **a** single finger tapping, **b** feet tapping, and **e** heel pressing. **c** Monitoring the heart beating of human body by attaching SBTNG device on the wrist. **d** Enlarged view of the generated peaks during heart beats

The SBTNG device detects this pulse pressure which is arising from the alternation of the systolic and diastolic pressure quickly and generates output voltage, shown in Fig. 7(d). Thus, fabricated device is very much sensitive and can be used in various medical equipment.

Besides this, SBTNG device has the capability to perceive another low-range mechanical energy which is generated during writing some words on the upper surface of the device. A paper sheet has been placed on the surface of the device and wrote some English letters on it; the SBTNG can harvest the mechanical energy from this writing process and generate some electrical energy, displayed in the output voltage vs. time graph in Fig. 8(c), which describes that the SBTNG devices show output voltage near about 0.5 V at the time of writing condition.

During stopped writing condition, no peak is observed in Fig. 8(c).Thus, SBTNG can be used as self-powered handwriting pad to identify signature. Moreover, the negative part of PBTNG device is attached with the space bar of the keyboard to catch the mechanical energy during keystroke. At the time of striking the space bar, each keystroke generates huge amount of mechanical energy and the device successfully coverts them into electrical energy easily. The generated output voltage of SBTNG device during keystroke is 2 V, as shown in Fig. 8(a). Hence, SBTNG can be utilized as the self-powered keyboards, keystroke speed recorder sensor, etc. External CD drive gives the vibrational energy at very low frequency range during running condition, and fabricated SBTNG device is highly sensitive and quite efficient to recognize this vibrational energy. During running condition, it can easily covert this vibrational energy into electrical energy and generate output voltage near about 200 mV. Figure 8(b) shows the output voltage vs. time graph of the CD drive at running conditions. Beside this, the fabricated SBTNG device has the ability to covert mechanical energy into electrical energy which is arising by clicking the mouse continuously. The generated output voltage is 1.8 V during mouse clicking condition, which is shown in Fig. 8(d).

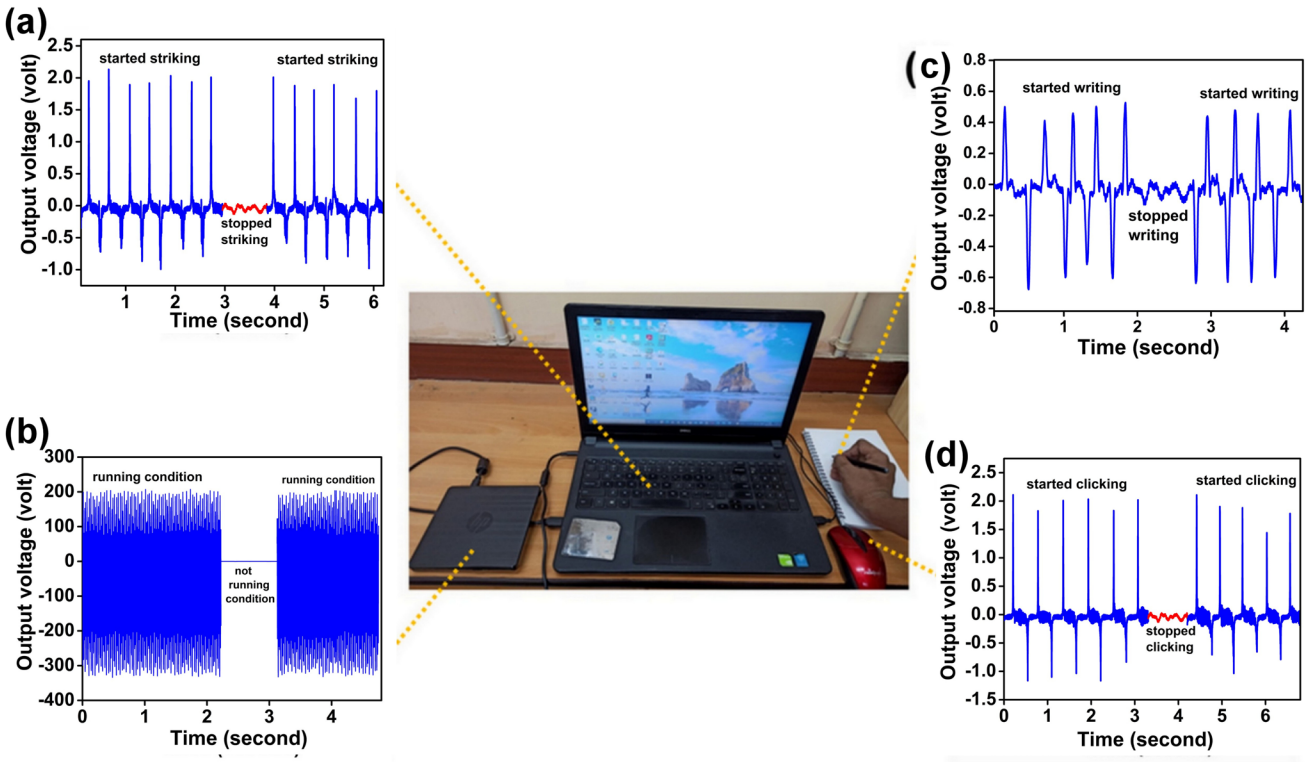


**Fig. 8** Catching small or low range mechanical energies with the help of SBTNG device from **a** striking space bar of keyboard, **b** external CD drive on running condition, **c** writing on device, and **d** mouse clicking

### 5.2 Realistic applications of PBTNG nanogenerator

The realistic applications of piezoelectric thin film–based triboelectric nanogenerator (PBTNG) have been investigated by charging capacitors and illuminating blue light-emitting diodes (LEDs). The PBTNG device is connected with bridge rectifier to charge the capacitors under periodic finger impartation. Figure 9(a) illustrates the capacitor charging graph which shows that the fabricated device has the capability to charge 1 µF, 2.2 µF, and 4.7 µF capacitors up to 3.97 V, 2.20 V, and 1.19 V within 60 s. Along with this, Fig. 9(a) also describes that with the increasing value of capacitance, the saturation voltage decreases gradually. Furthermore, the energy storage capacity of three capacitors has been measured. The energy ($E$) accumulated into the capacitors can be calculated by the following equation [55]:

$$E = \frac{1}{2}CV^2 \tag{9}$$

where $C$ = capacitance value of the capacitor and $V$ = voltage on the capacitor.

The amount of the energy accumulated in the three capacitors (1, 2.2, and 4.7µF) is shown in Fig. 9(c). The closer inspections of Fig. 9(c) describe that the capacitor having smaller capacitance value has larger energy storage capacity, which means 1 µF capacitor can accumulate larger amount of energy compared to the other two capacitors (2.2 and 4.7 µF). The amounts of energy accumulated in the 1, 2.2, and 4.7 µF are 7.88, 5.32 and 3.3 2 µJ, respectively. Thus, PBTNG device can be utilized to power up portable electronic gadgets. Apart from this, the fabricated device also has the potential to charge up transparent blue light emitting diodes (LEDs) under continuous finger impartation and heel pressing. The power generated from the PBTNG device can illuminate 84 blue LEDs under the periodic finger impartation and 30 blue LEDs under the heel pressing by connecting them in the series combination through a bridge rectifier, shown in Fig. 9(d) and (e). The durability of fabricated PBTNG has been investigated for 7 months and the device exhibits near about same output voltage throughout the whole time period, shown in Fig. 9(f).

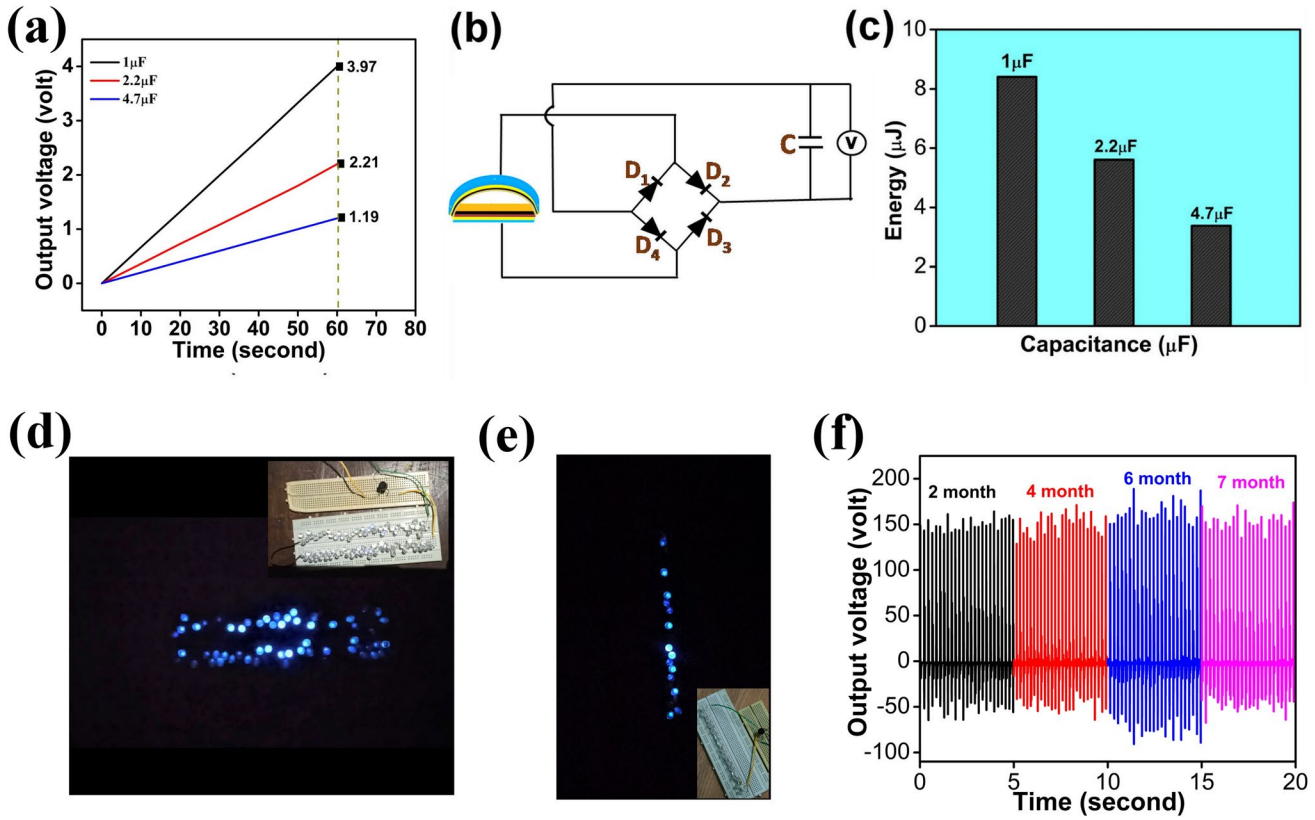


**Fig. 9** **a** Charging of capacitors by fabricated PBTNG device. **b** Circuit diagram of capacitor charging and illuminating of LEDs. **c** Accumulation of energies into the capacitors. Snapshots of blue LEDs lighting up by **d** periodic finger impartation and **e** heel pressing. **f** Durability performance of PBTNG device

## 6 Conclusion

In this present work, the arch shaped, self-powered, and wearable piezoelectric thin film with bismuth selenide based triboelectric nanogenerator, named as PBTNG, has been fabricated with the help of nanoporous $Bi_2Se_3$ and PVDF based piezoelectric thin (PBi) film, PVA thin film, PDMS and aluminum electrodes. The coupling effect between piezoelectricity and triboelectricity enhances the output performances of fabricated triboelectric nanogenerator. The PBTNG device converts different forms of mechanical energy into electrical energy easily. The single electrode bismuth selenide based triboelectric nanogenerator, named as SBTNG, exhibits high sensitivity (20.2 V/kPa) at low pressure region (< 0.5 kPa) which helps SBTNG to catch the small biomechanical energy generated by various body movements and convert them into electrical energy. Besides, the extra advantage of using this SBTNG device is that it can harness electrical energy from small scale range energy sources like keypad tapping, mouse clicking, writing on device, vibration of external CD drive at running mode etc., and each and every case shows very good output performance. The wearable and self-powered PBTNG device generates outstanding output voltage ($V_{OC}$) which is near about 171.8 V and short circuit current ($I_{SC}$) near about 11.7 μA at 5 Hz frequency under continuous finger impartation (near about 11.7 N). The maximum power density produced by PBTNG device is 2.03 W/m$^2$ at $10^7$ Ω. The PBTNG device also produces very good output voltage during heel pressing which has been utilized to illuminate 30 numbers of blue LEDs. The realistic importance of PBTNG device has been examined by charging three different capacitors within a short time span and lighting up 84 numbers of blue LEDs under periodic finger impartation. The device exhibits long term durability for 7 months by generating almost the same output performance throughout this period. The piezoelectric thin film with bismuth selenide based triboelectric nanogenerator (PBTNG) can be used in various versatile applications like weight sensor, mechanical and biomechanical energy harvester, blood flow sensor, etc. Furthermore, the device can be utilized as self-powered handwriting identifier, keystroke sensor and recorder, vibrational energy sensor, etc.

**Supplementary Information** The online version contains supplementary material available at https://doi.org/10.1007/s42114-023-00807-0.

**Acknowledgements** Moreover, authors would like to thank Jadavpur University, Department of Physics for the instrumental support through FIST and PURSE scheme of Department of Science and Technology, Govt. of India.

**Author contribution** Debmalya Sarkar: writing original draft, designing, computation, conceptualization, data acquisition, and manuscript preparation. Namrata Das: data acquisition and conceptualization. Md. Minarul Saikh: visualization. Shubham Roy: computation. Sumana Paul: methodology. Nur Amin Hoque: supervision and editing. Ruma Basu: supervision and editing. Sukhen Das: supervision and editing.

**Funding** This work is financially assisted by University Grants Commission, Govt. of India (No. 1413/(CSIR-UGC NET DEC.2018), 191620153244); Swami Vivekananda Merit-Cum-Means Scholarship (No. WBP191577101345); Science & Engineering Research Board (No. PDF/2022/002773); Science and Research Board, Govt. of India (Grant No. PDF/2019/001498); Science & Engineering Research Board (No. EEQ/2018/000747).

**Data availability** The data that supports the findings of this study are available from the corresponding author on reasonable request.

## Declarations

**Conflict of interest** Authors declare no competing interests.

## References

1. Jiang D, Lian M, Xu M, Sun Q, Xu BB, Thabet HK, El-Bahy SM, Ibrahim MM, Huang M, Guo Z (2023) Advances in triboelectric nanogenerator technology—applications in self-powered sensors, Internet of things, biomedicine, and blue energy. Adv Compos Hybrid Mater 6:57. https://doi.org/10.1007/s42114-023-00632-5
2. Li D, Hu J, Wang C, Guo L, Zhou J (2023) Metal-organic framework-induced edge-riched growth of layered $Bi_2Se_3$ towards ultrafast Na-ion storage. J Power Sources 555:232387. https://doi.org/10.1016/j.jpowsour.2022.232387
3. Li D, Liu H, Liu H, Chen Y, Wang C, Guo L (2023) A $NiCoSe_x$/CG heterostructure with strong interfacial interaction showing rapid diffusion kinetics as a flexible anode for high-rate sodium storage. Dalton Trans 52:5192–5201. https://doi.org/10.1039/D3DT00273J
4. Yuan G, Wan T, BaQais A, Mu Y, Cui D, Amin MA, Li X, Xu BB, Zhu X, Algadi H, Li H (2023) Boron and fluorine Co-doped laser-induced graphene towards high-performance micro-supercapacitors. Carbon 212:118101. https://doi.org/10.1016/j.carbon.2023.118101
5. Lin Z, Li X, Zhang H, Xu BB, Wasnik P, Li H, Singh MV, Ma Y, Li T, Guo Z (2023) Research progress of MXenes and layered double hydroxides for supercapacitors. Inorg Chem Front 10:4358–4392. https://doi.org/10.1039/D3QI00819C
6. Karthik A, Chiniwar DS, Das M, Prabhu P, Mulimani PA, Samanth K, Naik N (2021) Electric propulsion for fixed wing aircrafts–a review on classifications, designs, and challenges. Eng Sci 16:129–45. https://doi.org/10.30919/es8d573
7. Li T, Wei H, Zhang Y, Wan T, Cui D, Zhao S, Zhang T, Ji Y, Algadi H, Guo Z, Chu L (2023) Sodium alginate reinforced polyacrylamide/xanthan gum double network ionic hydrogels for stress sensing and self-powered wearable device applications. Carbohydr Polym 309:120678. https://doi.org/10.1016/j.carbpol.2023.120678
8. Akram W, Chen Q, Xia G, Fang J (2022) A review of single electrode triboelectric nanogenerators. Nano Energy 106:108043. https://doi.org/10.1016/j.nanoen.2022.108043
9. He J, Cao S, Zhang H (2020) Cylinder-based hybrid rotary nanogenerator for harvesting rotational energy from axles and self-powered tire pressure monitoring. Energy Sci Eng 8:291–299. https://doi.org/10.1002/ese3.560
10. Zou H, Zhang Y, Guo L, Wang P, He X, Dai G, Zheng H, Chen C, Wang AC, Xu C, Wang ZL (2019) Quantifying the triboelectric series Nat Commun 10:1427. https://doi.org/10.1038/s41467-019-09461-x
11. Wei X, Wang B, Wu Z, Wang ZL (2022) Open-environment tactile sensing system: towards simple and efficient material identification. Adv Mater 34:2203073. https://doi.org/10.1002/adma.202203073
12. Shawon SM, Sun AX, Vega VS, Chowdhury BD, Tran P, Carballo ZD, Tolentino JA, Li J, Rafaqut MS, Danti S, Uddin MJ (2021) Piezo-tribo dual effect hybrid nanogenerators for health monitoring. Nano Energy 82:105691. https://doi.org/10.1016/j.nanoen.2020.105691
13. Lopez D, Chowdhury AR, Abdullah AM, Sadaf MU, Martinez I, Choudhury BD, Danti S, Ellison CJ, Lozano K, Uddin MJ (2021) Polymer based triboelectric nanogenerator for cost-effective green energy generation and implementation of surface-charge engineering. Energy Technol 9:2001088. https://doi.org/10.1002/ente.202001088
14. Bhatta T, Maharjan P, Cho H, Park C, Yoon SH, Sharma S, Salauddin M, Rahman MT, Rana SS, Park JY (2021) High-performance triboelectric nanogenerator based on MXene functionalized polyvinylidene fluoride composite nanofibers. Nano Energy 81:105670. https://doi.org/10.1016/j.nanoen.2020.105670
15. He W, Fu X, Zhang D, Zhang Q, Zhuo K, Yuan Z, Ma R (2021) Recent progress of flexible/wearable self-charging power units based on triboelectric nanogenerators. Nano Energy 84:105880. https://doi.org/10.1016/j.nanoen.2021.105880
16. Li R, Wei X, Shi Y, Yuan Z, Wang B, Xu J, Wang L, Wu Z, Wang ZL (2022) Low-grade heat energy harvesting system based on the shape memory effect and hybrid triboelectric-electromagnetic nanogenerator. Nano Energy 96:107106. https://doi.org/10.1016/j.nanoen.2022.107106
17. Lin J, Li J, Feng S, Gu C, Li H, Lu H, Hu F, Pan D, Xu BB, Guo Z (2023) An active bacterial anti-adhesion strategy based on directional transportation of bacterial droplets driven by triboelectric nanogenerators. Nano Res 16:1052–1063. https://doi.org/10.1007/s12274-022-5177-6
18. Jia B, Lei M, Zou Y, Qin G, Zhang C, Han L, Zhang Q, Lu P (2022) The electron transfer mechanism between metal and silicon oxide composites for triboelectric nanogenerators. Adv Compos Hybrid Mater 5:3223–3231. https://doi.org/10.1007/s42114-022-00561-9
19. Zhang M, Du H, Liu K, Nie S, Xu T, Zhang X, Si C (2021) Fabrication and applications of cellulose-based nanogenerators. Adv Compos Hybrid Mater 4:865–884. https://doi.org/10.1007/s42114-021-00312-2
20. Ghafari E, Nantung T, Lu N (2019) An efficient polyvinylidene fluoride (PVDF) nanogenerator for energy harvesting in low frequency range. ES Mater Manuf 5:72–77. https://doi.org/10.30919/esmm5f321
21. Jirayupat C, Wongwiriyapan W, Kasamechonchung P, Wutikhun T, Tantisantisom K, Rayanasukha Y, Jiemsakul T, Tansarawiput C, Liangruksa M, Khanchaitit P, Horprathum M (2018) Piezoelectric-induced triboelectric hybrid nanogenerators based on the ZnO nanowire layer decorated on the Au/polydimethylsiloxane–Al

structure for enhanced triboelectric performance. ACS Appl Mater Interfaces 10:6433–6440. https://doi.org/10.1021/acsami.7b17314
22. Han C, Cao Z, Yuan Z, Zhang Z, Huo X, Zhang LA, Wu Z, Wang ZL (2022) Hybrid triboelectric-electromagnetic nanogenerator with a double-sided fluff and double Halbach array for wave energy harvesting. Adv Funct Mater 32:2205011. https://doi.org/10.1002/adfm.202205011
23. Wei X, Zhao Z, Wang L, Jin X, Yuan Z, Wu Z, Wang ZL (2022) Energy conversion system based on Curie effect and triboelectric nanogenerator for low-grade heat energy harvesting. Nano Energy 91:106652. https://doi.org/10.1016/j.nanoen.2021.106652
24. Suo G, Yu Y, Zhang Z, Wang S, Zhao P, Li J, Wang X (2016) Piezoelectric and triboelectric dual effects in mechanical-energy harvesting using $BaTiO_3$/polydimethylsiloxane composite film. ACS Appl Mater Interfaces 8:34335–34341. https://doi.org/10.1021/acsami.6b11108
25. Cheng H, Lu Z, Gao Q, Zuo Y, Liu X, Guo Z, Liu C, Shen C (2021) PVDF-Ni/PE-CNTs composite foams with co-continuous structure for electromagnetic interference shielding and photo-electro-thermal properties. Eng Sci 16:331–40. https://doi.org/10.30919/es8d518
26. Gao C, Deng W, Pan F, Feng X, Li Y (2020) Superhydrophobic electrospun PVDF membranes with silanization and fluorosilanization co-functionalized CNTs for improved direct contact membrane distillation. Eng Sci 9:35–43. https://doi.org/10.30919/es8d905
27. Wu Z, Wang X, Annamareddy SH, Gao S, Xu Q, Algadi H, Sridhar D, Wasnik P, Xu BB, Weng L, Guo Z (2023) Dielectric properties and thermal conductivity of polyvinylidene fluoride synergistically enhanced with silica@ multi-walled carbon nanotubes and boron nitride. ES Mater Manuf. https://doi.org/10.30919/esmm5f847
28. Sharafkhani S, Kokabi M (2022) Enhanced sensing performance of polyvinylidene fluoride nanofibers containing preferred oriented carbon nanotubes. Adv Compos Hybrid Mater 5:3081–3093. https://doi.org/10.1007/s42114-022-00565-5
29. Li GY, Li J, Li ZJ, Zhang YP, Zhang X, Wang ZJ, Han WP, Sun B, Long YZ, Zhang HD (2022) Hierarchical PVDF-HFP/ZnO composite nanofiber–based highly sensitive piezoelectric sensor for wireless workout monitoring. Adv Compos Hybrid Mater 5:766–775. https://doi.org/10.1007/s42114-021-00331-z
30. Liu Z, Li G, Qin Q, Mi L, Li G, Zheng G, Liu C, Li Q, Liu X (2021) Electrospun PVDF/PAN membrane for pressure sensor and sodium-ion battery separator. Adv Compos Hybrid Mater 4:1215–1225. https://doi.org/10.1007/s42114-021-00364-4
31. Das N, Sarkar D, Saikh MM, Biswas P, Das S, Hoque NA, Ray PP (2022) Piezoelectric activity assessment of size-dependent naturally acquired mud volcano clay nanoparticles assisted highly pressure sensitive nanogenerator for green mechanical energy harvesting and body motion sensing. Nano Energy 102:107628. https://doi.org/10.1016/j.nanoen.2022.107628
32. Hong M, Chasapis TC, Chen ZG, Yang L, Kanatzidis MG, Snyder GJ, Zou J (2016) n-type $Bi_2Te_{3-x}Se_x$ nanoplates with enhanced thermoelectric efficiency driven by wide-frequency phonon scatterings and synergistic carrier scatterings. ACS Nano 10:4719–4727. https://doi.org/10.1021/acsnano.6b01156
33. Gautam S, Aggarwal V, Singh B, Awana VP, Ganesan R, Kushvaha SS (2022) Signature of weak-antilocalization in sputtered topological insulator $Bi_2Se_3$ thin films with varying thickness. Sci Rep 12:9770. https://doi.org/10.1038/s41598-022-13600-8
34. Sun H, Jiang T, Zang Y, Zheng X, Gong Y, Yan Y, Xu Z, Liu Y, Fang L, He K (2017) Broadband ultrafast photovoltaic detectors based on large-scale topological insulator $Sb_2Te_3$/STO heterostructures. Nanoscale 9:9325–9332. https://doi.org/10.1039/C7NR01715D
35. Mishra SK, Satpathy S, Jepsen O (1997) Electronic structure and thermoelectric properties of bismuth telluride and bismuth selenide. J Phys Condens Matter 9:461. https://doi.org/10.1088/0953-8984/9/2/014
36. Yan Y, Wang LX, Yu DP, Liao ZM (2013) Large magnetoresistance in high mobility topological insulator $Bi_2Se_3$. Appl Phys Lett 103:033106. https://doi.org/10.1063/1.4813824
37. Yang WJ, Lee CW, Kim DS, Kim HS, Kim JH, Choi HY, Choi YJ, Kim JH, Park K, Cho MH (2018) Tuning of topological Dirac states via modification of van der Waals gap in strained ultrathin $Bi_2Se_3$ films. J Phys Chem C 122:23739–23748. https://doi.org/10.1021/acs.jpcc.8b06296
38. Mishra V, Baranwal V, Mishra RK, Sharma S, Paul B, Pandey AC (2017) Immunotoxicological impact and biodistribution assessment of bismuth selenide ($Bi_2Se_3$) nanoparticles following intratracheal instillation in mice. Sci Rep 7:18032. https://doi.org/10.1038/s41598-017-18126-y
39. Sharma A, Bhattacharyya B, Srivastava AK, Senguttuvan TD, Husale S (2016) High performance broadband photodetector using fabricated nanowires of bismuth selenide. Sci Rep 6:19138. https://doi.org/10.1038/srep19138
40. Zhang H, Zhang X, Liu C, Lee ST, Jie J (2016) High-responsivity, high-detectivity, ultrafast topological insulator $Bi_2Se_3$/silicon heterostructure broadband photodetectors. ACS Nano 10:5113–5122. https://doi.org/10.1021/acsnano.6b00272
41. Tang H, Liang D, Qiu RL, Gao XP (2011) Two-dimensional transport-induced linear magneto-resistance in topological insulator $Bi_2Se_3$ nanoribbons. ACS Nano 5:7510–7516. https://doi.org/10.1021/nn2024607
42. Zhang H, Liu CX, Qi XL, Dai X, Fang Z, Zhang SC (2009) Topological insulators in $Bi_2Se_3$, $Bi_2Te_3$ and $Sb_2Te_3$ with a single Dirac cone on the surface. Nat Phys 5:438–442. https://doi.org/10.1038/nphys1270
43. Li CH, Van 'T Erve OM, Robinson JT, Liu Y, Li L, Jonker BT, (2014) Electrical detection of charge-current-induced spin polarization due to spin-momentum locking in $Bi_2Se_3$. Nat Nanotechnol 9:218–224. https://doi.org/10.1038/nnano.2014.16
44. Mohyedin MZ, Taib MF, Malik NA, Alam NN, Mustaffa M, Ali AM, Hassan OH, Haq BU, Yahya MZ (2022) First-principles calculations of electronic and optical properties of orthorhombic $Bi_2Se_3$ nano thin film. Comput Condens Matter 30:e00618. https://doi.org/10.1016/j.cocom.2021.e00618
45. Sarkar D, Das N, Saikh MM, Biswas P, Roy S, Paul S, Hoque NA, Basu R, Das S (2023) High β-crystallinity comprising nitrogenous carbon dot/PVDF nanocomposite decorated self-powered and flexible piezoelectric nanogenerator for harvesting human movement mediated energy and sensing weights. Ceram Int 49:5466–5478. https://doi.org/10.1016/j.ceramint.2022.10.070
46. Wang ZL (2017) On Maxwell's displacement current for energy and sensors: the origin of nanogenerators. Mater Today 20:74–82. https://doi.org/10.1016/j.mattod.2016.12.001
47. He J, Qian S, Niu X, Zhang N, Qian J, Hou X, Mu J, Geng W, Chou X (2019) Piezoelectric-enhanced triboelectric nanogenerator fabric for biomechanical energy harvesting. Nano Energy 64:103933. https://doi.org/10.1016/j.nanoen.2019.103933
48. Guo Y, Zhang XS, Wang Y, Gong W, Zhang Q, Wang H, Brugger J (2018) All-fiber hybrid piezoelectric-enhanced triboelectric nanogenerator for wearable gesture monitoring. Nano Energy 48:152–160. https://doi.org/10.1016/j.nanoen.2018.03.033
49. Ajeel FN, Mohammed MH, Abd Ali RA (2017) Topological insulators in Bi2Se3 family nanostructured thin films: study topological nature and surface states. Uni Thi-Qar J 12:40_50-. https://doi.org/10.32792/utq/utj/vol12/1/5

50. Gupta V, Kumar A, Mondal B, Babu A, Ranpariya S, Sinha DK, Mandal D (2023) Machine learning-aided all-organic air-permeable piezoelectric nanogenerator. ACS Sustain Chem Eng 11:6173–6182. https://doi.org/10.1021/acssuschemeng.2c06779
51. Chen X, Song Y, Chen H, Zhang J, Zhang H (2017) An ultrathin stretchable triboelectric nanogenerator with coplanar electrode for energy harvesting and gesture sensing. J Mater Chem A 5:12361–12368. https://doi.org/10.1039/C7TA03092D
52. Roy S, Bardhan S, Pal K, Ghosh S, Mandal P, Das S, Das S (2018) Crystallinity mediated variation in optical and electrical properties of hydrothermally synthesized boehmite (γ-AlOOH) nanoparticles. J Alloys Compd 763:749–758. https://doi.org/10.1016/j.jallcom.2018.05.356
53. Das S, Das S, Sutradhar S (2017) Effect of $Gd^{3+}$ and $Al^{3+}$ on optical and dielectric properties of ZnO nanoparticle prepared by two-step hydrothermal method. Ceram Int 43:6932–6941. https://doi.org/10.1016/j.ceramint.2017.02.116
54. Jalili MA, Khosroshahi Z, Kheirabadi NR, Karimzadeh F, Enayati MH (2021) Green triboelectric nanogenerator based on waste polymers for electrophoretic deposition of titania nanoparticles. Nano Energy 90:106581. https://doi.org/10.1016/j.nanoen.2021.106581
55. Zheng F, Zhou Y, Hu S, Li R, Wang ZL, Wu Z (2022) A hybridized triboelectric-electromagnetic nanogenerator as a power supply of monitoring sensors for the ventilation system. Adv Energy Mater 12:2201966. https://doi.org/10.1002/aenm.202201966

Journal of Materials Chemistry C

ROYAL SOCIETY OF CHEMISTRY

PAPER

View Article Online
View Journal



Cite this: DOI: 10.1039/d3tc03822j

# Micro-patterned $BaTiO_3$@Ecoflex nanocomposite-assisted self-powered and wearable triboelectric nanogenerator with improved charge retention by 2D $MoTe_2$/PVDF nanofibrous layer†

Debmalya Sarkar,[a] Namrata Das,[a] Souvik Sau,[ac] Ruma Basu*[b] and Sukhen Das *[a]

With applications in robotic technology, human-machine interfaces and healthcare unit, the self-powered wearable triboelectric nanogenerator has the ability to detect different physical parameters. These aspects continue to be incredibly exciting for the researchers. Herein, a self-powered, skin-attachable and flexible triboelectric nanogenerator (EPMTNG) is designed with a charge generating layer using micro-patterned $BaTiO_3$@Ecoflex (EBTO) nanocomposite, nanofibrous trapping layer with 2D $MoTe_2$ and carbon tape as a charge collecting layer. Furthermore, charge recombination becomes the significant issue, which not only reduces the surface potential but also diminishes the output performance of TENG. For this, a 2D transition metal dichalcogenide ($MoTe_2$) incorporated PVDF nanofibrous (PM5) layer is introduced as a charge trapping layer to prevent the charge recombination and improve the output performance of the device. Additionally, the incorporation of 2D $MoTe_2$ nanoparticles reinforces the polarization effect by gathering more charge carriers and improves the dielectric property and conductivity of the device. To establish our concept of inclusion of an intermediate trapping layer in EPMTNG, a theoretical simulation model has been prepared confirming the rise of surface potential and output voltage in the presence of the trapping layer. Along with this, a surface modification technique has been resorted to create surface roughness and improve the output performance of EPMTNG. Thus, the intermediate trapping layer and micro-patterned nanocompositebased EPMTNG device generate a colossal output voltage of 319 V and an instantaneous power density of 2.9 W $m^{-2}$ under an axial pressure of 12 N. Also, the high sensitivity (32.5 V $kPa^{-1}$) of the device at low-pressure region assists in successfully detection of robotic gestures, including artificial finger bending and objects gripping. Moreover, the flexibility and skin attachable properties encourage the EPMTNG device in tracking human physiological signals coming from blood flow, glottis movement, neck up down, wrist bending, *etc.*, and monitor the wireless transmission of these signals. Therefore, the self-powered flexible device may be useful in health monitoring units and soft robotics applications.

Received 19th October 2023,
Accepted 1st December 2023

DOI: 10.1039/d3tc03822j

rsc.li/materials-c

## 1. Introduction

In the era of the Internet of Things, flexible, self-powered, and skin-attachable wearable electronic devices have gained tremendous attention due to their versatile utilizations in the field of robotics technology, human-machine interfaces, biomedical applications and healthcare units.[1–5] The main advantages of using these skin-attachable wearable devices are the detection and monitoring ability of different physical parameters, such as pressure, strain, sensitivity, and temperature. Along with this, these skin-attachable devices also have the capability to detect multiple stimuli at a single time.[6–8] Moreover, there have been some limitations in the use of conventional energy storage equipments, like daily charging requirements, large dimensions *etc.*, which restrict in long-term

[a] *Department of Physics, Jadavpur University, Kolkata 700032, West Bengal, India. E-mail: sdasphysics@gmail.com; Tel: +91-9433091337*
[b] *Department of Physics, Jogamaya Devi College, Kolkata 700026, West Bengal, India. E-mail: ruma.b1959@gmail.com; Tel: +91-9433115930*
[c] *Department of Physics, Bangabasi College, Kolkata 700009, West Bengal, India*

† Electronic supplementary information (ESI) available: Flexibility and weight of the EPMTNG device; synthesis method of $BaTiO_3$ (BTO); synthesis method of 2D $MoTe_2$ (MT) nanoparticles; thickness dependent output performance and twisting test of the EPMTNG device; calculation of applied force of EPMTNG; electrical properties of charge generating and charge trapping layer; monitoring swallowing and speaking ability of the device; circuit diagram of LED illumination and capacitor charging; effect of surface modification of EBTO nanocomposite on output performance; theoretical investigation of the effect of PM5 layer in charge loss; table of crystalline size and other parameters of BTO nanoparticles; table of crystalline size and other structural parameters of MT nanoparticles, table of comparison between EPMTNG device and previously reported 2D materials and nanofibers based TENGs; video of illuminating LEDs. See DOI: **https://doi.org/10.1039/d3tc03822j**

use and also unable to match the required power demand. To overcome these issues and fulfill the power demand, self-powered and wearable energy harvesting devices have been utilized.[9] Among the different types of energy harvesting devices, triboelectric nanogenerator (TENG) is the most suitable and promising candidate in energy harvesting techniques by converting waste mechanical energy into electrical energy. Generally, the fabrication of TENG depends on four basic components, *i.e.* charge generating layer, charge trapping layer, electrode layer and charge storage layer.[10] Among them, the charge generating layer and charge trapping layer play important roles in improving the output performance of TENG. However, the working performance of TENG depends on the coupling effect of generated triboelectric charges and induced electrostatic charges. Although, several techniques have been used to improve the power of TENG by inducing more triboelectrification in the charge generating layer, for example, selecting triboelectric materials from triboelectric series, chemical modification, using micro-structured materials *etc.*[11,12] Along with this, the utilization of functional substances with nanomaterials is a new technique to improve the power of TENG.[10] Rajagopalan *et al.* introduced a quasi-equilibrium state (made of nylon and aluminium oxide), which helps in better contact electrification processes and exhibits high output performance of fabricated TENG.[13] Moreover, Li *et al.* used $BaTiO_3$/polyimide nanocomposite to enhance the output performance of TENG.[14] But charge recombination takes place in the abovementioned studies, diminishing the surface charge density and yielding low output performance of TENG. Generally, when the charge generating layer and electrode layer get in contact with each other, an electrostatic potential is generated between them. As a result, due to the electric field, the surface charges of the charge generating layer drift easily towards the electrode layer and combine with the opposite charges which is induced on the electrode layer.[15] For this reason, charge recombination happens between the generating and electrode layers. This charge recombination directly affects the output performance of TENG by reducing the surface charge density. To overcome this problem, an intermediate layer has been placed between the charge collecting layer and electrode layer.[16] This intermediate layer not only traps the electrons but also enhances the output performance of TENG. Recently, polymer nanocomposites by incorporating 2D materials prove itself a potential candidate as intermediate layer by preventing charge recombination and enhancing the performance of TENG.[17] Moreover, 2D materials like MXene, reduced graphene oxide (rGO), transition metal dichalcogenides (TMD), black phosphorous, *etc.* have a large surface area, accelerating more charge accumulation and resulting in better output performance.[18] Along with the intermediate layer, surface modification also plays an important role to improve the performance of the TENG. Few pioneer works have been reported on surface modification processes, which include $C_{60}$ functionalized polyimidebased TENG by Lee *et al.*[19] and cation functionalized nanogenerator by Jae Park *et al.*[20] to enhance the output performance. But there are some drawbacks of utilizing these processes such as air breakdown, highcost fabrication process, low durability *etc.*[9] Thus, surface modification is required. In this work, our aim is to modify the surface and design charge generating and intermediate or trapping layers. To fulfill this aim, nanocomposite has been introduced. The benefits of using nanocomposites in TENG are their large surface area and controllable morphology, and the fabrication process is very simple.[21–23] Moreover, the introduction of functional substances into the nanocomposite helps in surface modification and increases the surface potential, directly enhancing the triboelectric charges.[10] Additionally, the large phase interaction between inorganic additives and polymer chains inside the nanocomposite improves the trapping ability of materials and prevents charge recombination.[24–26]

2D materials, especially transition metal dichalcogenides (TMDs), have excellent physical and structural properties, such as high in-plane conductivity, strong spin–orbit coupling, large magneto-resistance, large surface area, thermal stability, porosity *etc*.[27–30] Owing to these properties, 2D TMDs have broadened their utilization in versatile applications like energy storage and conversion, catalysis, hydrogen evolution, waste water purifications *etc.*[31–34] Amidst all 2D TMDs, molybdenum ditelluride ($MoTe_2$) is one of the compelling and barely explored material. It has semimetallic properties and topological electronic states.[35–37] Moreover, $MoTe_2$ can be synthesized in both semimetallic (1T') and semiconducting (2H) phases, as the energy gap between these two phases is very minimal (near about 40 meV). Also, layer-structured, semiconducting $MoTe_2$ exhibits a direct band gap of 1.1 eV.[37–39] These properties make it a potential choice in the field of electrical and optical applications.[40] Moreover, the excellent structural properties, large surface area, high-in-plane conductivity, and large spin-orbital coupling of $MoTe_2$ assist in creating conducting channels inside the nanocomposite and promoting charge transportation. This further helps in enhancing the trapping depth and restricting the recombination of triboelectric charges and induced charges.[34,40] Furthermore, by applying an external force, the inversion symmetry in the odd layer of $MoTe_2$ is broken, which helps in inducing polarization inside the material.[41–43] Thus, incorporating this material in the polymer matrix induces more polarization and enhances the trapping ability of the material.[36,43]

In the present work, we have designed a wearable, flexible, and skin-attachable triboelectric nanogenerator (EPMTNG) by using charge generating layer, charge trapping layer and carbon tape. Here, the $BaTiO_3$ (BTO) incorporated Ecoflex nanocomposite (EBTO) with micro-pattern serves as a charge generating layer. Moreover, the incorporation of BTO nanoparticles increases the surface potential and induces more triboelectric charges, which further helps in enhancement of output performance of the device. However, charge recombination occurs between the EBTO layer and carbon tape, which results in low output performance. To overcome this problem, 2D $MoTe_2$ (MT) incorporated PVDF nanofibers (PM5) have been inserted between the EBTO layer and carbon tape. The PM5 nanofibers not only serve as an intermediate trapping layer but also prevent the charge recombination process. This leads to the increment of the output performance of the device. The presence

 

of an intermediate trapping layer in the fabricated device is further established by using a theoretically simulated model. Moreover, our fabricated EPMTNG device generates an outstanding output voltage of 319 V and a power density of 2.9 W $m^{-2}$ under periodic finger impartation. Owing to the high sensitivity at a low-pressure region, the fabricated device easily detects different human physiological signals. These physiological signals include wrist bending, elbow movements, blood flow, vocal cord movement, *etc.* Moreover, the device has the ability to monitor robotic gestures. Also, the practical utilization of the device is monitored by capacitor charging and LEDs illuminating performance. Therefore, the EPMTNG can be used in health care monitoring and robotics applications.

## 2. Experimental section

### 2.1. Fabrication of micro-patterned $BaTiO_3$@Ecoflex nanocomposite

The nanocomposite was fabricated by applying simple solution-casting method. At first, 1 g of Ecoflex-A and 1 g of Ecoflex-B were measured in a Petri dish and the two solutions were mixed very well for 10 minutes. After mixing the two solutions, 0.5 wt% $BaTiO_3$ (BTO) was added to the mixed solution and stirred thoroughly at 500 rpm for 5 minutes. Thereafter, the final solution was cast on a 3D-printed rectangular mould to create roughness on the surface. After that, the rectangular mould was kept at room temperature (25 °C) for 9 h to cure the solution. After curing the solution, the sample was peeled off carefully and we finally obtained the $BaTiO_3$ incorporated Ecoflex nanocomposite with a micro-patterned surface and named as EBTO. Fig. 1(a) represents the schematic illustration of the fabrication process of the EBTO nanocomposite.

### 2.2. Formation of $MoTe_2$ (MT) incorporated PVDF nanofibers

The electrospinning technique was utilized to fabricate the nanofibers. First of all, stock solution was prepared by dissolving 12 wt% PVDF in 6 ml DMF and 4 ml acetone mixture and kept under stirring conditions (400 rpm) for 3 h at 60 °C. The required amount (1, 5, 10 wt%) of synthesized $MoTe_2$ nanoparticles was added to the prepared PVDF, DMF, and acetone solution and placed on the stirrer for another 3 h at the same temperature (60 °C). Moreover, the addition of nanoparticles transformed the transparent colour of the solution into blackish colour. In the next step, the blackishcoloured solution was sonicated for 15 minutes and we obtained the stock solution which was used in the electrospinning process.

A 10 ml syringe with a diameter of 8 mm was taken and filled with the prepared stock solutions. Thereafter, the stock solution-loaded syringe was placed in a syringe pump and the electrospinning process was performed by adjusting some parameters, including temperature (25 °C) and humidity (40%). To extract the solution by pump, the flow rate was adjusted to 0.4 ml $hour^{-1}$. Moreover, the distance between the needle of the syringe and the collector plate (Al foil) was maintained at 14 cm throughout the fabrication process of the nanofibers. Along with this, the nanofibers were fabricated at a 12 kV high voltage condition and extracted from the collector plate (Al foil). To recognize the nanoparticleincorporated nanofibers, we have named the 5 wt% $MoTe_2$ loaded nanofibers as PM5. The fabrication process of nanofibers is depicted in Fig. 1(b).

### 2.3. Fabrication of EPMTNG device

Our fabricated triboelectric nanogenerator (EPMTNG) is made of three layers: the charge generating layer, charge trapping

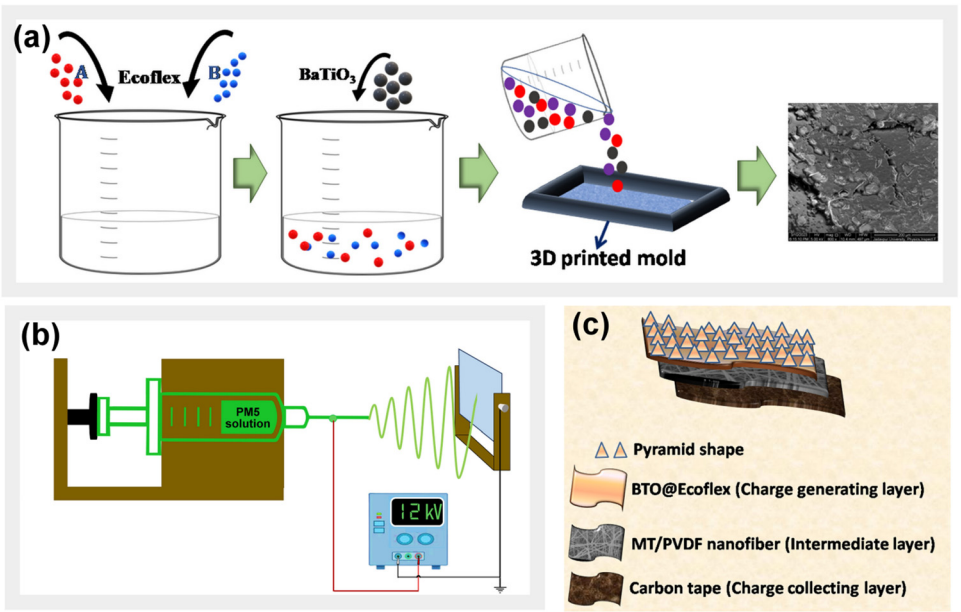


Fig. 1 Graphical representation of the fabrication process of (a) micro-patterned EBTO nanocomposite and (b) PM5 nanofiber. (c) The design of the fabricated EPMTNG device.

layer and charge collecting layer. Here, $BaTiO_3$@Ecoflex nanocomposite serves as a charge generating layer. For the charge trapping layer, we have selected $MoTe_2$ incorporated PVDF nanofibers. Carbon tape has been used as the charge collecting layer. Initially, nanofibers were prepared and affixed to the carbon tape. Thereafter, $BaTiO_3$ incorporated Ecoflex solution was cast on the other side of the nanofiber. Then, a 3D printed plate was attached to the upper surface of the $BaTiO_3$@Ecoflex layer and the whole system was kept at room temperature (25 °C) for 9 h to dry the Ecoflex solution. After completing the drying process, the 3D printed plate was peeled off from the upper surface of the Ecoflex layer and a copper wire was connected between the carbon tape and nanofibers to investigate the electrical performance. The dimension of the fabricated EPMTNG device is 4.4 cm × 2.5 cm. Fig. 1(c) exhibits the graphical representation of the fabricated device.

### 2.4. Characterization techniques

The structural and morphological properties of the synthesized nanoparticles and fabricated nanocomposites are examined by X-ray diffraction (XRD; Model-D8, Bruker AXS Inc., Madison, WI) and field emission scanning electron microscopy (FESEM; INSPECT F50). The EDS spectra and elemental colour mapping of the charge generating and intermediate layers are performed by Zeiss Gemini SEM 500. The electroactive phase formation of the intermediate layer is investigated by Fourier transform infrared (FTIR) spectroscopy (FTIR-8400S; Shimadzu). The electrical properties of charge generating and intermediate layers are investigated by a digital LCR meter (Agilent, E4980A). The output performance of the EPMTNG device is investigated by a Digital Oscilloscope (RTB2002).

## 3. Results and discussion

The structural and morphological properties of the charge generating layer and charge trapping layer have been analyzed by X-ray diffraction peaks, FTIR spectra and FESEM images.

### 3.1. Charge generating layer

BTO incorporated Ecoflex (EBTO) nanocomposite represents the charge generating layer. The synthesis procedure of BTO nanoparticles is elaborated in the ESI.† The characteristic XRD peaks at $2\theta$ = 22.2°, 31.1°, 38.8°, 45.5°, 56.1°, 65.7°, 70.3°, and 74.7° confirm the formation of BTO nanoparticles.[14] The FESEM image exhibits the spherulite microstructure of nanoparticles. The XRD peaks and FESEM image of BTO nanoparticles have been shown in Fig. S2(a) and (b) (ESI†). Moreover, the crystalline size ($D$) of nanoparticles is calculated from the XRD peaks using the Scherrer formula,

$$D = \frac{k\lambda}{\beta \cos\theta},$$

where $\lambda$ represents the wavelength of X-ray, $\beta$ is the full width at half maximum (FWHM) of peaks, and $k$ is the crystalline shape constant whose value is 0.9. The calculated average crystalline size of BTO nanoparticles is 9.4 nm. The table related to this calculation has been inserted in the ESI.† Thus, we have incorporated BTO nanoparticles into the Ecoflex polymer, named the nanocomposite as EBTO, and investigated the structural and morphological properties. Fig. 2(a) shows the XRD peaks of pure Ecoflex and EBTO nanocomposite. In the case of pure Ecoflex, the characteristic peaks at 12.7° and 21.6° are observed, whereas, in the case of the EBTO nanocomposite, an additional characteristic peak at 30.8° has been noticed, which occurs due to the BTO nanoparticles and also confirms the presence of BTO in the EBTO nanocomposite.[14,18] The surface morphology of the EBTO nanocomposite has been investigated by FESEM images. Fig. 2(b) exhibits the morphology of the nanocomposite. Furthermore, EDS spectra and elemental color mapping are performed to verify the atomic weight percentage and distribution of elements inside the nanocomposite. Fig. S5(a) (ESI†) reveals the atomic weight percentage of individual elements, silicon (Si), barium (Ba), titanium (Ti), and oxygen (O), which are present in the fabricated EBTO nanocomposite. The distributions of these elements are further verified by the colour mapping image, shown in Fig. S5(b) (ESI†). This confirms the homogeneous distribution of these elements inside the nanocomposite and concludes the successful fabrication of the EBTO nanocomposite. Furthermore, FESEM image has been captured to investigate the surface roughness of the device after 10 000 cycles (Fig. 2(f)). From the images, it can be seen that the micro-patterns of the EBTO layer remain almost the same after 10 000 cycles, and no damage is observed.

### 3.2. Charge trapping layer

The charge trapping layer consists of MT nanoparticle-incorporated PVDF nanofibers. The synthesis method of MT nanoparticles has been elaborated in the ESI.† The XRD peaks of MT nanoparticles are depicted in Fig. S3(a) (ESI†). The diffraction peaks at 23°, 27.5°, 40.4°, 49.6°, and 56.9° are well matched with JCPDS file no. 01-073-1650. Some additional peaks at 38.1°, 43.2° and 45.8° attribute due to weaker Te rings and also match with JCPDS file no 01-079-0736.[30] Thus, the XRD peaks confirm that synthesized nanoparticles are $MoTe_2$ (MT). The crystalline size of the synthesized nanoparticles has been measured by the Scherrer equation. The average crystalline size of MT nanoparticles is 30.2 nm. The surface morphology of MT nanoparticles has been investigated by FESEM, as shown in Fig. S3(b) (ESI†). From the FESEM image, we can observe the layered structure of MT nanoparticles, which also confirms that the synthesized nanoparticles have a 2D structure. Furthermore, we have incorporated these 2D $MoTe_2$ nanoparticles into the PVDF matrix and fabricated PM5 nanofibers. The structural properties of PM5 nanofibers have been examined through XRD and FTIR spectra. Fig. 2(c) represents the diffraction peaks of the nanofibers, where the characteristic peaks are at 20.3°, 27.3°, 38.1° and 40.4°. Among them, the last three peaks appear due to the presence of MT nanoparticles within the nanofibers. The first characteristic peak at 20.3° arises due to the nucleation of the β-crystalline phase within the PM5 nanofibers and also denotes the crystalline planes (110) and (200).

 

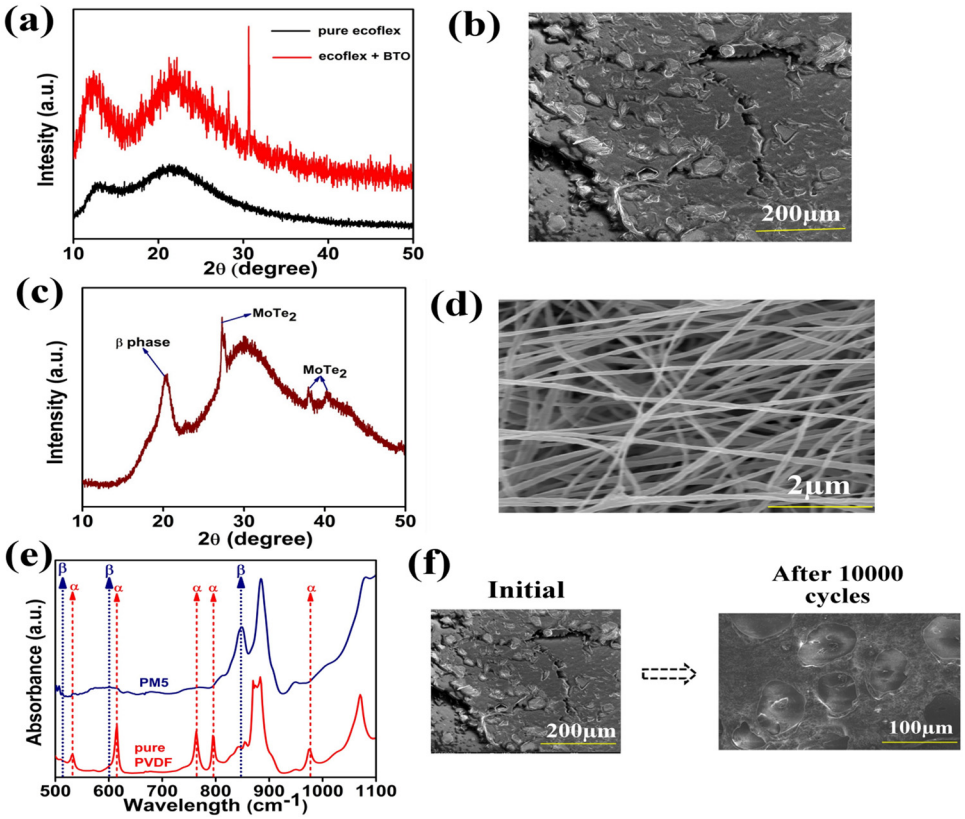


Fig. 2 (a) The X-ray diffraction peaks of pure Ecoflex and EBTO nanocomposite. (b) FESEM image, (c) the characteristic diffraction peaks of PM5 nanofibers. (d) FESEM image of PM5 nanofibers. (e) FTIR analysis of pure PVDF and PM5 nanofibers. (f) Surface roughness of the EBTO nanocomposite after 10 000 cycles.

The formation of this β-phase is occured due to electrostatic interactions between MT nanoparticles and the PVDF matrix, which helps in the conversion of the α-crystalline phase to β-crystalline phase. The nucleation of the β-phase inside the PM5 nanofibers is further confirmed by FTIR analysis depicted in Fig. 2(e). From literature reviews, the absorbance peaks of pure PVDF at 487 $cm^{-1}$ (due to $CF_2$ wagging), 531 $cm^{-1}$ (due to $CF_2$ bending), 616 and 764 $cm^{-1}$ (due to $CF_2$ and skeletal bending), 796 and 976 $cm^{-1}$ (due to $CH_2$ rocking) are observed, clearly indicating the presence of a non-polar α-crystalline phase. By incorporating MT nanoparticles into the PVDF matrix, the non-polar α-phase disappears and the β-crystalline phase rises. From Fig. 2(e), the observable absorption peaks at 445 $cm^{-1}$ ($CF_2$ and $CH_2$ rocking), 479 $cm^{-1}$ ($CF_2$ deformation), 510 $cm^{-1}$ ($CF_2$ stretching), 600 $cm^{-1}$ ($CF_2$ wagging), and 840 $cm^{-1}$ ($CH_2$ rocking, $CF_2$ and skeletal C–C stretching) clearly point out the presence of a polar electroactive β-phase. This β-crystalline phase of PM5 nanofibers improves the polarization effect and enhances the dielectric properties. Moreover, the amount of the β-phase content inside the nanofiber has been calculated using the Lambert–beer law,

$$F(\beta) = \frac{A_\beta}{\left(\frac{K_\beta}{K_\alpha}\right)A_\alpha + A_\beta}$$

where $F(\beta)$ is the fraction of β-crystalline phase content, $A_\alpha$ and $A_\beta$ are the absorbance values at 764 $cm^{-1}$ and 840 $cm^{-1}$, respectively. $K_\alpha$ and $K_\beta$ are the absorption coefficients at 764 and 840 $cm^{-1}$, whose values are $6.1 \times 10^4$ $cm^2$ $mol^{-1}$ and $7.7 \times 10^4$ $cm^2$ $mol^{-1}$, respectively.[44b,45] So, the calculated $F(\beta)$ value of PM5 nanofibers is 93%. The surface morphology of PM5 has been investigated by FESEM, which indicates the nanofibrous morphology, as depicted in Fig. 2(d). Also, the EDS spectra and elemental colour mapping are performed to examine the atomic weight percentage and elemental distribution inside the nanofibers. Fig. S5(c) (ESI†) represents the atomic weight percentage of nanofibers where the presence of fluorine (F), molybdenum (Mo), and tellurium (Te) is confirmed. The homogeneous distribution of these elements within the nanofibers is further verified by elemental colour mapping, as depicted in Fig. S5(d) (ESI†).

### 3.3. Working mechanism of the EPMTNG device

The schematic illustration of the working mechanism of the fabricated EPMTNG device and the influence of the trapping layer on the output performance are depicted in Fig. 3(a) and (b). The EPMTNG device is designed with three layers, *i.e.* charge generating layer, charge trapping layer and charge collecting layer. In this work, EBTO nanocomposite, PM5 nanofiber and carbon tape serve as the charge generating,

charge trapping and charge collecting layers, respectively. The combined effect of tribo-electrification and electrostatic induction plays an important role in the operating mechanism of the EPMTNG device. When the human hand gets into contact with the charge generating layer (EBTO), the EBTO layer generates negative triboelctric charges due to negative tribopolarity. On the contrary, the human hand induces positive triboelectric charges, as shown in step (i) of Fig. 3(a). In the next step, a relative separation between the human hand and the EBTO layer takes place. As a result, electrostatic charges are generated on the charge collecting layer (carbon tape) to balance the triboelectric charges. Thus, a potential difference develops between the ground and carbon tape, which further helps in the flow of electrons from the carbon tape to the ground through an external load, as depicted in step (ii) of Fig. 3(a). These electrons continue their flow until the EPMTNG device is separated completely (step (iii) of Fig. 3(a)). After completing the separation, the human hand comes closer to the EBTO layer again, decreasing the positive electrostatic charges generated on the charge collecting layer (carbon tape). Thus, the electrons return from the ground to the carbon tape and this flow continues until the human hand is fully in contact with the EBTO layer again, as shown in step (iv) of Fig. 3(a). With the help of this contact separation procedure, the EPMTNG device generates the output signal periodically.[9]

Generally, a triboelectric nanogenerator (TENG) consists of four representative layers: the charge generating layer, charge trapping layer, charge collecting layer, and charge storage layer. During triboelectrification, the charge generating layer induces the triboelectric charges, which can drift easily due to the effect of the driving force of the electric field and combines with the opposite induced charges generated in the charge collection layer. As a result, huge charge loss takes place, which reduces the surface charge density of TENG and diminishes the output performance of the nanogenerator.[10] To overcome the significant issue of charge loss and improve the performance of TENG, a charge trapping layer has been introduced in the intermediate of the charge generating layer and charge collection layer. The trapping layer restricts the combination of triboelectric charges and opposite induced charges and enhances the output performance of the nanogenerator by increasing the surface charge density. For this reason, we have introduced an intermediate trapping layer (PM5) in the designing process of the EPMTNG device. The effect of the intermediate trapping layer on the output performance of the EPMTNG device has been elaborated schematically in Fig. 3(b). In the absence of a charge trapping layer, the generated triboelectric charges of the EBTO layer get captured inside the trap sites. This helps in the accumulation of induced positive charges in the carbon tape, which results in the formation of an electric field between the EBTO layer and the carbon tape. As the charge trapping ability of the EBTO layer is very low, the triboelectric charges, which are trapped in the shallow trap of the EBTO layer easily drift to the carbon tape in the presence of a weak electric field and combine with the induced charges. As a result, huge charge loss takes place, which further results in low

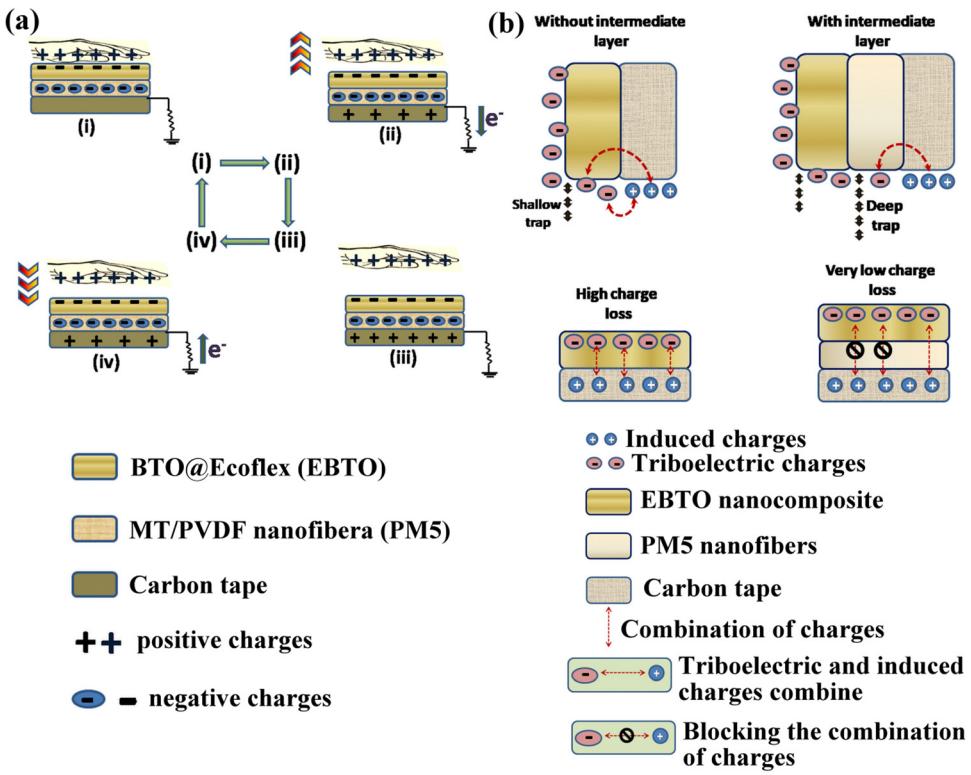


Fig. 3 (a) Working mechanism of the fabricated EPMTNG device. (b) Graphical representation of the effect of the trapping layer (PM5 nanofibers) on the output performance.

 

output performance. To improve the output performance and reduce the charge loss, an intermediate trapping layer (PM5 nanofiber) has been inserted between the EBTO layer and carbon tape. When the PM5 layer is introduced in the EPMTNG device, the phase interface between $MoTe_2$ and the PVDF matrix serves as efficient trap sites for the rapidly accumulating triboelectric charges. These trap networks retain the negative triboelectric charges while hindering the drifting of charges from the EBTO layer (charge generating layer) to the carbon tape (charge collecting layer), decreasing the neutralization of negative tribo-charges and positive induced charges. Moreover, the addition of $MoTe_2$ into the polymer matrix generates the induced charges under the application of an external field, owing to the excellent aspect ratio and high conducting properties of the nanoparticles and increases the Coulomb force, enhancing the polarization effect. This polarization effect arranges more capturing networks and then steadily traps the triboelectric charges by using the deep traps. Furthermore, the $MoTe_2$ nanoparticles strengthen the trapping depth of the triboelectric charges by creating conducting channels inside the PM5 layer and help in capturing more charges. Thus, the charges trapped in deep traps depart slowly from the trapping sites and extend the charge residence time, resulting in a decrement in charge loss by reducing the charge recombination process. Therefore, the incorporation of the PM5 layer in EPMTNG assists in the accumulation of more triboelectric charges on the surface of the EBTO layer and enhances the output performance of the device by increasing the surface charge density.[10,25]

### 3.4. Theoretical investigation of the effect of PM5 fibers on EPMTNG

The effect of the intermediate trapping layer (PM5 fibers) on the output performance of EPMTNG has been investigated theoretically using finite element analysis. Also, a simulation model using numerical analysis through Python has been prepared for the comparison of surface potential and output performance of TENG with respect to presence and absence of the intermediate layer. For this, fundamental numerical modeling has been applied and analyzed using Python 3.9 libraries on the Jupyter lab framework. Moreover, some libraries, including NumPy and Pandas, have been used in Python to analyze the numerical functions and data configurations. NumPy helps in numerical operations, including multidimensional array and matrix, elemental operations, *etc.*, and Panda assists in analyzing the organized and structured data frame. After successfully simulating the data in Python, the Matplotlib library is utilized to plot the excepted graph using the simulated data points. In the absence of the intermediate trapping layer (PM5), the *V*–*Q*–*x* relation of the conductor to the dielectric type triboelectric nanogenerator will be[16,46]

$$V = -\frac{Q}{S\varepsilon_0}(d_0 + x(t)) + \frac{\sigma x(t)}{\varepsilon_0},$$

where $d_0 = \frac{d_{EBTO}}{\varepsilon_{rEBTO}}$.

In the above equation, $Q$ is the amount of charge transferred; $S$ defines the area of EPMTNG; $\varepsilon_0$ represents the free space permittivity; $d_{EBTO}$ is the thickness of the charge generating layer (EBTO nanocomposite); $\varepsilon_{rEBTO}$ represents the relative permittivity of the EBTO nanocomposite; $x(t)$ is the distance between two triboelectric surfaces; $\sigma$ defines the surface charge density. For an open-circuit condition, $Q = 0$ that means no charge transfer process will occur. Therefore, the open-circuit voltage will be[47] $V_{OC} = \frac{\sigma x(t)}{\varepsilon_0}$. In the presence of the intermediate layer (PM5) within the EPMTNG device, *V*–*Q*–*x* relationship will be[46]

$$V = -\frac{Q}{S\varepsilon_0}(d_0 + x(t)) + \frac{\sigma x(t)}{\varepsilon_0},$$

where $d_0$ is the sum of the EBTO layer and PM5 layer. That means, $d_0 = \frac{d_{EBTO}}{\varepsilon_{rEBTO}} + \frac{d_{PM5}}{\varepsilon_{rPM5}}$. To simplify the calculations, some assumptions are taken which are

(a) The distribution of charges on the surface of triboelectric layers is uniform.

(b) Triboelectric charges stay only on the contact surfaces.

(c) Measured surface charge density is linearly related to the surface potential.

(d) The applying force on the device for all cases is the same.

(e) Thickness of the EBTO nanocomposite and PM5 layer are assumed to be 1 mm and 256 μm, respectively. The highest capacitance value is considered in the calculation. Areas of the EBTO nanocomposite and PM5 layer are 1.1 $cm^2$ and 1.4 $cm^2$, respectively. The surface charge densities of TENG with and without the PM5 layer are assumed to be $3.5 \times 10^{-4}$ C $m^{-2}$ and $1.3 \times 10^{-4}$ C $m^{-2}$, respectively.

Initially, we have calculated the relative permittivity ($\varepsilon_r$) of the EBTO nanocomposite and PM5 layer. As we know, the high permittivity based layer increases the surface charge density by inducing more polarization, and $\varepsilon_r$ has been measured using the equation[46]

$$\varepsilon_r = \frac{d_{film} C_0}{A\varepsilon_0}.$$

Here, $d_{film}$ stands for the thickness of the EBTO nanocomposite and PM5 layer, $C_0$ is the highest capacitance value, $A$ defines the area of the EBTO nanocomposite and PM5 layer, and $\varepsilon_0$ represents the free space permittivity. Thus, the calculated relative permittivity values of the EBTO nanocomposite and PM5 layer are 7 and 23 respectively.

Therefore, the high permittivity value of the PM5 layer assists in inducing a more polarization effect and enhances the surface charge density of the EPMTNG device. In the presence of the PM5 layer, the induced high surface charge density increases the output voltage of the device. The estimated output voltage of the EPMTNG device from finite element analysis is 304 V. Without the PM5 layer, the estimated voltage is 120 V, as shown in Fig. 4(a). Additionally, a diagram has been presented to investigate the theoretically and experimentally obtained output voltages in the absence and presence of the PM5 intermediate layer, shown in Fig. 4(b). Moreover, in addition to the changes in relative permittivity, the value of $d_0$ also changes for both cases (with and without the PM5 layer).

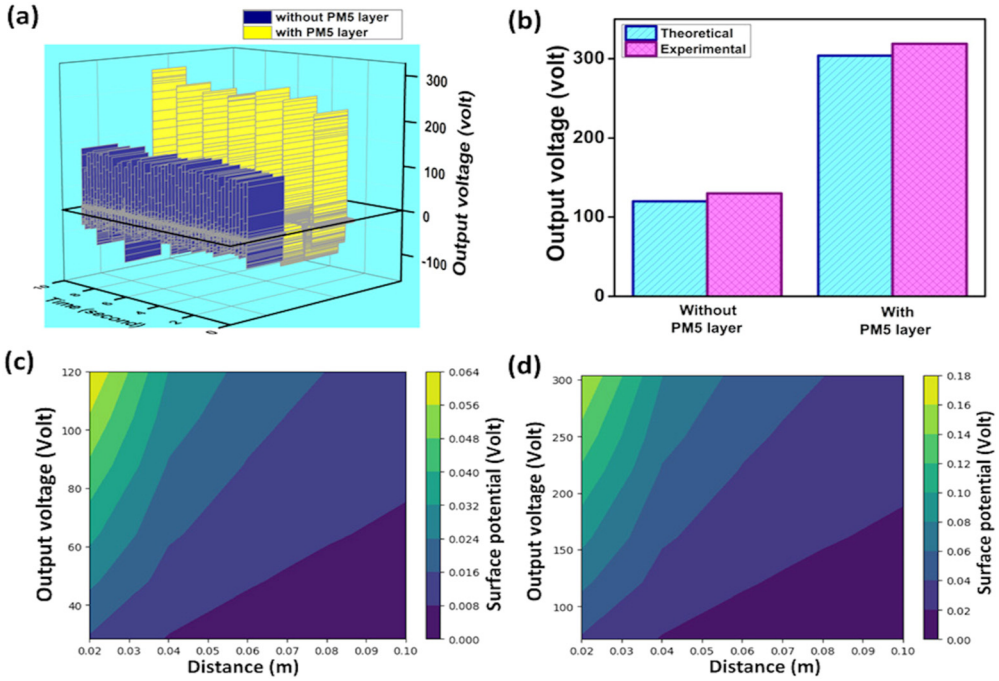


Fig. 4 (a) Theoretical evaluation of the effect of the PM5 layer on the output performance of EPMTNG. (b) Comparison of theoretically and experimentally obtained output voltages. Contour plot of surface potential during the (c) absence of PM5 layer and (d) presence of PM5 layer, with color bars.

Along with this, the amount of charge transfer ($Q$) in both cases is also varied with the surface charge density, as charge transfer is dependent on the surface charge density and contact area. In order to investigate the effect of the PM5 layer, the surface potential has been calculated theoretically using the equation:[18]

$$V = \frac{\sigma \times d_0}{\varepsilon_0 \times \varepsilon_r},$$

where $\sigma$ defines the surface charge density, $d_0$ represents the thickness of layer, $\varepsilon_0$ is the permittivity of free space, and $\varepsilon_r$ is the relative permittivity. The estimated results from the simulation describe that TENG with the PM5 layer has a surface potential of 0.18 V, which is higher than that of the TENG without the PM5 layer (surface potential of 0.064 V). Also, the variation of surface potential with different distances between the human hand and device has been mapped in both cases. The simulated data of the surface potential in both cases are represented in Fig. 4(c) and (d). The possible reasons behind the enhancement of surface charge density, surface potential, and output voltage in the presence of the intermediate trapping layer are (i) prevention of electron decay with positive induced charges, (ii) capturing more residual charges in the trap sites of the PM5 layer, (iii) reinforcing the polarization effect through trapping more charges and improving the conductivity. This further restricts the charge loss by preventing charge recombination and enhancing the surface potential. As a result, the output performance of EPMTNG is increased. Thus, the theoretical model clearly indicates the prominent advantages due to the presence of an intermediate layer in the fabricated device and establishes our proposed concept.

### 3.5. Output performance and electrical properties of the EPMTNG device

The three layers of the device not only increase the output performance but also make the device flexible and user-friendly. The flexibility of the device is shown in Fig. S1(a) and (b) (ESI†). Also, the weight of the device is measured, which confirms that the device is lightweight, as shown in Fig. S1(c) (ESI†). Furthermore, the output performance of the EPMTNG device has been investigated by connecting the device with DSO. The wearable and flexible device exhibits 319 V output voltage under continuous finger tapping conditions with a generated axial pressure of 12 N. Moreover, the influence of the intermediate layer is also observed. With the help of the intermediate layer, the EPMTNG device exhibits 319 V output voltage, whereas the device generates only 130 V output voltage in the absence of a charge trapping layer (Fig. 5(a)). The reason behind the high output is the influence of the trapping layer by capturing more charges within the trapping sites and increasing the charge storage ability of the device. From Coulomb's law, we can see that the electric field ($E$) among triboelectric ($Q_t$) and induced charges ($Q_e$) varies inversely to the square of the distance ($r$) between triboelectric charges and induced charges, *i.e.*,

$$E = \frac{K_e Q_t Q_e}{r^2}$$

where $K_e$ represents the Coulomb's constant. When the intermediate trapping layer is absent, a small amount of charge is trapped at a high electric field. Thereafter, these trapped charges drift easily and combine with induced charges as the

 

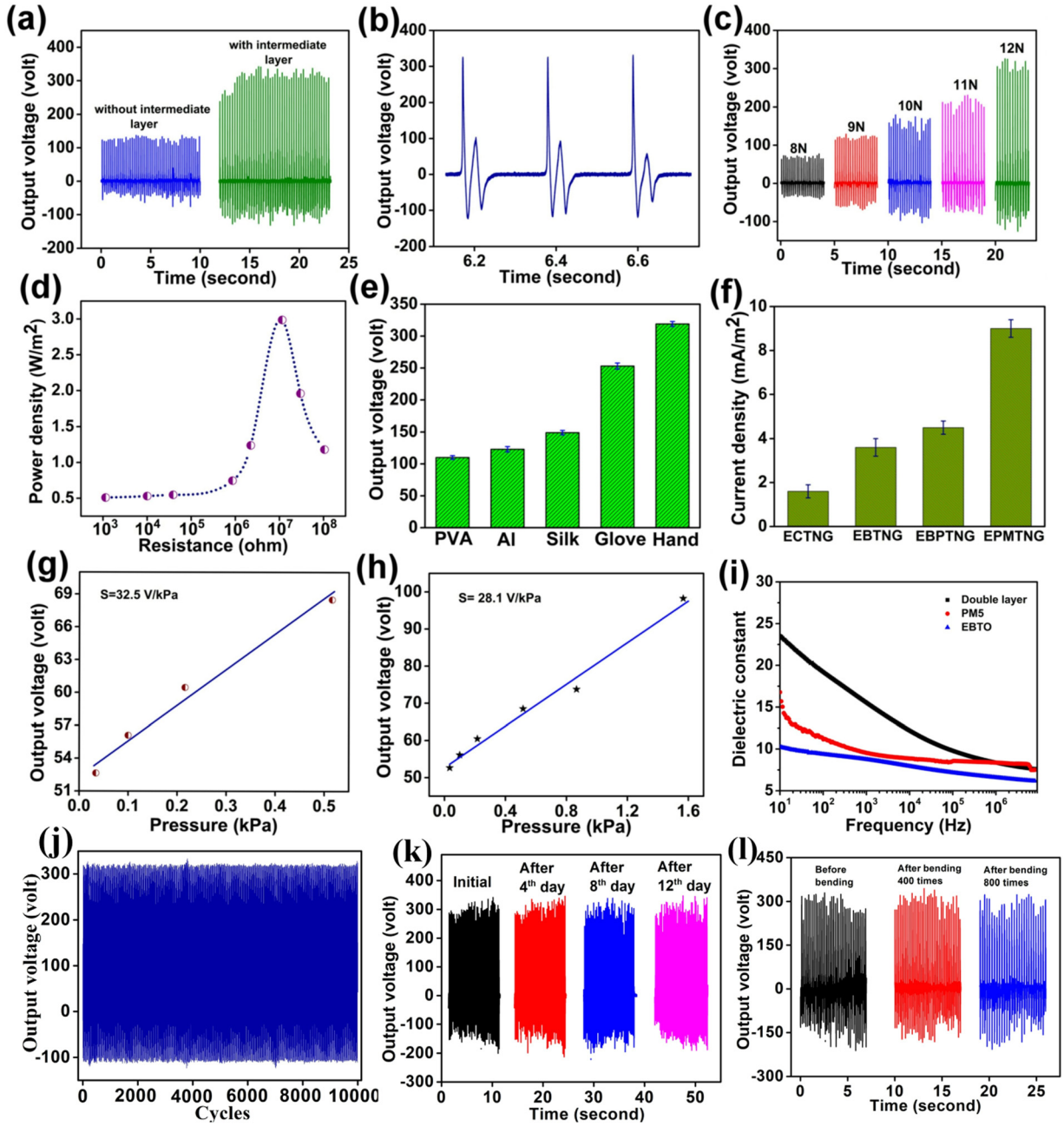


Fig. 5 (a) Output voltage of the EPMTNG device by periodic finger pressing (12 N). (b) Magnified outlook of the generated output voltage of our device during the same axial pressure. (c) Force dependent output voltage of the EPMTNG device. (d) Instantaneous power density with the variation of external load resistance. (e) Obtaining the output voltage by using different tribo positive materials. (f) Measuring the current densities of four devices (i) Ecoflex and carbon tape based TENG (ECTNG), (ii) BTO incorporated Ecoflex nanocomposite and carbon tape based TENG (EBTNG) (iii) EBTO layer, PVDF layer, and carbon tape based TENG (EBPTNG) and (iv) EBTO layer and MT incorporated PVDF nanofiber (EPMTNG). Sensitivity of the EPMTNG device at (g) low pressure (up to 0.5 kPa), (h) high pressure (>0.5 kPa) regions. (i) Dielectric constant of the EBTO nanocomposite, PM5 nanofibers, and dual layer. (j) Stability and (k) durability performance of the EPMTNG device. (l) Measuring the robustness of the fabricated device by bending it over 800 times.

drift velocity ($u$) depends on the electric field ($u = \mu E$).[17] That means, a high electric field induces high drift velocity, which helps in more charge recombination processes and induces a low output result. Meanwhile, the presence of a charge trapping layer increases the distance ($r$) between the charges and induces a weak electric field, which reduces the drift velocity of charges and prevents charge recombination. As a result, the EPMTNG device generates such high output voltage in the presence of an intermediate layer (PM5). Moreover, the enlarged view of the generated output voltage has been depicted in Fig. 5(b), where a positive peak appears when strain is applied to the EPMTNG device and a negative peak after recovering from the strain. The influence of an applied force on the output performance of the device has been monitored by applying

different forces on the device, as shown in Fig. 5(c). As we increase the applied force, the output voltage also increases. The possible reason is that with the increase in force, the contact between the two triboelectric layers also increases, which helps in more charge generation.[48,49] In order to explore the load capacity of our fabricated device, multiple valued load resistances have been used. The EPMTNG device exhibits different instantaneous power densities with the variation of load resistance changing from $10^3$ to $10^8$ Ω (Fig. 5(d)). The power density of the device has been calculated by using

$$P = \frac{V^2}{R_L \times A},$$

where $V$ represents the output voltage of the EPMTNG device, $R_L$ defines the value of load resistance, and $A$ is the surface area of the EPMTNG device (4.4 × 2.5 $cm^2$).[45] The obtained maximum power density is 2.9 W $m^{-2}$ at $10^7$ Ω. Furthermore, the thickness of the charge generating layer (EBTO nanocomposite) affects the output performance of the triboelectric nanogenerator. As we increase the thickness of the EBTO nanocomposite, the output voltage also decreases. The maximum voltage is obtained for 1 mm thickness, as depicted in Fig. S4(a) (ESI†). The reason behind this behavior is that the surface charge density reduces with the increasing thickness of EBTO, which results in lowering the output voltage. The equation validating this will be

$$\sigma = \frac{V\varepsilon_o\varepsilon_r}{d}$$

where $V$ describes the surface potential of the EBTO nanocomposite, $\varepsilon_0$ represents the dielectric constant of air, $\varepsilon_r$ represents the dielectric constant of the nanocomposite, $\sigma$ defines the surface charge density of the nanocomposite, and $d$ is the thickness of the EBTO nanocomposite.[18] Thus, it is clearly seen that increasing the thickness of the nanocomposite decreases the surface charge density, resulting in low output voltage as

$$V_{OC} = \frac{\sigma A}{2C_o}$$

where $V_{OC}$ is the output voltage of the EPMTNG device, $\sigma$ is the surface potential, and $A$ is the surface area of the EBTO nanocomposite, $C_o$ defines the capacitance of the device.[50] While measuring the output voltage of the device for more than one set of values, we get different results. This incident also happens when measuring the current density. The possible reasons behind the changes in the results are the errors arising from the external mechanical force, contact area, contact speed, frequency, *etc.*[51] Another leading factor of inducing the errors is the separation distance between the two triboelectric layers. When the separation distance is deviated from its optimal value, the charge transfer between electrodes also changes. As a result, we obtain different output results for the same device. Also, the contact area of the EPMTNG device is another source of error. Errors in the contact area result in fluctuations in charge density and provide inaccurate output values. Whenever, we measure the output voltage and current density for different cases of fabricated TENGs, some deviations are observed due to the above mentioned sources of errors. To improve the reliability, an error bar has been included. Moreover, the material selection of the positive layer of the EPMTNG device plays a significant role in the output performance. To demonstrate the excellent output performance of the fabricated device, its output result has been measured using different positive materials like PVA, aluminum sheet, silk, nitrile glove, and human hand, as shown in Fig. 5(e). The measured output voltages using different positive materials like PVA, aluminium sheet, silk, nitrile glove, and human hand are 110 ± 2.9 V, 123 ± 4.2 V, 149 ± 3.5 V, 253 ± 4.8 V, and 318 ± 3.9 V respectively. The findings indicate that the performance of the triboelectric nanogenerator is greatly impacted by the active layer materials and the human hand generates the maximum output voltage more than other positive materials as it is an extremely positive triboelectric material.[9] For this reason, we have selected the human hand as the positive layer in this present work. Furthermore, the current density of EPMTNG has been measured. Also, the influence of the trapping layer on the current density has been examined. We have prepared four devices (i) Ecoflex and carbon tape-based TENG, named as ECTNG, (ii) BTO incorporated Ecoflex nanocomposite and carbon tape based TENG, named as EBTNG, (iii) EBTO layer, PVDF layer and carbon tape based TENG, named as EBPTNG and (iv) EBTO layer and MT incorporated PVDF nanofiber (charge trapping layer) based EPMTNG. The measured current densities of these devices are shown in Fig. 5(f). The measured current densities of these four devices are 1.6 ± 0.2, 3.6 ± 0.4, 4.5 ± 0.3, 9 ± 0.4 mA $m^{-2}$ respectively. This result indicates that the intermediate trapping layer improves the current density of TENG compared to other devices. Generally, in the absence of a charge trapping layer, some charges of the EBTNG device are captured in the shallow trap sites of the BTO layer. Thereafter, these charges drift easily and combine with positive charges of the carbon tape, resulting in low surface charge density. Moreover, the presence of MT nanoparticles within the intermediate layer reinforces the polarization effect and prevents charge recombination. This increases the charge density and enhances the current density of EPMTNG. This can be mathematically expressed as

$$J_D = \sigma_T \frac{dH}{dt} \frac{\frac{d\varepsilon_o}{\varepsilon}}{dt\left(\frac{d\varepsilon_o}{\varepsilon} + z\right)\left(\frac{d\varepsilon_o}{\varepsilon} + z\right)} + \frac{d\sigma_T}{dt} \frac{H}{\left(\frac{d\varepsilon_o}{\varepsilon} + z\right)}$$

where $J_D$ represents the current density and $H$ represents the function of time associated with the contact frequency. This equation confirms that the current density is directly proportional to the charge density.[18] Thus, we get maximum current density in the case of the EPMTNG device compared to other devices. Also, the sensitivity of the fabricated EPMTNG device has been measured by dropping objects of different masses on the device. The equation to calculate the sensitivity of the device is

$$S = \frac{\Delta V}{\Delta P}$$

where $S$ is the sensitivity of the device, $\Delta V$ is the change in the obtained output voltage, and $\Delta P$ defines the change in applied

 

pressure.[45] The sensitivity of the device at a low pressure region (up to 0.5 kPa) is 32.5 V $kPa^{-1}$, as shown in Fig. 5(g). In the high-pressure region (>0.5 kPa), the sensitivity value of the device is 28.1 V $kPa^{-1}$, as shown in Fig. 5(h). Furthermore, the stability performance of the EPMTNG device has been analyzed over 10 000 cycles under the applied mechanical force by a human hand. Fig. 5(j) exhibits the stability performance of the device, showing that the device maintains nearly the same output voltage throughout the whole time period and no such degradation of output voltage is observed after 10 000 cycles. These results confirm the long-term stability of the EPMTNG device. The durability test of the EPMTNG device has been performed under the application of mechanical force by hand. The device exhibits about 314 V output voltage at 5 Hz frequency. The durability test has been conducted for 12 consecutive days and the results show that the EPMTNG device generates nearly the same output voltage throughout the whole time period and maintains over 98% of the initial output voltage, as shown in Fig. 5(k). Therefore, the results indicate that the EPMTNG device has exceptional durability and is suitable for long-term practical applications. To observe the robustness of the device, bending and twisting tests have been performed. Fig. 5(l) shows the bending performance of the EPMTNG device. After bending over 400 times, the device exhibits the same output voltage compared to its initial value and maintains 99% of the initial value. Thereafter, the device has been bent again 400 times more and maintained 98% of its initial value. The results of the bending test indicate the very good robustness of the device. Moreover, the twisting performance of the device is shown in Fig. S4(b) (ESI†). After twisting the device over 400 times, the device generates almost the same output voltage and maintains 98% of its initial value. To investigate the high robustness of the device, we have twisted it 400 times more and obtained nearly the same output voltage, maintaining 97% of its initial value. Therefore, the bending and twisting tests of the device exhibit the outstanding robust behavior of the EPMTNG device. Besides this, the output performance of the EPMTNG device is compared with the previously reported 2D materialbased TENGs and nanofiberbased TENGs. The comparison has been organized in table format and depicted in Table S3 (ESI†).

The electrical properties of the different layers of the fabricated EPMTNG device have been examined by dielectric measurements. Dielectric parameters play a significant role in enhancing the surface charge density and improving the output performance of the device. In this present work, we have prepared three systems, the EBTO layer, PM5 nanofiber, and dual layer (combining EBTO and PM5), by attaching the copper electrode on both sides of each system and measuring the dielectric parameters (for measurement of the prepared three systems) through an LCR meter by varying the frequency range from 10 Hz to 1 MHz. Fig. 5(i) exhibits the dielectric constant values of three systems by varying the frequencies. The relative dielectric constant can be expressed as $\varepsilon = \varepsilon' + j\varepsilon''$, where $\varepsilon'$ is the real part and $\varepsilon''$ is the imaginary part of the relative dielectric constant. The imaginary part contributes in energy dissipation inside the dielectric material, whereas the real part indicates the energy storage capacity of the dielectric substance. The real part of the dielectric constant can be calculated using this mathematical equation $\varepsilon' = (C \cdot d)/(\varepsilon_0 A)$ where $C$ represents the capacitance value of the respective system; $\varepsilon_0$ is free space permittivity whose value is $8.85 \times 10^{-12}$ F $m^{-1}$; $d$ is the thickness, and $A$ is the area of the respective systems. For the EBTO layer, the maximum dielectric constant is found to be 11 at 10 Hz frequency, which is very high compared to the dielectric constant (~3) of pure Ecoflex. The reasons behind getting high value of the dielectric constant are the formation of macroscopic dipoles and microcapacitor networks.[52] Moreover, the presence of oxygen (O) inside the BTO nanoparticles and hydrogen (H) inside the Ecoflex polymer helps in dipole formation, whereas the microcapacitors are induced between the nearest fillers (BTO nanoparticles). Each single microcapacitor contributes to build the microcapacitor network, which further leads to high dielectric values.[18] Thus, the EBTO layer shows the maximum dielectric value at 0.5 wt% of BTO. At higher doping concentrations (1 wt%), the dielectric value of the nanocomposite reduces due to the attainment of the percolation limit.[9] After reaching the percolation threshold, the interaction between fillers triggers the leakage current to increase. Additionally, the BTO nanoparticles set up a network of conductive molecules within the polymer matrix, which results in shifting from non-Ohmic to Ohmic conduction.[18] Due to these possible reasons, the dielectric value decreases at higher concentrations of BTO, as depicted in Fig. S6(a) (ESI†). For the PM5 nanofiber layer, the maximum dielectric constant is found to be 16 at 10 Hz frequency. Thereafter, the dielectric constant reduces gradually with the increasing frequency value. This phenomenon is attributed due to the Maxwell–Wagner interfacial polarization, which occurs while free charge carriers accumulate at high resistive grain edges. In detail, within the PM5 nanofiber layer, the edges of the insulated grains separate the conducting grains, which facilitate in trapping of free charge carriers and induce dipoles through the grain during their hopping,[44] yielding high values of dielectric constant. Additionally, a fast decrement of dielectric values at highfrequency zones has been observed as the dipole orientation polarization and electronic displacement polarization are unable to survive with the frequency variation.[53] In the case of a double layer, the maximum dielectric constant is 23 at 10 Hz frequency, which is relatively high compared to the EBTO layer. The possible reason behind this increment in dielectric value is the addition of the intermediate layer, which traps more residual charges in trapping sites. Moreover, the incorporation of MT nanoparticles into the PVDF matrix reinforces the polarization effect of the dual layer and enhances the number of charge carriers, which improves the dielectric property.[18]

Along with the dielectric value, tangent loss and ac conductivity of three systems have been observed and shown in Fig. S6(b) and (c) (ESI†). The EBTO layer, PM5 layer, and dual layer exhibit low tangent loss. From Fig. S6(b) (ESI†), a low tangent loss value is observed at a low-frequency region, whereas an increment of loss value at a higher-frequency region is visualized. The possible reason behind this phenomenon is the thermal agitation of the dipoles.[44] Thus, the high dielectric

value with low tangent loss of the EBTO layer, PM5 fiber, and double layer confirms the good storage capacity of the EPMTNG device.

### 3.6. Tracking different human physiological signals

The different body parts of the human body exhibit various characteristics of physiological signals. Owing to high sensitivity, stretchability, flexibility, and skin compatibility properties, the EPMTNG device can be used as a self-powered human physiological signal detector. These properties can have advanced implications in multiple areas, for example, human–machine interface, analysis of the performance in different sporting activities, medical rehabilitation *etc.*[9] To track the physiological signals, we have attached the EPMTNG device to the different parts of the human body like wrist, neck, throat, and elbow. As the device has high sensitivity in low pressure regions (32.5 V $kPa^{-1}$ up to 0.5 kPa), it can successfully detect the blood flow in the human body. When we attach the EPMTNG device to the wrist pulse, the device exhibits quite high output voltage (nearly 0.7 V) generated from blood flow, as shown in Fig. 6(a).

Systolic and diastolic are the two main components of blood pressure, which provide the peak and dip values of the pulse wave during blood flow.[45] Therefore, the fabricated device promptly detects the alternation of the systolic and diastolic pressure and generates output signals. From the following figure, it can be clearly seen that the EPMTNG device successfully detects 12 pulse beats in 10 seconds. That means the total number of pulse beats detected by our device in 60 seconds will be 72. This value matches the normal pulse rate of a healthy person in 60 seconds. Thus, the EPMTNG device may be useful in the clinical identification of hypertension and heart-related health problems.[54] Moreover, the capability of the EPMTNG device towards sensing thoracic pressure, generated by the vibration of the vocal cord at the time of coughing, has been monitored. The result exhibits that the fabricated device can detect every action of coughing (made up with opening burst, noisy airflow, and closing of the glottis) and generates an output voltage in every action, which is nearly 2 V. The detection of coughing action is depicted in Fig. 6(b). Therefore, the EPMTNG device can be utilized to track the airflow process during coughing and in diagnosing diseases related to coughing like bronchitis, asthma *etc.*[55] In addition, the swallowing process has been monitored through the EPMTNG device by affixing it to the throat of the human body. The corresponding fluctuation in output signal confirms the activity of the throat's muscle during the swallowing process, which occurs due to the opening and closing of the glottis (Fig. S7(a), ESI†). The detection of the swallowing process is further confirmed by a short time Fourier transform (STFT) spectrogram, as shown in Fig. S7(b) (ESI†). Thus, the fabricated device may be helpful

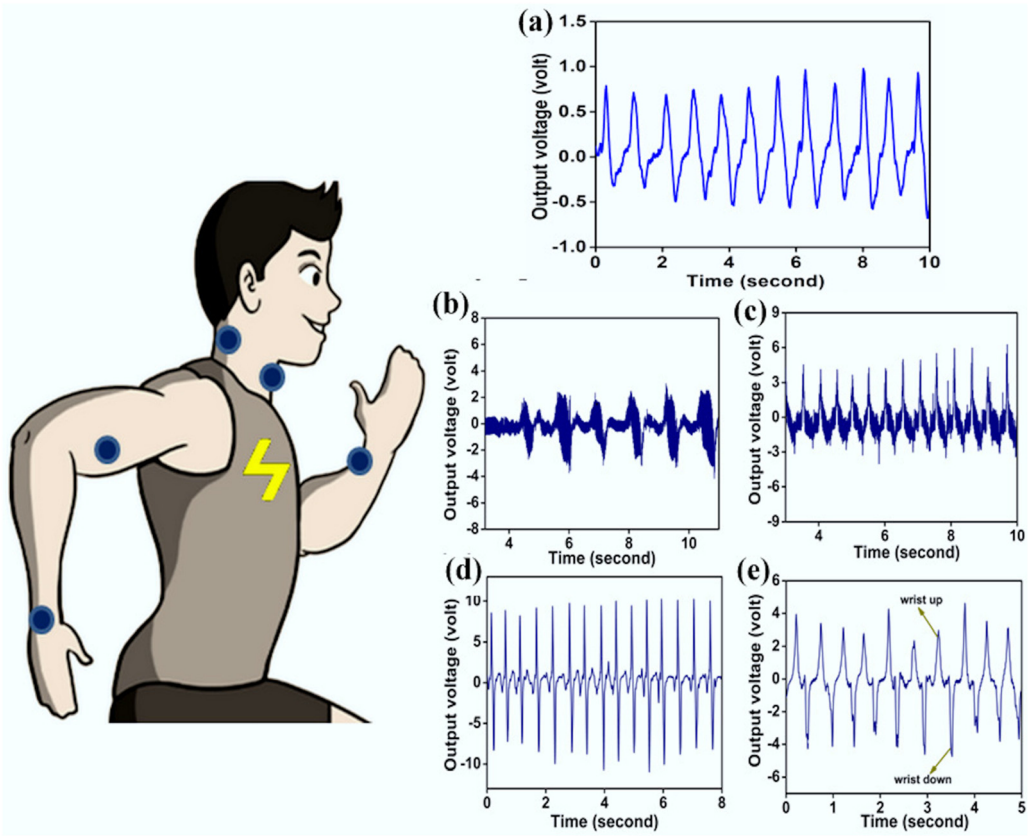


Fig. 6 Generating the output voltage from (a) blood flow by the fabricated EPMTNG device. Tracking the human physiological signals generated by the wearable device during (b) coughing, (c) neck movement, (d) flexion and extension of the elbow and (e) wrist up and down.

 

in the identification of Dysphagia and Odynophagia patients.[56] The fabricated device has the capability to sense muscle movements while speaking. At the time of speaking, the stress is induced due to the vibrations of the vocal cord. The EPMTNG device converts this stress into electric energy and gives us the output voltage, which is also confirmed by the STFT diagram, as depicted in Fig. S7(c) and (d) (ESI†). These results open up the utilization of the fabricated device in speech therapy. Moreover, the neck movement of the human body is also detected by the EPMTNG device. The device successfully detects the continuous up and down motion of the head and generates the output signal. During neck movement, the generated output voltage is about 5 V (Fig. 6(c)). The device was further affixed to synovial joints like the elbow and wrist to monitor the generated physiological signals. In the case of elbow movements, the EPMTNG device can promptly detect the flexion and extension of the elbow and convert this generated stress into an electrical signal, as shown in Fig. 6(d).[57] Additionally, the sensing ability of the device towards the wrist movement has been investigated. The EPMTNG device expands and emits rising and falling voltage signals as the wrist bending continuously occurs from outward to inward (Fig. 6(e)). This response is generated due to the combined effect of the wrist joint pressure and skin deformation.[48] Therefore, the fabricated device may be helpful in the area of sports like monitoring athlete movements and other sporting activities. All these results confirm the potential utilization of the EPMTNG device towards broad futuristic applications in healthcare and self-evaluation of health.

### 3.7. Robotic gesture detection

Owing to high sensitivity, low thickness, and flexibility, the wearable EPMTNG device has been utilized in robotic gesture detection. Firstly, the device is affixed with a hollow cylindrical object and the different responses of pressure generated by the full bending of each fingers of an artificial wooden hand has been monitored. Fig. 7(a)–(e) represents the digital snapshots of the device being pressed by the five fingers (index, middle, ring, middle, and thumb). For continuous pressing and releasing of artificial hand fingers, we get individual output responses from each finger, as shown in Fig. 7(f). Along with this, the positive peaks and the negative peaks of the generated output responses are also observed, which are attributed due to the pressing and releasing effect of fingers. As the generated

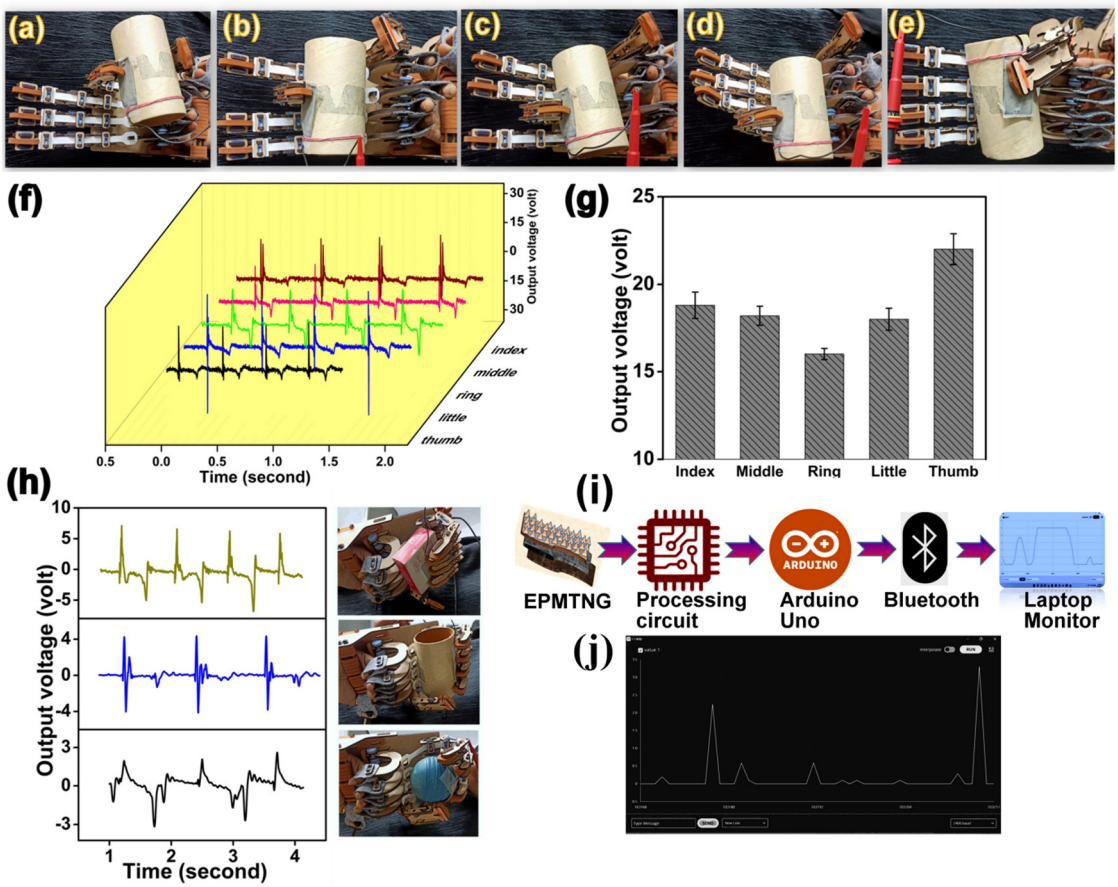


Fig. 7 (a)–(e) Digital snapshots and (f) output responses of five robotic fingers (index, middle, ring, middle, and thumb) at device touching conditions. (g) Obtaining the output voltage during each finger movement. (h) Output responses and digital images of gripping different objects (rectangular box, hollow cylinder, and rubber ball). (i) Schematic illustration of the wireless connection of transmitted signal. (j) Displaying the transmitted signal on a laptop monitor during artificial finger bending.

forces of the fingers on the EPMTNG device are different, the obtained output voltages of each finger movement are also different. During artificial finger bending, the generated error values are also included with the obtained output voltages of each finger movement (Fig. 7(g)). Therefore, the index, middle, and thumb fingers generate 19 ± 0.7 V, 18 ± 0.5 V, and 22 ± 0.8 V and the ring, little fingers exhibit 16 ± 0.3 V, 17 ± 0.6 V output voltage respectively. Thus, the flexible and wearable device can be utilized in robotic surgery and human-machine interface applications.[58] Furthermore, the sensing ability of the device opens up a new path of utilization in the field of soft robotic applications. The utilization of the device in soft robotic applications has been investigated by gripping different shaped objects. First of all, three differently shaped objects are selected, which are a rectangular box, a hollow cylindrical object and a rubber ball. Thereafter, the device is attached to these respective objects and monitor the responses during gripping. When the objects are gripped, the device generates positive peaks and negative peaks occur at the time of releasing the object, as shown in Fig. 7(h). Also, each differently shaped object generates different output responses during gripping and releasing due to different contact areas. Therefore, the rectangular box generates a high output voltage compared to other objects as the higher curvature induces a superior contact area, which leads to a high output signal.[59] Thus, the gripping ability and object distinguishable capability make the EPMTNG device a suitable candidate in soft robotic applications. Additionally, a wireless system has been introduced to monitor the bending movements of the robotics finger by transmitting the generated signal to a laptop through Arduino Uno Bluetooth system. Fig. 7(i) demonstrates the wireless connection of the transmitted signal. During the bending of the finger, the EPMTNG device generates an output signal that passes through a low-pass filter and rectifier module containing a processing circuit for rectifying the signal. After getting rectified, the signal is sent to Arduino Uno and also transferred wirelessly to the laptop *via* a Bluetooth system. The rectified signals during the bending motion are clearly displayed in the laptop monitor, as shown in Fig. 7(j).

### 3.8. Realistic approach of the fabricated EPMTNG device

To investigate the energy conversion ability and practical utilization of the EPMTNG device in our daily lives, LEDs illumination and capacitor charging have been performed. The LEDs are illuminated under a periodic finger pressing condition by connecting them into a series arrangement with the help of a

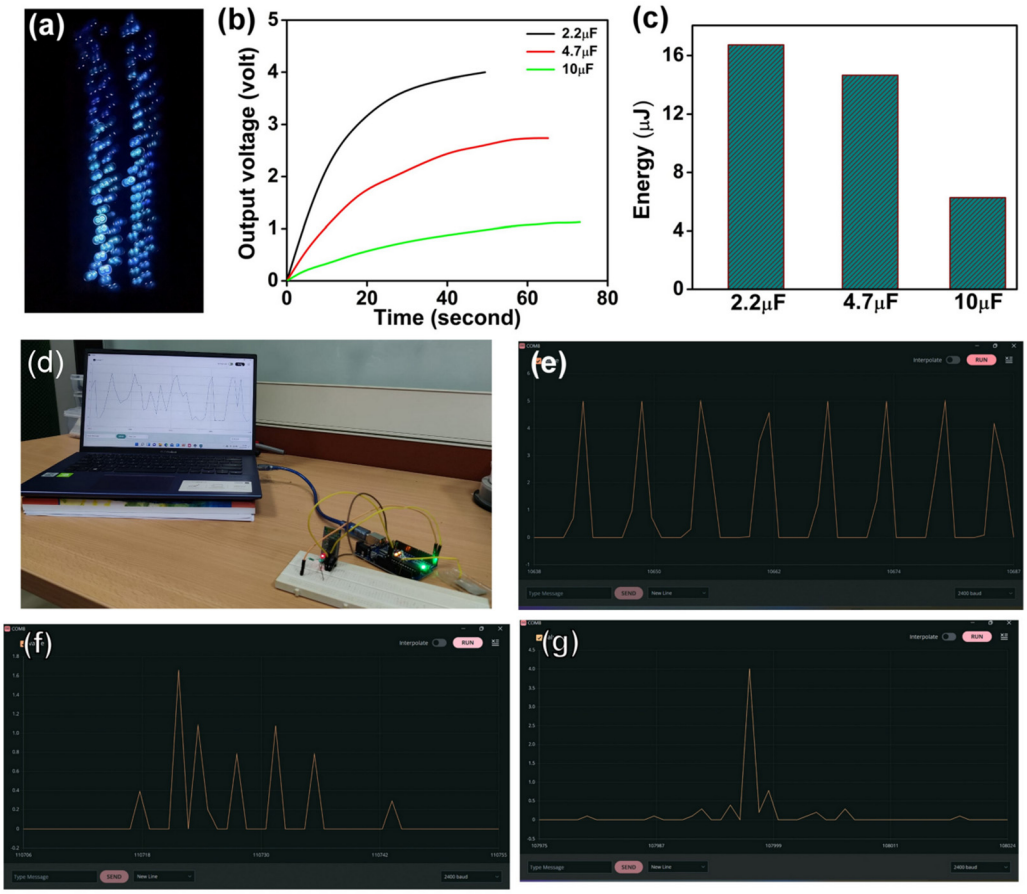


Fig. 8 (a) Digital image of illuminating blue LEDs under periodic finger pressing. (b) Charging of capacitors by the EPMTNG device. (c) Energy storage in three capacitors. (d) Pictorial representation of the wireless connection. Transmitting the generated signals wirelessly during (e) single finger tapping, (f) vocal cord vibration and (g) glottis movement.

 

bridge rectifier. The circuit diagram of LEDs illumination and charging capacitors has been depicted in Fig. S8 (ESI†). Fig. 8(a) represents the pictorial image of lighting up blue LEDs. This figure also depicts the capability of illuminating 140 blue LEDs of the EPMTNG device under periodic finger pressing. Furthermore, the fabricated device is wired with a bridge rectifier to charge up the capacitors under continuous finger pressing. Fig. 8(b) exhibits the capacitor charging curve, which clearly indicates that the EPMTNG device is capable of charging 2.2 μF, 4.7 μF and 10 μF capacitors up to 3.9 V, 2.5 V and 1 V within 75 seconds. Additionally, the capacitor charging curves illustrate how the saturation voltage gradually reduces with the increasing capacitance values. Moreover, the accumulation of energy inside the capacitors during the charging process has been calculated using

$$E = \frac{1}{2}CV^2,$$

where $E$ defines the accumulated energy, $C$ describes the capacitance value, and $V$ defines the voltage on the capacitor.

The total amount of energy gathered in the 2.2 μF, 4.7 μF and 10 μF capacitors are 16.7 μJ, 14.6 μJ and 6.2 μJ respectively, as depicted in Fig. 8(c). Thus, portable electronic appliances can be charged using this EPMTNG device, which has very good energy conversion and energy storage ability. Along with the capacitor charging and LEDs illumination, wireless transmission of the generated signal from the fabricated device has been visualized. First of all, the device is connected to the processing circuit to rectify the signal and then passed to Arduino Uno, which is further transmitted the signal in laptopthrough a Bluetooth connection. The digital snapshot of the wireless connection is represented in Fig. 8(d). The wireless transmission of signals generated from single finger tapping, coughing and speaking conditions are also monitored. Fig. 8(e) exhibits the transmitted signals wirelessly during single finger tapping. The vocal cord vibration and glottis movements are also monitored. Fig. 8(f) depicts the generated signals from the vocal cord vibration of a female person at the time of speaking some words. Each and every vibration is successfully displayed on the monitor of the laptop through waveforms. Moreover, the wireless transmission of signals induced from the glottis movement during single coughing has been visualized in Fig. 8(g).

## 4. Conclusion

The current work expresses the fabrication process and output performance of wearable and flexible EPMTNG devices. The designing of the device is made of micro-patterned $BaTiO_3$@Ecoflex (EBTO) nanocomposite, 2D layered $MoTe_2$ incorporated PVDF nanofibers (PM5) and carbon tape. The idea behind the utilization of surface modification of the EBTO nanocomposite is to create the surface area and improve the surface potential. The micro-patterned structure creates the surface roughness on the EBTO nanocomposite and assists in the increment of effective contact area between the human hand and the EBTO layer. Therefore, more triboelectric charges are induced on the surface of the EBTO layer and the human hand. As a result, potential difference increases during the triboelectrification process. This potential difference further helps in enhancing the output performance of the EPMTNG device. Furthermore, a charge trapping layer (PM5 nanofiber) has been introduced between the EBTO nanocomposite and carbon tape to prevent the charge recombination process and enhance the output performance of the fabricated device. The idea behind the addition of a charge trapping layer in designing EPMTNG has been established theoretically using a finite element simulation model, where the values of the theoretically calculated surface potential and output voltage in the presence of the PM5 layer are clearly indicated the validation of the proposed concept. Under continuous finger pressing (12 N) conditions, the self-powered and flexible device generates an output voltage of 319 V and a current density of 9 mA $m^{-2}$ respectively. Also, the device exhibits a very good power density of 2.9 W $m^{-2}$ at $10^7$ Ω under the same axial pressure. Moreover, the effect of PM5 nanofibers on the electrical properties of the device has been investigated by dielectric measurements. The incorporation of 2D $MoTe_2$ nanoparticles into the PVDF matrix increases the β-crystalline phase and reinforces the polarization effect by inducing more charge carriers inside the polymer matrix. This β-phase nucleation and polarization reinforcement help in the improvement of the dielectric properties of the device. In addition to this, the wearable EPMTNG device has high sensitivity (32.5 V $kPa^{-1}$) at low-pressure regions of up to 0.5 kPa. This high sensitivity value helps in the tracking of different human physiological signals and transmitting these signals wirelessly to a laptop. The additional significance of the device is the detection of robotic gestures. Furthermore, the realistic utilization of the fabricated device is monitored by illuminating LEDs and charging different capacitors. Thus, the self-powered and wearable EPMTNG device can be used in multidimensional applications, including monitoring sporting activity, speech therapy, medical rehabilitation, and identification of dysphagia and odynophagia patients *etc.* Also, the device has potential utilization in the field of robotic surgery and soft robotics applications. Therefore, the fabricated device may be useful in health care and human-machine interfaces.

## Author contributions

Debmalya Sarkar; writing original draft, designing, conceptualization, data acquisition, manuscript preparation. Namrata Das: data acquisition, conceptualization. Souvik Sau: theoretical modeling. Ruma Basu: supervision, editing. Sukhen Das: supervision, editing.

## Conflicts of interest

Authors declare that they have no competing interests.

## Acknowledgements

Authors are very thankful to Jadavpur University, Department of Physics, for the instrumental facility through the FIST and PURSE scheme of the Department of Science and Technology, Govt. of India. Authors would like to thank the SAIS department of the Indian Association for the Cultivation of Science, Govt. of India, for the FESEM facilities and experimental support. Moreover, this work is financially supported by the University Grants Commission, Govt. of India (No. 1413/(CSIR-UGC NET DEC.2018), 191620153244); UGC-DAE Consortium for Scientific Research (CSR/2021-22/02/514, CSR/2021-22/02/498).

## References

1 C. Chen, L. Chen, Z. Wu, H. Guo, W. Yu, Z. Du and Z. L. Wang, 3D double-faced interlock fabric triboelectric nanogenerator for bio-motion energy harvesting and as self-powered stretching and 3D tactile sensors, *Mater. Today*, 2020, **32**, 84–93.

2 S. S. Rana, M. A. Halim and M. H. Kabir, Design and implementation of a security improvement framework of Zigbee network for intelligent monitoring in IoT platform, *Appl. Sci.*, 2018, **8**, 2305.

3 D. Zhang, Z. Yang, P. Li, M. Pang and Q. Xue, Flexible self-powered high-performance ammonia sensor based on Au-decorated $MoSe_2$ nanoflowers driven by single layer $MoS_2$-flake piezoelectric nanogenerator, *Nano Energy*, 2019, **65**, 103974.

4 D. Wang, D. Zhang, J. Guo, Y. Hu, Y. Yang, T. Sun, H. Zhang and X. Liu, Multifunctional poly(vinyl alcohol)/Ag nanofibers-based triboelectric nanogenerator for self-powered MXene/tungsten oxide nanohybrid $NO_2$ gas sensor, *Nano Energy*, 2021, **89**, 106410.

5 H. Wu, Y. Huang, F. Xu, Y. Duan and Z. Yin, Energy harvesters for wearable and stretchable electronics: from flexibility to stretchability, *Adv. Mater.*, 2016, **28**, 9881–9919.

6 Q. Hua, J. Sun, H. Liu, R. Bao, R. Yu, J. Zhai, C. Pan and Z. L. Wang, Skin-inspired highly stretchable and conformable matrix networks for multifunctional sensing, *Nat. Commun.*, 2018, **9**, 244.

7 C. Zhang, S. Liu, X. Huang, W. Guo, Y. Li and H. Wu, A stretchable dual-mode sensor array for multifunctional robotic electronic skin, *Nano Energy*, 2019, **62**, 164–170.

8 T. Bu, T. Xiao, Z. Yang, G. Liu, X. Fu, J. Nie, T. Guo, Y. Pang, J. Zhao, F. Xi and C. Zhang, Stretchable triboelectric–photonic smart skin for tactile and gesture sensing, *Adv. Mater.*, 2018, **30**, 1800066.

9 M. T. Rahman, S. S. Rana, M. Salauddin, M. A. Zahed, S. Lee, E. S. Yoon and J. Y. Park, Silicone-incorporated nanoporous cobalt oxide and MXene nanocomposite-coated stretchable fabric for wearable triboelectric nanogenerator and self-powered sensing applications, *Nano Energy*, 2022, **100**, 107454.

10 Y. Xie, Q. Ma, B. Yue, X. Chen, Y. Jin, H. Qi, Y. Hu, W. Yu, X. Dong and H. Jiang, Triboelectric nanogenerator based on flexible Janus nanofiber membrane with simultaneous high charge generation and charge capturing abilities, *Chem. Eng. J.*, 2023, **452**, 139393.

11 H. Jiang, H. Lei, Z. Wen, J. Shi, D. Bao, C. Chen, J. Jiang, Q. Guan, X. Sun and S. T. Lee, Charge-trapping-blocking layer for enhanced triboelectric nanogenerators, *Nano Energy*, 2020, **75**, 105011.

12 B. Chai, K. Shi, H. Zou, P. Jiang, Z. Wu and X. Huang, Conductive interlayer modulated ferroelectric nanocomposites for high performance triboelectric nanogenerator, *Nano Energy*, 2022, **91**, 106668.

13 P. Rajagopalan, S. Huang, L. Shi, H. Kuang, H. Jin, S. Dong, W. Shi, X. Wang and J. Luo, Novel insights from the ultra-thin film, strain-modulated dynamic triboelectric characterizations, *Nano Energy*, 2021, **80**, 105560.

14 Z. Li, X. Wang, Y. Hu, L. Li and C. Wang, Triboelectric properties of BaTiO3/polyimide nanocomposite film, *Appl. Surf. Sci.*, 2022, **572**, 151391.

15 N. Cui, L. Gu, Y. Lei, J. Liu, Y. Qin, X. Ma, Y. Hao and Z. L. Wang, Dynamic behavior of the triboelectric charges and structural optimization of the friction layer for a triboelectric nanogenerator, *ACS Nano*, 2016, **10**, 6131–6138.

16 X. Xie, X. Chen, C. Zhao, Y. Liu, X. Sun, C. Zhao and Z. Wen, Intermediate layer for enhanced triboelectric nanogenerator, *Nano Energy*, 2021, **79**, 105439.

17 D. W. Kim, J. H. Lee, I. You, J. K. Kim and U. Jeong, Adding a stretchable deep-trap interlayer for high-performance stretchable triboelectric nanogenerators, *Nano Energy*, 2018, **50**, 192–200.

18 K. Shrestha, S. Sharma, G. B. Pradhan, T. Bhatta, P. Maharjan, S. S. Rana, S. Lee, S. Seonu, Y. Shin and J. Y. Park, A Siloxene/Ecoflex Nanocomposite-Based Triboelectric Nanogenerator with Enhanced Charge Retention by $MoS_2$/LIG for Self-Powered Touchless Sensor Applications, *Adv. Funct. Mater.*, 2022, **32**, 2113005.

19 J. W. Lee, S. Jung, J. Jo, G. H. Han, D. M. Lee, J. Oh, H. J. Hwang, D. Choi, S. W. Kim, J. H. Lee and C. Yang, Sustainable highly charged $C_{60}$-functionalized polyimide in a non-contact mode triboelectric nanogenerator, *Energy Environ. Sci.*, 2021, **14**, 1004–1015.

20 S. S. Rana, M. T. Rahman, S. Sharma, M. Salauddin, S. H. Yoon, C. Park, P. Maharjan, T. Bhatta and J. Y. Park, Cation functionalized nylon composite nanofibrous mat as a highly positive friction layer for robust, high output triboelectric nanogenerators and self-powered sensors, *Nano Energy*, 2021, **88**, 106300.

21 Y. Li, C. Zheng, S. Liu, L. Huang, T. Fang, J. X. Li, F. Xu and F. Li, Smart glove integrated with tunable MWNTs/PDMS fibers made of a one-step extrusion method for finger dexterity, gesture, and temperature recognition, *ACS Appl. Mater. Interfaces*, 2020, **12**, 23764–23773.

22 W. G. Kim, D. W. Kim, I. W. Tcho, J. K. Kim, M. S. Kim and Y. K. Choi, Triboelectric nanogenerator: Structure, mechanism, and applications, *ACS Nano*, 2021, **15**, 258–287.

23 Z. Qin, X. Chen, Y. Yin, G. Ma, Y. Jia, J. Deng and K. Pan, Flexible januselectrospun nanofiber films for wearable

 

triboelectric nanogenerator, *Adv. Mater. Technol.*, 2020, **5**, 1900859.

24 M. Tayyab, J. Wang, J. Wang, M. Maksutoglu, H. Yu, G. Sun, F. Yildiz, M. Eginligil and W. Huang, Enhanced output in polyvinylidene fluoride nanofibers based triboelectric nanogenerator by using printer ink as nano-fillers, *Nano Energy*, 2020, **77**, 105178.

25 H. Jiang, H. Lei, Z. Wen, J. Shi, D. Bao, C. Chen, J. Jiang, Q. Guan, X. Sun and S. T. Lee, Charge-trapping-blocking layer for enhanced triboelectric nanogenerators, *Nano Energy*, 2020, **75**, 105011.

26 D. W. Kim, J. H. Lee, I. You, J. K. Kim and U. Jeong, Adding a stretchable deep-trap interlayer for high-performance stretchable triboelectric nanogenerators, *Nano Energy*, 2018, **50**, 192–200.

27 J. Cui, P. Li, J. Zhou, W. Y. He, X. Huang, J. Yi, J. Fan, Z. Ji, X. Jing, F. Qu and Z. G. Cheng, Transport evidence of asymmetric spin–orbit coupling in few-layer superconducting 1T d-$MoTe_2$, *Nat. Commun.*, 2019, **10**, 2044.

28 S. Hao, J. Zeng, T. Xu, X. Cong, C. Wang, C. Wu, Y. Wang, X. Liu, T. Cao, G. Su and L. Jia, Low-temperature eutectic synthesis of $PtTe_2$ with Weak antilocalization and controlled layer thinning, *Adv. Funct. Mater.*, 2018, **28**, 1803746.

29 S. Lee, J. Jang, S. I. Kim, S. G. Jung, J. Kim, S. Cho, S. W. Kim, J. Y. Rhee, K. S. Park and T. Park, Origin of extremely large magnetoresistance in the candidate type-II Weyl semimetal $MoTe_{2-x}$, *Sci. Rep.*, 2018, **8**, 13937.

30 K. S. Bhat and H. S. Nagaraja, Performance evaluation of molybdenum dichalcogenide ($MoX_2$; X= S, Se, Te) nanostructures for hydrogen evolution reaction, *Int. J. Hydrogen Energy*, 2019, **44**, 17878–17886.

31 X. Yang, J. Han, J. Yu, Y. Chen, H. Zhang, M. Ding, C. Jia, J. Sun, Q. Sun and Z. L. Wang, Versatile triboiontronic transistor via proton conductor, *ACS Nano*, 2020, **14**, 8668–8677.

32 L. Lan, Y. Yao, J. Ping and Y. Ying, Ultrathin transition-metal dichalcogenide nanosheet-based colorimetric sensor for sensitive and label-free detection of DNA, *Sens. Actuators, B*, 2019, **290**, 565–572.

33 G. Gao, J. Yu, X. Yang, Y. Pang, J. Zhao, C. Pan, Q. Sun and Z. L. Wang, Triboiontronic transistor of $MoS_2$, *Adv. Mater.*, 2019, **31**, 1806905.

34 Y. Liu, J. Ping and Y. Ying, Recent progress in 2D-nanomaterial-based triboelectric nanogenerators, *Adv. Funct. Mater.*, 2021, **31**, 2009994.

35 N. R. Pradhan, D. Rhodes, S. Feng, Y. Xin, S. Memaran, B. H. Moon, H. Terrones, M. Terrones and L. Balicas, Field-effect transistors based on few-layered α-$MoTe_2$, *ACS Nano*, 2014, **8**, 5911–5920.

36 A. Bera, M. Kundu, B. Das, S. Kalimuddin, S. Bera, D. S. Roy, S. K. Pradhan, S. Naskar, S. K. De, B. Das and M. Mondal, Emergence of electric field-induced conducting states in single-crystalline $MoTe_2$ nanoflakes and its application in memristive devices, *Appl. Surf. Sci.*, 2023, **610**, 155409.

37 D. H. Keum, S. Cho, J. H. Kim, D. H. Choe, H. J. Sung, M. Kan, H. Kang, J. Y. Hwang, S. W. Kim, H. Yang and K. J. Chang, Bandgap opening in few-layered monoclinic $MoTe_2$, *Nat. Phys.*, 2015, **11**, 482–486.

38 C. Ruppert, B. Aslan and T. F. Heinz, Optical properties and band gap of single-and few-layer $MoTe_2$ crystals, *Nano Lett.*, 2014, **14**, 6231–6236.

39 K. A. Duerloo, Y. Li and E. J. Reed, Structural phase transitions in two-dimensional Mo-and W-dichalcogenide monolayers, *Nat. Commun.*, 2014, **5**, 4214.

40 J. H. Huang, K. Y. Deng, P. S. Liu, C. T. Wu, C. T. Chou, W. H. Chang, Y. J. Lee and T. H. Hou, Large-area 2D layered $MoTe_2$ by physical vapor deposition and solid-phase crystallization in a tellurium-free atmosphere, *Adv. Mater. Interfaces*, 2017, **4**, 1700157.

41 D. Seol, S. Kim, W. S. Jang, Y. Jin, S. Kang, S. Kim, D. Won, C. Lee, Y. M. Kim, J. Lee and H. Yang, Selective patterning of out-of-plane piezoelectricity in $MoTe_2$ via focused ion beam, *Nano Energy*, 2021, **79**, 105451.

42 L. Wang, S. Liu, X. Feng, C. Zhang, L. Zhu, J. Zhai, Y. Qin and Z. L. Wang, Flexoelectronics of centrosymmetric semiconductors, *Nat. Nanotechnol.*, 2020, **15**, 661–667.

43 Y. Chen, Z. Tian, X. Wang, N. Ran, C. Wang, A. Cui, H. Lu, M. Zhang, Z. Xue, Y. Mei and P. K. Chu, 2D Transition Metal Dichalcogenide with Increased Entropy for Piezoelectric Electronics, *Adv. Mater.*, 2022, **34**, 2201630.

44 (*a*) S. Roy, S. Bardhan, K. Pal, S. Ghosh, P. Mandal, S. Das and S. Das, Crystallinity mediated variation in optical and electrical properties of hydrothermally synthesized boehmite (γ-AlOOH) nanoparticles, *J. Alloys Compd.*, 2018, **763**, 749–758; (*b*) N. Das, D. Sarkar, M. M. Saikh, P. Biswas, S. Das, N. A. Hoque and P. P. Ray, Piezoelectric activity assessment of size-dependent naturally acquired mud volcano clay nanoparticles assisted highly pressure sensitive nanogenerator for green mechanical energy harvesting and body motion sensing, *Nano Energy*, 2022, **102**, 107628.

45 D. Sarkar, N. Das, M. M. Saikh, P. Biswas, S. Roy, S. Paul, N. A. Hoque, R. Basu and S. Das, High β-crystallinity comprising nitrogenous carbon dot/PVDF nanocomposite decorated self-powered and flexible piezoelectric nanogenerator for harvesting human movement mediated energy and sensing weights, *Ceram. Int.*, 2023, **49**, 5466–5478.

46 H. W. Park, N. D. Huynh, W. Kim, C. Lee, Y. Nam, S. Lee, K. B. Chung and D. Choi, Electron blocking layer-based interfacial design for highly-enhanced triboelectric nanogenerators, *Nano Energy*, 2018, **50**, 9–15.

47 S. Paria, R. Bera, S. K. Karan, A. Maitra, A. K. Das, S. K. Si, L. Halder, A. Bera and B. B. Khatua, Insight into cigarette wrapper and electroactive polymer based efficient TENG as biomechanical energy harvester for smart electronic applications, *ACS Appl. Energy Mater.*, 2018, **1**, 4963–4975.

48 M. He, W. Du, Y. Feng, S. Li, W. Wang, X. Zhang, A. Yu, L. Wan and J. Zhai, Flexible and stretchable triboelectric nanogenerator fabric for biomechanical energy harvesting and self-powered dual-mode human motion monitoring, *Nano Energy*, 2021, **86**, 106058.

49 X. Shen, W. Han, Y. Jiang, Q. Ding, X. Li, X. Zhao and Z. Li, Punching pores on cellulose fiber paper as the spacer of triboelectric nanogenerator for monitoring human motion, *Energy Rep.*, 2020, **6**, 2851–2860.

50 F. Yi, L. Lin, S. Niu, P. K. Yang, Z. Wang, J. Chen, Y. Zhou, Y. Zi, J. Wang, Q. Liao and Y. Zhang, Stretchable-rubber-based triboelectric nanogenerator and its application as self-powered body motion sensors, *Adv. Funct. Mater.*, 2015, **25**, 3688–3696.

51 D. Hong, Y. M. Choi and J. Jeong, Test bed for contact-mode triboelectric nanogenerator, *Rev. Sci. Instrum.*, 2018, **89**(6), DOI: **10.1063/1.5027764**.

52 L. Zhang, X. Shan, P. Bass, Y. Tong, T. D. Rolin, C. W. Hill, J. C. Brewer, D. S. Tucker and Z. Y. Cheng, Process and microstructure to achieve ultra-high dielectric constant in ceramic-polymer composites, *Sci. Rep.*, 2016, **6**, 35763.

53 S. Das, S. Das and S. Sutradhar, Effect of $Gd^{3+}$ and $Al^{3+}$ on optical and dielectricproperties of ZnO nanoparticle prepared by two step hydrothermal method, *Ceram. Int.*, 2017, **43**, 6932e6941.

54 D. Y. Park, D. J. Joe, D. H. Kim, H. Park, J. H. Han, C. K. Jeong, H. Park, J. G. Park, B. Joung and K. J. Lee, Self-Powered Real-Time Arterial Pulse Monitoring Using Ultrathin Epidermal Piezoelectric Sensors, *Adv. Mater.*, 2017, **29**, 1702308.

55 K. Roy, S. K. Ghosh, A. Sultana, S. Garain, M. Xie, C. R. Bowen, K. Henkel, D. Schmeißer and D. Mandal, A self-powered wearable pressure sensor and pyroelectric breathing sensor based on GO interfaced PVDF nanofibers, *ACS Appl. Nano Mater.*, 2019, **2**, 2013–2025.

56 B. Nicholls; C. S. Ang; C. Efstratiou; Y. Lee and W.-H. Yeo, In Swallowing Detection for Game Control: Using Skin-Like Electronics to Support People with Dysphagia, 2017 IEEE International Conference on Pervasive Computing and Communications Workshops (PerCom Workshops), IEEE, Kona, Hawaii, U.S.A., March 13–17, 2017, DOI: **10.1109/PERCOMW.2017.7917598**.

57 B. C. Tee, C. Wang, R. Allen and Z. Bao, An Electrically and Mechanically Self-Healing Composite with Pressure- and Flexion-Sensitive Properties for Electronic Skin Applications, *Nat. Nanotechnol.*, 2012, **7**, 825–832.

58 S. K. Ghosh, J. Kim, M. P. Kim, S. Na, J. Cho, J. J. Kim and H. Ko, Ferroelectricity-Coupled 2D-MXene-Based Hierarchically Designed High-Performance Stretchable Triboelectric Nanogenerator, *ACS Nano*, 2022, **16**, 11415–11427.

59 T. Jin, Z. Sun, L. Li, Q. Zhang, M. Zhu, Z. Zhang, G. Yuan, T. Chen, Y. Tian, X. Hou and C. Lee, Triboelectric nanogenerator sensors for soft robotics aiming at digital twin applications, *Nat. Commun.*, 2020, **11**, 5381.

 

# Seminars Attended

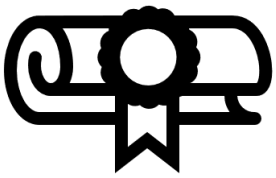

ASSOCIATION OF INDIAN UNIVERSITIES, NEW DELHI

&

JADAVPUR UNIVERSITY, KOLKATA

# ANVESHAN 2019-20

STUDENTS' RESEARCH CONVENTION (EAST ZONE)

## CERTIFICATE OF PARTCIPATION

This is to certify that Mr./Ms./Dr. *DEBMALYA SARKAR*,

Son/Daughter of Shri. *ASOK KUMAR SARKAR*

enrolled in *Ph.D*

Department/Faculty of *Basic science*

of *Jadavpur University* University/Institute participated in East Zone Student Research Convention held at Jadavpur University during February 12-13, 2020.

His/Her proposal/project entitled *Cotton Pappus Based Piezoelectric Nanogenerator and Touch-Sensor*

under the category of *BASIC SCIENCE* and secured *First* position.

Dr. Amarendra Pani
Jt. Director & Head, Research
Association of Indian Universities
New Delhi

Dr. Rajat Ray
Zonal Coordinator, Anveshan, 2019-20
&
Dean of Students, Jadavpur University

Prof. Suranjan Das
Vice-Chancellor
Jadavpur University

**DST-SERB Sponsored**

# One Day Workshop on Material Synthesis & Characterization Techniques

**Organized by: Department of Physics, Jadavpur University, Kolkata-700032**

## *Certificate of Presentation*

*This Certificate is awarded to*

*Mr/ Ms.* Debmalya Sarkar *for successfully presenting a paper entitled* Energy Harvester *in the Workshop organized by Department of Physics, Jadavpur University, Kolkata on 29th February 2020.*

29/02/2020

**Head, Department of Physics, Jadavpur University**

National Seminar on

**New Directions in Physical Sciences 2020 (NDPS 2020)**

Organised by

Department of Physics, Jadavpur University

In association with

Indian Photobiology Society

# Certificate of Participation

This is to certify that Prof./Dr./Mr./Ms. Debmalya Sarkar of Jadavpur University has participated/ presented a poster entitled Piezoelectric Nanogenerator Mediated Energy Harvesting at the seminar on 'New Directions in Physical Sciences 2020' at Jadavpur University, Kolkata on February 25, 2020.

25/2/2020

**Dr. Soumen Mondal**
Convener, NDPS 2020

**Prof. Mitali Mondal**
Convener, NDPS 2020

25/02/2020

**Prof. Sukhen Das**
Head, Dept. of Physics

*33rd AGM of MRSI and 4th Indian Material Conclave*

# IUMRS-ICA 2022

## CERTIFICATE OF PARTICIPATION

This is to certify that Mr./Ms/Dr./Prof **Debmalya Sarkar, Department of Physics, Jadavpur University** has given ~~Oral~~/Poster presentation of his work titled **"Self-powered and light weight electronic skin (e-skin) based on ZnS@PDMS nanocomposite for human body movements detection"** at the IUMRS-ICA 2022 conference held during 19-23 December, 2022, at Indian Institute of Technology, Jodhpur.

We wish you all the best for future endeavors!

**Prof. Mahesh Kumar**
**Chair IUMRS ICA 2022**

**Prof. Shree Prakash Tiwari**
**Co- Chair IUMRS ICA 2022**

REG-121

# 67th DAE Solid State Physics Symposium

*Organised by: Bhabha Atomic Research Centre, Mumbai*
*Sponsored by: Board of Research in Nuclear Sciences (BRNS)*
*Department of Atomic Energy, Government of India*

# CERTIFICATE

## of Participation

**Debmalya Sarkar**

Jadavpur University, Kolkata

has presented a paper and participated in this symposium held at GITAM Deemed to be University, Visakhapatnam, during 20- 24 December 2023

| | | |
|---|---|---|
| ***L. M. Pant*** | ***Mohit Tyagi*** | ***Jitendra Bahadur*** |
| *Convener* | *Scientific secretary* | *Scientific secretary* |
| *DAE SSPS 2023* | *DAE SSPS 2023* | *DAE SSPS 2023* |

*Dated: 24 Dec 2023*